

## Aspects of Gauge Theories Vacua

Présentée le 17 septembre 2020

à la Faculté des sciences de base  
Laboratoire de physique des particules et de cosmologie  
Programme doctoral en physique

pour l'obtention du grade de Docteur ès Sciences

par

**Adrien FLORIO**

Acceptée sur proposition du jury

Prof. J.-Ph. Ansermet, président du jury  
Prof. M. Chapochnikov, directeur de thèse  
Prof. H. Meyer, rapporteur  
Prof. G. Aarts, rapporteur  
Dr J. Waltraud Schober, rapporteuse



*À Papi et Mami*

# Acknowledgements

I am foremost extremely grateful to my supervisor Mikhail Shaposhnikov. In particular, I owe him for the trust he put in me, leaving me complete freedom as to what and with whom to work, while always being there to help and mentor. With freedom come responsibilities and I may not have always taken the wisest decisions as to what to do. But having had the possibility to take these decisions and see their consequences taught me to think a project through from scratch and to start understanding what is worth studying and what is not. This may well be the most valuable thing I learned during my PhD. It has of course also been a great pleasure and a chance to work with him and benefit from his deep understanding of physics. Beyond this, Misha has always been kind and supportive, which greatly contributed to making me live four amazing years of PhD.

I am also very grateful to Olaf Kaczmarek, who, from the start to the end of my PhD accepted to collaborate with me and allowed me to discover lattice QCD. He gave me access to an expertise and resources I would have otherwise not had. He also kindly invited me many times to Bielefeld, making me discover a second work environment and interact with new people. Moreover, he organised and encouraged me to participate to a summer school in Dubna, which was truly a life-changing experience.

I then want to thank Daniel G. Figueroa who, mostly during the second half of my PhD up to now, guided me through research. His friendliness and support have helped me a lot to finish this PhD. Atop of working together during my PhD, he also gave me the opportunity to collaborate on long-term projects, a collaboration which I hope to be, indeed, long and fruitful. I would also like to thank Gert Aarts, Harvey Meyer and Jennifer Waltraud Schober to have accepted to be members of my jury and Jean-Philippe Ansermet to preside over it.

I would not have managed through these four years without amazing colleagues. In random order, thank you to Gabriel Cuomo, Sasha Monin and Andrey Shkerin for their insights on physics and ping-pong, Gil Badel, Kamran Vaziri; Aditya Hebbar and Andrea Manenti for boardgames, Inar Timiryasov; Angelo Esposito for pushing when needed, Andrei Khmelnitsky, Marc Gillioz; Raffaele Tito d'Agnolo for his advices on life and food, David Pirtskhalva; Kin Mimouni for his advises, calm, ski and Corsica, Alfredo Glioti for Corsica and neutrinos, Siyu Chen, Marten Reehorst; Semeon Valgushev for his help and friendship, Jeanne Colbois and Francisco Kim to have bridged gaps between fields, Joao da Silva for his kindness, Anna Tokareva, Georgios Karananas, Denis Karateev, Davide Greco; Wessel Valkenburg for his



## Acknowledgements

---

commitment and impressive coding expertise, Sebastian Zell, Sasha Sobol; Juraj Klaric and Mario Herrero Valea to have beared with me as an office mate, Sander Mooij for the same, his sense of humour and life-mentorship, Francisco Torrenti for his patience and involvement when needed, Sergey Sibiryakov for illuminating physics discussion in the train, Aubry Jaquier for his patience, help and friendship, Misha Ivanov, for his help and hospitality. I also owe Joao Penedones to have shared some of his vast theoretical knowledge, and Riccardo Rattazi, who taught me quantum field theory and whose deep insights on physics, and also sometimes on research and life, I will carry away with me. I would also like to thank the CERN lattice group, in particular, Anthony Francis for his availability and inclusiveness and Mattia Bruno, who helped when it was needed, and to the Bielefeld crew, Lukas Mazur, Giuseppe Gagliardi, Lorenzo Dini, Marc Borell, Felix Ziesche, Jishnu Goswani, Simon Dentiger, Anna-Lena Kruse, David Clark, Aman Steinberg, Marc Klegrewe, who always made me feel at home when there. Of course, this PhD, not to mention life, would not be the same without my friends Cyrille, Dolma, Bianca, Dominika, Lily, Marc, Henry, Henry, Catalina, Ed, Will, Andy, Dasha, Rachel. I would also like to thank Marica and Luigi for their kindness. Last but far from least, I cannot say how much I owe to my parents who have been ever-loving, and to Anna Carla, whom I know to be there for me. Merci.

*Lausanne, August 17, 2020*

A. F.

# Abstract

This thesis is concerned with gauge theories, their complicated vacuum and resulting effects. After an introduction to the subject, it is divided into four parts.

Firstly, we treat the problem of chiral charge dynamics at finite temperature. Quantum field theory predicts a possibility for massless fermions to be transferred into electromagnetic fields with non-zero helicity and vice-versa. This phenomenon has applications ranging from cosmology to heavy-ions physics. We present a numerical investigation from first principles of the resulting complex dynamics and find a qualitative agreement with previous studies based on hydrodynamical approaches but measure rates that differ by up to an order of magnitude. We interpret this effect as contributions coming from small scales not previously taken into account.

Secondly, we present a study of open-boundary conditions in lattice QCD at finite temperature. They were designed to ease up the problem of "topological freezing", which plagues numerical simulations close to the continuum limit. In particular, we determine the length of the "boundary zone" for two different temperatures. We also use the boundary effects to extract screening masses.

Thirdly, we move on to present a compendium of lattice techniques, including some new algorithms, to perform real-time classical simulations of bosonic matter, Abelian and non-Abelian gauge fields in an expanding universe. We also briefly introduce *CosmoLattice*, a numerical software designed to perform such simulations, which are particularly interesting to study the reheating phase of our universe.

Finally, we study yet another technique to probe non-perturbative sectors of field theories. Namely, we show that one can reconstruct the Schwinger pair production rate, which is the rate of production of particles due to the presence of a strong electric field, using only a few terms of the weak magnetic field expansion. This surprising result is obtained by using techniques coming from the field of resurgence and the analysis of asymptotic expansions. We conclude this work by presenting some general outlooks, sharing aspects of all these different yet related topics.



# Résumé

Cette thèse traite des théories de jauge, en particulier de leurs états fondamentaux complexes et des effets qui en résultent. Suite à une introduction, ce travail est divisé en quatre parties. La première se charge d'étudier la dynamique de la charge chirale à températures finies. La théorie des champs quantiques prédit que les fermions de masse nulle aient la possibilité de se transformer en champ électromagnétique d'hélicité non-nulle et vice-versa. Ce phénomène a des applications tant en cosmologie qu'en collisions d'ions lourds. Nous présentons une étude numérique basée sur une théorie fondamentale de la dynamique compliquée associée à cet effet. Nos résultats sont en accord qualitatifs avec les études précédentes basées sur des approches hydrodynamiques bien que nous mesurons des "taux" qui diffèrent de jusqu'à un ordre de grandeur. Nous interprétons ce résultat comme venant de contributions associées à de faibles échelles d'énergies, non prises en compte jusque là.

Dans la seconde, nous présentons une étude sur l'utilisation de conditions aux bords dites "ouvertes" dans le contexte de la chromodynamique sur réseaux à températures finies. Ces conditions ont été introduites pour diminuer le problème de "figeage topologique", qui hante les simulations numériques proches de la limite du continu. En particulier, nous avons déterminé la longueur de la "zone de bord" pour deux températures différentes. Nous avons également utilisé les effets aux bords pour extraire des masses de Debye.

Troisièmement, nous présentons un recueil de techniques, dont certains nouveaux algorithmes, pour faire des simulations sur réseau de la dynamique classique de certains types de matière bosonique, qu'elle soit faite de champs de jauge Abéliens ou non, le tout dans un univers en expansion. Nous introduisons aussi brièvement *CosmoLattice*, un programme dédié à des simulations de ce genre, qui ont un intérêt particulier pour étudier la phase de "réchauffement" de notre univers.

Finalement, nous étudions encore une autre technique qui permet de sonder les secteurs non-perturbatifs d'une théorie des champs. Nous montrons que le taux de création de Schwinger, qui mesure le taux de particules créées par un champ électrique intense, peut être inféré seulement des quelques premiers termes de la série asymptotique pour un faible champ magnétique. Ce résultat surprenant a été obtenu en utilisant des techniques venant du domaine de la "résurgence" et de l'analyse des séries asymptotiques.

Nous concluons ce travail en présentant des directions de recherche mêlant différents aspects de ces projets.



# Foreword

The main focus of this thesis is gauge theories and various associated non-perturbative phenomena. After an introduction, parts II and III are concerned with anomalous processes and gauge topology, while parts IV and V cover particle creation in different contexts. All these effects happen only because of the complicated structure of gauge theories. They are interacting four-dimensional quantum field theories, potentially in presence of fermions, with a built-in redundancy and even a non-trivial internal topology in the non-Abelian case. To disentangle these different layers of complexity and identify the one responsible for a given process can be challenging. As such, we dedicate part I to a substantial general introduction to the topic. In chapter 1, after having justified the use of gauge theories in the first place and introduced Abelian and non-Abelian gauge fields, we describe, in what we think are "minimal settings", the effects and methods we study in later parts of this work. In chapter 2, we use the "quantum rotor", i.e. a quantum particle on a circle, to introduce key concepts related to vacuum degeneracy and the dynamics of vacuum transitions. We also use this model to introduce some tools, namely importance sampling simulations of Euclidean path integrals and the classical-statistical evolution of equations of motion and discuss their limitations. To discuss particle creation and anomalous processes, we move on to field theory in chapter 3. To keep it as simple as possible, we consider the Schwinger model and compute the particle production rate in a constant background electric field. We then discuss the "chiral anomaly", which relates the non-conservation of the fermionic chirality to variations of gauge fields. The advantage of this simple 1+1 dimensional model is that, while keeping the main features of the computations intact, it reduces the technical burden. To conclude the introduction, we move back to gauge theories and explain the spontaneous emergence of a non-trivial vacuum structure in non-Abelian gauge fields and present standard gauge-invariant techniques to discretise them.

Part II contains research material regarding the non-trivial dynamics induced by the chiral anomaly in systems with Abelian gauge fields. It is composed of two chapters. In chapter 5, we present relevant physical situations where this dynamic has an impact, together with the appropriate literature. Chapter 6 contains original work published in reference [1]. It reports classical real-time numerical simulations of an effective model that encodes chiral-anomaly induced effects on gauge fields.

Part III deals with Euclidean path integral simulations of  $SU(3)$  gauge fields and the use of

open-boundary conditions at finite temperature. Typically, numerical simulations in field theory use periodic boundary conditions to minimise effects of the boundaries. In the presence of topological sectors, such boundary conditions lead to poor sampling of the field space when approaching the continuum limit. This problem can be reduced by using open-boundary conditions. In chapter 7, we present some subtleties related to topology on the lattice and open-boundary conditions. Chapter 8 contains results published in reference [2] about the use of such boundary conditions in a finite-temperature set-up.

Part IV examines particle production in the early universe. Its main physical motivation is the study of the end of inflation and the subsequent production of standard model particles.

Chapter 9 presents relevant physics, namely the concept of "slow-roll" inflation and the "preheating" of the universe. Chapter 10 contains most of the material of reference [3], which is a compendium on real-time simulation techniques of reheating. In particular, it contains original evolution algorithms for dynamical gauge-fields. This chapter also includes a brief description of *CosmoLattice*, an open-source, modular, and user-friendly simulation software that was developed with references [3] and which will be made publicly available [4].

Part V is the last part of this thesis which contains original research. While also being concerned with particle production, it is somehow different from the other parts. It is related to the topic of resurgence. As explained in chapter 11, field theories have sometimes been conjectured to have a rich hidden analytic structure, based on the notion of "transseries", which are roughly speaking extensions of asymptotic series to the domain of analytically continuable functions. Chapter 12, published in reference [5], applies some recent ideas formulated in this context to the simple phenomenon of pair-creation in a constant electric field. In particular, it is shown that even if this phenomenon is non-perturbative, it can be reconstructed from a finite number of terms of the corresponding perturbative expansion. Finally, part VI draws conclusions and present general outlooks.

*Notations:* Throughout this work, we will use natural units with  $\hbar = c = 1$ . When working in Lorentzian signature, we will follow the "mostly plus" convention for our metric. Except when mentioned otherwise, we will adopt Einstein's convention; repeated indices are summed over.

# Contents

Acknowledgements	i
Abstract (English/Français)	iii
Foreword	vii
<b>I Introduction</b>	<b>1</b>
<b>1 A first look at gauge theories</b>	<b>3</b>
1.1 Motivation . . . . .	3
1.2 Scalar electrodynamics . . . . .	6
1.3 Non-Abelian gauge theory . . . . .	7
<b>2 A detour to lower dimensions: the quantum rotor</b>	<b>11</b>
2.1 Periodicity and $\theta$ -vacuum . . . . .	11
2.2 Topology-changing processes: classical vs quantum . . . . .	17
2.3 Euclidean path-integral simulations . . . . .	22
2.4 Classical simulations: "sphaleron" rate in a perdioidic potential . . . . .	27
2.5 A word of caution . . . . .	29
<b>3 A detour to lower dimensions: the Schwinger model</b>	<b>33</b>
3.1 Pair production . . . . .	34
3.2 Chiral anomaly . . . . .	39
3.2.1 Path integral measure . . . . .	40
3.2.2 Levels crossing . . . . .	43
<b>4 A second look at gauge theories</b>	<b>49</b>
4.1 Topology and $\theta$ -vacuum . . . . .	49
4.1.1 Semiclassics, instantons and $ n\rangle$ -vacua . . . . .	49
4.1.2 The $\theta$ -Vacuum . . . . .	53
4.2 Discretising gauge theories . . . . .	54
	ix



<b>II</b>	<b>Chiral Charge Dynamics</b>	<b>57</b>
<b>5</b>	<b>Chiral anomaly in practice</b>	<b>59</b>
5.1	Cosmology . . . . .	60
5.2	Chiral magnetic effect . . . . .	63
5.3	Foreword to [1] . . . . .	65
<b>6</b>	<i>Chiral charge dynamics in Abelian gauge theories at finite temperature [1]</i>	<b>67</b>
6.1	Introduction . . . . .	68
6.2	Lattice results . . . . .	72
6.2.1	Chemical potential decay . . . . .	72
6.2.2	Inverse cascade . . . . .	74
6.2.3	Decay in the presence of an external magnetic field . . . . .	76
6.2.4	Chiral magnetic rate . . . . .	79
6.3	Comparison to MHD . . . . .	83
6.3.1	Qualitative behaviour and initial plateaus . . . . .	85
6.3.2	Self-similarity and inverse cascade . . . . .	89
6.3.3	Chiral magnetic rate and MHD . . . . .	91
6.4	Conclusions . . . . .	94
6.5	Lattice set-up . . . . .	96
6.6	Fluctuation-dissipation theorem . . . . .	97
<b>III</b>	<b>Finite Temperature Lattice QCD</b>	<b>101</b>
<b>7</b>	<b>Topology on the lattice</b>	<b>103</b>
7.1	Topology of $SU(3)$ on the Lattice . . . . .	103
7.2	Open-boundary conditions . . . . .	105
7.3	Foreword to [2] . . . . .	108
<b>8</b>	<i>Open-Boundary Conditions in the Deconfined Phase [2]</i>	<b>111</b>
8.1	Introduction . . . . .	111
8.2	Open-boundary conditions and setup . . . . .	112
8.3	Boundary zone . . . . .	115
8.4	Screening masses . . . . .	117
8.4.1	Scalar screening mass . . . . .	118
8.4.2	Pseudo-scalar screening mass . . . . .	121
8.4.3	Discussion . . . . .	123
8.5	Topological susceptibility . . . . .	125
8.6	Conclusion . . . . .	128

<b>IV</b>	<b><i>CosmoLattice</i></b>	<b>131</b>
<b>9</b>	<b>Physical motivations: preheating</b>	<b>133</b>
9.1	Slow-roll inflation and its end . . . . .	133
9.2	Preheating and particle creation . . . . .	137
9.3	Foreword to [3] . . . . .	139
<b>10</b>	<b><i>The art of simulating the early Universe</i></b>	<b>141</b>
10.1	Introduction . . . . .	142
10.1.1	The <i>Numerical Early Universe</i> : a laboratory for non-linear high energy physics . . . . .	142
10.1.2	Purpose of this manuscript. Introducing <i>CosmoLattice</i> . . . . .	146
10.1.3	Conventions and notation . . . . .	150
10.2	Field dynamics in the continuum . . . . .	150
10.2.1	Scalar and Gauge field interactions in flat space-time . . . . .	151
10.2.2	Field dynamics in an expanding background . . . . .	154
10.2.3	Dynamics of the expanding background . . . . .	155
10.3	Field dynamics in a computer: the lattice approach . . . . .	157
10.3.1	Lattice definition and discrete Fourier transform . . . . .	157
10.3.2	Lattice representation of differential operators . . . . .	159
10.3.3	Evolution algorithms . . . . .	165
10.3.4	Higher-order integrators . . . . .	172
10.3.5	Integrator properties . . . . .	174
10.4	Lattice formulation of interacting scalar fields . . . . .	176
10.4.1	Continuum formulation and natural variables . . . . .	176
10.4.2	Lattice formulation of interacting scalar fields: $\mathcal{O}(dt^2)$ accuracy methods . . . . .	179
10.4.3	$\mathcal{O}(dt^n)$ Lattice formulation of interacting scalar fields . . . . .	184
10.4.4	Observables . . . . .	186
10.5	Lattice formulation of gauge fields, I: $U(1)$ interactions . . . . .	186
10.5.1	Continuum formulation and natural variables . . . . .	187
10.5.2	Non-compact Lattice formulation of scalar-gauge dynamics . . . . .	188
10.5.3	Compact Lattice formulation of scalar-gauge dynamics . . . . .	191
10.5.4	Observables . . . . .	195
10.6	Lattice formulation of gauge fields, II: $SU(N)$ interactions . . . . .	196
10.6.1	Continuum formulation and natural variables . . . . .	196
10.6.2	Lattice formulation of scalar-gauge dynamics . . . . .	197
10.6.3	Observables . . . . .	201
10.7	Initial conditions . . . . .	202
10.7.1	Stochastic spectrum of scalar fluctuations . . . . .	202
10.7.2	Charged scalars and gauge fields . . . . .	204
10.8	A working example: the $SU(2) \times U(1)$ gauge invariant inflaton . . . . .	208
10.8.1	Model details . . . . .	208
10.8.2	Lattice simulations: $U(1)$ gauge interactions . . . . .	214

## Contents

---

10.8.3 Lattice simulations: $SU(2) \times U(1)$ gauge interactions . . . . .	222
10.9 Summary and outlook . . . . .	226
10.10Cristoffel symbols . . . . .	230
10.11Friedmann's equations . . . . .	231
10.12FLRW with Cadabra2 . . . . .	232
<b>V Resurgence at Finite Order</b>	<b>237</b>
<b>11 A snapshot of resurgence</b>	<b>239</b>
11.1 A tale about transseries, Borel summation and others . . . . .	239
11.2 Foreword to [5] . . . . .	241
<b>12 <i>Schwinger pair production from Padé-Borel reconstruction</i> [5]</b>	<b>243</b>
12.1 Introduction . . . . .	243
12.2 Schwinger effect, generalities . . . . .	244
12.3 Strong-field regime from weak-field expansion . . . . .	246
12.4 Schwinger effect reconstructed . . . . .	248
12.5 Conclusion . . . . .	251
<b>VI Conclusion</b>	<b>253</b>
<b>Bibliography</b>	<b>259</b>
<b>Curriculum Vitae</b>	<b>281</b>

# Introduction **Part I**



# 1 A first look at gauge theories

Gauge theories are central to our current understanding of Nature. They are constructed by promoting invariance of the theory under specific reparametrisations of the fields to a building principle. In this respect, gauge theories are often said to be "gauge-invariant" or sometimes "gauge redundant", as this reparametrisation invariance is not a physical symmetry per se. In this section, we will present and recall the basic properties of Abelian and non-Abelian gauge theories.

## 1.1 Motivation

The appearance of gauge redundancy in electrodynamics can be traced to the requirement of Lorentz invariance. We will here briefly recall this argument, following references [6, 7].

We start with an experimental fact: at least at scales we can presently access, the principles of physics are invariant under Lorentz transformations. As explained at length in [6], this fact, once combined with the principles of quantum mechanics and some relatively mild assumptions about locality, leads naturally to the use of quantum fields which transforms under representations of the Lorentz group as building blocks of our theories. A second experimental fact is that electromagnetism can accurately be described by the theory of a massless vector of spin one. It makes us want to construct a massless quantum field of spin one, i.e. a field which transforms as

$$U(\Lambda) v_\mu(x) U^{-1}(\Lambda) = \Lambda_\mu^\nu v_\nu(x) \quad (1.1)$$

under the action of the Lorentz group. Unfortunately, because of the internal structure of the Lorentz group and as shown explicitly in reference [6], this cannot be done consistently. Instead, the best that can be done is to construct a field which transforms as

$$U(\Lambda) A_\mu(x) U^{-1}(\Lambda) = \Lambda_\mu^\nu A_\nu(x) + \partial_\mu \Omega(\Lambda, x) , \quad (1.2)$$

## Chapter 1. A first look at gauge theories

---

with  $\Omega(\Lambda, x)$  some known function.

Explicit Lorentz symmetry can be maintained by constructing a theory invariant under the change

$$A_\mu(x) \rightarrow A_\mu(x) + \partial_\mu \alpha(x) \quad (1.3)$$

for an arbitrary function  $\alpha$ . Solely out of  $A$ 's, we can only construct the following combination

$$F_{\mu\nu} = \partial_\mu A_\nu - \partial_\nu A_\mu, \quad (1.4)$$

which we will refer to as the field-strength tensor. The lowest order in derivative, non-trivial action which can be then built out of  $F_{\mu\nu}$  is

$$S_{F_{\mu\nu}} = \int d^4x \left( -\frac{1}{4} F_{\mu\nu} F^{\mu\nu} \right) \quad (1.5)$$

where the factor  $\frac{1}{4}$  is a canonical normalisation. This is of course nothing else than the action of free electromagnetism. The associated equations of motion

$$\partial_\mu F^{\mu\nu} = 0 \quad (1.6)$$

are half of Maxwell's equations, the other half being associated to Bianchi's identity

$$\partial_\mu \tilde{F}^{\mu\nu} = 0, \quad (1.7)$$

where we defined  $\tilde{F}_{\mu\nu} = \frac{1}{2} \epsilon_{\mu\nu\rho\sigma} F^{\rho\sigma}$ , the dual of  $F_{\mu\nu}$ .

An interesting question is to see what happens when we try to couple electromagnetism to matter. For the sake of clarity, let us consider the case of scalar fields. We need to find a construction that, despite the non-trivial transformation of the gauge fields under Lorentz (1.2), maintains explicit Lorentz invariance. A trivial way to achieve this is to use again only the field strength tensor. The lowest order in derivative interaction we can write is of the type

$$F^{\mu\nu} F_{\mu\nu} \phi, \quad (1.8)$$

with  $\phi$  some scalar field. It is a perfectly valid coupling but is, however, an operator of dimension five mediating short-range interactions. In particular, it does not lead to the expected Coulomb-type potential characteristic of electromagnetism. Fortunately, interactions of the type (1.8) are not the most general ones we can write down. In particular, the action

$$S_{int} = \int d^4x G[\Phi, \partial_\nu \Phi, A_\nu, F_{\nu\rho}] \quad (1.9)$$

can be invariant under (1.2) if  $G$  has the correct equations of motion. A simple example is

$$G = A_\mu j^\mu, \quad (1.10)$$

with  $j^\mu$  a conserved current  $\partial_\mu j^\mu = 0$ .

To couple dynamical matter, let us look at what is the appropriate transformation of  $G$  under an infinitesimal Lorentz transformation  $\epsilon(x)$ . Then, action (1.9) transforms as

$$S_{int}[A_\alpha + \partial_\alpha \epsilon] - S[A_\alpha] = \int d^4x \frac{\delta G}{\delta A_\alpha} \partial_\alpha \epsilon \quad (1.11)$$

$$= - \int d^4x \partial_\alpha \left( \frac{\delta G}{\delta A_\alpha} \right) \epsilon \quad (1.12)$$

which is equal to zero if

$$\partial_\alpha \left( \frac{\delta G}{\delta A_\alpha} \right) = 0. \quad (1.13)$$

A first trivial case corresponds to interactions only with  $F_{\mu\nu}$  like in (1.8). Then,  $\frac{\delta G}{\delta A_\alpha} = 0$ .

A key realisation to build more general interactions is that the relation (1.13) also occurs as the conservation law associated with the following joint *local* symmetry

$$A_\mu(x) \rightarrow A_\mu(x) + \partial_\mu \alpha(x) = A_\mu(x) + \partial_\mu \epsilon(x) \quad (1.14)$$

$$\Phi^a \rightarrow e^{i\alpha(x)T^a} \Phi^a \approx \Phi^a + i\epsilon(x)T^a \Phi^a \equiv \Phi^a + \delta \Phi^a, \quad (1.15)$$

with  $\Phi^a$  some matter content which transforms as specified,  $T^a$  is a charge associated to  $\Phi^a$ , no sum intended and we also wrote the corresponding infinitesimal transformations by  $\epsilon(x)$ . Under this joint transformation, action (1.9) transforms as

$$S_{int}[\Phi^a + \delta \Phi^a, \partial \Phi^a + \delta \partial \Phi^a, A_\alpha + \partial_\alpha \epsilon] = \int d^4x \left[ \frac{\delta G}{\delta \Phi^a} \delta \Phi^a + \frac{\delta G}{\delta \partial_\mu \Phi^a} \partial_\mu \delta \Phi^a + \frac{\delta G}{\delta A_\alpha} \partial_\alpha \epsilon \right] \quad (1.16)$$

$$= \int d^4x \left[ \frac{\delta G}{\delta \Phi^a} i\epsilon T^a \Phi^a + \frac{\delta G}{\delta \partial_\mu \Phi^a} \partial_\mu (i\epsilon T^a \Phi^a) + \frac{\delta G}{\delta A_\mu} \partial_\mu \epsilon \right] \quad (1.17)$$

$$= \int d^4x \left[ \frac{\delta G}{\delta \Phi^a} i\epsilon T^a \Phi^a - \partial_\mu \frac{\delta G}{\delta \partial_\mu \Phi^a} (i\epsilon T^a \Phi^a) - \partial_\mu \frac{\delta G}{\delta A_\mu} \epsilon \right] \quad (1.18)$$

$$= \int d^4x \left[ -\partial_\mu \frac{\delta G}{\delta A_\mu} \epsilon \right] = 0 \quad (1.19)$$

where we assumed that  $G$  depends only on first derivatives of  $\Phi$  and used equations of motion to cancel the two terms.

We can take the joint local symmetry (1.14) and (1.15) as a building tool; any matter action invariant under these transformations can be coupled to (1.8) in a Lorentz invariant way. Transformations (1.14) and (1.15) are referred to as gauge transformations. As we will see in the next section, it is often useful to take invariance under gauge transformations as a starting point. In this way, matter content which enjoys some global symmetries can be associated with some gauge fields by "gauging" these global symmetries, i.e. making them local and constructing the relevant invariant actions.



## 1.2 Scalar electrodynamics

In this section, we want to present the simplest theory of electromagnetism interacting with a matter field, namely scalar electrodynamics. Our task is to couple a free complex scalar field

$$S_\phi = \int d^4x (-\partial^\mu \phi^* \partial_\mu \phi - m^2 \phi^* \phi) , \quad (1.20)$$

to the action (1.5). This action is invariant under the transformation  $\phi \rightarrow e^{i\alpha} \phi$  but is not under  $\phi \rightarrow e^{i\alpha(x)} \phi$ . It can be made invariant by promoting the standard derivatives to gauge covariant derivatives

$$D_\mu \phi = \partial_\mu \phi - i g_A A_\mu \phi . \quad (1.21)$$

This covariant derivative then transforms as  $D_\mu \phi \rightarrow e^{i\alpha(x)} D_\mu \phi$  under

$$A_\mu \rightarrow A_\mu - \frac{i}{g_A} \partial_\mu \alpha(x) \quad (1.22)$$

$$\phi \rightarrow e^{i\alpha(x)} \phi \quad (1.23)$$

and the action

$$S = \int d^4x (- (D^\mu \phi)^* D_\mu \phi - m^2 \phi^* \phi) \quad (1.24)$$

is invariant under the same transformations. The factor  $g_A$  acts as a coupling constant and the factor of  $i$  is conventional. Together with the kinetic term for the gauge fields, it makes the action of scalar electrodynamics

$$S_{sem} = \int d^4x \left( -\frac{1}{4} F_{\mu\nu} F^{\mu\nu} - (D_\mu \phi)^* D^\mu \phi - m^2 \phi^* \phi \right) . \quad (1.25)$$

The associated conserved current (1.19) is

$$j_{U(1)}^\mu = g_A \Im \phi (D^\mu \phi)^* . \quad (1.26)$$

The equations of motion which follow from taking the variation of the action are

$$\partial_\nu F^{\nu\mu} = j_{U(1)}^\mu \quad (1.27)$$

$$D_\mu D^\mu \phi = m^2 \phi . \quad (1.28)$$

Of course, they reduce to the free electromagnetic (1.6) when we decouple the matter field. Note that we still have Bianchi's identities (1.7) as they are purely geometric; in the sense that they are an intrinsic property of  $F_{\mu\nu}$ .

Another fact we want to mention is that the field-strength tensor  $F_{\mu\nu}$  can be expressed solely in terms of covariant objects as a commutator of covariant derivatives

$$[D_\mu, D_\nu] \phi = i g_A F_{\mu\nu} \phi . \quad (1.29)$$

It will also be of interest to have the expressions for the energy-momentum tensor. Generically, for an action  $S = \int d^4x \sqrt{-g} L$  given in term of some Lagrangian density  $L$  in some metric  $g_{\mu\nu}$  with determinant  $g$ , the corresponding energy-momentum tensor is, see [8] for more details

$$T_{\mu\nu} = -2 \frac{\partial L}{\partial g^{\mu\nu}} + g_{\mu\nu} L . \quad (1.30)$$

In the case of action (1.25) in Minkowski space-time, we split it into a gauge field contribution  $T_{\mu\nu}^{em}$ , which is the same as for free electrodynamics, and a scalar contribution  $T_{\mu\nu}^s$ . We get

$$T_{\mu\nu}^{sem} = T_{\mu\nu}^{em} + T_{\mu\nu}^s \quad (1.31)$$

$$T_{\mu\nu}^{em} = F_{\mu\alpha} F_{\nu\beta} \eta^{\alpha\beta} - \eta_{\mu\nu} \frac{1}{4} F_{\alpha\beta} F^{\alpha\beta} \quad (1.32)$$

$$T_{\mu\nu}^s = 2(D_\mu \varphi)^* D_\nu \varphi - \eta_{\mu\nu} (D_\alpha \varphi)^* D^\alpha \varphi - \eta_{\mu\nu} m^2 \varphi^* \varphi . \quad (1.33)$$

As we will see later on in this work, the classical dynamics can be a valuable interest in many situations.

Before moving on to the non-Abelian theory, we want to point out that, at least at first sight, action (1.5) is not the only Lorentz scalar of dimension four which can be constructed out of  $F_{\mu\nu}$ . One can also write down

$$S_{\tilde{F}_{\mu\nu}} = \int d^4x \left( -\frac{\theta_{em}}{4} F_{\mu\nu} \tilde{F}^{\mu\nu} \right) , \quad (1.34)$$

with  $\tilde{F}_{\mu\nu} = \frac{1}{2} \epsilon_{\mu\nu\rho\sigma} F^{\rho\sigma}$  the dual field-strength tensor. In an Abelian theory and on its own, such a term has no consequences on the dynamics<sup>1</sup> as it can be rewritten as the following total derivative

$$F_{\mu\nu} \tilde{F}^{\mu\nu} = \partial_\mu K_A^\mu \quad (1.35)$$

$$K_A^\mu = \epsilon^{\mu\nu\rho\sigma} A_\nu \partial_\rho A_\sigma . \quad (1.36)$$

We will nonetheless see in part that II coupling this operator to some other fields describes rich physics. We will also see in chapter 4.1 these kinds of operators leads to some very interesting phenomena in non-Abelian theories.

### 1.3 Non-Abelian gauge theory

Thinking in terms of gauge invariance, it is useful to run the argument presented at the end of section 1.1 in reverse. Instead of starting from a Lorentz invariant gauge field and try to couple it to matter, leading to the "gauging" of the global symmetry, we can start from a

---

<sup>1</sup>Strictly speaking, this statement is not correct. Such a coupling is physical in the presence of background electromagnetic fields; it used for example to describe topological insulators. We refer the interested reader to reference [9] for a more thorough discussion.

## Chapter 1. A first look at gauge theories

---

globally symmetric matter action and demand its invariance under local transformations. This inevitably leads to the need of a gauge field which transforms appropriately under these local transformations. In this spirit, non-Abelian gauge theories arise naturally when gauging matter theories which have a global non-Abelian symmetry<sup>2</sup>.

For the sake of simplicity, let us consider a matter field which transforms under the fundamental representation of  $SU(N)$

$$\Phi = \begin{pmatrix} \Phi^1 \\ \vdots \\ \Phi^N \end{pmatrix} \in \mathbf{C}^N, \quad \Phi \rightarrow \Omega \Phi, \quad \Omega \in SU(N). \quad (1.37)$$

The following simple generalisation of the free action (1.20) is invariant under this transformation

$$S_\Phi = \int d^4x \left( -\partial^\mu \Phi^\dagger \partial_\mu \Phi - m^2 \Phi^\dagger \Phi \right). \quad (1.38)$$

For the same reasons, i.e. still because of the derivative, this is not invariant under a local  $SU(N)$  transformation. Indeed, we have

$$\partial_\mu \Phi \rightarrow \Omega \partial_\mu \Phi + (\partial_\mu \Omega) \Phi. \quad (1.39)$$

In analogy to (1.21), this can be fixed by introducing a vector potential  $A_\mu$  and a covariant derivative

$$D_\mu \Phi = \partial_\mu \Phi - i g_B A_\mu \Phi, \quad (1.40)$$

provided that  $A_\mu$  transforms as

$$A_\mu \rightarrow \Omega A_\mu \Omega^{-1} - i \frac{1}{g_B} \partial_\mu (\Omega) \Omega^{-1}. \quad (1.41)$$

Then, the action

$$S = \int d^4x \left( - (D^\mu \Phi)^\dagger D_\mu \Phi - m^2 \Phi^\dagger \Phi \right) \quad (1.42)$$

is invariant under local  $SU(N)$  transformations.

To build a covariant object out of  $A_\mu$ , let us compute, as in (1.29), the commutator of two covariant derivatives. In this case, we obtain

$$[D_\mu, D_\nu] \Phi = (\partial_\mu A_\nu - \partial_\nu A_\mu + [A_\mu, A_\nu]) \Phi \quad (1.43)$$

$$\equiv i g_B G_{\mu\nu} \Phi, \quad (1.44)$$

where we defined a non-Abelian field-strength tensor  $G_{\mu\nu}$ . We have that

---

<sup>2</sup>A more convincing argument, which is beyond the scope of this section, is given in [10], where it is shown that the requirement of tree-level unitarity, which is tied to renormalisability, implies gauge redundancy.

$[D_\mu, D_\nu]\Phi \rightarrow \Omega[D_\mu, D_\nu]\Phi$  and also  $\Phi \rightarrow \Omega\Phi$ , we obtain that  $G_{\mu\nu}$  transforms as

$$G_{\mu\nu} \rightarrow \Omega G_{\mu\nu} \Omega^{-1} . \quad (1.45)$$

So far, we have not specified to which set  $A_\mu$  and  $G_{\mu\nu}$  belong. We recognise in (1.45) the adjoint action of the group  $SU(N)$  and thus  $G_{\mu\nu}$  is a natural member of the Lie algebra  $\mathfrak{su}(N)$ . As such, it can be expanded onto a basis of generators of  $\mathfrak{su}(N)$

$$G_{\mu\nu} = G_{\mu\nu}^a T^a . \quad (1.46)$$

We follow the convention of taking  $T^a$  to be hermitian generators of  $\mathfrak{su}(N)$ , satisfying the following identities

$$[T^a, T^b] = i f_{abc} T^c, \text{Tr}(T^a, T^b) = \frac{1}{2} \delta^{ab} \quad (1.47)$$

$$\text{Tr}(T^a) = 0 \quad (1.48)$$

with the second line being the defining property of  $\mathfrak{su}(N)$ .

It is then consistent to take  $A_\mu$  to also be in the Lie algebra, as this is consistent with the gauge transformation (1.41). Indeed, the first term is nothing more than the action of the adjoint representation. Then, the term  $(\partial_\mu \Omega) \Omega^{-1}$  is also part of the algebra, as long as  $\Omega \in SU(N)$ . This is easily shown by using the exponential map from the algebra to the group and writing  $\Omega = \exp(i\omega_a T^a)$ .

As in the Abelian case, the lowest in derivatives scalar and gauge-invariant operators we can build from the gauge fields are

$$S_{G_{\mu\nu}} = - \int d^4x \left( \frac{1}{2} \text{Tr}(G_{\mu\nu} G^{\mu\nu}) + \frac{\theta}{2} \text{Tr}(G_{\mu\nu} \tilde{G}^{\mu\nu}) \right) . \quad (1.49)$$

The second term, referred to as the  $\theta$ -term, can again be rewritten as a total derivative, see for example [11]

$$\text{Tr}(G_{\mu\nu} \tilde{G}^{\mu\nu}) = \partial_\mu K_A^\mu \quad (1.50)$$

$$K^\mu = \epsilon^{\mu\nu\rho\sigma} \text{Tr} \left( A_\nu F_{\rho\sigma} - \frac{2}{3} A_\mu A_\nu A_\rho \right) . \quad (1.51)$$

As such, it also does not affect the classical equations of motion. Due to the complicated internal structure of the non-Abelian groups, it does, however, impact the quantum physics; we defer this discussion to chapters 4.1 and drop the  $\theta$ -term for the remainder of this section.

This said we can write down the relevant action with matter and  $SU(N)$  gauge fields

$$S_{NA} = \int d^4x \left( -\frac{1}{2} \text{Tr}(G_{\mu\nu} G^{\mu\nu}) - (D^\mu \Phi)^\dagger D_\mu \Phi - m^2 \Phi^\dagger \Phi \right) . \quad (1.52)$$

## Chapter 1. A first look at gauge theories

---

The classical equations of motion are a simple generalisation of the ones in the  $U(1)$  case. For the matter field,  $U(1)$  covariant derivatives become a  $SU(N)$  covariant derivative. The only difference appears in the gauge sector, where due to the non-Abelian nature of the fields, the normal derivative acting on the field strength is also replaced by a gauge covariant derivative, defined as

$$D_\mu G_{\nu\rho} = \partial_\mu G_{\nu\rho} + [G_\mu, G_{\nu\rho}] . \quad (1.53)$$

In this light, the equations of motion are

$$D_\nu G^{\nu\mu} = j_{SU(N)}^\mu \quad (1.54)$$

$$D_\mu D^\mu \phi = m^2 \Phi , \quad (1.55)$$

with  $j_{SU(N)}^\mu = g_B \mathfrak{Im} \Phi (D^\mu \Phi)^\dagger$ . The energy-momentum is also a straightforward generalisation of the Abelian case and is obtained by summing over the group components

$$T_{\mu\nu}^{NA} = T_{\mu\nu}^{SU(N)} + T_{\mu\nu}^s \quad (1.56)$$

$$T_{\mu\nu}^{SU(N)} = G_{\mu\alpha}^a G_{\nu\beta}^a \eta^{\alpha\beta} - \eta_{\mu\nu} \frac{1}{4} G_{\alpha\beta}^a G^{\alpha\beta a} \quad (1.57)$$

$$T_{\mu\nu}^s = 2(D_\mu \Phi)^\dagger D_\nu \Phi - \eta_{\mu\nu} (D_\alpha \Phi)^\dagger D^\alpha \Phi - \eta_{\mu\nu} m^2 \phi^\dagger \phi . \quad (1.58)$$

To conclude, let us mention that it is sometimes useful to reabsorb the coupling constant  $g_B$  (or  $g_A$  in the Abelian case) inside the gauge fields. In this case, the action of the gauge part become  $\int d^4x - \frac{1}{2g_B^2} \text{Tr}(G_{\mu\nu} G^{\mu\nu})$ . We will use sometimes this convention, depending on the context.

Before moving on and discuss some more intricate quantum effects, we will do two detours to lower dimensions to introduce some concepts in simpler set-ups, where analytical computations can be carried through.

## 2 A detour to lower dimensions: the quantum rotor

Arguably the simplest class of systems which display a non-trivial vacuum structure is the quantum mechanics of a periodic variable of period  $R$ . In this section, we will present its physics at length, as some subtleties of field theories already arise in this example, where everything can be computed explicitly. It is also a natural playground to illustrate the principles beyond the somewhat more involved numerical simulations which will be discussed later on in this work. References will be cited in due time, but let us mention that the main inspirations for this section are references [12–14].

### 2.1 Periodicity and $\theta$ -vacuum

Let us consider a free periodic particle

$$H_{per.} = \frac{\hat{p}^2}{2m} . \quad (2.1)$$

We impose periodicity on the wave-function amplitudes

$$|\psi(\phi + R)|^2 = |\psi(\phi)|^2 . \quad (2.2)$$

This can be realised if the eigenvectors  $|\phi\rangle$  satisfy

$$|\phi + R\rangle = e^{i\theta} |\phi\rangle , \quad (2.3)$$

with  $\theta \in [0, 2\pi)$  some phase. This condition is a restriction on the spectrum of the Hamiltonian

(2.1). This is seen as follow

$$|\phi + R\rangle = e^{iR\hat{p}} |\phi\rangle \quad (2.4)$$

$$= \sum_{p \in \text{Sp}(H_{per.})} e^{iRp} |p\rangle \langle p|\phi\rangle \quad (2.5)$$

$$\stackrel{!}{=} e^{i\theta} \sum_{p \in \text{Sp}(H_{per.})} |p\rangle \langle p|\phi\rangle \quad (2.6)$$

$$\Rightarrow e^{iRp} \stackrel{!}{=} e^{i\theta}, \quad \forall p \in \text{Sp}(H_{per.}) \quad (2.7)$$

with  $\sum_{p \in \text{Sp}(H_{per.})}$  a sum/integral over all eigenvalues in the spectrum  $\text{Sp}(H_{per.})$  of  $H_{per.}$  and we used in equation (2.4) that translations are generated by  $\hat{p}$ . We see that in order to satisfy relation (2.7), the eigenvalues need to be of the form

$$p \equiv p_l = \frac{2\pi l}{R} + \frac{\theta}{R}, \quad l \in \mathbb{N}. \quad (2.8)$$

and the spectrum of  $H_{per.}$  is discrete.

As we will soon see, this phase affects observables. Before moving on to this discussion, let us rephrase its origin in a fashion that will directly translate to more complicated theories which display similar behaviours. As already realised, the periodicity imposed by (2.3) is an invariance under translations by  $R$ , which are generated by the unitary operator  $\hat{U} = e^{iR\hat{p}}$ . It means that  $\hat{U}$  commutes with  $H_{per.}$  and as such, we can find a basis of our Hilbert space in which  $\hat{U}$  and  $H_{per.}$  are simultaneously diagonal. The operator  $\hat{U}$  has a continuous spectrum  $e^{i\lambda}$  with  $\lambda \in [0, 2\pi)$ . In other words, we can pick up a basis  $|p, \lambda\rangle$  such that  $H|p, \lambda\rangle = E|p, \lambda\rangle$  and  $\hat{U}|p, \lambda\rangle = e^{i\lambda}|p, \lambda\rangle$ . Condition (2.3) means that we restrict the Hilbert space to states with a given eigenvalue  $\theta$ .

A first interesting quantity we will look at is the free energy of the system. At zero temperature, it is nothing else than the ground state energy. Its high-temperature limit will also be of interest later on in this work. We thus want to compute

$$F(T, \theta) = -T \ln \mathcal{Z} \quad (2.9)$$

with  $T$  the temperature,  $\mathcal{Z} = \text{Tr} \hat{\rho}_0$  the partition function and  $\hat{\rho}_0 = e^{-\frac{H_{per.}}{T}}$  the equilibrium density matrix. In our simple case, the partition function can be written in these different

forms

$$\mathcal{Z}_{per.} = \sum_{l \in \mathbb{N}} \langle p_l | e^{-\frac{H_{per.}}{T}} | p_l \rangle \quad (2.10)$$

$$= \sum_{l \in \mathbb{N}} e^{-\frac{1}{2mT} \left( \frac{2\pi l}{R} + \frac{\theta}{R} \right)^2} = e^{-\frac{\theta^2}{2R^2 mT}} \sum_{l \in \mathbb{N}} e^{-\frac{2\pi}{R^2 mT} (\pi l^2 + l\theta)} \quad (2.11)$$

$$= e^{-\frac{\theta^2}{2R^2 mT}} \theta_3 \left( \frac{i\pi\theta}{R^2 mT}, \frac{2\pi i}{R^2 mT} \right) \quad (2.12)$$

$$= R \sqrt{\frac{mT}{2\pi}} \theta_3 \left( -\frac{\theta}{2}, \frac{iR^2 mT}{2\pi} \right) \quad (2.13)$$

$$= R \sqrt{\frac{mT}{2\pi}} \sum_{n \in \mathbb{N}} e^{-\left( \frac{mTR^2 n^2}{2} + i\theta n \right)} \quad (2.14)$$

with  $\theta_3(z|\tau)$  the third Jacobi  $\theta$ -function, see [15],

$$\theta_3(z|\tau) = \sum_{l \in \mathbb{N}} e^{i\pi\tau l^2} e^{2ilz} \quad (2.15)$$

which, by using Poisson summation formula on the defining sum, can be shown to satisfy the following functional relation

$$\theta_3(z|\tau) = (-i\tau)^{-1/2} e^{-i\frac{z^2}{\pi\tau}} \theta_3 \left( -\frac{z}{\tau}, -\frac{1}{\tau} \right). \quad (2.16)$$

Equations (2.11) and (2.14) correspond to respectively to a low and a high-temperature expansion of the partition function. We show the behaviour of the free energy as a function of  $\theta$  for different temperatures in figure 2.1. As can be understood from equation (2.11), the free energy develops cusps at odd-integer multiple of  $\pi$  in the limit  $T \rightarrow 0$ . There, only one of the exponential dominates and we have

$$\lim_{T \rightarrow 0} F(T, \theta) = \frac{1}{2mR^2} \min_{l \in \mathbb{N}} (\theta + 2\pi l)^2. \quad (2.17)$$

The other limit  $T \rightarrow \infty$  is understood from the sum (2.14). The leading contribution is a constant, coming from the terms with  $n = 0$ , and the leading  $\theta$ -dependence comes from the exponents with  $n = \pm 1$

$$F(T, \theta) \sim -T \left[ \log \left( R \sqrt{\frac{mT}{2\pi}} \right) + 2e^{-\frac{R^2 mT}{2}} \cos(\theta) \right] \quad (2.18)$$

Both of these limits are of special interests as they are the same as in more complicated models. They also both displays two key features of the  $\theta$ -parameter; the free energy depends on  $\theta$  and its minimum is at  $\theta = 0$ .

Equation (2.14) has a natural interpretation in terms of path integral. We recall that, given



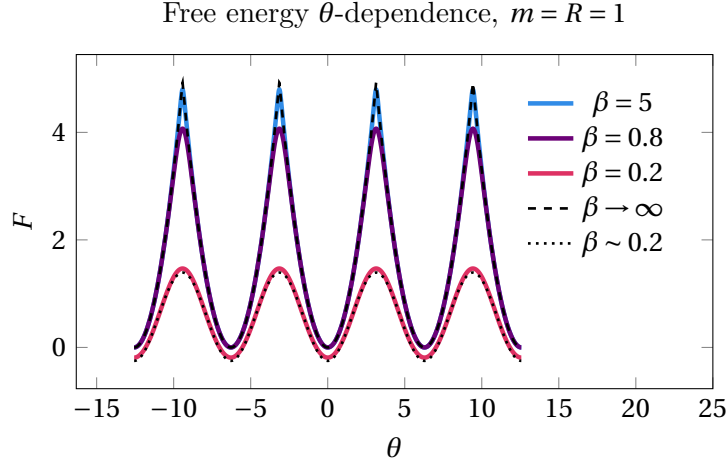


Figure 2.1 –  $\theta$ -dependence of the free energy for the quantum rotor, for different temperatures. The asymptotic expressions (2.17) and (2.18) are also depicted. The low-temperature expression develops characteristic cusps at multiple of  $\pi$  while the high-temperature expression is well approximated by an exponentially small cosine plus a constant.

the classical action which corresponding to (2.1)

$$S_{t_i, t_f} = \int_{t_i}^{t_f} dt \frac{1}{2} m \dot{\phi}^2, \quad (2.19)$$

transition amplitudes can be computed through the following functional integration

$$\langle \phi_i, t_i | \phi_f, t_f \rangle = \int \mathcal{D}\phi \exp(i S_{t_i, t_f}[\phi]), \quad (2.20)$$

where the measure  $\mathcal{D}\phi$  stands for all possible trajectories interpolating between  $x_i$  and  $x_f$ . Another salient feature of the path integral is that it can also be used to compute statistical ensemble averages; we refer the reader to [16] for a pedagogical introduction to the path integral formalism in quantum mechanics. It is achieved by an analytic continuation to Euclidean space  $t \rightarrow -i\tau$ . Then, any thermal average

$$\langle \mathcal{T}_{\mathcal{E}} \{ \hat{O}_1 \hat{O}_2 \dots \} \rangle_T = \text{Tr}(\hat{\rho} \mathcal{T}_{\mathcal{E}} \{ \hat{O}_1 \hat{O}_2 \dots \}) \quad (2.21)$$

can also be computed through a functional integral

$$\langle \mathcal{T}_{\mathcal{E}} \{ \hat{O}_1 \hat{O}_2 \dots \} \rangle_T = \int_{\phi(0)=\phi(\beta)} \mathcal{D}\phi O_1 O_2 \dots e^{-S_{0, \beta}^E}, \quad (2.22)$$

with  $\beta = \frac{1}{T}$  the inverse temperature and  $S^E$  the resulting Euclidean action. The operator  $\mathcal{T}_{\mathcal{E}}$  stands for Euclidean time ordering. In the presence of a potential, we have  $S_E = \int d\tau \frac{1}{2} m \dot{\phi}^2 + V(\phi)$  and one can think of it as describing the motion of a particle in an inverted potential. We see that in our particular case of a free particle, the Euclidean action is the same as the Minkowski one. Periodic boundary conditions in time are imposed to recover

the trace.

As we are interested in the non-interacting case, we are left with a Gaussian functional integral and can solve it explicitly. We will compute the partition function

$$\mathcal{Z} = \int_{\phi(0)=\phi(\beta)} \mathcal{D}\phi e^{-S_{0,\beta}^E} . \quad (2.23)$$

To do so, we compute the saddle point of the Euclidean action with the relevant periodic boundary conditions

$$\ddot{\phi} = 0 \quad (2.24)$$

$$\phi(0) = \phi(\beta) . \quad (2.25)$$

To highlight the differences, let us start by recalling what happens in infinite space rather than on a circle. Then, only solutions with  $\dot{\phi}_{cl} = 0$  are admissible. Namely, all classical solutions are given by

$$\phi_{cl} = \phi_0 , \quad \forall \tau \in [0, \beta] . \quad (2.26)$$

for all  $\phi_0 \in \mathbb{R}$ . The path integral becomes then

$$\int d\phi_0 \left( \int \mathcal{D}\delta\phi e^{-\int d\tau \frac{m}{2} \dot{\delta\phi}^2} \right) \quad (2.27)$$

where the integral over  $\phi_0$  is a "sum" over all classical solutions and the remaining functional integral over fluctuations is the usual fluctuation prefactor. It can be evaluated by using, for example, the Van Vleck-Pauli-Morette formula or the Gelfand-Yaglom formula, see for example [17]. In the particular case of a free particle, with our thermal conditions, it gives

$$\int \mathcal{D}\delta\phi e^{-\int d\tau \frac{m}{2} \dot{\delta\phi}^2} = \sqrt{\frac{mT}{2\pi}} . \quad (2.28)$$

The integral over  $\phi_0$  diverges in the case of the infinite line. We can regularise it by considering a line of size  $R$ . We then get

$$\mathcal{Z}_{line} = R \sqrt{\frac{mT}{2\pi}} . \quad (2.29)$$

We see that  $\mathcal{Z}_{line} \neq \mathcal{Z}_{per}$ . but that  $\mathcal{Z}_{line}$  is equal to the term with  $n = 0$  of  $\mathcal{Z}_{per}$ .

The other terms in  $\mathcal{Z}_{per}$  arise as other solutions to the classical equations of motion (2.25). Indeed, in a periodic system, the solution (2.26) is not the only valid classical solution. Thanks to the periodicity, the particle can move by a full period with a constant velocity, chosen such that the thermal periodic boundary conditions are satisfied, namely

$$\dot{\phi}_{cl}^n = TRn , \quad (2.30)$$

with  $n \in \mathbb{N}$  an integer. The fluctuation determinant is still given by (2.28) and we also get a factor  $R$  coming from the integration over the initial point  $\phi_0$ , but now we have contributions from several classical solutions to sum over

$$\mathcal{Z}_{per.} = R \sqrt{\frac{mT}{2\pi}} \left( \sum_n e^{-\frac{mTR^2 n^2}{2}} \right) \quad (2.31)$$

which is nothing else than (2.14) in the case  $\theta = 0$ .

Before discussing the case  $\theta \neq 0$  in this description, some comments are of order. First, we see that the effect of the periodicity is to allow for more classical solutions. The associated physical picture is the following. On a line, imposing periodic boundary condition is time, a classical particle is doomed not to move. Quantum corrections are only fluctuations around this classical solution. On the other hand, on a circle, the particle can wind around  $n$ -times with a constant velocity and be at its original location at the time  $\tau = \beta$ , hence solving the classical equations and the boundary conditions. Classically, the vacuum solution, i.e. the one of least energy, is still the one where the particle stays at rest. Quantum mechanically, the existence of other classical solutions with finite energy signals the fact that quantum tunnelling happens with a finite probability. The sum in (2.31) contains the corrections due to these tunnelling events and they are exponentially suppressed.

This description is exact in the case of a free particle as the path integral is Gaussian and all fluctuations are taken into account by the prefactor. Nonetheless, when interactions are present, the general picture does not change. In the presence of degenerate vacua, the existence of finite energy classical solutions that interpolates between them signals the presence of quantum tunnelling. The path integral can be sorted around as contributions of these tunnelling events and fluctuations around them. This is the semiclassical approximation. Note also that the appearance the "flat direction"  $\phi_0$  is due to the extra invariance by any translations of the free particle and is not a generic feature.

Now let us turn back to the appearance of the  $\theta$  parameter in the path integral description. We see that we can get the missing term in (2.31) by adding a term of the sort

$$S_{\tau_i, \tau_f}^\theta = i\theta \int_{\tau_i}^{\tau_f} d\tau \frac{\dot{x}}{R}, \quad (2.32)$$

to the classical action. This is actually the correct procedure and also has a natural interpretation in terms of trajectories. Paths that winds around  $n$ -times interpolates from the state  $|\phi\rangle$  to  $|\phi + nR\rangle$ . For  $\theta \neq 0$ , they pick up a phase as in equation (2.3), which can be incorporated to the action as the term (2.32), using  $nR = \int dt \dot{x}$ .

Once more we see that the origin of this  $\theta$ -angle is of pure quantum nature, as the term (2.32) does not affect the classical equations of motion, being a total derivative.

Before moving on to investigate other aspects of this model, let us sum-up the main features

## 2.2. Topology-changing processes: classical vs quantum

---

we described so far in terms that will, hopefully, resonate with field theories we will encounter in this work later on.

- Periodicity in field space is linked to a set of discrete transformations represented by an operator  $\hat{U}$ , here translations by  $nR$ .
- It creates a degeneracy of classical vacua. We can label them by picking up one at random, labelling it by  $0$  and then labelling by  $n$  the one we get by applying  $\hat{U}$   $n$ -times. The field space is "topologically non-trivial" and different vacua correspond to different topological sectors.
- Invariance under the action of  $\hat{U}$  of physical observables requires only invariance up to a phase  $\theta$  on the state vectors.
- A given  $\theta$  corresponds to a given eigenvalue of  $\hat{U}$ .
- Different  $\theta$  corresponds to different theories.
- The existence of classical solutions which interpolates between different vacuum indicates the presence of quantum tunnelling and the quantum vacuum is a superposition of the "classical" vacua.

## 2.2 Topology-changing processes: classical vs quantum

As we saw in section 2.1, the classical solutions which extend more than a period are associated with tunnelling events between classical vacua. The fact that fields can explore different vacua leads to a different physics. This is not specific to the quantum rotor and is a feature shared by all theories whose field-space has a non-trivial topology. A key information to grasp the contribution coming from the existence of these different topological sectors is how much the system explores them. In the case of the quantum rotor, a natural quantity to study is the distribution of solutions contributing to the path integral as a function of

$$n = \frac{1}{R} \int d\tau \dot{\phi} . \quad (2.33)$$

This is nothing else than the distance in units of the period; any solutions with  $n > 1$  will have travelled more than one period. Note that with thermal periodic boundary conditions,  $n$  is forced to be an integer. This distribution is can be characterised by the  $m$ -averages  $\langle n^m \rangle$  and, thanks to (2.32), they can conveniently be computed as

$$\langle n^m \rangle_T = \left. \frac{\partial^m \mathcal{Z}}{\partial \theta^m} \right|_{\theta=0} , \quad (2.34)$$

where we specified the discussion to the case  $\theta = 0$ . As  $\mathcal{Z}$  is an even function of  $\theta$ , only  $m$ -even averages are non-zero. A Gaussian distribution will only have its  $m = 2$  average non-zero; in this sense higher  $m$  characterise non-Gaussianities.

Actually, while the moments (2.34) contains the relevant information, they are not the cleanest way to package it. As often, it is more convenient to look only at the connected part of  $\langle n^m \rangle$ , which is obtained by taking the derivative of the logarithm of  $\mathcal{Z}$ , namely the free energy (2.9). Also, to have a well defined quantity in the thermodynamic limit, it is more conventional to consider the free energy density  $f = \frac{F}{R}$  instead of the free energy. Having this in mind, we can expand  $f$  as [13]

$$f(T, \theta) = f(T, 0) + \chi(T) \theta^2 \left( 1 + \sum_{n=1}^{\infty} b_{2n}(T) \theta^{2n} \right). \quad (2.35)$$

The coefficient  $\chi(T)$  is directly proportional to  $\langle n^2 \rangle$

$$\chi(T) = \frac{\langle n^2 \rangle}{R} \quad (2.36)$$

since  $\langle n \rangle = 0$  for  $\theta = 0$ . It is called the topological susceptibility. This name reflects the fact that it is the second derivative of the free energy and it also characterises the response to a would-be constant topological charge background. The other coefficients are higher-order moments of the free energy.

Again, in the case of the quantum rotor, this can be computed explicitly. And again, of particular interest are the high and low-temperature limits. From equations (2.17) and (2.18), we see that

$$\lim_{T \rightarrow 0} \chi(T) = \chi_0, \quad \lim_{T \rightarrow 0} b_{2n}(T) = 0 \quad (2.37)$$

$$\chi(T) \underset{T \rightarrow \infty}{\sim} e^{-\frac{R^2 m T}{2}}, \quad \lim_{T \rightarrow \infty} b_{2n}(T) = b_{2n}^{\infty}. \quad (2.38)$$

At zero temperature, the distribution of  $n$  is exactly Gaussian, while at high temperature the width of the distribution is exponentially suppressed and tunnelling becomes very unlikely.

A key point which is difficult to overemphasize is that all the discussion we just had is a *Euclidean* description and is related to quantum tunnelling processes. Even though it is not apparent in the free case we considered, the classical solutions the topological susceptibility measures the variance of are intrinsically solutions to the *Euclidean* equations of motion and are understood semiclassically as describing tunnelling processes. Equation (2.38) means that such tunnelling processes are suppressed at high-temperature. What equation (2.38) does *not* say is that the particle stays around the vacuum it started. Indeed, even classically, thermal fluctuations allow the particle to move along the period. The rate at which different vacuum are visited is even expected to grow with the temperature, as more energy is available.

To understand how this arises in the formalism, it is interesting to compute this rate explicitly, as presented in [12]. Let us define

$$n(\tau, 0) = \frac{1}{R} \int_0^{\tau} d\tau \dot{\phi} = \frac{1}{R} (\phi(\tau) - \phi(0)) \quad (2.39)$$

## 2.2. Topology-changing processes: classical vs quantum

and the following Euclidean correlator

$$G(\tau, \tau') = \langle \mathcal{T}_{\mathcal{E}} \{n(\tau, 0), n(\tau', 0)\} \rangle_T . \quad (2.40)$$

In these terms, we have

$$\chi(T) = \frac{G(\beta, \beta)}{R} . \quad (2.41)$$

The corresponding Minkowski correlator is given by

$$G(\tau, \tau') \rightarrow G(i\tau, i\tau') \equiv G(t, t') = \langle \mathcal{T}_{\mathcal{M}} \{n(t, 0), n(t', 0)\} \rangle_T , \quad (2.42)$$

which is nothing else than the usual real-time time-ordered propagator, as the notation  $\mathcal{T}_{\mathcal{M}}$  indicates.

Our goal is to understand how this two-point function is exponentially suppressed in Euclidean time but monotonically growing in Minkowski time, as a function of the temperature. To do so, we will explicitly compute the leading contribution in temperature to this two-point function. As we discussed above, can split contributions into topological sectors. The ones which do not belong to the sector  $n = 0$  are associated with quantum tunnelling and are exponentially suppressed. To look for a contribution which is not, it is thus enough to restrict the effort to the sector  $n = 0$ . In this context, it means we will do the computation as if we had not imposed periodicity (2.2); we will consider a truly free particle.

Restricting ourselves to equal times  $t > 0$ , in terms of (2.39), we need to compute

$$\langle \mathcal{T}_{\mathcal{M}} \{n(t, 0), n(t, 0)\} \rangle_T = \frac{1}{R^2} \langle \mathcal{T}_{\mathcal{M}} \{(\phi(t) - \phi(0))(\phi(t) - \phi(0))\} \rangle_T^F + O\left(e^{-\frac{mTR^2}{2}}\right) \quad (2.43)$$

$$= \frac{1}{R^2} \langle \phi(t)^2 - 2\phi(t)\phi(0) + \phi^2(0) \rangle_T + O\left(e^{-\frac{mTR^2}{2}}\right) \quad (2.44)$$

where we used the fact that  $t > 0$ , reordered the product according to the time ordering and kept track of the exponentially small effect we are neglecting by keeping explicit the  $O(e^{-n^2 T})$  contributions. The only quantity we need to know is  $\langle \phi(t)\phi(t') \rangle_T$  in a free theory. In the free case, to be well-defined, this quantity needs to be regulated. Following [12], we will obtain it as the zero-frequency limit of a harmonic oscillator. We thus consider the following system

$$H = \frac{1}{2m} \hat{p}^2 + \frac{1}{2} m \omega_\epsilon \hat{x}^2 \quad (2.45)$$

and will send the regulator  $\omega_\epsilon$  to zero at the end of the computation.

A detailed presentation of thermal field theory techniques is beyond the scope of this work and we refer the interested reader to [18, 19]. We will nonetheless recall some basic definitions to make this computation reasonably self-contained, mostly following the presentation of [18].

As in the zero temperature case, the ordering in time of operator is crucial and different

## Chapter 2. A detour to lower dimensions: the quantum rotor

---

orderings lead to different variables. The first two correlators we can define are the so-called Wightman's functions

$$G^>(t, t') = \langle \phi(t) \phi(t') \rangle_T \quad (2.46)$$

$$G^<(t, t') = \langle \phi(t') \phi(t) \rangle_T = G^>(t', t) . \quad (2.47)$$

Of interest is also be the spectral correlator

$$\rho^S(t, t') = G^>(t, t') - G^<(t, t') . \quad (2.48)$$

where the subscript  $S$  was added to differentiate it from the density matrix. In these terms, time ordered correlators are

$$G^{\mathcal{T}}(t, t') = \theta(t - t') G^>(t, t') + \theta(t' - t) G^<(t, t') . \quad (2.49)$$

These correlators can be defined in general, not only for a thermal ensemble. In this context, thermal equilibrium states that all these correlators are not independent but related one to another. It is the well-known Kubo-Martin-Schwinger (KMS) relation

$$G^>(t, t') = G^<(t + i\beta, t') , \quad (2.50)$$

which is easily obtained from (2.46) and (2.47) by writing down explicitly the thermal average and treating  $\hat{\rho}$  as an imaginary-time evolution operator.

It is often useful to manipulate these expressions in Fourier space. As equilibrium states are by definition time-translation invariant, all these correlators truly depend only on time differences and can be written Fourier space as

$$G^>(k_0) = \int_{-\infty}^{\infty} dt e^{ik_0 t} G^>(t, 0) \quad (2.51)$$

$$G^<(k_0) = \int_{-\infty}^{\infty} dt e^{ik_0 t} G^<(t, 0) \quad (2.52)$$

$$\rho^S(k_0) = G^>(k_0) - G^<(k_0) . \quad (2.53)$$

The KMS relation becomes

$$G^<(k_0) = e^{-\beta k_0} G^>(k_0) \quad (2.54)$$

and combined with (2.53) leads to the following two relations

$$G^>(k_0) = \left( 1 + \frac{1}{e^{\beta k_0} - 1} \right) \rho^S(k_0) \quad (2.55)$$

$$G^<(k_0) = \frac{\rho^S(k_0)}{e^{\beta k_0} - 1} . \quad (2.56)$$

This is all we need to compute (2.44). Indeed, in the case of the harmonic oscillator, the spectral correlator (2.48) can be easily computed, see for example [18]. The resulting spectral

## 2.2. Topology-changing processes: classical vs quantum

function is

$$\rho_{SHO}^S(k_0) = \frac{2\pi}{m} \text{sgn}(k_0) \delta(k_0^2 - \omega_\epsilon^2) \quad (2.57)$$

with  $\text{sgn}(k_0)$  the sign function. It is nothing else but the reflection of the fact that by definition a simple harmonic oscillator is monochromatic and of frequency  $\omega_\epsilon$ . With this at hand and realising that we only need to compute  $G^>(t, 0)$ , we simply plug (2.57) in (2.55) and compute its inverse Fourier transform

$$G^>(t, 0)_{SHO} = \frac{1}{2\pi} \int_{-\infty}^{\infty} e^{-ik_0 t} \left( 1 + \frac{1}{e^{\beta k_0} - 1} \right) \rho_{SHO}^S(k_0) \quad (2.58)$$

$$= \int_0^{\infty} dk_0 \left[ e^{-ik_0 t} \left( 1 + \frac{1}{e^{\beta k_0} - 1} \right) - e^{ik_0 t} \left( 1 + \frac{1}{e^{-\beta k_0} - 1} \right) \right] \frac{\delta(k_0 - \omega_\epsilon)}{2\omega m} \quad (2.59)$$

$$= \frac{1}{2m\omega} \left( -2i \sin(\omega_\epsilon t) + \frac{e^{-i\omega_\epsilon t}}{e^{\beta\omega_\epsilon} - 1} - \frac{e^{i\omega_\epsilon t}}{e^{-\beta\omega_\epsilon} - 1} \right) \quad (2.60)$$

where we split the initial integration in two to take into account the sign function explicitly. The special case of equal times reduces to

$$G^>(t, t)_{SHO} = G^>(0, 0)_{SHO} = \frac{1}{2m\omega_\epsilon} \coth\left(\frac{\beta\omega_\epsilon}{2}\right). \quad (2.61)$$

Altogether, equation (2.44) becomes

$$\langle \mathcal{T}_{\mathcal{M}} \{n(t, 0), n(t, 0)\} \rangle_T = \lim_{\omega_\epsilon \rightarrow 0} \left\{ \frac{1}{m\omega_\epsilon} \left( \coth\left(\frac{\beta\omega_\epsilon}{2}\right) + 2i \sin(\omega_\epsilon t) \right) \right. \quad (2.62)$$

$$\left. - \frac{e^{-i\omega_\epsilon t}}{e^{\beta\omega_\epsilon} - 1} + \frac{e^{i\omega_\epsilon t}}{e^{-\beta\omega_\epsilon} - 1} \right\} + O\left(e^{-\frac{mTR^2}{2}}\right) \\ = \frac{1}{m} \left( it + \frac{t^2}{\beta} \right) + O\left(e^{-\frac{mTR^2}{2}}\right). \quad (2.63)$$

The result (2.63), which was first derived in [12] is exactly the kind of expression we were hoping for. We started from the following apparent puzzle. In Euclidean space, the topological susceptibility, which is a two-point function of  $n(\tau)$  evaluated at  $\tau = \beta$ , is exponentially suppressed. On the other hand, even from classical physics, we expect the particles to travel more and more periods as the temperature rises, because of thermal fluctuations. This should also manifest itself in the two-point function of the topological charge. And as we can see in (2.63), it does. The *real-time* rate does grow as  $T$  rises. And upon analytic continuation  $t \rightarrow -i\beta$  we find back the Euclidean exponential suppression.

Actually, in this case it is informative to reinsert the factor of  $\hbar$ . We get

$$\langle \mathcal{T}_{\mathcal{M}} \{n(t, 0), n(t, 0)\} \rangle_T = \frac{1}{m} \left( it\hbar + \frac{t^2}{\beta} \right) + O\left(e^{-\frac{mTR^2}{2\hbar^2}}\right). \quad (2.64)$$



Taking the classical limit  $\hbar \rightarrow 0$ , we find no tunnelling at all and a real rate equal to

$$\langle \mathcal{T}_{\mathcal{M}} \{n(t,0), n(t,0)\} \rangle_T^{cl.} = \frac{t^2}{m\beta}, \quad (2.65)$$

which is exactly what the classical computation of the correlator would lead to, as the equipartition theorem states that  $\frac{1}{2}mv^2 = \frac{1}{2}T$ . Note also that the time ordering was crucial to find the result (2.63). If one does not reorder the term  $\phi(t)\phi(0) + \phi(0)\phi(t)$  in (2.44), one ends up computing  $G^>(t,0)_{SHO} + G^<(t,0)_{SHO}$  and the imaginary part of (2.63) drops out. The classical result is recovered, as it should since classical physics is not sensitive to time ordering. But this correlator does not continue to the correct one in Euclidean time and one cannot read out contributions to the topological susceptibility from there.

Let us summarise what was learnt in this section. As soon as a system possesses different topological sectors, transitions from one to another play an important role. Such transitions can happen in two ways, either through quantum tunnelling or thanks to thermal fluctuations. The former is a quantum phenomenon which is exponentially suppressed in the classical limit. The latter is a classical one which becomes more and more important as the temperature increases.

Before moving on, let us also comment on terminology. The classical solutions to the Euclidean equations of motions are generically called "instantons" and they describe tunnelling. When a potential is turned on, the real-time transitions are still triggered by thermal fluctuations, but the rate is more complicated to compute classically as the potential now competes against them. The leading contribution to the rate can be estimated by a specific solution to the real-time classical equations of motion and this solution is called "sphaleron" [20]. Correspondingly, the late time growth rate of correlators of the type (2.42) is called the "sphaleron rate".

### 2.3 Euclidean path-integral simulations

The quantum rotor is also a natural playground for numerical simulations. A particularly useful technique is to compute the Euclidean path integral numerically on a lattice. It can be done when the Euclidean action is positive definite, as in this case  $e^{-S_E}$  can be interpreted as a probability distribution and importance sampling methods can be applied to generate field configurations according to it. Plenty of algorithms are available and we defer the reader to [21, 22] for pedagogical introductions in the context of lattice QCD. In this section, we want to present some results obtained for the quantum rotor, mostly concerning topological transitions and the topological susceptibility. Already in this simple system, we will see the emergence of some difficulties in sampling correctly different topological sectors, difficulties that worsen for more complicated systems.

Here, we use the Metropolis algorithm presented in [13], the reference from which this section

is mostly inspired from. The idea behind Metropolis is to generate a Markov chain whose stationary distribution corresponds to the probability one wants to sample and then select states of the chain once it has reached its steady state. A mild complication in the case of the quantum rotor is to define a variable that is properly periodic and whose winding number (2.33) is integer. A way to do this is to consider the following action [13]

$$S_E^{sim.} = \frac{1}{2} \sum_{j=0}^{N-1} \frac{(x_{j+1} - x_j) \% \frac{1}{2}}{a} \quad (2.66)$$

where we fixed  $R = m = 1$ . We have then  $x \in [0, 1)$ . The time interval is discretised in  $N$  points separated by a Euclidean time  $a = \frac{\beta}{N}$  and  $x_j$  denotes  $x(j \cdot a)$ . Boundary conditions in time need to be imposed. To simulate a thermal system, we take them to be periodic. The quantity

$$(x - y) \% \frac{1}{2} = \begin{cases} x + y & \text{if } |x - y| \leq \frac{1}{2} \\ x + y - 1 & \text{if } x - y > \frac{1}{2} \\ x + y + 1 & \text{if } x - y < -\frac{1}{2} \end{cases} \quad (2.67)$$

measures the distance between two points on the circle.

The advantage of considering such a simple case is that some intuition on what is happening in the system can be gained by directly looking at configurations generated by the Markov chain. We do this in figure 2.2 where we plot a configuration together with  $n(\tau) = \int^\tau \dot{x} d\tau'$ . Note that for a periodic variable,  $n(\tau)$  is not quite  $x(\tau) - x(0)$ , as the former measures the net distance travelled whereas the second one is just a periodic coordinate. In other words,  $n(\tau)$  keeps track of the winding while  $x(\tau) - x(0)$  does not. This plot  $N = 2000$  and  $a = 0.01$ , giving  $T = 0.05$ . Recalling that we fixed  $R = m = 1$ , this corresponds to a low temperature and we do see that the Euclidean particle often changes topological sector, signalling frequent tunnelling. To understand qualitatively how a Euclidean transition looks like in an actual configuration, we restrict in figure 2.3 the Euclidean time range from 0 to 120 and plot the resulting trajectory in polar coordinates. We also show the corresponding classical solution in a plain line. And what we obtain is indeed a trajectory that winds around the circle once. We also note the presence of relatively strong fluctuations atop of the semiclassical solution.

To regain results in the continuum, we need to take the limit  $a \rightarrow 0$ . When trying to do that, we encounter a problem which is particularly severe for topological observables, the one of critical slowing down. Taking the continuum limit of a lattice model can be understood from a renormalisation group perspective as flowing a theory towards a continuum fixed point. Such fixed points are associated with second-order phase transitions and thus to diverging correlation lengths. Algorithms which are based on local steps are known not to perform well in such situations; they start to require an exponential amount of time to explore all of the relevant phase space, see for instance [23] for more information.

As we will see, we are also confronted with such a phenomenon in our simple toy model. The

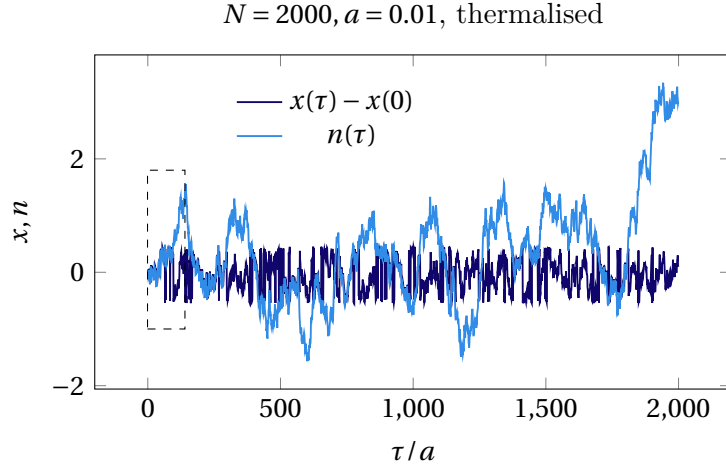


Figure 2.2 – A Euclidean configuration obtained from a Metropolis algorithm. In dark blue, we show the "compact" coordinates, which spans between  $-\frac{1}{2}$  and  $\frac{1}{2}$  and in lighter blue  $n(\tau) = \int d\tau \dot{x}$ , which keeps tracks of the total distance traveled from the origin. The dashed square highlight a part of the trajectory where a topological transition happens; this is the part which is shown in figure 2.3.

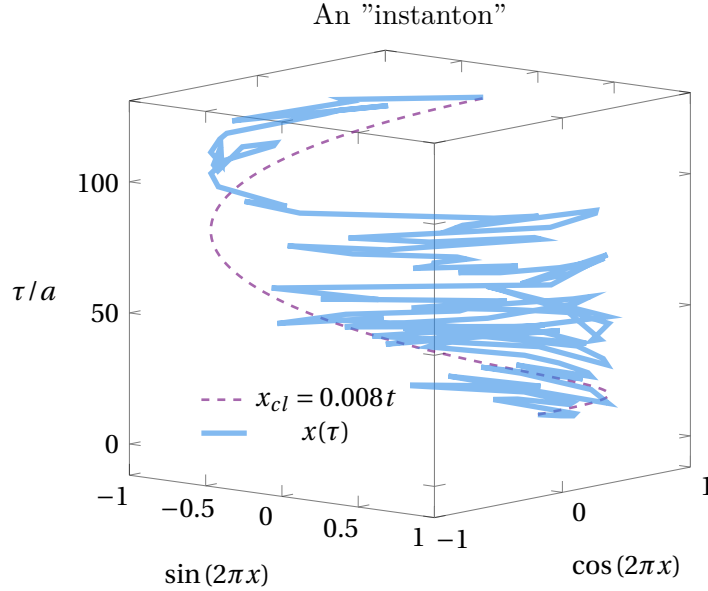


Figure 2.3 – Part of a Euclidean configuration which displays a tunnelling event, together with the corresponding semiclassical constant velocity solution. To get a better representation of what is happening, we treat it as an angle and plot it in polar coordinates.

existence of a topological charge, from a semiclassical point of view, splits the phase space into disconnected domains. They are disconnected because to deform a path with a given topological charge into one with a different topological charge, one needs to perform a discontinuous transformation, which strictly speaking corresponds to a contribution with an infinite action. In terms of the lattice model, what needs to be done is to be able to, with one update step of the algorithm, transform a path which winds around  $n$ -times into a path which winds around  $n \pm 1$  times. With a coarse discretisation, there is no problem as there is no clear notion of discontinuous transformations; the sectors are not disconnected and the action barrier between them is low. However, as the discretisation is refined, the action-cost related to transformations which add or remove winding to path grows together with the emergence of continuity.

The best way to get some understanding of this phenomenon is perhaps to watch it happening to the quantum rotor. We fix the temperature to be  $T = 0.5$ , which is still relatively low. As such we expect quantum transitions to give a non-negligible contribution to the path integral. In figure 2.4 we consider what happens to the topological charge for three different lattice spacings. We consider 100 configurations of our Markov chain, each separated by 500 iterations. The upper row shows the distribution of the topological charge as histograms, while the bottom row shows the topological charge history. We see that for the larger lattice spacing, there is no correlations between the different configurations and different topological sectors are sampled according to their weight in the path integral. Already for the second lattice spacing, we see this is not the case anymore. Different topological sectors are sampled but ineffectively. More problematically, we can see from the histories of the topological charge the presence of correlations between configurations we would like to be independent. The last lattice spacing, only 20% smaller than the intermediate one, displays no topological transitions at all, it is completely "frozen" in the  $Q = 0$  sector. This previous discussion can be made more quantitative by computing the autocorrelation time of the topological charge along the Markov chain, see [23] for a careful discussion. We will not do it here but we want to mention the result of [13] where this analysis was done for the quantum rotor. It was found that this autocorrelation time scales as  $\exp(1/a)$ , a scaling already found in other system possessing topological sectors, see [13] and references therein. This clarifies what was meant by the fact that the algorithm needs an exponential time to explore all the different sectors of the phase space.

To conclude this discussion on critical slow-down and topological freezing, we show on figure 2.5 two different full snapshots of configurations of total topological charge  $n = 0$ , both at the same temperature  $T = 0.5$ . The first one is for a lattice spacing of  $a = 0.01$  while the second one corresponds to  $a = 0.001$ . We can very visually see the effect of topological freezing. In the first case, the Euclidean particle constantly winds around the circle, but with a net amount of 0 turns. In the second case, the particle never goes around the circle.

To ease up this problem, several solutions have been proposed, see again [13] and references therein. Here we want to present one, namely using different boundary conditions. In the case

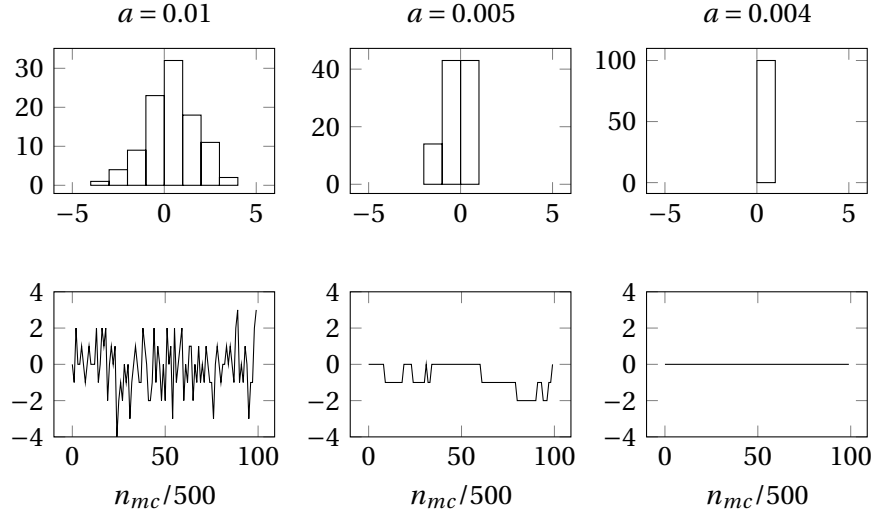


Figure 2.4 – Histograms and history of the topological along the Metropolis generated Markov chain, for different lattice spacings. As the continuum limit is approached, the topological transitions become sparser and sparser; the system "freezes" in the  $n = 0$  topological sector. The first sign of this freezing is the emergence of long autocorrelation in the charge's history, signalled by plateau's, as for the intermediate lattice spacing in this picture.

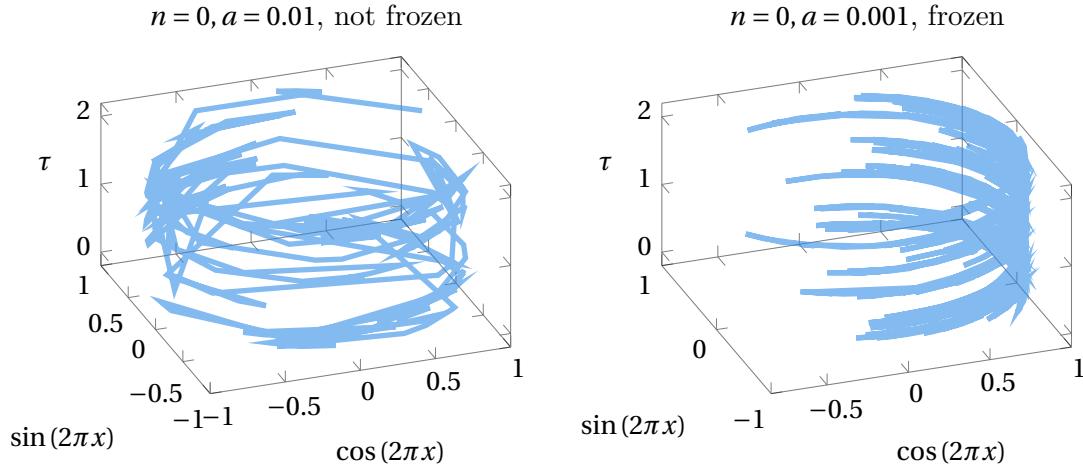


Figure 2.5 – Particle's trajectory for some generic configurations, far from the continuum (left-hand side) and close to the continuum (right-hand side). We see that in the first case, the path easily winds around the circle, even though the total number of winding sums-up to zero. On the contrary, the second case suffers from topological freezing and the particle never goes around the circle.

of quantum mechanics, once we decide to compute thermal averages, we do not have the choice of boundary conditions, so let us imagine for a moment we do not want to compute thermal correlators and that we indeed have a free choice of boundary conditions. We saw in the previous discussion that the appearance of topological freezing can be understood as the appearance of action barriers between topological sectors. In turns, these action barriers are related to the fact that one cannot continuously deform a path of a given topological charge into another. And this is intrinsically related to the fact that by imposing periodic boundary conditions, i.e. that the final position of the particle is the same than the initial one, we impose the number of turns to be integers, creating disconnected sectors. Were we to impose different boundary conditions, let us say setting  $x_{N_\tau} = 0$ , we would not be in the presence of disconnected sectors and we would expect a better sampling of the topological charge. In the case of the quantum rotor, this is precisely what happens and the autocorrelation time of the topological charge is found to scale as  $N_\tau^2$  [13]. As explained in this reference, a dependence on  $N_\tau$  rather than on  $a$  is expected in this case, as the gain in sampling the topological charge can be interpreted as flowing from the boundary and the information takes time to travel inwards.

The aim of this section was to introduce the concept of Euclidean path integral simulations and discuss the problem of topological freezing, which already appears in a simple model like the quantum rotor.

## 2.4 Classical simulations: "sphaleron" rate in a peridodic potential

We saw in section (2.2) that at finite temperature, topological transitions mostly happens thanks to thermal fluctuations. In cases were analytical results are not available, one needs to rely on numerical estimates. We described in the previous section how the Euclidean path integral can be simulated. The obstruction is that such simulations gives direct access to Euclidean correlators of the type (2.40) while the relevant information is encoded in the real-time ones of the type (2.42). In principle, as we are talking about thermal equilibrium and all different correlators are related, one can attempt to extract real-time information from the Euclidean data, by realising that the Euclidean correlator is related to the spectral function (2.53) as [18,19]

$$G(\tau, 0) = \int_0^\infty d\omega \rho(\omega) \frac{\cosh(\omega(\tau - \beta/2))}{\sinh(\beta\omega/2)} . \quad (2.68)$$

Once the spectral function is known, any real-time correlator can be recovered. All the problem lies in inverting numerically the integral equation (2.68). This is a notoriously hard problem which makes Euclidean simulations less appealing to extract Minkowski quantities. We refer interested readers to the recent review [24] and references therein for further discussions related to such inversions and to reference [25] for a discussion in relation to the sphaleron rate.

However, when the temperature is not negligible compared to the potential energy, we saw that the topological transitions were likely to be dominated by classical thermal fluctuations. When such cases arise, another path opens up to study these processes as it is now relevant to solve numerically the corresponding classical-statistical problem. In principle, we could continue to explore our free periodic particle. Its classical physics being completely trivial, it seems to us more appropriate to deviate from this example and consider the more interesting case of a periodic potential. To illustrate the method, we study the classical dynamics of a particle with the following Hamiltonian

$$H = \frac{1}{2}\dot{x}^2 + E_0 \sin^6(x) , \quad (2.69)$$

where the potential was chosen for its periodicity and for the fact that the corresponding equations of motion

$$\dot{p} = -6E_0 \sin^5(x) \cos(x) \quad (2.70)$$

$$\dot{x} = p \quad (2.71)$$

do not admit any obvious closed form.

To compute classical correlators of the type (2.65), we proceed as follow. First, we generate thermal initial conditions, namely a set of points  $x_0, v_0$  which are distributed according to the Boltzmann distribution  $e^{-\beta H}$ . This can be done by using the same techniques described in section (2.3), but in one dimension less (simply numbers in this case,  $n$ -dimensional fields for classical simulations in  $n+1$  dimensions). Then, for every initial conditions in this set, the classical equations of motion (2.70) and (2.71) are solved numerically. The correlators, or any other observable of interest, are then computed for every solution and averaged over. The result gives an estimator for the thermal average of the given observable.

To conclude this section and to illustrate the technique, we present some results obtained for the Hamiltonian (2.69) with  $E_0$ . In figure 2.6, we show the potential under consideration. In figure 2.7 we consider three temperatures. On the top two rows, we show the distributions of initial conditions obtained using a simple Metropolis algorithm. The velocities are simply Gaussian, with a variance proportional to the temperature. The positions (taken modulo the period for this plot) also behave in the expected way. For  $T \ll m$ , the initial point is located around the vacuum. the spread is larger for  $T = m$  but one still feels the effect of the potential. For  $T \gg m$ , the initial positions are almost uniformly distributed, as in the case of a free particle. These distributions of initial conditions also reflect themselves in the third row of the same figure, where we show a set of classical solutions obtained for some of these initial conditions. At low temperature, the particle is confined in the well it started. At intermediate temperature, thermal fluctuations with enough energy start to happen so that the particle can travel the valley of vacua. And at high temperature, this is what happens most of the time.

With these classical solutions at hand, we can now compute any statistical average we desire.

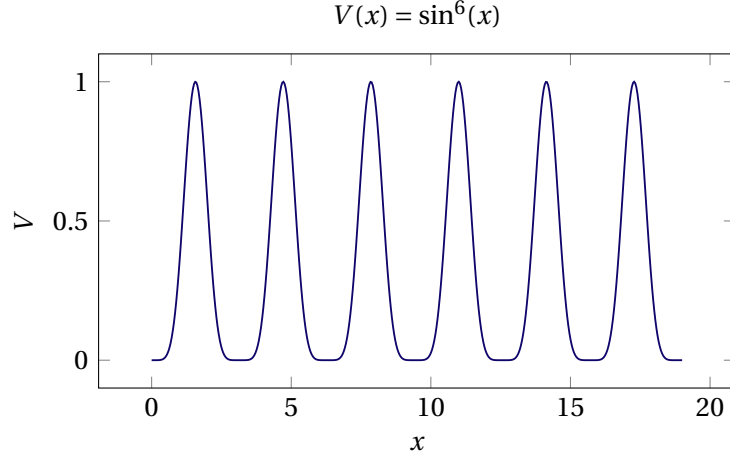


Figure 2.6 – Potential used to illustrate the use of classical simulation. It has a degenerate set of vacua at integer multiples of  $\pi$ .

We show in 2.8 a numerical determination of the correlator  $\langle (x(t) - x(0))^2 \rangle^{cl}$  for  $\frac{T}{m} = 1$  and  $\frac{T}{m} = 10$  (in the case  $\frac{T}{m} = 0.1$ , the topological transitions do not happen often enough so as to provide us with an easy way to measure this correlator). From the computation presented in section 2.2, equation (2.65), we expect it to go as  $t^2$  at high temperature when the system behaves like a free particle. This is what we observe. We also see that this  $t^2$  behaviour happens for smaller temperature as well. This is the case simply because, as soon as the particle has enough energy to pass a barrier, it will travel to infinity with a mean that grows linearly. Even if this would be beyond the scope of this illustratory study, one can also extract the coefficient in front of  $t^2$ , which would be in this case the equivalent of a field-theory "sphaleron-rate". One then would also study its dependence on the temperature and the energy barrier  $E_0$ .

To conclude this section, let us summarise its main point. When thermal fluctuations dominate over quantum tunnelling, it may be the case that classical-statistical physics is a good approximation. If this is so, classical simulations can be used to estimate relevant parameters. They are performed by solving the classical equations of motions using initial conditions distributed according to the thermal equilibrium distribution function and the results are obtained by averaging over them.

## 2.5 A word of caution

Despite all of the interesting physics that already arise in a simple quantum mechanical model, we wish to conclude this section with a word of caution: quantum mechanics is not field theory. And as such, we cannot expect to capture all field theoretical effects in this system. For example, no thermal collective effects or any other kind of many-body behaviour have a chance to be encoded in a single degree of freedom, be it quantum or not. Let us briefly discuss two



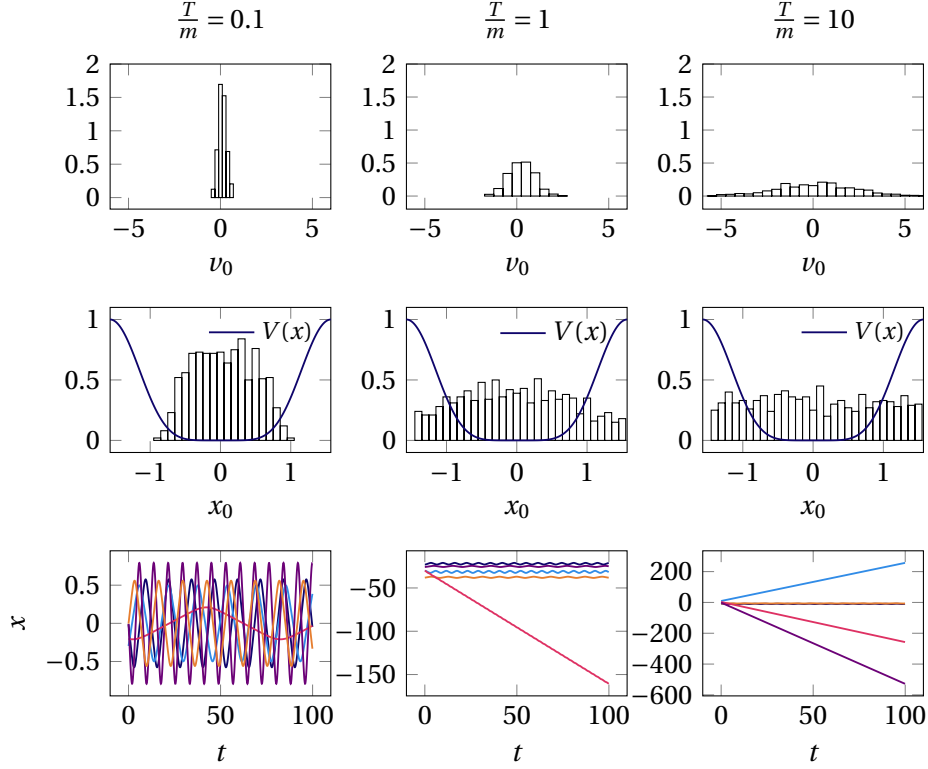


Figure 2.7 – Classical simulations for three different temperatures. The first row shows the Gaussian distribution of initial velocities, which becomes wider and wider as the temperature is increased. The second row shows the distribution of initial position modulo a period together with one period of the potential. As expected, at low temperature, most of the particles start at the bottom of the wells. At high temperature, they are uniformly distributed and at intermediate temperatures, we see the competition between thermal fluctuations and the potential. The third rows show classical solutions to the equations of motion, for some of the generated initial conditions; observables are computed by averaging over such solutions. At low temperature, it is very unlikely to escape the potential well and all trajectories stay in the well they started from. At high temperature, we get back a free particle which does not feel the potential. And for intermediate temperatures, both kinds of trajectories contribute.

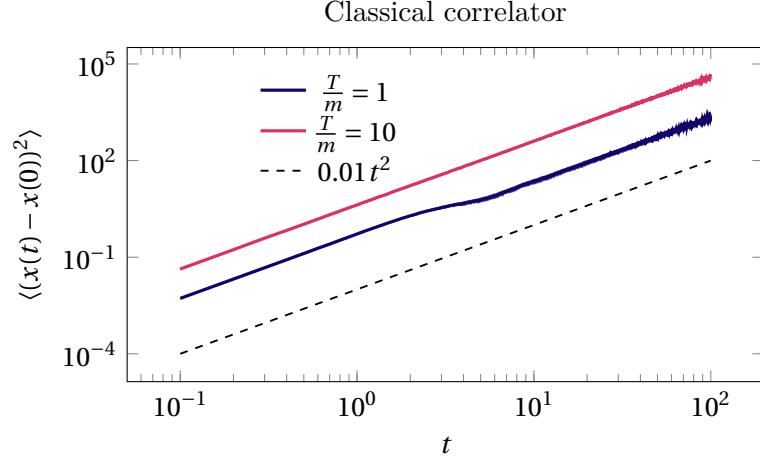


Figure 2.8 – Classical correlator linked to the “sphaleron-rate”. Errors were computed by considering 1000 classical solutions and using statistical bootstrap. The expected  $t^2$  growth is observed and we also observe a temperature dependence of the corresponding coefficient.

explicit cases when our quantum particle differs from what is expected from some quantum field theories.

Consider the asymptotic behaviour of the topological charge correlator at late time. We saw two examples in section 2.2 and 2.4 where this correlator grows as  $t^2$  for late times. This is actually something that has to be expected for one-dimensional systems. The phenomenon is dominated by classical dynamics. For a particle moving in a periodic potential, there are two kinds of solutions. First, the particle may not have enough energy to cross the potential barrier. These solutions do not contribute significantly to the correlator. The ones that do are the ones when the particle has enough energy to cross the barrier. But because of energy conservation, it means it will just continue to cross all barriers, forever. Integrated over a period, its motion will be effectively the one of a free particle, leading to  $n(t) \sim t$  and thus  $n(t)^2 \sim t^2$ . The prefactor will, of course, depend of the specifics of the problem.

The situation in field theory is different and the key reason is the following. A field theory is a theory of (infinitely) many degrees of freedom. A topological charge can be thought of as an effective dynamical degree of freedom emerging from this (infinitely) many-body system<sup>1</sup>. And as such, taken on its own, its dynamics will not be conservative. Picturing a complicated vacuum structure with many vacua, the intuition is that it will visit all these vacua following a random walk. This means that we should expect that  $\langle n^2 \rangle \sim t$ , as this is the behaviour of the variance of a random walk; we defer the reader to reference [27] for a statistical treatment of the topological charge dynamics. The point is that this intuition seems to be correct and this linear in time behaviour is what is observed in different field theories, see references [25, 28, 29] for examples.

<sup>1</sup>For a not-so-related-but-interesting discussion on this subject, see [26].

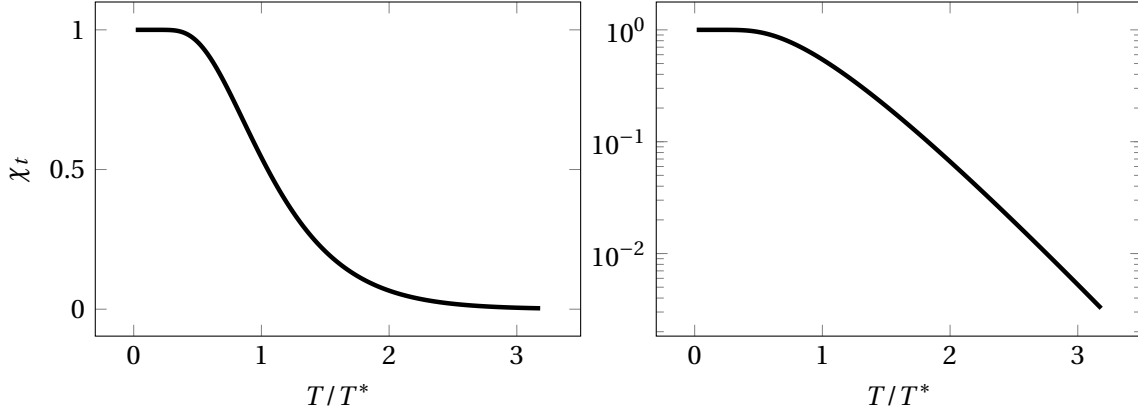


Figure 2.9 – Topological susceptibility of the quantum rotor for  $m = R = 1$  on in linear (left) and logarithmic (right) scales. The  $x$ -axis is normalised by the pseudo critical temperature. The linear scale shows in which sense  $T^*$  is a critical temperature; it connects two different behaviour of the theory. The logarithmic scale emphasise the logarithmic suppression which happens at high temperature.

A second example where our standard quantum particle in a periodic potential or on a circle cannot be used to describe the physics is when a phase transition is present, as phase transitions do not occur in local one-dimensional system [30]. For example, the asymptotic behaviour of the free particle's free energy (2.9) is identical to the one of a pure  $SU(N)$  gauge theory. However, this theory is known to experience a first-order phase transition at some critical temperature  $T_c$ , see for instance [19]. The topological susceptibility is expected to be discontinuous across the phase transition and thus cannot match exactly one obtained from a quantum particle.

It is interesting to note that except for the discontinuity, the behaviour is still qualitatively the same. Indeed, one can define a "pseudo critical temperature" in the case of the free particle, when the two different representations (2.11) and (2.14) of the path integral at  $\theta = 0$  are self-dual. This happens at  $T^* = \frac{2\pi}{mR^2}$  and we show in figure the topological susceptibility of the quantum rotor as a function of the temperature. Results for pure  $SU(3)$  can, for example, be found in reference [31] and their global trend is not so dissimilar.

These remarks close this part on free periodic quantum mechanics, which was shown to be an impressively rich toy model.

### 3 A detour to lower dimensions: the Schwinger model

We now move on to field theory to discuss some effects which are not present in normal quantum mechanics, namely the phenomenon of pair production in strong fields and the chiral anomaly. The former is tied to the fact that the particle number is not conserved in field theory. Under some conditions, here the presence of some strong background fields, it is energetically more favourable to create charged particles out of the vacuum to quench the fields instead of sustaining them. The latter is more subtle and is related to the intrinsic nature of fermions. In some situations, classical symmetries of the theory do not survive quantisation.

To study these, it is enough to go to 1+1 dimensions and consider fermions<sup>1</sup> coupled to a  $U(1)$  gauge field  $A_\mu$

$$S^E = \int d^2x \left[ \bar{\psi} (\not{\partial} + i \not{A} + m) \psi + \frac{1}{4g^2} F_{\mu\nu} F^{\mu\nu} \right], \quad (3.1)$$

where we directly wrote the action in Euclidean space,  $F_{\mu\nu} = \partial_\mu A_\nu - \partial_\nu A_\mu$  and where the "slash" notation denotes, as usual, contraction to gamma matrices  $\not{A} = \gamma^\mu A_\mu$ . We work with Euclidean  $\gamma$ -matrices which satisfy the Clifford algebra

$$\{\gamma^\mu, \gamma^\nu\} = 2\delta^{\mu\nu} \quad (3.2)$$

and define

$$\gamma^5 = i\gamma^0\gamma^1. \quad (3.3)$$

When needed, we use the following representation for the  $\gamma$ -matrices

$$\gamma_0 = \begin{pmatrix} 0 & -i \\ i & 0 \end{pmatrix}, \quad \gamma_1 = \begin{pmatrix} 0 & 1 \\ 1 & 0 \end{pmatrix}, \quad \gamma_5 = \begin{pmatrix} 1 & 0 \\ 0 & -1 \end{pmatrix}. \quad (3.4)$$

This model was studied early on in the massless case [32–34] where fermions were found to be confined. The study was extended to the massive case in [35, 36] and confinement was found to

---

<sup>1</sup>For pair production, charged scalars would also do.

persist. This model is also sensitive to the addition of a  $\theta$ -term [36]. Because of these features, it can be used as a toy-model for QCD.

### 3.1 Pair production

As previously mentioned, a genuine expectation in field theory is the possibility of creating pairs of particles out of the vacuum by applying strong fields. This was realised in the very early days of field theory, notably in reference [37]. A natural way to frame the question is the following. Consider quantum electrodynamics in some box of volume  $V$  and apply a constant electric field  $E$ . When will particles be created? It turns out that this question can be answered by neglecting the back-reaction of the created particles and simply considering the problem in a constant electric field. The problem was first solved in reference [38]. In such a case, the fermionic effective action can be computed exactly and displays an imaginary part, which is then interpreted as giving the rate of particle creation.

In this section, we want to present this computation. We will do it in the Schwinger model, where the computation simplifies, mostly because of the simpler Lorentz structure in  $1+1$  dimensions. It is worth noting that here it makes sense to use it as a proxy for QED only as long as we neglect the back-reaction since the dynamics of fermions are qualitatively different in both theories.

This aside, the computation proceeds in exactly the same way. We compute the effective action obtained by integrating out the fermionic part of the action

$$S_\psi^E = \int d^2x [\bar{\psi}(\partial + iA + m)\psi] \quad (3.5)$$

in the presence of a static and homogeneous  $F_{\mu\nu}$ . We write its only non-vanishing component as

$$F_{01} = E . \quad (3.6)$$

We also define a covariant derivative

$$D = \partial + iA . \quad (3.7)$$

To conduct the computation, we will fix the following gauge

$$\begin{aligned} A_0 &= 0 \\ A_1 &= Ex_0 . \end{aligned} \quad (3.8)$$

To have finite energy, we restrict our domain to be  $x_0 \in [0, T], x_1 \in [0, R]$ , but neglect finite size-effects.

Action (3.5) is quadratic and as such can be explicitly computed

$$-S_{eff} = \text{Ln det}(\mathcal{D} + m) \quad (3.9)$$

$$= \frac{1}{2} [\text{TrLn}(\mathcal{D} + m) + \text{TrLn}(\mathcal{D}^T + m)] \quad (3.10)$$

$$= \frac{1}{2} \text{TrLn}(m^2 - \mathcal{D}\mathcal{D}) , \quad (3.11)$$

where we used the cyclicity of the trace and the relation  $\gamma_\mu^T = -C\gamma_\mu C$  with  $C$  the charge conjugation operator. These manipulations are not necessary per se but make the next computations easier.

For convenience, we define the following operators

$$p_\mu = -i\partial_\mu \quad (3.12)$$

$$\Pi_\mu = p_\mu + A_\mu . \quad (3.13)$$

In particular  $\Pi_\mu = -iD_\mu$  and we want to compute

$$-S_{eff} = \frac{1}{2} \text{TrLn}(m^2 + \mathbb{M}\mathbb{M}) . \quad (3.14)$$

We then use Schwinger parametrisation. It is based on the following integrals

$$\log\left(\frac{b}{a}\right) = -\int_0^\infty du \left( \frac{e^{-bu} - e^{-au}}{u} \right) . \quad (3.15)$$

It allows us to rewrite

$$-S_{eff} = \frac{1}{2} \text{TrLn}\left(\frac{m^2 + \mathbb{M}\mathbb{M}}{\mu^2}\right) \quad (3.16)$$

$$= -\frac{1}{2} \int_0^\infty du \text{Tr} \left( \frac{e^{-m^2 u}}{u} \left( e^{-\mathbb{M}\mathbb{M}u} - e^{-(\mu^2 - m^2)u} \right) \right) . \quad (3.17)$$

We also have

$$\mathbb{M}\mathbb{M} = \Pi^2 - E\gamma_5 \quad (3.18)$$

and we focus on computing the traces<sup>2</sup>. Then

$$\text{Tr}(e^{-\mathbb{M}\mathbb{M}u}) = 2 \cosh(fEu) \text{Tr}(e^{-\Pi^2 u}) \quad (3.19)$$

$$= 2 \cosh(fEu) \int dx_0 dx_1 \langle x_0, x_1 | e^{-\Pi^2 u} | x_0, x_1 \rangle \quad (3.20)$$

$$= 2 \cosh(fEu) \int dx_0 dx_1 K_{\mathbb{R} \times S^1}(x_0, x_1, u; x_0, x_1, 0) \quad (3.21)$$

---

<sup>2</sup>With a slight abuse of notation, we use the same symbol to denote operator and matrix traces.

### Chapter 3. A detour to lower dimensions: the Schwinger model

---

with  $x_0, x_1$  labelling a complete basis of position eigen-states and

$$K(x_{b0}, x_{b1}, u; x_{a0}, x_{a1}, 0) = \langle x_{b0}, x_{b1} | e^{-\Pi^2 u} | x_{a0}, x_{a1} \rangle \quad (3.22)$$

is the position-kernel of the operator  $\Pi^2$ .

To compute this kernel, we deviate from reference [38], which solves some operator equations. Here, we present a path integral derivation of this result. Such a kernel admits the following path integral representation

$$K(x_{b0}, x_{b1}, s; x_{a0}, x_{a1}, 0) = C \int_{\substack{x_i(0)=x_{ia} \\ x_i(s)=x_{ib}}} \mathcal{D}x_0 \mathcal{D}x_1 \mathcal{D}p_0 \mathcal{D}p_1 \quad (3.23)$$

$$\exp \left( i \int ds' (p_0 \dot{x}_0 + p_1 \dot{x}_1 - H_{cl}(x_0, p_0, p_1)) \right) \quad (3.24)$$

with  $H_{cl}(x_0, p_0, p_1) = (p_0 - h_0)^2 + (p_1 - Ex_0 - h_1)^2$  and  $C$  is a normalisation constant. This Hamiltonian is nothing else than a two-dimensional harmonic oscillator and the path integral can be done. First, we integrate out the momenta. We get a  $-i\pi$  coefficient coming from the two Gaussian integrations. The remaining exponential is given by  $i$  times the classical action

$$K(x_{b0}, x_{b1}, s; x_{a0}, x_{a1}, 0) = -i\pi C \int_{\substack{x_i(0)=x_{ia} \\ x_i(s)=x_{ib}}} \mathcal{D}x_0 \mathcal{D}x_1 \quad (3.25)$$

$$\exp \left( i \int ds' L_{cl}(x_0, x_1) \right),$$

and  $L_{cl}$  is found to be

$$L_{cl} = \frac{1}{4} (\dot{x}_0^2 + \dot{x}_1^2) - E\dot{x}_1 x_0 - \dot{x}_0 h_0 - \dot{x}_1 h_1. \quad (3.26)$$

Since we are left with a quadratic Lagrangian, the saddle point method will give the exact result. We can write it as

$$K(x_{b0}, x_{b1}, s; x_{a0}, x_{a1}, 0) = -i\pi C \mathcal{N} \exp(i S_{cl}[x_{0a}, x_{1a}, x_{0b}, x_{1b}]) . \quad (3.27)$$

With  $\mathcal{N}$  a fluctuation prefactor, computed later on, and  $S_{cl}[x_{0a}, x_{1a}, x_{0b}, x_{1b}]$  the classical action  $\int ds' L_{cl}(x_0, x_1)$  computed over solutions to the classical equations of motion with boundary conditions  $x_0(0) = x_{0a}, x_1(0) = x_{1a}, x_0(s) = x_{0b}, x_1(s) = x_{1b}$ . They are found to be

$$x_0(s') = \frac{1}{2\cos(Es)} [\sin(E(2s' - s))(x_{0b} - x_{0a}) + \sin(Es)(x_{0b} + x_{0a}) \\ + (\cos(E(2s' - s)) - \cos(Es))(x_{1b} - x_{1a})] \quad (3.28)$$

$$x_1(s') = \frac{1}{2\cos(Es)} [\sin(E(2s' - s))(x_{1b} - x_{1a}) + \sin(Es)(x_{1b} + x_{1a}) \\ - (\cos(E(2s' - s)) - \cos(Es))(x_{0b} - x_{0a})] \quad (3.29)$$

and lead to the following functional

$$\begin{aligned}
 S_{cl}[x_{0a}, x_{1a}, x_{0b}, x_{1b}] = & \frac{1}{4} [E \cot(Es) ((x_{0b} - x_{0a})^2 + (x_{1b} - x_{1a})^2) \\
 & - 2E(x_{0b} + x_{0a})(x_{1b} - x_{1a})] \\
 & - h_0(x_{0b} - x_{0a}) - h_1(x_{1b} - x_{1a}) .
 \end{aligned} \tag{3.30}$$

We compute the prefactor  $\mathcal{N}$  using the Van-Vleck-Pauli-Morette formula [39], which asserts that

$$\mathcal{N}^2 = \det \left( \frac{\partial^2 S_{cl}}{\partial x_{ia} \partial x_{jb}} \right) \tag{3.31}$$

$$= \det \begin{pmatrix} -\frac{1}{2} E \cot(fEs) & -\frac{E}{2} \\ -\frac{E}{2} & -\frac{1}{2} f E \cot(Es) \end{pmatrix} \tag{3.32}$$

$$= \frac{E^2}{4} \frac{1}{\sin(Es)^2} . \tag{3.33}$$

All in all we obtain

$$\begin{aligned}
 K(x_{b0}, x_{b1}, s; x_{a0}, x_{a1}, 0) = & -i\pi C \frac{E}{2} \frac{1}{\sin(Es)} \\
 \exp \left( i \frac{1}{4} [E \cot(Es) ((x_{0b} - x_{0a})^2 + (x_{1b} - x_{1a})^2) \right. \\
 & \left. - 2(E(x_{0b} + x_{0a}))(x_{1b} - x_{1a})] - h_0(x_{0b} - x_{0a}) - h_1(x_{1b} - x_{1a}) \right) .
 \end{aligned} \tag{3.34}$$

We fix  $C$  by requiring that  $\lim_{s \rightarrow 0} K(x_{b0}, x_{b1}, s; x_{a0}, x_{a1}, 0) = \delta^2(x_{ib} - x_{ia})$

$$\begin{aligned}
 \int_{-\infty}^{\infty} dx_{0b} \int_{-\infty}^{\infty} dx_{1b} \lim_{s \rightarrow 0} K(x_{b0}, x_{b1}, s; x_{a0}, x_{a1}, 0) = & \lim_{s \rightarrow 0} -\frac{i\pi C}{2s} \int_{-\infty}^{\infty} dx_{0b} \int_{-\infty}^{\infty} dx_{1b} \\
 \exp \left( i \frac{1}{4} [E \cot(Es) ((x_{0b} - x_{0a})^2 + (x_{1b} - x_{1a})^2) \right. \\
 & \left. - 2(E(x_{0b} + x_{0a}))(x_{1b} - x_{1a})] - h_0(x_{0b} - x_{0a}) - h_1(x_{1b} - x_{1a}) \right)
 \end{aligned} \tag{3.35}$$

$$= 2\pi^2 C \stackrel{(!)}{=} 1 \tag{3.36}$$

and we get  $C = \frac{1}{2\pi^2}$ . At the end of the day, we obtain the expression for the kernel

$$\begin{aligned}
 K(x_{b0}, x_{b1}, s; x_{a0}, x_{a1}, 0) = & -i \frac{E}{4\pi} \frac{1}{\sin(Es)} \\
 \exp \left( i \frac{1}{4} [E \cot(Es) ((x_{0b} - x_{0a})^2 + (x_{1b} - x_{1a})^2) \right. \\
 & \left. - 2(E(x_{0b} + x_{0a}))(x_{1b} - x_{1a})] - h_0(x_{0b} - x_{0a}) - h_1(x_{1b} - x_{1a}) \right) .
 \end{aligned} \tag{3.37}$$



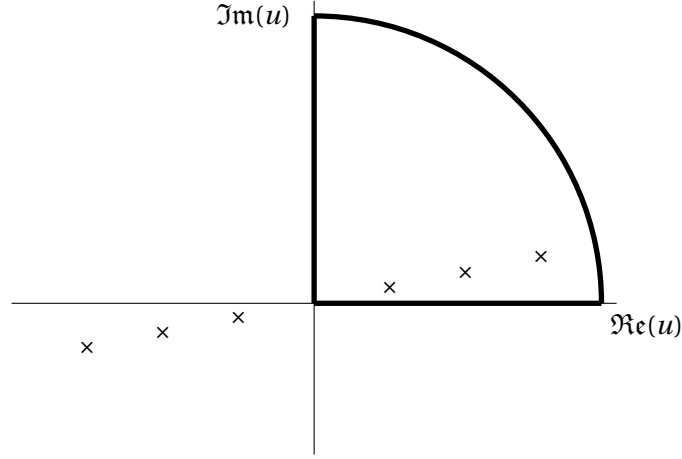


Figure 3.1 – Schwinger prescription and integration contour for the effective action.

With this result at hand, we obtain the following expression for the trace

$$\text{Tr}\left(e^{-\mathbb{M}u}\right) = \frac{RE}{2\pi} \coth(Eu) , \quad (3.38)$$

which leads to, taking  $\mu$  to cancel the  $s=0$  pole of the  $\coth$ ,

$$S_{eff} = \frac{RTE}{4\pi} \int_0^\infty du \frac{e^{-m^2 u}}{u} \left( \coth(Eu) - \frac{1}{Eu} \right) . \quad (3.39)$$

This expression is purely real but this is only because it is the effective action in Euclidean time. To obtain a real-time expression, we need to perform the analytic continuation  $T = iT_M, E = -iE_M$

$$S_M = iS_{eff} = -\frac{RT_ME_M}{4\pi} \int_0^\infty du \frac{e^{-m^2 u}}{u} \left( \cot(E_M u) - \frac{1}{E_M u} \right) . \quad (3.40)$$

Even if not apparent at a first look, this expression has an imaginary part. As such, it is not well defined, as the contour of integration runs over the poles of the cotangent. The correct prescription consists in not fully rotating back  $E \rightarrow e^{-i\pi/2}E_M$  but rather  $E \rightarrow e^{-i(\pi/2+\epsilon)}$ . Equivalently, one can shift the poles as  $u_n = \frac{n\pi}{E_M} e^{i\epsilon}$  and integrate (3.40) over the contour depicted in figure 3.1. The imaginary part is then computed as

$$\int_0^\infty du \frac{e^{-m^2 u}}{u} \left( \cot(E_M u) - \frac{1}{E_M u} \right) = i \int_0^\infty du \frac{e^{-im^2 u}}{u} \left( \coth(E_M u) - \frac{1}{E_M u} \right) + 2\pi i \sum_{n=1}^\infty \frac{e^{-n\pi \frac{m^2}{E_M}}}{n\pi} \quad (3.41)$$

$$\Im \left( \int_0^\infty du \frac{e^{-m^2 u}}{u} \left( \cot(E_M u) - \frac{1}{E_M u} \right) \right) = \Re \left( \int_0^\infty du \frac{e^{-im^2 u}}{u} \left( \coth(E_M u) - \frac{1}{E_M u} \right) \right) + 2 \sum_{n=1}^\infty \frac{e^{-n\pi \frac{m^2}{E_M}}}{n} . \quad (3.42)$$

Now the trick is to realise that the real part of this integral is symmetric under  $u \rightarrow -u$ . As such, we have the following relation

$$\Re \left( \int_0^\infty du \frac{e^{-im^2 u}}{u} \left( \coth(E_M u) - \frac{1}{E_M u} \right) \right) = \frac{1}{2} \Re \left( \int_{-\infty}^\infty du \frac{e^{-im^2 u}}{u} \left( \coth(E_M u) - \frac{1}{E_M u} \right) \right) . \quad (3.43)$$

This last integral can be evaluated using Cauchy's theorem again and receives contributions from the poles at  $u = -i \frac{n\pi}{E_M}$ . All in all, we find

$$\Im \left( \int_0^\infty du \frac{e^{-m^2 u}}{u} \left( \cot(E_M u) - \frac{1}{E_M u} \right) \right) = \sum_{n=1}^\infty \frac{e^{-n\pi \frac{m^2}{E_M}}}{n} \quad (3.44)$$

and thus

$$\Im(S_M) = -\frac{RT_M E_M}{4\pi} \sum_{n=1}^\infty \frac{e^{-n\pi \frac{m^2}{E_M}}}{n} . \quad (3.45)$$

The imaginary part we found is exponentially small, its largest contribution starting to be non-negligible only for strong fields  $E_M \sim m^2$ , as one would expect.

## 3.2 Chiral anomaly

A yet more subtle quantum phenomenon which can be studied with the help of Schwinger model is the one of the chiral anomaly. In the massless case  $m = 0$ , action (3.1) is invariant under global chiral rotations  $\psi \rightarrow e^{i\gamma_5 \alpha} \psi$ . It turns out that the only way, preserving gauge invariance, to quantise the theory breaks this symmetry. In terms of conserved quantities, this means that the axial current  $j_5^\mu = \bar{\psi} \gamma^\mu \gamma^5 \psi$  is not conserved at the quantum level. And its non-conservation is related to the gauge fields as follow

$$\partial_\mu j_5^\mu = \frac{\epsilon_{\mu\nu} F^{\mu\nu}}{2\pi} . \quad (3.46)$$

This section will aim at computing this relation in two different ways. For an extensive review and plenty of different derivations of the chiral anomaly in the Schwinger model, we refer the

reader to reference [40].

### 3.2.1 Path integral measure

The first derivation we want to present will be in the path integral formalism, as first introduced in reference [41], following the presentation of [40] and [42]. The breaking of chiral symmetry upon quantisation has a clear origin when thinking in terms of functional integral. Indeed, the action is not the only ingredient that needs to be invariant under a given symmetry; fields also enter the computation through the measure. And in the case of the chiral anomaly, this object is precisely not invariant and leads to the equation (3.46). To see so, we will explicitly compute how the fermionic path integral

$$\int \mathcal{D}\psi \mathcal{D}\bar{\psi} e^{-\int d^2x \bar{\psi}(\partial + i\mathbb{A})\psi} \quad (3.47)$$

transforms under an infinitesimal space-time dependent chiral rotation

$$\psi \rightarrow (1 + i\gamma^5 \epsilon) \psi \quad (3.48)$$

$$\bar{\psi} \rightarrow \bar{\psi} (1 + i\gamma^5 \epsilon) . \quad (3.49)$$

As we already know by Noether theorem, from the invariance of the action when  $\epsilon$  is constant, we will have

$$\int d^2x \bar{\psi} (\partial + i\mathbb{A}) \psi \rightarrow \int d^2x \bar{\psi} (\partial + i\mathbb{A}) \psi + \int d^2x \epsilon \partial_\mu J_5^\mu . \quad (3.50)$$

To compute the transformation of the measure, let us assume that we are working on a manifold such that  $i\mathbb{D}$  is a hermitian operator and that we have at hand a basis made out of its eigenfunctions

$$i\mathbb{D}\phi_n = \lambda_n \phi_n \quad (3.51)$$

$$\psi = \sum_n a_n \phi_n \quad (3.52)$$

$$\bar{\psi} = \sum_n b_n \phi_n^\dagger \quad (3.53)$$

$$\sum_n \phi_n(x) \phi_n^\dagger(y) = \delta^2(x - y) \quad (3.54)$$

$$\int d^2x \phi_m^\dagger(x) \phi_n(x) = \delta_{mn} , \quad (3.55)$$

with  $a_n, b_n$  anti-commuting Grassmann numbers. It transforms the fermionic measure as a product of the expansion coefficients

$$\mathcal{D}\psi \mathcal{D}\bar{\psi} = \prod_n da_n db_n , \quad (3.56)$$

and what is left to do is to understand how it transforms under an infinitesimal chiral rotation (3.48). Writing it out explicitly, we have

$$\sum_n a_n \phi_n \rightarrow \sum_n (a_n \phi_n + i\gamma^5 \epsilon a_n \phi_n) \equiv \sum_n a'_n \phi_n \quad (3.57)$$

$$\sum_n b_n \phi_n^\dagger \rightarrow \sum_n (b_n \phi_n^\dagger + b_n \phi_n^\dagger i\gamma^5 \epsilon) \equiv \sum_n b'_n \phi_n^\dagger \quad (3.58)$$

To rewrite that as an expansion over the  $\phi_n$  basis (recall that  $\gamma_5 \phi_n$  is not a basis eigenfunction), we extract the relevant coefficients  $a'_n$  using orthonormality (3.55)

$$a'_n = a_n + \sum_m \int d^2 x a_m \phi_n^\dagger i\gamma^5 \epsilon \phi_m \quad (3.59)$$

$$b'_n = b_n + \sum_m \int d^2 x b_m \phi_m^\dagger i\gamma^5 \epsilon \phi_n . \quad (3.60)$$

The associated Jacobian is given by

$$\mathcal{J} = \prod_n (1 + \text{Tr} \int d^2 x \phi_n^\dagger i\gamma^5 \epsilon \phi_n)^2 \quad (3.61)$$

or in exponential form as

$$\mathcal{J} = \exp \left( -2i \text{Tr} \int d^2 x \epsilon \sum_n \phi_n^\dagger \gamma_5 \phi_n \right) . \quad (3.62)$$

As  $\phi_n$  and  $\phi_n^\dagger$  are evaluated at the same point, this sum is divergent and needs to be regulated. A convenient way to do it is to rewrite it as follow

$$\sum_n \phi_n^\dagger \gamma^5 \phi_n = \sum_n \lim_{M \rightarrow \infty} \phi_n^\dagger \gamma^5 e^{-\frac{\lambda_n^2}{M^2}} \phi_n = \sum_n \lim_{M \rightarrow \infty} \phi_n^\dagger \gamma^5 e^{-\frac{(iD)^2}{M^2}} \phi_n \quad (3.63)$$

and define a regulated sum by swapping the limit and the sum. We are then left to evaluate

$$\lim_{M \rightarrow \infty} \sum_n \phi_n^\dagger \gamma^5 e^{-\frac{(iD)^2}{M^2}} \phi_n . \quad (3.64)$$

We expand  $\phi_n, \phi_n^\dagger$  in Fourier modes

$$\text{Tr} \sum_n \phi_n^\dagger \gamma^5 e^{-\frac{(iD)^2}{M^2}} \phi_n = \frac{1}{4\pi^2} \text{Tr} \int \int dk^2 dk'^2 \sum_n \phi_n^\dagger(k) e^{-ikx} \gamma^5 e^{-\frac{(iD)^2}{M^2}} \phi_n(k') e^{ik'x} \quad (3.65)$$

$$= \frac{1}{4\pi^2} \text{Tr} \gamma^5 \int dk^2 e^{-ikx} e^{-\frac{(iD)^2}{M^2}} e^{ikx} , \quad (3.66)$$

### Chapter 3. A detour to lower dimensions: the Schwinger model

where we used the cyclicity of the trace to reorder the expression together with the orthonormality (3.54) to perform one of the momentum integral. Once again, we have

$$-D^2 = -\gamma^\mu \gamma^\nu D_\mu D_\nu \quad (3.67)$$

$$= -\frac{1}{2} (\gamma^\mu \gamma^\nu D_\mu D_\nu + \gamma^\nu \gamma^\mu D_\nu D_\mu) \quad (3.68)$$

$$= -\frac{1}{2} (\gamma^\mu \gamma^\nu D_\mu D_\nu - \gamma^\mu \gamma^\nu D_\nu D_\mu + 2D^2) \quad (3.69)$$

$$= -D^2 - \frac{1}{2} \gamma^\mu \gamma^\nu [D_\mu D_\nu] \quad (3.70)$$

$$= -D^2 + i \frac{1}{2} \gamma^5 \epsilon^{\mu\nu} F_{\mu\nu} \quad (3.71)$$

and also

$$D^2 = (\partial^2 - A^2 + 2iA^\mu \partial_\mu + i\partial_\mu A^\mu) . \quad (3.72)$$

This leads to

$$\text{Tr} \gamma^5 e^{-\frac{i}{2} \gamma^5 \epsilon^{\mu\nu} F_{\mu\nu}} \int d^2 k e^{-ikx} e^{\frac{D^2}{M^2}} e^{ikx} = \text{Tr} \gamma^5 e^{\frac{1}{M^2} (-\frac{i}{2} \gamma^5 \epsilon^{\mu\nu} F_{\mu\nu} - \partial_\mu A^\mu)} \int d^2 k e^{-ikx} e^{\frac{1}{M^2} (-k^2 - 2A_\mu k^\mu)} e^{ikx} \quad (3.73)$$

$$= \text{Tr} \gamma^5 e^{\frac{1}{M^2} (-\frac{i}{2} \gamma^5 \epsilon^{\mu\nu} F_{\mu\nu} - \partial_\mu A^\mu)} \int d^2 k e^{\frac{1}{M^2} (-k^2 - 2A_\mu k^\mu)} \quad (3.74)$$

$$= \text{Tr} \gamma^5 e^{\frac{1}{M^2} (-\frac{i}{2} \gamma^5 \epsilon^{\mu\nu} F_{\mu\nu} - \partial_\mu A^\mu)} \int dk k e^{-\frac{k^2}{M^2}} \int d\theta e^{-\frac{2A_\mu k^\mu}{M^2}} . \quad (3.75)$$

We want now to keep only the terms which survive the  $M \rightarrow \infty$  limit. To do so, we do the change of variable  $k' = \frac{k}{M}$

$$\text{Tr} \gamma^5 e^{\frac{1}{M^2} (-\frac{i}{2} \gamma^5 \epsilon^{\mu\nu} F_{\mu\nu} - \partial_\mu A^\mu)} M^2 \int dk' k' e^{-k'^2} \int d\theta e^{-\frac{2Ak' \cos \theta}{M}} . \quad (3.76)$$

The only terms from the integral which survives both the limit  $M \rightarrow \infty$  and the trace will be the one of order one. Namely,

$$\int dk' k' e^{-k'^2} \int d\theta e^{-\frac{2Ak' \cos \theta}{M}} \sim 2\pi \int_0^\infty dk' k' e^{-k'^2} = \pi . \quad (3.77)$$

Finally, we get

$$\lim_{M \rightarrow \infty} \sum_n \phi_n^\dagger \gamma^5 e^{-\frac{(iD)^2}{M^2}} \phi_n = -\frac{i\epsilon_{\mu\nu} F^{\mu\nu}}{4\pi} \quad (3.78)$$

and the Jacobian (3.62) reads

$$\mathcal{J} = e^{-\int d^2 x \epsilon \frac{\epsilon_{\mu\nu} F^{\mu\nu}}{2\pi}} . \quad (3.79)$$

Altogether, the fermionic path integral (3.47) transforms as

$$\int \mathcal{D}\psi \mathcal{D}\bar{\psi} e^{-\int d^2 x \bar{\psi} (\partial + iA) \psi} \rightarrow \int \mathcal{D}\psi \mathcal{D}\bar{\psi} e^{-\int d^2 x \bar{\psi} (\partial + iA) \psi} \left( 1 + \int d^2 x \epsilon \left( \partial_\mu j_5^\mu - \frac{\epsilon_{\mu\nu} F^{\mu\nu}}{2\pi} \right) \right) \quad (3.80)$$

keeping only the leading terms in  $\epsilon$ . However, such a transformation is just a field redefinition and cannot change the path integral. It imposes that

$$\partial_\mu j_5^\mu = \frac{\epsilon_{\mu\nu} F^{\mu\nu}}{2\pi} \quad (3.81)$$

with this identity understood as a quantum average. This is the anomaly equation (3.46). This derivation shows that the anomaly can be understood as a quantum violation of Noether theorem, coming from the non-invariance of the fermionic measure in the path integral.

#### 3.2.2 Levels crossing

Even if the last derivation in terms of path integral clearly identifies the origin of the anomaly, it does not give much physical intuition about what is going on. Such intuition can be gained by understanding the energy spectrum of the theory in terms of chirality eigenstates and how it depends on the "electromagnetic" field. We will see that the anomaly can be understood as a "Hilbert's hotel"-like rearrangement of the spectrum caused by  $\epsilon_{\mu\nu} F^{\mu\nu}$ . This section is inspired from references [40, 43]. We also refer the interested reader to reference [44].

Let us consider again the massless Schwinger model. To regularise it, we will this time consider it on a spatial circle of length  $R$  and for tractability we will neglect the backreaction of fermions on the gauge field; in other words, we will treat  $A_\mu$  as an external background field. We moreover fix the gauge such that

$$A_0 = 0 \quad (3.82)$$

$$A_1 = A_1(t) . \quad (3.83)$$

We will want to compute the energy spectrum associated with the one-particle problem. As such, we can directly work in Minkowski space, with the following Lagrangian density

$$\mathcal{L} = \bar{\psi} i \mathcal{D} \psi , \quad (3.84)$$

which leads to the following Dirac equation

$$\mathcal{D} \psi = 0 . \quad (3.85)$$

In this context, it is best rewritten in terms of left and right-handed modes. Explicitly, choosing the following representation for the Minkowski  $\gamma$ -matrices

$$\gamma^0 = \begin{pmatrix} 0 & -i \\ i & 0 \end{pmatrix} , \quad \gamma^1 = \begin{pmatrix} 0 & -i \\ -i & 0 \end{pmatrix} , \quad \gamma^5 = \begin{pmatrix} -1 & 0 \\ 0 & 1 \end{pmatrix} , \quad (3.86)$$

we get

$$\begin{pmatrix} (i\partial_t + i\partial_x - A_1)\psi_R \\ (-i\partial_t + i\partial_x - A_1)\psi_L \end{pmatrix} = \begin{pmatrix} 0 \\ 0 \end{pmatrix}. \quad (3.87)$$

We need to choose boundary conditions for the fermions and we will take them to be antiperiodic, as would be done in a thermal setting, but periodic fermions would be as appropriate and lead to the same answer [43]. Thanks to this antiperiodicity, we have the following modes decomposition

$$\psi = \frac{1}{R} \sum_n \psi_n(t) e^{i \frac{2\pi(n+1/2)}{R} x}. \quad (3.88)$$

To find the energy spectrum, we consider left and right stationary waves

$$\phi_n^L(t) = \begin{pmatrix} e^{-iE_n^L t} \\ 0 \end{pmatrix}, \quad \phi_n^R(t) = \begin{pmatrix} 0 \\ e^{-iE_n^R t} \end{pmatrix}. \quad (3.89)$$

Plugging this back in equation (3.85), we find by comparison

$$E_n^{L/R} = \mp \left( n + \frac{1}{2} \right) \frac{2\pi}{R} \pm A_1. \quad (3.90)$$

Note that these stationary waves are a good approximation only when the time derivative of  $A_1$  can be neglected, which can always be engineered in this situation as  $A_1$  is treated as a background field under control.

A key discussion which has been missing up to now is what are the acceptable values for  $A_1$ . Schwinger model is a gauge theory invariant under gauge transformations of the type

$$\psi \rightarrow e^{i\alpha(t,x)} \psi. \quad (3.91)$$

It is enough to require invariance under *local* gauge transformations, i.e. gauge transformations for which  $\alpha(t, x)$  is continuous. On the circle, it is equivalent to ask for  $\alpha$  to be periodic  $\alpha(t, x+R) = \alpha(t, x)$ . Coincidentally, there is class of gauge transformations with discontinuous gauge function  $\alpha$  which also leaves invariant the theory. They are called *large* gauge transformations and are of the type  $\alpha_{large}(x, t) = \frac{2\pi n}{R} x$ . Their effect is simply to shift the gauge potential by a constant

$$A_1(t) \rightarrow A_1(t) + \frac{2\pi n}{R}. \quad (3.92)$$

In practice, this means that we can restrict  $A_1$  to be in the range  $[0, \frac{2\pi n}{R})$ ;  $A_1$  is naturally the coordinate of a circle.

Keeping this in mind, we can now draw the spectrum as a function of  $A_1$  and we get picture 3.2. We see that for non-zero values of  $A_1$ , the energy levels of left and right-handed particles

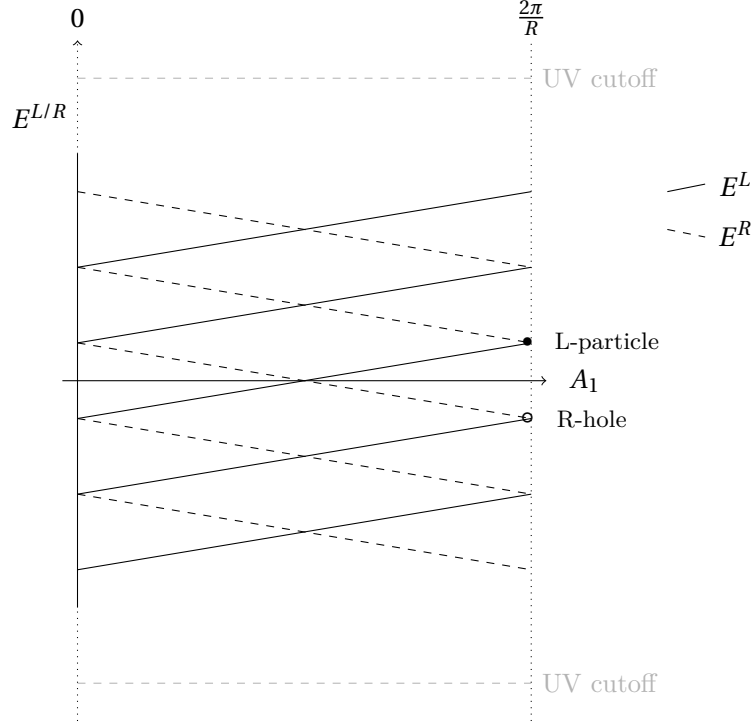


Figure 3.2 – Energy levels of left and right-handed particles in a background field  $A_1$ . The spectrum is degenerate only when  $A_1 \propto \frac{2\pi n}{R}$ .  $n \in \mathbf{N}$ . An adiabatic evolution of  $A_1$  by  $\frac{2\pi n}{R}$  reshuffles the spectrum and can be understood as the creation of left or right-handed particles. If the theory has a UV cutoff, the level crossing can be monitored there instead.

are not degenerate anymore, up until  $A_1$  reaches the value  $\frac{2\pi}{R}$ . At this point, the energies are again degenerate but the whole spectrum has reordered itself. Every right-handed level has been shifted upwards while every left-handed one has been shifted downwards. The physical consequences of this reordering of the spectrum can be understood by considering a state which is a vacuum sea *a la* Dirac. Take a state where all negative energy states are filled. Now turn on adiabatically  $A_1$  from 0 to  $\frac{2\pi}{R}$ . At this value, the energy states are again degenerate, but now a left-handed particle was created together with right-handed "hole", which in this picture is interpreted as a right-handed anti-particle. During this process, the vector ("electric") charge is conserved, as the hole and the particle have opposite vector charges, but the axial charge changes by two units, since both the hole and the particle have an axial charge of one

$$\Delta Q_A = 2. \quad (3.93)$$

In other words, every time  $A_1$  go through a period, the axial charge changes by two units, which can also be written per unit time as

$$\frac{\Delta Q_A}{\Delta t} = \frac{R}{\pi} \frac{\Delta A_1}{\Delta t}. \quad (3.94)$$



### Chapter 3. A detour to lower dimensions: the Schwinger model

---

In terms of the axial current, this is nothing else but the anomaly equation (3.46).

What may appear as surprising with respect to this derivation of the anomaly is the fact that it appears as an IR phenomenon, namely a reordering of the energy spectrum around the ground state, while in the path integral derivation it was clearly a UV effect. These two sides of the anomaly are a generic property. To illustrate this, we will present here a UV-derivation from the one-particle solution (3.89), following [40].

We can try to directly compute the currents on the Dirac sea. Before doing so we need to regularise them as the sum over infinitely many negative energy states do not converge. As in reference [40], we use the gauge-invariant point-splitting regularisation, introduced in reference [32]. The idea consists in tracking down the UV divergence to the fact that we want to evaluate the product of operators at the same point. One of the correlators is moved by an  $\epsilon$  and gauge invariance is maintained by introducing the appropriate parallel transporter  $e^{-i \int_x^{x+\epsilon} dx A_1}$

$$j^\mu = \lim_{\epsilon \rightarrow 0} \bar{\psi}(t, x + \epsilon) \gamma^\mu \psi(t, x) e^{-i \int_x^{x+\epsilon} dx A_1} \quad (3.95)$$

$$j_5^\mu = \lim_{\epsilon \rightarrow 0} \bar{\psi}(t, x + \epsilon) \gamma^\mu \gamma^5 \psi(t, x) e^{-i \int_x^{x+\epsilon} dx A_1} . \quad (3.96)$$

Explicitly, our Dirac sea is

$$\psi^D(t, x) = \frac{1}{R} \sum_{n=-1}^{-\infty} \phi_n^L(t) e^{i \frac{2\pi(n+1/2)}{R} x} + \frac{1}{R} \sum_{n=0}^{\infty} \phi_n^R(t) e^{i \frac{2\pi(n+1/2)}{R} x} . \quad (3.97)$$

We want to compute the associated charges

$$Q = \lim_{\epsilon \rightarrow 0} \int dx j^0 \quad (3.98)$$

$$Q_A = \lim_{\epsilon \rightarrow 0} \int dx j_5^0 . \quad (3.99)$$

To do so, we consider

$$j_D^\mu = \frac{1}{R} \lim_{\epsilon \rightarrow 0} \left( \sum_{n=-1}^{-\infty} e^{i \frac{2\pi(n+1/2)}{R} \epsilon} + \sum_{n=0}^{\infty} e^{i \frac{2\pi(n+1/2)}{R} \epsilon} \right) e^{-i \int_x^{x+\epsilon} dx A_1} \quad (3.100)$$

$$j_{5D}^\mu = \frac{1}{R} \lim_{\epsilon \rightarrow 0} \left( \sum_{n=-1}^{-\infty} e^{i \frac{2\pi(n+1/2)}{R} \epsilon} - \sum_{n=0}^{\infty} e^{i \frac{2\pi(n+1/2)}{R} \epsilon} \right) e^{-i \int_x^{x+\epsilon} dx A_1} . \quad (3.101)$$

The left and right-handed charges of the Dirac sea are then obtained as

$$Q^{L/R} = \frac{1}{2} (Q \pm Q_A) . \quad (3.102)$$

Remembering the fact that  $A_1$  is constant, we get

$$Q^L = \lim_{\epsilon \rightarrow 0} \sum_{n=-1}^{-\infty} e^{i\epsilon(\frac{2\pi(n+1/2)}{R} - A_1)} = \lim_{\epsilon \rightarrow 0} -\frac{ie^{-i\epsilon A_1}}{2\sin(\frac{\pi\epsilon}{R})} = -\frac{iR}{2\pi\epsilon} - \frac{A_1 R}{2\pi} \quad (3.103)$$

$$Q^R = \lim_{\epsilon \rightarrow 0} \sum_{n=0}^{\infty} e^{i\epsilon(\frac{2\pi(n+1/2)}{R} - A_1)} = \lim_{\epsilon \rightarrow 0} \frac{ie^{-i\epsilon A_1}}{2\sin(\frac{\pi\epsilon}{R})} = \frac{iR}{2\pi\epsilon} + \frac{A_1 R}{2\pi} . \quad (3.104)$$

This leads to  $Q = 0$ , as expected. On the other hand, we find

$$Q_A = \frac{iR}{\pi\epsilon} + \frac{A_1 R}{\pi} . \quad (3.105)$$

The divergent piece is subtracted off and we find a regulated  $Q_A$

$$Q_A = \frac{A_1 R}{\pi} \quad (3.106)$$

which leads to the anomaly in the form of equation (3.94).

In this case, the anomaly can be interpreted simultaneously as a UV and IR effect has an intuitive interpretation [43]. When considering the rearrangement of the spectrum (3.94), we counted how many levels crossed zero. Imagining now that the theory has some UV cutoff on highly excited states, the number of levels crossing zero is equal to the number of processes going beyond the cutoff. As such, it makes sense that the variation of  $A_1$  can be monitored by tracking out what happens there.

We encountered three different ways of computing the chiral anomaly. The first, computing the variation of the path integral measure, precisely pinpoints how a classical symmetry may not be a quantum one. The second and third, using the idea of level crossing and of Dirac sea, require more hand-waving but provide a physical intuition about what the anomaly is; the variation of the gauge field leads to a reshuffling of the matter energy spectra, leading to potential particle creation.

These are by far not the only ways to compute and understand the chiral anomaly. One can, for example, understand it as emerging from loop diagrams in the perturbative expansion; it is actually how this phenomenon was discovered [45, 46]. Another approach which sheds yet a different light on the phenomenon is the so-called index theorem, which predicts the anomaly from a purely geometrical perspective. Indeed, at least on compact manifolds,  $F_{\mu\nu}$  or its higher-dimensional equivalent is related to the number of left-handed minus the number of right-handed zero-modes of the Dirac operator, see for example [47].



## 4 A second look at gauge theories

The quantum rotor and the Schwinger model allowed us to introduce a variety of subtle effects in quantum theories. It is now time to move back to four dimensions and discuss how these effects manifest themselves in theories relevant to Nature. In particular, in this chapter, we will discuss why non-Abelian theories have an intrinsically complicated vacuum structure. Then, as quantum field theories in four dimensions are not analytically solvable and often numerical investigations can be of help, we will explain how one can discretise gauge theories preserving gauge invariance.

### 4.1 Topology and $\theta$ -vacuum

We want to start by discussing the vacuum structure of non-Abelian field theories. We will first see that, semiclassically, contributions to the path integral of non-Abelian theories can be sorted into different disconnected sectors. These sectors are interpreted as emerging from the non-trivial topology of the gauge group itself. They are tied to the existence of inequivalent classical-vacua which can be connected only by a class of "discrete" gauge transformations, the so-called large gauge transformations. As in the case of the quantum rotor, this picture leads to the existence of a  $\theta$ -vacuum, which can also be understood in terms of a Hamiltonian description and is tied to the existence of a non-zero topological susceptibility.

#### 4.1.1 Semiclassics, instantons and $|n\rangle$ -vacua

To keep the discussion simple, we will focus on the gauge group  $SU(2)$ . To try to gain some insights into the theory, we start from the Euclidean action

$$S_{SU(2)}^E = \frac{1}{g^2} \int d^4x \frac{1}{2} \text{Tr} (G_{\mu\nu} G^{\mu\nu} + i\theta \text{Tr} (G_{\mu\nu} \tilde{G}^{\mu\nu})) , \quad (4.1)$$

where we kept the  $\theta$ -term for the sake of generality and conventionally rescaled the field by the coupling constant  $g$ . Note that upon analytic continuation, the  $\theta$ -term picks up a factor of  $i$ .

We can now try to develop a semiclassical picture. This corresponds to a saddle point approximation of the corresponding path integral, so the first step is to find the saddle points. By definition, they are the stationary point of the classical action and as such are solutions to the classical equations of motion

$$D_\mu G^{\mu\nu} = 0 , \quad (4.2)$$

with  $G^{\mu\nu} \rightarrow 0$  at infinity. The trivial saddle  $G^{\mu\nu} = 0$  corresponds to an absolute minimum of the classical action and dominates the path integral. It is however not the only solution to the equations of motion. In particular, one can explicitly check that, for example,

$$\left( A_\mu^{inst.} \right)^a = \eta_{\mu\nu a} x^\nu \tau^a \frac{1}{r^2 + \rho^2} \quad (4.3)$$

$$\left( G_{\mu\nu}^{inst.} \right)^a = -2\eta_{\mu\nu a} \tau^a \frac{\rho^2}{(r^2 + \rho^2)^2} , \quad (4.4)$$

solve the equations of motion, see for example [11]. The symbols  $\eta_{\mu\nu a}$  are the t'Hooft symbols, whose non-vanishing components are given by

$$\eta_{0ia} = -\eta_{i0a} = \delta_{ia} \quad (4.5)$$

$$\eta_{ija} = \epsilon_{ija} . \quad (4.6)$$

The matrices  $\tau^a = \frac{\sigma^a}{2}$  with  $\sigma^a$  the Pauli matrices are taken as  $SU(2)$ 's generators. The parameter  $\rho$  is a free parameter and as such (4.3) and (4.4) are a one parameter family of solutions. Finally,  $r^2 = t^2 + x^i x_i$  is the Euclidean radius.

A key property of (4.4) is that it is a self-dual solution, in the sense that  $G_{\mu\nu} = \tilde{G}_{\mu\nu}$ . As such, the associated classical action is given by

$$S^{inst.} = \frac{8\pi^2}{g^2} (1 + i\theta) . \quad (4.7)$$

Remarkably, even though it is a total derivative, the term  $G_{\mu\nu} \tilde{G}^{\mu\nu}$  leads to a non-vanishing contribution to the action. This is very reminiscent of what happened in the case of the quantum rotor in section 2.1. There, the non-zero contribution could be associated to configurations with a non-trivial topology. The related observable was

$n = \frac{1}{R} \int d\tau \dot{x} = \frac{1}{R} (x(\beta) - x(0))$ . The solution with  $n = 1$  was the one with  $\dot{x} = \frac{R}{\beta}$ ; interpolating from the point  $x = 0$  to  $x = R$ .

Building on this analogy, we see that a quantity that may be of interest is the Chern-Simons form (1.51). To have a clear interpretation, we will work in the gauge  $A_0 = 0$ . Before transforming (4.3) and (4.4) into this gauge, let us define the Chern-Simons number

$$n_{cs}(t) = \int d^3x K^0 . \quad (4.8)$$

In the temporal gauge and taking into account  $G_{\mu\nu} \rightarrow 0$  at infinity, we have

$$\int d^4x \text{Tr}(G_{\mu\nu} \tilde{G}^{\mu\nu}) = \int_{-\infty}^{\infty} dt \partial_0 n_{cs}(t) \quad (4.9)$$

$$= n_{cs}(\infty) - n_{cs}(-\infty) . \quad (4.10)$$

More interestingly, we can now try to understand why this total derivative contributes to the action. As per the boundary conditions on the field strength  $G_{\mu\nu} \rightarrow 0$ , we have that

$$n_{cs}(\pm\infty) = -\frac{2}{3} \int d^3x \epsilon^{ijk} \text{Tr}(A_i A_j A_k) . \quad (4.11)$$

Moreover, to obtain  $G_{\mu\nu} \rightarrow 0$ , we need the gauge potential to asymptote to a pure gauge configuration

$$A_\mu \rightarrow i\Omega_{\pm\infty} \partial_\mu \Omega_{\pm\infty}^{-1}, \quad (4.12)$$

with  $\Omega_{\pm\infty}$  some  $SU(2)$  transformations. Plugging this back in (4.13), we obtain an expression of the form

$$n_{cs}(\pm\infty) = -\frac{2}{3} \int d^3x \epsilon^{ijk} \text{Tr}((\Omega_{\pm\infty} \partial_i \Omega_{\pm\infty}^{-1})(\Omega_{\pm\infty} \partial_j \Omega_{\pm\infty}^{-1})(\Omega_{\pm\infty} \partial_k \Omega_{\pm\infty}^{-1})) . \quad (4.13)$$

Following [11], we can compute explicitly what are the  $\Omega_\pm$  associated to (4.3) and (4.4). We are looking for a gauge transformation  $\Omega$

$$A_\mu^{inst} \rightarrow A_\mu^t = \Omega A_\mu^{inst} \Omega^{-1} - i \partial_\mu \Omega \Omega^{-1} . \quad (4.14)$$

The requirement  $A_0^t = 0$  imposes

$$\Omega^{-1} \partial_0 \Omega = A_0^{inst} = x_a \tau_a \frac{1}{x_i x^i + t^2 + \rho^2} , \quad (4.15)$$

which determines  $\Omega$  up to a gauge transformation which depends only on spatial coordinates. This remaining gauge freedom is just enough to set

$$\lim_{t \rightarrow -\infty} A_i^t = i \Omega_{-\infty} \partial_i \Omega_{-\infty}^{-1} = 0 , \quad (4.16)$$

where we used the fact that  $A_\mu^{inst} \rightarrow 0$  at  $t \pm \infty$  and thus  $\Omega_{\pm\infty} = \lim_{t \rightarrow \pm\infty} \Omega$ . Without loss of generality we thus set  $\Omega_- = 1$ . This acts as a boundary condition for (4.15) and allows to solve it explicitly. One then finds [11]

$$\Omega = e^{-i\tau^a \hat{x}^a F(x^i x_i, t)} , \quad (4.17)$$

$$F(x^i x_i, t) = \frac{\sqrt{x_i x^i}}{\sqrt{x_i x^i + \rho^2}} \left( \arctan \left( \frac{t}{\sqrt{x_i x^i + \rho^2}} \right) + \frac{\pi}{2} \right) , \quad (4.18)$$

with  $\hat{x}$  a unit vector of three-dimensional space. The advantage of having this explicit solution is that we can find the  $t \rightarrow \infty$  asymptote explicitly

$$\Omega_{+\infty} = e^{-i\tau^a \hat{x}^a F_1(x^i x_i)} \quad (4.19)$$

$$F(x^i x_i)_1 = \pi \frac{\sqrt{x_i x^i}}{\sqrt{x_i x^i + \rho^2}} . \quad (4.20)$$

This tells us that the classical solution (4.3) and (4.4), expressed in temporal gauge and after fixing the residual gauge redundancy, interpolate a vacuum state with  $A_\mu = 0$  to another with  $A_\mu$  a pure gauge different from zero. This may come as a surprise, as one might have thought that all pure gauge solutions to be strictly equivalent. As we just saw explicitly, this is not the case and can be understood by studying the internal structure of the gauge group. As explained in details in references [11] and [42], picking one or another  $\Omega_{\pm\infty}$  at infinity in our four-dimensional Euclidean space can be understood as a mapping from the three-sphere into  $SU(2)$ . For  $SU(2)$  (and any simple Lie group), such mappings split into a countable infinity of different families such that one cannot take a representative of a given family and continuously deform it into a representative of a different family. Moreover, one can assign a numbering to this set of family through some topological invariant. For  $SU(2)$ , the relevant invariant, sometimes called the Cartan-Maurer form [42], is

$$n[\Omega] = \frac{1}{24\pi^2} \int d^3 x \epsilon^{ijk} \text{Tr}((\Omega \partial_i \Omega^{-1})(\Omega \partial_j \Omega^{-1})(\Omega \partial_k \Omega^{-1})) . \quad (4.21)$$

Up to normalisation, it is nothing more than equation (4.13). Our non-Abelian theories possess different vacua, labelled by an integer, which can be retrieved by computing the Cartan-Maurer invariant. The Chern-Simons number is the Cartan-Maurer invariant when evaluated on vacuum configurations; for configurations that interpolate between different vacuum, it keeps track how many families apart the vacua are. Gauge transformations which are not smoothly connected to the identity are sometimes called large-gauge transformations.

These interpolating configurations, the "instantons" solutions, can be characterised by their topological charge

$$Q = \frac{1}{16\pi^2} \int d^4 x \text{Tr}(G_{\mu\nu} \tilde{G}^{\mu\nu}) , \quad (4.22)$$

which is nothing else than, in temporal gauge, the difference between Chern-Simons numbers. For instantons,  $Q$  is an integer. For generic fields, as in the case of the quantum rotor, this will depend on boundary conditions.

To summarise, we presented a non-trivial solution to the classical equations of motion for  $SU(2)$ , whose natural interpretation led us to discover that the theory has a set of disconnected vacuum. The solution (4.3) and (4.4) are referred to as "instantons" and they can be interpreted as tunnelling events from one to a neighbouring vacuum. This is embodied in the so-called topological charge, which is equal to one in the case of (4.3) and (4.4). From a semiclassical perspective, one has solutions with charges  $Q \in \mathbb{Z}$  and the path-integral can be

evaluated around these different saddles. For generic fields, the values of  $Q$  will depend on the boundary conditions imposed on the theory and may or may not be integer-valued.

#### 4.1.2 The $\theta$ -Vacuum

As in the case of the quantum rotor in section 2.1, the existence of a degenerate set of inequivalent vacua is tied to the existence of a  $\theta$ -parameter. We will see in this section that it can be understood beyond semiclassics from a Hamiltonian perspective.

Relevant references related to this discussion are [48–50]. We start with the following  $SU(N)$  Lagrangian (with no  $\theta$ -term) in Minkowski space

$$\mathcal{L} = -\frac{1}{2g^2} \text{Tr}(G_{\mu\nu} G^{\mu\nu}) . \quad (4.23)$$

We then move on and apply Dirac's procedure to canonically quantise the theory [51]. We represent the Lagrangian  $\mathcal{L}$  in terms of a generalised Hamiltonian  $\mathcal{H}$  of the form

$$\mathcal{L} = \frac{1}{2g^2} \left( \int d^3x B^a{}^i \dot{A}_i^a - \mathcal{H} + \int d^3x \partial_i B^a{}^i A_0^a \right) \quad (4.24)$$

$$\mathcal{H} = \int d^3x \left( \frac{1}{2} (B_i^a)^2 + \frac{1}{4} (F_{ij}^a)^2 \right) . \quad (4.25)$$

The extra part is to take into account Gauss law as a constraint

$$\partial^i B_i^a = 0 . \quad (4.26)$$

In this sense,  $A_0^a$  is not a dynamical variable but act as a Lagrange multiplier for the constraint. We further define the operator associated with Gauss law

$$G[A_0^a] = \int d^3x \partial_i B^a{}^i A_0^a . \quad (4.27)$$

For our purpose, we will not need to proceed through the whole associated quantisation procedure. The first comment we want to make is that the operator  $G[A_0^a]$  is the generator of gauge transformations with gauge function  $A_0^a$  [49]. It is seen by computing the associated classical Poisson-bracket

$$\{G[A_0], A_i^a\} = [A_i, A_0]^a + \partial_i A_0^a , \quad (4.28)$$

which is nothing else than the infinitesimal version of transformation (1.41). We recall the reader that the Poisson bracket are defined as, with  $p$  and  $q$  a pair of conjugate field variables and  $f$  and  $g$  arbitrary functions of them

$$\{f(p, q), g(p, q)\} = \frac{\delta f}{\delta q} \frac{\delta g}{\delta p} - \frac{\delta f}{\delta p} \frac{\delta g}{\delta q} , \quad (4.29)$$



with  $\frac{\delta f}{\delta q}$  standing for a functional derivative.

Restricting ourselves to continuous Lagrange parameters, we see that  $G[A_0]$  generates only gauge transformations which are connected to the identity. In the quantum theory, the physical Hilbert space is singled out by the condition

$$G[A_0]|\Psi_{phys.}\rangle = 0. \quad (4.30)$$

In the previous section, we saw that not all gauge transformations can be continuously obtained from the identity. Consider for example  $\Omega^1$  a large gauge transformation, of Cartan-Maurer index  $n = 1$ . It can be written as  $\Omega^1 = e^{iG[A_0^1]}$ , with  $A_0^1$  not smoothly connected to zero. As in the case of the quantum rotor and "large" translations of  $R$ , since  $G[A_0^1]$  commutes with the Hamiltonian, the operator  $\Omega^1$  can be simultaneously diagonalised with the Hamiltonian. Then, physical states can be classified according to the eigenvalues of  $\Omega^1$

$$\Omega^1|\Psi_{phys.}\rangle = e^{i\theta}|\Psi_{phys.}\rangle. \quad (4.31)$$

Because of the fact it commutes with the Hamiltonian, this becomes a "superselection rule"; time evolution happens only in a given  $\theta$  sector as  $\Omega^1 e^{iHt}|\Psi_{phys.}\rangle = e^{i\theta} e^{iHt}|\Psi_{phys.}\rangle$ .

Note that the choice of  $\Omega^1$  over  $\Omega^n$  for any  $n$  does not impact the discussion as we can show by induction than given (4.31), we have  $\Omega^n|\Psi_{phys.}\rangle = e^{in\theta}|\Psi_{phys.}\rangle$ .

As for the quantum rotor, this  $\theta$  parameter can be understood from different perspectives. From a semiclassical perspective, it affects the path integral because of topologically disconnected sectors in field space. From the operator perspective, it arises because of the presence of an extra discrete symmetry of the theory.

In any events, the sensitivity to the  $\theta$ -parameter goes in hand with the existence of a non-zero topological susceptibility, defined exactly in the same way as for the quantum rotor in equation (2.35). Moreover, its very-high temperature dependence is expected to be the same [52]. The zero-temperature limit is not exactly known, but expression (2.17) has been computed to be also the leading term in a large  $N$  expansion of the partition function [53, 54], with  $N$  the number of colors.

## 4.2 Discretising gauge theories

To conclude this introduction and to be able to move on to the main parts of this work, we want to discuss how gauge theories can be represented on a discrete lattice. First, this has an intrinsic theoretical interest, as a lattice can be used to regularise a quantum field theory. This was, for example, the pursued goal of [55], which pioneered the use of gauge fields on a lattice. Then, it is necessary to perform numerical simulations, be them of the sort presented in section 2.3 to simulate Euclidean path integrals or of the sort of the one presented in section

2.4 which deals with classical equations of motion.

As we saw in section 1.1, gauge invariance is required to build a consistent quantum representation of the Lorentz group. This is tied to the fact massive vector fields have more propagating degrees of freedom than massless ones. Gauge invariance is there to remove these extra degrees of freedom by "killing" the transverse modes. As such, to have a sound regularisation and capture only the degrees of freedom which are wanted, we need to find a discretisation of gauge fields which is gauge invariant at the lattice level. A pedagogical introduction to lattice techniques in the context of lattice QCD can, for example, be found in [22].

To illustrate the procedure and for concreteness, let us consider the action (1.52) in Euclidean space

$$S^E = \int d^4x \left( \frac{1}{2g^2} \text{Tr}(G_{\mu\nu}G^{\mu\nu}) + (D^\mu\Phi)^\dagger D_\mu\Phi + m^2\Phi^\dagger\Phi \right). \quad (4.32)$$

with  $G_{\mu\nu}$  a  $SU(N)$  gauge fields and  $\Phi$  a  $n$ -uplet complex scalar field. We introduce a four dimensional lattice  $\Lambda$  of size  $N^4$  and side-length  $L$ . Equivalently, we can define a lattice spacing  $a = \frac{N}{L}$ . The complex scalar field is discretised "naively", to every lattice point  $n \in \Lambda$  we associate a  $n$ -uplet  $\Phi(n)$ .

The naive approach does not lead to gauge covariant objects in the case of gauge fields. This can be easily seen from the matter covariant derivative. Were we to discretise the derivative using forward (or any other) finite differences and assigning  $\mathfrak{su}(n)$ -valued vectors  $A_\mu(n)$  to every lattice point, we would write

$$D_\mu^{naive}\Phi(n) = \frac{\Phi(n+a\hat{\mu}) - \Phi(n)}{a} + iA_\mu(n). \quad (4.33)$$

with  $\hat{\mu}$  a unit vector in the direction  $\mu$ . It is obviously not gauge covariant for any finite  $a$ . This can be traced back to the fact that  $\Phi(n+a\hat{\mu})$  are not evaluated at the same point and as such do not transform with the same gauge transformation.

We already encountered in section 3.2.2 a situation where it was needed to evaluate a gauge invariant combination of operators evaluated at different points when we consider the point-splitting regularisation. In this case, gauge invariance is preserved thanks to the introduction of a parallel transporter

$$U^\gamma(x, y) = \mathcal{P} e^{i \int_\gamma A_\mu dx^\mu}, \quad (4.34)$$

where  $\mathcal{P}$  is a path ordering operator and  $\gamma$  is a path running between  $x$  and  $y$ . These objects, which belong to the group  $SU(N)$  and not its Lie-algebra, have the convenient property of transforming as [22]

$$U^\gamma(x, y) \rightarrow \Omega(x) U^\gamma(x, y) \Omega(y)^\dagger. \quad (4.35)$$

## Chapter 4. A second look at gauge theories

---

This suggests the following. At every lattice point, introduce a set of four parallel transporters

$$U_\mu(n) = e^{i \int_n^{n+a\hat{\mu}} A_\nu dx^\nu} . \quad (4.36)$$

In particular, we can now build objects of the sort  $U_\mu(n)\Phi(n+a\hat{\mu})$  which transforms in the same way as  $\Phi(n)$ . It also means that a finite difference of the sort

$$D_\mu^+ \Phi = \frac{U_\mu(n)\Phi(n+a\hat{\mu}) - \Phi(n)}{a} \quad (4.37)$$

do transform covariantly. Moreover, simply by Taylor expanding in  $a$ , we see that we appropriately recover the continuum covariant derivative.

These parallel transporters which link neighbouring lattice points are naturally referred to as "link" variables. They can also be used to construct covariant objects which reproduce the field strength tensor  $G_{\mu\nu}$  in the continuum limit. The simplest such object is the so-called plaquette operator

$$P_{\mu\nu} = U(n)_\mu U(n+a\hat{\mu})_\nu U_\mu^\dagger(n+a\hat{\nu}) U_\nu^\dagger(n) , \quad (4.38)$$

whose expansion in  $a$  give [22]

$$P_{\mu\nu} = e^{ia^2 G_{\mu\nu}(n) + O(a^3)} . \quad (4.39)$$

Of course, as in the case of finite differences, one can always devise more complicated composite object which have a smaller discretisation error.

With these results, we have everything at hand to discretise the action (4.32)

$$S^\Lambda = S_G^\Lambda + S_\Phi^\Lambda \quad (4.40)$$

$$S_W^\Lambda = \frac{2}{g^2} \sum_{n \in \Lambda} \sum_{\mu < \nu} \Re \text{Tr}(\mathbf{1} - P_{\mu\nu}(n)) \quad (4.41)$$

$$S_\Phi^\Lambda = \sum_{n \in \Lambda} a^4 \left[ (D_\mu \Phi)^\dagger D_\mu \Phi + m^2 \Phi^\dagger \Phi \right] . \quad (4.42)$$

The particular discretisation (4.41) used for the gauge fields is the renowned Wilson's action, introduced in [55].

Such a discretisation scheme can then be used to perform MC simulations of the path integral of the type presented in section 2.3. The very same discretisation techniques can be applied to Minkowski field equations, as is needed for real-time simulations. We defer the reader to chapter 10 for additional discussion and specific examples of this type.

# Chiral Charge Dynamics **Part II**



## 5 Chiral anomaly in practice

The chiral anomaly is not a peculiarity of the Schwinger model or of 1+1 dimensions. Rather, it is a feature of gauge theories coupled to massless Dirac fermions. Consider a four-dimensional theory of the sort

$$S = \int d^4x \left( -\frac{1}{4} F_{\mu\nu} F^{\mu\nu} - \frac{1}{2} \text{Tr}(G_{\mu\nu} G^{\mu\nu}) + \bar{\psi} \mathcal{D} \psi \right) . \quad (5.1)$$

with  $F_{\mu\nu}$  a  $U(1)$  gauge field,  $G_{\mu\nu}$  a  $SU(2)$  gauge field,  $D_\mu \psi = \partial_\mu \psi + i g_A A_\mu + i g_B G_\mu$  the covariant derivative and  $A_\mu, G_\mu$  the gauge vectors associated to  $F_{\mu\nu}$  and  $G_{\mu\nu}$ . The story is the same as in section 3. At the classical level, it enjoys two global symmetries, vectorial and axial rotations

$$\Psi \rightarrow e^{i\alpha} \psi \quad (5.2)$$

$$\Psi \rightarrow e^{i\gamma_5 \alpha} \psi , \quad (5.3)$$

which are associated to two conserved currents

$$j^\mu = \bar{\psi} \gamma^\mu \psi \quad (5.4)$$

$$j_5^\mu = \bar{\psi} \gamma^\mu \gamma^5 \psi . \quad (5.5)$$

Quantisation requires some regularisation and such regularisation necessarily breaks one of these symmetries. As we cannot afford to break the vectorial one, as this would come in hand with a breaking of gauge invariance, we sacrifice the axial symmetry and the current is not conserved anymore. Following, for example, closely the argument presented in section 3.2.1, one finds [42, 56]

$$\langle \partial_\mu j_5^\mu \rangle = \frac{g_A}{8\pi^2} F_{\mu\nu} \tilde{F}^{\mu\nu} + \frac{g_B}{4\pi^2} \text{Tr}(G_{\mu\nu} \tilde{G}^{\mu\nu}) . \quad (5.6)$$

As in the 1+1 dimensional case, we see that the anomaly is a portal between the fermionic sector and the gauge sector. In particular, it couples to the topological operators  $F_{\mu\nu} \tilde{F}^{\mu\nu}$  and  $\text{Tr}(G_{\mu\nu} \tilde{G}^{\mu\nu})$ .

Early on, a lot of attention has been directed to the non-Abelian contribution to equation

(5.6), see for example [57–59] in the context of the axial  $U(1)$  problem in the standard model. or [60] for the role it can play in the context of baryogenesis. This contribution is of special interest because of the non-trivial topology of the non-Abelian group, as discussed in section 4.1. In particular, we saw there exists saddle-point solution to the path integral with non-vanishing  $G_{\mu\nu}\tilde{G}^{\mu\nu}$ . Despite their contributions being exponentially suppressed, they are not wild quantum excursions away from the classical vacuum. These contributions then lead to a spontaneous violation of the axial current.

Even though no such configuration exists in the Abelian case, because of the trivial topology of the  $U(1)$  group, the Abelian contribution to the chiral anomaly can still act as a portal between the fermionic and gauge sector. In particular, in a dynamical context, it is not difficult to envision situations where either fermionic chiral charge or "helical" gauge fields, i.e. gauge fields with a non-vanishing  $F_{\mu\nu}\tilde{F}^{\mu\nu}$ , are generated through unrelated processes. The anomaly can then be used to efficiently transfer one into the other.

In this part of this work, we will be concerned with this phenomenon and its dynamics. In particular, we will review in this chapter a few physical situations where the Abelian contribution to the chiral anomaly and the details of its dynamics is of crucial importance.

### 5.1 Cosmology

One of the first fields which recognised the potential importance of the Abelian contribution to the chiral anomaly is cosmology [61, 62]. Before moving on to describe specific scenarios, we need to discuss which anomalous symmetries are relevant. Let us first recall the fermionic content of the standard model; we refer the interested reader to [63] for a pedagogical introduction. From the perspective of the weak force  $SU(2)$ , it splits into left-handed doublets, which are charged under  $SU(2)$ , and into two right-handed singlets, which are not. The strong force  $SU(3)$  splits the particle between quarks, which are charged triplets under  $SU(3)$  and leptons, which are not. The  $U(1)_Y$ -hypercharge couples to all particle. This structure comes into three copies or "families". As such, we consider the following matter content

$$Q_L^i, u_R^i, d_R^i, l_L^i, e_R^i. \quad (5.7)$$

Rotating any of these fields by a single phase is not a symmetry of the Lagrangian and the associated currents are explicitly broken. However, atop of this explicit breaking, they each receive an anomalous contribution. The equivalent effect in Schwinger model is given by equations (3.103) and (3.104), where the left and right-handed rotations are both anomalous.

In particular, adapting from reference [64], these contributions are given by

$$\partial_\mu j_{Q_L}^\mu = +(N_c N_w y_Q^2) \frac{g'}{16\pi^2} Y_{\mu\nu} \tilde{Y}^{\mu\nu} + \dots = +\frac{1}{6} \frac{g'}{16\pi^2} Y_{\mu\nu} \tilde{Y}^{\mu\nu} + \dots \quad (5.8)$$

$$\partial_\mu j_{u_R^i}^\mu = -(N_c y_{u_R}^2) \frac{g'}{16\pi^2} Y_{\mu\nu} \tilde{Y}^{\mu\nu} + \dots = -\frac{4}{3} \frac{g'}{16\pi^2} Y_{\mu\nu} \tilde{Y}^{\mu\nu} + \dots \quad (5.9)$$

$$\partial_\mu j_{d_R^i}^\mu = -(N_c y_{d_R}^2) \frac{g'}{16\pi^2} Y_{\mu\nu} \tilde{Y}^{\mu\nu} + \dots = -\frac{1}{3} \frac{g'}{16\pi^2} Y_{\mu\nu} \tilde{Y}^{\mu\nu} + \dots \quad (5.10)$$

$$\partial_\mu j_{l_L^i}^\mu = +(N_w y_L^2) \frac{g'}{16\pi^2} Y_{\mu\nu} \tilde{Y}^{\mu\nu} + \dots = +\frac{1}{2} \frac{g'}{16\pi^2} Y_{\mu\nu} \tilde{Y}^{\mu\nu} + \dots \quad (5.11)$$

$$\partial_\mu j_{e_R^i}^\mu = -(y_{e_R}^2) \frac{g'}{16\pi^2} Y_{\mu\nu} \tilde{Y}^{\mu\nu} + \dots = -\frac{g'}{16\pi^2} Y_{\mu\nu} \tilde{Y}^{\mu\nu} + \dots, \quad (5.12)$$

where  $N_c = 3$  is the number of color and  $N_w = 2$  the number of flavour, the dots stand for the contributions coming from the explicit breaking and the anomaly associated with the other gauge fields. The constant  $g'$  is the gauge coupling to  $U(1)_Y$  and we used the value of the different hypercharges

$$y_Q = \frac{1}{6}, \quad y_{u_R} = \frac{2}{3}, \quad y_{d_R} = -\frac{1}{3}, \quad y_{l_L} = -\frac{1}{2}, \quad y_{e_R} = -1. \quad (5.13)$$

The standard model do possess classical symmetries, they are associated to baryon and lepton number. They are defined as

$$U(1)_B : Q_L^i, u_R^i, d_R^i, l_L^i, e_R^i \rightarrow e^{i\frac{1}{3}\alpha} Q_L^i, e^{i\frac{1}{3}\alpha} u_R^i, e^{i\frac{1}{3}\alpha} d_R^i, l_L^i, e_R^i \quad (5.14)$$

$$U(1)_l : Q_L^i, u_R^i, d_R^i, l_L^i, e_R^i \rightarrow Q_L^i, u_R^i, d_R^i, e^{i\alpha} l_L^i, e^{i\alpha} e_R^i. \quad (5.15)$$

They are both anomalously broken. We can see this explicitly for  $U(1)$  by combining the above contributions. We then get

$$\partial_\mu j_B^\mu = -\frac{g'}{32\pi^2} Y_{\mu\nu} \tilde{Y}^{\mu\nu} + \dots \quad (5.16)$$

$$\partial_\mu j_l^\mu = -\frac{g'}{32\pi^2} Y_{\mu\nu} \tilde{Y}^{\mu\nu} + \dots, \quad (5.17)$$

where the dots stand now only for the other anomalous contributions. From there, we see that at least with respect to the  $U(1)_Y$  sector, we can retrieve a symmetry that is non-anomalous by considering  $B - l$ ; do first a  $U(1)_B$  rotation of parameter  $\alpha$ , followed by a  $U(1)_l$  rotation of  $-\alpha$ . Actually, this combination is also not anomalous with respect to  $SU(2)$  and  $SU(3)$ . The remaining anomalous symmetry is conventionally taken to  $B + l$ , which consists in performing two rotations with the same parameter  $\alpha$ . This gives

$$\partial_\mu j_{B-l}^\mu = 0 \quad (5.18)$$

$$\partial_\mu j_{B+l}^\mu = -\frac{g'}{16\pi^2} Y_{\mu\nu} \tilde{Y}^{\mu\nu} + \dots. \quad (5.19)$$



In terms of conserved charges, this means that no processes in the standard model can change the number of baryons minus the number of leptons while fluctuations in gauge fields can change the number of baryons plus the number of leptons. It is, for example, the key idea behind models that try to achieve electroweak baryogenesis [60]. Below, we briefly review three different situations/scenarios where the  $U(1)$  contribution can also be of interest.

### Helical fields' contribution to baryogenesis

A relevant question to ask is whether the  $U(1)$  contribution can affect the process of baryogenesis in a similar fashion than the non-Abelian one. The naive answer is no, as no spontaneous variation of  $Y_{\mu\nu}\tilde{Y}^{\mu\nu}$  is expected. What can happen on the other hand, under some circumstances, is a transfer of preexisting helicity  $Y_{\mu\nu}\tilde{Y}^{\mu\nu}$  into fermions. This was first pointed out in [62, 65], where it was shown that inhomogeneous helical hypermagnetic fields could lead to potential  $B + l$  fluctuations. While the presence of an initial hypermagnetic field has to be postulated, different beyond the standard model scenarios can predict such kind of fields, see for example [66–68] and references therein.

The main obstacle for this idea to effectively affect baryogenesis is the problem of "sphaleron washout". As the electroweak phase transition is actually a crossover [69, 70], sphaleron processes, which are thermal fluctuations that carry a  $SU(2)$ -topological charge, are in thermal equilibrium and, through the  $SU(2)$  anomaly equations, tend to erase any preexisting  $B + l$  asymmetry. The question of whether contributions from hypermagnetic fields to baryogenesis can survive this crossover is still an open question [71, 72].

### Generation of helical fields in the unbroken phase

Another cosmological phenomenon that may be related to the Abelian contribution to the anomaly is the potential existence of primordial magnetic fields. Over the last decades, observational evidence has started to build up pointing towards the presence of coherent magnetic fields correlated over enormous distances, deep into the intergalactic voids, see reference [73] for a review. These large correlations are difficult to explain when considering the creation of magnetic fields by astrophysical processes, pointing towards "primordial" magnetic fields created in the very early stages of the universe.

Using the contribution from the chiral anomaly is an interesting idea as it naturally generates helical fields, which are by their nature coherent fields. It was first studied in [61], where the following mechanism was put forward. In equations (5.8)-(5.12), the right-handed electron has a special role. Indeed, the only anomalous contribution it receives when rotated by a phase comes from  $U(1)$ , as it is not charged under the other gauge groups. The explicit breaking, as for the other particles, is proportional to the Yukawa's coupling, which is notoriously small in the case of the electron. Hence, the associated reaction rate is small. In practice, this means that there is some temperature above which it can be completely neglected. Above this

temperature, rotation of the right-handed electron becomes an effective symmetry, with an anomalous  $U(1)_Y$  non-conservation. Reference [61] used this effective anomalous symmetry to create helical hypermagnetic fields starting from some hypothetical excess of right-handed fermions. The created hypermagnetic fields are then converted into regular magnetic fields at the electroweak phase transition.

The main problem of these kinds of scenarios is that they tend to produce magnetic fields which are not correlated over sufficiently large distances, see for example [68].

### Evolution of helical field in the Higgs phase

Until now, we only discussed phenomena happening in the symmetric phase of the electroweak theory. The symmetry  $B + l$  receives an anomalous contribution from the  $U(1)_Y$  because the left and right-handed charges are not the same. In this sense,  $U(1)_Y$  is a chiral interaction. This is not the case of  $U(1)_{e.m.}$  which couples to right and left-handed particles in the same way. As such, we do not have any anomalous Abelian contribution to the breaking of  $B + l$  in the Higgs phase.

It was however argued in references [74, 75] that effects associated to a  $U(1)$  anomalous contribution are relevant to the dynamics of magnetic fields even for a range of temperatures below the electroweak crossover. The argument is also based on the smallness of the electron Yukawa coupling. In the broken phase, the only interaction that refrains the chiral rotation  $e_L \rightarrow e^{i\alpha} e_L, e_R \rightarrow e^{-i\alpha} e_R$  from being a symmetry is the electrons Yukawa interaction. Even if active, a naive estimate of the chirality flipping processes that occur through this interaction shows that it does not overwhelm the  $U(1)_{e.m.}$  anomalous contribution associated to this chiral rotation. As such, to have a reliable model of magnetic field evolution, one has to take into account this interaction. This argument led to the development of numerical simulations of such models [76].

Note however that this effect depends on a precise and reliable estimate of both of the chirality flipping rate and of the rate at which the anomalous transfer occurs. It is not clear that such estimates exist at the moment and the intricacies of this complicated dynamics remain an open question.

## 5.2 Chiral magnetic effect

In a different context, another interesting effect related to the chiral anomaly is the so-called "chiral magnetic effect". Already many years ago, it was realised in [77] that a theory of massless fermions in presence of a chiral imbalance and subject to a background magnetic field will develop an electric current along the magnetic field.

The origin of this effect can be understood in several different ways, see [78]. We will follow

the argument first presented in [79]. Consider a Dirac fermion in a constant magnetic field oriented along the  $z$ -direction. Then, its motion is confined to the  $x-y$  plane and its spectrum is given by Landau levels [30] (a spectrum that can be mapped to the Schwinger model's one we considered in section 3.2.2). In the absence of background fields, the left and right-handed spectra are degenerate. A chiral imbalance can be introduced by introducing left and right-handed  $\mu_L, \mu_R$  chemical potential or equivalently a chiral chemical potential  $\mu_5 = \frac{1}{2}(\mu_L - \mu_R)$ . It creates an energy splitting of  $2\mu_5$  between the left and right-handed energy band.

To understand the dynamics of the system, we can resort to an energy balance argument. To convert a right-handed particle into a left-handed particle costs an energy of  $\Delta\epsilon = 2\mu_5$ , where the factor two is actually  $\Delta Q_A$  with  $Q_A$  the axial charge. In terms of rates, it gives

$$\frac{\Delta\epsilon}{\Delta t} = \frac{\mu_5 \Delta Q_A}{\Delta t} = \mu_5 \frac{g}{4\pi^2} \int d^3x \vec{E} \cdot \vec{B} , \quad (5.20)$$

thanks to the anomaly relation (5.6) and with  $\vec{E}$  and  $\vec{B}$  the  $U(1)$  electric and magnetic fields. This energy flux has to come from somewhere; we can extract it from an electric current  $\vec{j}_{CME}$ . The power delivered by an electric current is  $\int d^3x \vec{j} \cdot \vec{E}$  and we obtain the following relation

$$\int d^3x \vec{j}_{CME} \cdot \vec{E} = \mu_5 \frac{g}{4\pi^2} \int d^3x \vec{E} \cdot \vec{B} . \quad (5.21)$$

An expression of the current can then be obtained by taking the limit  $\vec{E} \rightarrow 0$ . We get

$$\vec{j}_{CME} = \mu_5 \frac{g}{4\pi^2} \vec{B} . \quad (5.22)$$

This current can be understood as the result of the fact that the magnetic fields lifts the spin degeneracy between particle and anti-particle; they will move in opposite directions and thus create an electric current.

The relevance of this effect in heavy-ions collisions and its potential observational signature in terms of charge separation was pointed out in references [80–82]. It was first observed in a tabletop condensed matter experiment, as reported in reference [83]. Its direct experimental observation in heavy-ions collisions is actively sought, with evidence of its occurrence building up over the year [84]. Recently, the STAR collaboration reported new observations of charge separation in proton-gold and gold-gold collisions [85], seemingly consistent with the chiral magnetic effect. A precise measurement of this effect in this context would be a unique way to probe experimentally topological properties of QCD, as the initial chiral imbalance which triggers the charge separation is expected to partly come from event-by-event QCD sphaleron processes.

Before concluding this section, we would like to mention an interesting idea to use the chiral magnetic effect in a controlled set-up to produced entangled two-states system to engineer quantum Q-bits [86, 87]. This shows how diverse the physics related to the Abelian

contribution to the chiral anomaly is.

### 5.3 Foreword to [1]

As we just saw, the chiral anomaly in four-dimensions, even through its Abelian contribution, leads to a variety of phenomena which can potentially be of great importance. As already mentioned, to make concrete predictions about these phenomena, we need to have a precise understanding of the chiral charge dynamics, not only at the qualitative level but also quantitatively. Both theoretical efforts, with the advent of chiral kinetic theory, see [88] and references therein, and progresses on chiral magneto-hydrodynamics (chiral MHD) [89], and numerical ones, with extended simulations of chiral MHD [76] and first principle simulations [90–93], have been undertaken. In the next part 6, we present our contribution [1] to this effort, in the instance of real-time classical simulations.



## 6 *Chiral charge dynamics in Abelian gauge theories at finite temperature [1]*

**Authors:** Daniel G. Figueroa, Adrien Florio, Mikhail Shaposhnikov

*Reference:* arXiv v2 of JHEP, 10:142, 2019, doi: 10.1007/JHEP10(2019)142

*Abstract:* We study fermion number non-conservation (or chirality breaking) in Abelian gauge theories at finite temperature. We consider the presence of a chemical potential  $\mu$  for the fermionic charge, and monitor its evolution with real-time classical lattice simulations. This method accounts for short-scale fluctuations not included in the usual effective magneto-hydrodynamics (MHD) treatment. We observe a self-similar decay of the chemical potential, accompanied by an inverse cascade process in the gauge field that leads to a production of long-range helical magnetic fields. We also study the chiral charge dynamics in the presence of an external magnetic field  $B$ , and extract its decay rate  $\Gamma_5 \equiv -\frac{d\log\mu}{dt}$ . We provide in this way a new determination of the gauge coupling and magnetic field dependence of the chiral rate, which exhibits a best fit scaling as  $\Gamma_5 \propto e^{11/2} B^2$ . We confirm numerically the fluctuation-dissipation relation between  $\Gamma_5$  and  $\Gamma_{\text{diff}}$ , the Chern-Simons diffusion rate, which was obtained in a previous study. Remarkably, even though we are outside the MHD range of validity, the dynamics observed are in qualitative agreement with MHD predictions. The magnitude of the chiral/diffusion rate is however a factor  $\sim 10$  times larger than expected in MHD, signaling that we are in reality exploring a different regime accounting for short scale fluctuations. This discrepancy calls for a revision of the implications of fermion number and chirality non-conservation in finite temperature Abelian gauge theories, though no definite conclusion can be made at this point until hard-thermal-loops are included in the lattice simulations.

*A.F. contribution:* Creation of the parallelised simulation software. Generation of the data. The analysis and the writing of the paper have been done jointly with the coauthors.

## 6.1 Introduction

Anomalous processes can be relevant in a large number of phenomena, from high energy particle physics to condensed matter. One of the most well-known applications is the explanation of the  $\pi^0 \rightarrow 2\gamma$  decay in quantum electrodynamics (QED), whereas in quantum chromodynamics (QCD) they play a decisive role in the resolution of the  $U_A(1)$  problem [57, 94]. The rate at which anomalous processes occur is actually a relevant quantity whenever we are dealing with out-of-equilibrium processes. In highly energetic and dense matter environments like in the early universe, the fluctuations of gauge and scalar fields – sphalerons [20] – lead to rapid fermion number non-conservation in the Standard Model (SM) [60], and to chirality non-conservation in QCD [95]. The  $SU(2)$  sphaleron rate is a crucial quantity to assess the viability of electroweak baryogenesis [60], and has been extensively studied across decades, both from a purely analytical side and with the help of numerical simulations. Studies have been carried out in the pure  $SU(2)$  theory in Refs. [96–106] and in the electroweak theory e.g. [107–110], see [70] for the latest up-to-date prediction using the measured Higgs-mass.

Anomalous  $U(1)$  processes have received some attention, especially in the cosmological context. In the electroweak theory of the SM, the anomaly in the fermionic and/or chiral current actually contains a  $U(1)$  contribution, which is associated with the hypercharge field in the Higgs unbroken phase and to the photon field of QED in the Higgs broken phase. As in Abelian gauge theories there are no large gauge transformations, nor vacuum configurations with different Chern-Simons numbers, there is no *irreversible* fermion (or chiral) number non-conservation, contrary to the case of non-Abelian theories. This does not prevent however the fermion/chiral number in Abelian theories to be transferred into gauge configurations carrying Chern-Simons number, and to re-appear back again due to changes in the gauge field background. These processes may have an important impact on the problems of baryogenesis [62, 67, 71, 72, 111], magnetic field generation in the early universe [61], and chiral asymmetry evolution at  $\sim \text{MeV}$  temperatures [74]. Anomalous  $U(1)$  processes have also received a renewed interest in the quark-gluon plasma community, where the chiral magnetic effect [77, 78] and its potential experimental signatures are being studied, see [84] for a review.

The above  $U(1)$  case have been studied mostly within the framework of magneto-hydrodynamics (MHD), which is an effective description accounting for distance scales exceeding the mean free path of the charged particles involved in the problem, see e.g. [89, 112], or [76] for recent numerical simulations. Despite the relevance of these processes, a full study beyond MHD, taking into account small scale fluctuations in detail, remains to be done. Some attempts in this direction were made in [90, 91], where out-of-equilibrium techniques were implemented. The main limitations of these studies were the intrinsic numerical cost associated with a full-fledged treatment of fermions. Another approach was initiated in [29], of which this paper is a natural continuation. To explain the aim of the present research, let us set up a working model and fix notation. We are interested in the study of physics described by scalar electrodynamics coupled to a massless vector-like fermion

field  $\Psi$ , so that our starting lagrangian is

$$\mathcal{L} = -\frac{1}{4}F_{\mu\nu}F^{\mu\nu} - \bar{\Psi}\gamma^\mu D_\mu\Psi - (D_\mu\phi)^*(D^\mu\phi) - V(\phi) , \quad (6.1)$$

where  $F_{\mu\nu}$  is the field strength tensor of the  $U(1)$  gauge field  $A_\mu$ ,  $D_\mu = \partial_\mu - ieA_\mu$  and

$$V(\phi) = m^2|\phi|^2 + \lambda|\phi|^4 . \quad (6.2)$$

Taking a positive squared mass  $m^2 > 0$ , we can chose its value so that the lagrangian (6.1) becomes a toy-model for the SM hypercharge sector close to the electroweak phase transition. The chiral fermionic current  $J^\mu = \bar{\Psi}\gamma^\mu\gamma_5\Psi$  is not conserved at the quantum level, and satisfies the anomaly equation

$$\partial_\mu J_5^\mu = \frac{e^2}{8\pi^2}F_{\mu\nu}\tilde{F}^{\mu\nu} = N_f\partial_\mu K^\mu , \quad (6.3)$$

where  $\tilde{F}_{\mu\nu} = \frac{1}{2}\epsilon_{\mu\nu\rho\sigma}F^{\rho\sigma}$  is the hodge-dual of  $F_{\mu\nu}$ ,  $N_f$  is the number of flavours and  $K^\mu = \frac{e^2}{8\pi^2}\epsilon^{\mu\nu\rho\sigma}A_\nu\partial_\rho A_\sigma$  is the Chern-Simons current. It follows that the Chern-Simons number  $N_{CS} = K^0$  is identified with the magnetic helicity density [we use a  $(-, +, +, +)$  signature and  $\epsilon^{0123} = -\epsilon_{0123} = 1$ ]

$$N_{CS} = \frac{e^2}{8\pi^2} \vec{A} \cdot \vec{B} . \quad (6.4)$$

In the particular case of a homogeneous fermion distribution, the anomaly equation reduces to (we fix  $N_f = 1$  from now on)

$$\partial_0 J_5^0 = \partial_\mu K^\mu . \quad (6.5)$$

This allows us to write an effective description without fermions. Integrating them out, they can be represented by a (homogeneous) chemical potential  $\mu$  sourced by the Chern-Simons number [113, 114]. Furthermore, in the case of massless fermions, the relation between the chiral current and the chemical potential can be written in a closed form as<sup>1</sup>

$$J_5^0 = \frac{1}{6}\mu T^2 + \frac{\mu^3}{6\pi^2} . \quad (6.6)$$

The anomaly, which represents a violation of chirality, can then be recast as an equation for  $\mu$

$$\frac{d}{dt} \left( \frac{1}{6}\mu T^2 + \frac{\mu^3}{6\pi^2} \right) = \frac{e^2}{8\pi^2} \frac{1}{V} \int d^3x F_{\mu\nu}\tilde{F}^{\mu\nu} . \quad (6.7)$$

The equations of motion of the scalar and gauge fields, together with the anomaly equation (6.7), can be actually derived from an effective action

---

<sup>1</sup>This is obtained for the ensemble average of the number density with the Fermi-Dirac distribution in the presence of a chemical potential:  $J_5^0 \equiv n_+ - n_-$ , with  $n_\pm = \frac{1}{2\pi^2} \int_0^\infty dE E^2 \left( 1 + e^{\frac{E \pm \mu}{T}} \right)^{-1}$ .



$$S_{eff} = - \int d^4x \left( (D_\mu \phi)^* (D^\mu \phi) - V(\phi) + \frac{1}{4} F_{\mu\nu} F^{\mu\nu} - \frac{1}{2} (\partial_0 a)^2 - \frac{1}{4M^4} (\partial_0 a)^4 - \frac{e^2}{(4\pi)^2} \frac{a}{\Lambda} F_{\mu\nu} \tilde{F}^{\mu\nu} \right), \quad (6.8)$$

upon identifying  $\partial_0 a = \Lambda \mu$ ,  $\Lambda^2 = T^2/12$  and  $M^4 = \frac{\pi^2 T^4}{9}$ , where  $T$  is the temperature of the system. The potential  $V(\phi)$  was given in Eq. (6.2).

The main aim of this work is to extract the decay rate of the chemical potential in the presence of an external magnetic field. This quantity is related to the Chern-Simons number diffusion rate in the absence of chemical potential through the fluctuation-dissipation theorem (we discuss this in detail in appendix 6.6). It is of special interest as the corresponding diffusion rate has been measured from (independent) simulations in Ref. [29]. The fluctuation-dissipation relation is a near-equilibrium relation, relevant for small chemical potentials  $\mu \ll T$ . Having this in mind, we will restrict our attention to the reduced system

$$S_{eff} = - \int d^4x \left( (D_\mu \phi)^* (D^\mu \phi) - V(\phi) + \frac{1}{4} F_{\mu\nu} F^{\mu\nu} - \frac{1}{2} (\partial_0 a)^2 - \frac{e^2}{(4\pi)^2} \frac{a}{\Lambda} F_{\mu\nu} \tilde{F}^{\mu\nu} \right), \quad (6.9)$$

which corresponds to neglecting the  $\mu^3$  term in the anomaly equation, hence leading to a linear dynamics in  $\mu$ . We have explored the dynamics of this system for different values of  $\mu$ , solving the linear equations of motion that follow from Eq. (6.9). In the case of large chemical potential  $\mu \gg T$ , the correct physical regime is rather described by the non-canonical kinetic term of  $a(t)$  that we have neglected in Eq (6.9). Keeping that term as in the full action (6.8), would lead however to a non-linear set of equations of motion, requiring a more complicated algorithm for solving the evolution of the system in a lattice. In this work we focus for simplicity in the linearised description (at the level of the equations of motion) of the system given by Eq. (6.9), independently whether this corresponds to the correct description of the physical regime expected for a given  $\mu$ . Fortunately, in order to extract the chiral decay rate of the chemical potential in the presence of a magnetic field, it is enough to explore the regime  $\mu < T$ , for which Eq. (6.9) represents the correct description of the system.

We start nonetheless studying the system with large non-vanishing initial values of the chemical potential,  $\mu > T$ . Even though, as mentioned, Eq. (6.9) does not correspond to the correct description of this physical regime, we still expect to get a qualitative understanding of the system dynamics. In this case, the chemical potential is expected to be unstable, forced to decay down to lower values. Due to volume effects unavoidable in any lattice simulation, the chemical potential cannot decay completely, and rather relaxes into a volume-dependent finite critical value  $\mu_c$ . By reaching a large enough volume in the lattice, we have achieved sufficiently small values of  $\mu_c$ , so that we can characterise well the chemical potential decay. In particular, we observe that the decay proceeds through a self-similar/power-law regime, while

at the same time the gauge field long-wavelengths develop an inverse cascade spectrum.

Next, we move into the main aim of our present work, studying the system in the presence of a background magnetic field. In this case, the theory becomes similar to its non-Abelian counterpart, as the vacuum becomes degenerate. In particular,  $\mu$  decays exponentially all the way down to zero. We have measured the corresponding rate  $\Gamma_5 \equiv -\frac{d\log\mu}{dt}$  in the regime of small  $\mu \leq T$ , where (6.9) describes the physically relevant theory. We provide in this way a new determination of the parametric dependence of the chiral rate  $\Gamma_5$ , which exhibits a best fit scaling as  $\Gamma_5 \propto e^{11/2} B^2$ , with no residual volume dependence, where  $B$  is the external magnetic strength. Furthermore, we have compared this prediction comparing the magnitude and parametric scaling of  $\Gamma_5$  obtained from our present lattice simulations against direct measurements of  $\Gamma_{\text{diff}}$  from (independent) simulations previously presented in Ref. [29], which according to the fluctuation-dissipation argument should be related as  $\Gamma_5 = 6\Gamma_{\text{diff}}/T^3$ , with  $T$  the temperature of the system.

On the technical side, the discretisation of this theory needs to be done with care, especially when considering the Chern-Simons number. An appropriate discretisation scheme for Abelian gauge theories, reproducing the continuum limit of the theory to quadratic order in the lattice spacing, was presented in [115]. It obeys the following properties on the lattice: *i*) the system is exactly gauge-invariant, and *ii*) shift symmetry of the axion is exact<sup>2</sup>. Property *i*) implies that physical constraints such as the Gauss law or Bianchi identities, are exactly verified on the lattice (up to machine precision). Property *ii*) implies that the lattice formulation naturally admits a construction of the topological number density with a total (lattice) derivative representation  $\mathcal{K} \equiv F_{\mu\nu}\tilde{F}^{\mu\nu} = \Delta_\mu^+ K^\mu$ , which reproduces the continuum expression  $\mathcal{K} = \partial_\mu K^\mu \propto \vec{E} \cdot \vec{B}$  up to  $\mathcal{O}(dx_\mu^2)$  corrections. Without this property, the interaction  $a F_{\mu\nu}\tilde{F}^{\mu\nu}$  cannot be interpreted as a derivative coupling, and hence is not really shift symmetric. As it is precisely the shift symmetry which justifies the functional form of the interaction in first place, it is therefore relevant to preserve exactly such symmetry at the lattice level. Hence, in the present work, we obtain results from numerical simulations based on the discretisation scheme presented in Ref. [115]. In appendix, we provide a summary of the key equations of such lattice formulation. For further technical details we refer the interested reader directly to Ref. [115].

Most of what is known about anomalous  $U(1)$  dynamics comes from MHD predictions, which represent the long-wavelength effective description of our system. To get analytic insights, it is interesting to compare our findings with this effective theory. The phenomena we observed (e.g. self-similar decay of the chemical potential, gauge field inverse cascade dynamics, etc) are qualitatively well-modeled by MHD-inspired models, even though these do not take into account the full-fledged short-scale dynamics present in our lattice simulations.

The paper is organised as follows. In section 6.2, we present the outcome of our lattice simulations. Namely, we study the evolution of an initially non-vanishing large chiral chemical

<sup>2</sup>An equivalent formulation for non-Abelian gauge theories was originally introduced in [116, 117]. In non-Abelian gauge theories the shift symmetry is however not preserved exactly on the lattice.

potential  $\mu$  in the absence of an external magnetic field. This leads to a characterisation of the self-similar decay of  $\mu$ , and of the gauge field inverse cascade dynamics. We then add an external magnetic field, which introduce a vacuum degeneracy, and allows for the complete decay of the chemical potential. This gives us a way to measure in the physically relevant regime the amplitude and parametric dependence of the decay rate  $\Gamma_5$ , which we compare with  $\Gamma_{\text{diff}}$  as inferred from previous simulations. Section 6.3 is devoted to the comparison of our results to MHD. We provide there a simplified MHD model which allows us to describe the gross feature of the system. We then characterise the inverse cascade phenomenon and see that its dynamical evolution can be well fit to an MHD-like *ansatz*. We also discuss the expected parametric dependence of the chiral rate. In section 6.4 we discuss our results and present future outlooks. Appendix 6.5 recaps the lattice setup and in appendix 6.6 we review the derivation of the fluctuation-dissipation relation between the chiral rate and the Chern-Simons diffusion one.

## 6.2 Lattice results

In this section, we report the results obtained from our lattice simulations. We select from a thermal ensemble (with  $\mu = 0$ ) initial configurations, which we then evolve following the (lattice version of) the classical equations of motions derived from (6.9), with initial condition  $\mu(0) = \mu_0 \neq 0$ . We follow the evolution of the chemical potential, which in the symmetric phase is expected to be unconditionally unstable, leading to the creation of long-range gauge fields [118, 119]. We start by investigating the general features of the chemical potential evolution in the absence of a background magnetic field, making sure that the volume dependence of our observables is under control. Then, we study the self-similar behaviour of the decay for large initial chemical potential, and characterise the associated inverse cascade dynamics of the gauge field. We show that the magnetic power spectrum flows to the infrared modes. After that, we switch on a homogeneous background magnetic field. This is achieved by the use of twisted boundary conditions [120], which are already introduced in the Monte-Carlo process that generates the initial configuration (we describe this in appendix 6.5). We observe different regimes, and in particular, we focus on the exponential decay induced by the presence of the external magnetic field. This allows us to extract the chiral magnetic decay rate  $\Gamma_5 = -\frac{d \log \mu}{dt}$ , and characterise its parametric dependence.

### 6.2.1 Chemical potential decay

The existence of an instability can be understood by looking at the free energy of the system under consideration. In momentum space, the usual magnetic term  $\mathcal{H}_{\text{mag}} = \frac{1}{2} \vec{B}^2 \sim \frac{1}{2} k^2 A^2$  competes with the chemical potential term  $\mathcal{H}_{\text{cs}} = \mu N_{\text{CS}} \sim \pm \frac{e^2}{8\pi^2} \mu k A^2$ , where the different sign corresponds to the different polarisations of the gauge field, reflecting the chiral nature of the coupling. The chiral term may become dominant at small momenta, and for the gauge field polarisation for which  $\mathcal{H}_{\text{cs}}$  and  $\mathcal{H}_{\text{mag}}$  have opposite sign, an instability occurs for sufficiently

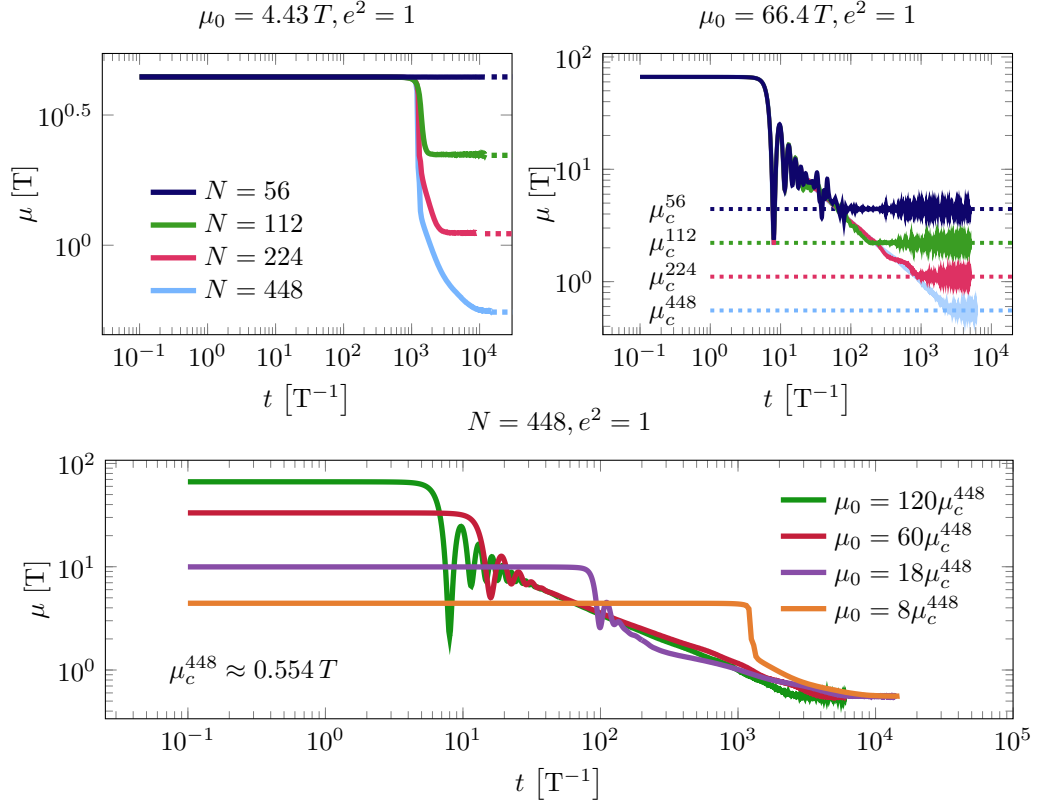


Figure 6.1 – Chemical potential evolution for different lattice sizes and initial values. *Upper panels:* Evolution of the chemical potential for different lattice sizes for a relatively small (left panel) and a relatively large (right panel) initial chemical potential. The dotted lines show the value of the critical potential predicted by equation (6.11). As expected, finite volume effects are observed for chemical potential close enough to critical. Far enough from the critical value, all lattices give the same results. *Lower panel:* Evolution of the chemical potential for different initial values, on the largest  $N = 448$  lattice we have simulated. As the initial value is decreased, the size of the initial *plateau* increases. For large chemical potential, we observe a power law decay, which is related to some self-similar behaviour.

infrared modes

$$k < \frac{e^2}{4\pi^2} \mu = k_c. \quad (6.10)$$

In particular, if all  $k$ 's on the lattice are larger than the critical  $k$ , no instability can develop. As the lattice momentum is discrete and has a minimum value  $k_{min}$ , it implies the existence of a critical chemical potential below which no instability can develop. Equation (6.10) can be rewritten to understand what is the largest chemical potential which is stable given a momentum resolution. Using the smallest momentum in a lattice  $k_{min} = \frac{2\pi}{Ndx}$ , with  $N$  the number of lattice points in one direction and  $dx$  the lattice spacing, we find

$$\mu_c = \frac{8\pi^3}{e^2 N dx}. \quad (6.11)$$

For  $\mu < \mu_c(e, N, dx)$  the instability is not captured any more for the given lattice. From now on we set  $Tdx = 1$ , as any re-scaling of the lattice spacing can be translated into an inverse re-scaling of the gauge coupling constant  $e^2$ . In this way, relevant scales are always guaranteed to be captured in the lattice (see [29] for more details). In the upper panels of figure 6.1 we show the behaviour of the chemical potential for different lattice sizes (in this figure and in the following, we indicate in brackets the corresponding units in powers of the temperature  $T$ ). The critical threshold predicted by (6.11) is clearly appreciated, as indicated by the dotted lines in the figure. As long as the chemical potential remains much larger than the critical value for a given lattice size  $N$ , all simulations agree, as expected, independently of the volume. On the other hand, some finite volume effects are observed around the critical value. In particular, we see in the top right panel that for the smallest volume considered  $N = 56$ , the chemical potential displays some oscillations just before approaching the critical value; such oscillations disappear for larger volumes. In the lower panel, we display the chemical potential evolution for different initial values, for the largest  $N = 448$  lattices we simulated. For large enough initial values, we observe a power law decay, which as we will explain in section 6.2.2, corresponds to a self-similar behaviour.

Another phenomenon we observe is that the smaller the initial chemical potential, the longer it takes for the decay to be triggered. In other words, we see the emergence of long *plateaus*, gradually longer the smaller the initial value of the chemical potential is. This phenomenon makes the regime of very small chemical potential difficult to be captured well on a lattice. Atop of requiring large volumes to decrease the critical chemical potential, one has to perform increasingly longer simulations.

### 6.2.2 Inverse cascade

In the previous subsection, we have seen that finite volume effects are under control for sufficiently large lattices  $N \gg 50$ , and that long initial *plateaus* appear for small chemical potentials. A remarkable feature of the chemical potential evolution in this context is that for large initial values, its decay corresponds to a universal power-law. We show this phenomenon in figure 6.2 for different charges and initial values of the chemical potential. After some transient behaviour, all decays enter a power-law regime well described by a  $t^{-1/2}$  behaviour. All the dependence on the parameters comes from the charge and lies in the prefactor as we illustrate in the right-hand side part of the figure.

Actually, this phenomenon goes in pair with what is known as an inverse magnetic cascade. The decay of the chemical potential induces a transfer of magnetic energy from the ultraviolet (UV) into the infrared (IR). In other words, long-range magnetic fields are created. We consider the magnetic power-spectrum

$$\epsilon_B(k) = \frac{1}{2\pi^2} \left( \frac{dx}{N} \right)^3 \langle k^3 |\tilde{B}(k)|^2 \rangle_{|k|}, \quad (6.12)$$

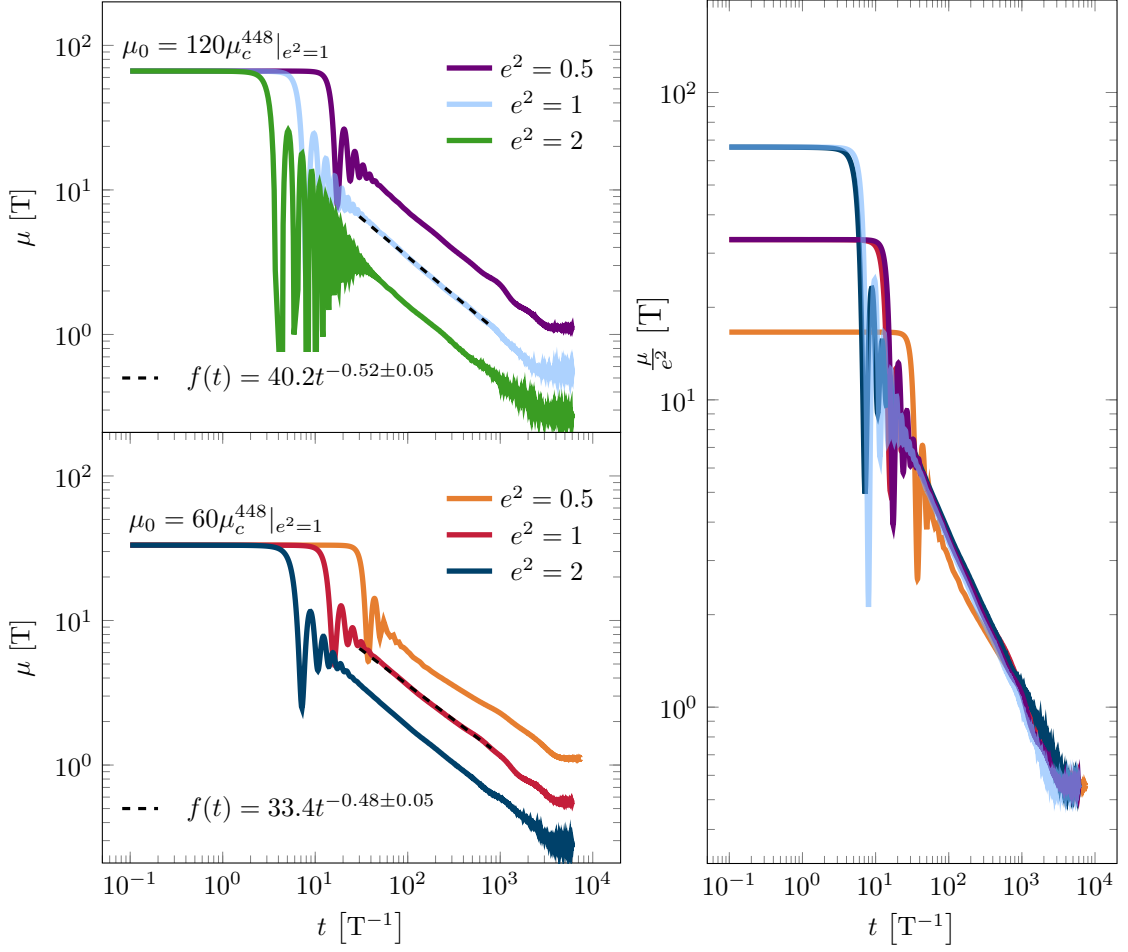


Figure 6.2 – *Left*: Chemical potential decay for different electric charges and different initial values. The dashed lines are the fits to a power-law (errors on the fit to the exponent are specified but not plotted). We see that the exponent is compatible with  $-\frac{1}{2}$ . *Right*: Chemical potential normalised by  $e^2$ . The data collapse shows that  $\mu(t) \propto e^2 g(t)$  with  $g(t)$  a function independent of  $e^2$ .

where the quantity  $\langle \dots \rangle_{|k|}$  denotes an angular average over the spherical shell of radii  $[|k| - \frac{1}{2}\Delta k, |k| + \frac{1}{2}\Delta k]$ , with  $\Delta k = k_{\min} \equiv \frac{2\pi}{Nd_x}$  the binning width. The quantity  $\tilde{B}(k) = \sum_x e^{-i\vec{k} \cdot \vec{x}} \tilde{B}(x)$  is the lattice discrete Fourier transform of  $\tilde{B}(x)$  and has the same units as  $\tilde{B}(x)$ . This definition has the advantage of being volume independent and it is simply related to the real-space volume average as  $\langle \tilde{B}^2 \rangle_v = \sum_k \frac{k_{\min}}{k} \epsilon_B(k)$  mimicking the continuum relation  $\langle \tilde{B}^2 \rangle = \int \frac{dk}{k} \epsilon_B(k)$ .

In figure 6.3, we plot the time evolution of the magnetic spectrum, where an energy flow from UV scales into IR scales, i.e. an inverse cascade, is clearly observed. As the chemical potential starts decaying, the magnetic energy is gradually transferred into the lower modes, so that at the end of the simulation most of it is peaked around the smallest lattice mode  $k_{\min}$ . Another way to display this information is by looking directly at the spatial distribution of the

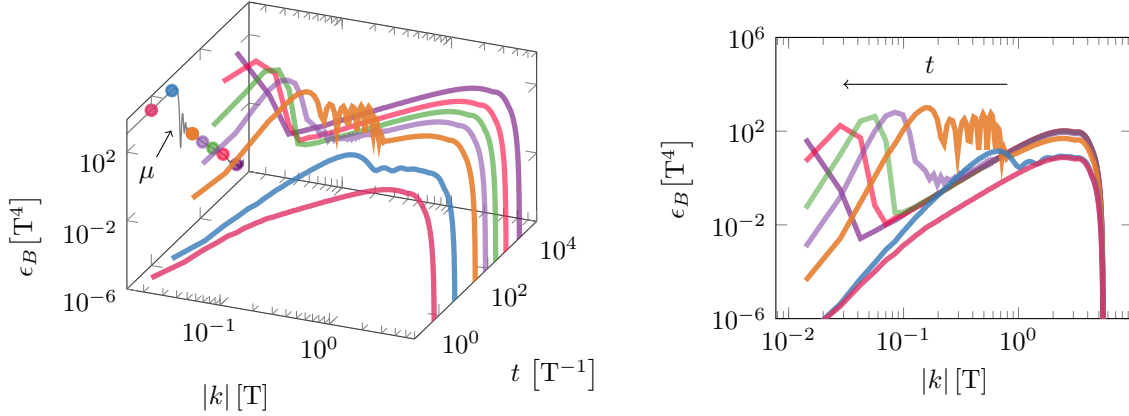


Figure 6.3 – Magnetic power spectrum on a  $448^3$  lattice with  $\mu_0 = 60\mu_c^{448}$  and  $e^2 = 1$ . In the 3D-plot, we also show the evolution of the chemical potential (the reader is referred to figure 6.2 for the correct scale). As the decay proceeds, we assist to a steady transfer of energy towards the IR. In the end, most of the magnetic energy is stored in the minimal frequency. The UV part of the spectrum is related to the intrinsic UV sickness of the classical theory.

magnetic field, as we do in figure 6.4. There we show snapshots of the magnetic field arrows, together with some representative field lines emanating from the center. In the left panel of figure 6.4, we see that, immediately after thermalisation, no characteristic structures in the magnetic field distribution are observed. However, after the inverse cascade process occurs, we see long-range magnetic fields, as depicted in the right panel of figure 6.4, where the field lines reach out through the whole lattice.

### 6.2.3 Decay in the presence of an external magnetic field

The dynamics of a chiral charge is of special interest in the presence of a background magnetic field  $B_i = \frac{1}{2}\epsilon_{ijk}F_{jk}$ . In this case, as detailed in [29], the vacuum of the theory is degenerate and the situation is closely related to its non-abelian counterpart. As already mentioned, such a background can be introduced on the lattice through the use of twisted boundary conditions [120]. The main difference from the case without magnetic field is that the chiral charge is now unconditionally unstable, and can decay all the way down to zero.

The early dynamics of the system depends crucially on the strength of the magnetic field. For large enough ones, it will drive the chiral charge decay from the beginning onward. For weak external magnetic fields, we expect the system to evolve initially like in the absence of magnetic field, and settle down to the critical value  $\mu_c$ . The chemical potential cannot stay however in the state  $\mu = \mu_c$  in the presence of a background magnetic field, and eventually decays to zero.

These two limiting situations can be well observed in our simulations. We can also study the transition between them, see in particular figure 6.5. There we plot the contribution to the

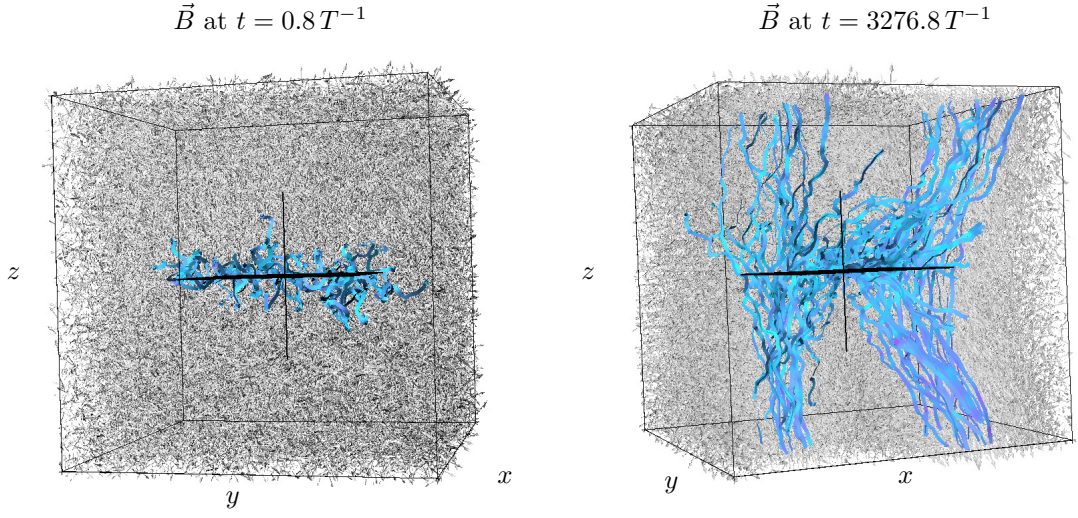


Figure 6.4 – Snapshots of the magnetic field just after thermalisation (left panel) and at the end of the inverse cascade (right panel) on a  $448^3$  lattice with  $\mu_0 = 60\mu_c^{448}$  and  $e^2 = 1$ . The blue ‘ribbons’ are field lines emanating from a small plane placed in the center of the box. They can, for instance, be drawn by following the motion of a test magnetic charge initially on the plane. At early times, no special structure is seen, since the magnetic field is homogeneous and well thermalised. At the end of the simulation, after the inverse cascade process has operated for a long while, the magnetic field has developed a long-range order, leading to structures which permeate the whole lattice. This is the spatial counterpart to the IR power displacement in Fourier space described below Eq. (6.3).



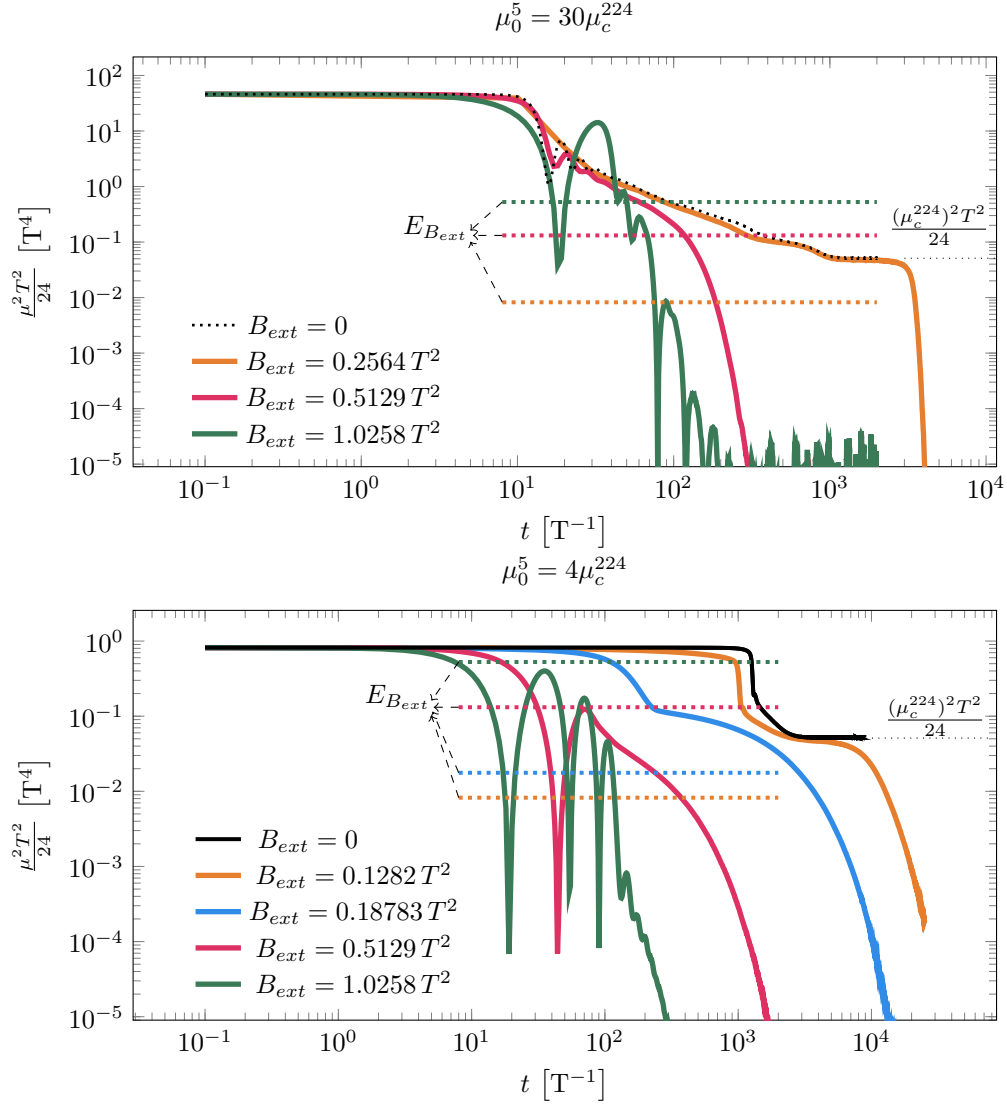


Figure 6.5 – Chiral chemical potential energy evolution for a variety of external magnetic fields. The lines  $E_{B_{ext}} = \frac{1}{2} B_{ext}^2$  are the energies of the external magnetic field, to give a reference point. *Upper plot:* Large initial chemical potential. We see three regimes. First, when the external magnetic field's energy is much smaller than the initial chemical potential energy, it has no effect on the initial dynamics; the system evolves as if there was no external background (orange curve). After some time spent in the critical *plateau*, the system eventually decays to a  $\mu = 0$  state. For a large external magnetic energy, the system does not enter the self-similar regime and the decay happens through the external magnetic field from the beginning (green curve). Between these two regimes, there is an intermediate one, where both effects contribute (pink curve). *Lower plot:* Small initial chemical potential. A similar discussion applies as in the upper plot, though the system exhibits now higher sensitivity to the external magnetic field, as the ratio between the chemical and magnetic energy is smaller.

total energy from the chemical potential  $\frac{\mu^2 T^2}{24}$ <sup>3</sup>. This allows us to compare the chemical potential energy with respect to that of the external magnetic field. In the upper panel, we plot configurations with large initial values of the chemical potential, whereas the analogous plots for weaker initial chemical potential values are presented in the lower panel. As a reference, we also display the outcome from simulations with the same initial chemical potential but no magnetic field. The dashed lines represent the magnetic energy carried by the external background. Looking first at the weakest magnetic fields, we see that its influence on the chemical potential is minimal. For larger initial chemical potentials, the simulations are almost not affected while in the case of smaller chemical potentials the length of the initial *plateau* is slightly reduced. As expected, we see that the chemical potential relaxes first to its critical value, before undergoing a secondary decay due to the presence of the background magnetic field. For stronger background magnetic fields (top red curve, and bottom red and blue curves), we observe a transition regime where both effects are competing. In this case, the system is not sensitive any more to the finite number of infrared modes; the chemical potential does not stabilise to a critical value. In both cases, it happens when the external magnetic energy is roughly two orders of magnitude smaller than the initial chemical potential energy. For even larger magnetic energies, we enter into a different dynamical regime, where the chemical potential decays quickly to zero through damped oscillations.

It is also instructive to look at the spatial distribution of the magnetic field. In figure 6.6, we show the magnetic field lines corresponding to the orange and red curves in the top panel of Fig. 6.5, associated with large initial chemical potentials. In the left panels of Fig. 6.6, we show the field lines just after thermalisation, and in the right panels we show the field line distribution at the final stage of the decay. As expected, the magnetic field is initially oriented along the direction of the external magnetic field (which, without loss of generality, was chosen to be oriented along the  $z$ -axis), and the stronger the external magnetic field the less important the thermal fluctuations are. In the final stage, we still see lattice-size structures. For weaker magnetic fields, the decay is essentially driven by the chiral instability of the chemical potential, so the field lines extend in all directions, as in the case without magnetic fields. Yet the effect it is still visible due to the presence of the external magnetic field, as more field lines expand along the  $z$ -direction. For a larger magnetic field background, the field lines which are not aligned to the  $z$ -axis are suppressed at the end of decay, and we essentially see only field strength lines along the  $z$ -axis.

#### 6.2.4 Chiral magnetic rate

As presented in the previous section, the evolution of the system in the presence of an external magnetic field is subject to two competing dynamics. On the one hand, there is the intricate evolution related to the anomaly-induced creation of long-range gauge fields. On the other hand, the external magnetic field acts as a vacuum reservoir and induces an exponential decay

<sup>3</sup>Of course this represents a "physical" energy only for  $\mu < T$ .

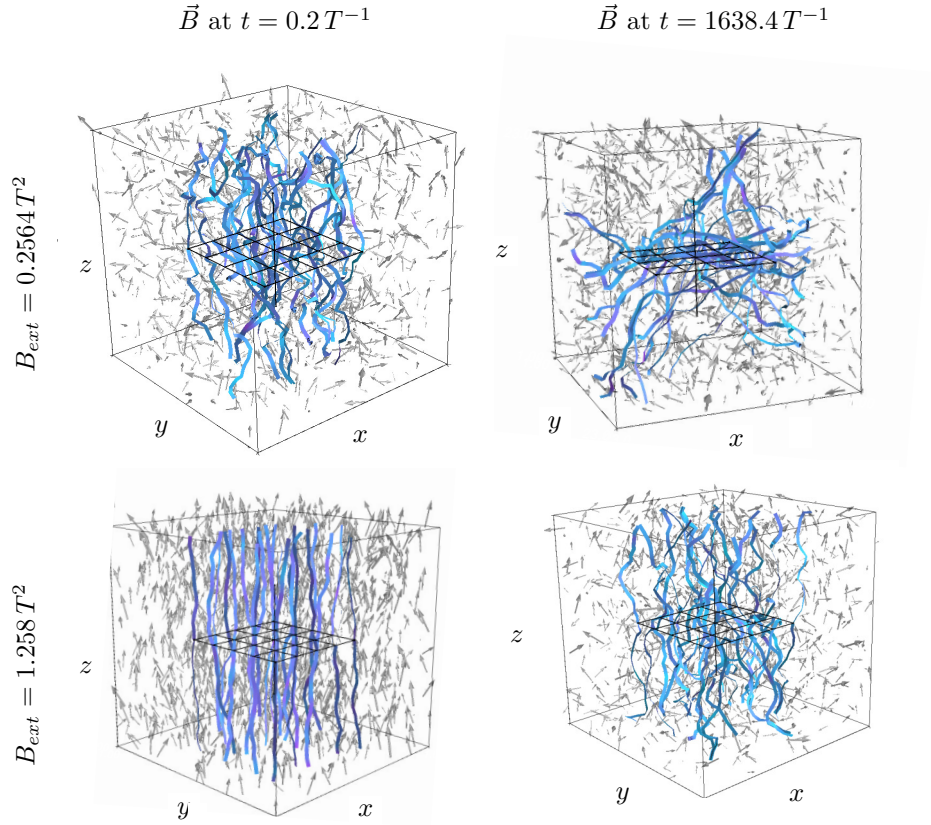


Figure 6.6 – Magnetic fields after thermalisation (left panels) and at the end of the evolution (right panels), obtained for  $N = 224$  and  $\mu_5^0 = 30\mu_c^{224}$ . Blue ribbons are the field lines emanating from a subplane in the center of the lattice. For both values of the external magnetic field, the initial configuration looks similar, with the magnetic field lines oriented along the  $z$ -direction. The final states are however different. For the weaker  $B_{\text{ext}}$  (orange curve of figure 6.5), the magnetic field develops long-range structures in transverse directions to the  $z$ -direction. For the larger  $B_{\text{ext}}$ , the final structures tend to be more aligned to the  $z$ -direction.

Fit quantity	Fit	$\chi^2/\text{dof}$
$\Gamma_5$	$10^{-2.094 \pm 0.008} (B)^{2.001 \pm 0.009} (e^2)^{2.76 \pm 0.01}$	0.88
$\frac{\Gamma_5}{B^2}$	$10^{-2.103 \pm 0.002} (e^2)^{2.75 \pm 0.01}$	1.13
$\frac{\Gamma_5}{e^{11/2}}$	$10^{-2.098 \pm 0.008} (B)^{2.005 \pm 0.008}$	1.13
$\frac{\Gamma_5}{e^6}$	$10^{-2.0 \pm 0.1} (B)^{2.1 \pm 0.1}$	155
$\frac{\Gamma_5}{e^{11/2} B^2}$	$10^{-2.10 \pm 0.02}$	1.16
$\frac{\Gamma_5}{e^6 B^2}$	$(1.9 \pm 0.1) \cdot 10^{-3} \ln\left(\frac{62 \pm 13}{e^2}\right)$	1.80

Table 6.1 – Chiral dissipation rate  $\Gamma_5$ . The errors are two standard deviations and are not rescaled by the  $\chi^2/\text{dof}$ .

of the chemical potential. In this section, we are interested in this dynamic.

To extract  $\Gamma_5$  from our simulations, we proceed as follow. To disentangle the magnetic driven decay from the rest of the dynamics, we take our initial chemical potential to be the critical one. Thanks to our large volumes, it also allow us to reach the physically relevant regime  $\mu < T$ . As explained in section 6.2.1, the anomaly-related instability does not develop for sub-critical chemical potentials. Representative evolution of the critical chemical potential in the presence of an external field are shown in the upper-left plot of 6.7. We see, as expected, a clear exponential decay. This allows us to measure  $\Gamma_5$ . We show its  $B^2$  dependence for different volumes in the upper-right panel of 6.7. We observe a good convergence to the infinite volume limit, as the  $N = 448$  and  $N = 224$  cases differ only in  $\sim 0.5\%$ . We thus pursue the investigation only on the  $N = 448$  lattices, adding a 1% systematic error to take into account any potential remaining volume dependence. We obtain that there is virtually no deviation from the expected  $B^2$  dependence.

In the lower-left panel of Fig. 6.7, we look at the charge dependence of the rate. Fitting our data, we find that they are well modeled by a  $\propto e^{11/2}$  dependence. This can also be seen in the lower-right panel of Fig. 6.7, where we show  $\frac{\Gamma_5}{e^{11/2} B_{ext}^2}$ . All the different determinations collapse to a constant; there is very little remaining dependence on the charge and magnetic field.

More quantitatively, we present in Table 6.1 the different fits we performed to our data. All the main fits agree with each other, giving an almost exact  $B^2$  magnetic dependence, an effective  $e^{11/2}$  charge dependence and a prefactor of  $10^{-2.1} \approx 0.0079$ . To check the robustness of the coefficients, we also tried to fit  $\frac{\Gamma_5}{e^6}$  with  $f(B) = \alpha B^\beta$ . Such a hypothesis is clearly excluded by the data as it leads to a  $\chi^2/\text{dof}$  of 155. We also present in this table a fit in  $\Gamma_5 = \alpha B^2 e^6 \ln\left(\frac{B}{e}\right)$  to show that the charge dependence can also potentially interpreted as logarithmic corrections to a leading  $e^6$  scaling. As we will discuss in section 6.3.3, this is what can be expected from theoretical predictions.

These numbers may be compared to the values of the topological charge diffusion rate, which

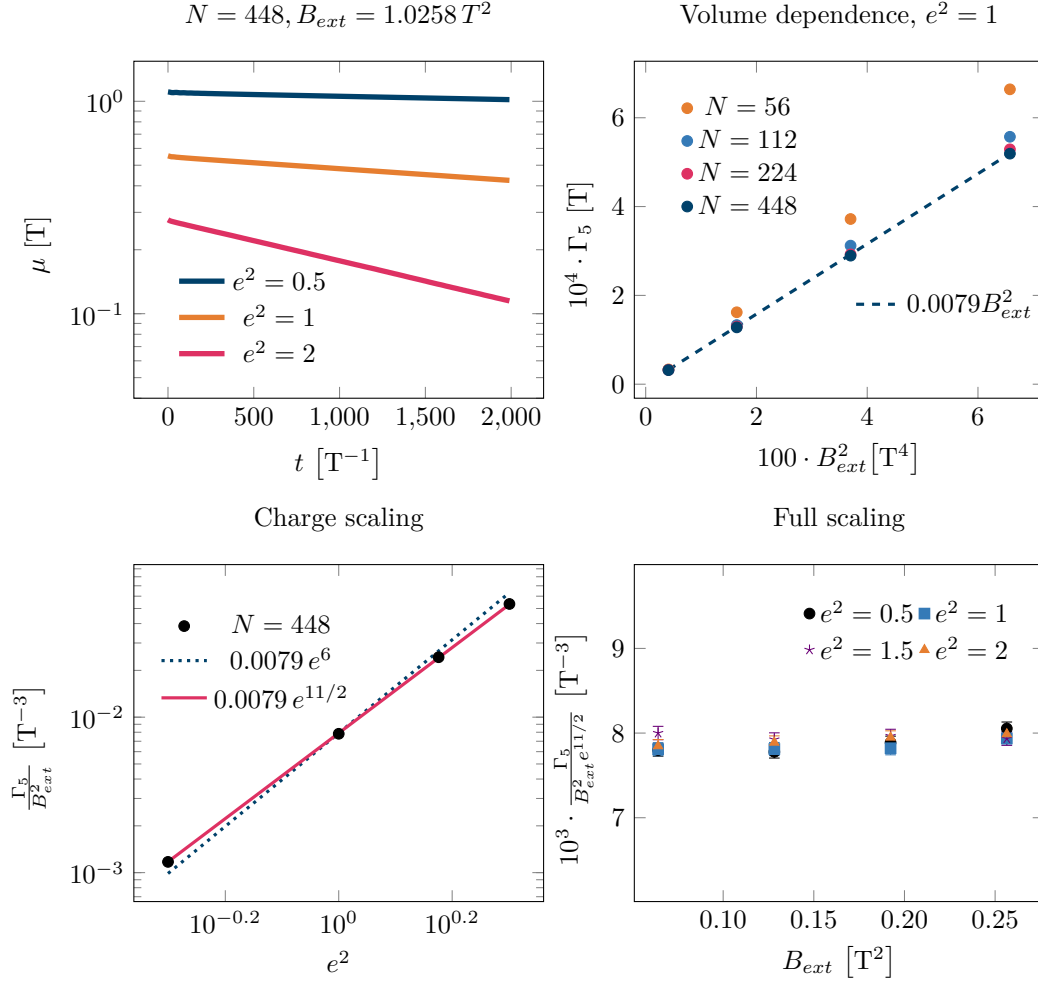


Figure 6.7 – *Upper left*: Exponential decay of the chemical potential for  $\mu_5^0 = \mu_c$ . *Upper right*: Volume dependence of the measured decay. We observe convergence to in the infinite volume limit. The  $N = 448$  results differ only in a few parts in thousands from a naive linear extrapolation using the  $N = 224$  and  $N = 448$  results. *Lower left*: Charge dependence of the decay rate. We observe a deviation from the dominant  $e^6$  scaling. We can well describe it by an effective  $e^{11/2}$  dependence. *Lower right*: Full scaling of the rate. We see that the quantity  $\frac{\Gamma_5}{e^{11/2} B_{ext}^2}$  is almost constant. The remaining charge and magnetic field dependence is very weak.

Fit quantity	Fit	$\chi^2/\text{dof}$
$\frac{\langle Q^2 \rangle}{Vt}$	$10^{-3.00 \pm 0.23} \cdot (e^2)^{2.87 \pm 0.12} \cdot B^{2.06 \pm 0.07} \cdot V^{0.05 \pm 0.09}$	0.67
$\frac{\langle Q^2 \rangle}{Vte^6}$	$10^{-3.06 \pm 0.24} \cdot 10^{-3} \cdot B^{2.05 \pm 0.08} \cdot V^{0.06 \pm 0.09}$	0.74
$\frac{\langle Q^2 \rangle}{Vte^{11/2}}$	$10^{-2.93 \pm 0.24} \cdot 10^{-3} \cdot B^{2.06 \pm 0.08} \cdot V^{0.03 \pm 0.06}$	0.74
$\frac{\langle Q^2 \rangle}{VtB^2}$	$10^{-2.91 \pm 0.21} \cdot 10^{-3} \cdot (e^2)^{2.87 \pm 0.12} \cdot V^{0.03 \pm 0.04}$	0.70
$\frac{\langle Q^2 \rangle}{Vte^6 B^2}$	$10^{-2.90 \pm 0.10} \cdot V^{0.06 \pm 0.08}$	0.76
$\frac{\langle Q^2 \rangle}{Vte^{11/2} B^2}$	$10^{-2.84 \pm 0.20} \cdot V^{0.00 \pm 0.04}$	0.77

Table 6.2 – Diffusion rate  $\Gamma_{\text{diff}}$  from [29], re-analysed. We take advantage of this re-analysis to take into account the statistical fluctuations in the fit, which was not done in [29]. The errors represent two standard deviations. The relatively small  $\chi^2/\text{dof}$  shows some degree of overfitting. As we do not use it to rescale the errors, they are probably overestimated.

at large time reads

$$\langle Q^2(t) \rangle = \Gamma_{\text{diff}} V t \quad (6.13)$$

with  $Q(t) = N_{cs}(t) - N_{cs}(0)$ ,  $N_{cs}(t) = \frac{e^2}{8\pi^2} \int d\mathbf{x}^3 \vec{A} \cdot \vec{B}$ . This quantity was measured in [29], and it is related to  $\Gamma_5$  through a standard fluctuation-dissipation argument<sup>4</sup>

$$\Gamma_5 = 6 \frac{\Gamma_{\text{diff}}}{T^3}. \quad (6.14)$$

For the sake of the comparison, we present in Table 6.2 a re-analysis of the data of Ref. [29]. Unfortunately, the diffusion rate is a harder quantity to extract and leads to a less precise quantification. As the results of [29] were obtained at different small volumes, we keep an explicit volume dependence in our fits, even if we find it to be weak. Taking as a measured value  $\Gamma_5 = 10^{-2.10 \pm 0.02} B^2 e^{11/2} / T^3$  leads to a prediction  $\Gamma_{\text{diff}} = 10^{-2.88 \pm 0.02} B^2 e^{11/2}$ . The prefactor and the magnetic field dependence are consistent with the measurements of  $\Gamma_{\text{diff}}$  reported in [29]. At first sight, the scaling with  $e^2$  seems to be in mild tension, but further analysis shows that the data from Ref. [29] does simply not constrain well enough the charge dependence of  $\Gamma_{\text{diff}}$ . This can be seen in the fits in Table 6.2, where either scalings  $\propto e^{11/2}$  and  $\propto e^6$  are compatible with the data, exhibiting a similar  $\chi^2/\text{dof}$ . We conclude that within the errors, the fluctuation-dissipation relation Eq. (6.14) is well verified.

### 6.3 Comparison to MHD

Different approaches can be followed to get some analytical understanding of a system in the presence of a chiral chemical potential. Recently, progresses have been made towards establishing a *chiral*-kinetic theory, which adds to the usual Boltzmann-like approach a

<sup>4</sup>Note that the corresponding expression in [29] contains a factor 2 wrong, see appendix 6.6 here, for a clarification of this.

self-consistent treatment of the anomaly, see [88] and references therein for more information. Valuable knowledge may also be gained in the hydrodynamical regime by studying the effective field theory of the long wavelength field modes together with the electromagnetic interactions. In this approach, matter is a fluid, characterised by its velocity field. A variety of interaction terms going from the simple linear response electric conductivity to direct coupling of the velocity which can induce turbulence can be added. This kind of approach is referred to as MHD. The equations can be further modified to take into account anomalous processes [61, 62], to give anomalous MHD. Recently, an extensive study was carried out, both at the theoretical level [89] and using numerical simulations, [76] of full anomalous MHD models. We refer the interested reader to these references for more details.

To try to gain some understanding of our results, we will attempt to model the system using a truncated set of MHD equations. Namely, we will focus on the magneto-dynamics part, not considering any hydrodynamics evolution.

$$\begin{aligned}\frac{\partial \vec{E}}{\partial t} &= e\vec{j} - \vec{\nabla} \times \vec{B} - \frac{e^2}{4\pi^2} \mu \vec{B}, & \frac{\partial \vec{B}}{\partial t} &= \vec{\nabla} \times \vec{E}, \\ \frac{d\mu}{dt} &= \frac{3e^2}{T^2\pi^2} \frac{1}{V} \int d^3x \vec{E} \cdot \vec{B}, & \vec{j} &= -\sigma \vec{E}.\end{aligned}\tag{6.15}$$

where  $\sigma$  is the linear-response electric conductivity.

This approximation will turn out to qualitatively work surprisingly well. Indeed, as our lattice simulations describes the full-dynamics of our matter field, there is no *a priori* reasons for the matter field to contribute little to the global dynamics. It is even likely that in some regimes not explored in this work, matter effects which would be described as turbulence in a hydrodynamic language should manifest themselves.

In particular, this model predicts the existence of a chiral magnetic rate. Indeed, the evolution equation for  $\mu$  can be rewritten as, neglecting the time derivative of the electric field,

$$\frac{d\mu}{dt} = -\frac{3e^2}{T^2\pi^2\sigma} \frac{1}{V} \int d^3x \left( \frac{e^2}{4\pi^2} \mu \vec{B} + \vec{\nabla} \times \vec{B} \right) \cdot \vec{B}.\tag{6.16}$$

Taking  $B$  to be constant, we then obtain

$$\mu \propto e^{-\Gamma_5^{(MHD)} t},\tag{6.17}$$

with  $\Gamma_5^{(MHD)} = \frac{3e^4 B^2}{4\pi^4 \sigma T^2}$ . We will compare it to our results in section 6.3.3.

Finally, note that from now on, when we refer to MHD or MHD-like predictions, we have in mind the specific model (6.15).

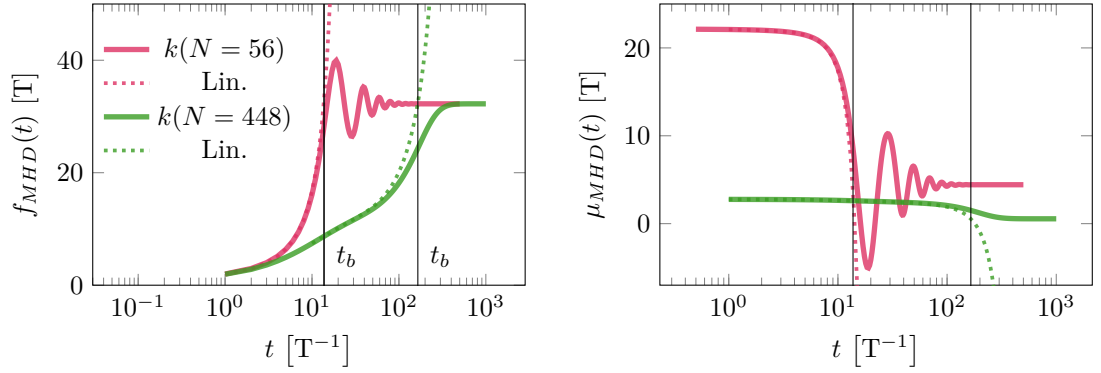


Figure 6.8 – *Left*: Single-mode MHD solution for some typical value of the parameters. The value of  $k$  is chosen to correspond to the minimal  $k$  which can be simulated on lattices of sizes  $N = 56$  and  $N = 448$ . We further set  $\sigma = 0.1, e^2 = 1$  and take  $f_0 = \dot{f}_0 = 1$  as initial values. We also plot the predicted breaking time, which gives a good estimate for the end of the exponential growth. *Right*: Corresponding chemical potentials.

### 6.3.1 Qualitative behaviour and initial plateaus

As presented in previous sections, the chemical potential is transferred into long-range helical magnetic fields which carry a non-vanishing Chern-Simons number. To understand at a qualitative level some of the observed features, like the existence of *plateaus* in the initial stage, we can consider the evolution of a maximally helical field under anomalous MHD-like dynamics. In the presence of a background magnetic field in the  $z$ -direction, this corresponds making the *ansatz* [118]

$$A_1 = f(t) \sin(kz) - \frac{B}{2} y, \quad A_2 = f(t) \cos(kz) + \frac{B}{2} x, \quad A_3 = f_z(t), \quad (6.18)$$

which leads to

$$\ddot{f} = kf \left( \frac{e^2 \mu}{4\pi^2} - k \right) - \sigma \dot{f}, \quad (6.19)$$

$$\dot{\mu} = \frac{3e^2}{T^2 \pi^2} (B \dot{f}_z - k f \dot{f}), \quad (6.20)$$

$$\ddot{f}_z = -\sigma \dot{f}_z - \frac{e^2}{4\pi^2} \mu B. \quad (6.21)$$

Let us first consider this toy-model without an external magnetic field ( $B = 0, f_z(t) = 0$ ). Then the system of equations reduces to

$$\ddot{f} = kf \left( \frac{e^2 \mu}{4\pi^2} - k \right) - \sigma \dot{f}, \quad \mu = -k \frac{3e^2}{2T^2 \pi^2} f^2 + k \frac{3e^2}{2T^2 \pi^2} f_0^2 + \mu_0. \quad (6.22)$$



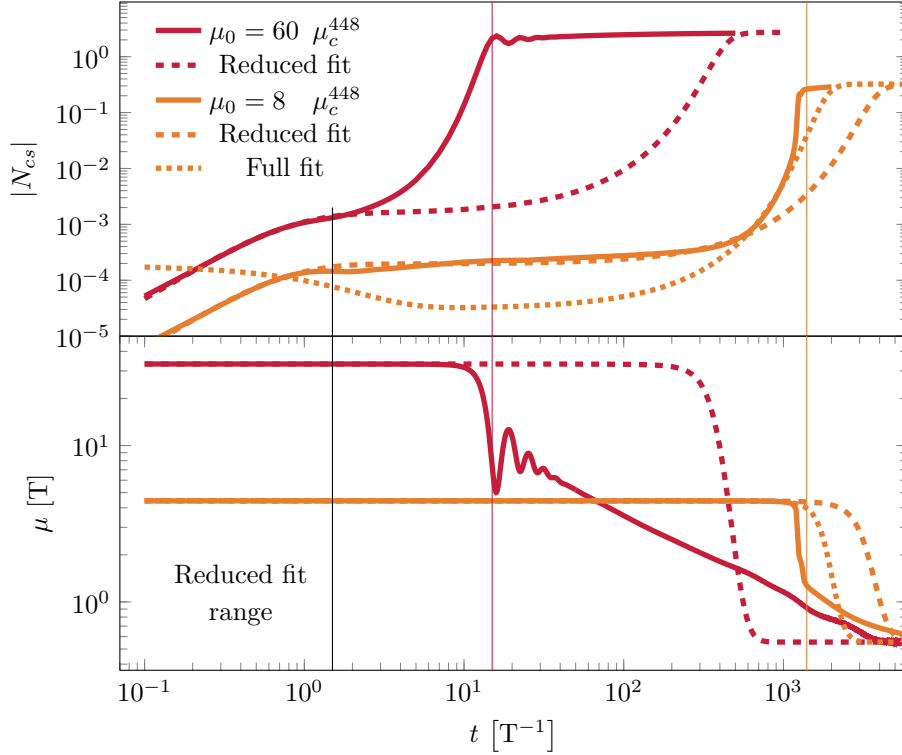


Figure 6.9 – *Upper panel:* Chern-Simons number evolution. *Lower panel:* Chemical potential. In both cases, non-solid lines are fits obtained from the model (6.22). Dotted ones correspond to a fit over the full time range whilst dashed lines were obtained by restricting  $t < 10$ . We see that the model is appropriate only for the initial part of the evolution.

By plugging in the expression for  $\mu$  into the first equation of (6.22), we obtain a non-linear equation for  $f(t)$ . Solving it numerically also gives us access to the evolution of  $\mu(t)$ . Here, we take  $f_0$  and  $\sigma$  to be some free parameters to be fitted. Examples of the time evolution of  $f(t)$  and  $\mu(t)$  obtained with this procedure, are shown in figure 6.8. Despite being in qualitative agreement, this simple modeling does not capture completely the fine details, especially for large initial chemical potentials. In figure 6.9, we compare the modeling based on the *ansatz* (6.18) with the numerical outcome from our lattice simulations. The lower panel shows the chemical potential whilst the upper panel shows the Chern-Simons number, which is useful to understand the initial dynamics. Solid lines were obtained from our simulations, while dashed and dotted ones are numerical solutions to equations (6.22) for different parameters (conductivity and initial conditions).

Let us first consider the case  $\mu_0 = 8\mu_c$ , as the model gives a better description for relatively small chemical potentials. The dotted curves were obtained by fitting the *ansatz* model to the whole range of data. When looking at the chemical potential, we see that the model is able to describe reasonably well the initial *plateau*, but fails to describe well the decay. Actually, when looking at the Chern-Simons number, we see that even the initial phase is not very well described by this fit. A remedy to this is to restrict the fitting range to early times, where the

system should be closer to the model. For example, the dashed curves are obtained by restricting the fitting range to times  $t < 10/T$  (delimited by a solid vertical black line). This gives a much better description of the initial phase; essentially the initial evolution is well captured by the simple *ansatz*. At a later stage, when a more complex dynamics has developed, such as the creation of long-range magnetic fields following a process of inverse cascade (or what can be described as a turbulent regime in MHD), the model is too simplistic to capture well the physics. The same can be said about large initial chemical potentials, as in the case of  $\mu_0 = 60\mu_c$  depicted in the figure. There, we see explicitly that the power-law decay (expected due to the generation of long-range magnetic field) is completely missed by the *ansatz* modeling. The red and orange vertical solid lines are a visual guide indicating the saturation of the Chern-Simons number and of the corresponding chemical potential.

We can get a better understanding of the early dynamics of  $f(t)$  and  $\mu(t)$  in the *ansatz* modeling, by simply perturbing equation (6.22), i.e. considering  $f(t) = f_0 + \delta f(t)$ , so that

$$f_0 k^2 - \frac{e^2}{4\pi^2} f_0 k \mu_0 + k^2 \delta f(t) + \frac{3e^4}{4\pi^4 T^2} f_0^2 k^2 \delta f(t) - \frac{e^2}{4\pi^2} k \mu_0 \delta f(t) + \sigma \dot{\delta f}(t) + \ddot{\delta f}(t) + \frac{9f_0 k^2 e^4}{8\pi^4 T^2} \delta f(t)^2 + \frac{3k^2 e^4}{8\pi^4 T^2} \delta f(t)^3 = 0. \quad (6.23)$$

Keeping the linear order terms in  $\delta f$  and neglecting the terms proportional to  $f_0^2$  (we do not start in a state with an helical field), the equation reduces to

$$\left(k^2 - \frac{e^2}{4\pi^2} k \mu_0\right) (f_0 + \delta f(t)) + \sigma \dot{\delta f}(t) + \ddot{\delta f}(t) = 0. \quad (6.24)$$

This is a driven harmonic oscillator which admits a solution as

$$\delta f(t) \approx \frac{e^{-\frac{\sigma}{2}t}}{2\omega_{eff}} (2f_0 \omega_{eff} \cosh(\omega_{eff} t) + (2\dot{f}_0 + f_0 \sigma) \sinh(\omega_{eff} t)) - f_0, \quad (6.25)$$

where  $\dot{f}_0$  is the initial time derivative of  $f(t)$ , and we have defined

$$\omega_{eff}^2 = \frac{e^2}{4\pi^2} k \mu_0 - k^2 + \left(\frac{\sigma}{2}\right)^2. \quad (6.26)$$

Eq. (6.25) indicates, first of all, that the solution corresponds to an IR instability for the modes  $k < \frac{e^2}{4\pi^2} \mu_0$ , which grow exponentially fast. Secondly, by estimating the range of validity of this solution, we can estimate the duration of the chemical potential *plateau* until the onset of its decay. Indeed, the breakdown of this approximation corresponds to the end of the exponential growth of  $f(t)$ , which in turn triggers the chemical potential decay. The approximations cease to be valid when higher order perturbations become non-negligible. To see this in detail, we keep only the exponentially growing part of the solution and neglect the constant term,

$$\delta f(t)_{as} \approx \frac{\exp\left(\left(-\frac{\sigma}{2} + \omega_{eff}\right)t\right)}{2\omega_{eff}} \left(f_0 \left(\omega_{eff} + \left(\frac{\sigma}{2}\right)\right) + \dot{f}_0\right). \quad (6.27)$$

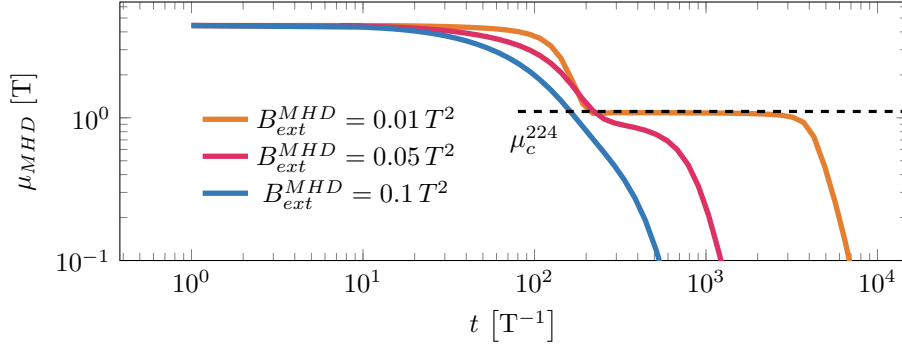


Figure 6.10 – Numerical solution to our single-mode MHD model for three different magnetic fields and some reasonable initial conditions. The behaviour is in qualitative agreement with the numerical outcome from lattice simulations, see Fig. 6.5. Three regimes appear to be present: one initially dominated by the chiral instability (orange curve), another where the decay is strongly induced by the external magnetic field (blue curve), and an intermediate regime (pink curve).

The relative weight between the linear to second-order perturbation terms in the equation of motion 6.23, and linear to third order terms, are defined by the ratios

$$r_2(t) = \frac{k^2 - \frac{e^2}{4\pi^2} k\mu_0}{\frac{9f_0 k^2 e^4}{8\pi^4 T^2}} \frac{1}{\delta f(t)_{as}}, \quad r_3(t) = \frac{k^2 - \frac{e^2}{4\pi^2} k\mu_0}{\frac{3k^2 e^4}{8\pi^4 T^2}} \frac{1}{\delta f(t)_{as}^2} \quad (6.28)$$

We expect the linear approximation to breakdown whenever either of these ratios become of order one. We thus define the breakdown time  $t_b$  to be

$$t_b \equiv \min(t_2, t_3), \quad \text{with } r_2(t_2) \equiv 1, \quad r_3(t_3) \equiv 1. \quad (6.29)$$

In figure 6.8, we show how this prediction performs, comparing the linearisation (dotted lines) to the numerical solution to Eq. (6.22). We see that  $t_b$  in (6.29) gives a reliable prediction of the range of validity of the linearisation regime. In conclusion, the duration of the initial *plateau* can be estimated well with our simple MHD-inspired *ansatz* equation (6.18).

In the presence of an external magnetic field, the system of equations (6.19) does not admit a simple enough analytic treatment. We can solve them nonetheless numerically. We show the chemical potential obtained from numerical integration of these equations in figure 6.10. As in the previous case, we see that it captures reasonably well the dynamics of small chemical potentials. For weak magnetic fields, it is dominated by the chiral instability of the chemical potential. The system evolves as in the absence of magnetic fields, reaches a *plateau* and only at later times it decays to zero because of the presence of the magnetic background field. For a sufficiently large background magnetic field, the decay is driven by the presence of such field, driving quickly the system into a  $\mu = 0$  state. For intermediate external magnetic fields, we have a superposition of the two effects.

### 6.3.2 Self-similarity and inverse cascade

The power law decay  $\propto t^{-1/2}$  of the chemical potential reported in section 6.2.2 was also predicted in the context of MHD in several works [61, 74, 75, 121, 122]. More specifically, various analysis of the time evolution of the magnetic spectrum, have been carried out in refs. [61, 121, 122]. We will now compare these modelings with the outcome from our numerical simulations. First of all, we repeat the analysis of refs. [61, 121, 122]. The starting point in MHD are equations (6.15). Taking the curl of the first equation and neglecting the second time derivative of  $\frac{\partial^2 \vec{B}}{\partial t^2} \approx 0$ , the equation for the magnetic field can be recast as

$$\sigma \frac{\partial \vec{B}}{\partial t} = \nabla^2 \vec{B} + \frac{e^2}{4\pi^2} \mu (\vec{\nabla} \times \vec{B}). \quad (6.30)$$

We can now decompose the magnetic field in an orthonormal helicity basis  $Q^\pm(\vec{k}, \vec{x})$ , which corresponds to a basis<sup>5</sup> of eigenvectors of the curl operator,

$$\vec{B}(x, t) = \int \frac{d^3 k}{(2\pi)^3} \left( \vec{\alpha}^+(t, \vec{k}) Q^+(\vec{k}, \vec{x}) + \vec{\alpha}^-(t, \vec{k}) Q^-(\vec{k}, \vec{x}) \right), \quad (6.31)$$

so that  $\vec{k} \times Q_\pm(\vec{k}) = \pm k Q_\pm(\vec{k})$ . In that basis Eq. (6.30) reduces to

$$\frac{\partial \alpha^\pm(t, \vec{k})}{\partial t} = \frac{1}{\sigma} \left( -k^2 \pm \frac{e^2}{4\pi^2} \mu(t) k \right) \alpha^\pm(t, \vec{k}), \quad (6.32)$$

which admits as a solution

$$\alpha^\pm(t, \vec{k}) = \alpha_0^\pm(\vec{k}) \exp \left[ \frac{1}{\sigma} \left( -k^2 t \pm k \frac{e^2}{4\pi^2} \int_{t_0}^t dt' \mu(t') \right) \right]. \quad (6.33)$$

Furthermore, as soon as  $\int_{t_0}^t dt' \mu(t')$  becomes sizable,  $\alpha^-(t, \vec{k})$  becomes sub-dominant. Neglecting the latter, we can then write

$$|B(t, \vec{k})|^2 \approx |\alpha_0^+(\vec{k})|^2 \exp \left[ \frac{2}{\sigma} \left( -k^2 t + k \frac{e^2}{4\pi^2} \int_{t_0}^t dt' \mu(t') \right) \right]. \quad (6.34)$$

Equation (6.34) represents a prediction based on MHD, which we can use to compare against our data. A further simplification we make, following [121], is to neglect the  $\vec{k}$  dependence<sup>6</sup> of the initial amplitude  $\alpha^+(\vec{k}) \approx \alpha_0^+$ . This leads us to write down the following function

$$B_{fit}^2(k, c_1, c_2, c_3) = \exp(c_1 k^2 + c_1 \cdot c_2 k + c_3), \quad (6.35)$$

<sup>5</sup>The precise form of the basis depends on the base space the analysis is performed, e.g. Ref. [61, 121] considers  $\mathbb{R}^3$  whilst Ref. [122] used a sphere. In the analytical description above we will simply work in a Euclidean base space  $\mathbb{R}^3$ , as we are describing the continuum theory. Were we to write down a basis for the torus, we could construct it nonetheless from a superposition of the basis of [121].

<sup>6</sup>Note that we could also get rid of it by considering ratios of  $|B(t, \vec{k})|^2$  at different times. An analysis using this method turned out to be less accurate, we believe because of the small number of momenta we can use for the fits.

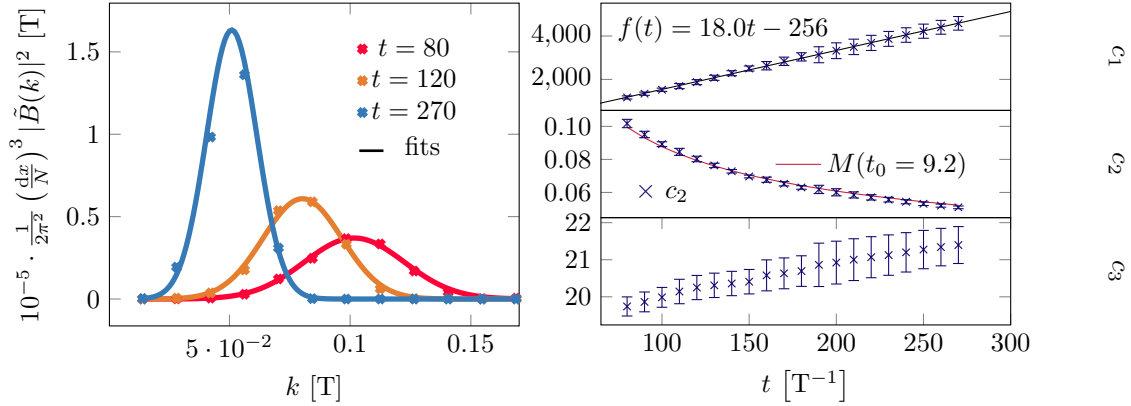


Figure 6.11 – *Left*: Time evolution of  $\frac{1}{2\pi^2} \left(\frac{dx}{N}\right)^3 |\tilde{B}(k)|^2$  against MHD inspired fits, see equation (6.12). *Right*: Fit’s parameters as a function of time. The coefficient  $c_1$  allows for a determination of an effective conductivity,  $\sigma_{eff}$ ,  $c_2$  can be used to check the validity of the fit, as it is expected to follow the evolution of the integrated chemical potential, which is indeed the case. Lastly,  $c_3$  can also be used as a *a posteriori* check, as it is supposed to be a constant. The fits are based on MHD predictions and show a remarkable agreement in the qualitative description.

which will be used as a fit to  $|B(k, t)|^2$  obtained from our simulated data at different times. This is precisely what we show in figure 6.11. In the left panel we plot  $|B(k, t)|^2$  for three different times together with a best fit of the form (6.35). Despite the limited number of modes available, we see that the data is well fit by a functional form as in Eq. (6.35).

Let us look now at the time dependence of the fit coefficients  $c_1, c_2$  and  $c_3$ . From comparing (6.35) and (6.34), we expect  $c_1$  to be a linear function of  $t$ . This is exactly what we observe in figure 6.11, where the top right panel displays a linear fit from our data as  $c_1(t) = (18.0 \pm 0.1)t + (256 \pm 20)$ . The crossing of the fit with the y-axis encodes actually various effects. First of all, we learn that  $t_0$  is not zero, and rather corresponds to an initial time at which  $|B(t, \vec{k})|^2$  is equal to  $|\alpha_0^+|^2$  (we will estimate it shortly, in a self-consistent manner, from the fit to the second coefficient  $c_2$ ). Secondly, a non-zero crossing may also reintroduce some  $k^2$  dependence in the initial condition, which will partially compensate for the approximation  $\alpha^+(\vec{k}) \approx \alpha_0^+$ .

The coefficient  $c_2$  is expected to go as  $M(t_0, t) \equiv \frac{1}{t} \frac{e^2}{4\pi^2} \int_{t_0}^t dt' \mu(t')$ . Its dependence on  $t_0$  allows us to estimate this initial time, by comparing it to  $M(t_0, t)$  for different values of  $t_0$ , and looking for the best match. This is shown in the middle right panel of figure 6.11. This procedure leads to an estimated value of as  $t_0 \approx 9.2/T$ . A last check is provided by the lower right panel of figure 6.11, which shows how close  $c_3$  is to a constant. The fact that this MHD-inspired model achieve such a good description of the data is a bit surprising, as the chemical potential probed here lie outside of the range of validity of (6.15). The relevant length scales which are to be compared are the typical instability length scale associated to the chemical potential decay,  $l_{inst} \sim \frac{1}{k_{inst}} = \frac{4\pi^2}{e^2\mu}$  to the typical mean free path in the plasma  $\lambda \sim \frac{1}{\alpha^2 T}$ . MHD is expected

to be valid for  $l_{inst} > \lambda$ , which happens for  $\mu < e^2 T$ . The only place where the "breaking" of the effective theory can be seen is if we try to extract a conductivity from the coefficient  $c_1$ . This gives an effective conductivity  $\sigma_{eff} = (0.11 \pm 0.01)T$ , which differs from the kinetic theory prediction, see section 6.3.3 for more details.

An interesting question would be to compare  $\sigma_{eff}$  to the intrinsic measurement of our system's conductivity with the use of the Kubo formula [123]. For classical field theories on a lattice with finite volume  $V$ , for a homogeneous and isotropic plasma,  $\sigma$  can be written as [29]

$$\sigma = \int dt \Sigma(t), \quad \Sigma(t) \equiv \frac{1}{VT} \frac{1}{3} \sum_{i=1}^3 \int d^3x \int d^3y \langle j_i(x, t) j_i(y, 0) \rangle, \quad (6.36)$$

where  $j_i$  are the spatial components of the electric current, and  $\langle \dots \rangle$  is an ensemble average over different realisations of our thermal initial conditions. This formula is readily to be implemented as an observable in our lattice simulations. The expression is however UV sensitive (in the free theory it is even linearly divergent with momentum), so the results are expected to be sensitive to the natural UV cutoff imposed by the lattice  $k_{\max} \sim 1/dx$ . The correlator in (6.36) is expected to decay exponentially in time,  $\Sigma(t) \sim \exp(-\gamma t)$ , and to oscillate with the plasma frequency. When obtaining numerically  $\Sigma(t)$  from our simulations, it exhibits an oscillatory pattern with frequency considerably smaller than  $1/T$ , which is presumably attributed to the plasma frequency (plots of this can be found in figure 7 (right panel) of Ref. [29], so we do not reproduce them here again). After some time, oscillations occur around zero, indicating the dumping. However, the presence of short time oscillations, associated with the lattice UV cutoff, is also very noticeable. These contribute to make the behaviour of  $\Sigma(t)$  very 'noisy', making difficult to obtain a trustworthy attempt to extract  $\sigma$  by this procedure.

Note that even if we were to extract a conductivity from this method, there is no reason to expect it to be equal to the quantum field theory computation. Indeed, as it is a UV-dominated quantity, it is sensitive to the distribution of large-momentum modes, which are intrinsically different between the classical and quantum field theory, see [100] for a careful discussion on this issue.

### 6.3.3 Chiral magnetic rate and MHD

As mentioned at the beginning of the section, one can infer a chiral magnetic-rate from MHD

$$\Gamma_5^{(MHD)} = \frac{3e^4 B^2}{4\pi^4 \sigma T^2}. \quad (6.37)$$

To be able to use this prediction, we need to use the kinetic theory prediction for the conductivity. The computation consists in finding the coefficient  $\sigma$  in the relation  $\vec{j} = -\sigma \vec{E}$  where  $\vec{E}$  is an external uniform and time-independent electric field and  $\vec{j}$  is the induced electric current. The main process to be taken into account is the mutual scattering of charged particles with an energy of the order of temperature. At leading-log order, for one charged

fermion species, it can be estimated as [124]

$$\sigma_F \simeq \frac{12^4 \zeta(3)^2}{\pi^3 (3\pi^2 + 32)} \frac{T}{e^2 \log(q_F/e)} . \quad (6.38)$$

For one charged scalar species, the conductivity has been also obtained recently as [125]

$$\sigma_S \simeq \frac{3^2 2^5 \zeta(3)^2}{\pi^3} \frac{T}{e^2 \log(q_S/e)} . \quad (6.39)$$

The coefficients  $q_F, q_S$  are  $\sim \mathcal{O}(1)$ , but can only be fixed from matching a computation at full leading order. The leading behaviour of the chiral rate is then expected to scale, independently of whether we use the fermion or scalar computation, as

$$\Gamma_5 \propto e^6 B^2 \ln(q/e) / T^3 , \quad (6.40)$$

with  $q$  some  $\mathcal{O}(1)$  parameter.

In the case of a charged fermion species, the coefficient  $q_F$  in the log can be determined using the full leading numerical result, for instance evaluated at  $e^2 = \frac{4\pi}{137.04}$ , as can be read out from table 2 of Ref. [126]. Matching such value to Eq. (6.38), leads to  $q_F = 4.2$ , and hence to

$$\sigma_F \simeq \frac{12^4 \zeta(3)^2}{\pi^3 (3\pi^2 + 32)} \frac{T}{e^2 \ln(4.2/e)} . \quad (6.41)$$

Unfortunately, there is no analogous full leading computation available for the scalar field case, so we cannot determine exactly the value of  $q_S$ . Assuming that  $q_S = q_F$ , then  $\sigma_S$  remains  $\sim 14.5\%$  smaller than  $\sigma_F$ . If we consider, however, values within the range e.g.  $q_F - 2 \leq q_S \leq q_F + 2$ , then  $\sigma_S$  ranges, for  $e = 1$ , between  $\sim 56\%$  larger and  $\sim 33\%$  smaller, compared to  $\sigma_F$  given by Eq (6.41) evaluated at  $e = 1$ . The difference becomes however smaller for smaller values of  $e$ .

In section 6.2.4, where we extracted this rate in the physical region  $\mu < T$ , we observed an almost perfect  $B^2$  dependence of  $\Gamma_5$ , but a certain deviation from an exact  $\propto e^6$  scaling. In particular, fitting to a simple power law  $\propto e^p$ , we obtain a best fit with  $p = 11/2$ , whereas fitting to a form  $e^6 \ln \frac{q}{e}$  we obtain  $q = 7.9$ , see Table 6.1<sup>7</sup>. Both of these fits describe well our data, although the logarithmic fit leads to a slightly worse  $\chi^2/dof$ . Given our limited range of values of  $e^2$ , we cannot clearly discriminate between these two options.

Using as a reference  $\sigma_F$ , we can now estimate a chiral magnetic decay rate from MHD and compare it to our simulations. Plugging in numbers, we get

$$\sigma_F \simeq \frac{31.4}{e^2 \log(17.6/e^2)} T , \quad (6.42)$$

---

<sup>7</sup>Note that we present there the result of the logarithmic fit as a function of  $q^2 \approx 62$ .

which for  $e^2 = 1$  gives  $\sigma_F \simeq 10.95 T$ . In the presence of a background magnetic field  $B$ , the chiral rate is actually inversely proportional to the conductivity, and it is given by

$$\Gamma_5^{(MHD)} = \frac{3e^4}{4\pi^4 \sigma_F T^2} B^2 \simeq 2.45 \cdot 10^{-4} \log(17.6/e^2) e^6 B^2 / T^3, \quad (6.43)$$

which for  $e^2 = 1$  is  $\Gamma_5^{(MHD)}(e^2 = 1) \simeq 7.0 \cdot 10^{-4} \cdot B^2 / T^3$ . In general then,  $\Gamma_5^{(MHD)} \sim 7 \times 10^{-4} \cdot e^6 \cdot B^2$ , modulo electric charge logarithmic corrections. Alternatively, from the fluctuation-dissipation relation  $\Gamma_{\text{diff}} = \frac{1}{6} \Gamma_5 T^3$ , the effective diffusion rate is expected in MHD as

$$\Gamma_{\text{diff}}^{(MHD)} \simeq 4.1 \cdot 10^{-5} \log(17.6/e^2) e^6 B^2, \quad (6.44)$$

which e.g. for  $e^2 = 1$  is  $\Gamma_{\text{diff}}^{(MHD)} \simeq 1.1 \cdot 10^{-4} \cdot B^2$ , or again in general  $\Gamma_{\text{diff}}^{(MHD)} \sim 10^{-4} \cdot e^6 B^2$  modulo logarithmic corrections on the electric charge.

Comparing these rates against our numerical fits to  $\Gamma_5$  (c.f. Table 6.1) or against the fits to  $\Gamma_{\text{diff}}$  from Ref. [29] (c.f. Table 6.2), we observe that the numerically extracted rates are a factor  $\sim 10$  larger than the MHD counterparts. In particular for  $e^2 = 1$  and imposing an exact scaling  $\propto B^2$  over our data (something that it is very well verified, recall the discussion in section 6.2.4), we obtain<sup>8</sup>

$$\left. \frac{\Gamma_5^{(num)}}{\Gamma_5^{(MHD)}} \right|_{e^2=1} = 11.2^{+0.1}_{-0.1}, \quad \left. \frac{\Gamma_{\text{diff}}^{(num)}}{\Gamma_{\text{diff}}^{(MHD)}} \right|_{e^2=1} = 10.5^{+6.5}_{-4.0}. \quad (6.45)$$

The two ratios in Eq. (6.45) are, as expected, consistent with each other, even if these are numbers independently obtained. This is simply due to the fact that the fluctuation-dissipation argument relating  $\Gamma_5$  and  $\Gamma_{\text{diff}}$ , is actually well verified in our data (within the errors of the diffusion rate), recall section 6.2.4. In summary, both the chiral decay rate or the Chern-Simons diffusion rate, obtained by completely independent simulations, lead to rates much larger than predicted in the MHD picture. This is the main quantitative result of our work.<sup>9</sup>

The equations (6.45) lead us to conclude that formula (6.37) is not describing correctly the rate of fermion number non-conservation in the presence of magnetic fields in our system. We take this as an evidence of the impact of short-scales fluctuations on the system dynamics. Assuming this to be correct, it calls for a revision of the cosmological implications of fermion number and chirality non-conservation in finite temperature Abelian gauge theories.

In fact, the failure of the MHD to predict correctly the CS diffusion rate in the presence of a magnetic field is not surprising. The MHD is only valid at distances larger than the mean free

<sup>8</sup>The ratio  $\Gamma_5^{(num)}/\Gamma_5^{(MHD)}$  of Eq. (6.45) was obtained with the power law fit  $\Gamma_5^{(num)} \propto e^{11/2}$ . If the ratio is obtained instead with the logarithmic fit  $\Gamma_5^{(num)} \propto e^6 \ln\left(\frac{62}{e^2}\right)$ , this yields (for  $e^2 = 1$ )  $\Gamma_5^{(num)}/\Gamma_5^{(MHD)} = 11.3^{+1.0}_{-1.4}$ , which is equally consistent with the other ratios.

<sup>9</sup>Note that this result can also be interpreted as having an effective conductivity 10 times smaller than that coming from kinetic theory.



path of particles in the plasma and thus it is not accounting correctly for the shorter scale electromagnetic fluctuations that may change the CS number and which are automatically included in our simulations. The similar phenomena exists in the diffusion of the CS number in non-Abelian theories, where the relevant distance scale  $\sim \frac{1}{\alpha T}$  is much smaller than the scattering length  $\sim \frac{1}{\alpha^2 T}$ . Though our lattice simulations, being classical in nature, do not include several effects - hard thermal loops (HTL) and scattering of energetic particles with energy  $\sim \mathcal{O}(T)$ , we do believe that they are reliable. The HTLs introduce a Debye-screening of the electric fields, plasmon masses for thermal excitations, and the Landau damping [127, 128]. All these effects have the energy scale  $\sim eT$ . In our discretised system, the similar effects are generated through lattice artifacts [129]. With our parametrisation, we have a UV cutoff of order  $\sim T$ , which will induce corrections mimicking HTLs [129]. Regarding the effect of collisions on the CS diffusion rate, we expect them to be negligible, as the longest scales which enters our problem is smaller than the mean free path. As detailed in section 2.2 of [29], the length scale associated to the chemical potential decay is the typical size of a configuration carrying CS-number one  $l_{CS} \sim \frac{1}{\alpha T}$ , while the mean free path in the plasma is of order  $l_{mf} \sim \frac{1}{\alpha^2 T}$ . These conjectures can be checked by including HTLs and effective collision terms into classical equations of motion along the lines of ref. [105, 130, 131]. We leave this for the future work.

## 6.4 Conclusions

In this work, we studied the evolution of the fermionic charge in an Abelian gauge theory at finite temperature, which can be a proxy either for fermion non-conservation or for chirality breaking. In section 6.2.1, we studied the dependence of the evolution on the initial value of the chemical potential. We observed that for small chemical potential, it develops long initial *plateaus*, before the decay is triggered. We saw in section 6.2.2 that for larger initial chemical potential, the decay happens through a self-similar process. This leads to a phenomenon of inverse cascade in the gauge field sector, with power transferred from UV to IR scales. We observed and quantified both of these phenomena, measuring the critical exponent of the chemical potential self-similar decay to be  $-\frac{1}{2}$ .

In section 6.2.3, we moved on to the study of the effect of an external magnetic field on the chemical potential evolution. Both for large and small initial chemical potential, three different situations can happen. First, when the external magnetic field is small, the chemical potential relaxes to its critical value, in the same way that in the absence of chemical potential. Then, from the critical value, it eventually decays to zero. For large external magnetic field, the dynamic is fully determined by the magnetic field, and the decay happens through damped oscillations. For moderate magnetic fields, both effects can be observed at the same time.

A way to isolate the effect of the external magnetic field influence is to study configurations with initial chemical potential equal to the critical one, as presented in 6.2.4. Then, only the exponential decay is visible. Following this procedure, we could extract a chiral dissipation rate and study its dependence on the parameters of the theory, finding

$\Gamma_5 = 10^{-2.10 \pm 0.02} B^2 e^{11/2} / T^3$ . We also compared this rate to the fluctuation rate of the topological charge in the absence of chemical potential, which was measured in Ref. [29]. These rates are related through a fluctuation-dissipation theorem. We found a good agreement between them, providing a solid self-consistency check for our framework.

In section 6.3 we analysed our results in light of MHD, which is the long-wavelength effective theory of our system. Despite being out of its range of validity, qualitative features of the chemical potential can be well described. For example, in section 6.3.1, we provide a simplified MHD modeling which reproduces the time-scale of the observed *plateaus* in the chemical potential decay. In section 6.3.2 we also showed that the spectrum evolution of the inverse cascade is well-modeled by a MHD-inspired description. In section 6.3.3, we studied the chiral rate in the physically relevant range of chemical potentials. We showed that our numerical rates are an order of magnitude larger than the MHD predictions. We interpreted this as evidence of the effect of short-scale fluctuations on the system dynamics. This can potentially shed a new light on the role of the abelian contribution to the anomaly on fermion number/chirality violating processes.

The main outlook of this work will be to confirm or refute these results. We intend to verify numerically the effects of hard thermal loops and collisions, using some effective theory, see e.g. [105, 130, 131].

Another direction which remains to be explored is the regime of extremely small chemical potential. This is however challenging from a technical point of view, as the smaller the initial values of the chemical potential, the larger the volume needs to be, given the existence of a critical value  $\mu_c$ . Moreover, one also need longer simulations, as the initial *plateau* gets longer. Our computer resources thus limits us to explore systematically this regime.

## Acknowledgements

The authors want to thank Oleksandr Sobol for relevant comments and Kohei Kamada for useful discussions. A.F. wishes to thank Hauke Sandmeyer for giving him access to his numerical fitting routines and Pavel Buividovich for an insightful discussion. This work was supported by the ERC-AdG-2015 grant 694896 and the Swiss National Science Foundation. The numerical simulations were performed on the Intel Broadwell based cluster Fidis, provided by the EPFL HPC center (SCITAS). The discrete Fourier transforms were performed with the AccFFT library [132].

## Appendices

### 6.5 Lattice set-up

The results presented in this work were obtained using the lattice discretisation presented in Ref. [115]. Initial conditions for the gauge fields and the scalar fields are drawn from a thermal ensemble, generated by a simple Metropolis algorithm. Gauss law is then enforced on the thermalised configurations. After that, the system is evolved along the classical trajectory specified by the set of discretised equations of motion

$$\pi = \Delta_o^+ \varphi \quad \Delta_o^- \pi = \sum_i D_i^- D_i^+ \varphi - V_{,\varphi^*} \quad (6.46)$$

$$E_i = \Delta_o^+ A_i \quad \Delta_o^- E_i = 2e, \text{Im}\{\varphi^* D_i^+ \varphi\} - \sum_{j,k} \epsilon_{ijk} \Delta_j^- B_k - \frac{e^2}{4\pi^2} \mu B_i^{(8)} \quad (6.47)$$

$$\mu = \frac{T}{2\sqrt{3}} \Delta_o^- a \quad \Delta_o^+ \mu = \frac{3}{\pi^2} \frac{1}{T^2} \frac{e^2}{N^3} \sum_{\vec{n}} \frac{1}{2} \sum_i E_i^{(2)} (B_i^{(4)} + B_{i,+0}^{(4)}) \quad (6.48)$$

$$\sum_i \Delta_i^- E_i = 2e \text{Im}\{\varphi^* \pi\} \quad (6.49)$$

with

$$E_i^{(2)} \equiv \frac{1}{2} (E_i + E_{i,-i}) \quad B_i^{(4)} \equiv \frac{1}{4} (B_i + B_{i,-j} + B_{i,-k} + B_{i,-j-k}) \quad (6.50)$$

$$B_i^{(8)} \equiv \frac{1}{2} (B_i^{(4)} + B_{i,+i}^{(4)}), \quad (6.51)$$

and  $\Delta_\mu^\pm f = \pm \frac{1}{dx} (f_{\pm\mu} - f)$ ,  $D_\mu^\pm f = \pm \frac{1}{dx} (e^{\mp iedx^\mu A_\mu(n \pm \frac{1}{2})} f_{\pm\mu} - f)$  the forward/backward finite difference operator and covariant derivatives. The notation  $f_{a,\mu}$  means that the component  $a$  of the vector field  $f$  is to be evaluated at the point  $\vec{n} + \hat{\mu}$ , with  $\hat{\mu}$  a unit displacement in the direction  $\mu$ ,  $f_{a,\mu} = f_a(n + \hat{\mu})$ . Notice that the equations are built out of composite field so that all the fields can be expanded consistently about the same point to reproduce the continuum equations to order  $O(dx^2)$ . The scalar fields live on lattice edges while the gauge fields are link variables; they live on half-integer sites. The time differential operators evolve by half a step in times. More details are to be found in [115].

The constant background magnetic field is introduced through twisted boundary conditions [120], which imposes a constant flux. To specify, we modify the periodic boundary conditions of the first component of our gauge field as follow

$$A_1(1, N, n_3) = A_1(1, 0, k) - \frac{2\pi n_{mag}}{dx} \quad \forall k \in [0, N-1]. \quad (6.52)$$

This corresponds to introducing a constant background magnetic field in the  $z$ -direction of

magnitude  $B = \frac{2\pi n_{mag}}{(\mathrm{d}xN)^2}$ .

For large volumes, it is essential to initiate the Monte-Carlo with configurations which already satisfy the twisted-boundary conditions (6.52). This can be achieved by taking as seed

$$A_1^{init}(i, j, k) = -\frac{2\pi n_{mag}}{\mathrm{d}xN^2}j - \delta_{j0}\frac{2\pi n_{mag}}{\mathrm{d}xN} + \delta_{j0}\delta_{i1}\frac{2\pi n_{mag}}{\mathrm{d}x} \quad (6.53)$$

$$A_2^{init}(i, j, k) = \delta_{j0}\frac{2\pi n_{mag}}{\mathrm{d}xN}i - \delta_{j0}\frac{2\pi n_{mag}}{\mathrm{d}x} + \delta_{j0}\delta_{i0}\frac{2\pi n_{mag}}{\mathrm{d}x} + \delta_{j0}\delta_{i1}\frac{2\pi n_{mag}}{\mathrm{d}x} \quad (6.54)$$

$$A_3^{init}(i, j, k) = 0, \quad (6.55)$$

where the non-trivial dependence of  $A_2$  ensures that  $A$  is consistent. In more details, a gauge field which lives on a periodic manifold must transform as

$$A_\mu(x + N \cdot \hat{i}) = A_\mu(x) + \partial_\mu \alpha_i(x), \quad (6.56)$$

with potentially three different gauge transformations  $\alpha_i$ , one by direction. These gauge transformations cannot be completely arbitrary, they satisfy so-called compatibility conditions. These are the requirement that the relation of the gauge field value at a given point  $x + N \cdot \hat{i} + N \cdot \hat{j}$  to its value at  $x$  better not depend on whether one first goes through the  $i$  or through the  $j$  boundary. In other words, we have

$$A_\mu(x + N \cdot \hat{i} + N \cdot \hat{j}) = A_\mu(x + N \cdot \hat{j} + N \cdot \hat{i}) \quad (6.57)$$

which implies

$$\partial_\mu(x) \alpha_i(x) + \partial_\mu \alpha_j(x + N \cdot \hat{i}) = \partial_\mu \alpha_j(x) + \partial_\mu \alpha_i(x + N \cdot \hat{j}) \quad (6.58)$$

The twisted boundary conditions (6.52) tells us that  $\partial_1 \alpha_2(1, j, k) = -\frac{2\pi n_{mag}}{\mathrm{d}x}$ . The choice of initial field (6.53) - (6.55) is made to satisfy the compatibility conditions (6.57).

## 6.6 Fluctuation-dissipation theorem

The dissipative chiral decay rate  $\Gamma_5$  is related to the diffusion rate of the topological charge  $\langle Q^2(t) \rangle = \Gamma V t$ . To derive this relation, we will use Zubarev's formalism [133], in the spirit of Ref. [27]. We treat  $\mu$  as a dynamical variable and want to understand its out of equilibrium properties. To do so, we introduce a "local equilibrium" partition function

$$\rho_{LE} = \exp(-\beta H + VT \chi(t) \mu(t)) \quad (6.59)$$

with  $\chi(t)$  some Lagrange parameter which drives  $\mu(t)$  locally out of equilibrium and the factor  $VT^2$  was introduced to make  $\chi(t)$  of the same dimensions than  $\mu$ . The function  $H$  is the Hamiltonian associated with our system. The relevant  $\mu$ -dependent part is

$$H_\mu = \frac{1}{24} \mu^2 VT^2 \quad (6.60)$$

This function is used to compute  $\langle \mu \rangle$  at any time [133] and thus determines  $\chi(t)$  as a function of  $\langle \mu \rangle$ .

$$\langle \mu \rangle = \frac{\int_{-\infty}^{\infty} d\mu \mu \exp\left(-\frac{1}{24} \mu^2 VT + \chi \mu VT\right)}{\int_{-\infty}^{\infty} d\mu \exp\left(-\frac{1}{24} \mu^2 VT + \chi \mu VT\right)} = 12\chi \quad (6.61)$$

However, it is *not* stationary, i.e. it does not satisfy Liouville's equation

$$\frac{d\rho}{dt} = \frac{\partial \rho}{\partial t} + \{\rho, H\} = 0, \quad (6.62)$$

with  $\langle \dots \rangle$  the usual Poisson brackets. A way to fix this is to introduce a second density matrix

$$\rho = N \lim_{\epsilon \rightarrow 0^+} \exp\left(-\frac{H}{T} + VT^2 \epsilon \int_{-\infty}^t e^{T\epsilon(t-t')} \chi(t') \mu(t') dt'\right) \quad (6.63)$$

with  $N$  such that  $\rho$  integrates to one. Integrating by part and neglecting  $\dot{\chi}(t)$ , i.e. considering slow processes, this can be recast as

$$\rho = N \lim_{\epsilon \rightarrow 0^+} \exp\left(-\frac{H}{T} + VT \chi \mu - VT \int_{-\infty}^t e^{T\epsilon(t-t')} \chi(t') \dot{\mu}(t') dt'\right) \quad (6.64)$$

$$\equiv N(h) \lim_{\epsilon \rightarrow 0^+} \exp\left(-\frac{H}{T} + h\right) \quad (6.65)$$

with  $h = VT \chi \mu - VT \int_{-\infty}^t e^{T\epsilon(t-t')} \chi(t') \dot{\mu}(t') dt'$ . Working at linear order in  $h$ , it becomes

$$\rho = \lim_{\epsilon \rightarrow 0^+} \rho_0 (1 + h + \langle h \rangle_0) \quad (6.66)$$

$$\approx \lim_{\epsilon \rightarrow 0^+} \rho_0 (1 + VT \chi \mu - VT \int_{-\infty}^t e^{T\epsilon(t-t')} \chi(t') \dot{\mu}(t') dt' + \langle h \rangle_0) \quad (6.67)$$

where  $\rho_0 = N_0 e^{-\frac{H}{T}}$  and  $\langle h \rangle_0$  is the average with respect to  $\rho_0$ .

To obtain a relation between the chiral decay rate and the diffusion rate of the topological charge, we compute  $\langle \dot{\mu} \rangle$  using eq. (6.67). Using the fact that in equilibrium we have  $\langle \dot{\mu} \rangle_0 = 0$

and  $\langle \dot{\mu} \mu \rangle_0 = 0$ , we obtain

$$\langle \dot{\mu} \rangle = -VT\chi(t) \lim_{\epsilon \rightarrow 0^+} \left\langle \int_{-\infty}^t e^{T\epsilon(t-t')} \dot{\mu}(t') \dot{\mu}(t) dt' \right\rangle_0 \quad (6.68)$$

where again we assumed that  $\chi(t)$  as a weak dependence on time. Now we can make use of the anomaly equation (6.7)

$$\begin{aligned} \langle \dot{\mu} \rangle &= -VT\chi(t) \left( \frac{3e^2}{4T^2\pi^2} \frac{1}{V} \right)^2 \cdot \\ &\lim_{\epsilon \rightarrow 0^+} \left\langle \int_{-\infty}^t e^{T\epsilon(t-t')} \int d^3x F_{\mu\nu} \tilde{F}^{\mu\nu}(x, t') \int d^3y F_{\mu\nu} \tilde{F}^{\mu\nu}(y, t) dt' \right\rangle_0 \end{aligned} \quad (6.69)$$

$$= -\chi(t) \frac{9 \cdot 16}{T^3 V} \lim_{\epsilon \rightarrow 0^+} \left\langle \int_{-\infty}^t e^{T\epsilon(t-t')} q(t') q(t) dt' \right\rangle_0, \quad (6.70)$$

with  $q(t) = \frac{e^2}{16\pi^2} \int d^3x F_{\mu\nu} \tilde{F}^{\mu\nu}(x, t)$  the topological charge density. With this notation and setting taking  $t = 0$  as a reference time, we can define the topological charge as

$$Q(t - t_0) = \int_{t_0}^t dt' q(t'). \quad (6.71)$$

Inserting Eq. (6.61) and setting  $\epsilon = 0$ , we then have

$$\langle \dot{\mu} \rangle = -\langle \mu \rangle \frac{12}{T^3 V} \lim_{t'' \rightarrow \infty} \langle Q(t'') q(0) \rangle_0, \quad (6.72)$$

This last quantity also appears in the diffusion rate of the topological charge. In the absence of chemical potential,  $Q(t)$  follows a random walk and we can define its diffusion rate by, following the convention of [29]

$$\langle Q^2(t - t_0) \rangle = \Gamma_{\text{diff}} V(t - t_0), \quad (6.73)$$

for times  $t$  much larger than a reference time  $t_0$ <sup>10</sup>. We can differentiate this expression by  $t_0$  to get

$$-2\langle Q(t - t_0) q(t_0) \rangle = -\Gamma_{\text{diff}} V \quad (6.74)$$

$$\implies \langle Q(t - t_0) q(t_0) \rangle = \frac{\Gamma_{\text{diff}} V}{2} \quad (6.75)$$

<sup>10</sup>In equation (6.13), we implicitly set  $t_0 = 0$ .

Finally, plugging this in (6.76), we get

$$\langle \dot{\mu} \rangle = -\langle \mu \rangle \frac{6}{T^3 V} \Gamma_{\text{diff}} V, \quad (6.76)$$

Leading to the relation

$$\Gamma_5 = 6 \frac{\Gamma_{\text{diff}}}{T^3}. \quad (6.77)$$

# Finite Temperature Lattice QCD

## Part III





# 7 Topology on the lattice

As we saw in chapter 2 and 4, not only thermal fluctuations but also quantum fluctuations of the topological charge are important in non-Abelian theories. A natural way to study these fluctuations is through importance sampling simulations of the path integral, as presented in section 2.3 for a quantum mechanical system. Before being able to study these fluctuations, we need to understand what happens to the topological structure of our theory once discretised. It will be the content of this section.

## 7.1 Topology of $SU(3)$ on the Lattice

In this work, we will only be concerned with gauge fields without any fermions. As described in section 4.2, the fundamental objects used in numerical simulations of non-Abelian gauge fields are the so-called link variables  $U_\mu(n)$ . At first glance, the situation on the lattice concerning topology is not promising. Indeed, our semiclassical discussion on topologically charged solutions in section 4.1.1 was based on the existence of the notion of paths in field space and the existence of disconnected classes of such paths which cannot continuously be deformed one into the other. These notions are tied to the notion of continuity and as such do not exist on the lattice; the topology of  $SU(N)$  on a lattice is, in a strict sense, trivial.

It would, however, seem likely that some notion of topological fields can be defined on the lattice, as fields will tend in the continuum limit to fields with a well-defined charge. Indeed, such a notion exists and was described in reference [134]. In the continuum, the fact that some fields cannot be deformed into one another by a continuous transformation can be rephrased as the fact that one cannot find an interpolating family of fields with a finite action for every intermediate field. On the lattice, the "infinite" is replaced by some finite value  $p$ . The statement is then the following. All fields such that their action is smaller than  $p$  can be grouped into equivalence classes of topological charge  $Q$ . Classes are disconnected, in the sense that fields belonging to different classes cannot be interpolated between by a family of fields such that all the fields have an action smaller than  $p$ . Moreover, this charge  $Q$  matches the

continuum definition of the topological charge.

The expressions for the discretised version of  $Q$  which emerge in this way are complicated and "non-local", in the sense that they involve many fields that do not live at the same point, see for instance the constructions in references [134, 135], making their use impractical. One would like to be able to obtain the topological charge by simply discretising the continuum operator  $G_{\mu\nu}\tilde{G}^{\mu\nu}$  and taking the continuum limit. The problem with this naive approach is that any of these discretisations will mix with other operators of the same dimensions, which generically require additional renormalisation to have a well-defined continuum limit, see references [25, 116, 136, 137] for related discussions.

This said, there are still several ways to extract an appropriate topological charge from such discretisations [138–142], which are all to some extent based on the idea of "smoothing out" the gauge fields to remove the dangerous UV fluctuations mentioned previously.

The method introduced in [141], the so-called "Wilson" or "gradient"-flow, has a very sound theoretical ground and many interesting properties which are of use beyond topology. The main idea behind its introduction was the concept of "trivialising maps" [143]. In spirit, they are very similar to the Hamilton-Jacobi formulation of classical mechanics. There, one looks for a canonical transformation of the conjugate variables that makes the dynamics of the new variables trivial; all the physics is then encoded in the transformation. Trivialising maps are field transformations whose Jacobian exactly cancels out the original action in the path integral, making it trivial. While trying to build exactly such maps for a strongly interacting theory like QCD is most likely hopeless, it was realised in reference [143] that some simple differentiable flow was an approximate trivialising map, in the case of the pure  $SU(3)$  theory. This flow can be written as [141]

$$\dot{V}_\mu(n, \tau) = -g^2 \delta_{V_\mu(n, \tau)} (S_W^\Lambda) V_\mu(n, \tau) \quad (7.1)$$

$$V_\mu(n, 0) = U_\mu(n) , \quad (7.2)$$

with  $\tau$  a fictitious flow time and where  $\delta_{V_\mu(x, \tau)}$  stands for the first order variation with respect to  $V_\mu(x, \tau)$ . The Wilson action  $S_W^\Lambda$  was defined in equation (4.41).

The fact that it is an approximation to a trivialisation map and that it smoothes out UV fluctuations is not so surprising, as this flow follows the steepest descent towards solutions which minimise the action. Another remarkable property of the Wilson flow is that it acts as a non-perturbative renormalisation scheme [141]; observables evaluated at non-zero flow-time are UV-finite.

Altogether, Wilson's flow is a particularly adequate tool to study the topology of  $SU(3)$  lattice configurations, by computing the topological charge

$$Q = \int d^4x q(x) = \frac{1}{32\pi^2} \int d^4x \epsilon^{\mu\nu\rho\sigma} \text{Tr} G_{\mu\nu} G_{\rho\sigma} \quad (7.3)$$

at finite flow-time. We show the effect of Wilson's flow on the topological charge density on some small toy-lattices ( $N = 20^4$  at  $\frac{6}{g^2} = 6.2$ ) in figure 7.1, reproduced from reference [144]. Starting from wildly fluctuating configurations at  $\tau = 0$ , the fields are gradually smoothed out and localised stable topological excitations are unravelled.

Before continuing, let us also mention another way to measure the topological charge. As briefly discussed in section 3.2.2, the topological charged can be extracted from the zero-modes of the Dirac operator, computed in the background of the gauge configurations. The advantage of the methods based on this index theorem is that they do not need regularisation. They are, on the other hand, very costly to implement, see [137] and references therein for more information.

## 7.2 Open-boundary conditions

The problem of topological freezing described in the case of quantum mechanics in section 2.3 is also present in pure Yang-Mills and QCD simulations, for essentially the same reasons. As the continuum is approached, continuity is better and better approximated and topological sectors become more and more well-separated. Algorithms get stuck in given sectors and stop being ergodic, see [145] for a detailed study.

A natural way to attempt to ease up this problem is to trade periodic boundary conditions, which forces the fields to have integer topological charge, for boundary conditions which do not constraint the topological charge. This can be achieved by imposing "open-boundary conditions" on the field-strength tensor [146], as we will summarise in this section.

Instead of usual periodic boundary conditions, consider a theory with the following "open" boundary conditions

$$G_{\mu\nu}(x)|_{x_\mu=0} = G_{\mu\nu}(x)|_{x_\mu=T} = 0 \quad , \quad \text{for a given } \mu \text{ and } \nu = 0, 1, 2, 3 \quad . \quad (7.4)$$

Even though boundary conditions should not matter once the thermodynamic and continuum limits are taken, they can and do impact the finite-size system. We can show for example that with such conditions, the topological charge is not quantised, following reference [146]. A special type of fields which satisfies (7.4) is given by

$$A_\mu = \partial_\nu A_\mu = 0 \quad \text{at } x_\mu = 0. \quad (7.5)$$

Any such field can be smoothly connected to zero without violating the boundary conditions. Now let us consider an arbitrary field which satisfies (7.4). Consider applying a gauge transformation and consider how its  $\mu$  component transforms

$$A_\mu \rightarrow \Omega A_\mu \Omega^{-1} - i \Omega \partial_\mu \Omega^{-1} \quad . \quad (7.6)$$

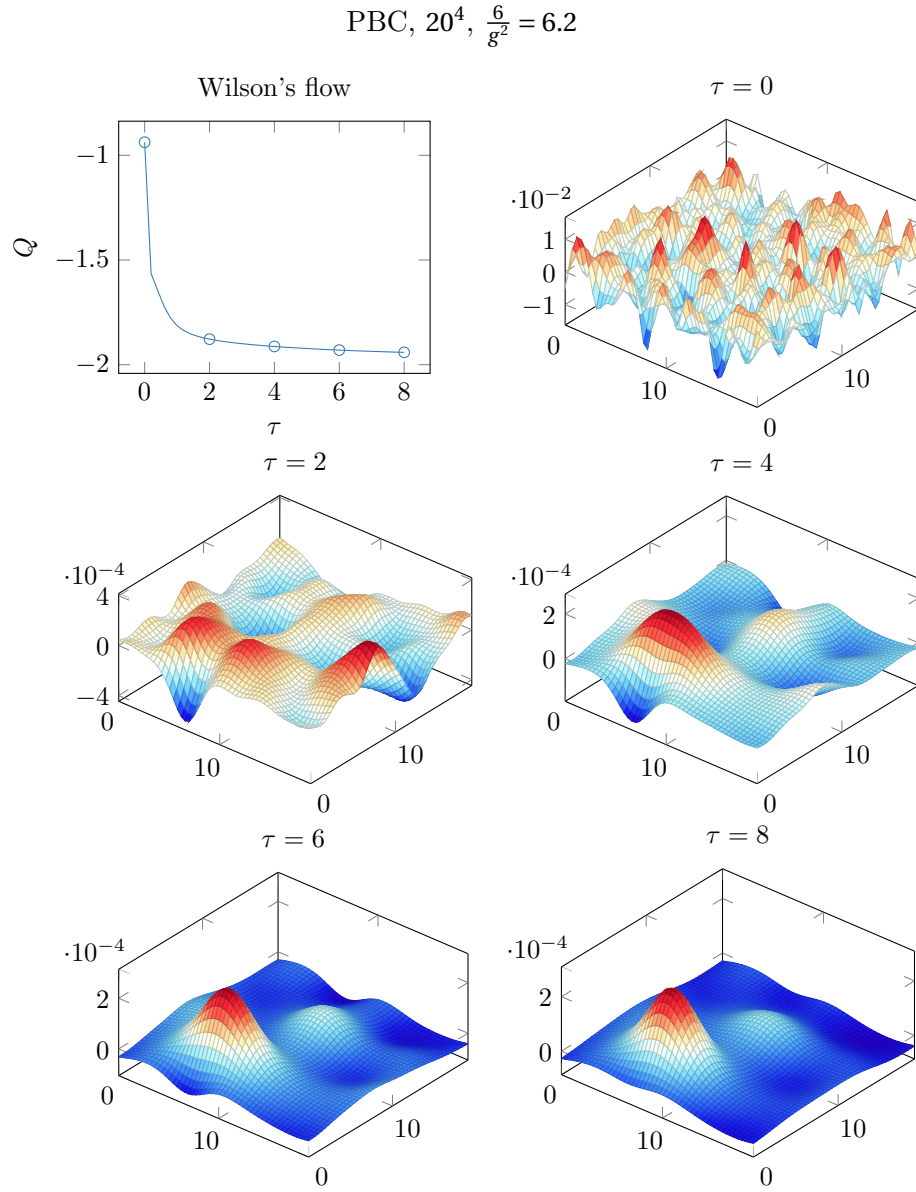


Figure 7.1 – Evolution of a two-dimensional slice of the topological charge density under Wilson flow, for some small lattices. The initial wild small scale fluctuations are tamed by the flow evolution and become smooth fields, with localised topological charge excitations. Reproduced from reference [144].

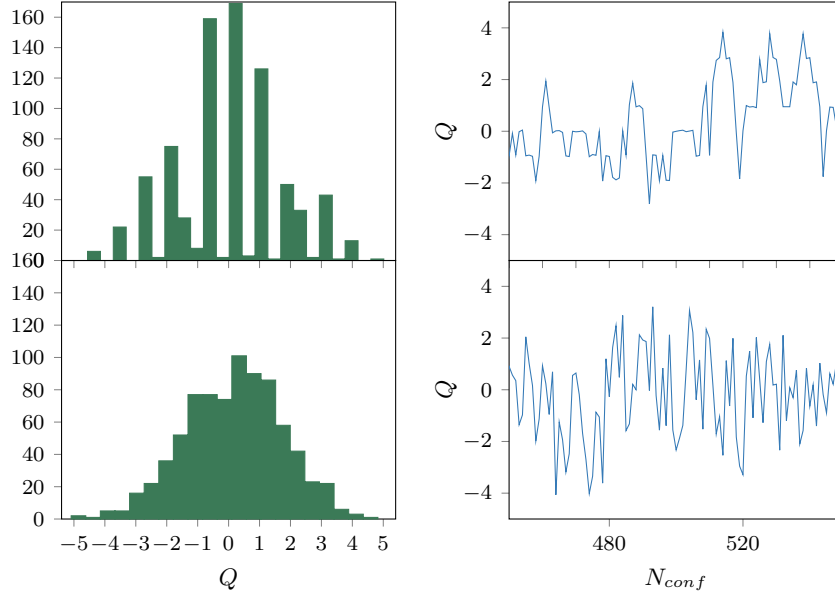


Figure 7.2 – Histogram and Monte-Carlo histories of the topological charge for periodic and open-boundary conditions in the spatial directions. In the former case, the charges are quantised while they are not in the latter case. Reproduced from reference [144].

The solution to the differential equation

$$A_\mu \Omega^{-1} - i \partial_\mu \Omega^{-1} = 0, \quad (7.7)$$

will send  $A_\mu$  to zero altogether. Moreover, the family of functions  $\Omega_s$  solving the differential equation

$$s A_\mu \Omega_s^{-1} - i \partial_\mu \Omega_s^{-1} = 0 \quad (7.8)$$

$$\Omega_s|_{x_\mu=0} = 0, \quad s \in [0, 1], \quad (7.9)$$

smoothly sends the field to a field which obeys conditions (7.5), which in turns can be smoothly mapped to zero. The field space is contractible and as a result, the topological charge is not quantised. Note also that one can impose open-boundary conditions in more than one directions without changing this result, as one can always impose successive gauge transformations in different directions without violating the boundary conditions.

In figure 7.2, also reproduced from reference [144], we illustrate these results with the same toy lattices with  $N = 20$ ,  $\frac{6}{g^2} = 6.2$  by measuring the topological charge on a set generated with periodic boundary conditions and one generated with open-boundary conditions in all three spatial directions, after some finite Wilson flow-time. In the first case, the topological charges are quantised, while they are not in the second case.

Despite this difference, and as expected from the fact the continuum/infinite volume physics

should not depend on boundary, the local aspect of the topological charge density is very similar in both cases. This can be seen on figure 7.3, reproduced from reference [144], where we show the topological charge density evolution under Wilson flow of one of our toy-lattices with open-boundary conditions. Except for the fact that the topological charge density vanishes on the boundary because of the boundary conditions, it is virtually indistinguishable from the equivalent figure with periodic boundary conditions, figure 7.1. Note also the fact that the total charge seems to converge to an integer is a misleading coincidence related to the specific configuration which was chosen to be displayed.

### 7.3 Foreword to [2]

Open-boundary conditions have been introduced in reference [146] in a zero temperature context, and have been successfully used in a number of study, amongst which [147–156]. Even if Euclidean topology-changing processes are suppressed at high temperatures, as discussed in section 2.2, they remain relevant at moderate ones and topological freezing can also be a hindrance. In reference [2], we carried the first study with open-boundary conditions in a spatial direction at finite-temperature and studied the generic temperature dependence of the boundary induced effects on observables. This study is the content of the next part.

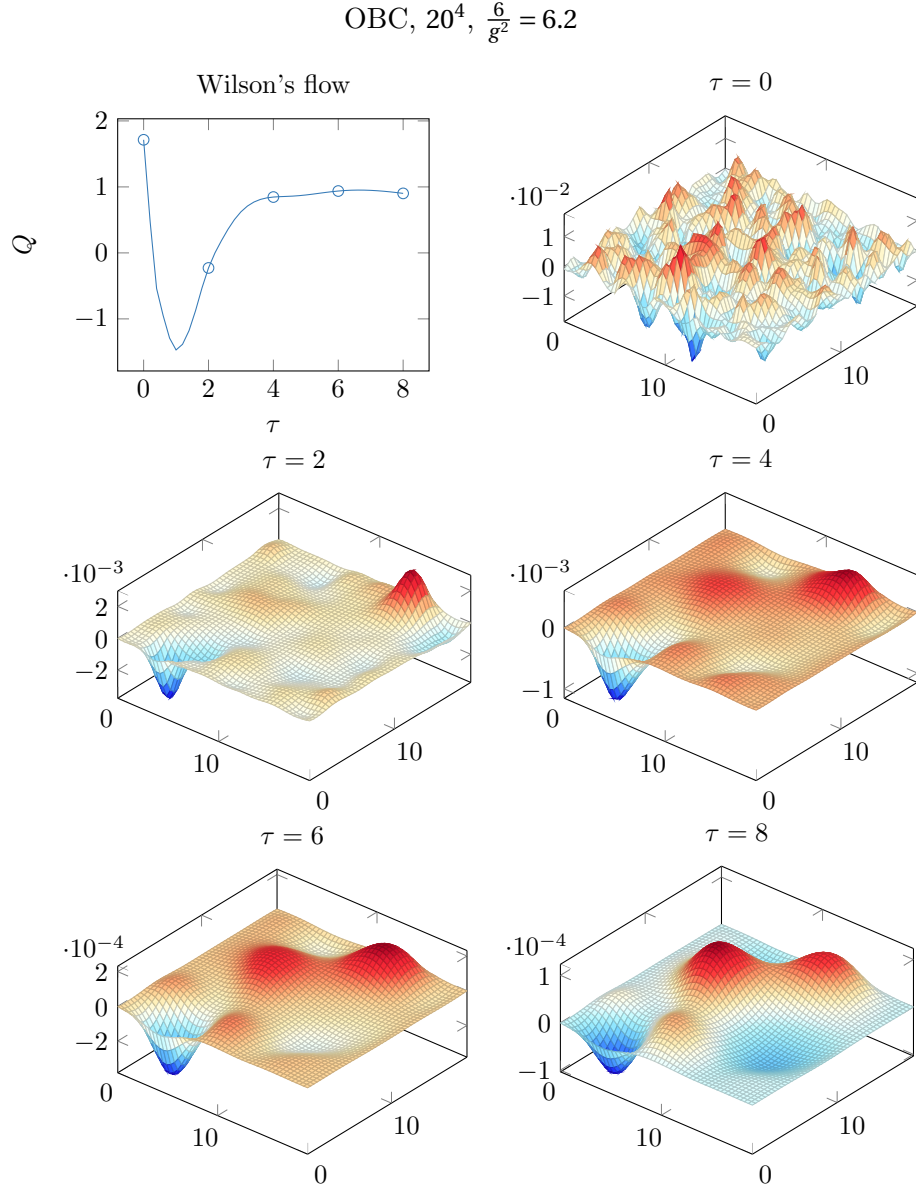


Figure 7.3 – Evolution of a two-dimensional slice of the topological charge density under Wilson flow, for some small lattices and open-boundary conditions. Except for the vanishing of the topological charge density on the boundary, the results are very similar to the one with periodic boundary conditions from figure 7.1, as expected. Reproduced from reference [144].





# 8 *Open-Boundary Conditions in the Deconfined Phase [2]*

**Authors:** Adrien Florio, Olaf Kaczmarek, Lukas Mazur

*Reference:* arXiv v2 of Eur. Phys. J. C, 79(12):1039, 2019, doi: 10.1140/epjc/s10052-019-7564-z

*Abstract:* In this work, we consider open-boundary conditions at high temperatures, as they can potentially be of help to measure the topological susceptibility. In particular, we measure the extent of the boundary effects at  $T = 1.5T_c$  and  $T = 2.7T_c$ . In the first case, it is larger than at  $T = 0$  while we find it to be smaller in the second case. The length of this "boundary zone" is controlled by the screening masses. We use this fact to measure the scalar and pseudo-scalar screening masses at these two temperatures. We observe a mass gap at  $T = 1.5T_c$  but not at  $T = 2.7T_c$ . Finally, we use our pseudo-scalar channel analysis to estimate the topological susceptibility. The results at  $T = 1.5T_c$  are in good agreement with the literature. At  $T = 2.7T_c$ , they appear to suffer from topological freezing, which prevents us from providing a precise determination of the topological susceptibility.

*A.F. contribution:* Idea of the project, large contribution to the writing of the paper. Analysis and numerical simulations done jointly with the coauthors.

## 8.1 Introduction

In general, finite-size systems differ from their infinite-volume counterpart. One of the most simple examples is the "particle-in-a-box" whose momenta are quantised. Not only the compactness, but also the boundary conditions affect the system. There, different choices lead to different quantisation conditions. The only restriction on such choices is that the infinite volume physics needs to be recovered in the thermodynamic limit. This requirement satisfied, the only remaining differences are related to the convergence to the infinite volume limit. When the system is discretised, discretisation effects may also vary between different types of boundary conditions.

In some circumstances, such differences may be used as algorithmic tools to improve numerical simulations. A typical example of this is the use of open-boundary conditions (OBC) in lattice QCD, which have been introduced in [146] as means to reduce autocorrelations of the topological charge. These autocorrelations become critical as the continuum is approached. and are signaled by the freezing of gauge field ensembles in given topological sectors. In this example, instead of considering QCD with periodic boundary conditions (PBC), which leads to a discrete topological charge

$$Q = \int d^4x q(x) = \frac{1}{32\pi^2} \int d^4x \epsilon^{\mu\nu\rho\sigma} \text{Tr} G_{\mu\nu} G_{\rho\sigma}, \quad (8.1)$$

the idea is to impose OBC in at least one of the directions. In this system,  $Q$  spans a continuum range of value. This then lifts the topological barrier responsible for the topological freezing and improves the sampling of the configuration space.

Having small autocorrelations is crucial to keep control of the statistical errors in Monte Carlo simulations [145, 157]. A poor sampling of the topological charge affects in principle all observables, leading to finite volume effects (see [158, 159] for practical examples). The situation is partially improved when considering QCD in the deconfined phase. For  $T > T_c$ , the order parameter which quantifies the variance of the topological charge, i.e. the topological susceptibility  $\chi = \frac{\langle Q^2 \rangle}{V}$ , decreases with  $T$ . At asymptotically-high temperatures, it is even suppressed as  $T^{-7}$  [52]. Nonetheless, for moderate temperatures,  $Q \neq 0$  configurations still contribute in a non-negligible way to the path-integral. In this context, OBC may also be of interest at non-zero temperatures<sup>1</sup>. However, before being able to use them systematically, an analysis of the influence of temperature on the boundary effects remains to be done. This is the content of this study, which focuses on pure  $SU(3)$  gauge theory, as dynamical matter is not expected to drastically change the results.

In section 8.2, we recall known facts about OBC and discuss our datasets and methodology. Then, in the spirit of the zero temperature analysis of [153], we investigate in section 8.3 the typical length over which the boundary effects propagate, the "boundary zone". We observe a noticeable temperature dependence. These differences can be understood in terms of the temperature dependence of the lightest propagating states' screening masses, which we study in section 8.4. As a by-product, we report in section 8.5 an extraction of the topological susceptibility from our rather large volumes simulations. We finally discuss our results in section 8.6.

## 8.2 Open-boundary conditions and setup

Conventional lattice QCD simulations use (anti-)periodic boundary conditions in all directions, for the obvious reason that they minimise boundary effects. In this study, we consider the use

---

<sup>1</sup>For a very exploratory study, see [160].

of OBC in one of the spatial directions (taken for definiteness to be the  $x$  direction). This amounts setting the field-strength tensor to zero outside the lattice. In this case the Wilson action reads [146]

$$S^{OBC} = -\frac{\beta}{3} \sum_P w(P) \text{Tr} \mathbf{1} - P, \quad (8.2)$$

where the sum runs over all the plaquettes

$$P_{\mu\nu} = U_\mu(n) U_\nu(n + \hat{\mu}) U_\mu(n + \hat{\nu})^\dagger U_\nu(n)^\dagger \quad (8.3)$$

whose corners are in the interval  $[x = 0, x = N_x - 1]$ . The  $U$ 's are the usual link variables and the quantity  $w(P)$  is an integration weight

$$w(P) = \begin{cases} 1 & \text{if } P \in \text{bulk} \\ \frac{1}{2} & \text{if } P \in x\text{-face} \end{cases}. \quad (8.4)$$

A bulk point is a point in the interval  $[1, N_x - 2]$ . A plaquette is on a  $x$ -face if it is not oriented along  $x$  and all of its corners are at  $x = 0$  or  $x = N_x - 1$ . As shown in [146], the continuum limit of this theory has a trivial topology in field space; all the admissible fields are connected by local gauge transformations.

Such boundary conditions break translational invariance and introduce boundary effects. These effects may be understood as the propagation of excited states from the boundary. Here we summarise the core of the argument, following [161–163].

For the sake of clarity, let us first recall the argument for OBC in the time direction; it straightforwardly transposes to OBC in the  $x$  direction. To quantise our Euclidean theory, we write down a transfer matrix  $\hat{T} = e^{-\hat{H}}$  with  $\hat{H}$  the Hamiltonian, the Euclidean equivalent of the evolution operator. It evolves states between temporal slices. In particular, going from the state  $|\gamma_i\rangle$  at  $t = 0$  to the state  $|\gamma_f\rangle$  at  $t = T$ , and given an operator  $O$  inserted at  $t$ , we can write

$$\langle O \rangle_{OBC} = \frac{1}{\mathcal{Z}} \langle \gamma_f | \hat{T}^{-(T-t)} O(t) \hat{T}^{-t} | \gamma_i \rangle. \quad (8.5)$$

To label our basis of states, we use the lattice version of the translation operators and get a basis consisting of  $|E_n(\vec{p})\rangle$ , with  $n$  labelling extra quantum numbers and  $\vec{p}$  the momentum eigenstates. Inserting a complete basis of states, we can then write

$$\langle O \rangle_{OBC} = \frac{1}{\mathcal{Z}} \sum_{n, \vec{p}, m, \vec{q}} \gamma_{n, \vec{p}}^i \gamma_{m, \vec{q}}^{f*} \cdot \langle E_m(\vec{q}) | \hat{T}^{-(T-t)} O(t) \hat{T}^{-t} | E_n(\vec{p}) \rangle \quad (8.6)$$

$$= \frac{1}{\mathcal{Z}} \sum_{n, \vec{p}, m, \vec{q}} \gamma_{n, \vec{p}}^i \gamma_{m, \vec{q}}^{f*} e^{-(T-t)E_m(\vec{q})} e^{-tE_n(\vec{p})} \cdot \langle E_m(\vec{q}) | O(t) | E_n(\vec{p}) \rangle, \quad (8.7)$$

with  $\gamma_{n, \vec{p}}^{i,f} = \langle E_n(\vec{p}) | \gamma^{i,f} \rangle$ . Now we see that the main contribution comes from the state with smallest energy. We then have a tower of exponentially suppressed corrections. More explicitly, using the fact that the main contribution to  $\mathcal{Z}$  is  $\gamma_0^i \gamma_0^{f*} e^{-E_0 T}$  (obtained by setting  $O(t) = \mathbf{1}$  in our expansion), we find

$$\langle O \rangle_{OBC} = \langle 0 | O | 0 \rangle + \alpha_1 e^{-(E_1 - E_0)t} + \beta_1 e^{-(E_1 - E_0)(T-t)} + \dots$$

with  $\alpha_1$  and  $\beta_1$  some matrix elements.

In other words, OBC do not project out directly on the vacuum state but are affected by states which propagate from the boundary. We also see that, at least in some limits, the corrections should be dominated by an exponential decay in the lightest state. We will take advantage of this in section 8.4. Note that this argument can be generalised to two-point functions [162] and higher-point functions.

In the case of OBC in the  $x$  direction, the previous analysis can be repeated by replacing the slicing in the  $t$  direction by a slicing in the  $x$  direction when quantising the system. Then  $H$  and  $\hat{P}_x$  exchange roles, with  $\hat{P}_x$  the translation operator in  $x$ . Modulo this, the derivation goes through.

To measure the topological correlators, we used the gluonic definition of the topological charge density. It requires some smoothing of the gauge fields, which was performed by using the gradient flow [141]. The fundamental gauge fields  $A_\mu(x)$  are evolved to finite flow-time  $\tau$ ,  $B(x, \tau)$ , using the flow equation

$$\dot{B}_\mu(x, \tau) = D_\nu G_{\nu\mu}(x, \tau), \quad B_\mu(x, \tau)|_{\tau=0} = A_\mu(x), \quad (8.8)$$

$$D_\mu = \partial_\mu + [B_\mu(x, \tau), \cdot]. \quad (8.9)$$

The associated smearing radius is  $\sqrt{8\tau}$ . It is implemented on the lattice by using the standard Wilson gauge action (Wilson flow). The integration is done using a third order Runge-Kutta algorithm with a step-size of 0.01, which was tested to be small enough for the lattice parameters of this study.

The configurations we used are listed in table 8.1. The quenched configurations were generated using a heat bath and an overrelaxation algorithm. One update consists of one heat bath and

$N_s^3 \times N_t$	$\beta$	$a[\text{fm}]$	$\frac{l}{\sqrt{8t_0}}$	$\frac{T}{T_c}$	$n_{OBC}$	$n_{PBC}$
$64^3 \times 6$	6.139	0.074	10.0	1.5	257	442
$88^3 \times 8$	6.335	0.056	10.4	1.5	430	533
$112^3 \times 10$	6.498	0.045	10.7	1.5	246	155
Continuum extrapolations for OBC				1.5	-	
Continuum extrapolations for PBC				1.5	-	
$64^3 \times 4$	6.253	0.063	8.52	2.7	533	512
$88^3 \times 6$	6.55	0.042	7.81	2.7	318	532
$120^3 \times 8$	6.778	0.031	7.86	2.7	533	532
Continuum extrapolations for OBC				2.7	-	
Continuum extrapolations for PBC				2.7	-	
$102^3 \times 6$	6.64	0.037	7.98	3.0	479	472

Table 8.1 – Lattices used in this study. The spatial size of the lattice is denoted  $l$ .

four overrelaxation steps. To make sure that the configurations are sufficiently thermalised we discard configurations from the first 4000 iterations. Configurations are measured every 500 Monte Carlo steps to minimise the autocorrelations. Working with flowed configurations, we use the scale  $t_0$  with the interpolation given in [164] to convert to physical units. The statistical errors were estimated by using Jackknife resampling.

To compute the topological charge and energy density we used the clover-shaped field strength tensor

$$G_{\mu\nu}(x) = \left( \frac{-i}{8a^2} (Q_{\mu\nu}(x) - Q_{\nu\mu}(x)) \right)_{AH}, \quad (8.10)$$

where  $AH$  is the projection on the traceless antihermitian part and  $Q_{\mu\nu}$  is defined as

$$Q_{\mu\nu}(x) = U_{\mu,\nu}(x) + U_{\nu,-\mu}(x) + U_{-\mu,-\nu}(x) + U_{-\nu,\mu}(x), \quad (8.11)$$

with the plaquette discretisation  $U_{\mu,\nu}$ .

### 8.3 Boundary zone

As explained in section 8.2, the presence of a boundary affects observables in the bulk, at least close to the boundary. The length of this "boundary zone" depends on how the observables couple to the lightest propagating states. To quantify this effect and in order to compare it to the zero temperature case, we adopted the method of [153]. We compute the value of the clover action density as a function of the distance to the boundary and extract the length of the boundary zone, i.e. the length over which this observable is significantly different from its bulk value. In more detail, for lattices with OBC in the  $x$  direction and some operator  $O$ , we define its sub-average at a distance  $r$ , inside a sub-volume of size  $(N_x - 2r) \times N_y \times N_z \times N_t$  from

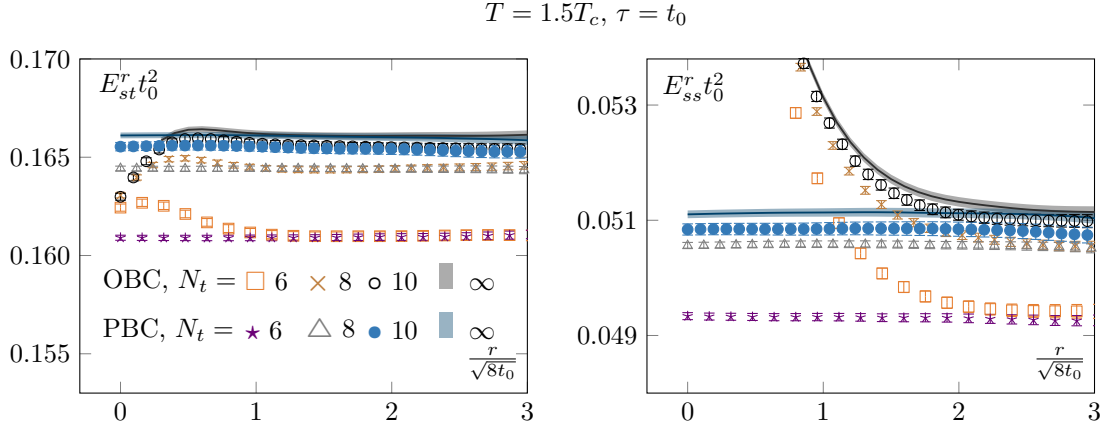


Figure 8.1 – Clover action density as a function of the distance from the open-boundary, at  $T = 1.5T_c$  configurations and reference flow-time  $t_0$ . **Left:** Electric component. **Right:** Magnetic component. Both components show a consistent scaling to the continuum and an agreement between OBC and PBC in the bulk. Also, we see the effect of the open-boundary. The fact that the two components are not equal is a finite temperature effect (see y-axis). We also see that they do not couple to the same boundary states.

the boundary, by

$$O^r = \frac{1}{N_y N_z N_t} \frac{1}{(N_x - 2r)} \sum_{y=0}^{N_y-1} \sum_{z=0}^{N_z-1} \sum_{t=0}^{N_t-1} \sum_{x=r}^{N_x-r-1} O(x, y, z, t), \quad (8.12)$$

with  $0 \leq r < N_x/2 - 1$ . For  $r = 0$ , we expect the strongest dependence on the boundary excitations. By studying the  $r$ -dependence, we can then characterise the typical size of the boundary contamination.

At non-zero temperature, the clover action density leads to two independent gluon condensates [165, 166]

$$E_{st} = \frac{1}{4} G_{0i}^a G_{0i}^a, \quad E_{ss} = \frac{1}{4} G_{ij}^a G_{ij}^a; \quad (8.13)$$

a "magnetic condensate"  $E_{ss}$  and an "electric condensate"  $E_{st}$ .

In figure 8.1, we show both densities at the reference flow-time  $t_0$  for our different configurations at  $T = 1.5T_c$ . All temperatures used in our study behave in a qualitatively similar way. First, we see as expected the existence of a boundary zone and an agreement between OBC and PBC in the bulk of the lattices, i.e. when  $r$  is sufficiently large to suppress the effects of the boundary on the sub-volume. Then we see that the component which displays the largest boundary zone is  $E_{ss}$ . The reason is that it couples to a lighter state than  $E_{st}$ .

To compare different results in all fairness, we proceed to a continuum extrapolation of both

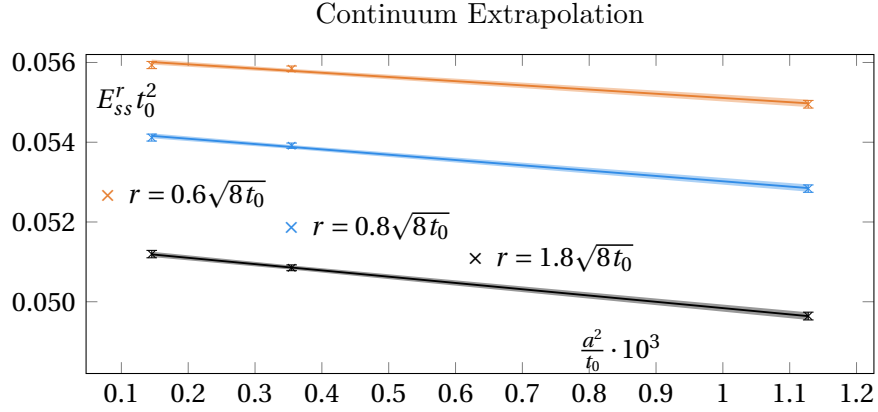


Figure 8.2 – Continuum extrapolation of the magnetic clover density for three different radii  $r = 0.6, 0.8, 1.8\sqrt{8t_0}$ .

condensates. In figure 8.2, we show this continuum extrapolation for  $T = 1.5T_c$  and three different radii. As reported in [141], the region close to the boundary is affected by linear lattice spacing artifacts when Wilson’s action is used without further improvements. We evade this complication by computing our continuum extrapolation only in the region where the  $O(a)$  corrections are negligible. This region turned out to be large enough for all purposes of this study.

Different temperatures are compared in figure 8.3, together with the zero temperature result of [153]. In this plot, we show the energy density normalised to its bulk value. We see that the length of the boundary zone depends on temperature. At  $1.5T_c$  we find it to be about 50% larger than at zero temperature while we find it reduced by 20% at  $2.7T_c$ , consistently with our fixed lattice spacing results at  $3T_c$ . This is also consistent with the temperature dependence of the screening masses. Actually, the behaviour of the observables in the boundary zone gives a handle on these screening masses, which will be discussed in the next section.

## 8.4 Screening masses

As explained in section 8.3, the boundary effects are controlled by the masses of the propagating states in the theory. In pure  $SU(3)$  gauge theory at finite temperature, these are the screening masses [167].

In this section, we will take advantage of the boundary effects to extract the lightest scalar and pseudo-scalar screening masses. In particular, as the lightest scalar mass is expected to be the lightest state in our system, its value controls the length of the boundary zone of section 8.3.



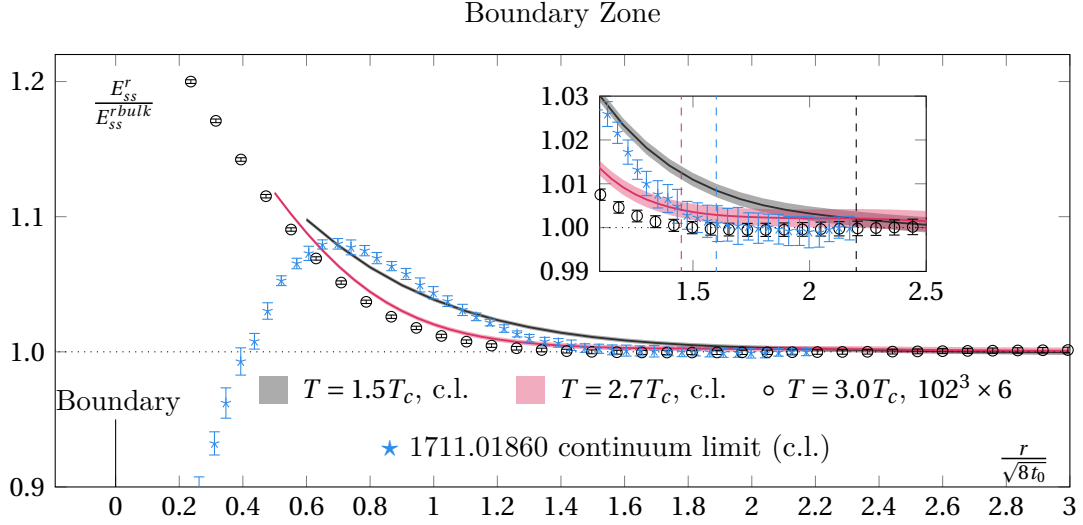


Figure 8.3 – Comparison of the normalised clover action between different temperatures. We report in this figure the zero temperature results of [153] in blue. We observe the length of the boundary zone to depend on temperature. At  $1.5T_c$ , we see that the boundary effects propagate over a larger distance than at zero-temperature. We take as a conservative estimate of the boundary zone at  $1.5T_c$  a length of  $l_b^{1.5T_c} \approx 2.2\sqrt{8t_0}$  (black dashed line). This has to be compared with the  $l_b^0 \approx 1.6\sqrt{8t_0}$  of [153] (blue dashed line). For higher temperatures, the boundary zone gets smaller again. At  $2.7T_c$  we estimate it to be of length  $l_b^{2.7T_c} \approx 1.45\sqrt{8t_0}$ .

#### 8.4.1 Scalar screening mass

The strong boundary contamination seen in the  $E_{ss}$  channel in figure 8.1 suggests that it might be an appropriate probe to extract the scalar screening mass  $m_{0+}$ , which will correspond to the lowest screening mass of the state which couples to  $E_{ss}$ . At zero temperature, it would be the lowest glueball state. Such a strategy was used in [148, 149] to extract glueball masses.

To make  $E_{ss}$  ultraviolet (UV) finite and be able to take the continuum limit, we study it at some finite flow-time. To have good control of our errors, we perform a simultaneous fit of the type

$$E_{ss}(r) = \alpha \exp(-m_{0+} r) + \beta + \gamma a^2 \quad (8.14)$$

with  $r$  a radius in the boundary zone (see section 8.3). The constant  $\beta$  has to reproduce the continuum bulk value and the  $\gamma$  factor encodes the  $a^2$  finite lattice spacing corrections.

We look for an intermediate range  $r \in [r_{min}, r_{max}]$  of values where we can extract a candidate mass  $m_{0+}$ . On the left-hand side of figure 8.4 we show the behaviour of  $\Delta E_{ss}^r t_0^2$  for different flow-times (top panel) together with the extraction of the screening mass for different  $r_{min}$  and different flow-times. We also checked that the results were not sensitive to the choice of  $r_{max}$ .

The extracted screening mass should be flow-time independent, being the mass of some states (the flow evolution will mix different operators but not change the operator basis), and we see

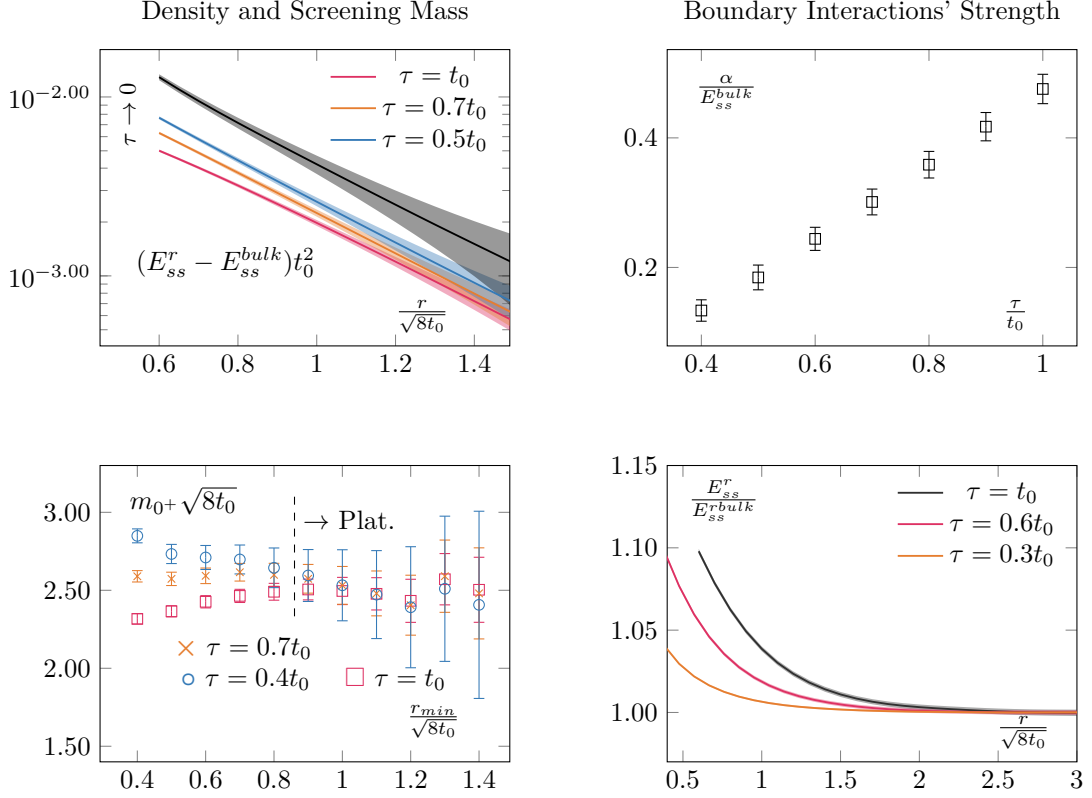


Figure 8.4 – **Top left:** Continuum extrapolated  $(E_{ss}^r - E_{ss}^{bulk})$  for different flow-times together with its  $\tau \rightarrow 0$  limit. Already qualitatively, one can see that there is an exponential decay, whose exponent does not seem to be sensitive to the flow-time, whilst its prefactor does. **Bottom left:** Extraction of the effective mass as a function of the minimal radius used in the exponential fit. We see that when the parameter saturates to a plateau, different flow-times lead to the same prediction, as expected. Note that our errors seem to be overestimated for large  $r_{min}$ ; we do not correct for this. **Top right:** Normalised prefactor of the exponential. This quantifies the interactions with the boundary states and increases with flow-time. This is due to the smoothing effect of the flow evolution; generically it increases the overlap between states. **Bottom right:** Corresponding effect on the boundary zone, its length increases with the flow-time as the bulk states interact more and more strongly with the boundary states.

that within our precision it is. Outside the plateau region, the masses differ but they do match once a plateau is reached. Typically, small flow-times lead to a worse signal. The reason lies in the smoothing effect of the flow. For larger flow-times, the errors are reduced and generally speaking overlap between states increases, as do their matrix elements. We can verify this by looking at the prefactor  $\alpha$  of our exponential fit, normalised by the bulk value. This quantifies the strength of the interaction with the  $0^+$  boundary state. We extract it using the same procedure as for the screening mass and report its flow-time dependence on the top panel on the right-hand side of figure 8.4. As expected, we see it growing with the flow-time. This also explains the behaviour of the boundary region as a function of the flow-time, which is shown in the lower panel on the right-hand side of figure 8.4. The more we flow, the stronger the interaction with the boundary gets and the larger the boundary zone becomes. This suggests that upon a good knowledge of the flow dependence of the observable under consideration, smaller flow-times are advantageous with respect to the boundary contaminations.

In this spirit, it is also instructive to perform the same mass extraction in the limit of zero Wilson flow. It serves two purposes. First, it allows checking the robustness of our results. Then, since  $E_{ss}$  is directly related to the energy-momentum tensor  $T_{\mu\nu}$ , taking the zero flow-time limit provides a properly renormalised observable. This would, for example, be required to extract any running quantities, such as the matrix elements encoded in  $\alpha$ . More precisely let us consider [168]

$$U_{\mu\nu}(x, \tau) = G_{\mu\rho}^a(x, \tau) G_{\nu\rho}^a(x, \tau) - \frac{1}{4} \delta_{\mu\nu} G_{\sigma\rho}^a(x, \tau) G_{\sigma\rho}^a(x, \tau) \quad (8.15)$$

$$E(x, \tau) = \frac{1}{4} G_{\sigma\rho}^a(x, \tau) G_{\sigma\rho}^a(x, \tau). \quad (8.16)$$

We can write

$$E_{ss}(x, \tau) = \frac{1}{4} (U_{ii}(x, \tau) - U_{00}(x, \tau)) - 2E(x, \tau). \quad (8.17)$$

The flow dependence then reads, using the expansions of [168],

$$E_{ss}(x, \tau) = \frac{c_T(\tau)}{4} (T_{ii}^R - T_{00}^R) - \frac{c_E(\tau)}{2} \{G_{\mu\nu} G_{\mu\nu}\}^R - c_1(\tau), \quad (8.18)$$

with  $T_{\mu\nu}^R$  the renormalised field strength tensor and  $\{G_{\mu\nu} G_{\mu\nu}\}^R$  the renormalised version of  $G_{\mu\nu} G_{\mu\nu}$ . The coefficients can be expanded perturbatively as

$$c_T(\tau) = g_0^2 + O\left(g^{\overline{\text{MS}}}((8\tau)^{-1/2})\right) \quad (8.19)$$

$$c_E(\tau) = 1 + O\left(g^{\overline{\text{MS}}}((8\tau)^{-1/2})\right), \quad (8.20)$$

with  $g_0$  the bare coupling and  $g^{\overline{\text{MS}}}$  the running coupling in the  $\overline{\text{MS}}$  scheme (see also [169]). The coefficient  $c_1$  is a mixing with unity and is set to  $c_1(\tau) = \langle E(\tau, x^{\text{bulk}}) \rangle$  where by  $x^{\text{bulk}}$  we mean the value in the centre of the lattice in the case of OBC. This sets the vacuum expectation of the trace of the energy-momentum tensor to zero [153]. Equation (8.18) allows

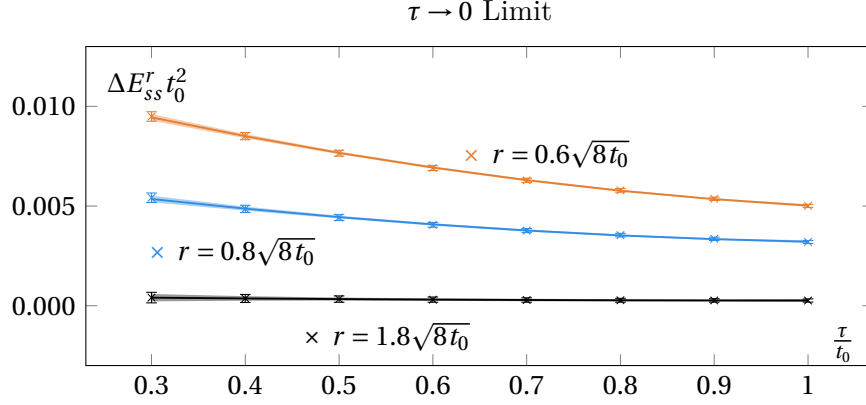


Figure 8.5 – Zero flow-time extrapolation of the continuum extrapolated  $(E_{ss}^r - E_{ss}^{bulk})$ .

to obtain a renormalised quantity to study the screening mass,

$$\Delta E_{ss}^r = \lim_{\tau \rightarrow 0} (E_{ss}^r(\tau) - E_{ss}^{bulk}(\tau)). \quad (8.21)$$

The zero flow-time extrapolation is shown in the top left plot of figure 8.4. To perform the extrapolation, we used a quadratic fit and checked that the result was insensitive to higher order corrections. An example at fixed radii is shown on figure 8.5. As expected, the extracted screening mass is compatible with the one obtained at other flow-times, as is shown in the left-hand side of figure 8.6.

We also extracted the screening mass at  $T = 2.7T_c$ , but did not extrapolate to zero flow-time; this is shown in figure the right-hand side of 8.6. Note that the mass is noticeably larger at  $2.7T_c$  than at  $1.5T_c$ ; see section 8.4.3 for a discussion. Consistently, the errors are also larger at  $2.7T_c$ . It also explains why we did not proceed to a zero flow-time extrapolation. As we may see, the signal quickly worsens at small flow-time and the noise reduction associated to the flow is crucial to extract the mass. It is thus extracted at  $t_0$ .

#### 8.4.2 Pseudo-scalar screening mass

Upon considering different operators, this method allows us to access the mass of the screening states of different quantum numbers. In this section, we will proceed with the mass determination of the pseudo-scalar screening state. One of the first continuum operators which come to mind and couples to the pseudo-scalar sector is the topological charge density

$$q(x) = \frac{1}{32\pi^2} \epsilon^{\mu\nu\rho\sigma} \text{Tr} G_{\mu\nu} G_{\rho\sigma} \quad (8.22)$$

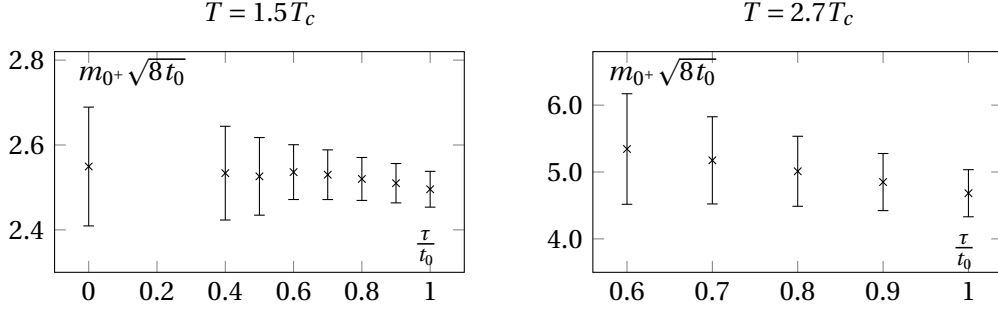


Figure 8.6 – **Left-hand side:** Measured screening masses at different flow-times, at  $T = 1.5T_c$ . They agree within statistical uncertainties. We clearly see the noise reduction associated with the Wilson flow. The relatively small value of the scalar screening mass allows for a precise measurement and a zero flow-time extrapolation. **Right-hand side:** Screening mass at different flow times at  $T = 2.7T_c$ . A larger mass is associated with larger uncertainties (mind the different scales).

Unfortunately, we cannot proceed with its integrated average, as we did in section 8.4.1 with the energy density, as  $\langle Q \rangle = 0$  in our case, with  $Q$  the topological charge (eq. (8.1)); in other words we are in the sector  $\theta = 0$ , with  $\theta$  the QCD  $\theta$ -angle. To circumvent this issue, we consider the two-point function of  $q$  over different sub-volumes,

$$\chi^r \equiv \langle q^2 \rangle^r = \frac{1}{N_y N_z N_t} \frac{1}{(N_x - 2r)} \langle \bar{q}^2(r) \rangle, \quad (8.23)$$

where we defined an averaged  $\bar{q}$ ,

$$\bar{q}(r) = \sum_{x=r}^{N_x-r-1} \sum_{y=0}^{N_y-1} \sum_{z=0}^{N_z-1} \sum_{t=0}^{N_t-1} q(x, y, z, t). \quad (8.24)$$

In other words,  $\chi^r$  is the average of topological charge square over a sub-volume. As the notation suggests, this quantity is related to the topological susceptibility, see section 8.5.<sup>2</sup> We show the  $r$  dependence of this quantity in figure 8.7 for various ensembles (some ensembles were omitted for the sake of clarity). Let us start discussing the ones at  $1.5T_c$  (left-hand side of figure 8.7). As expected, we see again a boundary zone in the case of OBC and a saturation away from it. In the very centre of the lattice,  $\chi^r$  displays a characteristic "bump". This feature is inherited from the behaviour of the correlator  $\langle q(x)q(0) \rangle$  around  $x = 0$  (see [170] for a detailed discussion).

The results at  $2.7T_c$  display the same global features as the ones at  $T = 1.5T_c$ , with a notable exception:  $\chi^r$  does not completely saturate; we observe a drift in its plateau value. We understand this effect as a manifestation of topological freezing (the lattices at  $2.7T_c$  are finer

<sup>2</sup>Note however that it is not the same quantity as is often used to study the topological susceptibility with OBC. Often, one considers the point-to-all two-point function of the topological charge, with the source far from the boundary (one can even average over different sources), see [151] for more details.

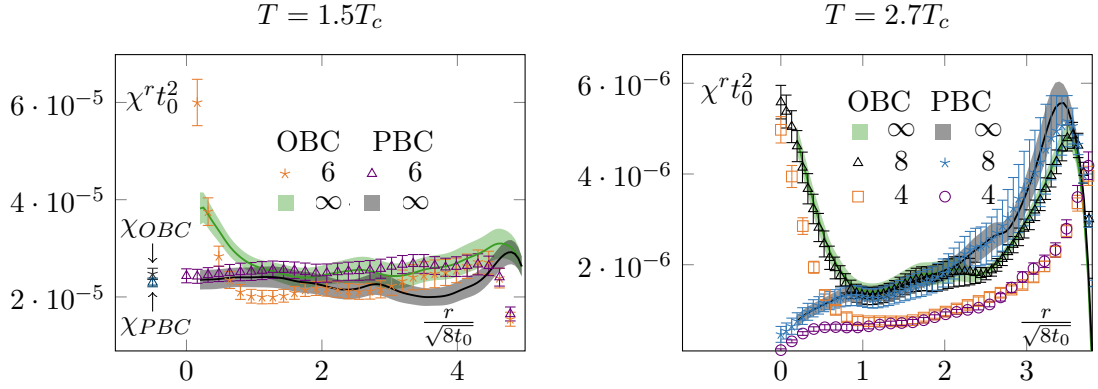


Figure 8.7 – Topological charge density square.. The legend’s labels correspond to  $N_t$ . For readability, we show only a subset of our data. At  $T = 1.5T_c$  (**left-hand side**), everything behaves as expected. The topological charge density square converges when integrated from the bulk and saturates to a constant value, which we can identify with the topological susceptibility. The OBC have the same bulk behaviour but suffer from exponentially suppressed contributions from the boundary states. The  $T = 2.7T_c$  case (**right-hand side**) is more interesting. We see that even the PBC charge density does not saturate. It can be interpreted as an indication of topological freezing, as it is known that the charge density over a sub-volume is less autocorrelated than the total charge [145]. The OBC presents a similar pattern, calling for a more careful analysis of their autocorrelation time.

than the one at  $1.5T_c$ ), see section 8.5 for a discussion.

In all cases, to extract the screening masses, we are only interested in the exponential decay from the boundary. We use the same strategy as in the previous section. As the pseudo-scalar is heavier, we perform the extraction at flow-time  $t_0$  to have a good signal to noise ratio; as in the case of the scalar mass at  $2.7T_c$ , the signal quickly deteriorates for smaller flow-times. We show the results in figure 8.8. The errors are comparable to the ones obtained for the scalar at  $2.7T_c$ , as the masses are of similar magnitude. We also checked that the masses are (within the statistical uncertainties) independent of the maximal radius used for the fit, as long as this radius is taken within the plateau region of  $\chi^r$ .

### 8.4.3 Discussion

All masses determined in this study are shown in physical units in figure 8.9. As expected, being less symmetric, the pseudo-scalar state is heavier than the scalar state. Whilst certainly present at  $T = 1.5T_c$ , the difference is not statistically significant at  $2.7T_c$ . This is an indication of dimensional reduction; at high temperature, the scalar and pseudo-scalar are expected to become degenerate [172].

On the same plot, we also show the values obtained in [171] by measuring the asymptotic behaviour of the energy density. The qualitative behaviour is the same but we observe a shift

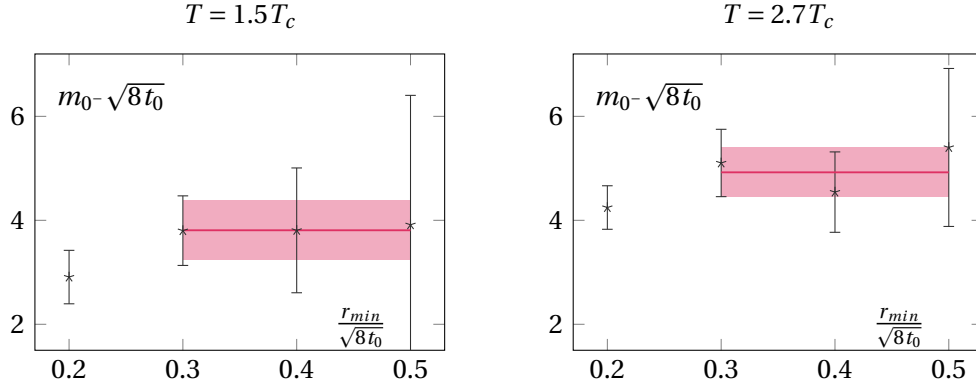


Figure 8.8 – **Left-hand side:** Extraction of the pseudo-scalar screening mass from the boundary pollution at  $T = 1.5T_c$ . The  $x$ -axis is the radius at which we start our single-exponential fit. We extract the mass from the plateau value. **Right-hand side:** Extraction of the pseudo-scalar screening mass from the boundary pollution at  $T = 2.7T_c$ . We observe a milder temperature dependence than in the scalar sector.

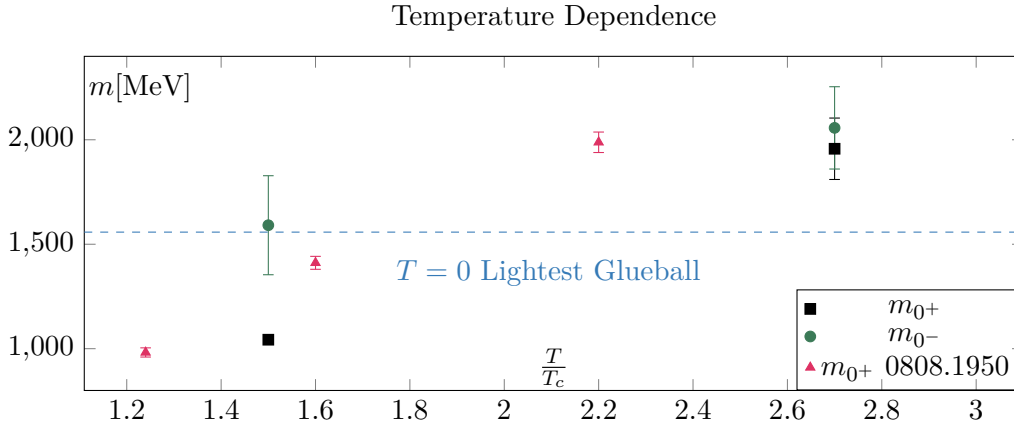


Figure 8.9 – Summary plot for the screening masses in [MeV]. Only statistical errors are shown. Firstly, as expected, the scalar screening mass is the lightest of the two states. Then, the behaviour of the masses is consistent with the behaviour of the boundary zone. At  $T = 1.5T_c$ , the scalar screening mass is lighter than the  $T = 0$  lightest glueball. At  $T = 2.7T_c$  it is heavier. The behaviour of the pseudo-scalar mass is also consistent; from a large mass gap between the two channels at  $T = 1.5T_c$ , we move to an almost degeneracy at  $T = 2.7T_c$ , which is a signal of dimensional reduction. On this figure, we also show the fixed lattice spacing results of [171]. The 15% discrepancy can most likely be attributed to systematic uncertainties (fixed lattice spacings, finite volume effects and conversion to physical units), even though a systematic difference between our methods cannot be excluded.

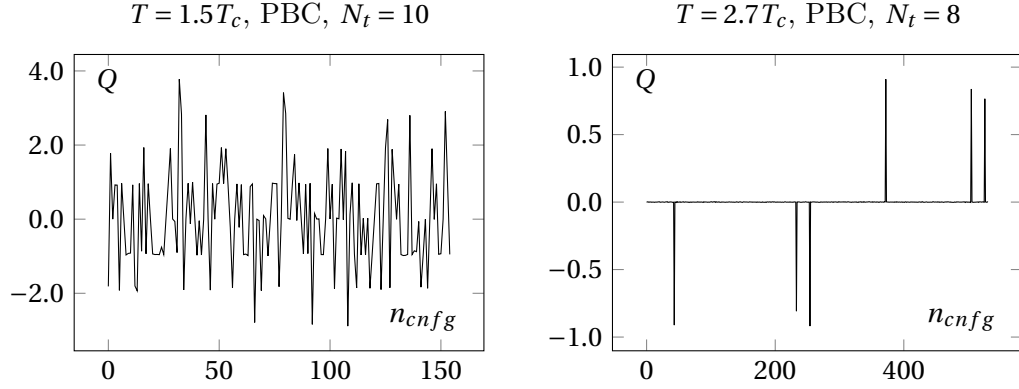


Figure 8.10 – **Left-hand side:** Topological charge history for PBC at  $1.5T_c$ . Every configuration is separated by 500 sweeps (see section 8.2). The different topological sectors are well sampled. **Right-hand side:** Topological charge history for PBC at  $2.7T_c$ . We observe clear signs of topological freezing at  $T = 2.7T_c$ . A very rough estimation gives  $\tau_{auto} > 300$ . This confirms the behaviour observed in figure 8.7.

of about 15%. Even if part of this discrepancy can presumably be explained by the fact that the results of [171] are at fixed lattice spacings and other systematics, an intrinsic difference between the two methods cannot be excluded.

Setting this aside, the data of [171] indicates that the main contribution to the pseudo-scalar mass is linear in  $T$ , as would be expected from perturbation theory at high temperatures. Taking this for granted, we can estimate that the scalar screening mass becomes heavier than the lightest glueball at around  $2T_c$ . This should correspond to the temperature at which the boundary zone becomes strictly smaller than the zero temperature one. And indeed, the fact that the scalar screening mass at  $1.5T_c$  is lighter than the lightest  $T = 0$  glueballs and that the  $T = 2.7T_c$  scalar screening mass is heavier is consistent with what was reported in figure 8.3 about the length of the boundary zone.

## 8.5 Topological susceptibility

Actually, the topological charge density square presented in section 8.4.2 also allows us to extract a value for the topological susceptibility. Indeed, as the continuum topological susceptibility is defined to be

$$\chi = \frac{d^2 E(\theta)}{d\theta^2} \quad (8.25)$$

$$= \frac{1}{V} \frac{1}{Z} \int \mathcal{D}A \left( \int d^4x \int d^4y q(x)q(y) \right) e^{-S[A]}, \quad (8.26)$$



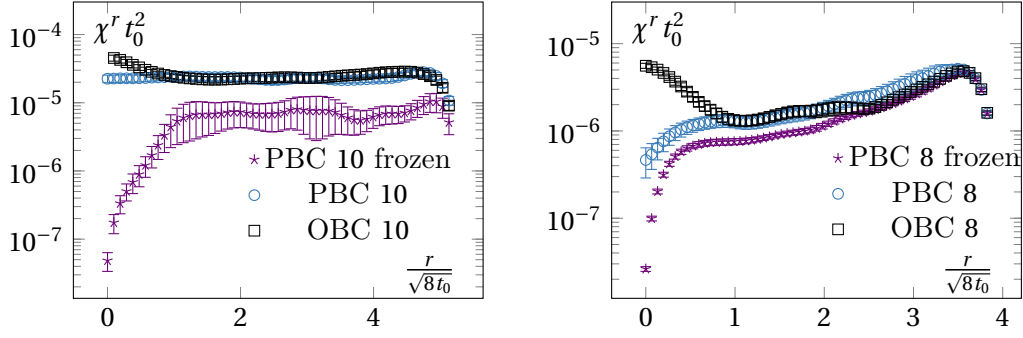


Figure 8.11 – **Left-hand side:** Topological charge density square on our finest lattice for OBC, PBC and  $Q=0$  PBC configurations at  $T = 1.5T_c$ . The numbers in the legend corresponds to  $N_t$ . **Right-hand side:** Topological charge density square on our finest lattice for OBC, PBC and  $Q=0$  PBC configurations at  $T = 2.7T_c$ . We see that the correlator behaves similarly to the  $Q=0$  restricted one at  $T = 1.5T_c$ . The numbers in the legend corresponds to  $N_t$ .

with the  $E(\theta)$  the vacuum energy at non-zero  $\theta$ ,<sup>3</sup>

$$E(\theta) = -\frac{1}{V} \ln \mathcal{Z}, \quad (8.27)$$

we expect the plateau value of  $\chi^r$  to give the topological susceptibility.

We show the obtained values in figure 8.7. The  $1.5T_c$  case is the most straightforward and leads to a clean signal. We perform a global fit on our three ensembles of the type  $f(a) = c_1 \cdot a^2 + \chi$  to remove the discretisation effect and extract the constant  $\chi$ . For PBC, we fit from the boundary up to  $r_{max} = 2\sqrt{8t_0}$ . In the case of OBC, we excluded the data in the boundary zone. Correspondingly, we used values in the range  $[1.3\sqrt{8t_0}, 2\sqrt{8t_0}]$ . It gives us measurements for the topological susceptibility

$$\chi_{OBC}(1.5T_c)t_0^2 = 2.47(15) \cdot 10^{-5} \quad (8.28)$$

$$\chi_{PBC}(1.5T_c)t_0^2 = 2.298(89) \cdot 10^{-5}, \quad (8.29)$$

which are in good agreement with  $\chi(1.5T_c)t_0^2 = 2.25(12) \cdot 10^{-5}$  of [170] and  $\chi_t(1.5T_c)t_0^2 \in [1.5 \cdot 10^{-5}, 4.4 \cdot 10^{-5}]$ , the global fit of reference [31]. They are also consistent with the fixed lattice spacing results of [173].

At  $2.7T_c$  the situation is more intricate, as it is not clear that  $\chi^r$  saturates to a plateau. The trouble comes from two reasons. First, as it was already discussed in [13] in the context of a toy model with OBC,  $\chi^r$  can present a slow convergence as a function of  $r$ . This is what we see in the centre of the lattice. Then, the behaviour of the PBC configurations seems to indicate that our ensembles are partially frozen.

<sup>3</sup>We recall that Euclidean  $SU(3)$  gauge theory at non-zero  $\theta$  can be described by the Lagrangian  $\mathcal{L} = L_{\theta=0}^{SU(3)} + i\theta q$ .

First, in figure 8.10, we show the history of the topological charge for PBC. We observe a clear difference between the two temperatures. At  $2.7T_c$ , the topological transitions are highly correlated. Then, in figure 8.11, we focus on our finest configurations at those two temperatures. We also display the results obtained when restricting ourselves to the  $Q = 0$  sector, i.e. by artificially freezing our lattices. Of course, at  $1.5T_c$ , the effect of freezing is drastic, as a lot of topological transitions are still to be expected. What is more interesting is the qualitative behaviour of  $\chi_r$ . For small sub-volumes, the value for the topological susceptibility is not so far from the unfrozen value but decreases for larger sub-volumes. It is consistent with the observation reported in [145], where it was observed that the topological charge measured on sub-volumes is less autocorrelated than the total charge. It is also intimately tied to the fact that the freezing of the topological charge is only a finite volume effect, one of the key ideas behind master field simulations [170, 174], where very large volumes are generated and the ensemble average is obtained by summing over decorrelated sub-volumes. The fact that we do not get the correct value for the topological susceptibility is only due to our volumes being too small to perform sub-volume averages in fixed sectors.

This discussion can also be applied to the  $2.7T_c$  case. However, there, the same kind of behaviour is present in the "unfrozen" case, which seems to indicate some partial freezing of our ensembles. This seems to be confirmed by the behaviour of the topological charge history of the PBC, which displays long correlations between jumps in topological sectors of the same sign; it shows correlations of at least 300 configurations. Unfortunately, the OBC shows a similar kind of behaviour. This stresses the point that OBC are not a remedy to the topological freezing but only a potential improvement.

This discussion shows that no reliable estimate of  $\chi(2.7T_c)$  can be extracted from figure 8.7 without further investigations of the autocorrelations. In particular, it confirms that even with these relatively large volumes, an extraction of the topological susceptibility from  $Q^2$  cannot be done reliably without a much larger statistics.

Note also that the way we extracted the topological susceptibility in this work is not the only way to do it. One can also consider the point-to-all integrated two-point function of the topological charge, with the source far-away from the boundary [151]

$$\chi^{2pt}(r, l) = \frac{1}{N_t N_y N_z} \frac{1}{2l} \sum_{x_0=N_x/2-l}^{N_x/2+l-1} \sum_{x=r}^{N_x-r-1} q^{av}(x_0) q^{av}(x_0 + x), \quad (8.30)$$

with

$$q^{av}(x) = \sum_{y=0}^{N_y-1} \sum_{z=0}^{N_z-1} \sum_{t=0}^{N_t-1} q(x, y, z, t). \quad (8.31)$$

The first sum in (8.30) is an average over sources that are far enough from the boundary while the second sum is a genuine integration. The quantity  $2l$  is the number of source points which

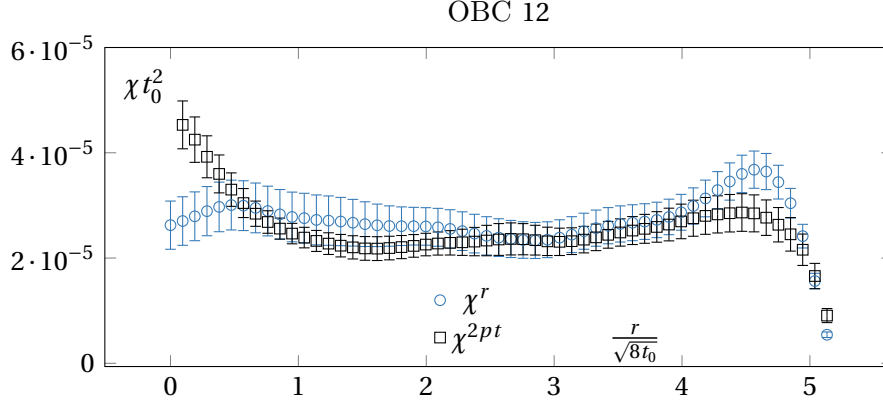


Figure 8.12 – Topological charge density square  $\chi^r$  versus topological charge integrated two-point function  $\chi^{2pt}$ . Both methods are consistent in their determination of the topological susceptibility. In this figure,  $\chi^{2pt}$  was averaged over 24 source points.

are averaged over. While we did not systematically study this quantity, we did check that our method is consistent with this definition. In figure 8.12, we show  $\chi^r$  and  $\chi^{2pt}(r, 12)$  for our largest configurations at  $T = 1.5T_c$ . Note that the choice  $l = 12$  is presumably not optimal and the error bars associated to  $\chi^{2pt}$  can presumably be reduced by tuning this parameter. We see that both methods are consistent; a careful study of their different systematics and how they relate is left as a potential interesting outlook.

## 8.6 Conclusion

In this study, we started a first systematic investigation of OBC at high temperature. The main difficulty in dealing with OBC is the presence of boundary effects. In section 8.3, we investigated the typical propagation length of these effects and compared it to the zero temperature results of [153]. At  $T = 1.5T_c$ , the boundary zone is larger than at  $T = 0$ , while it is smaller at  $T = 2.7T_c$  and  $T = 3.0T_c$ . These differences can be understood in terms of the temperature dependence of the mass of the lightest state in our system, namely the scalar screening mass. Actually, the boundary contamination gives us means to measure this screening mass, giving results which are consistent with the already existing literature (see section 8.4.3). In particular, we predict that the scalar starts to be heavier than the  $T = 0$  lightest glueball at around  $T = 2T_c$ . It tells us that the use of OBC in the region  $T \in [T_c, 2T_c]$  is more delicate than at  $T = 0$  but becomes gradually easier at temperatures above  $2T_c$ . This is potentially useful as it is the interesting range of temperatures to measure the topological susceptibility, for example [175]. Moreover, we do not expect the situation to change drastically in full QCD, in the deconfined phase.

We also used the boundary effects in the pseudo-scalar channel to estimate the corresponding screening mass. We measured a sizable mass gap between the scalar and pseudo-scalar at

$T = 1.5T_c$ . Moreover, we could confirm that this gap reduces at higher temperature, which is an expected signal of the dimensional reduction taking place at high enough temperatures.

As a by-product of the pseudo-scalar analysis, we could extract a precise measurement of the topological susceptibility at  $T = 1.5T_c$ , which is in good agreement with the recent results of [170]. Finally, the same analysis at  $T = 2.7T_c$  exhibits some signs of topological freezing. A potential interesting outlook consists in studying quantitatively how the autocorrelation time depends on the lattice spacing and temperature and how it compares to the master field approach [170]. Even so, it shows again that even with rather large volumes, the determination of the topological susceptibility is delicate. This supports the recent efforts [170, 176], which have been undertaken to reassess the robustness of high-temperature studies of the topological susceptibility. In particular, a careful reconsideration of the finite size effects on its determination, even in the quenched case, is called for.

## Acknowledgements

The authors wish to thank M. Lombardo for an interesting discussion, A. Francis, M. Bruno and S. Sharma for comments on a previous version of this manuscript and particularly R. Sommer for his help and suggestions. A.F. thanks A. Rago, M. Hansen, F. Knechtli and N. Husung for insightful discussions and A. Jaquier for his technical support. The work of A.F. is supported by the Swiss National Science Foundation. The authors acknowledge support by the Deutsche Forschungsgemeinschaft (DFG, German Research Foundation) through the CRC-TR 211 "Strong-interaction matter under extreme conditions" – project number 315477589 – TRR 211. Numerical calculations have been made possible through PRACE grants at CSCS, Switzerland, as well as grants at the GCS and at NIC-Jülich, Germany. These grants provided access to resources on Piz Daint at CSCS and JUWELS at NIC. Some of the numerical simulations have been performed on Fidus and Deneb, which are part of the EPFL HPC centre (SCITAS).



# *CosmoLattice* Part IV



## 9 Physical motivations: preheating

In this chapter, we will treat yet another aspect of non-perturbative field theory, particle creation after the end of the initial inflationary era of our universe. We will see that real-time numerical simulations are also needed in this case. Moreover, results depend on the model for inflation, and as the specifics of inflation are relatively poorly constrained, many different models are viable. All of these models require in principle dedicated numerical simulations. Publicly available software designed to perform such simulations exist [177–184], but at the time of writing none incorporate non-Abelian fields and only the recently announced [184] incorporate Abelian gauge fields. To fill in this gap, we wrote a new software, *CosmoLattice*, which is also able to simulate  $SU(2)$ -gauge fields. The algorithms designed to this purpose as well as demonstrations of its capability are presented in the next chapter; this is where the original research content can be found (most of which is also part of reference [3]). In this chapter, we present the relevant physics, namely recall basics of slow-roll inflation and the main mechanism behind particle creation at its end.

### 9.1 Slow-roll inflation and its end

In this section, we briefly recall basic facts about inflation. Introductions to this subject can be found in references [185, 186] or any modern textbook about cosmology. Cosmology is based on the observation that, at large scales, we live in a spatially homogeneous and isotropic universe. The only four-dimensional homogeneous and isotropic metric is the Friedmann-Lemaître-Robertson-Walker (FLRW) one and can be described by the following line element

$$ds^2 = dt^2 - a(t) \left( \frac{dr^2}{1 - Kr^2} + r^2 d\theta^2 + r^2 \sin^2(\theta) d\phi \right). \quad (9.1)$$

The constant  $K$  is the curvature of the space and  $a(t)$  is the scale factor. A negatively curved FLRW space is referred to as closed. A positively curved FLRW space is called open. When  $K = 0$  we talk about a flat space.

The only dynamical degree of freedom in this metric is the scale factor. Its equations of



## Chapter 9. Physical motivations: preheating

---

motion are found by developing Einstein's equations

$$G_{\mu\nu} = \frac{1}{m_p^2} T_{\mu\nu} \quad (9.2)$$

for the FLRW metric. In equation (9.2),  $G_{\mu\nu}$  is the Einstein's tensor,  $m_p^2 = \frac{1}{8\pi G_N}$  the reduced Planck mass,  $G_N$  Newton's constant and  $T_{\mu\nu}$  is the energy-momentum tensor defined in equation (1.30). Note also that we did not write down a cosmological constant  $\Lambda$ , as its presence is not relevant at early times. The resulting equations are called the Friedmann's equations and read

$$\frac{\dot{a}^2}{a^2} = \frac{\rho}{3m_p^2} - \frac{K}{a^2} \quad (9.3)$$

$$\frac{\ddot{a}}{a} = -\frac{\rho + 3p}{6m_p^2} . \quad (9.4)$$

The quantities  $p$  and  $\rho$  are the pressure and energy density associated with non-gravitational fields. They are defined in analogy to a perfect fluid, whose energy-momentum tensor is

$$T_{\mu\nu}^{fluid} = (p + \rho) v_\mu v_\nu + p g_{\mu\nu} \quad (9.5)$$

with  $v_\nu$  the fluid's velocity field. In the fluid's rest frame ( $v_i=0$ ,  $v_0=-1$ , so that  $v^\mu v_\mu = -1$ ), this gives

$$T_{00}^{fluid} = \rho \quad (9.6)$$

$$T_{ii}^{fluid} = p a^2 . \quad (9.7)$$

We then define, for generic matter content

$$\rho = T_{00} \quad (9.8)$$

$$p = \frac{a^{-2}}{3} \sum_{i=0}^3 T_{ii} . \quad (9.9)$$

Observations suggest that our universe is almost flat, possibly even exactly flat and the term in  $K$  in equation (9.3) can be neglected. Then, the evolution of the scale factor can be parametrised in terms of an equation of state for the non-gravitational fields

$$p = \omega \rho . \quad (9.10)$$

For  $\omega = \text{constant}$ , the Friedmann's equations can be solved and one finds

$$a(t) \propto t^{2/(3+3\omega)}, \quad \omega \neq -1 \quad (9.11)$$

$$a(t) \propto e^{ct} \quad \omega = -1 \quad (9.12)$$

with  $c$  some constant. The equation of state for purely non-relativistic matter is  $\omega = 0$  while the one of pure radiation is  $\omega = \frac{1}{3}$ .

Assuming that the evolution of the universe occurred only in phases where the dominant equation of state is the one of matter or radiation leads to some problems. First, the "flatness" problem, which comes about because of the present value of the measured curvature density  $\Omega_k = -\frac{K}{a^2}$ . Current bounds give [186]  $|\Omega_k| < 0.005$  and tracing it back in time with a power-law evolution of the scale factor leads to an extremely fine-tuned initial value for  $K$ . Second is the "horizon" problem. The observation of a largely homogeneous cosmic microwave background together with only a power-law like evolution of the scale factor would imply a causal correlation between different causal patches.

Both of these problems can be solved by assuming an initial era of expansion where the scale factor grows exponentially. This era is called inflation. As equation (9.12) indicates, this can be achieved if the field content which dominates has an equation of state of  $\omega = -1$ . The paradigmatic model of inflation consists of a homogeneous scalar field  $\phi$ , the "inflaton", evolving in some potential  $V$ . As we will derive in more details in the next chapter, the corresponding field equations are

$$\ddot{\phi} + 3\mathcal{H}\dot{\phi} + \frac{\partial V}{\partial \phi} = 0, \quad (9.13)$$

where we defined the Hubble rate as  $\mathcal{H} = \frac{\dot{a}}{a}$ . We are also interested in the energy components

$$\rho_\phi = \frac{1}{2}\dot{\phi}^2 + V(\phi), \quad p_\phi = \frac{1}{2}\dot{\phi}^2 - V(\phi). \quad (9.14)$$

We see that we can achieve the appropriate equation of state if

$$\frac{1}{2}\dot{\phi}^2 \ll V(\phi). \quad (9.15)$$

This will be our first "slow-roll" condition. In particular, with this assumption, the Friedmann's equation (9.3) simplifies to

$$\mathcal{H}^2 = \frac{1}{3m_p^2} V_\phi. \quad (9.16)$$

For inflation to last long enough (see references [185–187] for a quantitative description of this statement), we need our first slow-roll condition to be satisfied for long enough time. This will happen only if the friction term in the equation of motion (9.13) dominates over  $\ddot{\phi}$ . This leads to our second slow-roll condition

$$|\ddot{\phi}| \ll \mathcal{H}\dot{\phi}. \quad (9.17)$$

After some massaging, these two equations can be rewritten as dimensionless ratios involving

only the potential and its derivatives; these are the "potential" slow-roll parameters

$$\epsilon_V = \frac{m_p^2}{2} \left( \frac{\frac{\partial V}{\partial \phi}}{V(\phi)} \right)^2, \quad (9.18)$$

$$\eta_V = m_p^2 \left( \frac{\frac{\partial^2 V}{\partial \phi^2}}{V(\phi)} \right). \quad (9.19)$$

Both  $\epsilon_V$  and  $\eta_V$  must be much smaller than one to have slow-roll inflation. These two parameters are useful to decide whether a particular potential can sustain slow-roll inflation or not.

We can also directly consider the behaviour of  $H$  to characterise inflation. The trick is to rewrite  $\ddot{a} = a(\dot{\mathcal{H}} + \mathcal{H}^2)$ . To have inflation, we need at least  $\ddot{a} > 0$ , leading to the condition

$$\epsilon_H = -\frac{\dot{\mathcal{H}}}{\mathcal{H}^2} < 1. \quad (9.20)$$

Inflation ends when  $\epsilon_H = 1$ . We can also write a second slow-roll parameter to ensure that inflation occurs over sufficiently long times. It is defined as the rate of change of  $\epsilon_H$

$$\eta_H = \frac{\dot{\epsilon}_H}{\mathcal{H}\epsilon_H}, \quad (9.21)$$

and also needs to be smaller than one. For a careful discussion on slow-roll parameters, we refer the reader to reference [188].

Inflation needs to end at some point and the "inflaton" needs to transfer its energy into standard model fields, to populate the universe as we see it today. This transfer is called preheating and is the subject of the next section. To discuss it, it is important to understand how the inflaton behaves at the end of inflation. For concreteness, let us take  $V(\phi) = \frac{1}{2}m^2\phi^2$ . In figure 9.1, we show the numerical solution to the system of ordinary differential equations (9.13) together with the Friedmann equation for  $\mathcal{H}$ , with a large field amplitude as an initial condition. We can clearly see on the left-hand side of the figure the initial slow-roll phase, characterised, both by the mild change of the field amplitude and the smallness of  $\epsilon_H$ . At the end of this phase, around  $m_p t \approx 230$ , the field reaches the bottom of its potential and starts oscillating around it. As we will see, these oscillations around the minimum will drive preheating.

In the case of the quadratic potential, the form of these oscillations can be understood analytically. In a slow-phase approximation, one can show [186]

$$\phi(t) \approx \phi^{att.}(t) = \frac{2\sqrt{2}m_p \cos(m(t-t_f))}{\sqrt{3}m(t-t_f)} \left( 1 + \frac{\sin(2m(t-t_f))}{2m(t-t_f)} \right), \quad (9.22)$$

with  $t_f$  the time at which the slow-roll regime ends. This solution is compared to the full

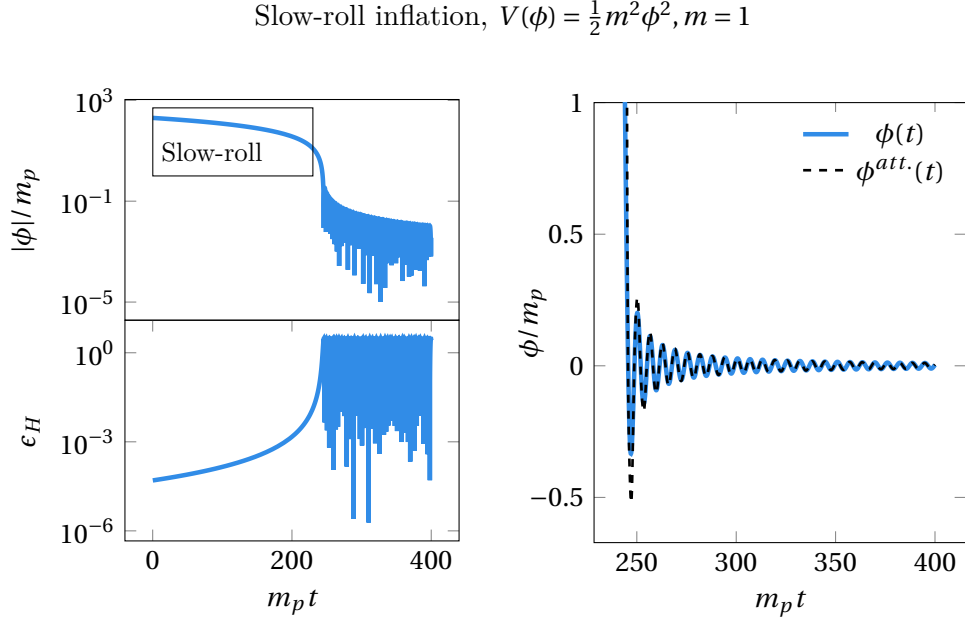


Figure 9.1 – **Left-hand side:** Numerical solution to the homogeneous scalar field equations and of the slow-roll parameter  $\epsilon_H$ . We see the slow-roll regime and its end, when  $\epsilon_H$  becomes of order one. **Right-hand side:** Evolution of the homogeneous inflaton just after the end of the slow-roll regime. An approximate analytic solution is also plotted.

numerical solution on the right-hand side of figure 9.1 and we see it is a good approximation. Moreover, for any potential with a quadratic minimum, the inflaton will be driven towards this solution.

To conclude this part, note that considering the inflaton to be a homogeneous field breaks down soon after the end of the slow roll regime, as we will discuss in the next section. Numerical solutions of the full partial differential equations are needed and this is what `CosmoLattice` is designed for.

## 9.2 Preheating and particle creation

Once the inflaton exits slow-roll, the universe is not expanding exponentially fast anymore. All the energy of the universe is stored in this field and now needs to be redistributed into other particles. This can happen because of quantum fluctuations. Any field is at least coupled to the inflaton through gravitation and can be dynamically fed energy.

An appropriate theoretical framework to treat this problem analytically is to consider the oscillating homogeneous mode of the inflaton as a classical background field to which quantum fluctuations are coupled [189]. We will present below one of the main process responsible for these energy transfers, namely parametric resonance. We will restrict ourselves to the simpler

## Chapter 9. Physical motivations: preheating

---

case without expansion, for a quadratic potential. For more details and a thorough analytical treatment of the effect of an expanding background, we refer the reader to reference [189].

We consider inflation with a quartic potential  $\frac{m^2}{2}\phi^2$  and model its evolution at the end of inflation by

$$\phi(t) = \Phi \cos(mt) . \quad (9.23)$$

To mimic interactions with other standard model particles, we add a quartic interaction to a daughter particle  $\phi$ , and consider the following potential

$$V(\phi, \chi) = \frac{m^2}{2}\phi^2 + \frac{g}{2}\phi^2\chi^2 , \quad (9.24)$$

with  $g$  some dimensionless coupling constant. Recalling that we treat  $\phi$  as a classical background, this means that we need to study the field operator  $\hat{\chi}$ , whose evolution is dictated by the following Hamiltonian

$$\hat{H} = \frac{1}{2}\hat{\Pi}_\chi^2 + \nabla\hat{\chi}^2 + \frac{g}{2}\hat{\chi}^2\Phi^2\cos^2(mt) . \quad (9.25)$$

This is nothing else than a simple harmonic oscillator with a time-varying frequency. The operator  $\hat{\chi}$  can also be expanded into creation and annihilation operators  $a_k, a_k^\dagger$  [187]

$$\hat{\chi}(x, t) = \int d^3k \chi_k(t)^* \hat{a}_k e^{i\vec{k}\cdot\vec{x}} + \chi_k(t) \hat{a}_k^\dagger e^{-i\vec{k}\cdot\vec{x}} , \quad (9.26)$$

provided the mode function solves the classical equations of motion with the time-varying frequency

$$\ddot{\chi}_k + (k^2 + g^2\Phi^2\sin^2(mt))\chi_k = 0 . \quad (9.27)$$

The main mechanism to drive particle creation comes from the fact that periodic ordinary differential equations of this type admit unstable solutions. The mathematical analysis of such equations is known as Floquet's theory. In our case, it tells us [186] that the most general solution is given in as

$$\chi_k(t) = e^{\mu_k t} v_+(t) + e^{-\mu_k t} v_-(t) , \quad (9.28)$$

with  $\mu_k$  the so-called Floquet's exponent and  $v_\pm(t) = v_\pm(t + T)$  some periodic functions of the same period  $T$  than the effective frequency ("Bloch waves" in a condensed matter context).

As outlined in [186], the Floquet's exponent can be exactly computed for every mode and given parameters by solving numerically the associated equation. To understand the phenomenon of particle creation, it is important to pin down which modes display an instability and for which set of parameters. This can be achieved through a parameter scan, often referred to as a Floquet's chart in this context.

In figure 9.2, we show the result of this analysis applied to equation (9.27). The colour-map

represents the real part of the Floquet's exponent; exponential growth happens only when it is non-zero. It is standard to map equation (9.27) to a Mathieu equation

$$\ddot{x}_k + (A_k - 2q \cos(2z))x_k = 0, \quad (9.29)$$

with a resonance parameter

$$q = \frac{g^2 \Phi^2}{4m^2} \quad (9.30)$$

and  $A_k = \frac{k^2}{m^2}$ . We see the emergence of resonance bands, where the Floquet's exponent has a non-zero real part, leading to an exponential growth of the corresponding mode. This exponential growth reflects itself in the particle occupation number and is then interpreted as particle creation.

This kind of instabilities are known as parametric resonances and are a feature of fields evolving in a periodic classical background. An interesting fact is that to have an exponential growth, some energy need to be already present in  $\chi_k(0)$  or  $\dot{\chi}_k(0)$ , has the only compatible solution of the type (9.28) with  $\chi_k(0) = 0$  and  $\dot{\chi}_k(0) = 0$  is  $\chi_k = 0$ . For preheating, quantum fluctuations play the role of seeds.

Parametric resonances remain when the expansion of the universe is accounted for, but the details are more intricate and we refer the interested reader to references [186, 187, 189].

The exponential creation of particles due to these parametric resonances brings the system into a classical regime with large occupation numbers and one expects the dynamics to be well captured by the classical field equations of motions. In particular, they can be solved numerically to take into account the inhomogeneities in the field  $\phi$ , which also grows exponentially due to parametric resonances and the back reaction of  $\chi$  into  $\phi$ , which is crucial to shut-off the exponential growth of  $\chi$ . Such kind of numerical simulations are what `ℳosmoℒattice` was designed for and are further described in the next chapter.

### 9.3 Foreword to [3]

As already mentioned several times, classical real-time simulations are essential to capture the non-linear dynamics responsible for the preheating of our universe. In reference [3], mostly reproduced in the next chapter, we present a compendium on lattice techniques to perform such simulations. In particular, we introduce a new set of algorithms to solve the dynamics of scalar, Abelian and non-Abelian gauge, precise of up to  $\mathcal{O}(dt^{10})$ . This work is meant to be the theory companion to `ℳosmoℒattice`, a scalable and user-friendly code, easily modifiable, which implements the presented algorithm and is to be publicly released [4].

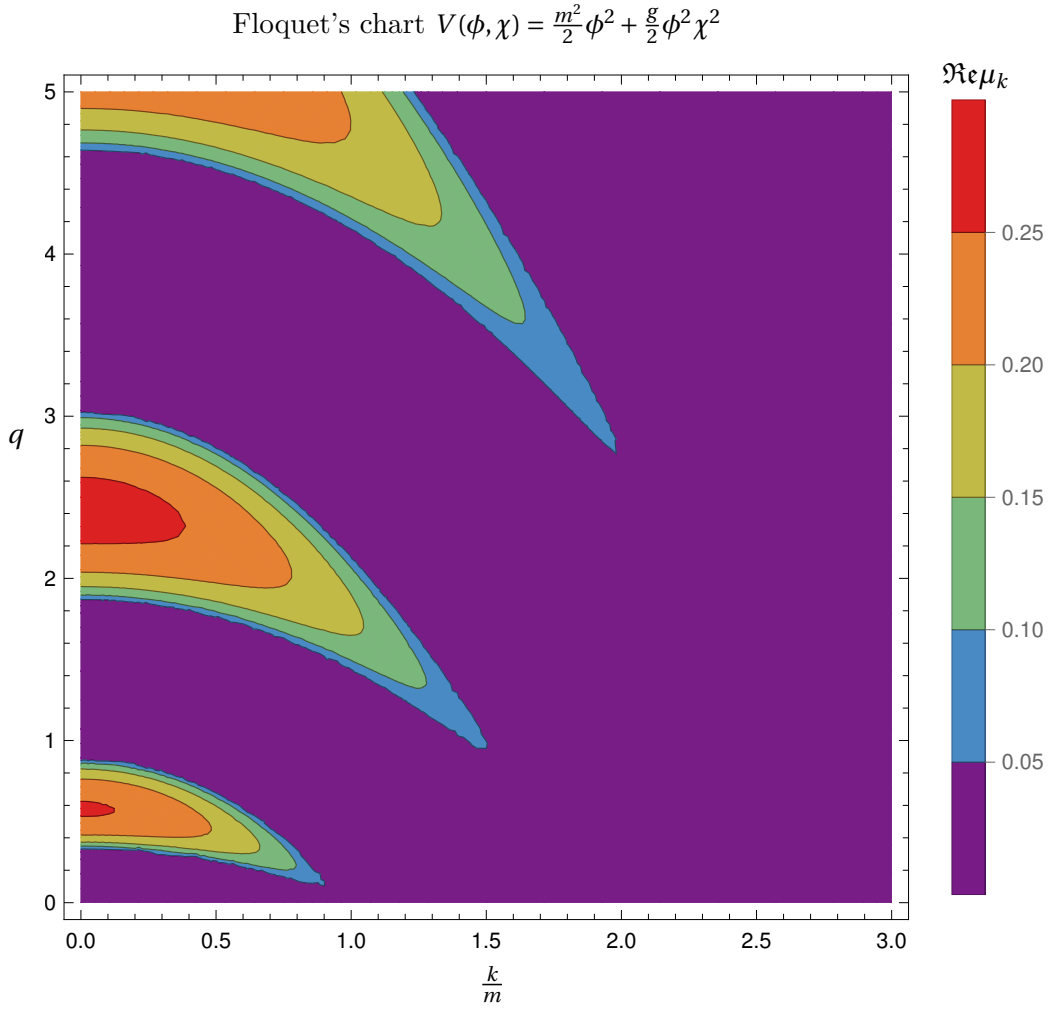
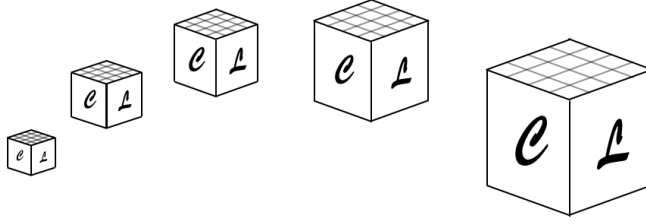


Figure 9.2 – Floquet's chart as a function of the momentum and the resonance parameter  $q = \frac{g^2\Phi^2}{4m^2}$  for the model  $V(\phi, \chi) = \frac{m^2}{2}\phi^2 + \frac{g}{2}\phi^2\chi^2$ . We see the appearance of resonance bands where the Floquet's exponent has a non-zero real part. Modes in this region will grow exponentially and lead to particle production.

# 10 *The art of simulating the early Universe* [3]<sup>\*</sup>



**Authors:** Daniel G. Figueroa, Adrien Florio, Francisco Torrenti, Wessel Valkenburg

*Reference:* arXiv:2006.15122

*Abstract:* We present a comprehensive discussion on lattice techniques for the simulation of scalar and gauge field dynamics in an expanding universe. After reviewing the continuum formulation of scalar and gauge field interactions in Minkowski and FLRW backgrounds, we introduce the basic tools for the discretization of field theories, including *lattice gauge invariant* techniques. Following, we discuss and classify numerical algorithms, ranging from methods of  $\mathcal{O}(\delta t^2)$  accuracy like *staggered leapfrog* and *Verlet integration* to the *Yoshida* integrators accurate up to  $\mathcal{O}(\delta t^{10})$ . We adapt these methods for their use in classical lattice simulations of the non-linear dynamics of scalar and gauge fields in an expanding grid in  $3+1$  dimensions, including the case of ‘self-consistent’ expansion sourced by the volume average of the fields’ energy and pressure densities. We present lattice formulations of canonical cases of: *i) Interacting scalar fields*, *ii) Abelian  $U(1)$  gauge theories*, and *iii) Non-Abelian  $SU(2)$  gauge theories*. In all three cases we provide symplectic integrators, with accuracy ranging from  $\mathcal{O}(\delta t^2)$  up to  $\mathcal{O}(\delta t^{10})$ . For each algorithm we provide the form of relevant observables, such as energy density components, field spectra and the Hubble constraint. We note that all our algorithms for gauge theories always respect the Gauss constraint to machine precision, even in the case of ‘self-consistent’ expansion. As a numerical example we analyze the post-inflationary dynamics of an oscillating inflaton charged under  $SU(2) \times U(1)$ . We note that the present manuscript is meant as part of the theoretical basis for the code *CosmoLattice*, a multi-purpose MPI-based package for simulating the non-linear evolution of field theories in an expanding universe, to be released in 2020.

<sup>\*</sup>*Content of this chapter:* Contrary to what is done in other chapters, we do not reproduce the



full content of reference [3]. We removed a few sections about some specific algorithms. Note that section 10.2.1 and section 10.3.2.2 have some overlap with material presented in chapter 1 and 4; we decided to include them anyhow to keep the integrity of the paper. Note also that we added appendices with some computations relating to the FLRW metric.

*Author’s contribution:* Development of about two third of the code, including the expression template gauge algebra, `CosmoLattice` interface, the measurements and the evolution algorithms. Design of the dedicated velocity-Verlet algorithms up to order  $O(dt^{10})$ . Contributions to the redaction of the paper.

## 10.1 Introduction

### 10.1.1 The Numerical Early Universe: a laboratory for non-linear high energy physics

Compelling evidence [190] supports the idea of *inflation*, a phase of accelerated expansion in the early universe, which provides both a solution to the shortcomings of the hot Big Bang framework [191–197], and an explanation for the origin of the primordial density perturbations [198–202]. Inflation is often assumed to be driven by a scalar field, the *inflaton*, with potential and initial conditions appropriately chosen to sustain a long enough period of accelerated expansion. To switch to the standard hot Big Bang cosmology, a *reheating* period must be ensured after inflation, converting the energy available into light degrees of freedom (*dof*), which eventually thermalize and dominate the universe energy budget. This transition process is an integral part of the inflationary paradigm, although observationally much less constrained than the inflationary period itself. For reviews on inflation and reheating, see [203–206] and [186, 187, 207, 208].

In many scenarios, the inflaton oscillates around the minimum of its potential following the end of inflation, initially in the form of a homogeneous condensate. Particle species coupled sufficiently strongly to it are then created in energetic bursts. If the particles are bosons, their production is driven by parametric resonance, resulting in an exponential transfer of energy within few oscillations of the inflaton [189, 209–215]. If the particles are fermion species, there can also be a significant transfer of energy [216–219], albeit no resonance can be developed due to Pauli blocking. Particle production in this way, of either bosons or fermions, corresponds to a non-perturbative effect, which cannot be described with standard quantum field theory (QFT) perturbative techniques. Furthermore, particle species created by these effects are typically far away from thermal equilibrium, and in the case of bosonic species their production is exponential, so they eventually ‘backreact’ onto the inflaton, breaking apart its initial homogeneous condition. The dynamics of the system becomes non-linear from that moment onward. All of these effects, from the initial particle production to the eventual development of non-linearities in the system, represent what is referred to as a *preheating* stage. In order to fully capture the non-perturbative, out-of-equilibrium and eventual

non-linearities of preheating, we need to study such phenomena on a lattice. This requires the use of classical field theory real-time simulations, an approach valid as long as the particle species involved in the problem have large occupation numbers  $n_k \gg 1$ , so that their quantum nature can be neglected [220, 221].

Parametric particle production can also be developed in the early universe, in circumstances other than preheating. For instance, in the curvaton scenario [222–225], the initially homogeneous curvaton (a spectator field during inflation) may decay after inflation via parametric resonance, transferring abruptly all its energy to other particle species [226–229]. If the Standard Model (SM) Higgs is weakly coupled to the inflationary sector, the Higgs can be excited either during inflation [230–232], or towards the end of it [233, 234], in the form of a condensate with large amplitude. The Higgs then decays naturally into the rest of the SM species via parametric effects [231, 234–239], some time after inflation<sup>1</sup>. In supersymmetric (SUSY) extensions of the SM we encounter flat directions [248, 249], configurations in field space where the renormalizable part of the scalar potential is exactly flat (as SUSY must be broken, the exact flatness is however typically uplifted by various effects [250]). During inflation, due to quantum fluctuations, field configurations can be developed with a large expectation value along these directions [249, 251]. If such scalar condensates have a soft mass, its amplitude starts oscillating after inflation once the Hubble rate becomes smaller than its mass [250, 252], possibly ensuing an explosive decay of the field condensate due to non-perturbative resonant effects [253–255].

In certain types of inflationary models where spontaneous symmetry breaking plays a central role, tachyonic effects can also lead to non-perturbative and out-of-equilibrium particle production, eventually driving the system into a non-linear regime. One example of this is Hybrid inflation [256], a family of models where the inflationary stage is sustained by the vacuum energy of a Higgs-like field. During inflation, the effective squared mass of the Higgs field is positive defined, but becomes negative when the inflaton eventually crosses around a critical point. The Higgs then sustains a tachyonic mass that leads into an exponential growth of the occupation number of its most infrared (IR) modes below its own tachyonic mass scale [257–260]. This continues until the mass square becomes positive again, due to the Higgs own self-interactions. In Hilltop-inflation, inflation is sustained while the inflaton slowly rolls from close to a maximum of its potential (the ‘hilltop’) towards its minimum, located at some non-vanishing scale. When the inflaton amplitude crosses a certain threshold, inflation ends, and the inflaton starts oscillating around its minimum. Its effective squared mass then alternates between positive and negative values, as the inflaton rolls back and forth between the minimum of its potential and the region of negative curvature where inflation ended. Fluctuations of the inflaton then grow exponentially during successive tachyonic phases.

Preheating effects have been also studied in models with gravitationally non-minimal coupled

---

<sup>1</sup>Note that this differs from the Higgs-Inflation scenario [240, 241], where the Higgs also decays after inflation into SM fields via parametric effects [236, 242–247], but as the Higgs plays the role of the inflaton, this scenario belongs to the category of preheating.

fields [246, 261–266], and in particular, recently, in multi-field inflation scenarios [267–271]. In the latter, a single-field attractor behavior is developed during inflation, later persisting during preheating. Due to this, particle production after inflation becomes more efficient than in multi-field models with minimal couplings, where a *de-phasing* effect of the background fields’ oscillations leads to a damping of the resonances [208, 272–275].

Furthermore, as gauge fields are naturally present in the SM and in many of its extensions, their presence in inflationary scenarios has also been considered. Due to their bosonic nature, gauge fields can exhibit highly nonlinear dynamics during preheating. For instance, if the inflaton enjoys a shift-symmetry, a topological coupling to a gauge sector is allowed. In the case of  $U(1)$  gauge fields, preheating effects have been studied in axion-inflation scenarios [276–281], showing that an interaction  $\phi F\tilde{F}$  leads to an extremely efficient way to reheat the universe, as well as to very interesting (potentially observable) phenomenology. In [1, 115, 279] an improved lattice formulation of an interaction  $\phi F\tilde{F}$  between an axion-like field and a  $U(1)$  gauge sector was constructed, demonstrating that the topological nature of  $F\tilde{F}$  as a total derivative  $\partial_\mu \mathcal{K}^\mu$ , can be actually realized exactly on a lattice (hence preserving exactly the shift symmetry at the lattice level). Interactions between a singlet inflaton and an Abelian gauge sector, via  $f(\phi)F^2$ , or a non-Abelian  $SU(2)$  gauge sector, via  $f(\phi)\text{Tr}G^2$ , have also been explored in the context of preheating [282, 283].

In Hybrid inflation models, the presence and excitation of gauge fields have also been addressed extensively, both for Abelian and non-Abelian scenarios, obtaining a very rich phenomenology, see e.g. [284–294]. The case of preheating via parametric resonance, with a charged inflaton under a gauge symmetry, has however not been considered very often in the literature<sup>2</sup>. Nothing is wrong *per se* about considering an inflaton charged under a gauge group [and hence coupled to some gauge field(s)], as long as one constructs a viable working model, respecting the observational constraints. In such a case, when the inflaton starts oscillating following the end of inflation, the corresponding gauge bosons will be parametrically excited. This has been studied in detail in Ref. [295], for both Abelian  $U(1)$  and non-Abelian  $SU(2)$  gauge groups. Actually, in this manuscript we also consider a similar model for which we compute the preheating stage via parametric resonance effects into  $U(1)$  and  $U(1) \times SU(2)$  sectors. A natural realization of an inflationary set-up where the inflaton is charged under a gauge group is the Higgs-Inflation scenario [240, 241], where the SM Higgs is the inflaton. There the electroweak gauge bosons and charged fermions of the SM are coupled to the Higgs, and thus they experience parametric excitation effects during the oscillations of the Higgs after inflation [236, 242–247]. If the SM Higgs is rather a spectator field during inflation, the post-inflationary decay of the Higgs into SM fields has also been considered in [238, 239, 296–298].

In general, the non-linear dynamics characteristic of preheating scenarios and in general of

---

<sup>2</sup>Possibly, this is partially due to the fact that there is no particular need to ‘gauge’ the inflationary sector, and partially because of the potential danger that gauge couplings may induce large radiative corrections in the inflaton potential, spoiling the conditions to sustain inflation.

non-perturbative particle production phenomena, are interesting not only by themselves, but also because they may lead to cosmologically relevant and potentially observable phenomena. Among these, we highlight:

- The generation of scalar metric perturbations [299–308], possibly leading to the formation of primordial black holes [309–317].
- The production of stochastic gravitational wave backgrounds by parametric effects [280, 281, 293, 318–334]. For a recent review see [335].
- The creation of topological defects, like cosmic string networks [184, 257, 293, 336, 337], and their evolution during the scaling regime [338–344] and corresponding emission of GWs [345].
- The creation of soliton-like structures like oscillons [324, 327, 328, 330, 333, 337, 346–351] and similar structures [306, 352–354].
- The realization of magnetogenesis [277, 291, 292, 355–358] and baryogenesis mechanisms [277, 284–286, 286–288, 359–366].
- The determination of the post-inflationary equation of state, and its implications for the CMB inflationary observables [347, 367–371], or for the dark matter relic abundance [372].

In general, the details of nonlinear phenomena are difficult to grasp, when not impossible, by analytic calculations. In order to fully understand the non-linearities developed in a given model, the use of numerical techniques becomes necessary. The non-trivial results arising from the non-linear dynamics of early universe high-energy phenomena, represents an important perspective in determining the best observational strategies to probe the unknown physics from this era. It is therefore crucial to develop numerical techniques, as efficient and robust as possible, to simulate these phenomena. Numerical algorithms developed for this purpose must satisfy a number of physical constraints (e.g. energy conservation), and keep the numerical integration errors under control. It is actually useful to develop as many techniques as possible, to validate and double check results from simulations. Only in this way, we will achieve a certain robustness in the predictions of the potentially observational implications from non-linear high energy phenomena. Furthermore, the techniques developed for studying nonlinear dynamics of classical fields, are common to many other non-linear problems in the early universe, like the dynamics of phase transitions [1, 29, 131, 131, 259, 260, 373–375] and their emission of gravitational waves [376–382], cosmic defect formation [175, 184, 293, 383–389], their later evolution [338–344, 390, 391] and gravitational wave emission [293, 345, 392], axion-like field dynamics [349, 353, 393–396], moduli dynamics [397, 398], etc. These techniques can also be used in applications of interest not only to cosmology, but also to other high energy physics areas. For example, classical-statistical simulations have been used to compute

quantities such as the sphaleron-rate [70, 96–110] and to study the Abelian [1, 29, 90–93] and non-Abelian [399] dynamics associated to the chiral anomaly, as well as for spectral quantities [400, 401], and some properties of the quark-gluon plasma [402–405].

### 10.1.2 Purpose of this manuscript. Introducing *CosmoLattice*

As just reviewed in the previous section, the phenomenology of high-energy non-linear processes in the early universe is vast and very rich. In order to make reliable predictions of their potentially observable consequences, we need appropriate numerical tools. The *Numerical Early Universe*, i.e. the study of high-energy non-linear field theory phenomena with numerical techniques, is an emerging field, and it is increasingly gaining relevance, especially as a methodology to assess our capabilities to experimentally constrain (or even determine) the physics of this (yet) unknown epoch. It is because we recognize the importance of this, that we have created this dissertation, the content and purpose of which we explain next.

The present manuscript is part of the theoretical basis for the code *CosmoLattice*, a modern multi-purpose MPI-based C++ package, to be publicly released in 2020 as a user-friendly software for lattice simulations of the non-linear dynamics of scalar and gauge field *dof* in an expanding background, with the expansion rate of the universe ‘self-consistently’ sourced by the fields themselves. Of course, exploring numerically the nonlinear dynamics of interacting fields during the early universe is not a new idea, as witnessed by the increasing number of lattice codes dedicated to this purpose that have appeared within the last years. With the exception of the recent *GFiRe* code [184], that includes integrators for Abelian gauge theories, previous public packages were dedicated only to interacting scalar fields, either with finite difference techniques in real space, like *Latticeeasy* [177], *Clustereasy* [178], *Defrost* [179], *CUDAeasy* [406], *HLattice* [181], *PyCOOL* [182] and *GABE* [183], or pseudo-spectral codes like *PSpectRe* [180] and *Stella* [348]. In most of the mentioned codes, metric perturbations (whenever present) are sourced passively, neglecting backreaction effects on the dynamics of the scalar fields. Notable exceptions to this are *HLATTICE v2.0*, and especially the recent *GABERel* [307], which allows for the full general relativistic evolution of non-linear scalar field dynamics. Given that all these codes are already available, one may wonder what is the point of releasing yet a new one. In order to answer this, let us explain the purpose of *CosmoLattice*, which is actually twofold:

1. *CosmoLattice* is meant to be a ‘platform’ for users to implement any system of equations suitable for discretization on a lattice. That is, *CosmoLattice* is not a code for doing one type of simulation with one specific integration technique, such as e.g. the real-time evolution of interacting scalar fields sourcing self-consistently the expansion of the universe. The idea is rather something else: *CosmoLattice* is a package that introduces its own *symbolic language*, by defining field variables and operations over them. Therefore, once the user becomes familiar with the basic ‘vocabulary’ of the new language, they can write their own code: be it for the time evolution of the field

variables in a given model of interest, or for some other operation, like a Monte-Carlo generator for thermal configurations. One of the main advantages of *CosmoLattice* is that it clearly separates the *physics* (i.e. fields living on a lattice and operations between them) from the *implementation details*, such as the handling of the parallelization or the Fourier transforms. For example, let us imagine a beginner user with little experience in programming, and with no experience at all in parallelization techniques. With *CosmoLattice*, they will be able to run a fully parallelized simulation of their favourite model (say using hundreds of processors in a cluster), while being completely oblivious to the technical details. They will just need to write a basic *model file* in the language of *CosmoLattice*, containing the details of the model being simulated. If, on the contrary, the user is rather an experienced one and wants to look inside the core routines of *CosmoLattice* and modify, for example, the MPI-implementation, they can always do so, and perhaps even contribute to improving them. On top of this, *CosmoLattice* includes already a *library* of basic routines and field-theoretical operations. This constitutes a clear advantage of using *CosmoLattice* as a platform to implement a given scenario over writing your own code from scratch. In particular, *CosmoLattice* comes with symbolic scalar, complex and  $SU(2)$  algebras, which allows to use vectorial and matrix notations without sacrificing performances. Furthermore, *CosmoLattice* is MPI-based and uses a discrete Fourier Transform parallelized in multiple spatial dimensions [407], making it very powerful for probing physical problems with well-separated scales, running very high resolution simulations, or simply very long ones. *CosmoLattice* will be made publicly available in 2020, and it will come with a detailed manual explaining its whole structure and the basic instructions to start running your own simulations.

2. *CosmoLattice* includes already a set of algorithms to evolve lattice scalar-gauge theories in real-time, which can be selected with a single ‘switch’ option. Part of this document can be actually considered as the theoretical basis for such algorithms. In fact, this manuscript is really meant to be a primer on lattice techniques for non-linear simulations, as we present a comprehensive discussion on such techniques, in particular for the simulation of scalar and gauge field dynamics in an expanding universe. In Section 10.2 we review first the formulation of scalar and gauge field interactions in the continuum, both in a flat space-time and in *Friedmann-Lemaître-Robertson-Walker* (FLRW) backgrounds. In Section 10.3 we introduce the basic tools for discretizing any bosonic field theory in an expanding background, including a discussion on *lattice gauge invariant* techniques for both *Abelian* and *non-Abelian* gauge theories. Next, we introduce and classify a series of numerical algorithms, starting from methods of  $\mathcal{O}(\delta t^2)$  accuracy, *staggered leapfrog* and *Verlet integration*, passing and covering higher-order integrators accurate up to  $\mathcal{O}(\delta t^{10})$ , such as the *Yoshida* methods. In the following Sections 10.4, 10.5 and 10.6, we adapt the previous algorithms to a specialized use for classical lattice simulations of scalar and gauge field dynamics in an expanding background in  $3+1$  dimensions. We put special care to include the possibility of ‘self-consistent’ expansion of the universe, sourcing the evolution of the scale factor by

the volume average of the fields' energy and pressure densities, independently of whether the fields are scalars, Abelian gauge fields, or non-Abelian gauge fields. In Section 10.4, we present a variety of lattice formulations of *interacting scalar fields*, consisting in different integrators which can reproduce the continuum theory to an accuracy ranging from  $\mathcal{O}(\delta t^2)$  to  $\mathcal{O}(\delta t^{10})$ . Analogously, in Sections 10.5 and 10.6, we present a set of algorithms for *Abelian  $U(1)$  gauge theories*, and *Non-Abelian  $SU(2)$  gauge theories*, respectively, again with an accuracy ranging between  $\mathcal{O}(\delta t^2)$  and  $\mathcal{O}(\delta t^{10})$ . In the case of interacting scalar field methods, we provide both symplectic and non-symplectic integrators, whereas for gauge fields only symplectic integrators are built. For every algorithm presented, we always provide the form of the most significant observables, such as the energy density components, relevant field spectra, and the form of the Hubble constraint. The latter is verified by our symplectic algorithms with an accuracy that depends on the integrator order, reaching even down to machine precision in the case of the highest order schemes. Furthermore, it is worth noting that our integration algorithms for gauge theories always respect exactly, down to machine precision, the Gauss constraint, independently of the order of the integrator. This remains true even in the case of self-consistent expansion, independently of whether the gauge sector is Abelian or non-Abelian. We note that all the explicit-in-time algorithms presented in Sections 10.4-10.6 are already implemented in *CosmoLattice*, and will be made therefore publicly available once *CosmoLattice* is released.

It should be also noticed that this manuscript represents only *Part I* of our intended discussion on lattice techniques for the simulation of scalar and gauge dynamics in an expanding universe. In this document we focus on the presentation of general integration techniques (Section 10.3), and in their use to build explicit-in-time integration algorithms for *canonical* scalar-gauge theories, i.e. for field theories with canonically normalized kinetic terms and standard scalar potential (Section 10.4) and scalar-gauge Abelian (Section 10.5) and non-Abelian (Section 10.6) interactions. We would like to highlight that we present higher-order integration algorithms for interacting scalar fields, similar to those in *HLattice* [181], which built algorithms with accuracy up to  $\mathcal{O}(\delta t^6)$ . We go a step beyond building also explicit implementations for all the orders, including the highest ones  $\mathcal{O}(\delta t^8)$  and  $\mathcal{O}(\delta t^{10})$ . Analogously, we also present higher-order integration algorithms for Abelian  $U(1)$  gauge theories, similar to those in *GFiRe* [184]. We demonstrate explicitly for the first time their numerical implementation for all accuracy orders, including now  $\mathcal{O}(\delta t^6)$ ,  $\mathcal{O}(\delta t^8)$  and  $\mathcal{O}(\delta t^{10})$ . Furthermore, we also present here, to the best of our knowledge for the first time, an algorithm for non-Abelian  $SU(N)$  gauge theories, which is symplectic, explicit in time, of arbitrary order, and preserving exactly the Gauss constraint, while solving for the expansion of the universe self-consistently. As a numerical example to test our algorithms in scalar-gauge canonical theories, we analyze the post-inflationary preheating dynamics of an oscillating inflaton charged under  $SU(2) \times U(1)$  in Section 10.8. We postpone the discussion about methods for non-canonical scenarios for *Part II* of our dissertation on lattice techniques, to be published elsewhere [408], together with the public release of their implementation in *CosmoLattice*. Non-canonical scenarios are

theories e.g. with non-minimal gravitational couplings, or more generally with kinetic terms with non-trivial field metrics, as considered e.g. in [183, 270, 271]. Non-canonical scenarios may also include interactions between field variables and their conjugate momenta, as naturally arising in exact derivative couplings between an axion-like field and gauge fields, as considered e.g. in [279]. Non-canonical interactions can be numerically complicated to deal with, and usually require integration techniques which are either non-symplectic or simply more involved, typically with high memory requirements, and often not explicit in time. It is precisely because of these circumstances that we naturally separate the methods for canonical scalar-gauge theories presented here in *Part I*, in Sections 10.4-10.6, from the numerical integrators that we will present for non-canonical interactions in *Part II* [408].

To conclude this section, let us mention that precisely because *ℳosmoLattice* is a platform rather than a specialized code for certain type of scenarios, there is a number of extensions (beyond the routines currently discussed here in *Part I*, or planned to be presented in *Part II*), which we would like to add in *ℳosmoLattice* in the mid-term, as we go updating and improving the code in time. We hope to eventually consider (perhaps in collaboration with you?) the following aspects:

- Addition of fermions. Even though this is numerically very costly, one can simulate out-of-thermal-equilibrium dynamics of classical bosonic fields coupled to quantum fermions. This has been done by [409] and successive works [410–412], combining the lattice implementation based on the the quantum mode equations proposed in [413], with the ‘low cost’ fermions introduced in [414].
- Computation of metric perturbations. This could be done for scalar and vector perturbations following [181], whereas tensor perturbations representing gravitational waves (GW), can be obtained following [415] (based on the idea originally proposed in [321]), as this allows for general GW sources built from either scalar and gauge fields (or even fermions if they were present).
- Addition of *relativistic hydrodynamics*. This can be useful to describe scenarios where a classical scalar field, playing the role of an *order parameter* in a phase transition, is coupled to a relativistic fluid by means of a phenomenological friction term. This is the basis to describe numerically the dynamics of first order phase transitions [1, 29, 131, 131, 259, 260, 373–375] and their emission of gravitational waves [376–382].
- Addition of new ‘initializer’ routines. So far we have only considered the initialization of field fluctuations in Fourier space (on top of homogeneous field values), given a theoretical spectrum as an input. However, in order to simulate e.g. the dynamics of a network of cosmic strings or other type of topological defects, different algorithms have been used to create



initially the defect network in configuration space, see e.g. [338–345, 390, 391, 416].

- Addition of ‘importance sampling’ algorithms. Monte-Carlo algorithms and Langevin dynamics are used to generate fields according to some probability distributions. They can be used to set up thermal initial conditions to study e.g. chiral charge dynamics in gauge theories at finite temperature [1, 29]. Alternatively, one could turn *CosmoLattice* into a general platform to sample positive definite path integrals. While specific and highly optimized open-source codes exist to simulate lattice QCD [417, 418], to the best of our knowledge, there is no truly versatile software to easily simulate other theories.

### 10.1.3 Conventions and notation

Unless otherwise specified, throughout the document we use the following conventions. We use natural units  $c = \hbar = 1$  and choose metric signature  $(-1, +1, +1, +1)$ . We use interchangeably the Newton constant  $G$ , the full Planck mass  $M_p \simeq 1.22 \cdot 10^{19}$  GeV, and the reduced Planck mass  $m_p \simeq 2.44 \cdot 10^{18}$  GeV, related through  $M_p^2 = 8\pi m_p^2 = 1/G$ . Concerning space-time coordinates, Latin indices  $i, j, k, \dots = 1, 2, 3$  are reserved for spatial dimensions, and Greek indices  $\alpha, \beta, \mu, \nu, \dots = 0, 1, 2, 3$  for space-time dimensions. We use the *Einstein convention* of summing over repeated indices only in the continuum, whereas on the lattice, in general, repeated indices do not represent summation. We consider a flat FLRW metric  $ds^2 = -a^{2\alpha}(\eta)d\eta^2 + a^2(\eta)\delta_{ij}dx^i dx^j$  with  $\alpha \in \mathcal{R}e$  a constant chosen conveniently in each scenario. For  $\alpha = 0$ ,  $\eta$  denotes the *coordinate time*  $t$ , whereas for  $\alpha = 1$ ,  $\eta$  denotes the *conformal time*  $\tau = \int \frac{dt'}{a(t')}$ . For arbitrary  $\alpha$ , we will refer to the time variable as the  $\alpha$ -time. We reserve the notation  $()'$  for derivatives with respect to cosmic time with  $\alpha = 0$ , and  $()^\alpha$  for derivatives with respect to  $\alpha$ -time with arbitrary  $\alpha$ . Physical momenta are represented by  $\mathbf{p}$ , comoving momenta by  $\mathbf{k}$ , the  $\alpha$ -time Hubble rate is given by  $\mathcal{H} = a'/a$ , whereas the physical Hubble rate is denoted by  $H = \mathcal{H}|_{\alpha=0}$ . Cosmological parameters are fixed to the CMB values given in [190, 419]. Our Fourier transform convention in the continuum is given by

$$f(\mathbf{x}) = \frac{1}{(2\pi)^3} \int d^3\mathbf{k} f(\mathbf{k}) e^{-i\mathbf{k}\mathbf{x}} \iff f(\mathbf{k}) = \int d^3\mathbf{x} f(\mathbf{x}) e^{+i\mathbf{k}\mathbf{x}}. \quad (10.1)$$

## 10.2 Field dynamics in the continuum

In this section, we describe briefly the formulation of scalar and gauge field dynamics in the continuum. We review first the case of interacting fields in a Minkowski background in Section 10.2.1, starting with scalar fields only, and then introducing gauge symmetries and the corresponding gauge field degrees of freedom (*dof*). We then promote the background metric into a curved manifold, and specialize our study to the case of a spatially-flat, homogeneous, and isotropic space-time, described by the FLRW metric. We consider the dynamics of scalar and gauge fields living in a FLRW background in Section 10.2.2, and the dynamics of the background itself, as sourced by the fields that live within it, in Section 10.2.3.

### 10.2.1 Scalar and Gauge field interactions in flat space-time

Let us consider first a set of  $N_s$  relativistic interacting scalar fields with action in flat space-time

$$S_S = - \int d^4x \left\{ \frac{1}{2} \partial^\mu \phi_i \partial_\mu \phi_i + V(\{\phi_j\}) \right\}, \quad (10.2)$$

where  $i, j = 1, \dots, N_s$  label the fields, and the potential  $V(\{\phi_j\})$  characterizes the interactions and self-interactions among fields. Because of the normalization constant  $1/2$  in front of the kinetic terms  $\partial^\mu \phi_i \partial_\mu \phi_i$ , we will refer to these fields as *canonically normalized scalar fields*. We note that space-time indices are raised with the Minkowski metric, e.g.  $\partial^\mu \phi \equiv \eta^{\mu\nu} \partial_\nu \phi$ . The equations of motion (EOM) of the system are obtained from minimizing Eq. (10.2). This leads to

$$-\square_\eta \phi_i + \frac{\partial V}{\partial \phi_i} = 0, \quad \text{with} \quad \square_\eta \equiv \eta^{\mu\nu} \partial_\mu \partial_\nu = \partial^\alpha \partial_\alpha. \quad (10.3)$$

In a more explicit form, the EOM can be written as

$$\ddot{\phi}_i - \vec{\nabla}^2 \phi_i + \frac{\partial V}{\partial \phi_i} = 0 \quad \Longleftrightarrow \quad \begin{cases} \dot{\phi}_i & \equiv \pi_i, \\ \dot{\pi}_i & = \vec{\nabla}^2 \phi_i - \frac{\partial V}{\partial \phi_i}. \end{cases} \quad (10.4)$$

Let us now consider a general scalar-gauge theory in the continuum, including three types of (canonically normalized) scalar fields: a singlet  $\phi$ , a  $U(1)$ -charged field  $\varphi$ , and a  $[SU(N) \times U(1)]$ -charged field  $\Phi$ ; as well as the corresponding Abelian  $A_\mu$  and non-Abelian  $B_\mu = C_\mu^a T_a$  gauge vector bosons. Here  $\{T_a\}$  are the  $N^2 - 1$  group generators of  $SU(N)$ , satisfying the properties of the  $SU(N)$  Lie algebra

$$[T_a, T_b] = i f_{abc} T_c, \quad \text{Tr}(T_a) = 0, \quad \text{Tr}(T_a T_b) = \frac{1}{2} \delta_{ab}, \quad T_a^\dagger = T_a, \quad (10.5)$$

with  $f_{abc}$  the totally anti-symmetric *structure constants* of  $SU(N)$ . In the particular case of  $SU(2)$ ,  $T_a \equiv \sigma_a/2$  ( $a = 1, 2, 3$ ), with  $\sigma_a$  the *Pauli matrices*

$$\sigma_1 = \begin{pmatrix} 0 & 1 \\ 1 & 0 \end{pmatrix}, \quad \sigma_2 = \begin{pmatrix} 0 & -i \\ i & 0 \end{pmatrix}, \quad \sigma_3 = \begin{pmatrix} 1 & 0 \\ 0 & -1 \end{pmatrix}. \quad (10.6)$$

For later convenience we also write some of their properties,

$$[\sigma_a, \sigma_b] = 2i \epsilon_{abc} \sigma_c, \quad \text{Tr}(\sigma_a) = 0, \quad \text{Tr}(\sigma_a \sigma_b) = 2 \delta_{ab}, \quad \sigma_a^\dagger = \sigma_a, \quad (10.7)$$

with  $\epsilon_{abc}$  the total anti-symmetric tensor.

We can write a gauge invariant action as

$$\begin{aligned}
 S &= - \int d^4x \left\{ \frac{1}{2} \partial_\mu \phi \partial^\mu \phi + (D_\mu^A \phi)^* (D_\mu^A \phi) + (D_\mu \Phi)^\dagger (D_\mu \Phi) + \frac{1}{4} F_{\mu\nu} F^{\mu\nu} + \frac{1}{2} \text{Tr}\{G_{\mu\nu} G^{\mu\nu}\} + V \right\} \\
 &= \int d^4x \left\{ \frac{\dot{\phi}^2}{2} - \frac{|\vec{\nabla}\phi|^2}{2} + |D_0\phi|^2 - |\vec{D}\phi|^2 + |D_0\Phi|^2 - |\vec{D}\Phi|^2 + \frac{|\vec{\mathcal{E}}|^2}{2} - \frac{|\vec{\mathcal{B}}|^2}{2} + \sum_a \left( \frac{|\vec{\mathcal{E}}_a|^2}{2} - \frac{|\vec{\mathcal{B}}_a|^2}{2} \right) - V \right\},
 \end{aligned} \quad (10.8)$$

with a potential  $V \equiv V(\phi, |\phi|, |\Phi|)$  describing the interactions among the scalar fields,

$$\phi \in \mathcal{R}e \quad , \quad \varphi \equiv \frac{1}{\sqrt{2}}(\varphi_0 + i\varphi_1) \quad , \quad \Phi = \begin{pmatrix} \varphi^{(0)} \\ \varphi^{(1)} \\ \vdots \\ \varphi^{(N-1)} \end{pmatrix} = \frac{1}{\sqrt{2}} \begin{pmatrix} \varphi_0 + i\varphi_1 \\ \varphi_2 + i\varphi_3 \\ \vdots \\ \varphi_{2N-2} + i\varphi_{2N-1} \end{pmatrix}, \quad (10.9)$$

and where we have introduced standard definitions of *covariant derivatives* (denoting  $Q_A$  and  $Q_B$  the Abelian and non-Abelian charges) and *field strength* tensors,

$$D_\mu^A \equiv \partial_\mu - i \frac{1}{2} Q_A g_A A_\mu, \quad (10.10)$$

$$D_\mu \equiv \mathcal{J} D_\mu^A - i g_B Q_B B_\mu^a T_a, \quad (10.11)$$

$$F_{\mu\nu} \equiv \partial_\mu A_\nu - \partial_\nu A_\mu, \quad (10.12)$$

$$G_{\mu\nu} \equiv \partial_\mu B_\nu - \partial_\nu B_\mu - i [B_\mu, B_\nu], \quad (10.13)$$

with  $\mathcal{J}$  the  $N \times N$  identity matrix. In the second line of (10.8) we have used the properties of the generators, displayed in Eq. (10.5), to obtain

$$G_{\mu\nu} \equiv G_{\mu\nu}^a T_a \quad \Rightarrow \quad \frac{1}{2} \text{Tr}(G_{\mu\nu} G^{\mu\nu}) \equiv \frac{1}{2} G_{\mu\nu}^a G_a^{\mu\nu}; \quad G_{\mu\nu}^a \equiv \partial_\mu B_\nu^a - \partial_\nu B_\mu^a + f^{abc} B_\mu^b B_\nu^c, \quad (10.14)$$

and introduced Abelian and non-Abelian electric and magnetic fields as

$$\mathcal{E}_i \equiv F_{0i}, \quad \mathcal{B}_i \equiv \frac{1}{2} \epsilon_{ijk} F^{jk}, \quad \mathcal{E}_i^a \equiv G_{0i}^a, \quad \mathcal{B}_i^a \equiv \frac{1}{2} \epsilon_{ijk} G_a^{jk}. \quad (10.15)$$

The equations of motion (EOM) of the system can be obtained from minimizing Eq. (10.8). They are

$$\begin{aligned}
 \partial^\mu \partial_\mu \phi &= \frac{\partial V}{\partial \phi} && [\text{Singlet}] \\
 D_A^\mu D_\mu^A \phi &= \frac{\partial V}{\partial |\phi|} \frac{\phi}{|\phi|} && [U(1)\text{-charged}] \\
 D^\mu D_\mu \Phi &= \frac{\partial V}{\partial |\Phi|} \frac{\Phi}{|\Phi|} && [U(1) \times SU(N)] \\
 \partial_\nu F^{\mu\nu} &= J_A^\mu && [\text{Abelian vector}] \\
 (\mathcal{D}_\nu)_{ab} G_b^{\mu\nu} &= J_a^\mu && [\text{Yang-Mills vector}]
 \end{aligned} \quad (10.16)$$

where  $(\mathcal{D}_\nu O)_a = (\mathcal{D}_\nu)_{ab} O_b \equiv (\delta_{ab} \partial_\nu - f_{abc} B_\nu^c) O_b$ , and the currents are given by

$$J_A^\mu \equiv g_A Q_A^{(\varphi)} \mathcal{J} m[\varphi^* (D_A^\mu \varphi)] + g_A Q_A^{(\Phi)} \mathcal{J} m[\Phi^\dagger (D^\mu \Phi)], \quad (10.17)$$

$$J_a^\mu \equiv 2g_B Q_B \mathcal{J} m[\Phi^\dagger T_a (D^\mu \Phi)]. \quad (10.18)$$

It is straightforward to show that both action (10.8) and the EOM (10.16) are invariant under the following set of gauge transformations,

$$\begin{aligned} \phi(x) &\longrightarrow \phi(x), \quad [\text{singlet}] \\ \varphi(x) &\longrightarrow \omega(x) \varphi(x), \quad \omega(x) = e^{-i \frac{g_A}{2} Q_A^{(\varphi)} \alpha(x)}, \\ \Phi(x) &\longrightarrow \omega(x) \Omega(x) \Phi(x), \quad \Omega(x) \equiv e^{-i g_B Q_B \beta_a(x) T_a}, \quad \omega(x) = e^{-i \frac{g_A}{2} Q_A^{(\Phi)} \alpha(x)}, \\ A_\mu(x) &\longrightarrow A_\mu(x) - \partial_\mu \alpha(x) \\ B_\mu(x) &\longrightarrow \Omega(x) B_\mu(x) \Omega^\dagger(x) - \frac{i}{g_B Q_B} [\partial_\mu \Omega(x)] \Omega^\dagger(x) \\ G_{\mu\nu}(x) &\longrightarrow \Omega(x) G_{\mu\nu}(x) \Omega^\dagger(x), \end{aligned} \quad (10.19)$$

with  $\alpha(x)$  and  $\beta_a(x)$  arbitrary real functions,  $Q_A^{(\varphi)}$  and  $Q_A^{(\Phi)}$  the Abelian charges of  $\varphi$  and  $\Phi$ , and  $Q_B$  the non-Abelian charge of  $\Phi$ .

Using the definitions in Eq. (10.15), we can also write the EOM in vectorial form, making more explicit the individual terms in each equation:

$$\ddot{\phi} - \vec{\nabla}^2 \phi = -V_{,\phi}, \quad (10.20)$$

$$\ddot{\varphi} - \vec{D}_A^2 \varphi = -V_{,|\varphi|} \cdot (\varphi/|\varphi|), \quad (10.21)$$

$$\ddot{\Phi} - \vec{D}^2 \Phi = -V_{,|\Phi|} \cdot (\Phi/|\Phi|), \quad (10.22)$$

$$\vec{\mathcal{E}} - \vec{\nabla} \times \vec{\mathcal{B}} = \vec{J}_A \equiv g_A Q_A^{(\varphi)} \mathcal{J} m[\varphi^* \vec{D}_A \varphi] + g_A Q_A^{(\Phi)} \mathcal{J} m[\Phi^\dagger \vec{D} \Phi], \quad (10.23)$$

$$(\vec{\mathcal{D}}_0 \vec{\mathcal{E}})_a - (\vec{\mathcal{D}} \times \vec{\mathcal{B}})_a = \vec{J}_a \equiv 2g_B Q_B^{(\Phi)} \mathcal{J} m[\Phi^\dagger T_a \vec{D} \Phi], \quad (10.24)$$

$$-\vec{\nabla} \vec{\mathcal{E}} = J_0^A \equiv g_A Q_A^{(\varphi)} \mathcal{J} m[\varphi^* (D_0^A \varphi)] + g_A Q_A^{(\Phi)} \mathcal{J} m[\Phi^\dagger (D_0 \Phi)], \quad (10.25)$$

$$-(\vec{\mathcal{D}} \vec{\mathcal{E}})_a = (J_0)_a \equiv 2g_B Q_B^{(\Phi)} \mathcal{J} m[\Phi^\dagger T_a (D_0 \Phi)]. \quad (10.26)$$

We note that the last two equations in Eq. (10.26) represent constraint equations, as they correspond to the equations associated with the temporal component of the gauge field, which is not dynamical. These constraints are equivalent to the standard *Gauss Law* of electromagnetism  $\vec{\nabla} \vec{\mathcal{E}} = \rho$ . In particular, they are the generators of gauge transformations [49].

## 10.2.2 Field dynamics in an expanding background

To describe the expansion of the Universe we consider a flat *Friedmann-Lemaître-Robertson-Walker* (FLRW) metric, with line element

$$ds^2 = g_{\mu\nu} dx^\mu dx^\nu = -a(\eta)^2 d\eta^2 + a(\eta)^2 \delta_{ij} dx^i dx^j . \quad (10.27)$$

where  $a(\eta)$  is the scale factor,  $\delta_{ij}$  is the Euclidean metric, and  $\alpha$  is a constant parameter that will be chosen conveniently in a case by case basis. The choice  $\alpha = 0$  identifies  $\eta$  with the *coordinate time*  $t$ , whereas  $\alpha = 1$  makes  $\eta$  the *conformal time*  $\tau \equiv \int \frac{dt'}{a(t')}$ . For the time being, we will consider  $\alpha$  as an unspecified constant, and we will refer to  $\eta$  as the  $\alpha$ -time variable. *Note* -. Recall that we reserve the symbol  $\dot{f} \equiv df/dt$  for derivatives with respect to the coordinate time, whereas  $f' \equiv df/d\eta$  will indicate derivative with respect to any  $\alpha$ -time variable.

For later convenience we write explicitly the metric and inverse metric elements,

$$g_{00} = -a(\eta)^{2\alpha} ; \quad g_{ij} = a(\eta)^2 \delta_{ij} ; \quad g^{00} = -a(\eta)^{-2\alpha} ; \quad g^{ij} = a(\eta)^{-2} \delta^{ij} . \quad (10.28)$$

To obtain the EOM in curved space, we follow the *minimal gravitational coupling* prescription, making the following replacements into the flat space-time equations,

$$\eta_{\mu\nu} \rightarrow g_{\mu\nu} , \quad (10.29)$$

$$\partial_\gamma V_{\mu\nu..}^{\alpha\beta..} \equiv V_{\mu\nu..,\gamma}^{\alpha\beta..} \rightarrow \nabla_\gamma V_{\mu\nu..}^{\alpha\beta..} \equiv V_{\mu\nu..;\gamma}^{\alpha\beta..} = V_{\mu\nu..,\gamma}^{\alpha\beta..} + \Gamma_{\gamma\sigma}^\alpha V_{\mu\nu..}^{\sigma\beta..} - \Gamma_{\gamma\mu}^\sigma V_{\sigma\nu..}^{\alpha\beta..} + \dots, \quad (10.30)$$

where  $V_{;\mu} = \nabla_\mu V$  represents a (gravitational) covariant derivative,  $\Gamma_{\alpha\beta}^\mu$  are the Christoffel symbols, and  $V_{\mu\nu..}^{\alpha\beta..}$  is an arbitrary tensor. Using the non-vanishing Christoffel symbols of the FLRW metric, see appendix 10.10,

$$\Gamma_{00}^0 = \alpha \frac{a'(\eta)}{a(\eta)} , \quad \Gamma_{ij}^0 = a^{-2\alpha+2} \frac{a'(\eta)}{a(\eta)} \delta_{ij} , \quad \Gamma_{i0}^i = \frac{a'(\eta)}{a(\eta)} , \quad (10.31)$$

we can obtain, via the minimal coupling prescription, the EOM in an expanding Universe. In practice, we can obtain directly the transformation of the derivative terms in the scalar and gauge field EOM, by making use of the following identities for the divergence of a vector and a rank-2 anti-symmetric tensor,

$$\nabla_\sigma V^\sigma = \frac{1}{\sqrt{g}} \frac{\partial(V^\sigma \sqrt{g})}{\partial x^\sigma} = \frac{1}{a^{3+\alpha}} \frac{\partial(V^\sigma a^{3+\alpha}(t))}{\partial x^\sigma} = g^{\sigma\lambda} \partial_\sigma V_\lambda + (3+\alpha) \frac{a'}{a} V^0 , \quad (10.32)$$

$$\nabla_\sigma F^{\sigma\lambda} = \frac{1}{\sqrt{g}} \frac{\partial(F^{\sigma\lambda} \sqrt{g})}{\partial x^\sigma} = \frac{1}{a^{3+\alpha}} \frac{\partial(F^{\sigma\lambda} a^{3+\alpha}(t))}{\partial x^\sigma} \quad (10.33)$$

$$= (3+\alpha) \frac{a'}{a} g^{0\lambda} g^{\alpha\beta} F_{\lambda\beta} + \partial_\sigma (g^{\sigma\lambda} g^{\alpha\beta} F_{\lambda\beta}) , \quad (10.34)$$

where  $g = -\det(g_{\mu\nu})$ . This leads to

$$\partial_\mu \partial^\mu \phi \longrightarrow \nabla_\mu [\partial^\mu \phi] = a^{-2\alpha} \phi'' - a^{-2} \partial_i \partial_i \phi + (3 - \alpha) \frac{a'}{a} \phi', \quad (10.35)$$

$$\begin{aligned} \partial_\mu F^{\mu\nu} \longrightarrow \nabla_\mu F^{\mu\nu} = g^{\nu\nu} \left( -a^{-2\alpha} \partial_0 F_{0\nu} + a^{-2} \partial_i F_{i\nu} - (3 - \alpha) a^{-2\alpha} \frac{a'}{a} F_{0\nu} \right) \\ - a^{-2\alpha} F_{0\nu} \partial_0 g^{\nu\nu}. \end{aligned} \quad (10.36)$$

Using these identities and the metric elements (10.28), we obtain the EOM in an expanding background as

$$\phi'' - a^{-2(1-\alpha)} \vec{\nabla}^2 \phi + (3 - \alpha) \frac{a'}{a} \phi' = -a^{2\alpha} V_{,\phi}, \quad (10.37)$$

$$\varphi'' - a^{-2(1-\alpha)} \vec{D}_A^2 \varphi + (3 - \alpha) \frac{a'}{a} \varphi' = -a^{2\alpha} V_{,|\varphi|} \cdot (\varphi/|\varphi|), \quad (10.38)$$

$$\Phi'' - a^{-2(1-\alpha)} \vec{D}^2 \Phi + (3 - \alpha) \frac{a'}{a} \Phi' = -a^{2\alpha} V_{,|\Phi|} \cdot (\Phi/|\Phi|), \quad (10.39)$$

$$\partial_0 F_{0i} - a^{-2(1-\alpha)} \partial_j F_{ji} + (1 - \alpha) \frac{a'}{a} F_{0i} = a^{2\alpha} J_i^A, \quad (10.40)$$

$$(\mathcal{D}_0)_{ab} (G_{0i})^b - a^{-2(1-\alpha)} (\mathcal{D}_j)_{ab} (G_{ji})^b + (1 - \alpha) \frac{a'}{a} (G_{0i})^b = a^{2\alpha} (J_i)_a, \quad (10.41)$$

$$\partial_i F_{0i} = a^2 J_0^A, \quad (10.42)$$

$$(\mathcal{D}_i)_{ab} (G_{0i})^b = a^2 (J_0)_a, \quad (10.43)$$

where the currents on the *rhs* of the gauge field EOM are still given by Eqs. (10.17)-(10.18). We note that Eqs. (10.42) and (10.43) are the generalization of the  $U(1)$  and  $SU(2)$  Gauss constraints in an expanding background. When we discretize the system of equations later on, we will use them as an indicator of the correctness of the discretization scheme, by checking whether the constraints are preserved at all times during the field evolution.

### 10.2.3 Dynamics of the expanding background

If the expansion of the Universe is dictated by some external *dof* different than the fields we are evolving, say e.g. a fluid with a given equation of state, we will refer to this case as *fixed background*. If on the contrary, the matter fields (scalar or gauge) for which we are solving their dynamics are the ones which govern the expansion of the Universe, we will refer to this case as *self-consistent expansion*. In general, the evolution of the scale factor  $a(\eta)$  is dictated by the stress-energy tensor of matter fields via the Friedmann equations. Denoting the background energy and pressure densities as  $\bar{\rho}$  and  $\bar{p}$ , the stress-energy tensor of a background *perfect fluid* is given by

$$\bar{T}_{\mu\nu} \equiv (\bar{\rho} + \bar{p}) u_\mu u_\nu + \bar{p} g_{\mu\nu}, \quad g_{\mu\nu} u^\mu u^\nu = -1 \quad \implies \quad \begin{cases} \bar{\rho} = a^{-2\alpha} \bar{T}_{00}, \\ \bar{p} = \frac{1}{3a^2} \Sigma_j \bar{T}_{jj}, \end{cases} \quad (10.44)$$

where we have used  $u_\mu = (a^\alpha, 0, 0, 0)$  and  $u^\mu = -(a^{-\alpha}, 0, 0, 0)$ . The evolution of the scale factor is then determined by the Friedmann equations, which, in  $\alpha$ -time, read as, see appendix 10.11,

$$\mathcal{H}^2 \equiv \left(\frac{a'}{a}\right)^2 = a^{2\alpha} \frac{\bar{\rho}}{3m_p^2}, \quad \frac{a''}{a} = \frac{a^{2\alpha}}{6m_p^2} [(2\alpha - 1)\bar{\rho} - 3\bar{p}]. \quad (10.45)$$

Let us consider first the case of a fixed background. If the expansion of the Universe is created by an external fluid with constant equation of state  $w \equiv p/\rho$ , the two Friedmann equations can be combined into a single equation as

$$2a'' + (1 + 3w - 2\alpha) \frac{a'^2}{a} = 0, \quad (10.46)$$

with solution

$$a(\eta) = a(\eta_i) \left(1 + \frac{1}{p} \mathcal{H}_i(\eta - \eta_i)\right)^p, \quad \mathcal{H}(\eta) = \frac{\mathcal{H}_i}{\left(1 + \frac{1}{p} \mathcal{H}_i(\eta - \eta_i)\right)} = \frac{\mathcal{H}_i}{\sqrt[p]{a(\eta)/a(\eta_i)}}, \quad p \equiv \frac{2}{3(1+w) - 2\alpha}, \quad (10.47)$$

where  $\eta_i$  is some initial time. In order to solve the scalar/gauge field dynamics, we just need then to plug in the above expressions for  $a(\eta)$  and  $\mathcal{H}(\eta)$  into the EOM of the matter fields.

In the case of self-consistent expansion, we need an expression for the energy momentum-tensor of the scalar/gauge matter fields, and then take a volume average of the corresponding local expressions of the energy and pressure densities, which source the Friedmann equations. From the Lagrangian in Eq. (10.8) we can actually derive a local expression for the stress-energy tensor of the scalar and gauge fields as

$$\begin{aligned} T_{\mu\nu} &= -\frac{2}{\sqrt{g}} \frac{\delta(\sqrt{g}\mathcal{L})}{\delta g^{\mu\nu}} = g_{\mu\nu}\mathcal{L} - 2 \frac{\delta\mathcal{L}}{\delta g^{\mu\nu}} \\ &= -g_{\mu\nu} \left( g^{\alpha\beta} \left[ (D_\alpha\Phi)^\dagger (D_\beta\Phi) + (D_\alpha^A\varphi)^* (D_\beta^A\varphi) + \frac{1}{2} (\partial_\alpha\phi)(\partial_\beta\phi) \right] + \frac{1}{4} g^{\alpha\delta} g^{\beta\lambda} (G_{\alpha\beta}^a G_{\delta\lambda}^a + F_{\alpha\beta} F_{\delta\lambda}) + V \right) \\ &\quad + \left[ 2(D_\mu\Phi)^\dagger (D_\nu\Phi) + 2(D_\mu^A\varphi)^* (D_\nu^A\varphi) + (\partial_\mu\phi)(\partial_\nu\phi) \right] + g^{\alpha\beta} \left( G_{\mu\alpha}^a G_{\nu\beta}^a + F_{\mu\alpha} F_{\nu\beta} \right), \end{aligned} \quad (10.48)$$

where in the first equality we used<sup>3</sup>  $\delta(\sqrt{g}) = -\frac{1}{2} g_{\mu\nu} \sqrt{g} \delta g^{\mu\nu}$ , and in the second we used  $\delta g^{\alpha\beta} = -g^{\alpha\mu} g^{\beta\nu} \delta g_{\mu\nu}$ . Using  $F^{\mu\nu} F_{\mu\nu} = -\frac{2}{a^{2(1+\alpha)}} \sum_i F_{0i}^2 + \frac{1}{a^4} \sum_{i,j} F_{ij}^2$  (similarly for  $G_{\mu\nu}^a$ ), and  $(D_\mu\Phi)^\dagger (D^\mu\Phi) = -a^{-2\alpha} (D_0\Phi)^\dagger (D_0\Phi) + a^{-2} (D_i\Phi)^\dagger (D_i\Phi)$  (similarly for the  $U(1)$ -charged and singlet scalar fields), we obtain for the energy and pressure densities,

$$\rho = K_\phi + K_\varphi + K_\Phi + G_\phi + G_\varphi + G_\Phi + K_{U(1)} + G_{U(1)} + K_{SU(2)} + G_{SU(2)} + V, \quad (10.49)$$

$$p = K_\phi + K_\varphi + K_\Phi - \frac{1}{3} (G_\phi + G_\varphi + G_\Phi) + \frac{1}{3} (K_{U(1)} + G_{U(1)}) + \frac{1}{3} (K_{SU(2)} + G_{SU(2)}) - V, \quad (10.50)$$

---

<sup>3</sup>Had we wanted to obtain  $T^{\mu\nu}$  with the space-time indices above, then we should use instead  $\delta(\sqrt{g}) = +\frac{1}{2} g^{\mu\nu} \sqrt{g} \delta g_{\mu\nu}$ .

### 10.3. Field dynamics in a computer: the lattice approach

with  $V$  the interacting scalar potential, whereas the kinetic and gradient energy densities are

$$\begin{aligned}
 K_\phi &= \frac{1}{2a^{2\alpha}} \phi'^2 & G_\phi &= \frac{1}{2a^2} \sum_i (\partial_i \phi)^2 & K_{U(1)} &= \frac{1}{2a^{2+2\alpha}} \sum_i F_{0i}^2 \\
 K_\varphi &= \frac{1}{a^{2\alpha}} (D_0^A \varphi)^* (D_0^A \varphi) \ ; \ G_\varphi &= \frac{1}{a^2} \sum_i (D_i^A \varphi)^* (D_i^A \varphi) \ ; & K_{SU(2)} &= \frac{1}{2a^{2+2\alpha}} \sum_{a,i} (G_{0i}^a)^2 \\
 K_\Phi &= \frac{1}{a^{2\alpha}} (D_0 \Phi)^\dagger (D_0 \Phi) & G_\Phi &= \frac{1}{a^2} \sum_i (D_i \Phi)^\dagger (D_i \Phi) & G_{U(1)} &= \frac{1}{2a^4} \sum_{i,j < i} F_{ij}^2 \\
 & & & & G_{SU(2)} &= \frac{1}{2a^4} \sum_{a,i,j < i} (G_{ij}^a)^2.
 \end{aligned} \tag{10.51}$$

(Kinetic-Scalar)                      (Gradient-Scalar)                      (Electric & Magnetic)

Whenever dealing with scenarios with self-consistent expansion of the Universe, we then need to take first a volume average of the local expressions in Eqs. (10.49), (10.50), so that we obtain the background energy and pressure densities  $\bar{\rho}$  and  $\bar{p}$ , within a given volume. Plugging back the background quantities into the Friedmann Eqs. (10.45), will determine then the evolution of the universe within the chosen volume, namely

$$\left( \frac{a'}{a} \right)^2 = \frac{a^{2\alpha}}{3m_p^2} \langle K_\phi + K_\varphi + K_\Phi + G_\phi + G_\varphi + G_\Phi + K_{U(1)} + G_{U(1)} + K_{SU(2)} + G_{SU(2)} + V \rangle, \tag{10.52}$$

$$\begin{aligned}
 \frac{a''}{a} &= \frac{a^{2\alpha}}{3m_p^2} \langle (\alpha - 2)(K_\phi + K_\varphi + K_\Phi) + \alpha(G_\phi + G_\varphi + G_\Phi) + (\alpha + 1)V \\
 &\quad + (\alpha - 1)(K_{U(1)} + G_{U(1)} + K_{SU(2)} + G_{SU(2)}) \rangle,
 \end{aligned} \tag{10.53}$$

where  $\langle \dots \rangle$  represents volume averaging. As long as the volume is sufficiently large compared to the scales excited in the matter fields, this approximation should lead to a well-defined notion of a 'homogeneous and isotropic' expanding background, within the given volume.

## 10.3 Field dynamics in a computer: the lattice approach

### 10.3.1 Lattice definition and discrete Fourier transform

In order to simulate the dynamics of interacting fields, we will consider a cubic lattice with  $N$  sites per dimension. As we are interested in three spatial dimensions, the lattice will have therefore  $N^3$  points in total, labeled as

$$\mathbf{n} = (n_1, n_2, n_3), \quad \text{with } n_i = 0, 1, \dots, N-1, \quad i = 1, 2, 3. \tag{10.54}$$

We will often refer to this set of points simply as the lattice, the *grid*, or even more colloquially, as the *box*. For convenience we define

$$\hat{1} \equiv (1, 0, 0), \quad \hat{2} \equiv (0, 1, 0), \quad \hat{3} \equiv (0, 0, 1), \tag{10.55}$$



as unit vectors on the lattice, corresponding to positive displacements of length

$$\delta x \equiv \frac{L}{N}, \quad (10.56)$$

in each of the independent directions in the continuum. We will refer to  $\delta x$  as the *lattice spacing*.

A continuum function  $\mathbf{f}(\mathbf{x})$  in space is represented by a lattice function  $f(\mathbf{n})$ , which has the same value as  $\mathbf{f}(\mathbf{x})$  at  $\mathbf{x} = \mathbf{n}\delta x$ . We note that whereas in a flat background, positions  $\{\mathbf{x}\}$  and their corresponding lattice sites  $\{\mathbf{n}\}$  represent physical spatial coordinates, in an expanding background they will rather represent *comoving* spatial coordinates. Unless specified otherwise, we will always consider *periodic boundary conditions* in the three spatial directions, so that  $f(\mathbf{n} + \hat{i}N) = f(\mathbf{n})$ ,  $i = 1, 2$  or  $3$ .

The periodic boundary conditions in coordinate space imply that momenta must be discretized, whereas the discretization of the spatial coordinates implies that any definition of a discrete Fourier transform must be periodic. For each lattice we can then consider always a reciprocal lattice representing *Fourier* modes, with sites labeled as

$$\tilde{\mathbf{n}} = (\tilde{n}_1, \tilde{n}_2, \tilde{n}_3), \quad \text{with } \tilde{n}_i = -\frac{N}{2} + 1, -\frac{N}{2} + 2, \dots, -1, 0, 1, \dots, \frac{N}{2} - 1, \frac{N}{2}, \quad i = 1, 2, 3. \quad (10.57)$$

We then define the discrete Fourier transform (DFT) as

$$f(\mathbf{n}) \equiv \frac{1}{N^3} \sum_{\tilde{\mathbf{n}}} e^{-i\frac{2\pi}{N}\tilde{\mathbf{n}}\mathbf{n}} f(\tilde{\mathbf{n}}) \quad \Leftrightarrow \quad f(\tilde{\mathbf{n}}) \equiv \sum_{\mathbf{n}} e^{+i\frac{2\pi}{N}\mathbf{n}\tilde{\mathbf{n}}} f(\mathbf{n}), \quad (10.58)$$

from where we obtain

$$\sum_{\mathbf{n}} e^{i\frac{2\pi}{N}\mathbf{n}\tilde{\mathbf{n}}} = N^3 \delta_{\mathbf{n}, \tilde{\mathbf{n}}}. \quad (10.59)$$

As expected, it follows that Fourier-transformed functions are periodic in the reciprocal lattice, with periodic boundary conditions as  $f(\tilde{\mathbf{n}} + \hat{i}N) = f(\tilde{\mathbf{n}})$ , with  $\hat{i}$  analogous unit vectors as in Eq. (10.55), but defined in the reciprocal lattice.

Let us emphasize that from the above discussion, it follows that we can only represent momenta down to a minimum infrared (IR) cut-off

$$k_{\text{IR}} = \frac{2\pi}{L} = \frac{2\pi}{N\delta x}, \quad (10.60)$$

such that  $\tilde{\mathbf{n}}$  labels the continuum momentum values  $\mathbf{k} = (\tilde{n}_1, \tilde{n}_2, \tilde{n}_3) k_{\text{IR}}$ . Furthermore, there is also a maximum ultraviolet (UV) momentum that we can capture in each spatial dimension,

$$k_{i,\text{UV}} = \frac{N}{2} k_{\text{IR}} = \frac{\pi}{\delta x}. \quad (10.61)$$

### 10.3. Field dynamics in a computer: the lattice approach

The maximum momentum we can capture in a three-dimensional reciprocal lattice is therefore

$$k_{\max} = \sqrt{k_{1,\text{UV}}^2 + k_{2,\text{UV}}^2 + k_{3,\text{UV}}^2} = \frac{\sqrt{3}}{2} N k_{\text{IR}} = \sqrt{3} \frac{\pi}{\delta x}. \quad (10.62)$$

In many situation, it will useful to define the *power – spectrum* of  $f$ , with ensemble average  $\langle f^2 \rangle$  in the continuum defined as

$$\langle f^2 \rangle = \int d \log k \mathcal{P}_f(k) \quad , \quad \langle f_k f_{k'} \rangle = (2\pi)^3 \frac{2\pi^2}{k^3} \mathcal{P}_f(k) \delta(\mathbf{k} - \mathbf{k}') \quad . \quad (10.63)$$

In a lattice, the ensemble average is substituted by a volume average,

$$\langle f^2 \rangle_V = \frac{dx^3}{V} \sum_{\mathbf{n}} f^2(n) \quad , \quad (10.64)$$

so that using the discrete Fourier transform we just defined, we obtain

$$\langle f^2 \rangle_V = \frac{1}{2\pi^2} \sum_{|\tilde{\mathbf{n}}|} \Delta \log k(\tilde{\mathbf{n}}) k^3(\tilde{\mathbf{n}}) \left( \frac{\delta x}{N} \right)^3 \langle |f(\tilde{n})|^2 \rangle_{R(\tilde{n})} \quad , \quad (10.65)$$

with  $\langle (...) \rangle \equiv \frac{1}{4\pi|\tilde{\mathbf{n}}|^2} \sum_{\tilde{\mathbf{n}}' \in R(\tilde{\mathbf{n}})} (...)$  an angular average over the spherical shell of radius  $\tilde{\mathbf{n}}' \in [|\tilde{\mathbf{n}}|, |\tilde{\mathbf{n}} + \Delta\tilde{\mathbf{n}}|]$ , and  $\Delta\tilde{\mathbf{n}}$  a given radial binning. We also defined  $\Delta \log k(\tilde{\mathbf{n}}) \equiv \frac{k_{\text{IR}}}{k(\tilde{\mathbf{n}})}$ . Identifying this with Eq. (10.63), we obtain the following expression for the discrete power spectrum

$$\mathcal{P}_f(k) \equiv \frac{k^3(\tilde{\mathbf{n}})}{2\pi^2} \left( \frac{\delta x}{N} \right)^3 \langle |f(\tilde{\mathbf{n}})|^2 \rangle_{R(\tilde{\mathbf{n}})} \quad . \quad (10.66)$$

Finally, let us notice that we will be dealing in general with spatially dependent functions representing field amplitudes at a given time. As time goes by in the simulation, the amplitude of the functions will change. We can therefore think of the above functions depending not only on their coordinates  $\mathbf{n}$  (or reciprocal coordinates  $\tilde{\mathbf{n}}$ ), but also depending on a discrete variable  $n_0 = 0, 1, 2, \dots$  counting the number of time iterations in a simulation. In general,  $n_0$  labels a time  $\eta = \eta_* + n_0 \delta\eta$ , where  $\delta\eta$  is the temporal step chosen in the evolution, and  $\eta_*$  denotes an initial time. We will think therefore of the above functions as 4-dimensional functions, and we will often write them as  $f(n) = f(n_0, \mathbf{n})$ , or  $f(\tilde{n}) = f(n_0, \tilde{\mathbf{n}})$ . We will use the notation  $\hat{0}$  to represent the advance of one time step, so e.g.  $f(n + \hat{0}) = f(n_0 + 1, \mathbf{n})$ .

#### 10.3.2 Lattice representation of differential operators

##### 10.3.2.1 Derivative operators and lattice momenta

The action or the equations of motion contain continuum derivatives, so we need to replace these with lattice expressions that have the correct continuum limit. A simple and symmetric

definition of a lattice derivative is e.g. the *centered* or *neutral* derivative

$$[\nabla_\mu^{(0)} f] = \frac{f(n + \hat{\mu}) - f(n - \hat{\mu})}{2\delta x^\mu} \longrightarrow \partial_i \mathbf{f}(x)|_{x \equiv \mathbf{n}\delta x + n_0\delta\eta} + \mathcal{O}(\delta x_\mu^2), \quad (10.67)$$

where in the case of spatial derivatives  $\delta x^\mu$  refers to the lattice spacing  $\delta x$ , whereas for temporal derivatives it refers to the time step  $\delta\eta$  (typically bounded to be smaller than  $\delta x$ ). The expression to the right-hand side of the arrow indicates where and to what order on the lattice spacing/time step the continuum limit is recovered. The neutral derivative in Eq. (10.67) has the drawback that it is insensitive to spatial variations at the smallest scale we can probe,  $\sim \delta x$ , or temporal variations within a time of the order of the actual time step  $\sim \delta\eta$ . Because of this, a definition involving the nearest spatial/temporal neighbors can be preferable. A standard way to do this, is to define the *forward* and *backward* derivatives

$$[\nabla_\mu^\pm f] = \frac{\pm f(n \pm \hat{\mu}) \mp f(n)}{\delta x^\mu} \longrightarrow \begin{cases} \partial_i \mathbf{f}(x)|_{x \equiv \mathbf{n}\delta x + n_0\delta\eta} + \mathcal{O}(\delta x_\mu) \\ \partial_i \mathbf{f}(x)|_{x \equiv (n \pm \hat{\mu}/2)\delta x^\mu} + \mathcal{O}(\delta x_\mu^2) \end{cases}, \quad (10.68)$$

which recover the continuum limit to linear or to quadratic order on the lattice spacing/time step, depending on whether we interpret that the discrete operator lives in  $\mathbf{n}$  or in between the two lattice sites involved  $\mathbf{n} \pm \hat{\mu}/2$ . This shows that in order to recover a continuum differential operation on the lattice, not only it is important to use a suitable discrete operator, but also to determine where it 'lives'. Depending on this choice, the operator might be symmetric or not with respect to the given location, hence recovering the continuum limit up to an even or an odd order on the lattice spacing/time step, respectively. To improve accuracy, one could also consider lattice derivatives which involve more points, typically leading to definitions that have a symmetry either around a lattice site or around half-way between lattice sites, see for instance [179].

Depending on the choice of lattice operator  $\nabla_i$  for the spatial derivatives, the discrete Fourier transform will lead to different *lattice momenta*. In general, for any given derivative operator, the value of the derivative  $[\nabla_i f]$  will be a linear combination of the field values at different lattice sites,  $[\nabla_i f](\mathbf{l}) = \sum_{\mathbf{m}} D_i(\mathbf{l}, \mathbf{m}) f(\mathbf{m})$ , with  $D_i(\mathbf{l}, \mathbf{m})$  a real-valued function of two variables on the lattice. Since we want the derivative to be translation invariant,  $D_i(\mathbf{l}, \mathbf{m})$  can only be a function of the difference  $\mathbf{l} - \mathbf{m}$ , i.e.  $D_i(\mathbf{l}, \mathbf{m}) = D_i(\mathbf{l} - \mathbf{m})$ , and we can write

$$[\nabla_i f](\mathbf{l}) = \sum_{\mathbf{m}} D_i(\mathbf{l}, \mathbf{m}) f(\mathbf{m}) = \sum_{\mathbf{m}} D_i(\mathbf{l} - \mathbf{m}) f(\mathbf{m}) = \sum_{\mathbf{m}'} D_i(\mathbf{m}') f(\mathbf{l} - \mathbf{m}'). \quad (10.69)$$

For example, for the neutral derivative (10.67),

$$D_i^0(\mathbf{m}') = \frac{\delta_{\mathbf{m}', -\hat{i}} - \delta_{\mathbf{m}', \hat{i}}}{2\delta x}, \quad (10.70)$$

whereas for the nearest-neighbor derivative (10.68),

$$D_i^\pm(\mathbf{m}') = \frac{\pm\delta_{\mathbf{m}', \mp\hat{i}/2} \mp \delta_{\mathbf{m}', \pm\hat{i}/2}}{\delta x} \quad \text{if } \mathbf{l} = \mathbf{n} + \frac{\hat{i}}{2}; \quad D_i^\pm(\mathbf{m}') = \frac{\pm\delta_{\mathbf{m}', \mp\hat{i}} \mp \delta_{\mathbf{m}', \mathbf{0}}}{\delta x} \quad \text{if } \mathbf{l} = \mathbf{n}. \quad (10.71)$$

The Fourier transform of the derivative  $[\nabla_i f]$  is

$$\nabla_i f(\tilde{\mathbf{n}}) = \sum_{\mathbf{n}} e^{\frac{2\pi i}{N} \tilde{\mathbf{n}} \cdot \mathbf{n}} \sum_{\mathbf{m}} D_i(\mathbf{n} - \mathbf{m}) f(\mathbf{m}) = \sum_{\mathbf{n}'} e^{\frac{2\pi i}{N} \tilde{\mathbf{n}} \cdot \mathbf{n}'} D_i(\mathbf{n}') \sum_{\mathbf{m}} e^{\frac{2\pi i}{N} \tilde{\mathbf{n}} \cdot \mathbf{m}} f(\mathbf{m}) \equiv -i \mathbf{k}_{\text{Lat}}(\tilde{\mathbf{n}}) f(\tilde{\mathbf{n}}), \quad (10.72)$$

leading to define the *lattice momentum*  $\mathbf{k}_{\text{Lat}}(\tilde{\mathbf{n}})$  as

$$\mathbf{k}_{\text{Lat}}(\tilde{\mathbf{n}}) = i \sum_{\mathbf{n}'} e^{\frac{2\pi i}{N} \tilde{\mathbf{n}} \cdot \mathbf{n}'} D_i(\mathbf{n}'). \quad (10.73)$$

Conversely, any function  $\mathbf{k}_{\text{Lat}}(\tilde{\mathbf{n}})$  with the correct leading behaviour  $\mathbf{k}_{\text{Lat}}(\tilde{\mathbf{n}}) \approx \tilde{\mathbf{n}} \mathbf{k}_{\text{IR}}$  in the IR limit  $|\tilde{\mathbf{n}}| \ll N$ , defines a lattice derivative through the inverse Fourier transform.

In practice, for the neutral derivative (10.67) we obtain

$$k_{\text{Lat},i}^0 = \frac{\sin(2\pi \tilde{n}_i/N)}{\delta x}, \quad (10.74)$$

whereas for the forward/backward derivatives (10.68),

$$k_{\text{Lat},i} = 2 \frac{\sin(\pi \tilde{n}_i/N)}{\delta x} \quad \text{if } \mathbf{l} = \mathbf{n} + \frac{\hat{i}}{2}; \quad k_{\text{Lat},i}^\pm = \frac{\sin(2\pi \tilde{n}_i/N)}{\delta x} \pm i \frac{1 - \cos(2\pi \tilde{n}_i/N)}{\delta x} \quad \text{if } \mathbf{l} = \mathbf{n}. \quad (10.75)$$

We note that for anti-symmetric lattice derivatives with  $D_i(-\mathbf{m}') = -D_i(\mathbf{m}')$ , the lattice momentum  $\mathbf{k}_{\text{Lat}}$  must be real.

### 10.3.2.2 Lattice gauge invariant techniques

Discretizing a gauge theory requires a special care in order to preserve gauge invariance at the lattice level. It is not enough to recover gauge invariance in the continuum, sending the lattice spacing/time step to zero, as gauge invariance is meant to remove spurious transverse degrees of freedom. If we were to discretize a gauge theory substituting all ordinary derivatives in the continuum EOM by finite differences like those in Eqs. (10.67), (10.68), the gauge symmetry would not be preserved on the lattice and these spurious degrees of freedom would be propagating.

In order to understand this, let us consider the simplest possible case of a gauge theory, say an Abelian-Higgs model in flat space-time, with Lagrangian  $-\mathcal{L} = (\partial_\mu + ieA_\mu)\varphi^*(\partial^\mu - ieA^\mu)\varphi + \frac{1}{4}F_{\mu\nu}F^{\mu\nu} + V(\varphi^*\varphi)$ . This system is invariant under continuum gauge transformations  $\varphi(x) \rightarrow e^{-i\alpha(x)}\varphi(x)$ ,  $A_\mu(x) \rightarrow A_\mu(x) - \frac{1}{e}\partial_\mu\alpha(x)$  simply because the transformation of  $\partial_\mu(e^{-i\alpha(x)}\varphi(x))$  leads to a term  $i\partial_\mu\alpha(x)e^{-i\alpha(x)}\varphi(x)$ , whereas the transformation of the gauge field in  $-ieA_\mu e^{-i\alpha(x)}$  leads to a term identical but of opposite sign,  $+i\partial_\mu\alpha(x)e^{-i\alpha(x)}\varphi(x)$ , which

cancels out the previous one. However, if we discretized the system by simply promoting continuum derivatives into finite differences, say  $\partial_\mu f(x) \rightarrow \Delta_\mu^+ f(x)$ , then  $\Delta_\mu^+(e^{-i\alpha(x)}\varphi(x)) \neq \Delta_\mu^+(e^{-i\alpha(x)})\varphi(x) + e^{-i\alpha(x)}\Delta_\mu^+\varphi(x)$ , and thus the transformation of the field derivative does not produce a term compensated by the gauge field transformation in  $-ieA_\mu e^{-i\alpha(x)}$ . The reason is simple, the *Leibniz* rule  $(fg)' = f'g + fg'$  does not hold for finite difference operators. The situation is no different in non-Abelian theories.

*How can we restore gauge invariance on the lattice?* To mimic a continuum gauge theory on the lattice, we must adopt a special discretization procedure that preserves some sort of discretized version of gauge transformations. Lattice gauge invariance is actually necessary in order to preserve constraints that follow from the EOM, in particular the Gauss laws. In order to introduce a general formalism valid for gauge theories (either Abelian or non-Abelian), let us consider the more general case of a  $SU(N)$  invariant theory. We introduce then a *parallel transporter*, connecting two points in space-time

$$U(x, y) = Pexp\left\{-i \int_x^y dx^\mu A_\mu\right\}, \quad (10.76)$$

where  $Pexp\{\dots\}$  means *path-ordered* along the trajectory. The crucial observation is that under a gauge transformation of the gauge fields, recall Eq. (10.19), the parallel transporter transforms as

$$U(x, y) \rightarrow \Omega(x)U(x, y)\Omega^\dagger(y), \quad (10.77)$$

which in the Abelian case reduces simply to  $U(x, y) \rightarrow U(x, y)e^{-i(\alpha(x)-\alpha(y))}$ . Therefore, according to Eq. (10.77), a parallel transporter transforms exactly as the field strength transforms for  $x = y$ , Eq. (10.19). Thus, considering the *minimal connector* between two space-time sites separated only by one lattice spacing/time step,  $x(n) \equiv \mathbf{n}\delta x + n_0\delta t$ ,  $x(n + \hat{\mu}) \equiv \mathbf{n}\delta x + n_0\delta t + \delta x_\mu$ , we define the *link* variables as

$$U_{0,n} \equiv Pexp\left\{-i \int_{x(n)}^{x(n+\hat{0})} dt' A_0\right\} \approx e^{-i\delta t A_0}, \quad U_{i,n} \equiv Pexp\left\{-i \int_{x(n)}^{x(n+\hat{i})} dx A_i\right\} \approx e^{-i\delta x A_i}, \quad (10.78)$$

where the gauge field, and hence the link, is considered to live in the point  $n + \frac{\hat{\mu}}{2}$ . We also define  $U_{-\mu,n} = U_{\mu,n-\hat{\mu}}^\dagger \equiv U_\mu^\dagger(n - \frac{1}{2}\hat{\mu})$ . Before we continue, it will be useful at this point to establish some conventions to simplify the notation of upcoming expressions.

*Convention -.* From now on, unless stated otherwise, a scalar field living in a generic lattice site  $n = (n_0, \mathbf{n}) = (n_0, n_1, n_2, n_3)$ , i.e.  $\varphi_n = \varphi(n)$ , will be simply denoted as  $\varphi$ . If the point is displaced in the  $\mu$ -direction by one unit lattice spacing/time step,  $n + \hat{\mu}$ , we will then use the notation  $n + \mu$  or simply by  $+\mu$  to indicate this, so that the field amplitude in the new point is expressed by  $\varphi_{+\mu} \equiv \varphi(n + \hat{\mu})$ . In the case of gauge fields, whenever represented explicitly on the lattice, we will automatically understand that they live in the middle of lattice points, i.e.  $A_\mu \equiv A_\mu(n + \frac{1}{2}\hat{\mu})$ . It follows then that e.g.  $A_{\mu,+\nu} \equiv A_\mu(n + \frac{1}{2}\hat{\mu} + \hat{\nu})$ . In the case of links, we

will use the notation  $U_\mu \equiv U_{\mu,n} \equiv U_\mu(n + \hat{\mu}/2)$ , and hence  $U_{\mu,\pm\nu} = U_{\mu,n\pm\nu} \equiv U_\mu(n + \hat{\mu}/2 \pm \hat{\nu})$ . Even though the lattice spacing  $\delta x$  and the time step  $\delta t$  do not need to be equal, we will loosely speak of corrections of order  $\mathcal{O}(\delta x)$ , independently of whether we are referring to the lattice spacing or the time step (the latter is actually always forced to be smaller than the former). In lattice expressions we will never consider summation over repeated indices.

In the continuum limit, we recover the gauge fields simply from

$$\frac{(\mathcal{J} - U_{\mu,n})}{i\delta x^\mu} \longrightarrow A_\mu\left(n + \frac{1}{2}\hat{\mu}\right) + \mathcal{O}(\delta x). \quad (10.79)$$

It turns out that we can actually build the action or EOM for any gauge theory, preserving a discretized version of the gauge symmetry, using only link variables and no gauge fields. That is known as the *compact formulation* of lattice gauge theories, which can be applied to both Abelian and non-Abelian gauge theories. Actually, in the case of non-Abelian theories, compact formulations are the only way to discretize them while respecting gauge invariance on the lattice. In Abelian gauge theories, however, it is still possible to make use of an explicit representation of the gauge fields, in the so called *non-compact formulation*. Below we provide both. We introduce now standard definitions for *links*, *plaquettes* and *lattice covariant derivatives*, specialized to both Abelian and non-Abelian gauge groups. We provide also basic definitions, together with useful approximations and expressions (in the case of Abelian theories for both compact and non-compact formulations):

— U(1) toolkit —

Links:  $V_\mu \equiv e^{-idx_\mu A_\mu} = \cos(dx_\mu A_\mu) - i \sin(dx_\mu A_\mu)$ ;  $V_{-\mu} \equiv V_{\mu,-\mu}^*$ ;  $V_\mu^* V_\mu = 1$ ;

Plaquettes:  $V_{\mu\nu} \equiv V_\mu V_{\mu+\nu} V_{\mu+\nu}^* V_\nu^* \simeq e^{-idx_\mu dx_\nu [F_{\mu\nu} + \mathcal{O}(\delta x)]}$ ;  $V_{\mu\nu}^* = V_{\nu\mu}$ ;

Covariant Derivs.:  $(D_\mu^\pm \varphi)(\mathbf{l}) = \pm \frac{1}{\delta x^\mu} (V_{\pm\mu} \varphi_{\pm\mu} - \varphi)$ ,  $\mathbf{l} = \mathbf{n} \pm \frac{1}{2}\hat{\mu}$

$$\text{Expansions: } \begin{cases} (D_\mu^\pm \varphi)(\mathbf{l}) \longrightarrow (D_\mu \varphi)(\mathbf{l}) + \mathcal{O}(\delta x^2) & \mathbf{l} = \mathbf{n} \pm \frac{1}{2}\hat{\mu} \\ \Re\{V_{\mu\nu}\} \longrightarrow 1 - \frac{1}{2}dx_\mu^2 dx_\nu^2 F_{\mu\nu}^2 + \mathcal{O}(\delta x^5), & \mathbf{l} = \mathbf{n} + \frac{1}{2}\hat{\mu} + \frac{1}{2}\hat{\nu} \\ \Im\{V_{\mu\nu}\} \longrightarrow -dx_\mu dx_\nu F_{\mu\nu} + \mathcal{O}(\delta x^3), & \mathbf{l} = \mathbf{n} + \frac{1}{2}\hat{\mu} + \frac{1}{2}\hat{\nu} \end{cases} \quad (10.80)$$

$$\text{Expressions: } \begin{cases} \left[ \begin{aligned} \sum_n \frac{1}{4} F_{\mu\nu}^2 &\cong -\frac{1}{2} \sum_n \frac{\Re\{V_{\mu\nu}\}}{dx_\mu^2 dx_\nu^2} = -\frac{1}{4} \sum_n \frac{(V_{\mu\nu} + V_{\mu\nu}^*)}{dx_\mu^2 dx_\nu^2} + \mathcal{O}(\delta x^2) \\ \sum_n \frac{1}{4} F_{\mu\nu}^2 &\simeq \sum_n \frac{1}{4} \frac{\Im^2\{V_{\mu\nu}\}}{dx_\mu^2 dx_\nu^2} = -\sum_n \frac{1}{4} \frac{(V_{\mu\nu} - V_{\mu\nu}^*)^2}{dx_\mu^2 dx_\nu^2} + \mathcal{O}(\delta x^2) \end{aligned} \right] & \text{(Compact)} \\ \left[ \sum_n \frac{1}{4} F_{\mu\nu}^2 \simeq \frac{1}{4} \sum_n (\Delta_\mu^+ A_\nu - \Delta_\nu^+ A_\mu)^2 + \mathcal{O}(\delta x^2) \right] & \text{(Non-Compact)} \end{cases}$$

$$\text{Gauge Trans} \left\{ \begin{array}{lcl} \phi & \longrightarrow & e^{+i\alpha} \phi \\ A_\mu & \longrightarrow & A_\mu + \frac{1}{e} \Delta_\mu^\dagger \alpha \\ U_{\pm\mu} & \longrightarrow & e^{+i\alpha} U_{\pm\mu} e^{-i\alpha_{\pm\mu}} \end{array} \right\} \Rightarrow \left\{ \begin{array}{lcl} D_\mu^\pm \phi & \longrightarrow & e^{+i\alpha} (D_\mu^\pm \phi) \\ U_{\mu\nu} & \longrightarrow & U_{\mu\nu} \text{ (gauge inv. !)} \end{array} \right.$$

— SU(N) toolkit —

$$\text{Links: } U_\mu \equiv e^{-idxB_\mu} = e^{-idxB_\mu^a T_a}; \quad U_{-\mu} \equiv U_{\mu,-\mu}^\dagger; \quad U_\mu^\dagger U_\mu = \mathcal{I}$$

$$\text{Plaquettes: } U_{\mu\nu} \equiv U_\mu U_{\nu,+\mu} U_{\mu,+\nu}^\dagger U_\nu^\dagger \simeq e^{-idx_\mu dx_\nu [G_{\mu\nu}^a T_a + \mathcal{O}(dx_\mu)]}; \quad U_{\mu\nu}^\dagger = U_{\nu\mu}$$

$$\text{Covariant Derivs.: } (D_\mu^\pm \Phi)(\mathbf{l}) = \pm \frac{1}{\delta x^\mu} (U_{\pm\mu} \Phi_{\pm\mu} - \Phi) \longrightarrow (D_\mu \Phi)(\mathbf{l}) + \mathcal{O}(\delta x^2), \quad \mathbf{l} = \mathbf{n} \pm \frac{1}{2} \hat{\mu}$$

$$\text{Expansions: } \left\{ \begin{array}{lcl} (D_\mu^\pm \Phi)(\mathbf{l}) & \longrightarrow & (D_\mu \Phi)(\mathbf{l}) + \mathcal{O}(\delta x^2), \quad \mathbf{l} = \mathbf{n} \pm \frac{1}{2} \hat{\mu} \\ (U_{\mu\nu} - U_{\mu\nu}^\dagger) & \longrightarrow & -2i\delta x_\mu \delta x_\nu G_{\mu\nu} + \mathcal{O}(dx_\mu^3), \quad \mathbf{l} = \mathbf{n} + \frac{1}{2} \hat{\mu} + \frac{1}{2} \hat{\nu} \\ \text{Tr}[U_{\mu\nu}] & \longrightarrow & 2 - \frac{dx_\mu^2 dx_\nu^2}{4} \sum_a (G_{\mu\nu}^a)^2 + \mathcal{O}(dx_\mu^5), \quad \mathbf{l} = \mathbf{n} + \frac{1}{2} \hat{\mu} + \frac{1}{2} \hat{\nu} \end{array} \right. \quad (10.81)$$

$$\text{Expressions: } \left\{ \begin{array}{l} \frac{1}{2} \text{Tr}[G_{\mu\nu} G^{\mu\nu}] = \frac{1}{4} \sum_a (G_{\mu\nu}^a)^2 \cong -\frac{\text{Tr}[U_{\mu\nu}]}{dx_\mu^2 dx_\nu^2} + \mathcal{O}(\delta x^2), \\ G_{\mu\nu} = G_{\mu\nu}^a T_a \simeq \frac{i}{2dx_\mu dx_\nu} (U_{\mu\nu} - U_{\mu\nu}^\dagger) + \mathcal{O}(\delta x^2), \\ G_{\mu\nu}^a \simeq \frac{1}{dx_\mu dx_\nu} \text{Tr}[(iT_a)(U_{\mu\nu} - U_{\mu\nu}^\dagger)] + \mathcal{O}(\delta x^2) \end{array} \right.$$

$$\text{Gauge Trans.} \left\{ \begin{array}{lcl} \Phi & \longrightarrow & \Omega \Phi, \quad \Omega \equiv e^{+i\alpha_a T_a} \\ U_{\pm\mu} & \longrightarrow & \Omega U_{\pm\mu} \Omega_{\pm\mu}^\dagger \end{array} \right\} \Rightarrow \left\{ \begin{array}{lcl} D_\mu^\pm \Phi & \longrightarrow & \Omega (D_\mu^\pm \Phi) \\ U_{\mu\nu} & \longrightarrow & \Omega U_{\mu\nu} \Omega^\dagger \\ \text{Tr}\{U_{\mu\nu}\} & \longrightarrow & \text{Tr}\{U_{\mu\nu}\} \end{array} \right.$$

In the case of  $SU(2)$ , any element can be written as

$$U_\mu = c_{\mu 0} \mathcal{I} + \sum_{a=1}^3 i c_{\mu a} \sigma_a = \sum_{\nu=0}^3 c_{\mu\nu} \bar{\sigma}_\nu, \quad \bar{\sigma}_a \equiv (1, i\vec{\sigma}), \quad \sum_{\nu=0}^3 c_{\mu\nu}^2 = 1, \quad (10.82)$$

or, in matrix form (in the gauge  $U_0 = \mathcal{I}$ )

$$U_i \equiv U_i(c_{i0}, c_{i1}, c_{i2}, c_{i3}) = \begin{pmatrix} c_{i0} + i c_{i3} & c_{i2} + i c_{i1} \\ -c_{i2} + i c_{i1} & c_{i0} - i c_{i3} \end{pmatrix}, \quad U_i^\dagger = U_i(c_{i0}, -c_{i1}, -c_{i2}, -c_{i3}). \quad (10.83)$$

Useful expressions for the electric and magnetic fields are

$$\mathcal{E}_i^a = G_{0i}^a \approx \frac{1}{\delta t \delta x} \text{Tr}[(iT_a)(U_{0i} - U_{i0})] = \frac{1}{\delta t \delta x} \text{Tr}[(iT_a)(U_{0i} - U_{0i}^\dagger)], \quad (10.84)$$

$$\mathcal{B}_i^a = \frac{1}{2} \epsilon_{ijk} G_{jk}^a \approx \frac{\epsilon_{ijk}}{2 \delta x^2} \text{Tr}[(iT_a)(U_{jk} - U_{kj})]. \quad (10.85)$$

### 10.3.3 Evolution algorithms

Solving the field dynamics in an expanding background in a lattice consists in writing some appropriate discrete version of the EOM [say Eqs. (10.37)-(10.39) for scalar fields, Eqs. (10.38)-(10.43) for gauge fields, and Eqs. (10.52)-(10.53) for the scale factor], and then iterate the discrete EOM for a finite number of time steps. In general we will have to follow the evolution in each spatial lattice site of a number of *dof* representing real field amplitudes, say one per singlet, two per complex field, four per doublet, etc, as well as the Lorentz components of each gauge field considered. Let us denote these *dof* collectively as the *field amplitudes*  $\{f_j\}$ , with  $j$  some index labeling all the real field amplitudes involved in a given scenario, and  $\{\pi_j\}$  their *conjugate momenta*. As the scale factor is only a homogeneous *dof* (sourced by the volume averaged energy and pressure densities built from the matter *dof*), we will not include it in the previous numbered list of *dof*'s, and we will rather treat it as a separate variable  $a(\eta)$ , with conjugate momenta  $\pi_a \equiv a'(\eta)$ . For example, in a theory with two singlet scalar fields, say  $\phi$  and  $\chi$ , and self-consistent expansion, we can consider  $\{f_1, f_2\} \equiv \{\phi(x), \chi(x)\}$  and  $\{\pi_1, \pi_2\} \equiv \{\phi'(x), \chi'(x)\}$ , and then separately  $a(\eta)$  and  $\pi_a(\eta) = a'(\eta)$ . Looking at the EOM in the continuum Eqs. (10.37)-(10.39) and scale factor Eqs. (10.52)-(10.53), we note the following structure in the system of equations (independently of the nature of fields involved),

$$\pi_a(\eta) = a'(\eta), \quad (10.86)$$

$$\pi'_a(\eta) = \mathcal{K}_a[a(\eta), \bar{V}(\eta), \bar{K}(\eta), \bar{G}(\eta)], \quad (10.87)$$

$$\pi_i(\mathbf{x}, \eta) = \mathcal{D}_i[f'_i(\mathbf{x}, \eta), a(\eta), \pi_a(\eta); \{f_j(\mathbf{x}, \eta)\}, \{f'_{j \neq i}(\mathbf{x}, \eta)\}], \quad (10.88)$$

$$\pi'_i(\mathbf{x}, \eta) = \mathcal{K}_i[f_i(\mathbf{x}, \eta), \pi_i(\mathbf{x}, \eta), a(\eta), \pi_a(\eta); \{f_{j \neq i}(\mathbf{x}, \eta)\}, \{\pi_{j \neq i}(\mathbf{x}, \eta)\}], \quad (10.89)$$

where  $\mathcal{D}_i[\dots]$  is a functional – the *drift* – that defines the conjugate momentum of the  $i$ th *dof*,  $\mathcal{K}_i[\dots]$  is another functional – the *kernel* or *kick* –, that determines the interactions of the  $i$ th *dof* with the rest of *dof*'s (possibly including itself), and finally  $\mathcal{K}_a[\dots]$  is given by the square root of the *rhs* of Eq. (10.53), based on the volume averages  $\langle \dots \rangle$  of the different *dof* contributions to the potential, kinetic and gradient energy densities,  $\bar{V}(\eta) \equiv \langle V \rangle$ ,  $\bar{K} \equiv \{\bar{K}_j(\eta); \bar{K}_j(\eta) \equiv \langle K_j \rangle\}$  and  $\bar{G} \equiv \{\bar{G}_j(\eta); \bar{G}_j(\eta) \equiv \langle G_j \rangle\}$ .

For canonical kinetic terms,  $\mathcal{D}_i$  depends on  $f'_i$  but not on any other  $f'_{j \neq i}$ . We note also that we have separated within the argument of each kernel  $\mathcal{K}_i$ , the amplitude and momentum of the  $i$ th *dof* itself, from the amplitudes and momenta of the rest of *dof*'s. The latter actually act merely as 'instantaneous' parameters for an infinitesimal evolution of the  $i$ th *dof*. Hence, in general, we will only care about the dependence of the  $i$ th kernel  $\mathcal{K}_i$  on  $f_i$  and  $\pi_i$ .



Furthermore, we will encounter often that the time derivative  $\pi'_i$  of a given *dof* can (and often will) depend on its amplitude  $f_i$ , but not on  $\pi_i$  itself. This is actually not a physical requisite, but rather a mathematical requisite we will seek. In fact, the EOM in the continuum as written so far, lead to kernels  $\mathcal{K}_i$  that depend on  $\pi_i$ , see e.g. the friction terms in Eqs. (10.37)-(10.41). However, from the point of view of the stability of the numerical algorithms used to solve the discrete EOM, it will be convenient to 'massage' appropriately the EOM, so that we arrive into effective kernels  $\mathcal{K}_i$  that do not depend<sup>4</sup> on  $\pi_i$ . We will see later on how to do this in a case by case basis. For the time being, we will consider that this condition has been achieved, implicitly assuming that pertinent manipulations (if any) of the field variables in the EOM have been made to grant it. Taking into account all the above considerations, the typical system of equations we will want to solve (for a theory with canonical kinetic terms) looks as follows

$$\pi_a(\eta) = a'(\eta), \quad (10.90)$$

$$\pi'_a(\eta) = \mathcal{K}_a[a(\eta), \bar{V}(\eta), \bar{K}(\eta), \bar{G}(\eta)], \quad (10.91)$$

$$\pi_i(\mathbf{x}, \eta) = \mathcal{D}_i[f'_i(\mathbf{x}, \eta), a(\eta); \dots], \quad (10.92)$$

$$\pi'_i(\mathbf{x}, \eta) = \mathcal{K}_i[f_i(\mathbf{x}, \eta), a(\eta), \pi_a(\eta); \dots]. \quad (10.93)$$

Let us note that, although any possible dependence of the drift  $\mathcal{D}_i$  on  $\pi_a$  would not pose a problem to the algorithms presented below, in practice we do not know of any theory that produces such dependence, so we have removed it as an explicit argument from  $\mathcal{D}_i$ . A discrete version of the EOM will then have a scheme similar to

$$\pi_a(\eta) = \Delta_0 a(\eta), \quad (10.94)$$

$$\Delta_0 \pi_a = \mathcal{K}_a[a(\eta), \bar{V}(\eta), \bar{K}(\eta), \bar{G}(\eta)], \quad (10.95)$$

$$\pi_i(\mathbf{x}, \eta) = \mathcal{D}_i[\Delta_0 f_i(\mathbf{x}, \eta), a(\eta); \dots], \quad (10.96)$$

$$\Delta_0 \pi_i(\mathbf{x}, \eta) = \mathcal{K}_i[f_i(\mathbf{x}, \eta), a(\eta), \pi_a(\eta); \dots], \quad (10.97)$$

with  $\Delta_0$  some discrete operator mimicking continuum time derivatives. As we will see in a moment, introducing time operators as simple as

$$(\Delta_0^{\pm r} f) = \frac{\pm f(n \pm r\delta t) \mp f(n)}{r\delta t} \longrightarrow \begin{cases} (\Delta_0^+ f) = \frac{f(n+\delta t) - f(n)}{\delta t} & , \text{Standard Forward Deriv.} \\ (\Delta_0^- f) = \frac{f(n) - f(n-\delta t)}{\delta t} & , \text{Standard Backward Deriv.} \\ (\Delta_0^{+\frac{1}{2}} f) = \frac{f(n+\delta t/2) - f(n)}{(\delta t/2)} & , +\frac{1}{2} \text{ Forward Deriv.} \\ (\Delta_0^{-\frac{1}{2}} f) = \frac{f(n) - f(n-\delta t/2)}{(\delta t/2)} & , -\frac{1}{2} \text{ Backward Deriv.} \end{cases} \quad (10.98)$$

will actually enable us to address all basic algorithms to iterate coupled finite difference equations like (10.94)-(10.97), mimicking continuum coupled differential equations like (10.90)-(10.93).

---

<sup>4</sup>The kernel  $\mathcal{K}_i$  will typically also not depend on the rest of conjugate momenta  $\{\pi_{i \neq j}\}$ , except in the case of non-canonically normalized kinetic terms. As already said, we leave this case for future work.

## 10.3.3.1 Staggered leapfrog

One of the simplest methods for solving second order differential equations is the *leapfrog* algorithm. Let us illustrate it by solving a simple one-dimensional problem, consisting in one *dof*  $x(t)$  that depends only on a time variable  $t$ , with EOM

$$\ddot{x}(t) = \mathcal{K}[x(t)]. \quad (10.99)$$

Taylor expanding the position at the next step we obtain

$$x(t + \delta t) = x(t) + \dot{x}(t)\delta t + \frac{1}{2}\mathcal{K}[x(t)]\delta t^2 + \dots \equiv x(t) + \dot{x}(t + \delta t/2)\delta t + \dots, \quad (10.100)$$

where in the second equality we have substituted the Taylor expansion of the velocity at half time step

$$\dot{x}(t + \delta t/2) = \dot{x}(t) + \frac{\delta t}{2}\mathcal{K}[x(t)] + \dots \equiv \dot{x}(t - \delta t/2) + \mathcal{K}[x(t)]\delta t + \dots, \quad (10.101)$$

and where we have used that  $\dot{x}(t) = \dot{x}(t - \delta t/2) + \mathcal{K}[x(t - \delta t/2)]\delta t + \mathcal{O}(\delta t^2)$  and  $\mathcal{K}[x(t - \delta t/2)]\delta t + \mathcal{O}(\delta t^2) = \mathcal{K}[x(t)]\delta t + \mathcal{O}(\delta t^2)$ . Applying recursively the above relations between velocity and position, we obtain

$$x(t) = x(t - \delta t) + \dot{x}(t - \delta t/2)\delta t, \quad (10.102)$$

$$\dot{x}(t + \delta t/2) = \dot{x}(t - \delta t/2) + \mathcal{K}[x(t)]\delta t, \quad (10.103)$$

$$x(t + \delta t) = x(t) + \dot{x}(t + \delta t/2)\delta t, \quad (10.104)$$

$$\dot{x}(t + 3\delta t/2) = \dot{x}(t + \delta t/2) + \mathcal{K}[x(t + \delta t)]\delta t, \quad (10.105)$$

....

The leapfrog method has an accuracy of order  $\mathcal{O}(\delta t^2)$ , because each step advances  $x$  or  $\pi_x$  in terms of its derivative at the middle of the step. This is better than the simpler *Euler* method, which has  $\mathcal{O}(\delta t)$  accuracy. This can be demonstrated by simply noting the accuracy of the derivative expressions  $(x(t + \delta t) - x(t))/\delta t \simeq \dot{x}(t + \delta t/2) + \mathcal{O}(\delta t^2)$  and  $(\dot{x}(t + \delta t/2) - \dot{x}(t - \delta t/2))/\delta t \simeq \ddot{x}(t) + \mathcal{O}(\delta t^2)$ . Let us label the initial time as  $t_0$ , and start with initial conditions  $x_0 \equiv x(t_0)$  and  $\dot{x}_0 \equiv \dot{x}(t_0)$ . We can obtain first  $\dot{x}(t_0 + \delta t/2) = \dot{x}_0 + 1/2\mathcal{K}[x_0]\delta t$ , and from then on, iterate as follows:  $(x(t_0), \dot{x}(t_0 + \delta t/2)) \rightarrow (x(t_1), \dot{x}(t_1 + \delta t/2)) \rightarrow \dots \rightarrow (x(t_n), \dot{x}(t_n + \delta t/2))$ , with  $t_n \equiv t_0 + n\delta t$ , and  $n$  the number of iterations.

In terms of the previously introduced time derivative operators, we can simply write the algorithm as

$$\Delta_0^+ x_n = \pi_{n+1/2}, \quad (10.106)$$

$$\Delta_0^+ \pi_{n+1/2} = \mathcal{K}[x_{n+1}], \quad (10.107)$$

understanding that  $x_n$  lives at 'integer' times  $t_n \equiv t_0 + n\delta t$  and  $\pi_x$  at 'semi-integer' times

$t_{n+1/2} \equiv t_n + \delta t/2 = t_0 + (n+1/2)\delta t$ , so that  $\Delta_0^+ x_n \equiv (x_{n+1} - x_n)\delta t$  lives at  $t_{n+1/2}$ , whereas  $\Delta_0^+ \pi_{n+1/2} \equiv (\pi_{n+3/2} - \pi_{n+1/2})\delta t$  lives at  $t_{n+1}$ . Due to this separation into variables that live at integer times and conjugate momenta that live at semi-integer times, sometimes people refer to this method as the 'staggered' leapfrog algorithm. We will content ourselves with simply referring to it as the leapfrog algorithm.

The leapfrog method, encapsulated in Eqs. (10.106)-(10.107) can be extended readily to multiple *dof*, simply labeling them with some index as  $x_n^i$  and  $\pi_{n+1/2}^i$ , with  $i = 1, 2, 3, \dots$  counting the number of *dof*. Namely

$$\Delta_0^+ x_n^i = \pi_{n+1/2}^i, \quad (10.108)$$

$$\Delta_0^+ \pi_{n+1/2}^i = \mathcal{K}_i \left[ x_{n+1}^i, \{x_{n+1}^{j \neq i}\} \right], \quad (10.109)$$

where the kernels  $\mathcal{K}_i$  represent the interaction of the  $i$ th *dof*  $x^i$  with the rest of *dofs*  $\{x^{j \neq i}\}$ . However, this method is only applicable to *conservative* forces<sup>5</sup>, i.e. to EOM with kernels that only depend on amplitude variables  $\mathcal{K} \equiv \mathcal{K}[\{x^i(t)\}]$ . This method can be therefore applied readily to our field theory EOM (10.94)-(10.97) in a flat space-time background. If the expansion of the Universe is switched off, i.e.  $a = 1$  and  $\dot{a} = \ddot{a} = 0$ , we can ignore the first two Eqs. (10.94)-(10.95) and take care of evolving only (10.96)-(10.97), which represent the evolution of the matter field *dof* in a flat background. Switching back to our  $\alpha$ -time variable, say  $\eta(n_0) \equiv \eta_0 + n_0 \delta \eta$  with  $n_0$  counting the number of time steps, we can solve Eqs. (10.96)-(10.97) with a leapfrog scheme simply as

$$\Delta_0^+ f_i(\mathbf{x}, n_0) = \pi_i(\mathbf{x}, n_0 + 1/2), \quad (10.110)$$

$$\Delta_0^+ \pi_i(\mathbf{x}, n_0 + 1/2) = \mathcal{K}_i[\{f_j(\mathbf{x}, n_0 + 1)\}], \quad (10.111)$$

with  $i = 1, 2, 3, \dots$  counting our field theory *dof*, e.g. scalar field real components and gauge field Lorentz components.

We note now that in any set of discrete EOM mimicking continuum EOM, the spatial coordinates  $\mathbf{x}$  are discretized, being represented by a finite set of lattice sites  $\mathbf{n} = (n_1, n_2, n_3)$  with  $n_i = 0, 1, 2, \dots, N-1$ , and  $N$  the number of lattice sites per spatial dimension (recall Section 10.3.1 for definitions). This implies that spatial derivatives appearing in the discrete EOM, e.g. the Laplacian operator for scalar fields  $\nabla^2 f$ , will be substituted by lattice derivative operators like in Eq. (10.68). Due to this, the kernels in the discretized EOM are not functions of the point  $\mathbf{n}$  only, but also of its nearest neighbours, e.g.  $\mathbf{n} \pm \hat{j}$ , with  $j = 1, 2, 3$ . The correct form of the discretized field EOM in a flat background will then look like

$$\Delta_0^+ f_i(\mathbf{n}, n_0) = \pi_i(\mathbf{n}, n_0 + 1/2), \quad (10.112)$$

$$\Delta_0^+ \pi_i(\mathbf{n}, n_0 + 1/2) = \mathcal{K}_i[\{f_j(\mathbf{m}, n_0 + 1)\}], \quad (10.113)$$

---

<sup>5</sup>In reality nothing prevents you from applying it to *non-conservative* forces with  $\mathcal{K} = \mathcal{K}[x(t), \dot{x}(t)]$ , but then its stability properties and its  $\mathcal{O}(\delta t^2)$  accuracy will be lost.

with  $\mathbf{m}$  representing  $\mathbf{n}$  and its nearest neighbours (to be determined in each case depending on the choice of lattice spatial derivatives).

Note that the leapfrog algorithm cannot be applied directly to scenarios where the expansion of the universe is considered (either background or self-consistent expansion), without a careful choice of which *dof* to evolve. Indeed, the EOM of matter fields in FLRW, c.f. Eq. (10.88), have kernels  $\mathcal{K}[\dots]$  containing conjugate momenta  $\pi_i$ , due to the presence of the friction terms  $\propto (a'/a)f'_i$  in the field EOM, see e.g. Eqs. (10.37)-(10.41). Furthermore, the Friedmann equation  $\pi'_a = \mathcal{K}_a[a, \bar{V}, \bar{K}, \bar{G}]$  [c.f. Eq. (10.87)], also contains the kinetic terms  $\bar{K} \equiv \{K_j\}$ , built from the conjugate momenta of the fields. As conjugate momenta  $\pi_i$  and  $\pi_a$  live, in a leapfrog algorithm, naturally at semi-integer times  $\eta_{n+1/2}$ , the leapfrog algorithm for kernels which contain conjugate momenta will not work, as they should rather live at integer times  $\eta_p$  for the algorithm to be stable and order  $\mathcal{O}(\delta t^2)$ . As we will show in Sections 10.4.2.1, it is possible to overtake this problem by means of field re-definitions and/or manipulations of the EOM, so that we can have a consistent iterative scheme with appropriate kernels, even in the presence of an expanding background. So for now, let us assume that we managed to obtain *dof* such that the kernels do not depend on the momenta. We then have the following leapfrog algorithm in an expanding universe

*Leapfrog in an expanding background*

$$\Delta_0^+ \pi_a(\mathbf{n}, n_0 - 1/2) = \mathcal{K}_a[a(n_0), \bar{V}(n_0), \bar{K}(n_0), \bar{G}(n_0)], \quad (10.114)$$

$$\Delta_0^+ \pi_i(\mathbf{n}, n_0 - 1/2) = \mathcal{K}_i[\{f_j(\mathbf{m}, n_0)\}, a(n_0)], \quad (10.115)$$

$$\Delta_0^+ a(n_0) = \pi_a(n_0 + 1/2), \quad (10.116)$$

$$\Delta_0^+ f_i(\mathbf{n}, n_0) = \mathcal{D}_i[\pi_i(\mathbf{n}, n_0 + 1/2), a(n_0 + 1/2)], \quad (10.117)$$

Its concrete applications to the case of interacting scalar, Abelian and non-Abelian gauge fields are discussed in Section 10.4 through 10.6.

#### 10.3.3.2 Verlet integration

Let us dig up again the one-dimensional problem of a single *dof* that depends only on time,  $x(t)$ , with EOM

$$\ddot{x}(t) = \mathcal{K}[x(t)], \quad (10.118)$$

say with initial condition  $t_0 = 0$ ,  $x(0) = x_0$  and  $\dot{x}(0) = \pi_0$ . Recall that in order to initiate the previously discussed leapfrog algorithm, we initially needed  $x_0$  and  $\pi_{1/2} \equiv \dot{x}(\delta t/2)$ , so we proposed to obtain the initial half-time step displaced velocity as  $\pi_{1/2} \simeq \pi_0 + \frac{1}{2}\delta t \mathcal{K}[x_0] + \mathcal{O}(\delta t^2)$  (or equivalently, from applying  $\Delta_{0/2}^+ \pi_0 = \frac{1}{2}\mathcal{K}[x_0]$ ). Now, following the leapfrog prescription, we would apply  $\Delta_0^+ x_0 = \pi_{1/2}$  leading to  $x_1$  at order  $\mathcal{O}(\delta t^2)$ , and then  $\Delta_0^+ \pi_{1/2} = \mathcal{K}[x_1]$  leading to  $\pi_{3/2}$

at order  $\mathcal{O}(\delta t^2)$ , and so on and so forth with successive iterations. However, after obtaining  $x_1$ , we might as well apply  $\Delta_{0/2}^+ \pi_{1/2} = \frac{1}{2} \mathcal{K}[x_1]$ , leading to  $\pi_1$ , also at order  $\mathcal{O}(\delta t^2)$ . Essentially, by applying the velocity part of the leapfrog algorithm at two equal and successive half time steps (with one position update in between), we can simply jump from  $(x_0, \pi_0)$  to  $(x_1, \pi_1)$ , and from there to  $(x_2, \pi_2)$ , and so on and so forth. In other words, we can actually obtain the position and velocity always at integer times, up at order  $\mathcal{O}(\delta t^2)$ , with a 'kick - drift - kick' scheme as

$$\left. \begin{aligned} \pi_{n+1/2} &= \pi_n + \frac{1}{2} \delta t \mathcal{K}[x_n], \\ x_{n+1} &= x_n + \pi_{n+1/2} \delta t, \\ \pi_{n+1} &= \pi_{n+1/2} + \frac{1}{2} \delta t \mathcal{K}[x_{n+1}], \end{aligned} \right\} \iff \left\{ \begin{aligned} \Delta_{0/2}^+ \pi_n &= \mathcal{K}[x_n], \\ \Delta_0^+ x_n &= \pi_{n+1/2}, \\ \Delta_{0/2}^+ \pi_{n+1/2} &= \mathcal{K}[x_{n+1}]. \end{aligned} \right. \quad (10.119)$$

In reality, this method is nothing else than the leapfrog algorithm, but adding an 'extra' computation of the conjugate momenta at integer times in each iteration,

$$\left. \begin{aligned} x_{n+1} &= x_n + \pi_{n+1/2} \delta t, \\ \pi_{n+3/2} &= \pi_{n+1/2} + \delta t \mathcal{K}[x_{n+1}], \\ \left( \pi_{n+1} &= \pi_{n+1/2} + \frac{1}{2} \delta t \mathcal{K}[x_{n+1}] \right) \end{aligned} \right\} \iff \left\{ \begin{aligned} \Delta_0^+ x_n &= \pi_{n+1/2}, \\ \Delta_0^+ \pi_{n+1/2} &= \mathcal{K}[x_{n+1}], \\ \left( \Delta_{0/2}^+ \pi_{n+1/2} &= \mathcal{K}[x_{n+1}] \right). \end{aligned} \right. \quad (10.120)$$

Alternatively, since we may only care about the amplitudes and conjugate momenta at the same moment, say at integer times, the scheme can be put into a 'drift-kick' scheme, simply by

$$\left. \begin{aligned} x_{n+1} &= x_n + \pi_n \delta t + \frac{1}{2} \mathcal{K}[x_n] \delta t^2, \\ \pi_{n+1} &= \pi_n + \frac{1}{2} (\mathcal{K}[x_n] + \mathcal{K}[x_{n+1}]) \delta t, \end{aligned} \right\} \iff \left\{ \begin{aligned} \Delta_0^+ x_n &= \pi_n + \frac{\delta t}{2} \mathcal{K}[x_n], \\ \Delta_0^+ \pi_n &= \frac{1}{2} (\mathcal{K}[x_n] + \mathcal{K}[x_{n+1}]). \end{aligned} \right. \quad (10.121)$$

The method, represented by either scheme Eq. (10.119), Eq. (10.120) or Eq. (10.121), is known as the *velocity-Verlet* algorithm. Let us remark that the 2-step scheme has actually no advantage versus the 3-step scheme, as in reality the number of operations is the same: the 2-step scheme simply contains the 'third' step in the drift (i.e. in the right hand side of the amplitude updates). The 2-step scheme is only a convenient way of writing the algorithm in a more compact way.

If instead we apply the coordinate part of the leapfrog algorithm at two equal and successive half time steps (with one velocity update in between), then the method turns into the *position-Verlet* algorithm, which in a 'drift-kick-drift' scheme, has the form

$$\left. \begin{aligned} x_{n+1/2} &= x_n + \frac{1}{2} \pi_n \delta t, \\ \pi_{n+1} &= \pi_n + \delta t \cdot \mathcal{K}[x_{n+1/2}], \\ x_{n+1} &= x_{n+1/2} + \frac{1}{2} \pi_{n+1} \delta t, \end{aligned} \right\} \iff \left\{ \begin{aligned} \Delta_{0/2}^+ x_n &= \pi_n, \\ \Delta_0^+ \pi_n &= \mathcal{K}[x_{n+1/2}], \\ \Delta_{0/2}^+ x_{n+1/2} &= \pi_{n+1}. \end{aligned} \right. \quad (10.122)$$

As before, this is nothing more than a standard leapfrog algorithm (with variables half time

### 10.3. Field dynamics in a computer: the lattice approach

step shifted), plus an extra computation at each time step. Position-Verlet is also an algorithm of order  $\mathcal{O}(\delta t^2)$ . The position-Verlet algorithm can also be put in a 2-step scheme like

$$\left. \begin{aligned} \pi_{n+1} &= \pi_n + \delta t \cdot \mathcal{K}[x_n + \frac{\delta t}{2} \pi_n], \\ x_{n+1} &= x_n + \frac{\delta t}{2}(\pi_n + \pi_{n+1}), \end{aligned} \right\} \iff \left\{ \begin{aligned} \Delta_0^+ \pi_n &= \mathcal{K}[x_n + \frac{\delta t}{2} \pi_n], \\ \Delta_0^+ x_n &= \frac{1}{2}(\pi_n + \pi_{n+1}), \end{aligned} \right. \quad (10.123)$$

which again is just a more compact manner to write the algorithm: the number of operations is still three at each time step, with the 'third' step now contained inside the argument of the kick.

The application of either Verlet algorithm to field theories in a flat space-time background is straightforward. Introducing again  $\eta(n_0) \equiv \eta_i + n_0 \delta \eta$  as the discrete  $\alpha$ -time variable ( $\eta_i$  some initial time), and  $i = 1, 2, 3, \dots$  labeling the field theory *dof* (namely scalar field real components and gauge field Lorentz components), the velocity-Verlet algorithm reads

$$\Delta_{\hat{0}/2}^+ \pi_i(\mathbf{n}, n_0) = \mathcal{K}_i[\{f_j(\mathbf{m}, n_0)\}], \quad (10.124)$$

$$\Delta_0^+ f_i(\mathbf{n}, n_0) = \pi_i(\mathbf{n}, n_0 + 1/2), \quad (10.125)$$

$$\Delta_{\hat{0}/2}^+ \pi_i(\mathbf{n}, n_0 + 1/2) = \mathcal{K}_i[\{f_j(\mathbf{m}, n_0 + 1)\}], \quad (10.126)$$

whereas the position-Verlet algorithm is

$$\Delta_{\hat{0}/2}^+ f_i(\mathbf{n}, n_0) = \pi_i(\mathbf{n}, n_0), \quad (10.127)$$

$$\Delta_0^+ \pi_i(\mathbf{n}, n_0) = \mathcal{K}_i[\{f_j(\mathbf{m}, n_0 + 1/2)\}], \quad (10.128)$$

$$\Delta_{\hat{0}/2}^+ f_i(\mathbf{n}, n_0 + 1/2) = \pi_i(\mathbf{n}, n_0 + 1). \quad (10.129)$$

Here, like in the staggered leapfrog algorithm,  $\mathbf{m}$  on the *rhs* represents  $\mathbf{n}$  and its nearest neighbours, which are determined by the choice of lattice spatial derivatives.

As in the case of leapfrog algorithms, to apply these algorithms to the case of an expanding universe, a careful choice of *dof* has to be taken. This choice will again be presented in Sections 10.4-10.6. Assuming we have *dof* such that the kernels are independent of the momenta, the velocity- and position-Verlet algorithms in respective 'kick-drift-kick' and 'drift-kick-drift' schemes read as

*Velocity-Verlet in an expanding background*

$$\Delta_{\hat{0}/2}^+ \pi_a(\mathbf{n}, n_0) = \mathcal{K}_a[a(n_0), \bar{V}(n_0), \bar{K}(n_0), \bar{G}(n_0)], \quad (10.130)$$

$$\Delta_{\hat{0}/2}^+ \pi_i(\mathbf{n}, n_0) = \mathcal{K}_i[\{f_j(\mathbf{m}, n_0)\}, a(n_0)], \quad (10.131)$$

$$\Delta_0^+ a(n_0) = \pi_a(n_0 + 1/2), \quad (10.132)$$

$$a(n_0 + 1/2) = \frac{1}{2}(a(n_0) + a(n_0 + 1)), \quad (10.133)$$

$$\Delta_0^+ f_i(\mathbf{n}, n_0) = \mathcal{D}_i[\pi_i(\mathbf{n}, n_0 + 1/2), a(n_0 + 1/2)], \quad (10.134)$$

$$\Delta_{0/2}^+ \pi_i(\mathbf{n}, n_0 + 1/2) = \mathcal{K}_i[\{f_j(\mathbf{m}, n_0 + 1)\}, a(n_0 + 1)], \quad (10.135)$$

$$\Delta_{0/2}^+ \pi_a(\mathbf{n}, n_0 + 1/2) = \mathcal{K}_a[a(n_0 + 1), \bar{V}(n_0 + 1), \bar{K}(n_0 + 1), \bar{G}(n_0 + 1)], \quad (10.136)$$

*Position-Verlet in an expanding background*

$$\Delta_{0/2}^+ f_i(\mathbf{n}, n_0) = \mathcal{D}_i[\pi_i(\mathbf{n}, n_0), a(n_0)], \quad (10.137)$$

$$\Delta_{0/2}^+ a(n_0) = \pi_a(n_0), \quad (10.138)$$

$$\Delta_0^+ \pi_i(\mathbf{n}, n_0) = \mathcal{K}_i[\{f_j(\mathbf{m}, n_0 + 1/2)\}, a(n_0 + 1/2)], \quad (10.139)$$

$$\bar{K}(n_0 + 1/2) = \frac{1}{2} (\bar{K}(n_0 + 1) + \bar{K}(n_0)) \quad (10.140)$$

$$\Delta_0^+ \pi_a(\mathbf{n}, n_0) = \mathcal{K}_a[a(n_0 + 1/2), \bar{K}(n_0 + 1/2), \bar{G}(n_0 + 1/2), \bar{V}(n_0 + 1/2)], \quad (10.141)$$

$$\Delta_{0/2}^+ a(n_0 + 1/2) = \pi_a(n_0 + 1), \quad (10.142)$$

$$\Delta_{0/2}^+ f_i(\mathbf{n}, n_0 + 1/2) = \mathcal{D}_i[\pi_i(\mathbf{n}, n_0 + 1), a(n_0 + 1)], \quad (10.143)$$

It is important to note that in both position- and velocity-Verlet algorithms for an expanding background, the kernels  $\mathcal{K}_i[\dots]$  of the matter *dof* must not depend on  $\pi_a$ , as the latter already depend on the conjugate momenta through the volume averaged kinetic energy  $\bar{K}[\{\pi_j\}]$ . An advantage of the Verlet algorithm(s) is that they can readily be turned into more accurate schemes, as will be explained in Section 10.3.4.1.

### 10.3.4 Higher-order integrators

Here we show the construction of higher-order integrators with accuracy  $\mathcal{O}(\delta t^4)$ ,  $\mathcal{O}(\delta t^6)$ ,  $\mathcal{O}(\delta t^8)$  and even  $\mathcal{O}(\delta t^{10})$ , based on the use of  $\mathcal{O}(\delta t^2)$  staggered/synchronous leapfrog algorithms as building blocks.

#### 10.3.4.1 Yoshida method: recursive Verlet integration

The  $\mathcal{O}(\delta t^2)$  Verlet integration methods, introduced in Section 10.3.3.2 to solve the problem  $\ddot{x}(t) = \mathcal{K}[x(t)]$  with initial conditions  $x(t_0) = x_0$ ,  $\dot{x}(t_0) = \pi_0$ , can be used recursively as building blocks to conveniently construct integrators of higher (even) order  $\mathcal{O}(\delta t^n)$ . The idea is to decompose appropriately a single time step  $\delta t$  into  $s$  sub-steps  $\delta t_i = w_i \delta t$  (with  $\sum_{i=1}^s w_i = 1$ ), in such a way that the errors of the intermediate steps cancel up to order  $n$ . In practice, the only thing that has to be done is to iterate  $s$ -times the Verlet algorithm (10.119) or (10.122), using each time the appropriate  $\delta t_i$  sub-step. For example, using (10.119) as the building

block, one full step  $\delta t$  of the algorithm must be divided in the sum of different  $\delta t_i$ 's as follows,

$$\left\{ \begin{array}{l} t^{(0)} = t_n \\ \pi^{(0)} \equiv \pi_n \\ x^{(0)} \equiv x_n \end{array} \right\} \Rightarrow \left\{ \begin{array}{l} \pi_{1/2}^{(i)} = \pi^{(i-1)} + \omega_i \frac{\delta t}{2} \mathcal{K}[x^{(i-1)}] \\ x^{(i)} = x^{(i-1)} + \pi_{1/2}^{(i)} \omega_i \delta t \\ \pi^{(i)} = \pi_{1/2}^{(i)} + \omega_i \frac{\delta t}{2} \mathcal{K}[x^{(i)}] \end{array} \right\}_{i=1, \dots, s} \Rightarrow \left\{ \begin{array}{l} t_{n+1} = t_n + \delta t \\ \pi_{n+1} \equiv \pi^{(s)} \\ x_{n+1} \equiv x^{(s)} \end{array} \right\}.$$

For information about how to construct a specific algorithm, i.e. how to find the corresponding weights  $\omega_i$ , we refer the interested reader to the original paper by Yoshida [420]. Here we simply collect in Table 10.1 sets of  $\delta t_i$ 's characterizing algorithms of order  $O(\delta t^4)$ ,  $O(\delta t^6)$ ,  $O(\delta t^8)$  and  $O(\delta t^{10})$ , see [420, 421] for their derivation. We will refer to these algorithms as *VV4*, *VV6*, *VV8* and *VV10*, while we will refer to the standard velocity Verlet building block as *VV2*.

Some comments are, however, in order. First, the number of steps required to reach a given accuracy grows quickly. For example, *VV4* requires only 3 times more operations than *VV2*, while *VV10* requires 31 times more operations than *VV2*. Actually, to go from one algorithm to the next, the number of steps in each iteration is slightly more than doubled every time. This gives a rule of thumb as of when it is beneficial to use the next more accurate algorithm: if in order to reach some target precision, the time step must be decreased by more than a factor two, then we should consider using the next more accurate algorithm.

This said, let us write for completeness how this algorithm reads for our expanding fields, again assuming that a clever choice of *dof* has been made

$$\left\{ \begin{array}{l} \pi_i^{(0)} \equiv \pi_i(\mathbf{n}, n_0) \\ f_i^{(0)} \equiv f_i(\mathbf{n}, n_0) \\ a^{(0)} \equiv a(n_0) \\ \pi_a^{(0)} \equiv \pi_a(n_0) \end{array} \right\} \Rightarrow \left\{ \begin{array}{l} \pi_{a,1/2}^{(p)} = \pi_a^{(p-1)} + \frac{\omega_p \delta \eta}{2} \mathcal{K}_a[a^{(p-1)}, \bar{K}^{(p-1)}, \bar{G}^{(p-1)}, \bar{V}^{(p-1)}] \\ \pi_{i,1/2}^{(p)} = \pi_i^{(p-1)} + \frac{\omega_p \delta \eta}{2} \mathcal{K}_i[a^{(p-1)}, f_j^{(p-1)}] \\ a^{(p)} = a^{(p-1)} + \omega_p \delta \eta \pi_{a,1/2}^{(p)} \\ a_{1/2}^{(p)} = \frac{1}{2} (a^{(p)} + a^{(p-1)}) \\ f_i^{(p)} = f_i^{(p-1)} + \omega_p \delta \eta \mathcal{D}[a_{1/2}^{(p)}, \pi_{i,1/2}^{(p)}] \\ \pi_i^{(p)} = \pi_{i,1/2}^{(p)} + \frac{\omega_p \delta \eta}{2} \mathcal{K}_i[a^{(p)}, f_j^{(p)}] \\ \pi_a^{(p)} = \pi_{a,1/2}^{(p)} + \frac{\omega_p \delta \eta}{2} \mathcal{K}_a[a^{(p)}, \bar{K}^{(p)}, \bar{G}^{(p)}, \bar{V}^{(p)}] \end{array} \right\}_{p=1, \dots, s} \Rightarrow \left\{ \begin{array}{l} \pi_i(\mathbf{n}, n_0 + 1) \equiv \pi_i^{(s)} \\ f_i(\mathbf{n}, n_0 + 1) \equiv f_i^{(s)} \\ a(n_0 + 1) \equiv a^{(s)} \\ b(n_0 + 1) \equiv b^{(s)} \end{array} \right. \quad (10.144)$$



where  $a_{1/2}^{(p)}, \pi_{i\ 1/2}^{(p)}, \pi_a^{(p)}$  are intermediate values and we explicitly wrote down the temporal derivatives. Note also that the same can be done using position-Verlet as a building block.

### 10.3.5 Integrator properties

Finally, before we move into the discussion of applications of standard algorithms into our interactive field theories, let us mention the list of desired properties that we may want to demand in order to have a good numerical integrator:

- *Time reversal.* Dynamical processes are time-reversible if their EOM are invariant under a change in the sign of the time variable. Since this is an exact symmetry of the continuum EOM, it is desirable that a numerical approximation respects the same property. An evolution algorithm for discrete EOM respects time reversibility if we can integrate forward  $p$  steps, and then reverse the direction of integration and integrate backwards  $p$  steps, to arrive exactly at the original starting initial condition.
- *Symplectic nature.* Dynamical processes driven by conservative forces (i.e. from kernels that do not depend on conjugate momenta or on any time-dependent external function) respect the *Liouville's theorem*; the infinitesimal phase-space area per degree of freedom is preserved as the system evolves. As this area-preserving property is an exact feature of the continuum EOM which we want to solve, it is desirable that a numerical integrator respects such a conservation law. Numerical schemes that do so are referred to as *symplectic*. The relevance of having a symplectic integrator is that they possess a great stability: since the phase-space area is preserved during the evolution, there cannot be situations where the field amplitudes or their conjugate momenta (and hence their energy) increase without bound, because this would expand the phase-space area. Symplectic integrators offer therefore numerical conservation of energy<sup>6</sup> to a good degree, which improves the higher the accuracy  $\mathcal{O}(\delta t^p)$  of the integrator itself.
- *Integration accuracy.* Depending on the nature of a given numerical integrator method, we may obtain an accuracy in the integrated field amplitudes and conjugate momenta of the order  $\mathcal{O}(\delta t^p)$ , typically with  $p = 2, 4, 6, 8$  or even 10. Our default algorithms have always an accuracy  $\mathcal{O}(\delta t^2)$ . However, basic  $\mathcal{O}(\delta t^2)$  integrators can be converted into higher-order integrators using techniques due to *Haruo Yoshida*. Essentially, by applying the basic algorithm over a number of adjusted different timesteps chosen so that the errors cancel, far higher-order integrators can be obtained. For symplectic integrators this is particularly interesting, as the degree of conservation of energy (Hubble constraint for expanding backgrounds) will increase significantly as we improve the integrator accuracy.

---

<sup>6</sup>In the case of scenarios with an expanding background, by conservation of energy we actually mean the preservation of the Hubble constraint  $3m_p^2 H^2 = \rho$ .

### 10.3. Field dynamics in a computer: the lattice approach

Name	Order	$w_i = \frac{\delta t_i}{\delta t}$	$q$
VV4	$O(\delta t^4)$	$w_1 = w_3 = 1.351207191959657771818$ $w_2 = -1.702414403875838200264$	3
VV6	$O(\delta t^6)$	$w_1 = w_7 = 0.78451361047755726382$ $w_2 = w_6 = 0.23557321335935813368$ $w_3 = w_5 = -1.1776799841788710069$ $w_4 = 1.3151863206839112189$	7
VV8	$O(\delta t^8)$	$w_1 = w_{15} = 0.74167036435061295345$ $w_2 = w_{14} = -0.40910082580003159400$ $w_3 = w_{13} = 0.19075471029623837995$ $w_4 = w_{12} = -0.57386247111608226666$ $w_5 = w_{11} = 0.29906418130365592384$ $w_6 = w_{10} = 0.33462491824529818378$ $w_7 = w_9 = 0.31529309239676659663$ $w_8 = -0.79688793935291635402$	15
VV10	$O(\delta t^{10})$	$w_1 = w_{31} = -0.48159895600253002870$ $w_2 = w_{30} = 0.0036303931544595926879$ $w_3 = w_{29} = 0.50180317558723140279$ $w_4 = w_{28} = 0.28298402624506254868$ $w_5 = w_{27} = 0.80702967895372223806$ $w_6 = w_{26} = -0.026090580538592205447$ $w_7 = w_{25} = -0.87286590146318071547$ $w_8 = w_{24} = -0.52373568062510581643$ $w_9 = w_{23} = 0.44521844299952789252$ $w_{10} = w_{22} = 0.18612289547097907887$ $w_{11} = w_{21} = 0.23137327866438360633$ $w_{12} = w_{20} = -0.52191036590418628905$ $w_{13} = w_{19} = 0.74866113714499296793$ $w_{14} = w_{18} = 0.066736511890604057532$ $w_{15} = w_{17} = -0.80360324375670830316$ $w_{16} = 0.91249037635867994571$	31

Table 10.1 – Time steps required to construct higher-order velocity Verlet algorithms. A given algorithm requires  $q$  iterations. The coefficients are symmetric, in each case, with respect to the intermediate  $w_i$  parameter. Note that we reported here only the algorithms of a given order with the minimal number of steps. For others, see Ref. [421].

- *Efficiency.* We obviously want to make our numerical integration as fast as possible, so if we need to choose between two integration methods with the same accuracy  $\mathcal{O}(\delta t^p)$  but different levels of energy conservation, we might still prefer the faster integrator even if it has worse energy conservation (as long as it can be confronted against the outcome from other integrators with better energy conservation).

## 10.4 Lattice formulation of interacting scalar fields

### 10.4.1 Continuum formulation and natural variables

Let us consider a set of interacting real scalar fields  $\{\phi_a\}$  with canonically normalized kinetic terms. If they live in a FLRW background  $g_{\mu\nu} = \text{diag}(-a^{2\alpha}, a^2, a^2, a^2)$ , with line element  $ds^2 = -a^{2\alpha}\delta\eta^2 + a^2(\eta)d\vec{x}^2$  and  $\alpha$ -time  $\eta$ , their action can be written like

$$S = - \int d^4x \sqrt{-g} \left( \frac{1}{2} \partial_\mu \phi_b \partial^\mu \phi_b + V(\{\phi_c\}) \right) = \left( \frac{f_*}{\omega_*} \right)^2 \tilde{S}, \quad (10.145)$$

with

$$\tilde{S} = \int d^3\tilde{x} \delta\tilde{\eta} \left\{ \frac{1}{2} a^{3-\alpha} \sum_b \tilde{\phi}_b'^2 - \frac{1}{2} a^{1+\alpha} \sum_{b,k} (\tilde{\nabla}_k \tilde{\phi}_b)^2 - a^{3+\alpha} \tilde{V}(\{\tilde{\phi}_c\}) \right\}, \quad (10.146)$$

the action expressed in the dimensionless variables

$$\tilde{\phi}_a \equiv \frac{\phi_a}{f_*}, \quad \delta\tilde{\eta} \equiv a^{-\alpha} \omega_* dt, \quad d\tilde{x}^i \equiv \omega_* dx^i, \quad (10.147)$$

where  $' \equiv d/d\tilde{\tau}$  and  $\tilde{\nabla}_i \equiv \partial/\partial\tilde{x}^i$ , and where a dimensionless potential has been introduced as

$$\tilde{V}(\{\tilde{\phi}_c\}) \equiv \frac{1}{f_*^2 \omega_*^2} V(\{\phi_c\}) \Big|_{\phi_c = f_* \tilde{\phi}_c}. \quad (10.148)$$

The EOM in the dimensionless variables follow immediately from varying the action  $\tilde{S}$ ,

$$\tilde{\phi}_a'' - a^{-2(1-\alpha)} \tilde{\nabla}^2 \tilde{\phi}_a + (3-\alpha) \frac{a'}{a} \tilde{\phi}_a' + a^{2\alpha} \tilde{V}_{,\tilde{\phi}_a} = 0. \quad (10.149)$$

The expansion of the universe, on the other hand, is dictated by the Friedmann equations, sourced by the volume averaged energy and pressure densities  $\langle \rho_\phi \rangle$ ,  $\langle p_\phi \rangle$  of the fields. Writing the relevant part of Eqs. (10.52), (10.53) in program variables (10.147), we have

$$a'' = a^{2\alpha+1} \left( \frac{f_*}{m_p} \right)^2 \frac{1}{6} [(2\alpha-1)\langle \tilde{\rho}_\phi \rangle - 3\langle \tilde{p}_\phi \rangle], \quad a'^2 = a^{2\alpha+2} \left( \frac{f_*}{m_p} \right)^2 \frac{1}{3} \langle \tilde{\rho}_\phi \rangle, \quad (10.150)$$

## 10.4. Lattice formulation of interacting scalar fields

with *program energy* and *pressure densities* defined as

$$\bar{\rho}_\phi \equiv \frac{\rho}{f_*^2 \omega_*^2} = \tilde{K}_\phi + \tilde{G}_\phi + \tilde{V}, \quad ; \quad \bar{p}_\phi \equiv \frac{p}{f_*^2 \omega_*^2} = \tilde{K}_\phi - \frac{1}{3} \tilde{G}_\phi - \tilde{V}, \quad (10.151)$$

where

$$\tilde{K}_\phi = \frac{1}{2a^{2\alpha}} \sum_i (\tilde{\phi}'_i)^2, \quad \tilde{G}_\phi = \frac{1}{2a^2} \sum_{i,k} (\tilde{V}_k \tilde{\phi}_i)^2. \quad (10.152)$$

As in reality we need the volume averages  $\langle \dots \rangle$  of expressions (10.152), we define for convenience

$$E_K \equiv \frac{1}{2a^{2\alpha}} \sum_i \langle (\tilde{\phi}'_i)^2 \rangle, \quad E_G \equiv \frac{1}{2a^2} \sum_{i,k} \langle (\tilde{V}_k \tilde{\phi}_i)^2 \rangle, \quad E_V \equiv \langle \tilde{V}(\{\tilde{\phi}_j\}) \rangle, \quad (10.153)$$

so that the Friedmann equations read

$$\left( \frac{a'}{a} \right)^2 = \frac{a^{2\alpha}}{3} \left( \frac{f_*}{m_p} \right)^2 [E_K + E_G + E_V], \quad (10.154)$$

$$\frac{a''}{a} = \frac{a^{2\alpha}}{3} \left( \frac{f_*}{m_p} \right)^2 [(\alpha - 2)E_K + \alpha E_G + (\alpha + 1)E_V]. \quad (10.155)$$

If on the contrary the expansion of the universe is sourced by an external fluid, say with constant *barotropic* equation of state  $w \equiv \langle p \rangle / \langle \rho \rangle$ , then we obtain the scale factor simply from the analytical expression

$$a(\tilde{\eta}) = a_0 \left( 1 + \frac{1}{p} \tilde{\mathcal{H}}_0 (\tilde{\eta} - \tilde{\eta}_0) \right)^p, \quad \text{with} \quad p = \frac{2}{3(1+w) - 2\alpha}, \quad (10.156)$$

where we fixed the initial conditions at an initial time  $\tilde{\eta}_0$  ( $= 0$ , typically) to  $a_0 = a(\tilde{\eta}_0)$  and  $\tilde{\mathcal{H}}_0 \equiv \tilde{\mathcal{H}}(\tilde{\eta}_0)$ , and introduced a dimensionless *program Hubble rate*  $\tilde{\mathcal{H}} = \frac{a^\alpha}{\omega_*} H$ , with  $H \equiv \dot{a}/a$  the physical Hubble parameter.

*Program variables* –. We will refer to the dimensionless field and space-time variables in Eq. (10.147) as the *lattice* or *program variables*, and to the dimensionless potential in Eq. (10.148) as the *lattice* or *program potential*<sup>7</sup>. The values of  $\alpha$ ,  $f_*$  and  $\omega_*$  can be chosen, in principle, arbitrarily. However, certain choices can be more convenient than others, depending on the form of the potential  $V$ . First, let us consider the choice of  $\alpha$ . In principle, this could be chosen at will: we could take  $\alpha = 0$  if we wanted to solve our dynamics in cosmic time, whereas we could choose  $\alpha = 1$  if we wanted to solve it in conformal time (up to dimensionful constant factors). However, there are many situations in which an oscillatory field dominates the energy budget of the system for a long time, with a time-dependent oscillation period  $T_{\text{osc}}(t)$ . As the integration techniques introduced in the previous sections assume a constant time step, we would not be able to resolve later oscillations of the field with the same accuracy as early ones. This could cause stability problems in the simulation at late times, if the

<sup>7</sup>We will also define dimensionless *program variables* for the charged scalars and gauge fields in Eqs. (10.226) and (10.309).

oscillation period were to decrease with time. Therefore, if we were in such a situation, it would be extremely convenient to choose a value of  $\alpha$  that makes the oscillation period constant in the new  $\alpha$ -time variable. In Section 10.8 we show an example of this in the context of a scalar field oscillating around the minimum of a monomial potential.

Let us now consider  $f_*$ . For this, let us imagine a scenario in which one scalar field (say  $\phi$ ) has initially a homogeneous configuration with a certain initial amplitude  $\Phi_*$ . A natural choice would be to fix the dimensionful normalization constant as  $f_* = \Phi_*$ , so that as long as that field dominates the energy budget during the dynamics, its normalized amplitude  $\tilde{\phi}$  will be of order unity (modulo red-shifting dilution factors due to the expansion of the universe). This is often the case in models with parametric resonance, such as the preheating scenario presented in Section 10.8. If on the contrary, relevant field(s) in the dynamics start with vanishing (or small) amplitude but acquire a vacuum expectation value  $\langle\phi\rangle = v$  later on, it might be convenient to take  $f_* = v$ . This will be the case e.g. in models with spontaneous symmetry breaking, like in phase transitions and cosmic defect formation. Finally, let us consider  $\omega_*$ . If the dominant scalar field of the system oscillates say with a frequency  $\Omega_{\text{osc}}(\eta)$  (possibly time-dependent), it can be convenient to take, for instance,  $\omega_* = \Omega_{\text{osc}}(\eta_*)$ , at the time  $\eta = \eta_*$  of onset of field oscillations. However, if the time scale  $\Delta\eta_*$  of excitation of other fields is rather the relevant time scale in the problem, it might be more convenient to choose  $\omega_*$  of the order of  $1/\Delta\eta_*$ . Another possibility would be to simply set  $f_* = \omega_*$ , so we prevent ratios  $f_*/\omega_*$  (naturally appearing e.g. in the initial condition of scalar field fluctuations) to become tiny or extremely large, see Section 10.7.

In summary, if the choice of  $\alpha$ ,  $f_*$  and  $\omega_*$  is made judiciously, it will lead to order unity field amplitudes and time scales, in the naturally dimensionless program variables. This would achieve a twofold objective. first, a better handle of the program variables in the computer, as order unity numbers are more convenient to deal with from a computational point of view. And second, an easier and more transparent conversion of the dimensionless computer program variables into physical mass/time scales characteristic of each given scenario. From now on, we assume that independently of the scenario we are dealing with, a convenient choice of  $(\alpha, f_*, \omega_*)$  has been made. In order to solve the dynamics of the interacting scalar fields on a computer, we need now to obtain some discretized version of the continuum EOM (10.149) expressed in the natural variables (10.147), (10.148). We need to do two things: first, to substitute somehow the time and spatial continuum derivatives by lattice operators mimicking such continuum differential operations up to some order  $\mathcal{O}(\delta x^\mu)$ ; and second, to solve the resulting discrete lattice EOM with some algorithms. Our toolkit to address these two aspects was provided in Section 10.3, where we introduced both lattice differential operators and evolution algorithms. Armed with such toolkit, we have essentially two options: 1) *Lattice action approach*. This is based on discretizing the continuum action, so that it is substituted by a lattice version. Varying such lattice action with respect to the lattice field *dof*, leads to lattice EOM enjoying whichever symmetry the lattice action enjoyed in first place. Constraint equations (expected as a consequence of the symmetries) are then automatically satisfied at the lattice level.

2) *EOM discretization approach*. This is based on discretizing the continuum EOM directly. Here we simply substitute the partial derivatives involved in certain terms of the continuum EOM by appropriate lattice operators mimicking those continuum derivatives. This method allows to envisage lattice EOM adapted to essentially any evolution algorithm we wish to use. Either approach 1) or 2) may have its advantages and disadvantages depending on the model and circumstances. Whereas for EOM in flat space-time the two approaches are essentially very similar, this might not be case in an expanding universe, particularly in the presence of gauge fields. As for the time being we only deal with scalar sectors in expanding backgrounds in this section, we will simply present next the series of algorithms that one can envisage to engineer lattice EOM that can be solved with the evolution algorithms we introduced in Section 10.3.

## 10.4.2 Lattice formulation of interacting scalar fields: $\mathcal{O}(dt^2)$ accuracy methods

### 10.4.2.1 Staggered leapfrog from a lattice action

A lattice version of action (10.146) can be written using e.g. forward derivatives [c.f. Eq. (10.68)] for the time derivatives and the spatial gradients. Promoting integrals into discrete sums  $\int d\eta(\dots) \equiv \delta\eta \sum_{n_0}(\dots)$ ,  $\int dx^3(\dots) \equiv \delta x^3 \sum_{\mathbf{n}}(\dots)$ , we obtain

$$\tilde{S}_L = \delta\tilde{\eta}\delta\tilde{x}^3 \sum_{n_0} \sum_{\mathbf{n}} \left\{ \frac{1}{2} a_{+0/2}^{3-\alpha} \sum_b (\tilde{\Delta}_0^+ \tilde{\phi}^b)^2 - \frac{1}{2} a^{1+\alpha} \sum_{b,k} (\tilde{\Delta}_k^+ \tilde{\phi}^b)^2 - a^{3+\alpha} \tilde{V}(\{\tilde{\phi}_c\}) \right\}. \quad (10.157)$$

Note that we have not determined yet at what times the scale factor lives in, and we have rather referred to a scale factor at integer and half-integers times, whenever appropriate. The logic to specify where the scale factor lives in each term of the action, is to consider the time the operator it is multiplied to lives in. Thus, as  $(\tilde{\Delta}_0^+ \tilde{\phi}^{(a)})^2$  lives at  $n_0 + 1/2$ , we write its pre-factor as  $a_{+0/2}^{3-\alpha}$ , whereas  $(\tilde{\Delta}_k^+ \tilde{\phi}^{(a)})^2$  lives at  $n_0$ , so we write its pre-factor as  $a^{1+\alpha}$ , etc. Varying this action with respect each field *dof*,  $\delta_{\phi_a} S_L = 0$ , leads to the discrete EOM

$$\tilde{\Delta}_0^- [a_{+0/2}^{3-\alpha} \tilde{\Delta}_0^+ \tilde{\phi}_b] = a^{1+\alpha} \sum_k \tilde{\Delta}_k^- \tilde{\Delta}_k^+ \tilde{\phi}_b - a^{3+\alpha} \tilde{V}_{,\tilde{\phi}_b}, \quad b = 1, 2, \dots, N_s \quad (10.158)$$

with  $N_s$  the total number of scalar fields.

Let us now deal with the expansion of the universe. We need to express the Friedmann equations as a function of program expressions for the volume averaged field energy and pressure densities  $\langle \rho_\phi \rangle$ ,  $\langle p_\phi \rangle$ . We introduce first a discretized version of  $E_K, E_G$  and  $E_V$ , c.f. Eq. (10.153),

$$E_K \equiv \frac{1}{2a_{+0/2}^{2\alpha}} \sum_a \langle (\tilde{\Delta}_0^+ \tilde{\phi}_a)^2 \rangle, \quad E_G \equiv \frac{1}{2a^2} \sum_{a,k} \langle (\tilde{\Delta}_k^+ \tilde{\phi}_a)^2 \rangle, \quad E_V \equiv \langle \tilde{V}(\{\tilde{\phi}_c\}) \rangle \quad (10.159)$$

with  $E_G$  and  $E_V$  naturally living at integer times  $n_0$ , and  $E_K$  at semi-integer times  $n_0 + 1/2$ . We need to decide now whether we consider a scale factor living 'naturally' at integer or semi-integer times. If we consider that  $a$  lives at semi-integer times, then it is natural to define the operator  $b \equiv \tilde{\Delta}_0^+ a_{-0/2}$  living at integer times, and hence identify the first and second derivative [via the Friedmann equations in (10.154), (10.155)] of the scale factor as

$$a' \rightarrow \tilde{\Delta}_0^+ a_{-0/2} \equiv b, \quad (10.160)$$

$$a'' \rightarrow \tilde{\Delta}_0^+ b = \frac{1}{3} \left( \frac{f_*}{m_p} \right)^2 a_{+0/2}^{1+2\alpha} \left[ (\alpha - 2)E_K + \alpha \overline{E_G} + (\alpha + 1)\overline{E_V} \right]. \quad (10.161)$$

with  $\overline{E_G} \equiv (E_G + E_{G,+0})/2$  and  $\overline{E_V} \equiv (E_V + E_{V,+0})/2$ , so that they live at semi-integer times, like the scale factor and  $E_K$ . Alternatively, if we think of the scale factor living at integer times, we can define the operator  $b_{+0/2} \equiv (\tilde{\Delta}_0^+ a)$  living at semi-integer times, and identify the first and second derivative of the scale factor as

$$a' \rightarrow \tilde{\Delta}_0^+ a \equiv b_{+0/2}, \quad (10.162)$$

$$a'' \rightarrow \tilde{\Delta}_0^+ b_{-0/2} = \frac{1}{6} \left( \frac{f_*}{m_p} \right)^2 a^{1+2\alpha} \left[ (\alpha - 2)\overline{E_K} + \alpha E_G + (\alpha + 1)E_V \right], \quad (10.163)$$

with  $\overline{E_K} \equiv (E_{K,-0/2} + E_{K,+0/2})/2$  living at integer times, as much as  $a, E_G$  and  $E_V$ .

From a practical or computational point of view, choosing a scale factor living at integer or semi-integer times, is actually irrelevant. If we choose that it lives at e.g. integer times, we will always be forced to obtain it also, within each iteration, at semi-integer times, from the semi-sum of its two values at the closest integer times. And vice versa. In order to provide an iterative scheme, we still need to decide on the *conjugate momenta*  $\tilde{\pi}_{+0/2}^{(a)}$ , which will be implemented through forward derivative operators. The question is whether to choose that  $\tilde{\pi}_{+0/2}^{(a)}$  represents the time-derivative of each field, i.e.  $\phi'_a$ , or rather represents  $a^{3-\alpha}\phi'_a$ , as the EOM actually naturally suggest. It turns out that depending on this choice the integrator will be accurate to order  $\mathcal{O}(\delta\eta)$  or  $\mathcal{O}(\delta\eta^2)$ . All together, we can obtain the following implementations of a staggered leapfrog algorithm (here *IC* stands for *Initial Condition*, and *HC* for *Hubble Constraint*):

#### 10.4. Lattice formulation of interacting scalar fields

I) Iterative scheme for  $\tilde{\pi}_{+0/2}^{(a)} \equiv \tilde{\Delta}_0^+ \tilde{\phi}_a$  and scale factor  $a(n_0 + 1/2)$ :

$$IC : \quad \{\tilde{\phi}_a, b\} \text{ at } \tilde{\eta}_0, \quad \{\tilde{\pi}_{-0/2}^{(a)}, a_{-0/2}\} \text{ at } \tilde{\eta}_0 - 0.5\delta\tilde{\eta} \quad (10.164)$$

$$a_{+0/2} = a_{-0/2} + b\delta\tilde{\eta} \longrightarrow a \equiv (a_{+0/2} + a_{-0/2})/2 \quad (10.165)$$

$$\tilde{\pi}_{+0/2}^{(a)} = \left(\frac{a_{-0/2}}{a_{+0/2}}\right)^{3-\alpha} \tilde{\pi}_{-0/2}^{(a)} + a_{+0/2}^{-(3-\alpha)} \left( a^{1+\alpha} \sum_k \tilde{\Delta}_k^- \tilde{\Delta}_k^+ \tilde{\phi}^{(a)} - a^{3+\alpha} \tilde{V}_{\tilde{\phi}^{(a)}} \right) \quad (10.166)$$

$$\tilde{\phi}_{+0}^{(a)} = \tilde{\phi}^{(a)} + \delta\tilde{\eta} \tilde{\pi}_{+0/2}^{(a)} \quad (10.167)$$

$$b_{+0} = b + \frac{\delta\tilde{\eta}}{3} \left(\frac{f_*}{m_p}\right)^2 a_{+0/2}^{1+2\alpha} \left[ (\alpha-2)E_K + \alpha\overline{E_G} + (\alpha+1)\overline{E_V} \right], \quad (10.168)$$

$$HC : \quad b^2 = \frac{1}{3} \left(\frac{f_*}{m_p}\right)^2 a^{2\alpha+1} \left( \overline{E_K} + E_G + E_V \right). \quad (10.169)$$

II) Iterative scheme for  $\tilde{\pi}^{(a)} \equiv \tilde{\Delta}_0^+ \tilde{\phi}_{-0/2}^{(a)}$  and scale factor  $a(n_0)$

$$IC : \quad \{\tilde{a}, \tilde{\pi}^{(a)}\} \text{ at } \tilde{\eta}_0, \quad \{\tilde{\phi}_{-0/2}^{(a)}, b_{-0/2}\} \text{ at } \tilde{\eta}_0 - 0.5\delta\tilde{\eta} \quad (10.170)$$

$$\tilde{\phi}_{+0/2}^{(a)} = \tilde{\phi}_{-0/2}^{(a)} + \delta\tilde{\eta} \tilde{\pi}^{(a)} \quad (10.171)$$

$$b_{+0/2} = b_{-0/2} + \frac{\delta\tilde{\eta}}{3} \left(\frac{f_*}{m_p}\right)^2 a^{1+2\alpha} \left[ (\alpha-2)E_K + \alpha\overline{E_G} + (\alpha+1)\overline{E_V} \right], \quad (10.172)$$

$$a_{+0} = a + b_{+0/2} \delta\tilde{\eta} \longrightarrow a_{+0/2} \equiv (a_0 + a)/2, \quad (10.173)$$

$$\tilde{\pi}_{+0}^{(a)} = \left(\frac{a}{a_{+0}}\right)^{3-\alpha} \tilde{\pi}^{(a)} + a_{+0}^{-(3-\alpha)} \left( a_{+0/2}^{1+\alpha} \sum_k \tilde{\Delta}_k^- \tilde{\Delta}_k^+ \tilde{\phi}_{+0/2}^{(a)} - a_{+0/2}^{3+\alpha} \tilde{V}_{\tilde{\phi}^{(a)}} \Big|_{+0/2} \right), \quad (10.174)$$

$$HC : \quad b_{+0/2}^2 = \frac{1}{3} \left(\frac{f_*}{m_p}\right)^2 a_{+0/2}^{2\alpha+1} \left( \overline{E_K} + E_{G,+0/2} + E_{V,+0/2} \right), \quad (10.175)$$

III) Iterative scheme for  $\tilde{\pi}_{+0/2}^{(a)} \equiv a_{+0/2}^{3-\alpha} \tilde{\Delta}_0^+ \tilde{\phi}_a$  and scale factor  $a(n_0)$

$$IC : \quad \{\tilde{\phi}^{(a)}, a\} \text{ at } \tilde{\eta}_0, \quad \{\tilde{\pi}_{-0/2}^{(a)}, b_{-0/2}\} \text{ at } \tilde{\eta}_0 - 0.5\delta\tilde{\eta} \quad (10.176)$$

$$\tilde{\pi}_{+0/2}^{(a)} = \tilde{\pi}_{-0/2}^{(a)} + \left( a^{1+\alpha} \sum_k \tilde{\Delta}_k^- \tilde{\Delta}_k^+ \tilde{\phi}^{(a)} - a^{3+\alpha} \tilde{V}_{\tilde{\phi}^{(a)}} \right) \quad (10.177)$$

$$b_{+0/2} = b_{-0/2} + \frac{\delta\tilde{\eta}}{3} \left(\frac{f_*}{m_p}\right)^2 a^{1+2\alpha} \left[ (\alpha-2)\overline{E_K} + \alpha E_G + (\alpha+1)E_V \right], \quad (10.178)$$

$$a_{+0} = a + b_{+0/2} \delta\tilde{\eta} \longrightarrow a_{+0/2} \equiv (a_{+0} + a_0)/2, \quad (10.179)$$

$$\tilde{\phi}_{+0}^{(a)} = \tilde{\phi}^{(a)} + \delta\tilde{\eta} \tilde{\pi}_{+0/2}^{(a)} a_{+0/2}^{-(3-\alpha)}, \quad (10.180)$$

$$HC : \quad b_{+0/2}^2 = \frac{1}{3} \left(\frac{f_*}{m_p}\right)^2 a_{+0/2}^{2\alpha+1} \left( E_K + \overline{E_G} + \overline{E_V} \right), \quad (10.181)$$



IV) Iterative scheme for  $\tilde{\pi}^{(a)} \equiv a^{3-\alpha} \tilde{\Delta}_0^+ \tilde{\phi}_{-0/2}^{(a)}$  and scale factor  $a(n_0 + 1/2)$

$$IC : \quad \{\tilde{\pi}^{(a)}, b\} \text{ at } \tilde{\eta}_0, \quad \{\tilde{\phi}_{-0/2}^{(a)}, a_{-0/2}\} \text{ at } \tilde{\eta}_0 - 0.5\delta\tilde{\eta} \quad (10.182)$$

$$a_{+0/2} = a_{-0/2} + b\delta\tilde{\eta} \longrightarrow a \equiv (a_{+0/2} + a_{-0/2})/2 \quad (10.183)$$

$$\tilde{\phi}_{+0/2}^{(a)} = \tilde{\phi}_{-0/2}^{(a)} + \delta\tilde{\eta} \tilde{\pi}^{(a)} a^{-(3-\alpha)} \quad (10.184)$$

$$\tilde{\pi}_{+0}^{(a)} = \tilde{\pi}^{(a)} + a_{+0/2}^{1+\alpha} \sum_k \tilde{\Delta}_k^- \tilde{\Delta}_k^+ \tilde{\phi}_{+0/2}^{(a)} - a_{+0/2}^{3+\alpha} \tilde{V}_{,\tilde{\phi}^{(a)}} \Big|_{+0/2} \quad (10.185)$$

$$b_{+0} = b + \frac{\delta\tilde{\eta}}{3} \left( \frac{f_*}{m_p} \right)^2 a_{+0/2}^{1+2\alpha} \left[ (\alpha-2) \overline{E_K} + \alpha E_{G,+0/2} + (\alpha+1) E_{V,+0/2} \right], \quad (10.186)$$

$$HC : \quad b^2 = \frac{1}{3} \left( \frac{f_*}{m_p} \right)^2 a^{2\alpha+1} (E_K + \overline{E_G} + \overline{E_V}). \quad (10.187)$$

While all these iterative schemes descent from the same action (10.157), they are truly different algorithms, based on the choice of conjugate momenta and time domain of the scale factor. In fact, iterative schemes *I* and *II*, which are basically very similar as they are based on (discretized versions of) the same choice  $\pi_a \equiv \phi'_a$ , are only accurate to order  $\mathcal{O}(\delta\eta)$ . Iterative schemes *III* and *IV*, also very similar to each other as they are based on (discretized versions of) the choice  $\pi_a \equiv a^{3-\alpha} \phi'_a$ , are however accurate to order  $\mathcal{O}(\delta\eta^2)$ . This becomes manifest in numerical simulations by monitoring the Hubble constraint  $3m_p^2 H^2 = \rho$ , which in the case of schemes *I* and *II* is only verified to order  $\mathcal{O}(\delta\eta)$  by Eqs. (10.169), (10.175), whereas in the schemes *III* and *IV*, Eqs. (10.181), (10.187) are verified to order  $\mathcal{O}(\delta\eta^2)$ . This is a first illustration of the importance of choosing the appropriate conjugate momentum to evolve the equations.

#### 10.4.2.2 Synchronized Leapfrog: Position- and Velocity-Verlet

While in Section 10.4.2.1 our starting point was a lattice action from which we derived the lattice EOM, here we will rather discretize directly the continuum EOM, without introducing a conformal rescaling, similarly to what was done in Section 10.4.2.1, using a re-definition of the field variables. Considering again the EOM of  $N_s$  scalar fields canonically normalized, c.f. Eq. (10.149), we immediately conclude that the field variables' kernel depend on the conjugate momenta through the friction term  $(3-\alpha)\mathcal{H}\tilde{\phi}'_b$ . This seemingly appears as an impediment to apply staggered or synchronized leapfrog methods. The EOM as derived initially from the continuum action (10.145), can however be written as

$$(a^{(3-\alpha)} \tilde{\phi}'_b)' - a^{1+\alpha} \tilde{\nabla}^2 \tilde{\phi}_b + a^{3+\alpha} \tilde{V}_{,\tilde{\phi}_b} = 0, \quad b = 1, 2, \dots, N_s, \quad (10.188)$$

so that only when expanding the first term (and after multiplying by  $a^{-(3-\alpha)}$ ), the standard second derivative and friction terms  $\tilde{\phi}''_b + (3-\alpha)\mathcal{H}\tilde{\phi}'_b$  become explicit. Instead of expanding such terms, the form of Eqs. (10.188) invites to rather re-write them more naturally in a

#### 10.4. Lattice formulation of interacting scalar fields

Hamiltonian-like scheme as

$$\tilde{\phi}'_b = a^{-(3-\alpha)} \tilde{\pi}_b, \quad (10.189)$$

$$\tilde{\pi}'_b = a^{1+\alpha} \tilde{\nabla}^2 \tilde{\phi}_b - a^{3+\alpha} \tilde{V}_{,\tilde{\phi}_b}, \quad (10.190)$$

where it is manifest that the kernel does not depend on the conjugate momenta. Analogously, the second Friedmann equation (10.155) can then be written as

$$a' = b, \quad (10.191)$$

$$b' = \frac{a^{1+2\alpha}}{3} \left( \frac{f_*}{m_p} \right)^2 \left[ (\alpha-2)E_K + \alpha E_G + (\alpha+1)E_V \right], \quad (10.192)$$

$$\text{where} \quad E_K \equiv \frac{1}{2a^6} \sum_i \langle (\tilde{\pi}_i)^2 \rangle, \quad E_G \equiv \frac{1}{2a^2} \sum_{i,k} \langle (\tilde{\nabla}_k \tilde{\phi}_i)^2 \rangle, \quad E_V \equiv \langle \tilde{V}(\{\tilde{\phi}_j\}) \rangle, \quad (10.193)$$

This immediately invites for the application of either staggered or synchronized leapfrog methods. In fact, the methods *III* and *IV* from Section 10.4.2.1 correspond precisely to the application of a staggered leapfrog scheme. We will thus focus now on the application of synchronized leapfrog schemes, also known as Verlet integrators, either velocity- or position-based. Following Section 10.4.2.2, these algorithms read:

*I) Velocity-Verlet scheme for interacting scalar fields in an expanding background*

$$IC : \quad \{\tilde{\phi}^{(i)}, \tilde{\pi}^{(i)}, a, b\} \text{ at } \tilde{\eta}_0, \quad (10.194)$$

$$b_{+0/2} = b + \frac{1}{3} \left( \frac{f_*}{m_p} \right)^2 a^{1+2\alpha} \left[ (\alpha-2)E_K + \alpha E_G + (\alpha+1)E_V \right] \frac{\delta \tilde{\eta}}{2}, \quad (10.195)$$

$$\tilde{\pi}_{+0/2}^{(i)} = \tilde{\pi}^{(i)} + \left( a^{1+\alpha} \sum_k \tilde{\Delta}_k^- \tilde{\Delta}_k^+ \tilde{\phi}^{(i)} - a^{3+\alpha} \tilde{V}_{,\tilde{\phi}^{(i)}} \right) \frac{\delta \tilde{\eta}}{2}, \quad (10.196)$$

$$a_{+0} = a + b_{+0/2} \delta \tilde{\eta}, \quad (10.197)$$

$$a_{+0/2} = \frac{a_{+0} + a}{2}, \quad (10.198)$$

$$\tilde{\phi}_{+0}^{(i)} = \tilde{\phi}^{(i)} + \delta \tilde{\eta} \tilde{\pi}_{+0/2}^{(i)} a_{+0/2}^{-(3-\alpha)}, \quad (10.199)$$

$$\tilde{\pi}_{+0}^{(i)} = \tilde{\pi}_{+0/2}^{(i)} + \left( a_{+0}^{1+\alpha} \sum_k \tilde{\Delta}_k^- \tilde{\Delta}_k^+ \tilde{\phi}_{+0}^{(i)} - a_{+0}^{3+\alpha} \tilde{V}_{,\tilde{\phi}^{(i)}} \Big|_{+0} \right) \frac{\delta \tilde{\eta}}{2}, \quad (10.200)$$

$$b_{+0} = b_{+0/2} + \frac{1}{3} \left( \frac{f_*}{m_p} \right)^2 a_{+0}^{1+2\alpha} \left[ (\alpha-2)E_{K,+0} + \alpha E_{G,+0} + (\alpha+1)E_{V,+0} \right] \frac{\delta \tilde{\eta}}{2}, \quad (10.201)$$

$$HC : \quad b^2 = \frac{1}{3} \left( \frac{f_*}{m_p} \right)^2 a^{2(\alpha+1)} (E_K + E_G + E_V), \quad (10.202)$$

*II) Position-Verlet scheme for interacting scalar fields in an expanding background*

$$IC : \quad \{\tilde{\phi}^{(i)}, \tilde{\pi}^{(i)}, a, b\} \text{ at } \tilde{\eta}_0, \quad (10.203)$$

$$a_{+0/2} = a + b \frac{\delta \tilde{\eta}}{2}, \quad (10.204)$$

$$\tilde{\phi}_{+0/2}^{(i)} = \tilde{\phi}^{(i)} + \frac{\delta\tilde{\eta}}{2} \tilde{\pi}^{(i)} a^{-(3-\alpha)}, \quad (10.205)$$

$$\tilde{\pi}_{+0}^{(i)} = \tilde{\pi}^{(i)} + \left( a_{+0/2}^{1+\alpha} \sum_k \tilde{\Delta}_k^- \tilde{\Delta}_k^+ \tilde{\phi}_{+0/2}^{(i)} - a_{+0/2}^{3+\alpha} \tilde{V}_{,\tilde{\phi}^{(i)}} \Big|_{+0/2} \right) \delta\tilde{\eta}, \quad (10.206)$$

$$E_{K,+0/2} = \frac{E_{K,+0} + E_K}{2}, \quad (10.207)$$

$$b_{+0} = b + \frac{1}{3} \left( \frac{f_*}{m_p} \right)^2 a_{+0/2}^{1+2\alpha} \left[ (\alpha-2)E_{K,+0/2} + \alpha E_{G,+0/2} + (\alpha+1)E_{V,+0/2} \right] \delta\tilde{\eta}, \quad (10.208)$$

$$a_{+0} = a_{+0/2} + b_{+0} \frac{\delta\tilde{\eta}}{2}, \quad (10.209)$$

$$\tilde{\phi}_{+0}^{(i)} = \tilde{\phi}_{+0/2}^{(i)} + \frac{\delta\tilde{\eta}}{2} \tilde{\pi}_{+0}^{(i)} a_{+0}^{-(3-\alpha)}. \quad (10.210)$$

$$HC : b^2 = \frac{1}{3} \left( \frac{f_*}{m_p} \right)^2 a^{2(\alpha+1)} (E_K + E_G + E_V), \quad (10.211)$$

Both algorithms have  $\mathcal{O}(\delta\eta^2)$  accuracy and are equivalent in efficiency (number of steps per iteration, complexity of the steps), so one can equally use one or the other, and obtain the same results. Verlet integrators have however three steps per iteration (as they come in a *kick-drift-kick* or *drift-kick-drift* fashion) versus two steps of the staggered leapfrog integrators *III* and *IV* from Section 10.4.2.1 (which come in a *drift-kick* or *kick-drift* scheme). Verlet integrators is therefore some  $\sim 30-40\%$  slower than staggered leapfrog algorithms. They can however be used to implement higher-order in  $\delta\eta$  with the method presented in Section 10.3.4.1, see Section 10.4.3.1.

### 10.4.3 $\mathcal{O}(dt^n)$ Lattice formulation of interacting scalar fields

#### 10.4.3.1 Verlet Integration $n$ th order

In order to consider any of the higher-order Verlet integrators that we introduced in Section 10.3.4.1, we need to re-write first the EOM (10.189)-(10.192) for  $N_s$  interacting scalar fields dictating the expansion of the universe, as follows

$$a' = b, \quad (10.212)$$

$$\tilde{\phi}'_i = a^{-(3-\alpha)} \tilde{\pi}_i, \quad (10.213)$$

$$\tilde{\pi}'_i = \mathcal{K}_i[a, \{\tilde{\phi}_j\}], \quad (10.214)$$

$$b' = \mathcal{K}_a[a, E_K, E_G, E_V], \quad (10.215)$$

where

$$\mathcal{K}_i[a, \{\tilde{\phi}_j\}] \equiv a^{1+\alpha} \tilde{\nabla}^2 \tilde{\phi}_i - a^{3+\alpha} \tilde{V}_{\tilde{\phi}_i}, \quad (10.216)$$

$$\mathcal{K}_a[a, E_K, E_G, E_V] \equiv \frac{1}{3} \left( \frac{f_*}{m_p} \right)^2 a^{1+2\alpha} [(\alpha-2)E_K + \alpha E_G + (\alpha+1)E_V], \quad (10.217)$$

$$E_K \equiv \frac{1}{2a^6} \sum_i \langle \tilde{\pi}_i^2 \rangle, \quad E_G \equiv \frac{1}{2a^2} \sum_{i,k} \langle (\tilde{\nabla}_k \tilde{\phi}_i)^2 \rangle, \quad E_V \equiv \langle \tilde{V}(\{\tilde{\phi}_j\}) \rangle. \quad (10.218)$$

Decomposing one time step  $\delta\eta = \sum_{p=1}^s \delta\eta_p$  into  $s$  sub-steps  $\delta\eta_p = w_p \delta t$ , so that  $\sum_{p=1}^s w_p = 1$ , the idea is to iterate  $s$ -times one of the Verlet algorithms, (10.119) or (10.122), using each time the appropriate  $\delta\eta_p$  sub-step. Without loss of generality we use the Velocity Verlet algorithm (10.119) as the building block, obtaining

$$\left\{ \begin{array}{l} \tilde{\pi}_i^{(0)} \equiv \tilde{\pi}_i(\mathbf{n}, n_0) \\ \tilde{\phi}_i^{(0)} \equiv \tilde{\phi}_i(\mathbf{n}, n_0) \\ a^{(0)} \equiv a(n_0) \\ b^{(0)} \equiv b(n_0) \end{array} \right\} \Rightarrow \left\{ \begin{array}{l} b_{1/2}^{(p)} = b^{(p-1)} + w_p \frac{\delta\tilde{\eta}}{2} \mathcal{K}_a[a^{(p-1)}, E_K^{(p-1)}, E_G^{(p-1)}, E_V^{(p-1)}] \\ \tilde{\pi}_{i,1/2}^{(p)} = \tilde{\pi}_i^{(p-1)} + w_p \frac{\delta\tilde{\eta}}{2} \mathcal{K}_i[a^{(p-1)}, \{\tilde{\phi}_j^{(p-1)}\}] \\ a_{1/2}^{(p)} = a^{(p-1)} + b_{1/2}^{(p)} w_p \frac{\delta\tilde{\eta}}{2} \\ \tilde{\phi}_i^{(p)} = \tilde{\phi}_i^{(p-1)} + w_p \delta\tilde{\eta} \tilde{\pi}_{i,1/2}^{(p)} (a_{1/2}^{(p)})^{-(3-\alpha)}, \\ a^{(p)} = a_{1/2}^{(p)} + b_{1/2}^{(p)} w_p \frac{\delta\tilde{\eta}}{2}, \\ \tilde{\pi}_i^{(p)} = \tilde{\pi}_{i,1/2}^{(p)} + w_p \frac{\delta\tilde{\eta}}{2} \mathcal{K}_i[a^{(p)}, \{\tilde{\phi}_j^{(p)}\}] \\ b^{(p)} = b_{1/2}^{(p)} + w_p \frac{\delta\tilde{\eta}}{2} \mathcal{K}_a[a^{(p)}, E_K^{(p)}, E_G^{(p)}, E_V^{(p)}] \end{array} \right\}_{p=1, \dots, s} \Rightarrow \left\{ \begin{array}{l} \tilde{\pi}_i(\mathbf{n}, n_0 + 1) \equiv \tilde{\pi}_i^{(s)} \\ \tilde{\phi}_i(\mathbf{n}, n_0 + 1) \equiv \tilde{\phi}_i^{(s)} \\ a(n_0 + 1) \equiv a^{(s)} \\ b(n_0 + 1) \equiv b^{(s)}. \end{array} \right. \quad (10.219)$$

By choosing the appropriate weights  $w_p$ 's from Table 10.1, the errors of the intermediate steps cancel up to order  $\mathcal{O}(\delta\eta^n)$ , with  $n = 4, 6, 8$  and  $10$  for  $s = 3, 7, 15$  and  $31$ , respectively.

Finally we deal with the Hubble constraint. Like in the *RK4* case, here both field amplitudes and conjugate momenta live at the same integer times (after each full iteration over the  $s$ -subintervals), so we simply write

$$HC : b^2 = \frac{1}{3} \left( \frac{f_*}{m_p} \right)^2 a^{2(\alpha+1)} (E_K + E_G + E_V), \quad (10.220)$$

evaluated at any integer time. Note that a similar algorithm of accuracy  $\mathcal{O}(\delta t^6)$  has been previously introduced in Ref. [181].

### 10.4.4 Observables

To conclude this section, we collect the main observables of interest, such as energies and power-spectra. In the case of scalar fields, we are mostly concerned with the fields and conjugate momenta themselves,  $\tilde{\phi}_i$  and  $\tilde{\pi}_i$ . In particular, we typically monitor their mean value and their variance.

#### 10.4.4.1 Energy components

We can define the kinetic and gradient energy for each field as follows,

$$E_K^{\phi_i} = \frac{1}{a^6} \langle (\tilde{\pi}_i)^2 \rangle, \quad E_G^{\phi_i} = \frac{1}{a^2} \sum_j \langle (\tilde{\Delta}_j^+ \tilde{\phi}_i)^2 \rangle, \quad (10.221)$$

while the total potential energy is defined as

$$E_V = \langle \tilde{V}(\{\tilde{\phi}_i\}) \rangle. \quad (10.222)$$

In most cases, the potential can naturally be written as a sum of  $p$  different terms  $V(\{\tilde{\phi}_i\}) = \sum_a V_a(\{\tilde{\phi}_i\})$ , which are typically the different mass terms and interactions of the fields. Therefore, we also measure

$$E_{V_a} = \langle \tilde{V}_a(\{\tilde{\phi}_i\}) \rangle. \quad (10.223)$$

#### 10.4.4.2 Spectra

Finally, we can also consider the power spectrum of each individual field. Following our conventions in Eq. (10.66), we define

$$\mathcal{P}_{\tilde{\phi}_i}(k(\tilde{n})) = \frac{k^3(\tilde{n})}{2\pi^2} \left( \frac{\delta \tilde{x}}{N} \right)^3 \langle |(\tilde{\phi}_i)(\tilde{n})|^2 \rangle_{R(\tilde{n})}, \quad (10.224)$$

$$\mathcal{P}_{\tilde{\pi}_i}(k(\tilde{n})) = \frac{k^3(\tilde{n})}{2\pi^2} \left( \frac{\delta \tilde{x}}{N} \right)^3 \langle |\tilde{\pi}_i(\tilde{n})|^2 \rangle_{R(\tilde{n})}. \quad (10.225)$$

## 10.5 Lattice formulation of gauge fields, I: $U(1)$ interactions

We can now move on to the lattice formulation of the  $U(1)$  gauge sector, which consists in developing an appropriate discretization for Eqs. (10.38) and (10.40), together with Friedmann's law (10.53). In particular, we will generalize the staggered leapfrog algorithm of Section 10.4.2.1, the velocity-Verlet one of Section 10.4.2.2, and its higher-order generalizations introduced in Section 10.4.3.1. For simplicity, we restrict the presentation to the case of a single complex scalar field  $\varphi$  coupled to a single Abelian gauge field  $A_\mu$ , as the generalization to a larger number of fields is straightforward. Note also that for conciseness, we present explicitly only the velocity-Verlet versions of the Verlet's algorithm. The position one is

straightforwardly obtained by inverting the roles of the momenta and fields, as explained in Section 10.4.2.2.

### 10.5.1 Continuum formulation and natural variables

We define the following *program* variables for the  $U(1)$ -charged scalars and the Abelian gauge fields as

$$\tilde{\varphi} = \frac{1}{f_*} \varphi, \quad \tilde{A}_\mu = \frac{1}{\omega_*} A_\mu. \quad (10.226)$$

The normalization of the charged scalar is identical to the one of the scalar singlet, introduced in Eq. (10.147). However, the gauge field is normalized with respect  $\omega_*$ , so it cancels the one coming from  $\delta \tilde{x}^\mu$  in the link, i.e.  $V_\mu \equiv e^{-i\delta x_\mu A_\mu} = e^{-i\delta \tilde{x}_\mu \tilde{A}_\mu} \equiv \tilde{V}_\mu$ . The continuum equations of motion in these variables are, in the temporal gauge  $\tilde{A}_0 = 0$ ,

$$(a^{3-\alpha} \tilde{\varphi}')' - a^{1+\alpha} \tilde{D}_A^2 \tilde{\varphi} = -a^{\alpha+3} \tilde{V}_{|\tilde{\varphi}|} \frac{\tilde{\varphi}}{|\tilde{\varphi}|}, \quad (10.227)$$

$$\tilde{\partial}_0(a^{1-\alpha} \tilde{F}_{0i}) - a^{\alpha-1} \partial_j \tilde{F}_{ji} = a^{1+\alpha} \tilde{J}_i^A, \quad (10.228)$$

where all field and spacetime variables are program variables, and as such, are indicated with a ‘ $\sim$ ’. By inspecting these equations, we can naturally identify appropriate definitions for the conjugate momenta of the field variables as

$$\tilde{\pi}_\varphi \equiv a^{3-\alpha} \tilde{\varphi}', \quad (10.229)$$

$$(\tilde{\pi}_A)_i \equiv a^{1-\alpha} \tilde{F}_{0i}. \quad (10.230)$$

We define the *program* kinetic energies of the fields as

$$E_K^\varphi = \frac{1}{a^6} \langle \tilde{\pi}_\varphi^2 \rangle, \quad (10.231)$$

$$E_K^A = \frac{1}{2a^4} \sum_{i=1}^3 \langle (\tilde{\pi}_A)_i^2 \rangle. \quad (10.232)$$

For convenience, let us also define the following kernels for each of the amplitudes and momenta,

$$(\tilde{\pi}_\varphi)' = \mathcal{K}^\varphi[a, \tilde{\varphi}, \tilde{A}_i], \quad (10.233)$$

$$(\tilde{\pi}_A)_i' = \mathcal{K}_i^A[a, \tilde{\varphi}, \tilde{A}_i], \quad (10.234)$$

$$\mathcal{K}^\varphi[a, \tilde{\varphi}, \tilde{A}_i] \equiv -a^{\alpha+3} \tilde{V}_{|\tilde{\varphi}|} \frac{\tilde{\varphi}}{|\tilde{\varphi}|} + a^{1+\alpha} \tilde{D}_A^2 \tilde{\varphi}, \quad (10.235)$$

$$\mathcal{K}^A[a, \tilde{\varphi}, \tilde{A}_i]_i \equiv a^{1+\alpha} \tilde{J}_i^A + a^{\alpha-1} \tilde{\partial}_j \tilde{F}_{ji}. \quad (10.236)$$

## 10.5.2 Non-compact Lattice formulation of scalar-gauge dynamics

We first present here a spatial discretization of the kernels using non-compact variables, which means that the variables to evolve are the field amplitudes and momenta themselves,  $\{\tilde{\varphi}, \tilde{\pi}_\varphi, \tilde{A}_i, (\tilde{\pi}_A)_i\}$ . Using our  $U(1)$ -toolkit (10.3.2.2), we get

$$\mathcal{K}^\varphi[a, \tilde{\varphi}, \tilde{A}_i] = -a^{\alpha+3} \tilde{V}_{|\tilde{\varphi}|} \frac{\tilde{\varphi}}{|\tilde{\varphi}|} + a^{1+\alpha} \sum_i \tilde{D}_i^- \tilde{D}_i^+ \tilde{\varphi}, \quad (10.237)$$

$$\mathcal{K}^A[a, \tilde{\varphi}, \tilde{A}_i]_i = a^{1+\alpha} \left( g_A Q_A^{(\tilde{\varphi})} \mathcal{J}m[\tilde{\varphi}^* \tilde{V}_i \tilde{\varphi}] + \dots \right) + a^{\alpha-1} \sum_j \left( \tilde{\Delta}_j^- \tilde{\Delta}_j^+ \tilde{A}_i - \tilde{\Delta}_j^- \tilde{\Delta}_i^+ \tilde{A}_j \right), \quad (10.238)$$

where the dots are here to remind the reader that any fields coupled to the  $U(1)$  gauge field will contribute to its kernel through the gauge current. For example, an  $SU(N)$ -doublet  $\tilde{\Phi}$  would add a contribution of the sort  $g_A Q_A^{(\tilde{\Phi})} \mathcal{J}m[\tilde{\Phi}^\dagger \tilde{V}_i \tilde{\Phi}]$ . For conciseness, let us also define a kernel for the scale factor as

$$\begin{aligned} \mathcal{K}^b[a, \tilde{\varphi}, \tilde{\pi}_\varphi, \tilde{A}_i, (\tilde{\pi}_A)_i] = & \frac{a^{2\alpha+1}}{3m_p^2} (\alpha-2)(E_K^\varphi + \dots) + \alpha(E_G^\varphi + \dots) \\ & + (\alpha+1)E_V + (\alpha-1)(E_K^A + E_G^A \dots), \end{aligned} \quad (10.239)$$

corresponding to Friedmann's equation (10.53). We reproduced only the terms directly relevant to the  $U(1)$  gauge sector; the dots are here again to remind the reader that other contributions will enter if some other sectors are also present (e.g. scalar singlets). The kinetic energies are defined in (10.231) and (10.232). We discretize the remaining gradient and potential energies as follows,

$$E_G^\varphi = \frac{1}{a^2} \sum_i \langle (\tilde{D}_i^A + \tilde{\varphi})^* (\tilde{D}_i^A + \tilde{\varphi}) \rangle, \quad (10.240)$$

$$E_G^A = \frac{1}{2a^4} \sum_{i,j < i} \langle (\tilde{\Delta}_i^+ \tilde{A}_j - \tilde{\Delta}_i^- \tilde{A}_j)^2 \rangle, \quad (10.241)$$

$$E_V = \langle \tilde{V}(\tilde{\varphi}, \dots) \rangle. \quad (10.242)$$

Finally, a crucial quantity to monitor is the Gauss law, which must be obeyed at all times during the simulation. It is written in the continuum in Eq. (10.42). In terms of program variables, we can discretize it as follows,

$$-\sum_i \Delta_i^- (\tilde{\pi}_A)_i = g_A Q_A^{(\varphi)} \mathcal{J}m[\tilde{\varphi}^* \tilde{\pi}_\varphi]. \quad (10.243)$$

### 10.5.2.1 Staggered Leap-Frog

Let us now consider the time evolution of these equations. We first present an adaptation of the staggered leapfrog algorithm of order  $O(\delta\eta^2)$  to our system. Momenta are evaluated at semi-integer times, while fields live at integer times. When needed, the former/latter can be

## 10.5. Lattice formulation of gauge fields, I: $U(1)$ interactions

evaluated at integer/semi-integer times by interpolation. In particular, this is needed in the scale-factor kernels,

$$\begin{aligned} \mathcal{K}^b[a, \tilde{\varphi}, \tilde{\pi}_\varphi, \tilde{A}_i, (\tilde{\pi}_A)_i] &= \frac{a^{2\alpha+1}}{3m_p^2} (\alpha-2) \overline{E_K^\varphi} + \dots + \alpha(E_G^\varphi + \dots) + (\alpha+1)E_V \\ &\quad + (\alpha-1) \left( \overline{E_K^A} + E_G^A \right) \dots \end{aligned} \quad (10.244)$$

The algorithm to evolve the fields and their momenta by one time step proceeds as follows:

*Staggered Leapfrog Non-Compact*

$$IC : \{a, b_{-1/2}, \tilde{\varphi}, (\tilde{\pi}_\varphi)_{-1/2}, \tilde{A}_i, (\tilde{\pi}_A)_{i,-1/2}\} \text{ at } \tilde{\eta}_0. \quad (10.245)$$

$$(\tilde{\pi}_\varphi)_{+1/2} = (\tilde{\pi}_\varphi)_{-1/2} + \delta\tilde{\eta} \mathcal{K}^\varphi[a, \tilde{\varphi}, \tilde{A}_i], \quad (10.246)$$

$$(\tilde{\pi}_A)_{i,+1/2} = (\tilde{\pi}_A)_{i,-1/2} + \delta\tilde{\eta} \mathcal{K}^A[a, \tilde{\varphi}, \tilde{A}_i]_i, \quad (10.247)$$

$$b_{+1/2} = b_{-1/2} + \delta\tilde{\eta} \mathcal{K}^b[a, \tilde{\varphi}, \tilde{\pi}_\varphi, \tilde{A}_i, (\tilde{\pi}_A)_i], \quad (10.248)$$

$$a_{+0} = a + \delta\tilde{\eta} b_{+1/2}, \quad (10.249)$$

$$a_{+1/2} = \frac{a_{+0} + a}{2}, \quad (10.250)$$

$$\tilde{\varphi}_{+0} = \tilde{\varphi} + \delta\tilde{\eta} \frac{(\tilde{\pi}_\varphi)_{+1/2}}{a_{+1/2}^{3-\alpha}}, \quad (10.251)$$

$$\tilde{A}_{i,+0} = \tilde{A}_i + \delta\tilde{\eta} \frac{(\tilde{\pi}_A)_{i,+1/2}}{a_{+1/2}^{1-\alpha}}, \quad (10.252)$$

$$HC : b^2 = \frac{1}{3} \left( \frac{f^*}{m_p} \right)^2 a^{2(\alpha+1)} \left( \overline{E_K^\varphi} + E_G^\varphi + \overline{E_K^A} + E_G^A + E_V \right), \quad (10.253)$$

where the last line is the corresponding Hubble constraint. We see that the scale factor also needs to be interpolated, as it enters into the relation between the conjugate momenta and the fields' time derivative. Note also that this scheme can be obtained from an action principle, similar to the analogous scalar singlet case.

### 10.5.2.2 Velocity-Verlet

The equations can also be solved with a velocity-Verlet scheme of order  $O(\delta\tilde{\eta}^2)$ , similarly to the analogous scalar case. The algorithm to update the system proceeds as follows,

*Velocity-Verlet VV2 Non-Compact*

$$IC : \{a, b, \tilde{\varphi}, \tilde{\pi}_\varphi, \tilde{A}_i, (\tilde{\pi}_A)_i\} \text{ at } \eta_0. \quad (10.254)$$

$$(\tilde{\pi}_\varphi)_{+1/2} = \tilde{\pi}_\varphi + \frac{\delta\tilde{\eta}}{2} \mathcal{K}^\varphi[a, \tilde{\varphi}, \tilde{A}_i], \quad (10.255)$$



$$(\tilde{\pi}_A)_{i,+1/2} = (\tilde{\pi}_A)_i + \frac{\delta\tilde{\eta}}{2} \mathcal{K}^A[a, \tilde{\varphi}, \tilde{A}_i]_i, \quad (10.256)$$

$$b_{+1/2} = b + \frac{\delta\tilde{\eta}}{2} \mathcal{K}^b[a, \tilde{\varphi}, \tilde{\pi}_\varphi, \tilde{A}_i, (\tilde{\pi}_A)_i], \quad (10.257)$$

$$a_{+0} = a + \delta\tilde{\eta} b_{+1/2}, \quad (10.258)$$

$$a_{+1/2} = \frac{a_{+0} + a}{2}, \quad (10.259)$$

$$\tilde{\varphi}_{+0} = \tilde{\varphi} + \delta\tilde{\eta} \frac{(\tilde{\pi}_\varphi)_{+1/2}}{a_{+1/2}^{3-\alpha}}, \quad (10.260)$$

$$\tilde{A}_{i,+0} = \tilde{A}_i + \delta\tilde{\eta} \frac{(\tilde{\pi}_A)_{+1/2}}{a_{+1/2}^{1-\alpha}}, \quad (10.261)$$

$$(\tilde{\pi}_\varphi)_{+0} = (\tilde{\pi}_\varphi)_{+1/2} + \frac{\delta\tilde{\eta}}{2} \mathcal{K}^\varphi[a_{+0}, \tilde{\varphi}_{+0}, \tilde{A}_{i,+0}], \quad (10.262)$$

$$(\tilde{\pi}_A)_{i,+0} = (\tilde{\pi}_A)_{i,+1/2} + \frac{\delta\tilde{\eta}}{2} \mathcal{K}_i^A[a_{+0}, \tilde{\varphi}_{+0}, \tilde{A}_{i,+0}]_i, \quad (10.263)$$

$$b_{+0} = b_{+1/2} + \frac{\delta\tilde{\eta}}{2} \mathcal{K}^b[a_{+0}, \tilde{\varphi}_{+0}, (\tilde{\pi}_\varphi)_{+0}, \tilde{A}_{i,+0}, (\tilde{\pi}_A)_{i,+0}], \quad (10.264)$$

$$HC : b^2 = \frac{1}{3} \left( \frac{f_*}{m_p} \right)^2 a^{2(\alpha+1)} (E_K^\varphi + E_G^\varphi + E_K^A + E_G^A + E_V), \quad (10.265)$$

where the last line is again the Hubble constraint. Note that a similar integrator, based on a position-Verlet method, was recently presented in Ref. [184].

### 10.5.2.3 Velocity-Verlet $n$ th order

In order to construct the higher order integrators VV4, VV6, VV8 and VV10, one simply needs to apply the method described in Section 10.3.4.1. Explicitly, by choosing  $\omega_p$  in Table 10.1, it proceeds as follows,

$$\left. \begin{aligned} \tilde{\pi}_\varphi^{(0)} &\equiv \tilde{\pi}_\varphi(\mathbf{n}, n_0) \\ \tilde{\varphi}^{(0)} &\equiv \tilde{\varphi}(\mathbf{n}, n_0) \\ \tilde{A}_i^{(0)} &\equiv \tilde{A}_i(\mathbf{n}, n_0) \\ (\tilde{\pi}_A)_i^{(0)} &\equiv (\tilde{\pi}_A)_i(\mathbf{n}, n_0) \\ a^{(0)} &\equiv a(n_0) \\ b^{(0)} &\equiv b(n_0) \end{aligned} \right\} \Rightarrow \quad (10.266)$$

$$\Rightarrow \left\{ \begin{array}{l} (\tilde{\pi}_\varphi)_{1/2}^{(p)} = \tilde{\pi}_\varphi^{(p-1)} + \frac{\omega_p \delta \tilde{\eta}}{2} \mathcal{K}^\varphi \left[ a^{(p-1)}, \tilde{\varphi}^{(p-1)}, \tilde{A}_i^{(p-1)} \right] \\ (\tilde{\pi}_A)_{i,1/2}^{(p)} = (\tilde{\pi}_A)_i^{(p-1)} + \frac{\omega_p \delta \tilde{\eta}}{2} \mathcal{K}^A \left[ a^{(p-1)}, \tilde{\varphi}^{(p-1)}, \tilde{A}_i^{(p-1)} \right]_i \\ b_{1/2}^{(p)} = b^{(p-1)} + \frac{\omega_p \delta \tilde{\eta}}{2} \mathcal{K}^b \left[ a^{(p-1)}, \tilde{\varphi}^{(p-1)}, \tilde{\pi}_\varphi^{(p-1)}, \tilde{A}_i^{(p-1)}, (\tilde{\pi}_A)_i^{(p-1)} \right] \\ a^{(p)} = a^{(p-1)} + \omega_p \delta \tilde{\eta} b_{1/2}^{(p)} \\ a_{1/2}^{(p)} = \frac{a^{(p)} + a^{(p-1)}}{2} \\ \tilde{\varphi}^{(p)} = \tilde{\varphi}^{(p-1)} + \delta \tilde{\eta} \frac{(\tilde{\pi}_\varphi)_{1/2}^{(p)}}{(a_{1/2}^{(p)})^{3-\alpha}} \\ \tilde{A}_i^{(p)} = \tilde{A}_i^{(p-1)} + \omega_p \delta \tilde{\eta} \frac{(\tilde{\pi}_A)_{1/2}^{(p)}}{(a_{1/2}^{(p)})^{1-\alpha}} \\ (\tilde{\pi}_\varphi)^{(p)} = (\tilde{\pi}_\varphi)_{1/2}^{(p)} + \frac{\omega_p \delta \tilde{\eta}}{2} \mathcal{K}^\varphi \left[ a^{(p)}, \tilde{\varphi}^{(p)}, \tilde{A}_i^{(p)} \right] \\ (\tilde{\pi}_A)_i^{(p)} = (\tilde{\pi}_A)_{i,1/2}^{(p)} + \frac{\omega_p \delta \tilde{\eta}}{2} \mathcal{K}^A \left[ a^{(p)}, \tilde{\varphi}^{(p)}, \tilde{A}_i^{(p)} \right]_i \\ b^{(p)} = b_{1/2}^{(p)} + \frac{\omega_p \delta \tilde{\eta}}{2} \mathcal{K}^b \left[ a^{(p)}, \tilde{\varphi}^{(p)}, (\tilde{\pi}_\varphi)^{(p)}, \tilde{A}_i^{(p)}, (\tilde{\pi}_A)_i^{(p)} \right] , \end{array} \right\}_{p=1, \dots, s} \quad (10.267)$$

$$\Rightarrow \left\{ \begin{array}{l} \tilde{\pi}_\varphi(\mathbf{n}, n_0) \equiv \tilde{\pi}_\varphi^{(s)} \\ \tilde{\varphi}(\mathbf{n}, n_0) \equiv \tilde{\varphi}^{(s)} \\ \tilde{A}_i(\mathbf{n}, n_0) \equiv \tilde{A}_i^{(s)} \\ (\tilde{\pi}_A)_i(\mathbf{n}, n_0) \equiv (\tilde{\pi}_A)_i^{(s)} \\ a(n_0) \equiv a^{(s)} \\ b(n_0) \equiv b^{(s)} , \end{array} \right. \quad (10.268)$$

$$HC : b^2 = \frac{1}{3} \left( \frac{f_*}{m_p} \right)^2 a^{2(\alpha+1)} (E_K^\varphi + E_G^\varphi + E_K^A + E_G^A + E_V) . \quad (10.269)$$

### 10.5.3 Compact Lattice formulation of scalar-gauge dynamics

As presented in Section 10.3.2.2, the link variables  $V_i$  can also be used as “fundamental” variables to be solved, instead of the gauge field amplitudes  $A_i$ . This leads to a ‘compact’ discretization of the  $U(1)$  gauge sector. In this approach, we keep the same definitions for momenta as before, (10.229) and (10.230). However, we take for the gauge fields’ kernel,

$$\mathcal{K}_i^A[a, \tilde{\varphi}, \tilde{V}_i]_i = a^{1+\alpha} \left( g_A Q_A^{(\varphi)} \mathcal{J} m[\tilde{\varphi}^* \tilde{V}_i \tilde{\varphi}] + \dots \right) + \frac{a^{\alpha-1}}{\delta \tilde{x}^3} \sum_j (\tilde{V}_{ij} - \tilde{V}_{ij-j}) . \quad (10.270)$$

where the second term is a backward discretization of  $\tilde{\partial}_j \tilde{F}_{ji}$ . This can of course be replaced by some other discretization, this precise one corresponds to a discrete action made out of a

plaquettes. The magnetic energy can be approximated by

$$E_G^A = \frac{2}{a^4 \delta \tilde{x}^4} \sum_{i,j < i} (1 - \Re e(\tilde{V}_{ij}))^2 . \quad (10.271)$$

The last difference with respect to the non-compact formulation is how the link variables are evolved in time. In order to understand this, let us compute the continuum time derivative of a link

$$(\tilde{V}_i)' = \partial_0 e^{-i\delta \tilde{x} \tilde{A}_i} = -i\delta \tilde{x} (\tilde{A}_i)' \tilde{V}_i , \quad (10.272)$$

or in terms of the conjugate momenta,

$$(\tilde{V}_i)' = -i \frac{\delta \tilde{x}}{a^{1-\alpha}} (\tilde{\pi}_A)_i \tilde{V}_i . \quad (10.273)$$

The scale factor kernel  $\mathcal{K}^b[a, \tilde{\varphi}, \tilde{\pi}_\varphi, \tilde{V}_i, (\tilde{\pi}_A)_i]$  is then understood to be computed with these energies. Having defined all the necessary ingredients, we can write down the corresponding modified evolution algorithms for the compact formulation.

### 10.5.3.1 Staggered Leap-Frog

In this case, the only difference with respect to the non-compact formulation is how the drifts are given. The algorithm is

*Staggered Leapfrog Compact*

$$IC : \{a, b_{-1/2}, \tilde{\varphi}, (\tilde{\pi}_\varphi)_{-1/2}, \tilde{V}_i, (\tilde{\pi}_A)_{i,-1/2}\} \text{ at } \eta_0. \quad (10.274)$$

$$(\tilde{\pi}_\varphi)_{+1/2} = (\tilde{\pi}_\varphi)_{-1/2} + \delta \tilde{\eta} \mathcal{K}^\varphi[a, \tilde{\varphi}, \tilde{V}_i], \quad (10.275)$$

$$(\tilde{\pi}_A)_{i,+1/2} = (\tilde{\pi}_A)_{i,-1/2} + \delta \tilde{\eta} \mathcal{K}^A[a, \tilde{\varphi}, \tilde{V}_i]_i, \quad (10.276)$$

$$b_{+1/2} = b_{-1/2} + \delta \tilde{\eta} \mathcal{K}^b[a, \tilde{\varphi}, \tilde{\pi}_\varphi, \tilde{V}_i, (\tilde{\pi}_A)_i], \quad (10.277)$$

$$a_{+0} = a + \delta \tilde{\eta} b_{+1/2}, \quad (10.278)$$

$$\tilde{\varphi}_{+0} = \tilde{\varphi} + \delta \tilde{\eta} \frac{(\tilde{\pi}_\varphi)_{+1/2}}{a_{+1/2}^{3-\alpha}}, \quad (10.279)$$

$$\tilde{V}_{i,+0} = \tilde{V}_i - i\delta \tilde{\eta} \delta \tilde{x} \frac{(\tilde{\pi}_A)_{i,+1/2}}{a_{+1/2}^{1-\alpha}} \tilde{V}_i, \quad (10.280)$$

$$HC : b^2 = \frac{1}{3} \left( \frac{f_*}{m_p} \right)^2 a^{2(\alpha+1)} \left( \overline{E_K^\varphi} + E_G^\varphi + \overline{E_K^A} + E_G^A + E_V \right) . \quad (10.281)$$

## 10.5.3.2 Velocity-Verlet

Again, only the drifts differ in the velocity-Verlet algorithm with respect to the non-compact case. We get

*Velocity-Verlet VV2 Compact*

$$IC : \{a, b, \tilde{\varphi}, \tilde{\pi}_\varphi, \tilde{V}_i, (\tilde{\pi}_A)_i\} \text{ at } \eta_0. \quad (10.282)$$

$$(\tilde{\pi}_\varphi)_{+1/2} = \tilde{\pi}_\varphi + \frac{\delta\tilde{\eta}}{2} \mathcal{K}^\varphi[a, \tilde{\varphi}, \tilde{V}_i], \quad (10.283)$$

$$(\tilde{\pi}_A)_{i,+1/2} = (\tilde{\pi}_A)_i + \frac{\delta\tilde{\eta}}{2} \mathcal{K}^A[a, \tilde{\varphi}, \tilde{V}_i]_i, \quad (10.284)$$

$$b_{+1/2} = b + \frac{\delta\tilde{\eta}}{2} \mathcal{K}^b[a, \tilde{\varphi}, \tilde{\pi}_\varphi, \tilde{V}_i, (\tilde{\pi}_A)_i], \quad (10.285)$$

$$a_{+0} = a + \delta\tilde{\eta} b_{+1/2}, \quad (10.286)$$

$$a_{+1/2} = \frac{a_{+0} + a}{2}, \quad (10.287)$$

$$\tilde{\varphi}_{+0} = \tilde{\varphi} + \delta\tilde{\eta} \frac{(\tilde{\pi}_\varphi)_{+1/2}}{a_{+1/2}^{3-\alpha}}, \quad (10.288)$$

$$\tilde{V}_{i,+0} = \tilde{V}_i - i\delta\tilde{\eta}\delta\tilde{x} \frac{(\tilde{\pi}_A)_{i,+1/2}}{a_{+1/2}^{1-\alpha}} \tilde{V}_i, \quad (10.289)$$

$$(\tilde{\pi}_\varphi)_{+0} = (\tilde{\pi}_\varphi)_{+1/2} + \frac{\delta\tilde{\eta}}{2} \mathcal{K}^\varphi[a_{+0}, \tilde{\varphi}_{+0}, \tilde{V}_{i,+0}], \quad (10.290)$$

$$(\tilde{\pi}_A)_{i,+0} = (\tilde{\pi}_A)_{i,+1/2} + \frac{\delta\tilde{\eta}}{2} \mathcal{K}_i^A[a_{+0}, \tilde{\varphi}_{+0}, \tilde{V}_{i,+0}]_i, \quad (10.291)$$

$$b_{+0} = b_{+1/2} + \frac{\delta\tilde{\eta}}{2} \mathcal{K}^b[a_{+0}, \tilde{\varphi}_{+0}, (\tilde{\pi}_\varphi)_{+0}, \tilde{V}_{i,+0}, (\tilde{\pi}_A)_{i,+0}], \quad (10.292)$$

$$HC : b^2 = \frac{1}{3} \left( \frac{f_*}{m_p} \right)^2 a^{2(\alpha+1)} (E_K^\varphi + E_G^\varphi + E_K^A + E_G^A + E_V). \quad (10.293)$$

10.5.3.3 Velocity-Verlet  $n$ th order

The higher order integrators VV4, VV6, VV8 and VV10 for the compact formulation are also obtained by a simple modification of the drifts,

$$\left. \begin{aligned} \tilde{\pi}_\varphi^{(0)} &\equiv \tilde{\pi}_\varphi(\mathbf{n}, n_0) \\ \tilde{\varphi}^{(0)} &\equiv \tilde{\varphi}(\mathbf{n}, n_0) \\ \tilde{V}_i^{(0)} &\equiv \tilde{V}_i(\mathbf{n}, n_0) \\ (\tilde{\pi}_A)_i^{(0)} &\equiv (\tilde{\pi}_A)_i(\mathbf{n}, n_0) \\ a^{(0)} &\equiv a(n_0) \\ b^{(0)} &\equiv b(n_0) , \end{aligned} \right\} \Rightarrow \quad (10.294)$$

$$\Rightarrow \left\{ \begin{aligned} (\tilde{\pi}_\varphi)_{1/2}^{(p)} &= \tilde{\pi}_\varphi^{(p-1)} + \frac{\omega_p \delta \tilde{\eta}}{2} \mathcal{K}^\varphi \left[ a^{(p-1)}, \tilde{\varphi}^{(p-1)}, \tilde{V}_i^{(p-1)} \right] \\ (\tilde{\pi}_A)_{i,1/2}^{(p)} &= (\tilde{\pi}_A)_i^{(p-1)} + \frac{\omega_p \delta \tilde{\eta}}{2} \mathcal{K}^A \left[ a^{(p-1)}, \tilde{\varphi}^{(p-1)}, \tilde{V}_i^{(p-1)} \right]_i \\ b_{1/2}^{(p)} &= b^{(p-1)} + \frac{\omega_p \delta \tilde{\eta}}{2} \mathcal{K}^b \left[ a^{(p-1)}, \tilde{\varphi}^{(p-1)}, \tilde{\pi}_\varphi^{(p-1)}, \tilde{V}_i^{(p-1)}, (\tilde{\pi}_A)_i^{(p-1)} \right] \\ a^{(p)} &= a^{(p-1)} + \omega_p \delta \tilde{\eta} b_{1/2}^{(p)} \\ a_{1/2}^{(p)} &= \frac{a^{(p)} + a^{(p-1)}}{2} \\ \tilde{\varphi}^{(p)} &= \tilde{\varphi}^{(p-1)} + \delta \tilde{\eta} \frac{(\tilde{\pi}_\varphi)_{1/2}^{(p)}}{(a_{1/2}^{(p)})^{3-\alpha}} \\ V_i^{(p)} &= V_i^{(p-1)} - i \delta \tilde{\eta} \delta \tilde{x} \frac{(\tilde{\pi}_A)_{1/2}^{(p)}}{(a_{1/2}^{(p)})^{3-\alpha}} V_i^{(p)} \\ (\tilde{\pi}_\varphi)^{(p)} &= (\tilde{\pi}_\varphi)_{1/2}^{(p)} + \frac{\omega_p \delta \tilde{\eta}}{2} \mathcal{K}^\varphi \left[ a^{(p)}, \tilde{\varphi}^{(p)}, \tilde{V}_i^{(p)} \right] \\ (\tilde{\pi}_A)_i^{(p)} &= (\tilde{\pi}_A)_{i,1/2}^{(p)} + \frac{\omega_p \delta \tilde{\eta}}{2} \mathcal{K}^A \left[ a^{(p)}, \tilde{\varphi}^{(p)}, \tilde{V}_i^{(p)} \right]_i \\ b^{(p)} &= b_{1/2}^{(p)} + \frac{\omega_p \delta \tilde{\eta}}{2} \mathcal{K}^b \left[ a^{(p)}, \tilde{\varphi}^{(p)}, (\tilde{\pi}_\varphi)^{(p)}, \tilde{V}_i^{(p)}, (\tilde{\pi}_A)_i^{(p)} \right] , \end{aligned} \right\}_{p=1, \dots, s} \quad (10.295)$$

$$\Rightarrow \left\{ \begin{aligned} \tilde{\pi}_\varphi(\mathbf{n}, n_0) &\equiv \tilde{\pi}_\varphi^{(s)} \\ \tilde{\varphi}(\mathbf{n}, n_0) &\equiv \tilde{\varphi}^{(s)} \\ \tilde{V}_i(\mathbf{n}, n_0) &\equiv \tilde{V}_i^{(s)} \\ (\tilde{\pi}_A)_i(\mathbf{n}, n_0) &\equiv (\tilde{\pi}_A)_i^{(s)} \\ a(n_0) &\equiv a^{(s)} \\ b(n_0) &\equiv b^{(s)} , \end{aligned} \right.$$

$$HC : b^2 = \frac{1}{3} \left( \frac{f_*}{m_p} \right)^2 a^{2(\alpha+1)} (E_K^\varphi + E_G^\varphi + E_K^A + E_G^A + E_V) . \quad (10.296)$$

As we will see in next section, an advantage of the compact formulation is that it directly generalizes to non-Abelian groups, contrary to the non-compact one. However, before moving on, let us introduce some relevant observables for the  $U(1)$  gauge sector.

### 10.5.4 Observables

We group here observables whose mean value and variance are of interest,

$$U(1) \text{ matter: } \mathcal{R}e[\tilde{\varphi}] , \mathcal{I}m[\tilde{\varphi}] , \mathcal{R}e[\tilde{\pi}_\varphi] , \mathcal{I}m[\tilde{\pi}_\varphi] , |\tilde{\varphi}| , |\tilde{\pi}_\varphi| . \quad (10.297)$$

$$U(1) \text{ gauge fields, non-compact: } \tilde{\mathcal{E}}_i = \frac{1}{a^{1-\alpha}} (\tilde{\pi}_A)_i , \tilde{\mathcal{B}}_i = \frac{1}{2} \sum_{jk} \epsilon_{ijk} (\tilde{\Delta}_j^+ \tilde{A}_k - \tilde{\Delta}_k^+ \tilde{A}_j) , \\ |\tilde{\mathcal{E}}| , |\tilde{\mathcal{B}}| . \quad (10.298)$$

$$U(1) \text{ gauge fields, compact: } \tilde{\mathcal{E}}_i = \frac{1}{a^{1-\alpha}} (\tilde{\pi}_A)_i , \tilde{\mathcal{B}}_i = -\frac{1}{2\delta\tilde{x}^4} \sum_{jk} \epsilon_{ijk} (\mathcal{R}e(\tilde{V}_{jk})) , \\ |\tilde{\mathcal{E}}| , |\tilde{\mathcal{B}}| . \quad (10.299)$$

Note that, as presented in the  $U(1)$ -toolkit (10.3.2.2), other discretizations are possible for the magnetic field.

#### 10.5.4.1 Energy components

We collect here the different expressions for the energy components of the system,

$$U(1) \text{ matter: } E_K^\varphi = \frac{1}{a^6} \langle \tilde{\pi}_\varphi^2 \rangle , E_G^\varphi = \frac{1}{a^2} \sum_i \langle (\tilde{D}_i^{A+} \tilde{\varphi})^* (\tilde{D}_i^{A+} \tilde{\varphi}) \rangle . \quad (10.300)$$

$$U(1) \text{ gauge fields, non-compact: } E_K^A = \frac{1}{2a^4} \sum_{i=1}^3 \langle (\tilde{\pi}_A)_i^2 \rangle , \\ E_G^A = \frac{1}{2a^4} \sum_{i,j<i} \langle (\tilde{\Delta}_i^+ \tilde{A}_j - \tilde{\Delta}_j^+ \tilde{A}_i)^2 \rangle . \quad (10.301)$$

$$U(1) \text{ gauge fields, compact: } E_K^A = \frac{1}{2a^4} \sum_{i=1}^3 \langle (\tilde{\pi}_A)_i^2 \rangle , \\ E_G^A = \frac{2}{a^4 \delta\tilde{x}^4} \sum_{i,j<i} (1 - \mathcal{R}e(\tilde{V}_{ij}))^2 . \quad (10.302)$$

$$\text{Potential: } E_V = \langle \tilde{V}(\tilde{\varphi}, \dots) \rangle , \quad (10.303)$$

where ‘K’, ‘G’, and ‘V’ indicate kinetic, gradient, and potential energies.

#### 10.5.4.2 Spectra

The last quantities of interest are the power spectra, which according to the discrete expression of Eq. (10.66), we define as follow,

$$\mathcal{P}_{\tilde{\varphi}}(k(\tilde{n})) = \frac{k^3(\tilde{n})}{2\pi^2} \left( \frac{\delta \tilde{x}}{N} \right)^3 \langle |\mathcal{R}e(\tilde{\varphi})(\tilde{n})|^2 + |\mathcal{I}m(\tilde{\varphi})(\tilde{n})|^2 \rangle_{R(\tilde{n})} , \quad (10.304)$$

$$\mathcal{P}_{\tilde{\pi}_\varphi}(k(\tilde{n})) = \frac{k^3(\tilde{n})}{2\pi^2} \left( \frac{\delta \tilde{x}}{N} \right)^3 \langle |\mathcal{R}e(\tilde{\pi}_\varphi)(\tilde{n})|^2 + |\mathcal{I}m(\tilde{\pi}_\varphi)(\tilde{n})|^2 \rangle_{R(\tilde{n})} , \quad (10.305)$$

$$\mathcal{P}_{\tilde{\mathcal{E}}}^A(k(\tilde{n})) = \frac{k^3(\tilde{n})}{2\pi^2} \left( \frac{\delta \tilde{x}}{N} \right)^3 \langle \sum_i |\tilde{\mathcal{E}}_i(\tilde{n})|^2 \rangle_{R(\tilde{n})} , \quad (10.306)$$

$$\mathcal{P}_{\tilde{\mathcal{B}}}^A(k(\tilde{n})) = \frac{k^5(\tilde{n})}{2\pi^2} \left( \frac{\delta \tilde{x}}{N} \right)^3 \langle \sum_i |\tilde{A}_i(\tilde{n})|^2 \rangle_{R(\tilde{n})} , \text{ [non-compact]} , \quad (10.307)$$

$$\mathcal{P}_{\tilde{\mathcal{B}}}^A(k(\tilde{n})) = \frac{k^3(\tilde{n})}{2\pi^2} \left( \frac{\delta \tilde{x}}{N} \right)^3 \langle \sum_i |\tilde{\mathcal{B}}_i(\tilde{n})|^2 \rangle_{R(\tilde{n})} , \text{ [compact]} , \quad (10.308)$$

with the electric and magnetic fields defined as in equations (10.298) and (10.299). The extra powers of  $k(\tilde{n})$  in the non-compact magnetic field spectra come from the spatial derivative of  $\tilde{A}_i$ .

## 10.6 Lattice formulation of gauge fields, II: $SU(N)$ interactions

Let us now introduce a set of new Gauss-preserving evolution algorithms for a  $SU(N)$  gauge sector with self-consistent expansion of the universe. We will follow closely what has been done for the compact  $U(1)$  formulation. As in the previous section, we explicitly present only a velocity-Verlet algorithm; the corresponding position Verlet one is straightforwardly obtained from there.

### 10.6.1 Continuum formulation and natural variables

We define the following *program variables* for the non-Abelian gauge fields and complex doublet, as follows

$$\tilde{\Phi} = \frac{\Phi}{f_*} , \quad \tilde{B}_\mu^a = \frac{B_\mu^a}{\omega_*} , \quad (10.309)$$

mimicking the definition for the  $U(1)$  gauge sector, see Eq. (10.226). Again, our lattice formulation will be based in these variables.

We start again by identifying an appropriate set of conjugate momenta. This is again achieved by rewriting the continuum equations (10.39) and (10.41) appropriately. In the temporal gauge, they are

$$(a^{3-\alpha} \tilde{\Phi}')' - a^{1+\alpha} \tilde{D}^2 \tilde{\Phi} = -a^{\alpha+3} \tilde{V}_{|\tilde{\Phi}|} \frac{\tilde{\Phi}}{|\tilde{\Phi}|} , \quad (10.310)$$

$$\partial_0(a^{1-\alpha}(\tilde{G}_{0i})^a) - a^{\alpha-1}(\tilde{\mathcal{D}}_j)_{ab}(\tilde{G}_{ji})^b = a^{1+\alpha} \tilde{f}_i^a . \quad (10.311)$$

## 10.6. Lattice formulation of gauge fields, II: $SU(N)$ interactions

From here, we define the conjugate momenta as

$$\tilde{\pi}_\Phi = a^{3-\alpha} \tilde{\Phi}' , \quad (10.312)$$

$$(\tilde{\pi}_B)^a = a^{1-\alpha} \tilde{G}_{0i}^a . \quad (10.313)$$

The associated kinetic energies of the two field sectors become

$$E_K^\Phi = \frac{1}{a^6} \langle \tilde{\pi}_\Phi^\dagger \tilde{\pi}_\Phi \rangle , \quad (10.314)$$

$$E_K^B = \frac{1}{2a^4} \sum_{a,i} \langle (\tilde{\pi}_B)_i^a \rangle^2 . \quad (10.315)$$

Finally, we define the following kernels as

$$(\tilde{\pi}_\Phi)' = \mathcal{K}^\Phi[a, \tilde{\Phi}, \tilde{U}_i] , \quad (10.316)$$

$$((\tilde{\pi}_B)_i^a)' = \mathcal{K}^B[a, \tilde{\Phi}, \tilde{U}_i]_i^a , \quad (10.317)$$

$$\mathcal{K}^\Phi[a, \tilde{\Phi}, \tilde{U}_i] \equiv -a^{\alpha+3} \tilde{V}_{|\tilde{\Phi}|} \frac{\tilde{\Phi}}{|\tilde{\Phi}|} + a^{1+\alpha} \tilde{D}_A^2 \tilde{\Phi} , \quad (10.318)$$

$$\mathcal{K}^B[a, \tilde{\Phi}, \tilde{U}_i]_i^a \equiv a^{1+\alpha} \tilde{J}_i^a + a^{\alpha-1} (\tilde{\mathcal{D}}_j)_{ab} (\tilde{G}_{ji})^b , \quad (10.319)$$

which allows us to proceed with the discretization and time evolution of the EOM.

### 10.6.2 Lattice formulation of scalar-gauge dynamics

For non-Abelian gauge fields, we do not have the choice between compact and non-compact variables: the compact formulation is required to maintain gauge invariance. As such, we discretize the kernels as follows,

$$\mathcal{K}^\Phi[a, \tilde{\Phi}, \tilde{U}_i] = -a^{\alpha+3} \tilde{V}_{|\tilde{\Phi}|} \frac{\tilde{\Phi}}{|\tilde{\Phi}|} + a^{1+\alpha} \sum_i \tilde{D}_i^- \tilde{D}_i^+ \tilde{\Phi} , \quad (10.320)$$

$$\mathcal{K}^B[a, \tilde{\Phi}, \tilde{U}_i]_i = a^{1+\alpha} \left( 2g_B Q_B^{(\Phi)} \mathcal{J} m[\tilde{\Phi}^\dagger \tilde{U}_i \tilde{\Phi}] + \dots \right) + \frac{a^{\alpha-1}}{\delta \tilde{x}^3} \sum_j \left( \tilde{U}_{ij} - \tilde{U}_{j,-j}^\dagger \tilde{U}_{ij} - \tilde{U}_{j,-j} \tilde{U}_{ij} \right) , \quad (10.321)$$

where the second term in the  $SU(N)$  kernel is a backward finite difference approximation of the gauge covariant derivative  $\tilde{\mathcal{D}} \tilde{G}_{ij}$ . We also used matrix notation, for conciseness. Using our  $SU(N)$ -toolkit (10.81), we see that the magnetic energy can be written as

$$E_G^B = \frac{2}{g_B a^4 \delta \tilde{x}^4} \sum_{a,i,j < i} \langle \text{Tr}(i T_a \tilde{U}_{ij})^2 \rangle . \quad (10.322)$$



As in the compact  $U(1)$  case, we need to relate our conjugate momenta to the time derivative of the link. We use the same relation in the continuum as before,

$$(\tilde{U}_i)' = \partial_0 e^{-i\delta\tilde{x}\tilde{B}_i} \approx -i\delta\tilde{x}(\tilde{B}_i)'\tilde{U}_i, \quad (10.323)$$

which in terms of the conjugate momenta is

$$(\tilde{U}_i)' \approx -i \frac{\delta\tilde{x}}{a^{1-\alpha}} (\tilde{\pi}_B)_i \tilde{U}_i, \quad (10.324)$$

with no sum intended. Note that in this case, this relation is valid only at leading order in  $\delta x$  because of the non-commutativity of the fields.

Finally, a crucial quantity to monitor is the Gauss law, which must be obeyed at all times during the simulation. Based on the continuum expression in Eq. (10.43), we discretize it in matrix notation as

$$-\sum_i \Delta_i^- (\tilde{\pi}_B)_i = 2g_B Q_B^{(\Phi)} \mathcal{J} m [\tilde{\Phi}^\dagger \tilde{\pi}_\Phi]. \quad (10.325)$$

### 10.6.2.1 Staggered Leap-Frog

Let us now consider different evolution algorithms to solve the field dynamics in the compact formulation, following closely the same script as for the  $U(1)$  gauge sector. We begin with a straightforward generalization of the staggered leap-frog algorithm. It gives

*Staggered Leapfrog*

$$IC : \{a, b_{-1/2}, \tilde{\Phi}, (\tilde{\pi}_\Phi)_{-1/2}, \tilde{U}_i, (\tilde{\pi}_B)_{i,-1/2}\} \text{ at } \eta_0. \quad (10.326)$$

$$(\tilde{\pi}_\Phi)_{i,+1/2} = (\tilde{\pi}_\Phi)_{-1/2} + \delta\tilde{\eta} \mathcal{K}^\Phi [a, \tilde{\Phi}, \tilde{U}_i]_i, \quad (10.327)$$

$$(\tilde{\pi}_B)_{i,+1/2} = (\tilde{\pi}_B)_{i,-1/2} + \delta\tilde{\eta} \mathcal{K}^B [a, \tilde{\Phi}, \tilde{U}_i]_i, \quad (10.328)$$

$$b_{+1/2} = b_{-1/2} + \delta\tilde{\eta} \mathcal{K}^b [a, \tilde{\Phi}, \tilde{\pi}_\Phi, \tilde{U}_i, (\tilde{\pi}_B)_i], \quad (10.329)$$

$$a_{+0} = a + \delta\tilde{\eta} b_{+1/2}, \quad (10.330)$$

$$a_{+1/2} = \frac{a_{+0} + a}{2}, \quad (10.331)$$

$$\tilde{\Phi}_{+0} = \tilde{\Phi} + \delta\tilde{\eta} \frac{(\tilde{\pi}_\Phi)_{+1/2}}{a_{+1/2}^{3-\alpha}}, \quad (10.332)$$

$$\tilde{U}_{i,+0} = \tilde{U}_i - i\delta\tilde{\eta} \delta\tilde{x} \frac{(\tilde{\pi}_B)_{i,+1/2}}{a_{+1/2}^{1-\alpha}} \tilde{U}_i, \quad (10.333)$$

$$HC : b^2 = \frac{1}{3} \left( \frac{f_*}{m_p} \right)^2 a^{2(\alpha+1)} \left( \overline{E_K^\Phi} + E_G^\Phi + \overline{E_K^B} + E_G^B + E_V \right). \quad (10.334)$$

In particular, note that the scale factor kernel is also evaluated using semi-sums of the different kinetic energies.

## 10.6.2.2 Velocity Verlet

Mimicking the algorithm developed for the analogous  $U(1)$  gauge sector, we obtain

*Velocity Verlet VV2*

$$IC : \{a, b, \tilde{\Phi}, \tilde{\pi}_\Phi, \tilde{U}_i, (\tilde{\pi}_B)_i\} \text{ at } \eta_0. \quad (10.335)$$

$$(\tilde{\pi}_\Phi)_{+1/2} = \tilde{\pi}_\Phi + \frac{\delta\tilde{\eta}}{2} \mathcal{K}^\Phi[a, \tilde{\Phi}, \tilde{U}_i], \quad (10.336)$$

$$(\tilde{\pi}_B)_{i,+1/2} = (\tilde{\pi}_B)_i + \frac{\delta\tilde{\eta}}{2} \mathcal{K}^B[a, \tilde{\Phi}, \tilde{U}_i]_i, \quad (10.337)$$

$$b_{+1/2} = b + \frac{\delta\tilde{\eta}}{2} \mathcal{K}^b[a, \tilde{\Phi}, \tilde{\pi}_\Phi, \tilde{U}_i, (\tilde{\pi}_B)_i], \quad (10.338)$$

$$a_{+0} = a + \delta\tilde{\eta} b_{+1/2}, \quad (10.339)$$

$$a_{+1/2} = \frac{a_{+0} + a}{2}, \quad (10.340)$$

$$\tilde{\Phi}_{+0} = \tilde{\Phi} + \delta\tilde{\eta} \frac{(\tilde{\pi}_\Phi)_{+1/2}}{a_{+1/2}^{3-\alpha}}, \quad (10.341)$$

$$\tilde{U}_{i,+0} = \tilde{U}_i - i\delta\tilde{\eta}\delta\tilde{x} \frac{(\tilde{\pi}_B)_{i,+1/2}}{a_{+1/2}^{1-\alpha}} \tilde{U}_i, \quad (10.342)$$

$$(\tilde{\pi}_\Phi)_{+0} = (\tilde{\pi}_\Phi)_{+1/2} + \frac{\delta\tilde{\eta}}{2} \mathcal{K}^\Phi[a_{+0}, \tilde{\Phi}_{+0}, \tilde{U}_{i,+0}], \quad (10.343)$$

$$(\tilde{\pi}_B)_{i,+0} = (\tilde{\pi}_B)_{i,+1/2} + \frac{\delta\tilde{\eta}}{2} \mathcal{K}_i^B[a_{+0}, \tilde{\Phi}_{+0}, \tilde{U}_{i,+0}]_i, \quad (10.344)$$

$$b_{+0} = b_{+1/2} + \frac{\delta\tilde{\eta}}{2} \mathcal{K}^b[a_{+0}, \tilde{\Phi}_{+0}, (\tilde{\pi}_\Phi)_{+0}, \tilde{U}_{i,+0}, (\tilde{\pi}_B)_{i,+0}], \quad (10.345)$$

$$HC : b^2 = \frac{1}{3} \left( \frac{f_*}{m_p} \right)^2 a^{2(\alpha+1)} (E_K^\Phi + E_G^\Phi + E_K^B + E_G^B + E_V). \quad (10.346)$$

 10.6.2.3 Velocity Verlet  $n$ th order

The higher-order integrators VV4, VV6, VV8 and VV10 are also obtained by a simple modification of the drifts,

$$\left. \begin{aligned} \tilde{\pi}_{\Phi}^{(0)} &\equiv (\tilde{\pi}_{\Phi})(\mathbf{n}, n_0) \\ \tilde{\Phi}^{(0)} &\equiv \tilde{\Phi}(\mathbf{n}, n_0) \\ \tilde{U}_i^{(0)} &\equiv \tilde{U}_i(\mathbf{n}, n_0) \\ (\tilde{\pi}_B)_i^{(0)} &\equiv (\tilde{\pi}_B)_i(\mathbf{n}, n_0) \\ a^{(0)} &\equiv a(n_0) \\ b^{(0)} &\equiv b(n_0) , \end{aligned} \right\} \Rightarrow \quad (10.347)$$

$$\Rightarrow \left\{ \begin{aligned} (\tilde{\pi}_{\Phi})_{1/2}^{(p)} &= (\tilde{\pi}_{\Phi})^{(p-1)} + \frac{\omega_p \delta \tilde{\eta}}{2} \mathcal{K}^{\Phi} [a^{(p-1)}, \tilde{\Phi}^{(p-1)}, \tilde{U}_i^{(p-1)}] \\ (\tilde{\pi}_B)_{i,1/2}^{(p)} &= (\tilde{\pi}_B)_i^{(p-1)} + \frac{\omega_p \delta \tilde{\eta}}{2} \mathcal{K}^B [a^{(p-1)}, \tilde{\Phi}^{(p-1)}, \tilde{U}_i^{(p-1)}]_i \\ b_{1/2}^{(p)} &= b^{(p-1)} + \frac{\omega_p \delta \tilde{\eta}}{2} \mathcal{K}^b [a^{(p-1)}, \tilde{\Phi}^{(p-1)}, \tilde{\pi}^{\Phi (p-1)}, \tilde{U}_i^{(p-1)}, (\tilde{\pi}_B)_i^{(p-1)}] \\ a^{(p)} &= a^{(p-1)} + \omega_p \delta \tilde{\eta} b_{1/2}^{(p)} \\ \tilde{\Phi}^{(p)} &= \tilde{\Phi}^{(p-1)} + \delta \tilde{\eta} \frac{(\tilde{\pi}_{\Phi})_{1/2}^{(p)}}{a_{1/2}^{(p) \frac{1}{3-\alpha}}} \\ \tilde{U}_i^{(p)} &= \tilde{U}_i^{(p-1)} - i \delta \tilde{\eta} \delta \tilde{x} \frac{(\tilde{\pi}_B)_{i,1/2}^{(p)}}{a_{1/2}^{(p) \frac{1}{1-\alpha}}} \tilde{U}_i^{(p-1)} \\ (\tilde{\pi}_{\Phi})^{(p)} &= (\tilde{\pi}_{\Phi})_{1/2}^{(p)} + \frac{\omega_p \delta \tilde{\eta}}{2} \mathcal{K}^{\Phi} [a^{(p)}, \tilde{\Phi}^{(p)}, \tilde{U}_i^{(p)}] \\ (\tilde{\pi}_B)_i^{(p)} &= (\tilde{\pi}_B)_{i,1/2}^{(p)} + \frac{\omega_p \delta \tilde{\eta}}{2} \mathcal{K}^B [a^{(p)}, \tilde{\Phi}^{(p)}, \tilde{U}_i^{(p)}]_i \\ b^{(p)} &= b_{1/2}^{(p)} + \frac{\omega_p \delta \tilde{\eta}}{2} \mathcal{K}^b [a^{(p)}, \tilde{\Phi}^{(p)}, \tilde{\pi}^{\Phi (p)}, \tilde{U}_i^{(p)}, (\tilde{\pi}_B)_i^{(p)}] , \end{aligned} \right\}_{p=1, \dots, s} \quad (10.348)$$

$$\Rightarrow \left\{ \begin{aligned} (\tilde{\pi}_{\Phi})(\mathbf{n}, n_0) &\equiv (\tilde{\pi}_{\Phi})_i^{(s)} \\ \tilde{\Phi}(\mathbf{n}, n_0) &\equiv \tilde{\Phi}^{(s)} \\ \tilde{U}_i(\mathbf{n}, n_0) &\equiv \tilde{U}_i^{(s)} \\ (\tilde{\pi}_B)_i(\mathbf{n}, n_0) &\equiv (\tilde{\pi}_B)_i^{(s)} \\ a(n_0) &\equiv a^{(s)} \\ b(n_0) &\equiv b^{(s)} , \end{aligned} \right\} \quad (10.349)$$

$$HC : \quad b^2 = \frac{1}{3} \left( \frac{f_*}{m_p} \right)^2 a^{2(\alpha+1)} (E_K^{\Phi} + E_G^{\Phi} + E_K^B + E_G^B + E_V) . \quad (10.350)$$

### 10.6.3 Observables

Finally, we write here several observables that are of interest. Let us start with the following averages,

$$SU(2) \text{ matter: } \tilde{\Phi}^a, (\tilde{\pi}_\Phi)^a, |\tilde{\Phi}|, |\tilde{\pi}_\Phi|. \quad (10.351)$$

$$\begin{aligned} SU(2) \text{ gauge fields: } \tilde{\mathcal{E}}_i^a &= \frac{1}{a^{1-\alpha}} (\tilde{\pi}_B)_i^a, \quad \tilde{\mathcal{B}}_i^a = \frac{\epsilon_{ijk}}{2\delta\tilde{x}^2} \text{Tr}[(iT_a)(\tilde{U}_{jk} - \tilde{U}_{kj})], \\ |\tilde{\mathcal{E}}^B| &= \sum_{a,i} (\tilde{\mathcal{E}}_i^a)^2, \quad |\tilde{\mathcal{B}}^B| = \sum_{a,i} (\tilde{\mathcal{B}}_i^a)^2. \end{aligned} \quad (10.352)$$

#### 10.6.3.1 Energy components

The different energies associated to the  $SU(N)$  gauge sector are

$$SU(2) \text{ matter: } E_K^\Phi = \frac{1}{a^6} \langle \tilde{\pi}_\Phi^\dagger \tilde{\pi}_\Phi \rangle, \quad E_G^\Phi = \frac{1}{a^2} \sum_i \langle (\tilde{D}_i^+ \tilde{\Phi})^* (\tilde{D}_i^+ \tilde{\Phi}) \rangle. \quad (10.353)$$

$$SU(2) \text{ gauge fields: } E_K^B = \frac{1}{2a^4} \sum_{a,i} \langle ((\tilde{\pi}_B)_i^a)^2 \rangle, \quad E_G^B = \frac{2}{g_B a^4 \delta\tilde{x}^4} \sum_{a,i,j<i} \langle \text{Tr}(iT_a \tilde{U}_{ij})^2 \rangle. \quad (10.354)$$

$$\text{Potential: } E_V = \langle \tilde{V}(\tilde{\Phi}, \dots) \rangle, \quad (10.355)$$

where ‘K’, ‘G’ and ‘V’ refer to kinetic, gradient, and potential energy.

#### 10.6.3.2 Spectra

We also define the associated power-spectra of each field sector as follows,

$$\mathcal{P}_\Phi(k(\tilde{n})) = \frac{k^3(\tilde{n})}{2\pi^2} \left( \frac{\delta\tilde{x}}{N} \right)^3 \left\langle \sum_a |\tilde{\Phi}^a(\tilde{n})|^2 \right\rangle_{R(\tilde{n})}, \quad (10.356)$$

$$\mathcal{P}_{\tilde{\pi}_\Phi}(k(\tilde{n})) = \frac{k^3(\tilde{n})}{2\pi^2} \left( \frac{\delta\tilde{x}}{N} \right)^3 \left\langle \sum_a |(\tilde{\pi}_\Phi)^a(\tilde{n})|^2 \right\rangle_{R(\tilde{n})}, \quad (10.357)$$

$$\mathcal{P}_{\tilde{\mathcal{E}}}^B(k(\tilde{n})) = \frac{k^3(\tilde{n})}{2\pi^2} \left( \frac{\delta\tilde{x}}{N} \right)^3 \left\langle \sum_{i,a} |\tilde{\mathcal{E}}_i^a(\tilde{n})|^2 \right\rangle_{R(\tilde{n})}, \quad (10.358)$$

$$\mathcal{P}_{\tilde{\mathcal{B}}}^B(k(\tilde{n})) = \frac{k^3(\tilde{n})}{2\pi^2} \left( \frac{\delta\tilde{x}}{N} \right)^3 \left\langle \sum_{i,a} |\tilde{\mathcal{B}}_i^a(\tilde{n})|^2 \right\rangle_{R(\tilde{n})}, \quad (10.359)$$

with the electric and magnetic fields defined as in equations (10.352). We note that the spectra are homogeneized over all directions in space and field-space.

## 10.7 Initial conditions

We describe in this section how to set the initial conditions of the different fields, both in the continuum and on the lattice. The initial condition of any field consists of a homogeneous mode, over which a particular spectrum of fluctuations is added. In particular, let us denote the initial time of our simulations as  $t_*$ , and add the subindex “\*” to any quantity evaluated at such time. The initial conditions of e.g. a scalar singlet can be written, in our notation, as

$$\phi(\mathbf{x}, t_*) \equiv \bar{\phi}_* + \delta\phi_*(\mathbf{x}) , \quad (10.360)$$

$$\dot{\phi}(\mathbf{x}, t_*) \equiv \bar{\dot{\phi}}_* + \delta\dot{\phi}_*(\mathbf{x}) , \quad (10.361)$$

where the bar denotes the homogeneous component of a given quantity. The numerical values of  $\bar{\phi}_*$  and  $\bar{\dot{\phi}}_*$  depend on the details of the specific field model being simulated. For example, in Section 10.8, we take the scalar field  $\phi$  as the inflaton field sourcing the accelerated expansion of the Universe, so in this context,  $\bar{\phi}_*$  and  $\bar{\dot{\phi}}_*$  can be conveniently chosen as the inflaton amplitude and derivative at the end of inflation, i.e. when the inflaton oscillatory regime starts.

In this section we focus on how to set the initial fluctuations of the different fields. We first explain in Section 10.7.1 how to set a spectrum of scalar fluctuations on the lattice, so that they recover the expected distribution of fluctuations in the continuum limit. After that, we explain in Section 10.7.2 how to set the initial fluctuations of the charged fields and the (Abelian and non-Abelian) gauge fields, putting a special emphasis on achieving preservation of the Gauss constraint(s) up to machine precision.

### 10.7.1 Stochastic spectrum of scalar fluctuations

Let us consider the scalar field given in Eqs. (10.360)-(10.361). Given the homogeneous modes  $\bar{\phi}_*$  and  $\bar{\dot{\phi}}_*$ , we want to set an appropriate set of classical fluctuations  $\delta\phi_*(\mathbf{x})$  and  $\delta\dot{\phi}_*(\mathbf{x})$  at time  $t = t_*$ , in order to mimic quantum vacuum fluctuations as well as possible. In the continuum, we can write

$$\langle \delta\phi^2 \rangle = \frac{1}{2\pi^2} \int d\log k \, k^3 \mathcal{P}_{\delta\phi}(k) , \quad \langle \delta\phi_{\mathbf{k}} \delta\phi_{\mathbf{k}'} \rangle \equiv (2\pi)^3 \mathcal{P}_{\delta\phi}(k) \delta(\mathbf{k} - \mathbf{k}') , \quad (10.362)$$

where  $\langle \dots \rangle$  represents an ensemble average, and  $\mathcal{P}_{\delta\phi}(k)$  is the power spectrum. Although these quantities must obviously be evaluated at the time  $t = t_*$ , here we have dropped the “\*” to simplify notation, as we will do in the remainder of this section. For initial conditions representing quantum vacuum fluctuations, we choose

$$\mathcal{P}_{\delta\phi}(k) \equiv \frac{1}{2\omega_{k,\phi}} \equiv \frac{1}{2\sqrt{k^2 + m_\phi^2}} , \quad m_\phi^2 \equiv \frac{\partial^2 V}{\partial \phi^2}(\phi = \bar{\phi}) , \quad (10.363)$$

where  $\omega_{k,\phi} \equiv \sqrt{k^2 + m_\phi^2}$  is the frequency of the mode, and  $m_\phi$  is the effective mass of the field, evaluated in terms of the homogeneous field components.

On the lattice, we want to set the fluctuations of the scalar field so that expression (10.362) is recovered in the continuum limit. In the discrete we substitute the stochastic expectation value by a volume average as

$$\langle \delta\phi^2 \rangle_V = \frac{\delta x^3}{V} \sum_n \delta\phi^2(n) = \frac{1}{N^6} \sum_{\tilde{n}} |\delta\phi(\tilde{n})|^2, \quad (10.364)$$

where we have used Eq. (10.59). Decomposing the summation into radial and angular parts, we obtain

$$\langle \delta\phi^2 \rangle_V = \frac{1}{N^6} \sum_{|\tilde{n}|} \sum_{\tilde{n}' \in R(\tilde{n})} |\delta\phi(\tilde{n})|^2 = \frac{4\pi}{N^6} \sum_{|\tilde{n}|} |\tilde{n}|^2 \langle |\delta\phi(\tilde{n})|^2 \rangle_{R(\tilde{n})}, \quad (10.365)$$

where  $\langle (\dots) \rangle_{R(\tilde{n})} \equiv \frac{1}{4\pi|\tilde{n}|^2} \sum_{\tilde{n}' \in R(\tilde{n})} (\dots)$  is an angular average over the spherical shell of radius  $\tilde{n}' \in [|\tilde{n}|, |\tilde{n}| + \Delta\tilde{n}]$ , with  $\Delta\tilde{n}$  a given radial binning. This leads to

$$\langle \delta\phi^2 \rangle_V = \frac{4\pi}{k_{\text{IR}}^3 N^6} \sum_{|\tilde{n}|} \Delta \log k(\tilde{n}) k^3(\tilde{n}) \langle |\delta\phi(\tilde{n})|^2 \rangle_{R(\tilde{n})}, \quad (10.366)$$

$$= \frac{1}{2\pi^2} \sum_{|\tilde{n}|} \Delta \log k(\tilde{n}) k^3(\tilde{n}) \frac{L^3}{N^6} \langle |\delta\phi(\tilde{n})|^2 \rangle_{R(\tilde{n})}, \quad (10.367)$$

where  $\Delta \log k(\tilde{n}) \equiv \frac{k_{\text{IR}}}{k(\tilde{n})}$ ,  $\mathbf{k}(\tilde{n}) \equiv k_{\text{IR}} \tilde{n}$  and  $k_{\text{IR}} \equiv \frac{2\pi}{L}$ . In order to mimic on the lattice the continuum stochastic initial condition, we impose

$$\langle \delta\phi^2 \rangle_V = \frac{1}{2\pi^2} \sum_{|\tilde{n}|} \Delta \log k(\tilde{n}) k^3(\tilde{n}) \mathcal{P}_{\delta\phi}(k), \quad (10.368)$$

from where we identify

$$\langle |\delta\phi(\tilde{n})|^2 \rangle_{R(\tilde{n})} = \left( \frac{N}{\delta x} \right)^3 \mathcal{P}_{\delta\phi}(k). \quad (10.369)$$

The initial variance of the Fourier modes on the lattice, expressed in the program variables of Eq. (10.147), must be taken therefore as

$$|\delta\tilde{\phi}(\tilde{n})|^2 \equiv \left( \frac{\omega_*}{f_*} \right)^2 \left( \frac{N}{\delta \tilde{x}} \right)^3 \tilde{\mathcal{P}}_{\delta\phi}(\tilde{k}(\tilde{n})), \quad (10.370)$$

where  $\tilde{\mathcal{P}}_{\delta\phi} \equiv \omega_* \mathcal{P}_{\delta\phi}$  is the (dimensionless) power spectrum in program units. With this choice, we reproduce the continuum correctly,

$$\langle \delta\phi^2 \rangle_V = \frac{1}{2\pi^2} \sum_{|\tilde{n}|} \Delta \log k(\tilde{n}) k^3(\tilde{n}) \mathcal{P}_{\delta\phi}(k(\tilde{n})) \quad \longrightarrow \quad \frac{1}{2\pi^2} \int d\log k k^3 \mathcal{P}_{\delta\phi}(k). \quad (10.371)$$

The key point of the identification made in Eq. (10.369), is that  $\langle \delta\phi^2 \rangle_V$  in Eq. (10.371) does not depend explicitly on the volume  $V = (N \cdot \delta x)^3$ , as required in order to correctly reproduce the continuum result. For quantum fluctuations with distribution (10.363), we shall write

$$|\delta\tilde{\phi}(\tilde{n})|^2 \equiv \left(\frac{\omega_*}{f_*}\right)^2 \left(\frac{N}{\delta\tilde{x}}\right)^3 \frac{1}{2\sqrt{\tilde{k}^2(\tilde{n}) + \tilde{m}_\phi^2}}, \quad \tilde{m}_\phi^2 \equiv \frac{\partial^2 \tilde{V}}{\partial \tilde{\phi}^2}(\tilde{\phi} = \tilde{\phi}), \quad (10.372)$$

where  $\tilde{k} \equiv k/\omega_*$  and  $\tilde{m}_\phi \equiv m_\phi/\omega_*$  are the momentum and effective mass in program variables.

Note that this expression gives an account of the appropriate radial distribution of the amplitude of the fluctuations on the lattice, but does not describe how the amplitude changes point by point. Moreover, we also need to consider the fluctuations of the time-derivative of the field. In this regard, let us note that the field modes have a time-dependence as  $\delta\phi_{\mathbf{k}} \propto (1/a)e^{\pm i\omega_k t}$ , with  $a$  the scale factor. The frequency  $\omega_k$  may depend on time, but we assume that the initial conditions are set in an adiabatic regime,  $\dot{\omega}_k/\omega_k^2 \ll 1$ . Taking the time-derivative of the field mode, we get  $\delta\dot{\phi}_{\mathbf{k}} = (\pm i\omega_k - H)\delta\phi_{\mathbf{k}}$ . Choosing one sign in this expression is equivalent to choosing a preferred direction in position space, so although this effect should be irrelevant in the dynamics once the non-linearities of the simulated process kick in, we follow the prescription of `Latticeeasy` to define isotropic initial conditions [177]. In particular, at each lattice point in momentum space, we add to the field amplitude in program units a sum of left-moving and right-moving waves as follows,

$$\delta\tilde{\phi}(\tilde{\mathbf{n}}) = \frac{1}{\sqrt{2}}(\delta\tilde{\phi}_1(\tilde{\mathbf{n}})e^{i\theta_1(\tilde{\mathbf{n}})} + \delta\tilde{\phi}_2(\tilde{\mathbf{n}})e^{i\theta_2(\tilde{\mathbf{n}})}), \quad (10.373)$$

$$\delta\tilde{\phi}'(\tilde{\mathbf{n}}) = \frac{1}{\sqrt{2}}i\tilde{\omega}_k(\delta\tilde{\phi}_1(\tilde{\mathbf{n}})e^{i\theta_1(\tilde{\mathbf{n}})} - \delta\tilde{\phi}_2(\tilde{\mathbf{n}})e^{i\theta_2(\tilde{\mathbf{n}})}) - \tilde{H}\delta\tilde{\phi}(\tilde{\mathbf{n}}), \quad (10.374)$$

where  $\tilde{\omega}_k \equiv \sqrt{\tilde{k}^2(\tilde{n}) + \tilde{m}_\phi^2}$  and  $\tilde{H} \equiv H/\omega_*$  are the frequency of the mode and the Hubble parameter in program units. In this expression,  $\theta_1(\tilde{\mathbf{n}})$  and  $\theta_2(\tilde{\mathbf{n}})$  are two random phases which vary uniformly in the range  $[0, 2\pi)$  from point to point, and  $\delta\tilde{\phi}_1(\tilde{\mathbf{n}})$  and  $\delta\tilde{\phi}_2(\tilde{\mathbf{n}})$  are two amplitudes that also vary from point to point, according to a Gaussian distribution with the corresponding variance to reproduce (10.372). Note that `Latticeeasy` imposes an additional constraint  $\delta\tilde{\phi}_1(\tilde{\mathbf{n}}) = \delta\tilde{\phi}_2(\tilde{\mathbf{n}})$  at each lattice site, which could pose problems in non-gaussianity studies (see the discussion in [179]). This is in principle not necessary for real scalar singlets, but the situation is different for charged scalar fields under a gauge group, see the discussion below.

### 10.7.2 Charged scalars and gauge fields

Let us now consider the initial conditions for the gauge fields, as well as of the charged fields coupled to them. In this work we are considering scalar fields charged under  $U(1)$  and  $SU(N) \times U(1)$  gauge groups, which we denote as  $\varphi$  and  $\Phi$  respectively. We recall that these fields are composed of multiple real components: 2 in the case of  $\varphi$ , and  $2N$  in the case of  $\Phi$ .

As the potential only depends on the absolute value of these fields, we can set the same initial amplitude to the homogeneous modes of all their components. In particular, we set for each real component  $\varphi_n$  of the charged field ( $n = 0, 1, \dots, 2N-1$ ),

$$\varphi_n(\mathbf{x}, t_*) \equiv \frac{|\varphi_*|}{2^{N/2}} + \delta\varphi_*(\mathbf{x}) , \quad (10.375)$$

$$\dot{\varphi}_n(\mathbf{x}, t_*) \equiv \frac{|\dot{\varphi}_*|}{2^{N/2}} + \delta\dot{\varphi}_*(\mathbf{x}) , \quad (10.376)$$

where  $|\varphi_*|$  and  $|\dot{\varphi}_*|$  are the initial homogeneous components of the complex field norm and its time derivative (which must be chosen for each particular model), and  $\delta\varphi_*(\mathbf{x})$  and  $\delta\dot{\varphi}_*(\mathbf{x})$  are the corresponding initial fluctuations spectra. For simplicity, we will drop the “\*” notation from now on. Mimicking the functional form of the scalar singlet fluctuations (10.373)-(10.374), we impose to the charged scalar fields on the lattice the following fluctuations,

$$\delta\tilde{\varphi}_n(\tilde{\mathbf{n}}) = \frac{1}{\sqrt{2}}(\delta\tilde{\varphi}_{n1}(\tilde{\mathbf{n}})e^{i\theta_{n1}(\tilde{\mathbf{n}})} + \delta\tilde{\varphi}_{n2}(\tilde{\mathbf{n}})e^{i\theta_{n2}(\tilde{\mathbf{n}})}) , \quad (10.377)$$

$$\delta\tilde{\varphi}'_n(\tilde{\mathbf{n}}) = \frac{1}{\sqrt{2}}i\tilde{\omega}_{k,n}(\delta\tilde{\varphi}_{n1}(\tilde{\mathbf{n}})e^{i\theta_{n1}(\tilde{\mathbf{n}})} - \delta\tilde{\varphi}_{n2}(\tilde{\mathbf{n}})e^{i\theta_{n2}(\tilde{\mathbf{n}})}) - \tilde{H}\delta\tilde{\varphi}_n(\tilde{\mathbf{n}}) , \quad (10.378)$$

where  $\tilde{\omega}_{k,n} \equiv \omega_{k,n}/\omega_* = \sqrt{\tilde{k}^2 + (\partial^2 \tilde{V}/\partial \tilde{\varphi}_n^2)}$  is the initial effective frequency of the field mode of each component in program units. Therefore, for a charged field with  $2N$  real components, there are  $8N$  functions to be fixed,  $(f_{n1}, f_{n2}, \theta_{n1}, \theta_{n2})$  (with  $n = 0, 1, \dots, 2N-1$ ). In principle, all of these functions should change from lattice point to lattice point according to the probability distributions described above, i.e. Eq. (10.372) for  $f_{n1}$  and  $f_{n2}$ , and uniformly in the range  $[0, 2\pi)$  for  $\theta_{n1}$  and  $\theta_{n2}$ . However, as we shall see, we will need to impose certain constraints to these functions in order to preserve the Gauss constraints initially.

Let us now consider the fluctuations of the Abelian and non-Abelian gauge fields. We will consider first the fluctuations in the continuum, and generalize to the discretized case later on. For the gauge fields we shall impose

$$A_i(\mathbf{x}, t_*) \equiv 0 , \quad (10.379)$$

$$B_i^a(\mathbf{x}, t_*) \equiv 0 , \quad (10.380)$$

$$\dot{A}_i(\mathbf{x}, t_*) \equiv \delta\dot{A}_{i*}(\mathbf{x}) , \quad (10.381)$$

$$\dot{B}_i^a(\mathbf{x}, t_*) \equiv \delta\dot{B}_{i*}^a(\mathbf{x}) , \quad (10.382)$$

i.e. we impose the amplitude of the gauge fields to be *exactly* zero at all lattice points, while we set an initial spectrum of fluctuations to their time-derivatives (but no homogeneous components). Because of this, the magnetic energy is exactly zero initially, while there will be some amount of electric energy, due to the fluctuations of the time-derivatives. The fluctuations of the charged scalars and gauge fields must be imposed in such a way that the Gauss constraints are initially preserved. If this is achieved, then the dynamical evolution of the field EOM will guarantee that these constraints are preserved at later times. The Gauss



constraints for the  $SU(2) \times U(1)$  gauge-invariant theory considered in this work are given in (10.42)-(10.43). These are

$$\partial_i F_{0i}(\mathbf{x}) = J_0^A(\mathbf{x}) , \quad J_0^A(\mathbf{x}) \equiv g_A Q_A^{(\varphi)} \mathcal{J}m[\varphi^* \varphi'] + g_A Q_A^{(\Phi)} \mathcal{J}m[\Phi^\dagger \Phi'] , \quad (10.383)$$

$$(\mathcal{D}_i)_{ab}(G_{0i})^b(\mathbf{x}) = J_0^a(\mathbf{x}) , \quad J_0^a(\mathbf{x}) \equiv 2g_B Q_B \mathcal{J}m[\Phi^\dagger T_a \Phi'] . \quad (10.384)$$

where we have set the initial scale factor to  $a = 1$  for simplicity. By Fourier transforming both sides of the equation, we get

$$k^i A'_i(\mathbf{k}) = J_0^A(\mathbf{k}) , \quad k^i B'_{i'}(\mathbf{k}) = J_0^a(\mathbf{k}) . \quad (10.385)$$

where  $J_0^A(\mathbf{k})$  and  $J_0^a(\mathbf{k})$  are the Fourier transforms of each current. Finally, by multiplying each side by  $k^i$ , we get

$$A'_i(\mathbf{k}) = i \frac{k_i}{k^2} J_0^A(\mathbf{k}) , \quad B'_{i'}(\mathbf{k}) = i \frac{k_{i'}}{k^2} J_0^a(\mathbf{k}) . \quad (10.386)$$

The complex scalar fields fluctuations  $\delta\varphi_*(\mathbf{x})$  and  $\delta\phi_*(\mathbf{x})$  are given by Eqs. (10.377)-(10.378) (we are still working in the continuum, so all involved functions must be interpreted as functions of the continuous spatial coordinate  $\mathbf{x}$ , instead of the lattice point  $\mathbf{n}$ ). They generate fluctuations on the currents  $J_0^A(\mathbf{x})$ , and  $J_0^a(\mathbf{x})$ . Therefore, we can impose fluctuations to the gauge fields in momentum space via Eqs. (10.386), and then transform back to position space to obtain  $\delta\dot{A}_{i*}(\mathbf{x})$ ,  $\delta\dot{B}_{i'}^a(\mathbf{x})$ .

The above procedure should, in principle, initially preserve the Gauss constraints. However, we must guarantee that the imposition of Eq. (10.386) does not add a spurious non-zero homogeneous mode to the gauge fields. We must then check that  $J_0^A(\mathbf{k} = \mathbf{0}) = J_0^a(\mathbf{k} = \mathbf{0}) = 0$  (note that if this is not implicitly assumed in (10.386), we would be dividing the right hand side by zero). For concreteness, let us consider the case of a complex doublet  $\Phi$  charged under a  $U(1) \times SU(2)$  gauge group (the case of the  $U(1)$ -charged field  $\varphi$  is just a particular case, as we explain below). The homogeneous modes of the Abelian and non-Abelian currents (10.383) and (10.384) can be written in terms of the complex field fluctuations as

$$\begin{aligned} J_0^A(\mathbf{k} = \mathbf{0}) &= \int d^3\mathbf{x} J_0^A(\mathbf{x}) \propto \int d^3\mathbf{k} \mathcal{R}e[\varphi_0^*(\mathbf{k})\varphi'_1(\mathbf{k}) - \varphi'_0(\mathbf{k})\varphi_1^*(\mathbf{k}) + \varphi_2^*(\mathbf{k})\varphi'_3(\mathbf{k}) - \varphi'_2(\mathbf{k})\varphi_3^*(\mathbf{k})] = 0 , \\ J_0^1(\mathbf{k} = \mathbf{0}) &= \int d^3\mathbf{x} J_0^1(\mathbf{x}) \propto \int d^3\mathbf{k} \mathcal{R}e[\varphi_3^*(\mathbf{k})\varphi'_0(\mathbf{k}) - \varphi'_3(\mathbf{k})\varphi_0^*(\mathbf{k}) + \varphi_1^*(\mathbf{k})\varphi'_2(\mathbf{k}) - \varphi'_1(\mathbf{k})\varphi_2^*(\mathbf{k})] = 0 , \\ J_0^2(\mathbf{k} = \mathbf{0}) &= \int d^3\mathbf{x} J_0^2(\mathbf{x}) \propto \int d^3\mathbf{k} \mathcal{R}e[\varphi_0^*(\mathbf{k})\varphi'_2(\mathbf{k}) - \varphi'_0(\mathbf{k})\varphi_2^*(\mathbf{k}) + \varphi_1^*(\mathbf{k})\varphi'_3(\mathbf{k}) - \varphi'_1(\mathbf{k})\varphi_3^*(\mathbf{k})] = 0 , \\ J_0^3(\mathbf{k} = \mathbf{0}) &= \int d^3\mathbf{x} J_0^3(\mathbf{x}) \propto \int d^3\mathbf{k} \mathcal{R}e[\varphi_1^*(\mathbf{k})\varphi'_0(\mathbf{k}) - \varphi'_1(\mathbf{k})\varphi_0^*(\mathbf{k}) + \varphi_2^*(\mathbf{k})\varphi'_3(\mathbf{k}) - \varphi'_2(\mathbf{k})\varphi_3^*(\mathbf{k})] = 0 . \end{aligned}$$

One way to guarantee these conditions are respected is to set all the integrands to zero. By solving the corresponding system of linear equations, we get the following three conditions,

$$\mathcal{R}e[\varphi'_m(\mathbf{k})\varphi_0^*(\mathbf{k}) - \varphi'_0(\mathbf{k})\varphi_m^*(\mathbf{k})] = 0 , \quad m = 1, 2, 3 , \quad (10.387)$$

which mix the different real components of the doublet. This condition is in general *not* fulfilled when all the functions  $f_{n1}$ ,  $f_{n2}$ ,  $\theta_{n1}$  and  $\theta_{n2}$  in the scalar fluctuations (10.373) and (10.374) are unconstrained. However, by substituting these expressions into Eq. (10.387), we can prove that the above condition is satisfied when the following relations hold,

$$\delta\varphi_{n1}(\mathbf{k}) = \delta\varphi_{n2}(\mathbf{k}) , \quad n = 0, 1, 2, 3 , \quad (10.388)$$

$$\theta_{m2}(\mathbf{k}) = \theta_{02}(\mathbf{k}) + \theta_{m1}(\mathbf{k}) - \theta_{01}(\mathbf{k}) , \quad m = 1, 2, 3 . \quad (10.389)$$

The first relation imposes the same amplitude to the left and right waves of each real scalar component's fluctuations. The second line consists in a set of three different constraints that must be imposed to the eight phases appearing in the four components of the doublet. Therefore, in the case of the  $SU(2)$ -charged doublet, one can simply generate randomly  $\delta\varphi_{01}$ ,  $\delta\varphi_{02}$ ,  $\delta\varphi_{10}$ ,  $\delta\varphi_{20}$ ,  $\delta\varphi_{30}$ ,  $\theta_{01}$ ,  $\theta_{02}$ ,  $\theta_{11}$ ,  $\theta_{21}$ , and  $\theta_{31}$  according to the corresponding probability distributions, and then impose  $\delta\varphi_{11}$ ,  $\delta\varphi_{21}$ ,  $\delta\varphi_{31}$ ,  $\theta_{12}$ ,  $\theta_{22}$  and  $\theta_{32}$  via Eqs. (10.388)-(10.389). This procedure guarantees that the homogeneous modes of the current is zero initially, and hence that the Gauss laws are preserved<sup>8</sup>.

Let us remark that a similar procedure can be applied to the simpler case of a  $U(1)$ -charged field  $\varphi$ . In this case there are only two real scalar components,  $\delta\varphi_0(\mathbf{k})$  and  $\delta\varphi_1(\mathbf{k})$ , so there are only three constraints to be fulfilled:  $\delta\varphi_{01}(\mathbf{k}) = \delta\varphi_{02}(\mathbf{k})$ ,  $\delta\varphi_{11}(\mathbf{k}) = \delta\varphi_{12}(\mathbf{k})$ , and  $\theta_{12}(\mathbf{k}) = \theta_{02}(\mathbf{k}) + \theta_{11}(\mathbf{k}) - \theta_{01}(\mathbf{k})$ . The procedure to set the initial fluctuations is therefore analogous to the  $SU(2) \times U(1)$  case.

Finally, let us consider the translation of this procedure developed in the continuum to the lattice. For charged scalar fields, the only difference is that the different functions  $\delta\varphi_{ab}$  and  $\theta_{ab}$  are only defined in each lattice point, instead of being continuum functions. Therefore, some of these parameters must be randomly generated at each lattice site  $\mathbf{\tilde{n}}$  according to the corresponding probability distribution, while the others must be imposed at each lattice site via the constraint equations (10.388)-(10.389). On the other hand, for gauge fields we must start from the discrete Gauss equations. As we are not imposing fluctuations to the amplitude of the gauge fields, the discrete Gauss constraints (10.243) and (10.325) simply become, in position space and in physical variables,

$$\sum_i \Delta_i^- \Delta_0^+ A_i(\mathbf{n}) = J_0^A(\mathbf{n}) , \quad \sum_i \Delta_i^- \Delta_0^+ B_i^a(\mathbf{n}) = J_0^a(\mathbf{n}) , \quad (a = 1, 2, 3) . \quad (10.390)$$

<sup>8</sup>Another possibility to guarantee constraints (10.387) would be to just impose the relations,  $\varphi'_m(\mathbf{k}) = \varphi'_0(\mathbf{k})\varphi_m^*(\mathbf{k})/\varphi_0^*(\mathbf{k})$  directly for  $m = 1, 2, 3$ , where the functions in the *rhs* of this expression are to be generated according to the probability distributions (10.373) and (10.374), without imposing the constraints (10.388) and (10.389). However, using this procedure, the fluctuations generated for the *0th*-component have typically very different amplitudes than for the other components, of one or more orders of magnitude of difference. Moreover, the spectra of the *0th*-component depends very much on the particular random realization of the fields. This makes us prefer the procedure described in the bulk text.

By taking a discrete Fourier transform in both sides of the equation, we get

$$\Delta_0^+ A_i(\tilde{\mathbf{n}}) = i \frac{k_{\text{Lat},i}^-}{(k_{\text{Lat},i}^-)^2} J_0^A(\tilde{\mathbf{n}}) , \quad \Delta_0^+ B_i^a(\tilde{\mathbf{n}}) = i \frac{k_{\text{Lat},i}^-}{(k_{\text{Lat},i}^-)^2} J_0^a(\tilde{\mathbf{n}}) , \quad (a = 1, 2, 3) . \quad (10.391)$$

Note that, as we are taking the backward spatial derivative  $\Delta_i^-$  in Eq. (10.390), then the corresponding complex lattice momentum  $k_{\text{Lat},i}^-$  must appear in Eq. (10.391) after Fourier transforming, which is defined in Eq. (10.75). Therefore, in order to set the fluctuations of the gauge field derivatives on the lattice, we first add the fluctuations to the real components to compute the corresponding currents, then transform the currents to momentum space and impose expressions (10.391) to the gauge fields, and finally transform the gauge fields back to position space.

## 10.8 A working example: the $SU(2) \times U(1)$ gauge invariant inflaton

In order to illustrate some of the techniques and concepts explained previously, we study in this section the dynamics of a specific scalar-gauge field theory using lattice simulations. In particular, we are going to consider an observationally viable single-field inflationary model, with monomial potential energy  $V(\phi) \propto \phi^p$  around the minimum, and a 'flattening' at large field amplitudes. We will study the post-inflationary stage of preheating, which is triggered by the inflaton oscillations around the minimum of its potential. As an example of the gauge-invariant lattice techniques presented above, we will couple the inflaton to both scalar and gauge fields (which we denote indistinctly as *daughter fields* from now on), and study the transfer of energy from the inflaton to these fields.

The structure of this section is as follows. First, we present in Section 10.8.1 the details of how inflation and preheating proceed in the model under consideration. In particular, we will review the two resonant phenomena that govern the post-inflationary dynamics: parametric resonance of the daughter field(s), and self-resonance of the inflaton. After that, we present the results of our lattice simulations. In Section 10.8.2 we consider the case of a  $U(1)$  gauge invariant inflaton, coupled to an Abelian gauge field through a covariant derivative. In Section 10.8.3 we consider the case of a  $SU(2) \times U(1)$  gauge invariant inflaton, coupled simultaneously to a  $SU(2) \times U(1)$  gauge sector (formed by Abelian and non-Abelian gauge fields) and a massless scalar singlet.

### 10.8.1 Model details

Let us consider a scalar field  $\phi$  with the following potential energy,

$$V(\phi) = \frac{\Lambda^4}{p} \tanh^p \left( \frac{|\phi|}{M} \right) , \quad (10.392)$$

where  $\Lambda$  and  $M$  have dimensions of energy, and  $p$  is a positive number. The particular form of this potential is based on  $\alpha$ -attractor models of inflation, see Ref. [422]. The field amplitude is introduced as an absolute value, so the potential has a minimum at  $\phi = 0$  independently of the choice of  $p$ . Similarly, the potential develops a plateau  $V(\phi) \rightarrow \Lambda^4/p$  at large field amplitudes  $\phi \gg M$ . We take  $\phi$  as the *inflaton* field responsible of the early inflationary stage of the Universe, and consider in detail the following stage of preheating. Although the numerical values of the model parameters ( $\Lambda$ ,  $M$ ,  $p$ ) are in principle independent, they are in practice constrained by the observed amplitude of the scalar perturbations in the CMB, i.e.  $\Lambda = \Lambda(M, N_{\text{CMB}}, p)$ , with  $N_{\text{CMB}} = 50 - 60$  the number of e-folds between the end of inflation and the horizon crossing of the relevant perturbations.

The potential (10.392) can be expanded around the minimum as the following monomial function,

$$V(\phi) = \frac{1}{p} \lambda \mu^{4-p} |\phi|^p, \quad \lambda \mu^{4-p} \equiv \Lambda^4 M^{-p}, \quad (10.393)$$

where  $\lambda$  is dimensionless and  $\mu$  has dimensions of energy. The product of parameters  $\lambda \mu^{4-p}$  in Eq. (10.393) is fixed in terms of ( $\Lambda$ ,  $M$ ,  $p$ ) to match the exact potential (10.392) in the limit  $\phi \ll M$ . The field value that separates the monomial and plateau regimes in the exact potential can be estimated by computing its inflection point, i.e. the amplitude at which  $V_{,\phi\phi}(\phi_i) = 0$ . It is given by

$$\phi_i = \text{Marcsinh} \left( \sqrt{\frac{p-1}{2}} \right). \quad (10.394)$$

The monomial potential (10.393) is a very good approximation to the exact potential (10.392) for field amplitudes  $\phi \ll M$ . In particular, in the limit  $M \rightarrow \infty$ , the inflaton potential (10.392) recovers the monomial function (10.393) exactly, recovering this way the well-known chaotic inflation scenario.

Inflation takes place during the slow-roll decay of the inflaton, which starts at large field amplitudes and proceeds towards the minimum of the potential. The inflaton acquires a sizable effective mass approximately when the slow-roll conditions break down, and as a consequence, starts oscillating around the minimum. The field amplitude  $\phi_*$  when the slow-roll parameter  $\epsilon_V \equiv m_{\text{pl}}^2 V_{,\phi}^2 / (2V^2)$  obeys  $\epsilon_V(\phi_*) = 1$  is

$$\phi_* \equiv \frac{M}{2} \text{arcsinh} \left( \frac{\sqrt{2} p m_{\text{pl}}}{M} \right) \xrightarrow{M \rightarrow \infty} \frac{p m_{\text{pl}}}{\sqrt{2}}, \quad (10.395)$$

where we have also written the corresponding inflaton amplitude in the limit  $M \rightarrow \infty$ . In this model, inflation happens for field amplitudes  $\phi \gtrsim \phi_*$ , while the oscillatory regime which follows takes place for  $\phi \lesssim \phi_*$ . Therefore, the field amplitude  $\phi = \phi_*$  constitutes a natural initial condition for our lattice simulations. If  $M \gtrsim m_p$ , we have that  $\phi_* \ll \phi_i$ , so the inflaton is already in the positive-curvature region of the potential when the slow-roll regime breaks, and does not enter into the tachyonic region during the subsequent inflaton oscillations. In that

case, we can safely take the monomial potential (10.393) as a very good approximation to the exact potential (10.392) during preheating. On the other hand, if  $M \lesssim m_p$  we have that  $\phi_* \gg \phi_i$ , so the inflaton does enter into the tachyonic region during at least the first oscillations. Here we consider only the first scenario, so our results do not depend very much on the details of the transition between the monomial function and the plateau. In particular, we will fix the value  $M = 10m_p$  on the lattice simulations, whose results we present below.

The equation of motion of the homogeneous component of the inflaton in the limit  $M \rightarrow \infty$  is

$$\ddot{\phi} + 3H\dot{\phi} + \Omega^2(\phi)\phi = 0, \quad \Omega(\phi) \equiv \sqrt{\lambda}\mu^{\frac{4-p}{2}}|\phi|^{\frac{p-2}{2}}, \quad (10.396)$$

which corresponds to a harmonic oscillator with time-dependent effective frequency  $\Omega(\phi)$  and friction term  $\propto 3H\dot{\phi}$ , induced by the expansion of the universe. The oscillation frequency is constant for  $p = 2$ , but depends explicitly on the field amplitude (and hence on time) for  $p \neq 2$ . This equation can be solved together with the Friedmann equation (10.52) in the homogeneous approximation, with initial conditions deep in slow-roll. During inflation we have  $\phi \gg \phi_*$ , or equivalently,  $H(\phi) \gg \Omega(\phi)$ . Eventually, when the field amplitude becomes approximately  $\phi \simeq \phi_*$ , the condition  $H(\phi) = \Omega(\phi)$  holds, and the inflaton starts oscillating. The solutions for the inflaton amplitude and scale factor can be approximated during the oscillatory regime as [423]

$$\phi(t) \simeq \Phi(t)F(t), \quad \Phi(t) = \Phi_* \left( \frac{t}{t_*} \right)^{-2/p}, \quad (10.397)$$

$$a(t) \propto a_* \left( 1 + \frac{3p}{2+p} H_* t \right)^{\frac{2+p}{3p}} \sim t^{\frac{2+p}{3p}}. \quad (10.398)$$

In Eq. (10.397),  $\Phi(t)$  is a decaying amplitude that starts at a certain time  $t_*$  from some initial amplitude  $\Phi_* \simeq \phi_*$ , while  $F(t)$  is an oscillatory function that is periodic for  $p = 2$  and non-periodic for  $p \neq 2$ . The quantities  $a_*$  and  $H_*$  are the scale factor and Hubble parameter at time  $t = t_*$ . Note that this field configuration gives rise, for times  $H_* t \gg 1$ , to a matter/radiation-dominated equation of state for  $p = 2, 4$  respectively.

In order to do lattice simulations of this system, we have to appropriately fix the program variables ( $f_*$ ,  $\alpha$ ,  $\omega_*$ ), defined in Eq. (10.147). First, we want to use variables that guarantee that typical numbers of certain physical quantities (such as field amplitudes or range of excited momenta) are of order unity. And second, as the evolution algorithms discussed above assume a constant time step, we want to use a program time variable that guarantees an approximately constant oscillation frequency. This way, each oscillation period is well resolved independently of how long the simulation time is. In this regard, we get from Eqs. (10.397) and (10.398) that the inflaton oscillation frequency (defined in Eq. 10.396) scales with the scale factor as

$$\Omega(\phi) \sim \omega_* \left( \frac{t}{t_*} \right)^{4/p-2} \sim \left( \frac{a}{a_*} \right)^{\frac{-3(p-2)}{(p+2)}}, \quad \omega_* \equiv \sqrt{\lambda}\mu^{\frac{4-p}{2}}\phi_*^{\frac{p-2}{2}}, \quad (10.399)$$

where  $\omega_*$  is the oscillation frequency at the onset of oscillations. Therefore, a convenient choice of program variables is

$$\alpha = 3 \frac{p-2}{p+2}, \quad f_* \equiv \phi_*, \quad \omega_* \equiv \Lambda^2 M^{-\frac{p}{2}} \phi_*^{\frac{p-2}{2}}. \quad (10.400)$$

Note that for this choice of units, program time corresponds to cosmic/conformal time for  $p=2,4$  respectively, up to a dimensionful constant factor. The corresponding program potential  $\tilde{V}(\tilde{\phi})$  of our model, defined in Eq. (10.148), can be then written as

$$\begin{aligned} \tilde{V}(\tilde{\phi}) &\equiv \frac{1}{f_*^2 \omega_*^2} V(\tilde{\phi}) \\ &= \frac{1}{p} \left( \frac{M}{\phi_*} \right)^p \tanh^p \left( \frac{\phi_* |\tilde{\phi}|}{M} \right), \end{aligned} \quad (10.401)$$

and its first and second derivatives are

$$\frac{\partial \tilde{V}}{\partial \tilde{\phi}} = 2 \left( \frac{M}{\phi_*} \right)^{p-1} \frac{\tanh^p(\phi_* |\tilde{\phi}|/M)}{\sinh(2\phi_* |\tilde{\phi}|/M)} \text{sgn}(\tilde{\phi}), \quad (10.402)$$

$$\frac{\partial^2 \tilde{V}}{\partial \tilde{\phi}^2} = 4 \left( \frac{M}{\phi_*} \right)^{p-2} (p - \cosh(2\phi_* |\tilde{\phi}|/M)) \frac{\tanh^p(\phi_* |\tilde{\phi}|/M)}{\sinh^2(2\phi_* |\tilde{\phi}|/M)}, \quad (10.403)$$

where  $\text{sgn}(\tilde{\phi})$  is the sign function.

### 10.8.1.1 Preheating

Let us now review how preheating proceeds in this model. The post-inflationary dynamics of an inflaton with potential (10.392) has been studied with lattice simulations in the past: in the absence of inflaton interactions to other species in [347, 368], with interactions to a second scalar field with non-canonical kinetic terms in [370], and more recently, with quadratic interactions to a daughter field in [371]. In all of these studies, the fields involved were real scalars. Here, in order to illustrate the gauge-invariant lattice techniques introduced in the previous sections, we couple for the first time the inflaton field to a gauge structure.

Let us start by considering a daughter massless scalar field  $\chi$ , coupled to the inflaton via a quadratic interaction. The potential of such a theory can be written as

$$V(\phi, \chi) = \frac{1}{p} \lambda \mu^{4-p} |\phi|^p + \frac{1}{2} g^2 \phi^2 \chi^2, \quad (10.404)$$

where  $g$  is a dimensionless coupling constant, and we have taken the limit  $M \rightarrow \infty$  in the inflaton potential. When inflation ends at the amplitude  $\phi = \phi_*$ , the energy budget of the Universe is dominated by the homogeneous component of the inflaton. Therefore, the evolution of the inflaton amplitude and scale factor can be described approximately by Eqs. (10.397)-(10.398) during the first inflaton oscillations, and it is natural to also use the

program variables defined in (10.400) in this context. With this choice, the program potential (again in the limit  $M \rightarrow \infty$ ) is

$$\begin{aligned}\tilde{V}(\tilde{\phi}, \tilde{\chi}) &\equiv \frac{1}{f_*^2 \omega_*^2} V(\tilde{\phi}, \tilde{\chi}) \\ &= \frac{1}{p} |\tilde{\phi}|^p + \frac{1}{2} q_* \tilde{\phi}^2 \tilde{\chi}^2 ,\end{aligned}\tag{10.405}$$

where the *resonance parameter*  $q_*$  is defined as the following dimensionless ratio,

$$q_* \equiv \frac{g^2 \phi_*^2}{\omega_*^2} .\tag{10.406}$$

The first and second derivatives of the program potential with respect to the two fields are

$$\frac{\partial \tilde{V}}{\partial \tilde{\phi}} = |\tilde{\phi}|^{p-2} \tilde{\phi} + q_* \tilde{\chi}^2 \tilde{\phi} , \quad \frac{\partial \tilde{V}}{\partial \tilde{\chi}} = q_* \tilde{\phi}^2 \tilde{\chi} ,\tag{10.407}$$

$$\frac{\partial^2 \tilde{V}}{\partial \tilde{\phi}^2} = (p-1) |\tilde{\phi}|^{p-2} + q_* \tilde{\chi}^2 , \quad \frac{\partial^2 \tilde{V}}{\partial \tilde{\chi}^2} = q_* \tilde{\phi}^2 .\tag{10.408}$$

During the first stages of preheating, the linearized fluctuations of both fields have time-dependent effective masses, induced by the oscillations of the inflaton homogeneous mode. These masses vary non-adiabatically each time the inflaton crosses zero, which triggers an exponential growth of the amplitude of the field modes for certain bands of momenta. More specifically, the post-inflationary dynamics is governed by the interplay of two different resonant phenomena, which may or may not be present for certain choices of model parameters. These are:

- **Self-resonance of the inflaton:** The inflaton has a time-dependent effective mass  $m_\phi^2 \propto |\phi|^{p-2}$  for  $p \neq 2$ , see Eq. (10.404). In these cases, the (conformally rescaled) inflaton fluctuations can grow exponentially during this regime as  $|\delta \tilde{\phi}_k|^2 \propto e^{2\nu_k z}$ , where  $\Re e(\nu_k) > 0$  for certain momenta bands, and  $\nu_k \equiv \nu_k(k; p)$  the corresponding so-called Floquet index. These bands are always narrow for all reasonable values of  $p$ ,  $\Delta k / \bar{k} \lesssim 0.1$  (with  $\bar{k}$  the average momentum inside the band), and the maximum Floquet index within each band is maximum  $\Re e(\nu_k) \lesssim 0.035$ .
- **Parametric resonance of the daughter field:** Similarly, the daughter field also has a time-dependent mass  $m^2 \propto g^2 \chi^2$  for any of choice of  $p$  as long as the quadratic interaction is present, see Eq. (10.404). Due to this, the (conformally rescaled) daughter field fluctuations can also grow exponentially as  $|\delta \tilde{\chi}_k|^2 \propto e^{2\mu_k z}$ , with  $\Re e(\mu_k) > 0$  for certain ranges of momenta, and  $\mu_k \equiv \mu_k(k, q_*; p)$  the corresponding Floquet index. The key parameter signaling the strength of the resonance is the *effective resonance*

## 10.8. A working example: the $SU(2) \times U(1)$ gauge invariant inflaton

parameter  $q_{\text{res}}$ , which is defined as

$$q_{\text{res}} \equiv q_* a^{\frac{6(p-4)}{p+2}}, \quad (10.409)$$

and evolves with the expansion of the universe. If  $q_{\text{res}} \gtrsim 1$ , the parametric resonance is *broad*: the width of the resonance bands for all values of  $p$  is  $\Delta k/\bar{k} \sim 1$ , and the maximum Floquet index within those bands is typically  $\Re(\mu_k) \sim 0.1 - 0.2$ . In this case, the maximum momenta excited by the main resonance band scales as  $k \sim q_{\text{res}}^{1/4} \omega_*$ , modulo some multiplying scale factor term. On the other hand, if  $q_{\text{res}} \ll 1$ , the width of the bands is very small  $\Delta k/\bar{k} \ll 1$ , and we say that the resonance is *narrow*. This second effect cannot be typically captured on the lattice due to lack of resolution. Note that  $q_{\text{res}}$  changes with time, so the type of resonance may change during preheating: it decreases with time for  $p < 4$ , grows for  $p > 4$ , and remains constant for  $p = 4$ . Therefore, the type of parametric resonance (either broad or narrow) can change as the Universe expands.

If broad parametric resonance of the daughter field is present (i.e. if  $q_{\text{res}} > 1$ ), it is almost always a stronger effect than the inflaton self-resonance. However, parametric resonance eventually becomes narrow for  $p < 4$ , even if it was broad initially. This contrasts with inflaton self-resonance, which is always present independently of the value of  $p$ , as long as  $p \neq 2$ . The different behaviour of these phenomena for different model parameters is key to understand how energy distributes between the different field sectors during preheating, as well as the evolution of the post-inflationary evolution of the equation of state.

Let us now consider a scenario in which the inflaton (in this case a complex doublet  $\Phi$ ) is coupled to a  $SU(2) \times U(1)$  gauge sector via a gauge-invariant covariant derivative. Fortunately, the simpler scalar theory described above constitutes an excellent proxy for this more complex model, as the dominant interaction term generated by the covariant derivative is also quadratic. In order to see this, let us consider the covariant derivative term in action (10.8), which contains the interaction between the inflaton and the gauge fields. It can be expanded as

$$(\vec{D}_\mu \Phi)^\dagger (\vec{D}^\mu \Phi) = (\partial_\mu \Phi)^\dagger \partial^\mu \Phi + \frac{1}{4} Q_A^2 g_A^2 |\Phi|^2 |\vec{A}|^2 + \frac{1}{4} Q_B^2 g_B^2 |\Phi|^2 \sum_a |\vec{B}^a|^2 + Q_A g_A Q_B g_B \sum_a \vec{A} \cdot \vec{B}^a (\Phi^\dagger T_a \Phi) \dots, \quad (10.410)$$

where we have ignored terms of the type  $\sim (\partial_\mu \Phi) \Phi$ , which are subdominant during the early linear regime. The first term in Eq. (10.410) gives rise to the usual Laplacian in the field equations. The second and third terms constitute quadratic interactions between the inflaton and the Abelian and non-Abelian gauge fields respectively. These are analogous to the quadratic interaction of Eq. (10.404) between the inflaton and a secondary scalar field, with the identification  $g \rightarrow Q_A g_A/2$  and  $g \rightarrow Q_B g_B/2$  in each case. Mimicking the notation of Eq. (10.406), it is then natural to define the resonance parameters of the Abelian and non-Abelian gauge fields as

$$q_{A*} \equiv \frac{Q_A^2 g_A^2 |\Phi_*|^2}{4\omega_*^2}, \quad q_{B*} \equiv \frac{Q_B^2 g_B^2 |\Phi_*|^2}{4\omega_*^2}, \quad (10.411)$$



where  $|\Phi_*| \equiv \phi_*$  is the amplitude of the inflaton norm at the end of inflation, which we set equal to Eq. (10.395). Therefore, we can use the scalar theory as a proxy to study the equivalent  $U(1)$  or  $SU(2)$  gauge-invariant theories, at least during the initial linear regime. In particular, in the gauge scenario the inflaton can also develop fluctuations via self-resonance, while the gauge fields can also get excited via parametric resonance. However, non-linearities become relevant at later times, so important differences between the scalar and gauge theories may appear later on. Finally, the fourth term in Eq. (10.410) appears when the inflaton is coupled to a full  $SU(2) \times U(1)$  gauge sector. One can prove that the effect of such term is to couple the EOM of the Abelian and non-Abelian gauge fields, so that they experience parametric resonance with a common resonance parameter  $q_{\text{eff}*} = q_{A*} + q_{B*}$ . The details of the parametric resonance process in the presence of Abelian and non-Abelian gauge fields, as well as the relevance of that term, will be discussed in more detail in an upcoming work [424]. This goes beyond the objective of this manuscript, which is mainly to illustrate lattice gauge-invariant techniques in a specific physics model.

### 10.8.2 Lattice simulations: $U(1)$ gauge interactions

Simulation	$p$	$M/m_p$	$\Lambda^4$	$q_*$	$N$	$\tilde{k}_{\text{IR}}$	$\delta\tilde{t}$
U(1)	2	10	$1.8 \cdot 10^{65}$	$4 \cdot 10^4$	128	4	$5 \cdot 10^{-3}$
U(1)	4	10	$4.3 \cdot 10^{65}$	$10^2$	128	0.6	$10^{-2}$
U(1)	6	10	$6.8 \cdot 10^{65}$	1	128	0.15	$7 \cdot 10^{-4}$
$SU(2) \times U(1) + \chi$	2	10	$1.8 \cdot 10^{65}$	$4 \cdot 10^4$	128	4	$3 \cdot 10^{-4}$
$SU(2) \times U(1) + \chi$	4	10	$4.3 \cdot 10^{65}$	$10^2$	128	0.6	$10^{-2}$

Table 10.2 – Benchmark model and lattice parameters used in the  $U(1)$  and  $SU(2) \times U(1) + \chi$  gauge simulations

We now proceed to discuss the results from our lattice simulations. We start by considering the post-inflationary dynamics of a complex inflaton field  $\varphi \equiv \frac{1}{\sqrt{2}}(\varphi_0 + i\varphi_1)$  with potential energy (10.392) [where we must substitute  $\phi \rightarrow \varphi$ ], coupled to an Abelian gauge boson  $A_\mu$  via a gauge-invariant covariant derivative. The model and lattice parameters considered in the simulations are provided in Table 10.2. We have chosen a set of three representative power-law coefficients,  $p = 2, 4, 6$ . In each case, the resonance parameter  $q_{A*}$  is fixed to guarantee broad parametric resonances at the onset of the inflaton oscillatory regime. We have fixed the value  $M = 10m_p$  as a benchmark, which guarantees that the inflationary slow-roll condition breaks down in the positive-curvature region of the potential. As described above, the initial exponential growth of the gauge field modes during broad parametric resonance takes place mainly within an infrared band of width  $p \lesssim p_* \equiv q_{A*}^{1/4} \omega_*$  (modulo a multiplying scale factor term). However, when the energy transferred to the gauge fields is large enough, they backreact onto the inflaton homogeneous condensate, which triggers a propagation of the spectra of all fields to the ultraviolet. Due to this, the minimum momenta  $\tilde{k}_{\text{IR}}$  and number of

points per lattice side  $N$  are chosen, in each case, to guarantee that both the initial infrared growth and the following ultraviolet propagation are well resolved on the lattice.

We start by showing in Fig. 10.1 the evolution of the volume-averaged inflaton norm  $|\varphi| \equiv \sqrt{\varphi_0^2 + \varphi_1^2}$ , equation of state  $w \equiv p/\rho$ , and scale factor as a function of program time  $\tilde{\eta}$  [ $d\tilde{\eta} \equiv a^{-\alpha} \omega_* dt$ , c.f. (10.147)], for each of the three power-law coefficients  $p = 2, 4, 6$ . As described above, the inflaton can be approximated as a homogeneous condensate during its first oscillations, and the evolution of the inflaton amplitude and scale factor are approximately given by Eqs. (10.397)-(10.398). From these expressions, we deduce that the amplitude of the inflaton oscillations scales initially as  $|\varphi| \sim a^{\frac{-6}{p+2}}$ , so  $|\varphi| \sim a^{-3/2}, a^{-1}, a^{-3/4}$  for  $p = 2, 4, 6$ , respectively. Therefore, in the Figure we have multiplied the inflaton norm by the inverse of these factors, so the amplitude of the rescaled inflaton oscillations is initially constant. Although the inflaton homogeneous regime holds qualitatively well during the first inflaton oscillations, the energy stored in gauge fields and inflaton gradients grows exponentially due to broad parametric resonance. Eventually, the fraction of transferred energy is so large that they backreact onto the inflaton, destroying the homogeneity of the condensate. We identify this time scale as the *backreaction time*  $\tilde{\eta}_{\text{br}}$ . From the simulation, we get  $\tilde{\eta}_{\text{br}} \simeq 130, 40, 70$  for  $p = 2, 4, 6$  respectively.

Let us now focus on the post-inflationary evolution of the equation of state  $w \equiv p/\rho$ , i.e. the ratio between the (volume-averaged) pressure and energy densities of the system. Initially, the inflaton oscillates coherently around the minimum, which gives rise to similar oscillations in the equation of state in the range  $-1 < w < 1$ . From Eqs. (10.397)-(10.398), we can compute that the *effective* (i.e. oscillation-averaged) equation of state in this regime is approximately  $\bar{w} \equiv (p-2)/(p+2)$ . This corresponds to  $\bar{w} = 0, 1/3, 1/2$  for  $p = 2, 4, 6$  respectively, which agrees with our lattice results, see the middle column of Fig. 10.1. After backreaction, the equation of state stops oscillating, and slowly evolves towards the asymptotic values  $w \rightarrow 0$  (for  $p = 2$ ) and  $w \rightarrow 1/3$  (for  $p = 4, 6$ ). We will be able to understand these results better in light of the evolution of the energy distribution, which we discuss below. We also show the scale factor as a function of program time in the right panels of Fig. 10.1. We know that during the initial linear regime, the scale factor evolves in cosmic time as  $a \sim t^{\frac{2+p}{3p}}$  [c.f. (10.398)]. By substituting this expression in the program time definition (10.147), we get that the scale factor evolves as  $a \sim \tilde{\eta}^{\frac{p+2}{6}}$  in terms of program time, in agreement to what we see on the lattice.

We can understand better the evolution of these quantities if we focus on the evolution of the energy distribution. In the left panels of Fig. 10.2 we show the total energy of the system as a function of time (Eq. 10.49), for the considered power-law coefficients  $p = 2, 4, 6$ . We also depict the evolution of each of its individual contributions: the kinetic, gradient, and potential energies of the inflaton, as well as the electric and magnetic energies of the gauge fields (see Eq. (10.51) for their exact expressions). As described above, the effective equation of state during the initial linear regime is  $\bar{w} \simeq (p-2)/(p+2)$ , so the total energy decays during the initial regime as  $\rho \sim a^{-3(1+\bar{w})} = a^{\frac{-6p}{p+2}}$ , which corresponds to  $\rho \sim a^{-3}, a^{-4}, a^{-4.5}$  for  $p = 2, 4, 6$ ,

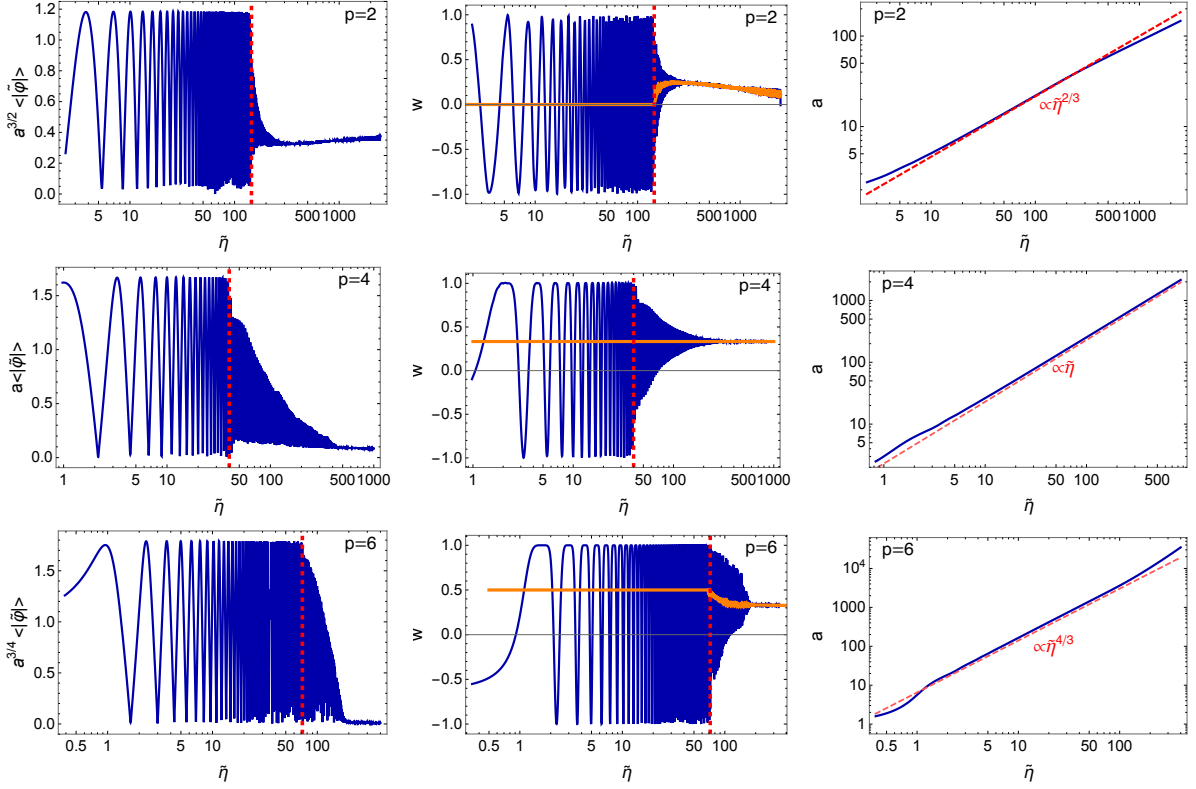


Figure 10.1 – Average values of the scalar field norm, equation of state  $w$ , and scale factor as a function of time, for three  $U(1)$  gauge simulations with  $p = 2$  (top row),  $p = 4$  (middle row), and  $p = 6$  (bottom row). The effective equation of state is indicated by orange solid lines. The backreaction time  $\tilde{\eta}_{\text{br}}$  is indicated for the first two quantities with a vertical dashed line. In the scale factor panels we have added the prediction  $a \sim \tilde{\eta}^{\frac{p+2}{6}}$ , coming from the linear regime of homogeneous inflaton oscillations.

respectively. Therefore, we have multiplied the energies by the inverse of those factors, so that the rescaled total energy is constant initially. We also depict in the right panels of Fig. 10.2 the evolution of the energy *ratios*  $\epsilon_i \equiv \tilde{\rho}_i / \tilde{\rho}$  for the same simulations, i.e. the relative contribution of each of the energy components to the total energy. By construction, the sum of all ratios is one.

As expected, the energy budget of the Universe is initially dominated by the kinetic and potential energies of the inflaton, while the other energies are subdominant, i.e.  $\langle E_K^A \rangle, \langle E_G^A \rangle, \langle E_G^\varphi \rangle \ll \langle E_K^\varphi \rangle, \langle E_V \rangle$ . However, a very small fraction of the initial energy is stored in the electric and inflaton gradient energies, due to the spectrum of fluctuations imposed to  $\varphi$  and  $\dot{A}_i$ . In contrast, the initial magnetic energy is exactly zero (up to machine precision), as we do not set fluctuations to the amplitude of the gauge field  $A_i$ , see Eqs. (10.379)-(10.382). In any case, these energies soon start growing exponentially due to parametric resonance, as seen in the three simulations. These energies become sizable approximately at the backreaction time  $\tilde{\eta} \simeq \tilde{\eta}_{\text{br}}$ , and the inflaton homogeneous condensate gets destroyed via backreaction effects. From then on, non-linear effects become relevant, and the system eventually achieving a stationary regime at late times. Remarkably, we observe that the inflaton gets virialized very quickly after inflation, with their oscillation-averaged energies satisfying the relation  $\langle E_K^\varphi \rangle \simeq \langle E_G^\varphi \rangle + \frac{p}{2} \langle E_V \rangle$ , for the three cases  $p = 2, 4, 6$ . Similarly, we observe equipartition between the electric and magnetic energies at late times,  $\langle E_K^A \rangle \simeq \langle E_G^A \rangle$ .

It is very interesting to analyze how the energy is distributed at very late times in the simulation, i.e. well within the non-linear regime. This was studied recently in Ref. [371] in the context of a real singlet inflaton with the same potential as here, coupled to a massless scalar singlet via a quadratic interaction. Although here we are considering a gauge sector, the explanation developed in Ref. [371] also applies here. In particular, we find that the energy distribution at late times is determined by the choice of  $p$  in the inflaton potential. For  $p = 2$ , the inflaton cannot get excited via self-resonance, but the daughter field does get excited via broad parametric resonance because  $q_{A*} > 1$ . However, the effective resonance parameter (10.409) decreases with time, so parametric resonance eventually becomes narrow. After that, the inflaton kinetic and potential energies dilute as matter, while the other ones dilute as radiation or faster. Due to this, at very late times we get the energy ratios  $\epsilon_K^\varphi, \epsilon_V \rightarrow 0.5$ , with the other ratios becoming negligible. This explains why the effective equation of state goes to  $w \rightarrow 0$  at late times in Fig. 10.1. On the other hand, for  $p = 4, 6$ , both the inflaton and the gauge fields are always being excited resonantly at late times: inflaton self-resonance is always present for  $p > 2$ , while parametric resonance is always broad at late times because  $q_{\text{res}}$  is either constant (for  $p = 4$ ) or grows with time (for  $p > 4$ ). Therefore, the energy contributions of both field sectors are sizeable at late times. In the case  $p = 4$ , the inflaton possesses 60% of the total energy of the system at very late times (divided by half between kinetic and gradient energy), while the gauge fields possess the other 40% (divided also by half between electric and magnetic energy). Moreover, the inflaton potential energy becomes negligible, which explains why the effective equation of state goes to  $w \rightarrow 1/3$  at late times in Fig. 10.1. We expect this final distribution to be quite independent on the choice of  $q_*$ , as will be seen in Ref. [424] in a

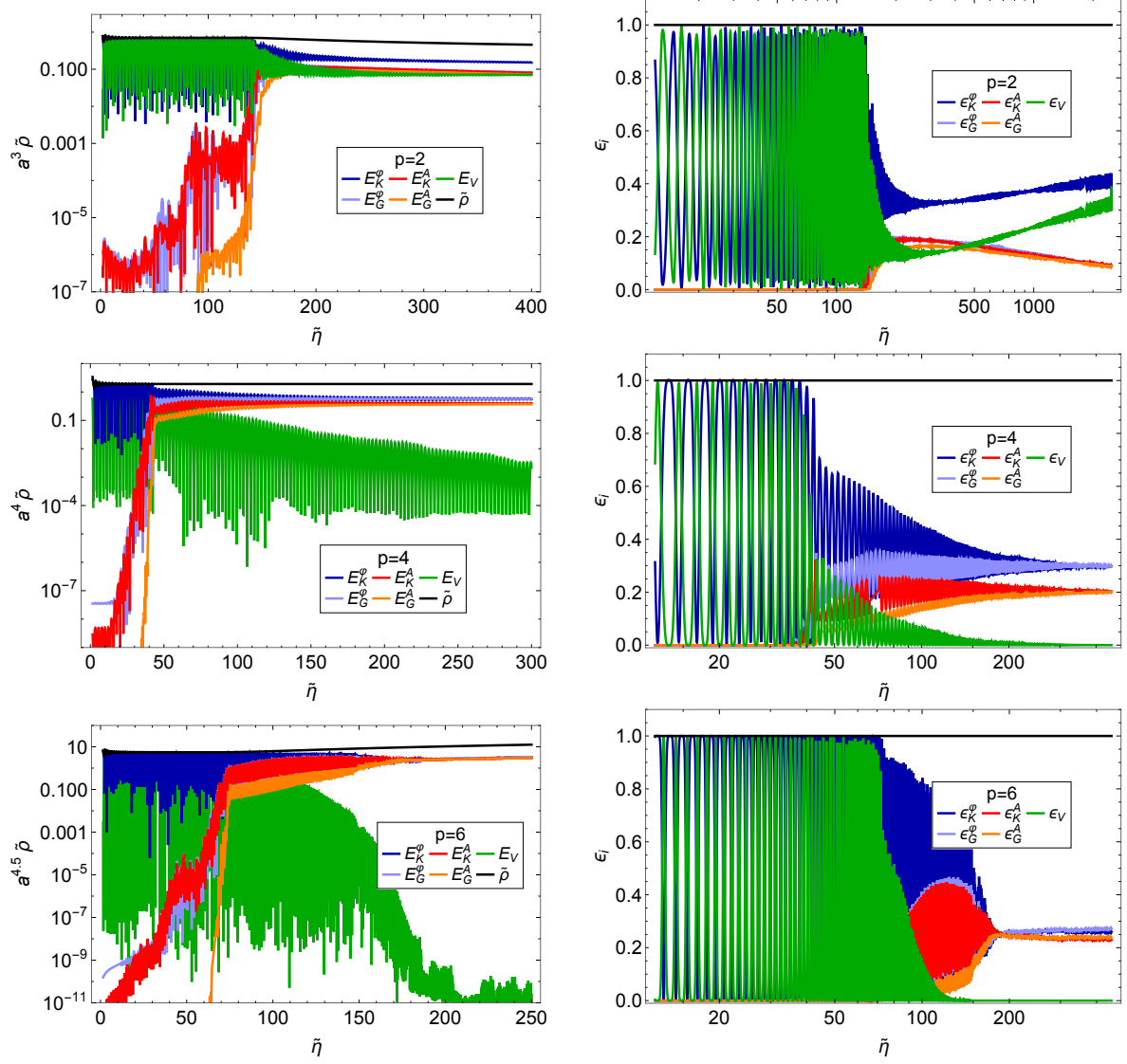


Figure 10.2 – Left panel: Evolution of the total energy  $\tilde{\rho} \equiv \rho/(f_*^2 \omega_*^2)$  for the  $U(1)$  gauge simulation and  $p=2, 4, 6$ , as well as of each of its individual contributions: kinetic, gradient, and potential energies of the inflaton, as well as electric and magnetic energies of the gauge field. These quantities are multiplied by the factor  $\sim a^{\frac{6p}{p+2}}$ . Right panel: Evolution of the energy ratios  $\epsilon_i \equiv \tilde{\rho}_i/\tilde{\rho}$  for the same simulations as in corresponding left panel. The sum of all ratios is one.

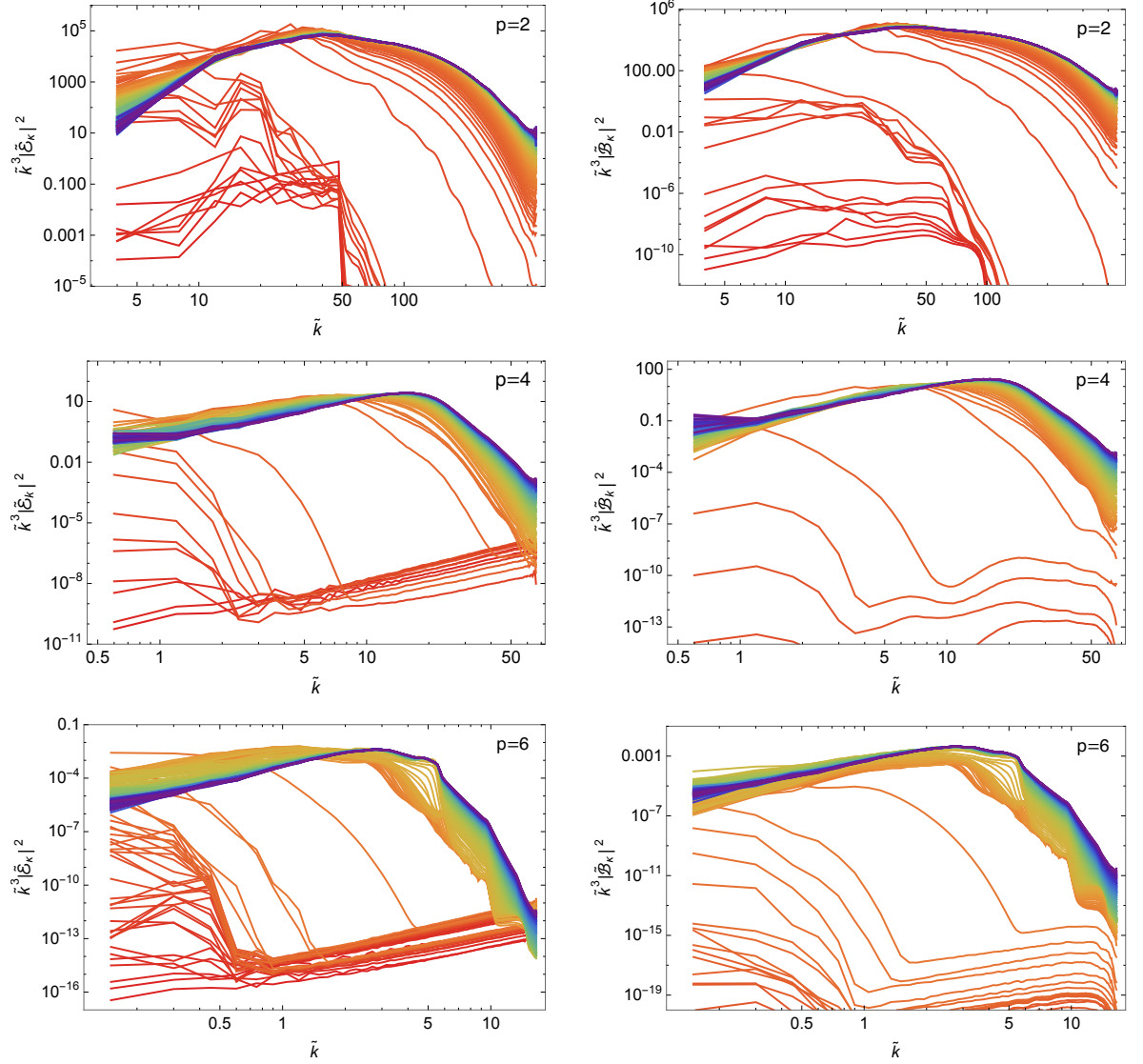


Figure 10.3 – Spectral evolution of the electric field  $\tilde{k}^3 |\tilde{\mathcal{E}}_k|^2$  (left panels) and magnetic field  $\tilde{k}^3 |\tilde{\mathcal{B}}_k|^2$  (right panels), as a function of  $\tilde{k} \equiv k/\omega_*$ , for the  $U(1)$  gauge simulations with  $p = 2, 4, 6$ . Each line shows the spectra at different moments of the evolution, going from red lines (early times) to purple lines (late times).

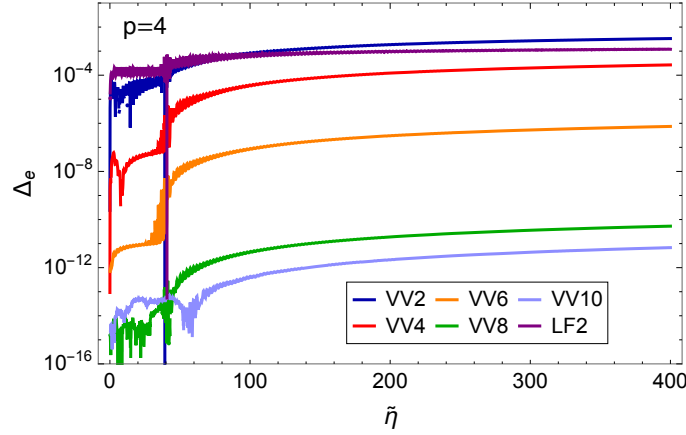


Figure 10.4 – Comparison of “energy conservation” in the  $U(1)$  gauge simulation with  $p = 4$ , for different evolution algorithms: velocity-Verlet (orders 2, 4, 6, 8, and 10), as well as staggered leapfrog (order 2).

slightly different context. This contrasts with the simulations of the analogous scalar theory simulated in Ref. [371], where the energy is distributed 50%-50% between the inflaton and the daughter field. On the other hand, in the gauge simulations for  $p = 6$  we do observe equipartition between inflaton and gauge energies at late times, although the simulation is not long enough in this case to determine if this distribution will hold for later times, or if it will slowly evolve towards the 60%-40% distribution observed for  $p = 4$ .

Finally, we show in Fig. 10.3 the spectra of the electric and magnetic fields for the three power-law potentials  $p = 2, 4, 6$  considered here. As expected from the linear analysis, mainly field modes within an infrared band  $\tilde{k} \equiv k/\omega_* \lesssim q_*^{1/4}$  grow exponentially during the initial linear regime, at times  $\tilde{\eta} < \tilde{\eta}_{\text{br}}$ . However, when backreaction happens at time  $\tilde{\eta} = \tilde{\eta}_{\text{br}}$ , the growth of the infrared band saturates, and the different fields start populating modes of increasingly high momenta due to rescattering. The spectra eventually saturate, showing a peak at larger scales. This process is qualitatively similar for the different choices of  $p$  considered here.

### 10.8.2.1 Accuracy tests

In flat space and in conservative systems, energy conservation can be used to monitor the precision of evolution algorithms. However, we are now considering an expanding Universe, and in particular, we are using the second Friedmann equation (10.155) to evolve the scale factor. In this context we can instead check that the first Friedmann equation (10.154) holds during the evolution. However, contrary to the Gauss laws (which are preserved by design when the discretized equations are gauge invariant), the first Friedmann’s law will be only approximately respected. We will loosely refer to this second Friedmann’s equation being respected as “energy conservation”, in analogy to the flat case. In particular, we require that the relative difference between the left and right hand sides of Eq. (10.154), which we denote

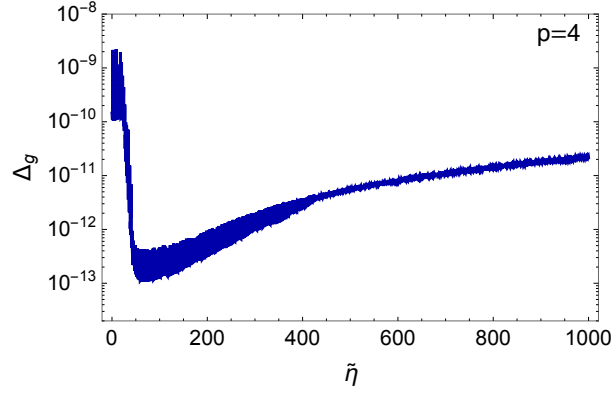


Figure 10.5 – Conservation of the Gauss law as a function of time for the  $U(1)$  gauge simulation with  $p = 4$ .

by  $\Delta_e$ , obeys always  $\Delta_e \ll 1$ . The better the accuracy of the evolution algorithm used to solve the lattice equations, the better “energy” is preserved. In order to illustrate this, we show in Fig. 10.4 the evolution of  $\Delta_e$  as a function of time, for the case  $p = 4$ . The lattice equations have been solved with different accuracy orders of the velocity Verlet algorithm, introduced in Section 10.3.3.2. As expected, the higher the order, the better the “energy” is preserved: the violation of “energy conservation” at time  $\tilde{\eta} \approx 400$  is  $\Delta_e \approx 3 \cdot 10^{-3}$ ,  $2 \cdot 10^{-4}$ ,  $7 \cdot 10^{-7}$ ,  $5 \cdot 10^{-11}$ , and  $6 \cdot 10^{-12}$ , for VV2, VV4, VV6, VV8, and VV10 respectively. This means that “energy conservation” improves by factors  $\sim 12$ ,  $360$ ,  $10^4$ , and  $8$ , as we increase the order of the integrator from one to the next one, i.e. from VV2 to VV4, VV4 to VV6, etc. Interestingly, the value of  $\Delta_e$  saturates for VV10: in that case, the error in the scale factor constraint is due exclusively to an accumulation of machine precision errors, so using velocity-Verlet algorithms of higher-orders than VV10 will not improve the energy constraint anymore. Of course, the negative side of using higher-order iterators is the increase of the required computation time. Finally, we have also solved the field dynamics with a second-order staggered leapfrog algorithm (see Section 10.3.3.1), which we denote as LF2. Remarkably, this algorithm slightly improves “energy conservation” at late times with respect VV2, as observed in the Figure.

Let us now focus on the conservation of the Gauss constraint, given in Eq. (10.42). As already mentioned, the Gauss constraint must be always satisfied up to machine precision, *independently of the accuracy of the integrator*, as it is a direct consequence of the lattice equations of motion: a violation of the Gauss constraints is a violation of gauge invariance. We show in Fig. 10.5 the relative difference between the left and right hand sides of Eq. (10.42) as a function of time, which we denote as  $\Delta_g$ . At the onset of the simulation we get  $\Delta_g \sim 10^{-9}$ , which is explained by the  $\sim 7$  orders of magnitude of difference between the amplitudes of the inflaton homogeneous mode and its fluctuations. After backreaction, the relative difference decreases down to  $\Delta_g \sim 10^{-13}$ , and starts increasing slowly from then on, due to a constant accumulation of machine precision errors.



### 10.8.3 Lattice simulations: $SU(2) \times U(1)$ gauge interactions

We now consider a scenario in which a complex doublet  $\Phi$  with potential (10.392) [where we must substitute  $\phi \rightarrow \Phi$ ] acts as an inflaton field, and it is simultaneously coupled to 1) a  $SU(2) \times U(1)$  gauge sector via a gauge-invariant covariant derivative, and 2) a massless secondary scalar field  $\chi$  via a quadratic interaction  $V_{\text{int}}(|\Phi|, \chi) \equiv (1/2)g^2|\Phi|^2\chi^2$ , with  $g$  a dimensionless coupling constant. The strength of the parametric resonance is determined, in each case, by the corresponding resonance parameter:  $q_*$  for the scalar field (see Eq. 10.406), and  $q_{A*}$  and  $q_{B*}$  for the  $U(1)$  and  $SU(2)$  gauge fields (see Eqs. 10.411). Here we fix  $q_{A*} = q_{B*} = q_*$  for illustrative purposes, with  $q_* > 1$  to have broad parametric resonance for all daughter field sectors. We have simulated the preheating process for the power-law coefficients  $p = 2, 4$ , and studied the post-inflationary dynamics of the system. The lattice and model parameters chosen for the simulations are given in Table 10.2, and are similar to the analogous  $U(1)$  simulations. In particular, we choose again  $M = 10m_p$ , which ensures that the inflaton always oscillates in the positive-curvature region of its potential. Similarly, the number of points and volume of the lattice are chosen, in each case, to resolve well both the infrared resonant bands, as well as the following propagation of the spectra towards the UV after backreaction.

The evolution of the inflaton amplitude, equation of state, and scale factor are, in this case, qualitatively similar to the examples shown for the  $U(1)$  gauge simulation in the previous section. Therefore, we proceed to consider directly the evolution of the energy distribution, which differs in some aspects with respect to the  $U(1)$  case. We show in Fig. 10.6 the evolution of the total energy of the system during preheating, as well as of each of its different contributions, for  $p = 2, 4$ . These are the kinetic and gradient energies of the scalars  $\Phi$  and  $\chi$ , the electric and magnetic energies of the  $U(1)$  and  $SU(2)$  gauge sectors, the inflaton potential energy  $\tilde{V}_{\text{pot}} \equiv |\tilde{\Phi}|^4$ , and the interaction energy  $\tilde{V}_{\text{int}} \equiv (1/2)q_*|\tilde{\Phi}|^2\tilde{\chi}^2$  between  $\Phi$  and  $\chi$ . As in the  $U(1)$  case, we have multiplied the different energies by the appropriate scale factor term, so that the (oscillation-averaged) total energy is constant during the initial linear regime. We also show the evolution of the energy ratios  $\epsilon_i \equiv \tilde{\rho}_i/\tilde{\rho}$ , which sum one by construction.

As expected, the energy budget is dominated by the inflaton homogeneous mode initially, so the kinetic and potential energies of the inflaton dominate over all the other energy contributions. However, the kinetic and gradient energies of all daughter fields grow exponentially due to broad parametric resonance, as well as the inflaton gradient energy. These contributions become sizeable enough at a certain time scale, destroying the inflaton homogeneous condensate via backreaction effects. As before, we denote this time scale as the *backreaction time*  $\tilde{\eta}_{\text{br}}$ . From the simulations, we get  $\tilde{\eta}_{\text{br}} \simeq 60, 40$  for  $p = 2, 4$  respectively. From then on, the non-linearities of the field EOM can no longer be ignored, and affect the dynamics of the system, achieving a stationary regime at late times. As in the  $U(1)$  gauge simulation, we observe that the system gets virialized very quickly, with the inflaton energies obeying  $\langle E_K^\Phi \rangle \simeq \langle E_G^\Phi \rangle + \frac{p}{2}\langle E_V \rangle + \langle E_{\text{int}} \rangle$  when averaged over oscillations. Also, we also have equipartition between the kinetic and gradient energies of all daughter field sectors at late

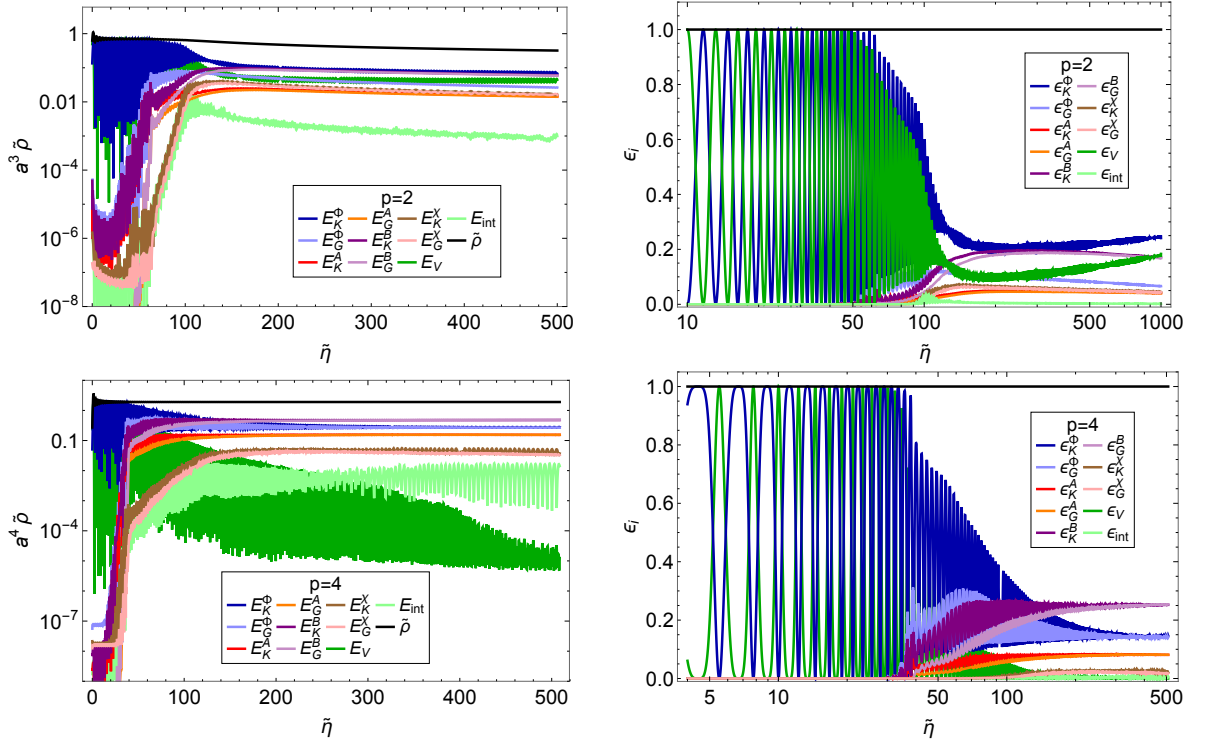


Figure 10.6 – Left panel: Evolution of the total energy in program units,  $\bar{\rho} \equiv \rho/\omega_*$ , as well as of each of its energy contributions, for the  $SU(2) \times U(1) + \chi$  gauge simulations with  $p = 2, 4$ . Quantities are multiplied by the factor  $\sim a^{\frac{6p}{p+2}}$ . Right panel: Evolution of the energy ratios for the same simulations as in the left panels.

times, as can be observed in the Figure.

Let us now comment about how the energy distributes at very late times. Let us consider first the case  $p = 2$ . Here we observe a qualitatively similar behaviour than in the equivalent  $U(1)$  simulation: although the inflaton kinetic and potential energy ratios decay around backreaction time, at later times they start growing again. The reason is the same as in the  $U(1)$  simulations: the inflaton does not get excited via self-resonance for  $p = 2$ , while the parametric resonance of the daughter fields eventually becomes narrow (because the effective resonance parameter (10.409) decreases with time). Therefore, at very late times neither of the two resonant phenomena is present, and the inflaton slowly recovers all the energy of the system due to the different dilution rates of the energy contributions (the inflaton behaves as matter, while the daughter fields as radiation). Due to this, although our simulations are not long enough to observe this effect, we expect that  $\epsilon_K^\phi, \epsilon_V \rightarrow 0.5$  at asymptotically late times. Moreover, this energy configuration also gives rise to a matter-dominated equation of state at late times,  $w \rightarrow 0$ .

Let us focus now on the simulation with  $p = 4$ . In this case, the effective resonance parameter

(10.409) remains constant. Therefore, as we have fixed  $q_* = q_{\text{eff}} > 1$  for all daughter field species (scalar  $\chi$ , Abelian and non-Abelian gauge bosons), they experience a broad parametric excitation during the whole time evolution of the system, including at late times. Similarly, the inflaton is also being excited due to the oscillations of its own homogeneous mode, and develops fluctuations via self-resonance. Neither of the two effects dies out, which could explain why neither of the two field sectors (inflaton or daughter fields) possesses 100% of the total energy at asymptotically late times. In our particular scenario, we observe that at the end of the simulation, the inflaton possesses  $\sim 30\%$  of the total energy, the scalar singlet  $\sim 4\%$ , the  $U(1)$  gauge sector  $\sim 16\%$ , and the  $SU(2)$  gauge sector  $\sim 50\%$ . In each of the four cases, the energy is divided half and half between kinetic and gradient contributions. These results are in contrast with the analogous  $U(1)$  simulation, which show that  $\sim 60\%$  of the total energy remains in the inflaton at late times. From this result, we can conclude the (somewhat expected) result that the larger the number of daughter fields, the larger the amount of energy that gets transferred to them from the inflaton. Finally, let us also observe that the inflaton potential and inflaton- $\chi$  interaction energies go to zero at late times,  $\epsilon_V, \epsilon_{\text{int}} \rightarrow 0$ , as in the analogous  $U(1)$  gauge simulation. Due to this, the effective equation of state goes to  $w \rightarrow 1/3$  at late times.

We also show in Fig. 10.7 the evolution of the spectra of all fields involved: the norm of the inflaton  $|\Phi|$ , the scalar singlet  $\chi$ , and the electric and magnetic energies of the  $U(1)$  and  $SU(2)$  sector. We observe in all cases the same qualitative behaviour: first an exponential growth of the field modes within an infrared band, which saturates at backreaction time, followed by a propagation of the spectra towards the UV, populating modes of higher and higher momenta. The initial infrared growth of the gauge fields is in agreement with the linear analysis presented above, except in the case of the inflaton, which does not experience broad parametric resonance. The inflaton growth is, instead, triggered by backreaction effects from the daughter fields.

### 10.8.3.1 Accuracy tests

Finally, it is always important to check that both “energy conservation” and the Gauss constraints are preserved at all times during the simulation. Let us consider first the left of panel of Fig. 10.8, where we show the relative difference between the left and right hand sides of the 1st Friedmann equation as a function of time (denoted as  $\Delta_e$ ), for  $p = 4$ . Naturally, we require  $\Delta_e \ll 1$  in order to trust the results of our simulations. For illustrative purposes, we have solved the field dynamics with velocity-Verlet evolution algorithms of orders 2 and 4, for the same lattice and model parameters. As expected, the higher the accuracy of the integrator, the better “energy” is preserved: at time  $\tilde{\eta} \approx 340$  we get  $\Delta_e \approx 2.2 \cdot 10^{-3}$  for VV2, and  $\Delta_e \approx 1.1 \cdot 10^{-4}$  for VV4, i.e. VV4 preserves “energy” a factor  $\sim 20$  better than VV2. However, the negative side is that the required simulation time for VV4 increases with respect VV2, as expected. In principle, one should be able to improve the accuracy of the integrator arbitrarily up to machine precision, as in the analogous  $U(1)$  gauge simulation shown in Fig. 10.4. This

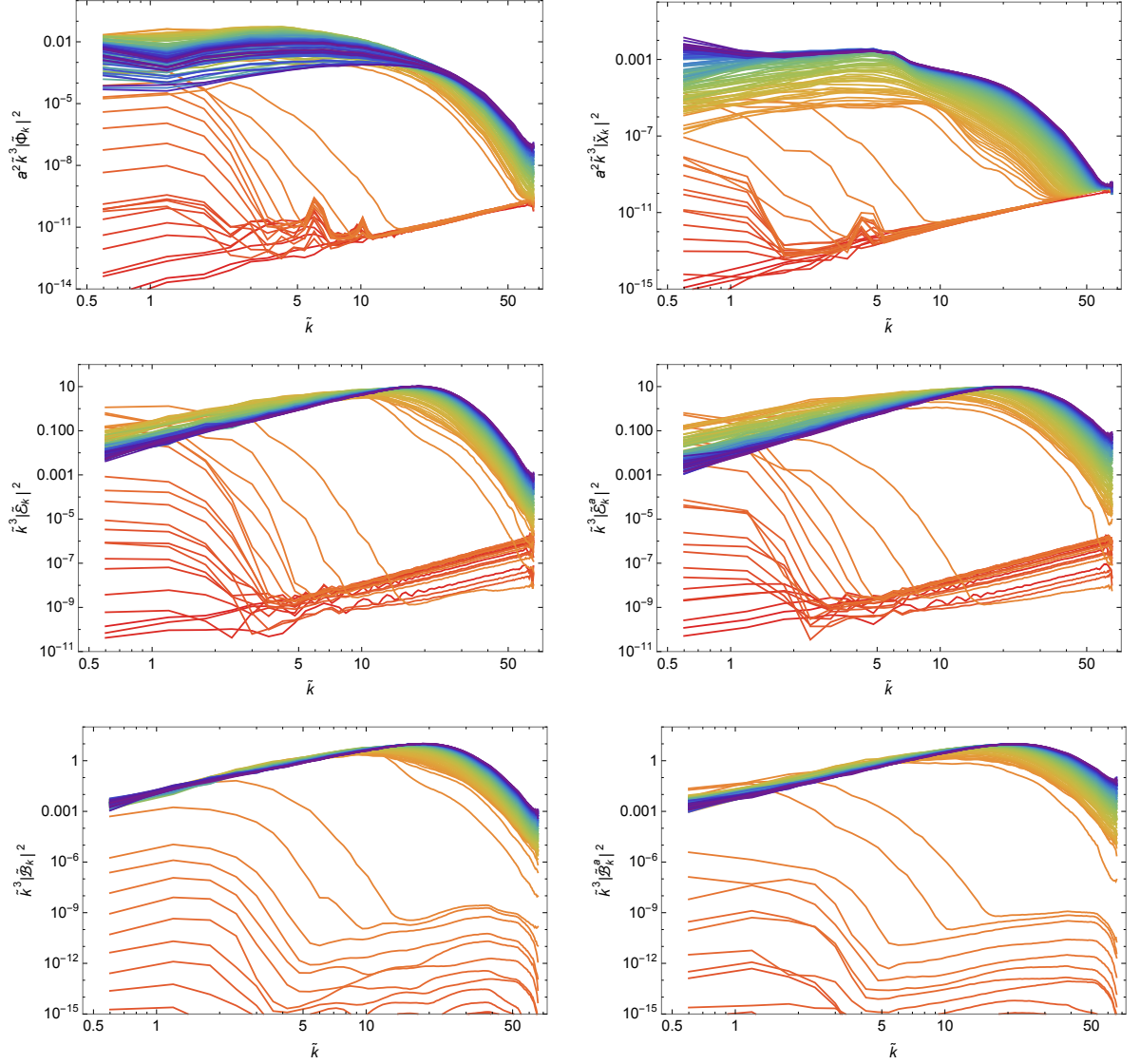


Figure 10.7 – Spectral evolution of all the fields involved in the  $SU(2) \times U(1) + \chi$  lattice simulations as a function of  $\tilde{k} \equiv k/\omega_*$ , for  $p = 4$ . From left to right and from top to bottom, we show the inflaton, the massless scalar  $\chi$ , the electric and magnetic fields of the  $U(1)$  gauge sector, and electric and magnetic fields of the  $SU(2)$  gauge sector. Each line shows the spectra at different times during the field evolution, from red (early times) to purple (late times).

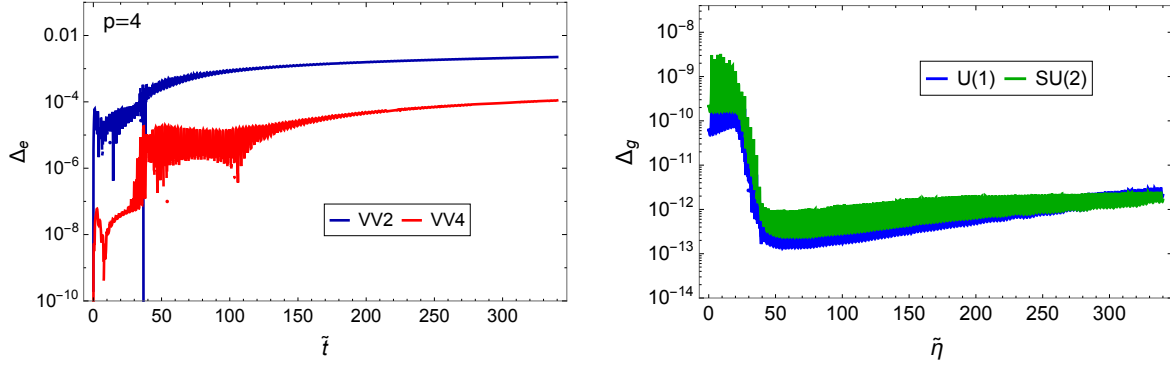


Figure 10.8 – Left panel: Evolution of the relative error in “energy conservation” for the  $SU(2) \times U(1) + \chi$  simulation with  $p = 4$ , obtained for the VV2 and VV4 algorithms. Right panel: Evolution of the relative error in the Gauss constraints of the  $U(1)$  and  $SU(2)$  gauge sectors, for the same simulation.

can be useful if one wants to apply this algorithm to any particular scenario requiring extremely good energy conservation. This is always at the expense, of course, of longer simulation times.

In the right panel of Fig. 10.8 we show how the Gauss laws are preserved during the simulation. In this case there are two Gauss laws that must be satisfied: one for the  $U(1)$  sector (given in Eq. 10.25), and another one for the  $SU(2)$  sector (given in Eq. 10.26). We measure this by the parameter  $\Delta_g$ , which as defined before, is the relative difference between the left and hand sides of the corresponding Gauss constraints. As explained before, these constraints must be preserved up to machine precision independently of the chosen evolution algorithm, as they are a direct consequence of the gauge invariance that our careful discretization techniques maintain on the lattice equations. We observe a similar behaviour as in the analogous  $U(1)$  gauge simulations: before backreaction we have  $\Delta_g \sim 10^{-9}$  for both gauge sectors, due to the large relative difference between the amplitudes of the inflaton homogeneous mode and its fluctuations. After backreaction we get  $\Delta_g \simeq 10^{-13}$ , and from then on, the error slowly grows due to a constant accumulation of machine precision errors in each time step. At time  $\tilde{t} \simeq 340$  we get  $\Delta_g \sim 10^{-12}$  for both  $U(1)$  and  $SU(2)$  gauge sectors, which shows that both Gauss constraints are exceptionally well preserved during the simulation.

## 10.9 Summary and outlook

The present document represents *Part I* of a comprehensive dissertation on lattice techniques for the simulation of non-linear dynamics in the early Universe. Here we have focused on the lattice treatment of canonical scalar-gauge field theories in an expanding Universe, considering an arbitrary number of interacting (real and complex) scalars and (Abelian and non-Abelian) gauge fields. This suffices to describe the majority of physically relevant scenarios from the early universe. In addition, we plan to discuss methods for non-canonical interactions in an

upcoming *Part II* [408], like those in theories with non-minimal gravitational couplings, or in general with non-minimal kinetic terms, as well as non-canonical interactions defined by the product between field variables and their conjugate momenta.

Let us summarize the content of the present work. In Section 10.2 we reviewed first the field dynamics of scalar-gauge theories in a continuum space-time, both with and without expansion of the Universe. We considered a theory containing different kinds of scalars (singlets,  $U(1)$ -charged, and  $SU(N) \times U(1)$ -charged scalars) and (Abelian and non-Abelian) gauge fields. We wrote explicitly the EOM of such theory, as well as introduced the notation later used throughout the document. We then introduced in Section 10.3 basic concepts of lattice techniques, with a special emphasis on how to discretize appropriately gauge theories to preserve gauge invariance on the lattice. We then introduced basic evolution algorithms for the integration of the field EOM: staggered leapfrog and Verlet methods, with accuracy  $\mathcal{O}(\delta t^2)$ . We also showed how some of these basic algorithms can be used as building blocks for the higher-order Yoshida integrators, with accuracy up to  $\mathcal{O}(\delta t^{10})$ .

In the following three sections we focused on developing lattice formulations for the different field sectors of the canonical theories considered here. In Section 10.4 we considered the case of multiple interacting scalar fields. We first have introduced a set of dimensionless field and spacetime variables, which we have call the *lattice* or *program* variables. When thoughtfully defined, these variables can be very useful when working on a lattice. Our lattice algorithms are therefore written in terms of these variables. We explained how to apply different evolution algorithms to solve the scalar EOM, as well as define different useful observables. In Section 10.5 we developed the same ideas for gauge theories with  $U(1)$  interactions, and in Section 10.6 we did the same for gauge theories with  $SU(N)$  interactions. In Section 10.7 we described how to set the initial conditions for the different kinds of fields, both in the continuum and on the lattice. For scalar fields, we imposed a spectrum of classical vacuum fluctuations, which mimics the expected spectrum of quantum fluctuations in a FLRW Universe. For gauge fields, we discussed how to set their initial conditions so that Gauss constraint is preserved from the beginning.

Finally, in Section 10.8, we simulated the dynamics of a specific scalar-gauge field model with *CosmoLattice*, to illustrate some of the techniques presented in the previous sections. In particular, we considered the preheating dynamics of a charged inflaton, with monomial shape around the minimum of its potential. We considered two different scenarios: 1) a  $U(1)$ -charged scalar coupled to an Abelian gauge field, and 2) a  $SU(2) \times U(1)$  charged scalar coupled to Abelian and non-Abelian gauge fields simultaneously, as well as to a scalar singlet. We considered different model parameters, and in particular, we studied different power-law coefficients in the monomial function. We studied the evolution during preheating of several relevant observables: the inflaton mean amplitude value, the evolution of the scale factor and of the equation of state, the energy distributions among field components, and the relevant field spectra. We showed explicitly how each Gauss constraint is preserved to machine precision during the evolution of the system. We also demonstrated the power of the

higher-order Verlet evolution algorithms implemented in `CosmoLattice`, which can be used to obtain energy conservation up to machine precision in simulations of scalar-gauge theories in an expanding Universe.

Let us emphasize here that, to the best of our knowledge, we are presenting for the first time an algorithm for non-Abelian  $SU(N)$  gauge theories, which is symplectic, explicit in time, and preserving exactly the Gauss constraint, while solving for the expansion of the universe self-consistently. Furthermore, it can be made of arbitrary order. Besides, we also present higher-order integration algorithms for Abelian  $U(1)$  gauge theories, similar to those in `GFiRe` [184], demonstrating explicitly for the first time their numerical implementation for the highest orders, in particular for  $\mathcal{O}(\delta t^6)$ ,  $\mathcal{O}(\delta t^8)$  and  $\mathcal{O}(\delta t^{10})$ . Similarly, we also present higher-order integration algorithms for interacting scalar theories, similar to those in `HLattice` [181], but going also to higher-orders, in particular building explicit implementations for  $\mathcal{O}(\delta t^8)$  and  $\mathcal{O}(\delta t^{10})$ .

The concepts and techniques discussed in this dissertation, in particular the explicit-in-time algorithms presented in Sections 10.4-10.6, are already implemented in our present code `CosmoLattice`, a *user-friendly* and highly modular C++ MPI-based code for lattice simulations of non-linear classical dynamics in an expanding universe, that we plan to publicly release before the end of 2020. Most of the algorithms presented in this work are bundled in a high-level interface which allows the user to add almost effortlessly models with different interaction potentials, and easily add new integration algorithms. Moreover, the library has been designed in such a way to allow the user to use complex, vectorial and matricial representation of fields, to keep the lattice equations resembling as much as possible to the continuum ones. This level of abstraction is achieved through the use of compile-time code generation, using C++ expression templates, so that performance is never sacrificed.

The aim of this manuscript has been to illustrate different concepts of lattice gauge-invariant techniques and of general integration methods, which we have then specialized and adapted for their use in the context of canonical scalar-gauge field theories. We expect that the work we have developed so far here (soon to be complemented by *Part II* [408]) shall be useful for a large fraction of the research community interested in the early universe, let it be completely inexperienced researchers in lattice field theory simulations, or very experienced ones.

To conclude, we comment on several aspects that we plan to explore in forthcoming works (either in *Part II* or elsewhere), both in the near and in the mid-term future:

- The development of lattice techniques for the discretization of theories with non-minimal kinetic terms. As the *drift* and *kick* functionals in these theories typically contain a linear combination of conjugate momenta of other fields, explicit-in-time symplectic integrators (such as staggered leapfrog or Verlet integrators) are not appropriate. However, one can resort to explicit (non-symplectic) Runge-Kutta methods (this has been done in e.g. [183]), or even to higher-order implicit (yet symplectic) integrators like

the Gauss-Legendre methods. As mentioned before, we postpone a specialized discussion of these problems to *Part II* of our dissertation on lattice techniques [408]. The implementation of the corresponding algorithms in *CosmoLattice* will also be made publicly available in that moment.

- In a similar spirit, the axial couplings of a pseudo-scalar field with a gauge sector is also of great interest. An implicit method for the interaction of an axion-like field  $\phi$  with a  $U(1)$ -gauge sector through a shift invariant coupling  $\phi F^{\mu\nu} \tilde{F}_{\mu\nu}$ , has been in fact explored in [115, 276–281]. In particular, an exactly lattice-shift-symmetric formulation was developed in [115], and was later on generalized to an expanding background in [279]. We could revisit and generalize this kind of approaches in light of the algorithms presented here in Section 10.3, coming possibly with many potential outlooks. We plan to present a specialized discussion on these interactions in *Part II* [408].
- The creation of tensor perturbation representing gravitational waves [280, 281, 293, 318–335], as well as the dynamics of scalar metric perturbations [299–308] (possibly leading to the formation of primordial black holes [309–317]) are all topics of great interest. In the case of tensor perturbations, we plan to follow [415] (based on an idea originally proposed in [321]), as this technique allows for generic sources independently of the field content of the theory studied. Although we have not decided about a clear strategy for a general solver of scalar metric perturbations yet, one possibility would be to follow [181].
- The inclusion of fermions in the simulations. Of course, the notion of ‘classical fermions’ does not exist due to Pauli-blocking, and hence a straightforward discretization and evolution of the Dirac equation would not be useful. However, as first realised in [413], one can still study real-time fermions’ dynamics in a semi-classical formulation of the out-of-equilibrium Schwinger-Keldysh formulation, see also references [90, 92, 425]. Combining the lattice implementation proposed in [413], with the ‘low cost’ fermions introduced in [414], [409–412] have succeeded in simulating out-of-equilibrium dynamics of classical scalar fields coupled to quantum fermions. These simulations are however very costly in terms of computer memory, and only very small lattices have been considered until now.
- The addition of other initialization procedures. Depending on the problem, initializing fields in real space might be more convenient than imposing a certain mode spectrum in Fourier space, as we did in Section 10.7. As mentioned in the introduction, to simulate e.g. the dynamics of field string networks or any other type of cosmic defects, one needs to create in first place the defect network in configuration space, see e.g. [338–345, 390, 391, 416], and then evolve the field configuration from then onward (typically after a diffusion phase to force the system to reach a scaling regime as fast as possible). Although different problems may require completely different initializers, it might be useful to consider making a library for specialized ones for cosmic strings, other topological defects, and other circumstances.



- The addition of ‘cooling’ procedures for the initial condition for gauge fields. Another improvement would be to use cooling algorithms to initialize gauge fields. Instead of imposing the Gauss constraints by hand as we have done in Section 10.7.2, one can impose completely unconstrained fluctuations to the gauge fields, and then remove the unwanted transverse degree’s of freedom by a minimization procedure [28, 116]. For thermal initial conditions, one can also thermalize the system while exactly preserving Gauss law through some Langevin dynamics [426]. Studying such algorithms will allow us to consider different initial conditions and thus study yet another variety of models.

## Acknowledgments

The authors would like to thank Andrei Frolov for useful discussions, and in particular for pointing us out the Gauss-Legendre methods. D.G.F. and F.T. acknowledge hospitality from KITP-UCSB, where part of this work was carried out under support by the National Science Foundation under Grant No. NSF PHY-1748958. F.T. thanks M. Shaposhnikov for his kind invitation to EPFL during the development of this work. A.F. wants to thank S. Antusch for his kind invitation to Basel. D.G.F. (ORCID 0000-0002-4005-8915) is supported by a Ramón y Cajal contract by Spanish Ministry MINECO, with Ref. RYC-2017-23493. A.F. acknowledges support from the Swiss National Science Foundation. F.T. also acknowledges support from the Swiss National Science Foundation (project number 200020/175502).

## Appendices

### 10.10 Cristoffel symbols

The most straightforward way to obtain them is by deriving the geodesic equations. To do so, we start from the action from a unit mass free particle

$$S_{free}^{1part} = \int ds g_{\mu\nu} \dot{x}^\mu \dot{x}^\nu = \int ds \left( -a(\eta)^{2\alpha} \dot{\eta}^2 + a(\eta)^2 \delta_{ij} \dot{x}^i \dot{x}^j \right), \quad (10.412)$$

where  $\dot{f}$  denotes the differentiation with respect to  $s$ . From now on, we will also write  $f'$  for the differentiation with respect to  $\eta$ . Then, we compute the variation with respect to the coordinates and compare to the canonical form of the geodesic equations

$$\ddot{x}^\mu + \Gamma_{\alpha\beta}^\mu \dot{x}^\alpha \dot{x}^\beta = 0. \quad (10.413)$$

We start with the  $\eta$ -variation. Using the relations

$$(a(\eta + \delta\eta)^{2\alpha} - a(\eta)^{2\alpha})^{lin} = 2\alpha a(\eta)^{2\alpha-1} a'(\eta) \delta\eta \quad (10.414)$$

$$\dot{a}(\eta) = a'(\eta) \dot{\eta}, \quad (10.415)$$

and integrating by part the terms of the sort  $\delta \dot{f}$ , we find

$$\begin{aligned} \left( S_{free}^{1part}[\eta + \delta\eta] - S_{free}^{1part}[\eta] \right)^{lin} &= \int ds \left( -2\alpha a(\eta)^{2\alpha-1} a'(\eta) \dot{\eta}^2 \delta\eta - 2a(\eta)^{2\alpha} \dot{\eta} \delta\dot{\eta} \right. \\ &\quad \left. + 2a(\eta) a'(\eta) \delta_{ij} \dot{x}^i \dot{x}^j \delta\eta \right) \end{aligned} \quad (10.416)$$

$$\begin{aligned} &= 2 \int ds \left( \alpha a(\eta)^{2\alpha-1} a'(\eta) \dot{\eta}^2 + a(\eta)^{2\alpha} \ddot{\eta} \right. \\ &\quad \left. + a(\eta) a'(\eta) \delta_{ij} \dot{x}^i \dot{x}^j \right) \delta\eta = 0 \end{aligned} \quad (10.417)$$

$$\left( S_{free}^{1part}[x_i + \delta x_i] - S_{free}^{1part}[x_i] \right)^{lin} = \int ds \left( a(\eta)^2 \delta_{ij} \dot{x}^j \delta \dot{x}^i \right) \quad (10.418)$$

$$= \int ds \left( -a(\eta)^2 \ddot{x}^i - 2a(\eta) a'(\eta) \dot{\eta} \dot{x}^i \right) \delta x_i \quad (10.419)$$

In canonical form, this gives us the following geodesic equations for

$$\ddot{\eta} + \alpha \frac{a'(\eta)}{a(\eta)} \dot{\eta}^2 + a^{-2\alpha+2} \frac{a'(\eta)}{a(\eta)} \delta_{ij} \dot{x}^i \dot{x}^j = 0 \quad (10.420)$$

$$\ddot{x}^i + 2 \frac{a'(\eta)}{a(\eta)} \dot{\eta} \dot{x}^i = 0 . \quad (10.421)$$

It tells us that the following Cristoffel symbols are non-vanishing

$$\Gamma_{00}^0 = \alpha \frac{a'(\eta)}{a(\eta)} \quad (10.422)$$

$$\Gamma_{ij}^0 = a^{-2\alpha+2} \frac{a'(\eta)}{a(\eta)} \delta_{ij} \quad (10.423)$$

$$\Gamma_{i0}^i = \frac{a'(\eta)}{a(\eta)} . \quad (10.424)$$

With the Cristoffel's symbols at hand, we can move on to derive the Friedmann's equations (9.3) and (9.4) for the line element (10.27).

## 10.11 Friedmann's equations

The Friedmann's equations are obtained by computing the Einstein tensor associated to (10.27) and plugging it in Einstein's equations (9.2). Rather than repeating here explicitly the derivation of the FLRW Einstein tensor, we join in appendix 10.12 a Cadabra notebook [427, 428] which computes it from the metric. The non-vanishing components are

$$G_{00} = 3a'(\eta)^2 a(\eta)^{-2} \quad (10.425)$$

$$G_{ii} = \left( (2\alpha - 1) a'(\eta)^2 - 2a(\eta) a''(\eta) \right) a(\eta)^{-2\alpha} \quad (10.426)$$

As already mentioned, in a cosmological context, these equations are often rewritten in terms of energy density  $\rho$  and pressure  $p$ . They are defined in analogy by comparing to the

energy-momentum tensor of a perfect fluid.

$$T_{\mu\nu}^{fluid} = (p + \rho) v_\mu v_\nu + p g_{\mu\nu} \quad (10.427)$$

with  $v_\nu$  the fluid's velocity field. In the fluid's rest frame,  $v_i=0$ ,  $v_0 = -a^\alpha$ , so that  $v^\mu v_\mu = -1$ ), giving

$$T_{00}^{fluid} = \rho a^{2\alpha} \quad (10.428)$$

$$T_{ii}^{fluid} = p a^2. \quad (10.429)$$

We thus define, for generic matter content

$$\rho = a^{-2\alpha} T_{00} \quad (10.430)$$

$$p = \frac{a^{-2}}{3} \sum_{i=0}^3 T_{ii} \quad (10.431)$$

and rewrite Einstein's equations as

$$a'(\eta)^2 = \frac{a^{2\alpha+2}}{3m_p^2} \rho \quad (10.432)$$

$$((2\alpha - 1)a'(\eta)^2 - 2a(\eta)a''(\eta)) = \frac{1}{m_p^2} a^{2\alpha+2} p \quad (10.433)$$

For further uses, it is convenient to combine equations (10.432) and (10.433) to get an equation for  $a''(\eta)$

$$a''(\eta) = \frac{1}{6m_p^2} a^{2\alpha+1} ((2\alpha - 1)\rho - 3p). \quad (10.434)$$

## 10.12 FLRW with Cadabra2

In this appendix, we present computations of the rescaled FLRW Einstein's tensor using the Cadabra software [427, 428].

In this notebook, we compute the Einstein's tensor for FLRW, with a rescaled time.

```
1 {t,x,y,z}::Coordinate.
2 {\mu,\nu,\alpha,\beta,\sigma,\rho}::Indices(values={t,x,y,z}, position=fixed).
3 \partial{#}::PartialDerivative.
4 g_{\mu\nu}::Metric.
5 g^{\mu\nu}::InverseMetric.
6 a::Depends(t).
```

We start by defining our FLRW metric. The parameter  $b$  allows to go from coordinate time to conformal time, or any other time rescaling.

```
1 flrw := {g_{t t}=-a**(2b), g_{x x}=a**2, g_{y y}=a**2, g_{z z}=a**2}.
2 complete(flrw, $g^{\mu \nu}$);
```

$$\left[ g_{tt} = -a^{2b}, \quad g_{xx} = a^2, \quad g_{yy} = a^2, \quad g_{zz} = a^2, \quad g^{tt} = -a^{-2b}, \quad g^{xx} = a^{-2}, \quad g^{yy} = a^{-2}, \quad g^{zz} = a^{-2} \right]$$

We then compute the Cristoffel's symbols, Riemann tensor, Ricci tensor and Ricci scalar.

```

1  ch:= \Gamma^{\mu}_{\nu\rho} = 1/2 g^{\mu\sigma} (
2      \partial_{\rho} g_{\nu\sigma}
3      +\partial_{\nu} g_{\rho\sigma}
4      -\partial_{\sigma} g_{\nu\rho} ):
5  evaluate(ch, flrw, rhsonly=True);

```

$$\Gamma^{\mu}_{\nu\rho} = \frac{1}{2} g^{\mu\sigma} (\partial_{\rho} g_{\nu\sigma} + \partial_{\nu} g_{\rho\sigma} - \partial_{\sigma} g_{\nu\rho})$$

$$\Gamma^{\mu}_{\nu\rho} = \square_{\nu\rho}^{\mu} \left\{ \begin{array}{l} \square_{zt}^z = \partial_t a a^{-1} \\ \square_{yt}^y = \partial_t a a^{-1} \\ \square_{xt}^x = \partial_t a a^{-1} \\ \square_{tt}^t = b \partial_t a a^{-1} \\ \square_{tz}^z = \partial_t a a^{-1} \\ \square_{ty}^y = \partial_t a a^{-1} \\ \square_{tx}^x = \partial_t a a^{-1} \\ \square_{zz}^t = a^{(-2b+1)} \partial_t a \\ \square_{yy}^t = a^{(-2b+1)} \partial_t a \\ \square_{xx}^t = a^{(-2b+1)} \partial_t a \end{array} \right.$$

In more compact notations, this gives  $\Gamma_{it}^i = \frac{a'}{a}$ ,  $\Gamma_{tt}^t = b \frac{a'}{a}$ ,  $\Gamma_{ij}^t = a^{-2b+2} \frac{a'}{a} \delta_{ij}$ .

```

1  rm:= R^{\mu}_{\nu\alpha\beta} = \partial_{\alpha} \Gamma^{\mu}_{\nu\beta}
2      -\partial_{\beta} \Gamma^{\mu}_{\nu\alpha}
3      +\Gamma^{\mu}_{\sigma\alpha} \Gamma^{\sigma}_{\nu\beta}
4      -\Gamma^{\mu}_{\sigma\beta} \Gamma^{\sigma}_{\nu\alpha};

```

$$R^{\mu}_{\nu\alpha\beta} = \partial_{\alpha} \Gamma^{\mu}_{\nu\beta} - \partial_{\beta} \Gamma^{\mu}_{\nu\alpha} + \Gamma^{\mu}_{\sigma\alpha} \Gamma^{\sigma}_{\nu\beta} - \Gamma^{\mu}_{\sigma\beta} \Gamma^{\sigma}_{\nu\alpha}$$

```

1  substitute(rm, ch)
2  evaluate(rm, flrw, rhsonly=True);

```

$$R^\mu{}_{\nu\alpha\beta} = \square_{\nu\beta}{}^\mu{}_\alpha \left\{ \begin{array}{l} \square_{xx}{}^t{}_t = (-b(\partial_t a)^2 + a\partial_{tt}a) a^{-2b} \\ \square_{yy}{}^t{}_t = (-b(\partial_t a)^2 + a\partial_{tt}a) a^{-2b} \\ \square_{zz}{}^t{}_t = (-b(\partial_t a)^2 + a\partial_{tt}a) a^{-2b} \\ \square_{tx}{}^x{}_t = (-b(\partial_t a)^2 + a\partial_{tt}a) a^{-2} \\ \square_{ty}{}^y{}_t = (-b(\partial_t a)^2 + a\partial_{tt}a) a^{-2} \\ \square_{tz}{}^z{}_t = (-b(\partial_t a)^2 + a\partial_{tt}a) a^{-2} \\ \square_{xt}{}^t{}_x = (b(\partial_t a)^2 - a\partial_{tt}a) a^{-2b} \\ \square_{yt}{}^t{}_y = (b(\partial_t a)^2 - a\partial_{tt}a) a^{-2b} \\ \square_{zt}{}^t{}_z = (b(\partial_t a)^2 - a\partial_{tt}a) a^{-2b} \\ \square_{tx}{}^x{}_x = (b(\partial_t a)^2 - a\partial_{tt}a) a^{-2} \\ \square_{ty}{}^y{}_y = (b(\partial_t a)^2 - a\partial_{tt}a) a^{-2} \\ \square_{tz}{}^z{}_z = (b(\partial_t a)^2 - a\partial_{tt}a) a^{-2} \\ \square_{yy}{}^z{}_z = a^{-2b}(\partial_t a)^2 \\ \square_{xx}{}^z{}_z = a^{-2b}(\partial_t a)^2 \\ \square_{zz}{}^y{}_y = a^{-2b}(\partial_t a)^2 \\ \square_{xx}{}^y{}_y = a^{-2b}(\partial_t a)^2 \\ \square_{zz}{}^x{}_x = a^{-2b}(\partial_t a)^2 \\ \square_{yy}{}^x{}_x = a^{-2b}(\partial_t a)^2 \\ \square_{yz}{}^z{}_y = -a^{-2b}(\partial_t a)^2 \\ \square_{xz}{}^z{}_x = -a^{-2b}(\partial_t a)^2 \\ \square_{zy}{}^y{}_z = -a^{-2b}(\partial_t a)^2 \\ \square_{xy}{}^y{}_x = -a^{-2b}(\partial_t a)^2 \\ \square_{zx}{}^x{}_z = -a^{-2b}(\partial_t a)^2 \\ \square_{yx}{}^x{}_y = -a^{-2b}(\partial_t a)^2 \end{array} \right.$$

Or in other words  $R^t{}_{tti} = (-ba'^2 + aa'')a^{-2b}$ ,  $R^i{}_{tti} = (-ba'^2 + aa'')a^{-2}$  and  $R^i{}_{jjj} = a^{-2b}a'^2$ .

```
1 rc:= R_{\sigma\nu} = R^{\rho}_{\sigma\rho\nu};
2 substitute(rc, rm)
3 evaluate(rc, flrw, rhsonly=True);
```

$$R_{\sigma\nu} = R^\rho{}_{\sigma\rho\nu}$$

$$R_{\sigma\nu} = \square_{\sigma\nu} \left\{ \begin{array}{l} \square_{xx} = (-b(\partial_t a)^2 + a\partial_{tt}a + 2(\partial_t a)^2) a^{-2b} \\ \square_{yy} = (-b(\partial_t a)^2 + a\partial_{tt}a + 2(\partial_t a)^2) a^{-2b} \\ \square_{zz} = (-b(\partial_t a)^2 + a\partial_{tt}a + 2(\partial_t a)^2) a^{-2b} \\ \square_{tt} = 3(b(\partial_t a)^2 - a\partial_{tt}a) a^{-2} \end{array} \right.$$

```
1 rs:= R = g^{\mu\nu} R_{\mu\nu};
2 substitute(rs,rc)
3 evaluate(rs,flrw, rhsonly=True);
```

$$R = g^{\mu\nu} R_{\mu\nu}$$

$$R = 6(-b(\partial_t a)^2 + a\partial_{tt}a + (\partial_t a)^2) a^{(-2b-2)}$$

```
1 et := G_{\mu\nu} = R_{\mu\nu} - R/2 g_{\mu\nu};
2 substitute(et,rc)
```

```

3  substitute(et,rs)
4  evaluate(et,flrw, rhsonly=True);

```

$$G_{\mu\nu} = R_{\mu\nu} - \frac{1}{2} R g_{\mu\nu}$$

$$G_{\mu\nu} = \square_{\mu\nu} \begin{cases} \square_{xx} = (2b(\partial_t a)^2 - 2a\partial_{tt}a - (\partial_t a)^2) a^{-2b} \\ \square_{yy} = (2b(\partial_t a)^2 - 2a\partial_{tt}a - (\partial_t a)^2) a^{-2b} \\ \square_{zz} = (2b(\partial_t a)^2 - 2a\partial_{tt}a - (\partial_t a)^2) a^{-2b} \\ \square_{tt} = 3(\partial_t a)^2 a^{-2} \end{cases}$$

Or in other words  $G_{ii} = \left( (2b-1)a'^2 - 2aa'' \right) a^{-2b}$  and  $G_{tt} = 3a'^2 a^{-2}$ .



# Resurgence at Finite Order **Part V**





# 11 A snapshot of resurgence

In the last part of this work, we leave the realm of numerical simulations and discuss a different tool to make non-perturbative predictions, namely the concept of resurgence. We will be concerned with series expansions, complex functions and analytic continuations. A series is defined by its radius of convergence; when infinite, it means that it corresponds to an analytic function. A finite radius of convergence signals a singularity.

Quantum field theory seems to fare worse in this respect, as most of perturbation theory is expected to have zero radius of convergence; perturbative series are expected to be "asymptotic" [429]. Typically, the coefficients of asymptotic series are factorially growing, sometimes worse. The inclusion of  $n_{opt}$  terms onward improves the precision of the computation and from the  $n_{opt} + 1$  term the series starts to differ exponentially fast from the expected answer.

The program of resurgence is based on tools which allow reconstructing entire functions from asymptotic series in a well-defined way. As such, it intimately connects what would normally be considered as perturbative phenomena to non-perturbative ones, which are a crucial part of the full answer. In this chapter, we will briefly outline some of the key ideas relevant to the work presented in the next chapter. We refer the reader to references [430–432] for real introductions to the subject.

## 11.1 A tale about transseries, Borel summation and others

As it was already discussed in this work, the semiclassical expansion is constructed from a saddle point approximation. In simple cases, observables  $O$  are computed schematically as

$$O = \underbrace{\sum_n a_n \left(\frac{1}{x}\right)^n}_{\text{perturbative expansion}} + \sum_{s^*} \overbrace{e^{-S[s^*]}}^{\text{semiclassical action}} \underbrace{\sum_n a_n^{s^*} \left(\frac{1}{x}\right)^n}_{\text{perturbative expansion around saddle } s^*}, \quad (11.1)$$

with  $s^*$  a potentially infinite family of saddle point and  $(\frac{1}{x})$  a small parameter. First, we have as the main contribution the perturbative expansion around the vacuum, to which we add saddle points or "instantons" contributions. These effects are exponentially small and come together with extra perturbative expansions computed in the background of the saddle solutions, see for example [433, 434]. Typically, all of the perturbative expansions present in this expression are only asymptotic.

The mathematical concept behind this kind of concatenated asymptotic series weighted by "non-perturbative" factors such as exponentials and logarithms is the one of "transseries". They are used in the context of asymptotic analysis of partial differential equations. Their main feature is that the collection of all transseries is closed under analytic continuation [430]. In other words, a transseries is well behaved under analytic continuation. This has to be contrasted with simple asymptotic expansions, which are not. An intuitive example of why they cannot be is the following. By the nature of an asymptotic expansion, functions that differ only by an exponentially small correction in the expansion parameter will have the same asymptotic expansion. However, once analytically continued in the complex plane, the exponentially small corrections can become of order one and are completely missed by the asymptotic expansion.

What makes the theory of transseries potentially relevant to physics is that transseries are not arbitrary. In particular, the asymptotic series associated to different "non-perturbative" factor are connected one to another through "bridge equations" [432], which are "compatibility" conditions in the complex plane, similar in spirit to the WKB matching conditions around turning points in quantum mechanics. In particular, it means that starting only from, for instance, the perturbative expansion around the vacuum, one can infer information about the expansion around the "instanton" solution.

A key tool in these discussions is the Borel summation. It is a resummation technique that can be used to assign in a well-defined way a function to an asymptotic series. It can be understood as being based on the following formal manipulation. Given a series

$\Sigma(x) = a_0 + \sum_{n=1}^{\infty} a_n \left(\frac{1}{x}\right)^n$ , write [431]

$$\Sigma(x) = a_0 + \sum_{n=1}^{\infty} a_n \frac{1}{(n-1)!} \int_0^{\infty} dp e^{-px} p^{n-1} \quad (11.2)$$

$$\rightarrow a_0 + \int_0^{\infty} dp e^{-px} \sum_{n=1}^{\infty} \frac{a_n}{(n-1)!} p^{n-1} \equiv \int_0^{\infty} dp e^{-px} \mathcal{B}(\Sigma)(p) . \quad (11.3)$$

For absolutely convergent series, going from equation (11.2) to equation (11.3) is an equality. In the case of asymptotic series, it is only a formal manipulation, as the sum is not convergent. It is the key step of Borel summation. The quantity

$$\mathcal{B}(\Sigma)(p) = \sum_{n=1}^{\infty} \frac{a_n}{(n-1)!} p^{n-1} \quad (11.4)$$

is called the Borel transform of  $\Sigma(x)$ . Thanks to the division by  $(n-1)!$ , it converts asymptotic series into convergent series, provided that the original coefficients do not grow faster than factorially. In this case, equation (11.3) corresponds to a well-defined function and is the Borel resummation of  $\Sigma(x)$ .

Actually, the analytical structure of  $\mathcal{B}(\Sigma)(p)$  is of crucial importance. For example, the integral over  $p$  in (11.3), which is nothing else than a Laplace transform, can only be taken unambiguously in directions in the complex  $p$  plane absent of singularities. The presence of these singularities, associated with the so-called Stokes phenomenon, is what eventually lead to the "bridge equations" mentioned previously, which link perturbative expansions in different sectors.

## 11.2 Foreword to [5]

Over the past years, many impressive works have been carried on the topic of resurgence and its potential use in quantum mechanics, field theory and string theory, see for instance [432, 435–441]. One of the most exciting aspects of this program is that a careful analysis of the all-orders vacuum perturbative expansion is enough to reconstruct non-perturbative phenomena. This aspect is also potentially what could make these techniques useless in any realistic strongly interacting field theory, as there one can in principle compute only a few terms of the perturbative expansion.

Recently, reference [442] started a rigorous analysis of the following question. How much information about non-perturbative contributions in a transseries is it possible to extract by knowing only a finite number of terms from the leading asymptotic expansion? They investigated this in the context of the Painlevé I equation and were surprisingly able to reconstruct the whole complicated analytic structure of its solutions with a finite number of terms of its asymptotic expansion around real infinity.

In the next section, whose content is reference [5], we applied the reasoning of reference [442] to the case of Schwinger pair creation, explained in section 3.1. This simpler situation turned out to be an ideal playground to illustrate the potential power of such techniques.



## 12 *Schwinger pair production from Padé-Borel reconstruction [5]*

**Author:** Adrien Florio

*Reference:* arXiv v2 of Phys. Rev. D, 101(1):013007, 2020, doi: 10.1103/PhysRevD.101.013007

*Abstract:* In this work, we show how the knowledge of the first few terms of the Euler-Heisenberg Lagrangian's weak-field expansion in a magnetic field background is enough to reconstruct the pair-production rate in a strong electric field background. To this end, we study its associated truncated Borel sum using Padé approximants, as advocated in a recent work by Costin and Dunne, J. Phys. A52, 445205 (2019).

### 12.1 Introduction

In recent years, the program of "resurgence" has started to collect a number of successes in quantum mechanics and field theory. The idea behind it is that the typical asymptotic expansions that are to be dealt with, for example usual weak coupling expansions, are to be understood as being part of a transseries. In simple terms, transseries are sums of asymptotic series weighted by non-perturbative factors such as exponentials and logarithms. A typical example is the semi-classical expansion, which is a sum of perturbative/asymptotic expansions around different saddle points. We refer the reader to [430, 431] for pedagogical introductions to the topic.

The very analytic structure of transseries implies consistency relations between the different constituent asymptotic series. In particular, large order coefficients of a given expansion are known to be related to the small order coefficients of neighboring expansions. While being seemingly a mathematical curiosity, these relations have, for example, been used to predict the loop expansion around an instanton background for the quantum mechanical Sine-Gordon potential [435], predictions which have been explicitly verified up to three loops using diagrammatic methods [434]. For other interesting examples and reviews, we defer the reader to [432, 437–440] and references therein.

An immediate complaint against the potential practical usefulness of such approaches is that the knowledge of large orders terms of realistic quantum field theories expansions is not necessarily available. In this spirit, reference [442] started to investigate the amount of "non-perturbative" information that can be extracted from a finite number of terms of an asymptotic expansion. Stunningly, using relatively few terms of the asymptotic expansion of solutions to the Painlevé I equation around real infinity, they were able to reconstruct the whole highly non-trivial analytic structure of this solution throughout the whole complex plane. In a similar spirit, the works [443, 444] successfully explored the phase diagram of the  $\lambda\phi^4$  field theory by computing weak coupling expansions up to nine loops and studying their associated Borel sums.

Having in mind general quantum field theories, these are proofs of principle that a lot of non-perturbative information might be at our hand, waiting to be extracted from perturbative expansions.

This short note's aim is to illustrate again the potential use of some of the ideas developed in these works in field theory, using one of the simplest "non-perturbative" effects at hand, namely Schwinger pair production. In particular, we will present two results. First, the knowledge of a few terms of the weak-field expansion of the Euler-Heisenberg effective Lagrangian in a background magnetic field is enough to reconstruct its strong-field behavior. Then, and perhaps more interestingly, the same knowledge is enough to reconstruct the Euler-Heisenberg effective Lagrangian in a background electric field, for weak and strong fields, including its imaginary part. This means that this imaginary part, which gives the particle production rate in a constant electric field, can be inferred from a few terms of a perturbative expansion.

## 12.2 Schwinger effect, generalities

Schwinger pair production is one of the most basics field-theoretic non-perturbative effect, see [445] for an extensive review. Its simplest realization is the vacuum emission of charged particles in the presence of strong electric fields. A way to study it is to compute the one-loop fermionic effective action in a background electromagnetic field. Then, the phenomenon of pair-productions is signaled by the appearance of an imaginary part in the effective action. For the sake of simplicity, we will hereafter restrict ourselves to the constant background case. There, one can explicitly write down the effective Lagrangian [37]. For a purely magnetic field, it admits the following closed-form [445]

$$\mathcal{L}_{eff}(B) = \frac{(eB)^2}{2\pi^2} \left[ \zeta'_H \left( -1, \frac{m^2}{2eB} \right) + \zeta_H \left( -1, \frac{m^2}{2eB} \right) \ln \left( \frac{m^2}{2eB} \right) - \frac{1}{12} + \frac{1}{4} \left( \frac{m^2}{2eB} \right)^2 \right], \quad (12.1)$$

with  $\zeta_H(s, a)$  the Hurwitz zeta function and  $\zeta'_H(s, a)$  its derivative with respect to  $s$ . The parameters  $m$  and  $e$  are respectively the fermion's mass and electric charge, while  $B$  is the

strength of the constant background magnetic field. This expression is real and there is no pair-production in a magnetic background, as there is apriori no magnetically charged particle to be produced. The case of a pure electric field background is recovered by analytically continuing  $B \rightarrow \pm iE$  [446] (note that in this sense (12.1) can also be understood as the Euclidean space effective Lagrangian in an electric field background). Then, the effective Lagrangian does develop an imaginary part, which can be written as [446]

$$\Im(\mathcal{L}_{eff}(E)) = \frac{m^4}{8\pi^3} \left( \frac{eE}{m^2} \right)^2 \text{Li}_2 \left( e^{-\frac{m^2\pi}{eE}} \right) \quad (12.2)$$

$$= \frac{m^4}{8\pi^3} \left( \frac{eE}{m^2} \right)^2 \left[ e^{-\frac{m^2\pi}{eE}} + \dots \right], \quad (12.3)$$

with  $\text{Li}_2$  the second polylogarithm. From this expression, it is easy to see the famous exponential suppression to the production rate  $\Gamma_{prod}$ , which by definition is [445]

$$\Gamma_{prod} = 2\Im(\mathcal{L}_{eff}). \quad (12.4)$$

Another representation of (12.1) that will be of use is the following Laplace-type integral [37, 38]

$$\mathcal{L}_{eff}(B) = -\frac{e^2 B^2}{8\pi^2} \int_0^\infty \frac{dp}{p^2} \left( \coth p - \frac{1}{p} - \frac{p}{3} \right) e^{-\frac{m^2 p}{eB}}. \quad (12.5)$$

From this representation, it is clear that the imaginary part in the electric case comes from the contribution to the integral of the poles of the hyperbolic cotangent at integer multiples of  $i\pi$ .

In the rest of this work, we will be concerned with the weak-field expansion of (12.1). It is given as [445, 447]

$$\mathcal{L}_{eff}(B) \sim \frac{m^4}{4\pi^2} \sum_{n=0}^{\infty} (-1)^n (2n+1)! \frac{\zeta(2n+4)}{(2\pi)^{2n+4}} \left( \frac{2eB}{m^2} \right)^{2n+4}, \quad (12.6)$$

with  $\zeta(x)$  the Riemann zeta function. For the electric field, the expansion reads

$$\mathcal{L}_{eff}(E) \sim \frac{m^4}{4\pi^2} \sum_{n=0}^{\infty} (2n+1)! \frac{\zeta(2n+4)}{(2\pi)^{2n+4}} \left( \frac{2eE}{m^2} \right)^{2n+4}. \quad (12.7)$$

Both series are asymptotic because of the factorial growth of their coefficients. They are also both real to all orders. It is in this sense that the rate (12.4) is a non-perturbative quantity; at any given order in (12.7),  $\Gamma_{prod} = 0$ .



Actually, these weak-field expansions can be resummed to (12.5) using Borel summation. In this language, again, the imaginary part appears because of the presence of poles in the Laplace transform; (12.6) is "Borel summable" while (12.7) is not.

### 12.3 Strong-field regime from weak-field expansion

Following [442], we want to understand how much of the full Lagrangian (12.1) we can reconstruct using a finite number of terms in (12.6). To this purpose, again as in [442], we construct the corresponding truncated Borel sum. From it, we build Padé approximants, which are then used to compute a resummed Lagrangian  $\mathcal{L}_{eff}^{res}$  through a Laplace transform. The idea behind this procedure is to try to exploit the fact that, while the original expansion is only asymptotic, its Borel transform is convergent. Note also that very similar techniques were already used in the 80's, see for example [448] for a thorough review on QCD strong coupling expansion.

To keep notations clear, we set  $x = \frac{m^2}{2eB}$  and write the asymptotic expansion (12.6), truncated at order  $N$ , as

$$\frac{\mathcal{L}_{eff}(x, N)}{m^4} \sim \frac{1}{64\pi^6} \frac{1}{x^4} \sum_{n=0}^N (-1)^n (2n+1)! \frac{\zeta(2n+4)}{(2\pi)^{2n}} \left(\frac{1}{x}\right)^{2n} \quad (12.8)$$

$$= \frac{1}{64\pi^6} \frac{1}{x^4} \sum_{n=0}^N a_{2n} \left(\frac{1}{x}\right)^{2n}, \quad (12.9)$$

with  $a_{2n} = (-1)^n (2n+1)! \frac{\zeta(2n+4)}{(2\pi)^{2n}}$ . We also define a truncated Borel sum

$$\mathcal{B}\mathcal{L}_{eff}(p, N) = \sum_{n=1}^N \frac{a_{2n}}{(2n-1)!} p^{2n-1}. \quad (12.10)$$

With these definitions, we construct a Padé approximant of (12.10). Padé approximants are rational functions constructed to match a given series at specific points. They are typically used to try to reproduce the analytical structure of a function by extrapolating it away from some regions. Their rational nature allows for the emergence of poles and branch cuts, which appear as accumulations of poles. They can be found in a variety of places in the physics literature. As a specific example, we can mention attempts to analytically continue Euclidean lattice data to Minkowski space through Padé approximants, see [24] and references therein.

To have easy access to the poles of our Padé function and have good control over the

### 12.3. Strong-field regime from weak-field expansion

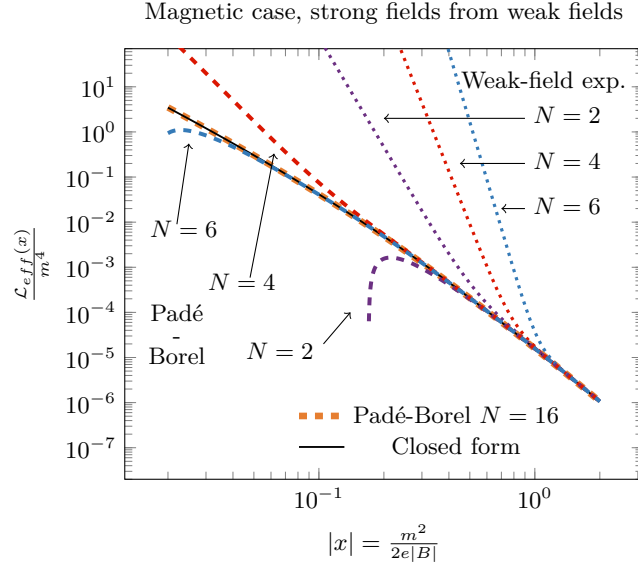


Figure 12.1 – Magnetic field effective Lagrangian. Closed-form (plain line), weak-field expansion (dotted lines) and Padé-Borel reconstruction (dashed lines) for different truncation order  $N$ . The weak-field expansion has a typical asymptotic behavior; every order makes it break down faster. The Padé-Borel reconstruction takes advantage of the fact that the Borel sum is convergent; every order improves the answer.

numerical Laplace transform, we use Padé approximants of the type

$$\mathcal{P}^{2N} \mathcal{B} \mathcal{L}_{eff}(p, N) = \sum_{n=1}^N \frac{c_n}{1 + b_n p}. \quad (12.11)$$

The coefficients  $c_n, b_n$ , which are in principle complex numbers, are computed by matching this expression to (12.10) around  $p = 0$ , see [449] for an explicit algorithm.

Finally, we compute our resummed Lagrangian as follows

$$\frac{\mathcal{L}_{eff}^{res}(x, N)}{m^4} = \frac{1}{64\pi^6} \frac{1}{x^4} \left( a_0 + \int_0^\infty dp e^{-px} \mathcal{P}^{2N} \mathcal{B} \mathcal{L}_{eff}(p, N) \right). \quad (12.12)$$

Note in particular that without the Padé interpolation, we would have achieved nothing, as in this case (12.12) would literally be equal to (12.9).

We show the result of this procedure, which from now on we will refer to as Padé-Borel reconstruction, in figure 12.1. The plain black line is the closed-form (12.1). The dotted lines are the truncated weak-field expansions, for different truncation  $N$ . The dashed lines are the Padé-Borel reconstructed expressions for the same  $N$ . Note that  $x \rightarrow \infty$  resp.  $x \rightarrow 0$  corresponds to the weak resp. strong-field regime, the goal being to be able to extrapolate from the former to the latter. Being an asymptotic expansion, every order makes it break down for larger values of  $x$ , i.e. for weaker fields. On the contrary, the Padé-Borel reconstruction

improves as  $N$  increases. This boils down to the fact that the Borel sum (12.10) is convergent; every new order contributes making the result more accurate. For example, only four terms of the weak-field expansion can be used to probe the strongly-coupled regime as far as  $x = 0.2$ .

This is our first result. With the knowledge of only the first few terms of the weak-field expansion (12.6), it is possible to explore the regime of strong magnetic fields by first constructing the corresponding truncated Borel sum, Padé approximating it and computing its Laplace transform.

## 12.4 Schwinger effect reconstructed

Now, we will show that this method, using the same data, actually also gives access to the regime of strong electric fields. In particular, we will see that we can use it to recover the Schwinger pair production rate.

To consider an electric field, we proceed with the analytic continuation  $x \rightarrow \mp ix$ . This leads us to study

$$\frac{\mathcal{L}_{eff}^{res}(\mp ix, N)}{m^4} = \frac{1}{64\pi^6} \frac{1}{x^4} \left( a_0 + \int_0^\infty dp e^{\pm ipx} \mathcal{P}^{2N} \mathcal{B} \mathcal{L}_{eff}(p, N) \right). \quad (12.13)$$

Technically, to compute this Laplace transform, we consider all the different fractions of (12.11) separately. We then rotate the integration contour in the complex plane by some angle and take into account any poles we might have crossed in the process.

Let us first look at what we obtain for the real part of the resummed electric field effective Lagrangian obtained through this analytic continuation, figure 12.2. As in the magnetic case, few terms of the weak Lagrangian allows for a precise extrapolation up into the strong-field regime. In particular, the reconstruction is able to predict correctly non-trivial features such as the change of signs which happens around  $x = 0.1$  (note that we are plotting the absolute value).

More interesting are the results for the imaginary part of the effective Lagrangian, i.e. the pair-production rate. They are shown in figure 12.3. They behave in exactly the same way; few terms of the weak-field expansion still give a quantitatively correct prediction of the rate. As little as the first two terms are required to reconstruct an imaginary part which is qualitatively correct at weak-field. With only the first six terms one can make quantitative predictions up to strong fields. This has to be contrasted again with the original asymptotic series, which uses the same data but is real to all orders.

The perhaps surprising capability of the Padé-Borel reconstruction to recover the

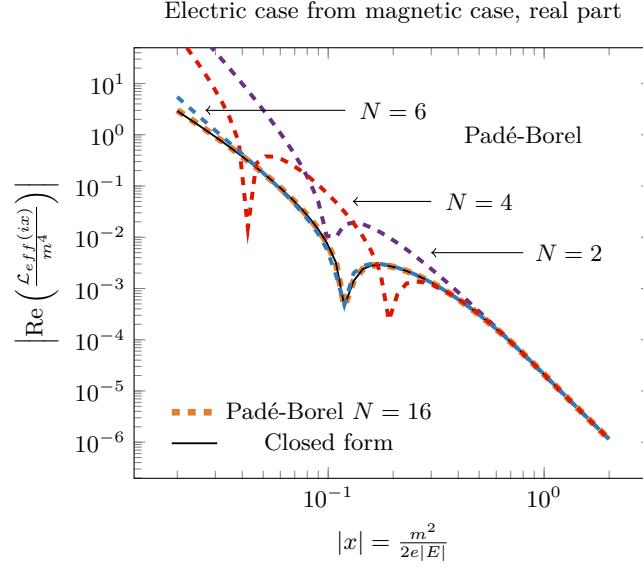


Figure 12.2 – Real part of electric field effective Lagrangian. Closed-form (plain line) and Padé-Borel reconstruction (dashed lines) for different truncation order  $N$ . The Padé-Borel reconstruction leads to correct and convergent results even after analytic continuation.

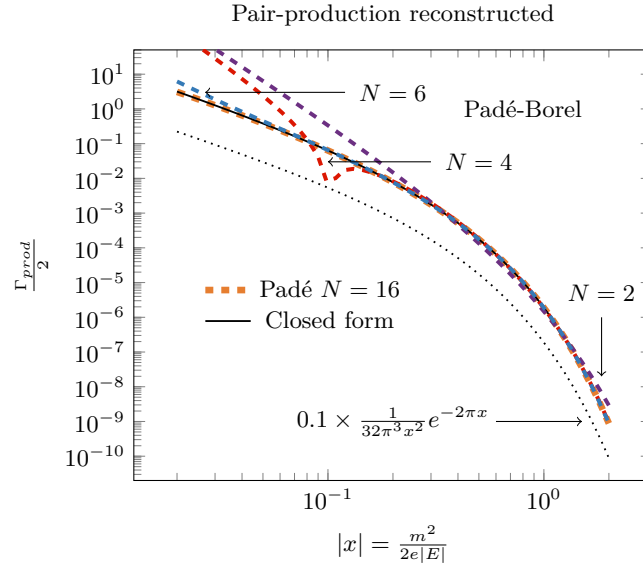


Figure 12.3 – Pair-production rate in a background electric field (imaginary part of the electric field effective Lagrangian). Closed-form (plain line) and Padé-Borel reconstruction (dashed lines) for different truncation order  $N$ . The dotted line is the leading exponential suppression to the Schwinger rate (shifted for readability). While  $N=2$  gives an imaginary part which is only qualitatively correct for weak-field,  $N=4$  and larger leads to a quantitatively correct prediction of the Schwinger rate for a whole range of field-strengths.

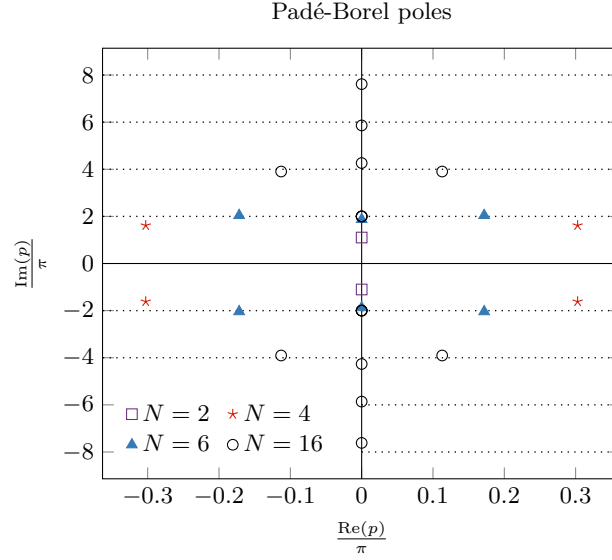


Figure 12.4 – Poles of the Padé-Borel reconstruction in the Borel plane, for different truncation order  $N$ . Dotted lines are multiples of  $2\pi i$ , where poles accumulate as  $N$  is taken larger. This is the correct analytic structure of the actual Borel sum, which has single poles at non-zero multiples of  $2\pi i$ . Note that the Padé-Borel approximation requires more than a single pole per multiple of  $2\pi i$  to reproduce the correct functional dependence.

pair-production rate is due to the fact that the Padé approximants of the truncated Borel sums are able to reproduce the correct analytic structure of the Borel sum. In terms of our variable  $x$ , the actual Borel sum (12.5) is a meromorphic function with single poles at  $x = 2\pi i n$  for  $n \in \mathbf{Z}, n \neq 0$ . As already mentioned, the imaginary part (12.3) can be understood as coming from the contribution of every single pole. It is dominated by the lowest-lying ones at  $x = \pm 2\pi i$

$$\frac{\Gamma_{prod}^{lead.}}{2} = \frac{1}{32\pi^3 x^2} e^{-2\pi x}, \quad (12.14)$$

which we also show in figure 12.3.

As the Padé-Borel approximants are constructed only from an asymptotic expansion around the real axis it is, however, a non-trivial fact that they are able to mimic correctly this analytic structure. We show it occurring in figure 12.4, where we display the poles of our Padé approximants. As the truncation order  $N$  is taken to be larger, they accumulate around  $x = 2\pi i n$ . Note that to approximate the correct prefactors, a single pole is replaced by a combination of different ones centered around  $x = 2\pi i n$ . The leading poles at  $\pm 2\pi i$  are first reproduced accurately by the truncation order  $N = 6$ , which is consistent with the behavior of the results presented in figure 12.3.

This is our second and most important result. The knowledge of a few terms of the weak-field expansion of the effective Euler-Heisenberg Lagrangian in a magnetic field background is

enough to reconstruct the particle production rate in a strong electric field.

## 12.5 Conclusion

This work can be summarized as follows: using only the truncated weak-field asymptotic expansion of the Euler-Heisenberg effective Lagrangian in a magnetic background, we were able to reconstruct the full Euler-Heisenberg Lagrangian, including its imaginary part which gives the Schwinger pair production rate. This may come as a surprise, as this rate is zero at all-orders of the weak-field asymptotic expansion.

What this result suggests, as already realized in [442], is that all coefficients in such asymptotic expansions contain information about the analytic structure of the underlying transseries in the whole complex plane. This information can be extracted by studying the associated Borel sum even upon truncation to a finite number of terms, by taking advantage of the fact that the Borel sum is a convergent series. Another remarkable fact is that the knowledge of the truncated Borel sum along the real axis is enough to gain information about its analytic structure, using Padé approximants, throughout the complex plane. In particular, this means that the underlying transseries is constrained enough to force the Padé approximants to develop poles at the correct locations.

The precise mechanism behind this phenomenon remains to be better understood; this will be essential to apply this method to unsolved problems and obtain trustworthy predictions. The aim of this work was however to illustrate its potential use in a simple physical problem.

*Acknowledgments.* The author wants to thank G. Dunne for an inspiring talk, S. Valgushev for stimulating conversations and its invitation to BNL, where the aforementioned talk was given, and M. Shaposhnikov for feedback on this work. The author is supported by the Swiss National Science Foundation.



# Conclusion **Part VI**





---

## The end...

Both the dynamics and the vacuum structure of gauge theories are extremely rich. In this thesis, we studied four such instances.

The first problem we tackled is the effect of the chiral anomaly on the evolution of an electromagnetic plasma in the presence of a chiral imbalance. As we argued, a precise understanding of the underlying dynamics would have implications in fields ranging from cosmology to heavy-ions physics. Current knowledge and quantitative predictions are mostly based on hydrodynamic-like approaches [89, 112] and therefore cannot account independently for fluctuations smaller than the mean free path of the system. Recently, an effort to accommodate such effects from first principles simulations was started, directly studying fermions [90–93]. In reference [1], presented in chapter 6, we aimed to achieve the same understanding following another road. We conducted classical real-time simulations of a scalar plasma, incorporating the effect of the anomaly in an effective way using a chiral chemical potential. The main result of this study can be framed as follows. While the qualitative features of this system are particularly well described by the relevant hydrodynamic approach, the quantitative predictions taking into account short-scale fluctuations can vary by an order of magnitude from the hydrodynamical predictions. In particular, we extracted the chiral decay rate, which quantifies the exponentially swift relaxation of a chiral chemical potential into gauge fields in the presence of a background magnetic field. We found this rate to be ten times larger than the one predicted by hydrodynamic. Such a difference, together with other discrepancies reported in [92, 93], strongly motivates further studies to elucidate the impact of short-scale fluctuations on the chiral dynamics.

In part III, we left Abelian gauge fields and Minkowski space to consider non-Abelian fields and Euclidean path integral simulations. In particular, motivated by the problem of topological freezing, namely the poor sampling of different topological sectors as the continuum limit is taken, we studied in reference [2], the content of chapter 8, the use of open-boundary conditions at finite temperature. A crucial quantity to determine when using open-boundary conditions is the "boundary zone", namely the length over which boundary effects are not negligible. In a field theory setting, these interactions of operators with the boundary can be understood as being mediated by propagating states of the underlying theory. In this sense, one expects the typical length of the boundary zone to be inversely proportional to the lightest propagating state. We measured this length for two different temperatures. Its value and temperature dependence were found to be compatible with the former interpretation. It was in turn used to determine screening masses at finite temperatures using an independent approach from what was previously done in the literature.

Combining aspects of the two previous projects, we presented in chapter 10 a compendium on lattice techniques to perform real-time classical simulations of scalars, Abelian and non-Abelian gauge fields, in an expanding Friedmann-Robertson-Lemaître-Walker universe. Their main applications lie in, but are not limited to, the fields of early cosmology and

---

reheating. In particular, we reported new algorithms, some with remarkable accuracy, to evolve gauge fields and demonstrated their robustness in a simulation combining  $U(1)$  and  $SU(2)$  gauge fields with their matter content. Alongside this project, we developed a scalable, user-friendly, extendable code, *CosmoLattice*, to perform these kinds of simulations. One of the main advantages of its flexibility is that its main module could also serve as a base to perform simulations of the type presented in chapter 6.

At last, in part V, we diverted from the realm of numerical simulations to study another way to probe non-perturbative physics, by using techniques coming from the field of "resurgence". For some years now, a research program has been built on the idea that quantum field theories may have a rather constrained hidden analytical structure and that elucidating these constraints may be used as a tool to probe physics. In reference [5], presented in chapter 12, we applied recent ideas from this topic [442] to the simple problem of Schwinger pair-production. Such processes, namely the creation of particles by strong electric fields, are considered to be non-perturbative, as they are seemingly not captured by the weak-field perturbative expansion. Surprisingly, by only using a few terms from the weak-field expansion in a background *magnetic*-field, we were able to reconstruct the strong field behaviour, both for electric and magnetic fields. It means in particular that we were able to extract the Schwinger pair-production rate only starting from the weak-magnetic field expansion at finite order.

All these four different topics present surprising connections. For instance, ideas emerging from the field of resurgence are actively being researched in lattice QCD to ease the so-called "sign-problem", see for instance [450] for a review. Importance sampling algorithms can only be used to sample probability distributions. Euclidean path-integrals cannot be interpreted as such when the action is not positive definite and these algorithms cannot be applied directly. A way to parametrise the constrained analytical structure predicted in the context of resurgence is the so-called Lefschetz thimbles. The field space is complexified and the path integral is deformed in some specific complex directions, the "thimbles". It was realised in reference [451] that these ideas might be applied to numerical simulations, to reduce the sign problem. Next, to conclude this thesis looking forward, we will discuss a potential outlook which takes advantage of, albeit different, similar connections.

### **... or not**

The research presented in this work opens up many possibilities for further explorations. Chiral charge dynamics is not a solved problem and further investigation is required. Open-boundary conditions can be used at finite temperature to improve the determination of topology-sensitive observables above the phase transition. The preheating of zillions of inflationary models needs to be studied. Resurgence at finite order needs to find a situation where original predictions can be made.

Rather than developing on specific outlooks of each project, which are still mentioned in their

---

respective conclusions, we want to pitch a potential direction of research that groups aspects of these four different projects.

We saw in chapter 6 that classical real-time simulations of a chirally charged scalar plasma lead to a prediction of the chiral decay rate ten times larger than one would expect from a hydrodynamical approach. We also argued that even if interesting in and of itself, one need to assess the effects of quantum and thermal corrections to make this result robust. Lastly, we also saw that this rate is related through a fluctuation-dissipation theorem to helicity diffusion in the absence of chiral chemical potential.

Such a "helicity-diffusion rate" can in principle be extracted directly from Euclidean path integral simulations of a  $U(1)$  gauge field coupled to a complex scalar, thus taking directly into account quantum and thermal effects. Moreover, studying this system would be interesting towards extracting similar quantities in more complicated theories such as QCD. Indeed, as we already mentioned in section 2.4, extraction of dynamical rates, or more generically "transport coefficients", from Euclidean data is a notoriously difficult problem, as it involves reconstructing Minkowski correlators from a finite number of points of the Euclidean correlators. Despite having been performed with some success for different quantities, see for instance [452] and references therein, coefficients coming from "topological correlators", such as the sphaleron rate, are believed to be even harder to extract [25]. This is related to the fact that the topological charge is not easy to define on a lattice, see chapter 7. This problem can be both circumvented or mimicked by a non-compact or compact formulation of the  $U(1)$  gauge fields. Moreover, this study would motivate the development of a Monte-Carlo interface on top of the same core module as *CosmoLattice*, which would be of great help to study all different models that do not have dedicated code as QCD does.

In any events, gauge theories still abound of fascinating problems to be solved and as such remain an exciting playground for research.



# Bibliography

- [1] D. G. Figueroa, A. Florio, and M. Shaposhnikov, JHEP **10**, 142 (2019), 1904.11892.
- [2] A. Florio, O. Kaczmarek, and L. Mazur, Eur. Phys. J. C **79**, 1039 (2019), 1903.02894.
- [3] D. G. Figueroa, A. Florio, F. Torrenti, and W. Valkenburg, (2020), 2006.15122.
- [4] D. G. Figueroa, A. Florio, F. Torrenti, and W. Valkenburg, In preparation. .
- [5] A. Florio, Phys. Rev. D **101**, 013007 (2020), 1911.03489.
- [6] S. Weinberg, *The Quantum theory of fields. Vol. 1: Foundations* (Cambridge University Press, 2005).
- [7] S. Weinberg, What is quantum field theory, and what did we think it is?, in *Conceptual foundations of quantum field theory. Proceedings, Symposium and Workshop, Boston, USA, March 1-3, 1996*, pp. 241–251, 1996, hep-th/9702027.
- [8] C. W. Misner, K. S. Thorne, and J. A. Wheeler, *Gravitation* (W. H. Freeman, San Francisco, 1973).
- [9] D. Tong, Gauge theory, 2018.
- [10] J. M. Cornwall, D. N. Levin, and G. Tiktopoulos, Phys. Rev. **D10**, 1145 (1974), [Erratum: Phys. Rev.D11,972(1975)].
- [11] V. A. Rubakov, *Classical theory of gauge fields* (, 2002).
- [12] P. B. Arnold and L. D. McLerran, Phys. Rev. D **37**, 1020 (1988).
- [13] C. Bonati and M. D’Elia, Phys. Rev. E **98**, 013308 (2018), 1709.10034.
- [14] A. Ramamurti, E. Shuryak, and I. Zahed, Phys. Rev. D **97**, 114028 (2018), 1802.10509.
- [15] *NIST Digital Library of Mathematical Functions*, <http://dlmf.nist.gov/>, Release 1.0.26 of 2020-03-15, F. W. J. Olver, A. B. Olde Daalhuis, D. W. Lozier, B. I. Schneider, R. F. Boisvert, C. W. Clark, B. R. Miller, B. V. Saunders, H. S. Cohl, and M. A. McClain, eds.
- [16] R. Feynman, A. Hibbs, and D. Styer, *Quantum Mechanics and Path Integrals*, Dover Books on Physics (Dover Publications, 2010).

## Bibliography

---

- [17] M. Blau, Lecture notes on the path integral approach to quantum mechanics, 2019.
- [18] M. Le Bellac, *Thermal Field Theory* Cambridge Monographs on Mathematical Physics, (Cambridge University Press, 1996).
- [19] J. I. Kapusta and C. Gale, *Finite-Temperature Field Theory: Principles and Applications*, Cambridge Monographs on Mathematical Physics, 2 ed. (Cambridge University Press, 2006).
- [20] F. R. Klinkhamer and N. Manton, Phys. Rev. D **30**, 2212 (1984).
- [21] G. Lepage, Lattice QCD for novices, in *13th Annual HUGS AT CEBAF (HUGS 98)*, pp. 49–90, 1998, hep-lat/0506036.
- [22] C. Gattringer and C. B. Lang, Lect. Notes Phys. **788**, 1 (2010).
- [23] ALPHA, S. Schaefer, R. Sommer, and F. Virotta, Nucl. Phys. B **845**, 93 (2011), 1009.5228.
- [24] R.-A. Tripolt, P. Gubler, M. Ulybyshev, and L. Von Smekal, Comput. Phys. Commun. **237**, 129 (2019), 1801.10348.
- [25] G. D. Moore and M. Tassler, JHEP **02**, 105 (2011), 1011.1167.
- [26] G. Dvali, C. Gomez, L. Gruending, and T. Rug, Nucl. Phys. B **901**, 338 (2015), 1508.03074.
- [27] S. Khlebnikov and M. Shaposhnikov, Nucl. Phys. B **308**, 885 (1988).
- [28] J. Ambjorn, T. Askgaard, H. Porter, and M. Shaposhnikov, Nucl. Phys. B **353**, 346 (1991).
- [29] D. G. Figueroa and M. Shaposhnikov, JHEP **04**, 026 (2018), 1707.09967.
- [30] L. Landau and E. Lifshitz, *Statistical Physics: Volume 5* (Elsevier Science, 2013).
- [31] S. Borsanyi *et al.*, Phys. Lett. B **752**, 175 (2016), 1508.06917.
- [32] J. S. Schwinger, Phys. Rev. **128**, 2425 (1962).
- [33] J. Lowenstein and J. Swieca, Annals Phys. **68**, 172 (1971).
- [34] A. Casher, J. B. Kogut, and L. Susskind, Phys. Rev. D **10**, 732 (1974).
- [35] S. R. Coleman, R. Jackiw, and L. Susskind, Annals Phys. **93**, 267 (1975).
- [36] S. R. Coleman, Annals Phys. **101**, 239 (1976).
- [37] W. Heisenberg and H. Euler, Z. Phys. **98**, 714 (1936), physics/0605038.
- [38] J. S. Schwinger, Phys. Rev. **82**, 664 (1951).

- 
- [39] C. Morette, Phys. Rev. **81**, 848 (1951).
- [40] C. Adam, R. Bertlmann, and P. Hofer, Riv. Nuovo Cim. **16N8**, 1 (1993).
- [41] K. Fujikawa, Phys. Rev. Lett. **42**, 1195 (1979).
- [42] S. Weinberg, *The quantum theory of fields. Vol. 2: Modern applications* (Cambridge University Press, 2013).
- [43] M. Shifman, *Advanced topics in quantum field theory.: A lecture course* (Cambridge Univ. Press, Cambridge, UK, 2012).
- [44] J. Ambjorn, J. Greensite, and C. Peterson, Nucl. Phys. B **221**, 381 (1983).
- [45] S. L. Adler and W. A. Bardeen, Phys. Rev. **182**, 1517 (1969).
- [46] J. Bell and R. Jackiw, Nuovo Cim. A **60**, 47 (1969).
- [47] M. Nakahara, *Geometry, topology and physics* (, 2003).
- [48] L. Faddeev and A. Slavnov, *Gauge Fields. Introduction to Quantum Theory*, Vol. 50 (Benjamin/Cummings, 1980).
- [49] V. Vlasov, V. Matveev, A. Tavkhelidze, S. Khlebnikov, and M. Shaposhnikov, Fiz. Elem. Chast. Atom. Yadra **18**, 5 (1987).
- [50] M. Shaposhnikov, Anomalous fermion number nonconservation, in *Summer School in High-energy Physics and Cosmology*, pp. 338–374, 1991.
- [51] P. A. M. Dirac, *Lectures on Quantum Mechanics*, Belfer Graduate School Sci. Mono. (Belfer Graduate School of Science, New York, NY, 1964), Photocopy.
- [52] D. J. Gross, R. D. Pisarski, and L. G. Yaffe, Rev. Mod. Phys. **53**, 43 (1981).
- [53] E. Witten, Nucl. Phys. **B156**, 269 (1979).
- [54] G. Veneziano, Nucl. Phys. **B159**, 213 (1979).
- [55] K. G. Wilson, p. 45 (1974).
- [56] J. Donoghue, E. Golowich, and B. R. Holstein, *Dynamics of the standard model*, Vol. 2 (CUP, 2014).
- [57] G. 't Hooft, Phys. Rev. Lett. **37**, 8 (1976), [,226(1976)].
- [58] R. Jackiw and C. Rebbi, Phys. Rev. Lett. **37**, 172 (1976).
- [59] J. Callan, Curtis G., R. Dashen, and D. J. Gross, Phys. Lett. B **63**, 334 (1976).
- [60] V. A. Kuzmin, V. A. Rubakov, and M. E. Shaposhnikov, Phys. Lett. **155B**, 36 (1985).



## Bibliography

---

- [61] M. Joyce and M. E. Shaposhnikov, Phys. Rev. Lett. **79**, 1193 (1997), astro-ph/9703005.
- [62] M. Giovannini and M. E. Shaposhnikov, Phys. Rev. **D57**, 2186 (1998), hep-ph/9710234.
- [63] M. D. Schwartz, *Quantum Field Theory and the Standard Model* (Cambridge University Press, 2014).
- [64] A. J. Long, E. Sabancilar, and T. Vachaspati, JCAP **02**, 036 (2014), 1309.2315.
- [65] M. Giovannini and M. Shaposhnikov, Phys. Rev. Lett. **80**, 22 (1998), hep-ph/9708303.
- [66] K. Bamba, Phys. Rev. D **74**, 123504 (2006), hep-ph/0611152.
- [67] K. Kamada, Phys. Rev. **D97**, 103506 (2018), 1802.03055.
- [68] K. Kamada, Y. Tsai, and T. Vachaspati, Phys. Rev. D **98**, 043501 (2018), 1803.08051.
- [69] K. Kajantie, M. Laine, K. Rummukainen, and M. E. Shaposhnikov, Phys. Rev. Lett. **77**, 2887 (1996), hep-ph/9605288.
- [70] M. D’Onofrio and K. Rummukainen, Phys. Rev. **D93**, 025003 (2016), 1508.07161.
- [71] K. Kamada and A. J. Long, Phys. Rev. **D94**, 123509 (2016), 1610.03074.
- [72] K. Kamada and A. J. Long, Phys. Rev. **D94**, 063501 (2016), 1606.08891.
- [73] R. Durrer and A. Neronov, Astron. Astrophys. Rev. **21**, 62 (2013), 1303.7121.
- [74] A. Boyarsky, J. Fröhlich, and O. Ruchayskiy, Phys. Rev. Lett. **108**, 031301 (2012), 1109.3350.
- [75] A. Boyarsky, J. Fröhlich, and O. Ruchayskiy, Phys. Rev. **D92**, 043004 (2015), 1504.04854.
- [76] J. Schober *et al.*, Astrophys. J. **858**, 124 (2018), 1711.09733.
- [77] A. Vilenkin, Phys. Rev. **D22**, 3080 (1980).
- [78] K. Fukushima, D. E. Kharzeev, and H. J. Warringa, Phys. Rev. **D78**, 074033 (2008), 0808.3382.
- [79] H. B. Nielsen and M. Ninomiya, Phys. Lett. B **130**, 389 (1983).
- [80] D. Kharzeev and A. Zhitnitsky, Nucl. Phys. A **797**, 67 (2007), 0706.1026.
- [81] D. E. Kharzeev, L. D. McLerran, and H. J. Warringa, Nucl. Phys. A **803**, 227 (2008), 0711.0950.
- [82] H. J. Warringa, J. Phys. G **35**, 104012 (2008), 0805.1384.
- [83] Q. Li *et al.*, Nature Phys. **12**, 550 (2016), 1412.6543.

- 
- [84] D. E. Kharzeev, J. Liao, S. A. Voloshin, and G. Wang, *Prog. Part. Nucl. Phys.* **88**, 1 (2016), 1511.04050.
  - [85] STAR, (2020), 2006.04251.
  - [86] D. E. Kharzeev and Q. Li, (2019), 1903.07133.
  - [87] M. Chernodub, J. Garaud, and D. Kharzeev, (2019), 1908.00392.
  - [88] J.-Y. Chen, D. T. Son, and M. A. Stephanov, *Phys. Rev. Lett.* **115**, 021601 (2015), 1502.06966.
  - [89] I. Rogachevskii *et al.*, *Astrophys. J.* **846**, 153 (2017), 1705.00378.
  - [90] P. V. Buividovich and M. V. Ulybyshev, *Phys. Rev.* **D94**, 025009 (2016), 1509.02076.
  - [91] P. V. Buividovich and S. N. Valgushev, (2016), 1611.05294, [PoSLATTICE2016,253(2016)].
  - [92] M. Mace, N. Mueller, S. Schlichting, and S. Sharma, *Phys. Rev. Lett.* **124**, 191604 (2020), 1910.01654.
  - [93] M. Mace, N. Mueller, S. Schlichting, and S. Sharma, Chirality transfer & chiral turbulence in gauge theories, in *28th International Conference on Ultrarelativistic Nucleus-Nucleus Collisions*, 2020, 2003.00763.
  - [94] G. 't Hooft, *Phys. Rev.* **D14**, 3432 (1976), [,70(1976)].
  - [95] L. D. McLerran, E. Mottola, and M. E. Shaposhnikov, *Phys. Rev.* **D43**, 2027 (1991).
  - [96] O. Philipsen, *Phys. Lett.* **B358**, 210 (1995), hep-ph/9506478.
  - [97] J. Ambjorn and A. Krasnitz, *Phys. Lett.* **B362**, 97 (1995), hep-ph/9508202.
  - [98] P. B. Arnold and L. G. Yaffe, *Phys. Rev.* **D52**, 7208 (1995), hep-ph/9508280.
  - [99] P. B. Arnold, D. Son, and L. G. Yaffe, *Phys. Rev.* **D55**, 6264 (1997), hep-ph/9609481.
  - [100] P. B. Arnold, *Phys. Rev.* **D55**, 7781 (1997), hep-ph/9701393.
  - [101] G. D. Moore, C.-r. Hu, and B. Muller, *Phys. Rev.* **D58**, 045001 (1998), hep-ph/9710436.
  - [102] D. Bodeker, *Phys. Lett.* **B426**, 351 (1998), hep-ph/9801430.
  - [103] G. D. Moore, *Nucl. Phys.* **B568**, 367 (2000), hep-ph/9810313.
  - [104] G. D. Moore and K. Rummukainen, *Phys. Rev.* **D61**, 105008 (2000), hep-ph/9906259.
  - [105] D. Bodeker, G. D. Moore, and K. Rummukainen, *Phys. Rev.* **D61**, 056003 (2000), hep-ph/9907545.

## Bibliography

---

- [106] P. B. Arnold and L. G. Yaffe, Phys. Rev. **D62**, 125014 (2000), hep-ph/9912306.
- [107] W.-H. Tang and J. Smit, Nucl. Phys. **B482**, 265 (1996), hep-lat/9605016.
- [108] J. Ambjorn and A. Krasnitz, Nucl. Phys. **B506**, 387 (1997), hep-ph/9705380.
- [109] G. D. Moore, Phys. Rev. **D62**, 085011 (2000), hep-ph/0001216.
- [110] M. D’Onofrio, K. Rummukainen, and A. Tranberg, JHEP **08**, 123 (2012), 1207.0685.
- [111] T. Fujita and K. Kamada, Phys. Rev. **D93**, 083520 (2016), 1602.02109.
- [112] A. Brandenburg *et al.*, Astrophys. J. **845**, L21 (2017), 1707.03385.
- [113] A. N. Redlich and L. C. R. Wijewardhana, Phys. Rev. Lett. **54**, 970 (1985).
- [114] A. J. Niemi and G. W. Semenoff, Phys. Rev. Lett. **54**, 2166 (1985).
- [115] D. G. Figueroa and M. Shaposhnikov, Nucl. Phys. **B926**, 544 (2018), 1705.09629.
- [116] G. D. Moore, Nucl. Phys. **B480**, 657 (1996), hep-ph/9603384.
- [117] G. D. Moore, Nucl. Phys. **B480**, 689 (1996), hep-lat/9605001.
- [118] V. A. Rubakov, Prog. Theor. Phys. **75**, 366 (1986).
- [119] V. A. Rubakov and A. N. Tavkhelidze, Phys. Lett. **165B**, 109 (1985).
- [120] K. Kajantie, M. Laine, J. Peisa, K. Rummukainen, and M. E. Shaposhnikov, Nucl. Phys. **B544**, 357 (1999), hep-lat/9809004.
- [121] H. Tashiro, T. Vachaspati, and A. Vilenkin, Phys. Rev. **D86**, 105033 (2012), 1206.5549.
- [122] Y. Hirono, D. Kharzeev, and Y. Yin, Phys. Rev. **D92**, 125031 (2015), 1509.07790.
- [123] R. Kubo, J. Phys. Soc. Jap. **12**, 570 (1957).
- [124] P. B. Arnold, G. D. Moore, and L. G. Yaffe, JHEP **11**, 001 (2000), hep-ph/0010177.
- [125] O. Sobol, Phys. Rev. D **100**, 056012 (2019), 1905.08190.
- [126] P. B. Arnold, G. D. Moore, and L. G. Yaffe, JHEP **05**, 051 (2003), hep-ph/0302165.
- [127] E. Braaten and R. D. Pisarski, Nucl. Phys. **B337**, 569 (1990).
- [128] J. O. Andersen, E. Braaten, and M. Strickland, Phys. Rev. **D61**, 014017 (2000), hep-ph/9905337.
- [129] D. Bodeker, L. D. McLerran, and A. V. Smilga, Phys. Rev. **D52**, 4675 (1995), hep-th/9504123.
- [130] A. Rajantie and M. Hindmarsh, Phys. Rev. **D60**, 096001 (1999), hep-ph/9904270.

- [131] M. Hindmarsh and A. Rajantie, Phys. Rev. **D64**, 065016 (2001), hep-ph/0103311.
- [132] A. Gholami, J. Hill, D. Malhotra, and G. Biros, arXiv e-prints , arXiv:1506.07933 (2015), 1506.07933.
- [133] D. Zubarev, *Nonequilibrium Statistical Thermodynamics* Studies in Soviet science (Consultants Bureau, 1974).
- [134] M. Luscher, Commun. Math. Phys. **85**, 39 (1982).
- [135] A. Phillips and D. Stone, Commun. Math. Phys. **103**, 599 (1986).
- [136] G. D. Moore, Do we understand the sphaleron rate?, in *4th International Conference on Strong and Electroweak Matter*, pp. 82–94, 2000, hep-ph/0009161.
- [137] M. P. Lombardo and A. Trunin, (2020), 2005.06547.
- [138] A. Hasenfratz and F. Knechtli, Phys. Rev. D **64**, 034504 (2001), hep-lat/0103029.
- [139] S. O. Bilson-Thompson, F. Bonnet, D. Leinweber, and A. G. Williams, Nucl. Phys. B Proc. Suppl. **109A**, 116 (2002), hep-lat/0112034.
- [140] C. Morningstar and M. J. Peardon, Phys. Rev. D **69**, 054501 (2004), hep-lat/0311018.
- [141] M. Lüscher, JHEP **08**, 071 (2010), 1006.4518, [Erratum: JHEP03,092(2014)].
- [142] M. Müller-Preussker, PoS **LATTICE2014**, 003 (2015), 1503.01254.
- [143] M. Luscher, Commun. Math. Phys. **293**, 899 (2010), 0907.5491.
- [144] A. Florio, Gluonic observables in lattice QCD, 2016, Master MSc project, EPFL.
- [145] ALPHA, S. Schaefer, R. Sommer, and F. Virota, Nucl. Phys. **B845**, 93 (2011), 1009.5228.
- [146] M. Lüscher and S. Schaefer, JHEP **07**, 036 (2011), 1105.4749.
- [147] M. Luscher and S. Schaefer, Comput. Phys. Commun. **184**, 519 (2013), 1206.2809.
- [148] A. Chowdhury, A. Harindranath, and J. Maiti, JHEP **06**, 067 (2014), 1402.7138.
- [149] A. Chowdhury, A. Harindranath, and J. Maiti, Phys. Rev. **D91**, 074507 (2015), 1409.6459.
- [150] G. McGlynn and R. D. Mawhinney, PoS **LATTICE2014**, 026 (2014).
- [151] ALPHA, M. Bruno, S. Schaefer, and R. Sommer, JHEP **08**, 150 (2014), 1406.5363.
- [152] M. Bruno, T. Korzec, and S. Schaefer, Phys. Rev. D **95**, 074504 (2017), 1608.08900.
- [153] N. Husung, M. Koren, P. Krah, and R. Sommer, EPJ Web Conf. **175**, 14024 (2018), 1711.01860.

## Bibliography

---

- [154] A. Gérardin, H. B. Meyer, and A. Nyffeler, Phys. Rev. D **100**, 034520 (2019), 1903.09471.
- [155] RQCD, G. S. Bali *et al.*, Eur. Phys. J. A **55**, 116 (2019), 1903.12590.
- [156] ALPHA, R. Höllwieser, F. Knechtli, and T. Korzec, Eur. Phys. J. C **80**, 349 (2020), 2002.02866.
- [157] ALPHA, U. Wolff, Comput. Phys. Commun. **156**, 143 (2004), hep-lat/0306017, [Erratum: Comput. Phys. Commun.176,383(2007)].
- [158] S. Aoki, H. Fukaya, S. Hashimoto, and T. Onogi, Phys. Rev. **D76**, 054508 (2007), 0707.0396.
- [159] W. Bietenholz *et al.*, Phys. Rev. **D93**, 114516 (2016), 1603.05630.
- [160] Y. Burnier, A. Florio, O. Kaczmarek, and L. Mazur, EPJ Web Conf. **175**, 07004 (2018), 1710.06472.
- [161] ALPHA, M. Guagnelli, J. Heitger, R. Sommer, and H. Wittig, Nucl. Phys. **B560**, 465 (1999), hep-lat/9903040.
- [162] M. Bruno, *The energy scale of the 3-flavour Lambda parameter*, PhD thesis, Humboldt-Universität zu Berlin, Mathematisch-Naturwissenschaftliche Fakultät, 2016.
- [163] M. F. García Vera, *Investigating the large  $N$  limit of  $SU(N)$  Yang-Mills gauge theories on the lattice*, PhD thesis, Humboldt-Universität zu Berlin, Mathematisch-Naturwissenschaftliche Fakultät, 2017.
- [164] A. Francis, O. Kaczmarek, M. Laine, T. Neuhaus, and H. Ohno, Phys. Rev. **D91**, 096002 (2015), 1503.05652.
- [165] S. Datta, S. Gupta, and A. Lytle, Phys. Rev. **D94**, 094502 (2016), 1512.04892.
- [166] M. Wandelt and F. Knechtli and M. Günther, JHEP **10**, 061 (2016), 1603.05532.
- [167] S. Nadkarni, Phys. Rev. **D33**, 3738 (1986).
- [168] H. Suzuki, PTEP **2013**, 083B03 (2013), 1304.0533, [Erratum: PTEP2015,079201(2015)].
- [169] L. Del Debbio, A. Patella, and A. Rago, JHEP **11**, 212 (2013), 1306.1173.
- [170] L. Giusti and M. Lüscher, (2018), 1812.02062.
- [171] H. B. Meyer, Phys. Rev. **D79**, 011502 (2009), 0808.1950.
- [172] S. Datta and S. Gupta, Nucl. Phys. **B534**, 392 (1998), hep-lat/9806034.
- [173] E. Berkowitz, M. I. Buchoff, and E. Rinaldi, Phys. Rev. **D92**, 034507 (2015), 1505.07455.
- [174] Lüscher, Martin, EPJ Web Conf. **175**, 01002 (2018), 1707.09758.

- 
- [175] G. D. Moore, EPJ Web Conf. **175**, 01009 (2018), 1709.09466.
- [176] P. T. Jahn, G. D. Moore, and D. Robaina, Phys. Rev. **D98**, 054512 (2018), 1806.01162.
- [177] G. N. Felder and I. Tkachev, Comput. Phys. Commun. **178**, 929 (2008), hep-ph/0011159.
- [178] G. N. Felder, Comput. Phys. Commun. **179**, 604 (2008), 0712.0813.
- [179] A. V. Frolov, JCAP **11**, 009 (2008), 0809.4904.
- [180] R. Easther, H. Finkel, and N. Roth, JCAP **10**, 025 (2010), 1005.1921.
- [181] Z. Huang, Phys. Rev. D **83**, 123509 (2011), 1102.0227.
- [182] J. Sainio, JCAP **04**, 038 (2012), 1201.5029.
- [183] H. L. Child, J. Giblin, John T., R. H. Ribeiro, and D. Seery, Phys. Rev. Lett. **111**, 051301 (2013), 1305.0561.
- [184] K. D. Lozanov and M. A. Amin, JCAP **04**, 058 (2020), 1911.06827.
- [185] S. Weinberg, *Cosmology* Cosmology (OUP Oxford, 2008).
- [186] K. D. Lozanov, (2019), 1907.04402.
- [187] R. Allahverdi, R. Brandenberger, F.-Y. Cyr-Racine, and A. Mazumdar, Ann. Rev. Nucl. Part. Sci. **60**, 27 (2010), 1001.2600.
- [188] A. R. Liddle, P. Parsons, and J. D. Barrow, Phys. Rev. D **50**, 7222 (1994), astro-ph/9408015.
- [189] L. Kofman, A. D. Linde, and A. A. Starobinsky, Phys. Rev. D **56**, 3258 (1997), hep-ph/9704452.
- [190] Planck, Y. Akrami *et al.*, (2018), 1807.06211.
- [191] A. H. Guth, Adv. Ser. Astrophys. Cosmol. **3**, 139 (1987).
- [192] A. D. Linde, p. 185 (1981).
- [193] A. Albrecht and P. J. Steinhardt, Adv. Ser. Astrophys. Cosmol. **3**, 158 (1987).
- [194] R. Brout, F. Englert, and E. Gunzig, Annals Phys. **115**, 78 (1978).
- [195] A. A. Starobinsky, Adv. Ser. Astrophys. Cosmol. **3**, 130 (1987).
- [196] D. Kazanas, Astrophys. J. Lett. **241**, L59 (1980).
- [197] K. Sato, Mon. Not. Roy. Astron. Soc. **195**, 467 (1981).
- [198] V. F. Mukhanov and G. V. Chibisov, JETP Lett. **33**, 532 (1981).

## Bibliography

---

- [199] A. H. Guth and S. Pi, Phys. Rev. Lett. **49**, 1110 (1982).
- [200] A. A. Starobinsky, Phys. Lett. B **117**, 175 (1982).
- [201] S. Hawking, Phys. Lett. B **115**, 295 (1982).
- [202] J. M. Bardeen, P. J. Steinhardt, and M. S. Turner, Phys. Rev. D **28**, 679 (1983).
- [203] D. H. Lyth and A. Riotto, Phys. Rept. **314**, 1 (1999), hep-ph/9807278.
- [204] A. Riotto, ICTP Lect. Notes Ser. **14**, 317 (2003), hep-ph/0210162.
- [205] A. D. Linde, Lect. Notes Phys. **738**, 1 (2008), 0705.0164.
- [206] D. Baumann, Inflation, in *Theoretical Advanced Study Institute in Elementary Particle Physics: Physics of the Large and the Small*, pp. 523–686, 2011, 0907.5424.
- [207] B. A. Bassett, S. Tsujikawa, and D. Wands, Rev. Mod. Phys. **78**, 537 (2006), astro-ph/0507632.
- [208] M. A. Amin, M. P. Hertzberg, D. I. Kaiser, and J. Karouby, Int. J. Mod. Phys. D **24**, 1530003 (2014), 1410.3808.
- [209] J. H. Traschen and R. H. Brandenberger, Phys. Rev. D **42**, 2491 (1990).
- [210] L. Kofman, A. D. Linde, and A. A. Starobinsky, Phys. Rev. Lett. **73**, 3195 (1994), hep-th/9405187.
- [211] Y. Shtanov, J. H. Traschen, and R. H. Brandenberger, Phys. Rev. D **51**, 5438 (1995), hep-ph/9407247.
- [212] D. I. Kaiser, Phys. Rev. D **53**, 1776 (1996), astro-ph/9507108.
- [213] P. B. Greene, L. Kofman, A. D. Linde, and A. A. Starobinsky, Phys. Rev. D **56**, 6175 (1997), hep-ph/9705347.
- [214] D. I. Kaiser, Phys. Rev. D **56**, 706 (1997), hep-ph/9702244.
- [215] D. I. Kaiser, Phys. Rev. D **57**, 702 (1998), hep-ph/9707516.
- [216] P. B. Greene and L. Kofman, Phys. Lett. B **448**, 6 (1999), hep-ph/9807339.
- [217] P. B. Greene and L. Kofman, Phys. Rev. D **62**, 123516 (2000), hep-ph/0003018.
- [218] M. Peloso and L. Sorbo, JHEP **05**, 016 (2000), hep-ph/0003045.
- [219] J. Berges, D. Gelfand, and J. Pruschke, Phys. Rev. Lett. **107**, 061301 (2011), 1012.4632.
- [220] S. Khlebnikov and I. Tkachev, Phys. Rev. Lett. **77**, 219 (1996), hep-ph/9603378.
- [221] T. Prokopec and T. G. Roos, Phys. Rev. D **55**, 3768 (1997), hep-ph/9610400.

- [222] K. Enqvist and M. S. Sloth, Nucl. Phys. B **626**, 395 (2002), hep-ph/0109214.
- [223] D. H. Lyth and D. Wands, Phys. Lett. B **524**, 5 (2002), hep-ph/0110002.
- [224] T. Moroi and T. Takahashi, Phys. Lett. B **522**, 215 (2001), hep-ph/0110096, [Erratum: Phys.Lett.B 539, 303–303 (2002)].
- [225] A. Mazumdar and J. Rocher, Phys. Rept. **497**, 85 (2011), 1001.0993.
- [226] K. Enqvist, S. Nurmi, and G. Rigopoulos, JCAP **10**, 013 (2008), 0807.0382.
- [227] K. Enqvist, D. G. Figueroa, and R. N. Lerner, JCAP **01**, 040 (2013), 1211.5028.
- [228] K. Enqvist, R. N. Lerner, and S. Rusak, JCAP **11**, 034 (2013), 1308.3321.
- [229] K. Enqvist, R. N. Lerner, and T. Takahashi, JCAP **01**, 006 (2014), 1310.1374.
- [230] A. A. Starobinsky and J. Yokoyama, Phys. Rev. D **50**, 6357 (1994), astro-ph/9407016.
- [231] K. Enqvist, T. Meriniemi, and S. Nurmi, JCAP **10**, 057 (2013), 1306.4511.
- [232] A. De Simone and A. Riotto, JCAP **02**, 014 (2013), 1208.1344.
- [233] M. Herranen, T. Markkanen, S. Nurmi, and A. Rajantie, Phys. Rev. Lett. **115**, 241301 (2015), 1506.04065.
- [234] D. G. Figueroa and C. T. Byrnes, Phys. Lett. B **767**, 272 (2017), 1604.03905.
- [235] K. Enqvist, S. Nurmi, and S. Rusak, JCAP **10**, 064 (2014), 1404.3631.
- [236] D. G. Figueroa, JHEP **11**, 145 (2014), 1402.1345.
- [237] A. Kusenko, L. Pearce, and L. Yang, Phys. Rev. Lett. **114**, 061302 (2015), 1410.0722.
- [238] D. G. Figueroa, J. Garcia-Bellido, and F. Torrenti, Phys. Rev. D **92**, 083511 (2015), 1504.04600.
- [239] K. Enqvist, S. Nurmi, S. Rusak, and D. Weir, JCAP **02**, 057 (2016), 1506.06895.
- [240] F. L. Bezrukov and M. Shaposhnikov, Phys. Lett. B **659**, 703 (2008), 0710.3755.
- [241] F. Bezrukov, A. Magnin, M. Shaposhnikov, and S. Sibiryakov, JHEP **01**, 016 (2011), 1008.5157.
- [242] F. Bezrukov, D. Gorbunov, and M. Shaposhnikov, JCAP **06**, 029 (2009), 0812.3622.
- [243] J. Garcia-Bellido, D. G. Figueroa, and J. Rubio, Phys. Rev. D **79**, 063531 (2009), 0812.4624.
- [244] D. G. Figueroa, AIP Conf. Proc. **1241**, 578 (2010), 0911.1465.
- [245] J. Repond and J. Rubio, JCAP **07**, 043 (2016), 1604.08238.



## Bibliography

---

- [246] Y. Ema, R. Jinno, K. Mukaida, and K. Nakayama, JCAP **02**, 045 (2017), 1609.05209.
- [247] E. I. Sfakianakis and J. van de Vis, Phys. Rev. D **99**, 083519 (2019), 1810.01304.
- [248] T. Gherghetta, C. F. Kolda, and S. P. Martin, Nucl. Phys. B **468**, 37 (1996), hep-ph/9510370.
- [249] K. Enqvist and A. Mazumdar, Phys. Rept. **380**, 99 (2003), hep-ph/0209244.
- [250] M. Dine, L. Randall, and S. D. Thomas, Nucl. Phys. B **458**, 291 (1996), hep-ph/9507453.
- [251] I. Affleck and M. Dine, Nucl. Phys. B **249**, 361 (1985).
- [252] M. K. Gaillard, H. Murayama, and K. A. Olive, Phys. Lett. B **355**, 71 (1995), hep-ph/9504307.
- [253] K. A. Olive and M. Peloso, Phys. Rev. D **74**, 103514 (2006), hep-ph/0608096.
- [254] A. Basboll, D. Maybury, F. Riva, and S. M. West, Phys. Rev. D **76**, 065005 (2007), hep-ph/0703015.
- [255] A. Gumrukcuoglu, K. A. Olive, M. Peloso, and M. Sexton, Phys. Rev. D **78**, 063512 (2008), 0805.0273.
- [256] A. D. Linde, Phys. Rev. D **49**, 748 (1994), astro-ph/9307002.
- [257] G. N. Felder *et al.*, Phys. Rev. Lett. **87**, 011601 (2001), hep-ph/0012142.
- [258] G. N. Felder, L. Kofman, and A. D. Linde, Phys. Rev. D **64**, 123517 (2001), hep-th/0106179.
- [259] E. J. Copeland, S. Pascoli, and A. Rajantie, Phys. Rev. D **65**, 103517 (2002), hep-ph/0202031.
- [260] J. Garcia-Bellido, M. Garcia Perez, and A. Gonzalez-Arroyo, Phys. Rev. D **67**, 103501 (2003), hep-ph/0208228.
- [261] B. A. Bassett and S. Liberati, Phys. Rev. D **58**, 021302 (1998), hep-ph/9709417, [Erratum: Phys.Rev.D 60, 049902 (1999)].
- [262] S. Tsujikawa, K.-i. Maeda, and T. Torii, Phys. Rev. D **60**, 063515 (1999), hep-ph/9901306.
- [263] S. Tsujikawa, K.-i. Maeda, and T. Torii, Phys. Rev. D **60**, 123505 (1999), hep-ph/9906501.
- [264] S. Tsujikawa, K.-i. Maeda, and T. Torii, Phys. Rev. D **61**, 103501 (2000), hep-ph/9910214.

- 
- [265] J. Crespo and H. de Oliveira, JCAP **12**, 045 (2019), 1905.13647.
- [266] J. Crespo and H. de Oliveira, (2019), 1906.00802.
- [267] M. P. DeCross, D. I. Kaiser, A. Prabhu, C. Prescod-Weinstein, and E. I. Sfakianakis, Phys. Rev. D **97**, 023526 (2018), 1510.08553.
- [268] M. P. DeCross, D. I. Kaiser, A. Prabhu, C. Prescod-Weinstein, and E. I. Sfakianakis, Phys. Rev. D **97**, 023527 (2018), 1610.08868.
- [269] M. P. DeCross, D. I. Kaiser, A. Prabhu, C. Prescod-Weinstein, and E. I. Sfakianakis, Phys. Rev. D **97**, 023528 (2018), 1610.08916.
- [270] R. Nguyen, J. van de Vis, E. I. Sfakianakis, J. T. Giblin, and D. I. Kaiser, Phys. Rev. Lett. **123**, 171301 (2019), 1905.12562.
- [271] J. van de Vis, R. Nguyen, E. I. Sfakianakis, J. T. Giblin, and D. I. Kaiser, (2020), 2005.00433.
- [272] D. Battefeld, Nucl. Phys. B Proc. Suppl. **192-193**, 126 (2009), 0809.3455.
- [273] D. Battefeld and S. Kawai, Phys. Rev. D **77**, 123507 (2008), 0803.0321.
- [274] D. Battefeld, T. Battefeld, and J. T. Giblin, Phys. Rev. D **79**, 123510 (2009), 0904.2778.
- [275] J. Braden, L. Kofman, and N. Barnaby, JCAP **07**, 016 (2010), 1005.2196.
- [276] P. Adshead, J. T. Giblin, T. R. Scully, and E. I. Sfakianakis, JCAP **12**, 034 (2015), 1502.06506.
- [277] P. Adshead, J. T. Giblin, T. R. Scully, and E. I. Sfakianakis, JCAP **10**, 039 (2016), 1606.08474.
- [278] P. Adshead, J. T. Giblin, and Z. J. Weiner, Phys. Rev. D **98**, 043525 (2018), 1805.04550.
- [279] J. R. C. Cuissa and D. G. Figueroa, JCAP **06**, 002 (2019), 1812.03132.
- [280] P. Adshead, J. T. Giblin, M. Pieroni, and Z. J. Weiner, Phys. Rev. D **101**, 083534 (2020), 1909.12842.
- [281] P. Adshead, J. T. Giblin, M. Pieroni, and Z. J. Weiner, Phys. Rev. Lett. **124**, 171301 (2020), 1909.12843.
- [282] J. Deskins, J. T. Giblin, and R. R. Caldwell, Phys. Rev. D **88**, 063530 (2013), 1305.7226.
- [283] P. Adshead, J. T. Giblin, and Z. J. Weiner, Phys. Rev. D **96**, 123512 (2017), 1708.02944.
- [284] A. Rajantie, P. Saffin, and E. J. Copeland, Phys. Rev. D **63**, 123512 (2001), hep-ph/0012097.

## Bibliography

---

- [285] E. J. Copeland, D. Lyth, A. Rajantie, and M. Trodden, Phys. Rev. D **64**, 043506 (2001), hep-ph/0103231.
- [286] J. Smit and A. Tranberg, JHEP **12**, 020 (2002), hep-ph/0211243.
- [287] J. Garcia-Bellido, M. Garcia-Perez, and A. Gonzalez-Arroyo, Phys. Rev. D **69**, 023504 (2004), hep-ph/0304285.
- [288] A. Tranberg and J. Smit, JHEP **11**, 016 (2003), hep-ph/0310342.
- [289] J.-I. Skullerud, J. Smit, and A. Tranberg, JHEP **08**, 045 (2003), hep-ph/0307094.
- [290] M. van der Meulen, D. Sexty, J. Smit, and A. Tranberg, JHEP **02**, 029 (2006), hep-ph/0511080.
- [291] A. Diaz-Gil, J. Garcia-Bellido, M. Garcia Perez, and A. Gonzalez-Arroyo, Phys. Rev. Lett. **100**, 241301 (2008), 0712.4263.
- [292] A. Diaz-Gil, J. Garcia-Bellido, M. Garcia Perez, and A. Gonzalez-Arroyo, JHEP **07**, 043 (2008), 0805.4159.
- [293] J.-F. Dufaux, D. G. Figueroa, and J. Garcia-Bellido, Phys. Rev. D **82**, 083518 (2010), 1006.0217.
- [294] A. Tranberg, S. Tähtinen, and D. J. Weir, JCAP **04**, 012 (2018), 1706.02365.
- [295] K. D. Lozanov and M. A. Amin, JCAP **06**, 032 (2016), 1603.05663.
- [296] K. Kohri and H. Matsui, Phys. Rev. D **94**, 103509 (2016), 1602.02100.
- [297] D. G. Figueroa, A. Rajantie, and F. Torrenti, Phys. Rev. D **98**, 023532 (2018), 1709.00398.
- [298] Y. Ema, M. Karciauskas, O. Lebedev, and M. Zatta, JCAP **06**, 054 (2017), 1703.04681.
- [299] B. A. Bassett, D. I. Kaiser, and R. Maartens, Phys. Lett. B **455**, 84 (1999), hep-ph/9808404.
- [300] B. A. Bassett, F. Tamburini, D. I. Kaiser, and R. Maartens, Nucl. Phys. B **561**, 188 (1999), hep-ph/9901319.
- [301] B. A. Bassett, C. Gordon, R. Maartens, and D. I. Kaiser, Phys. Rev. D **61**, 061302 (2000), hep-ph/9909482.
- [302] F. Finelli and R. H. Brandenberger, Phys. Rev. D **62**, 083502 (2000), hep-ph/0003172.
- [303] A. Chambers and A. Rajantie, Phys. Rev. Lett. **100**, 041302 (2008), 0710.4133, [Erratum: Phys.Rev.Lett. 101, 149903 (2008)].

- 
- [304] J. Bond, A. V. Frolov, Z. Huang, and L. Kofman, Phys. Rev. Lett. **103**, 071301 (2009), 0903.3407.
- [305] S. V. Imrith, D. J. Mulryne, and A. Rajantie, Phys. Rev. D **100**, 043543 (2019), 1903.07487.
- [306] N. Musoke, S. Hotchkiss, and R. Easther, Phys. Rev. Lett. **124**, 061301 (2020), 1909.11678.
- [307] J. T. Giblin and A. J. Tishue, Phys. Rev. D **100**, 063543 (2019), 1907.10601.
- [308] J. Martin, T. Papanikolaou, L. Pinol, and V. Vennin, JCAP **05**, 003 (2020), 2002.01820.
- [309] E. Cotner, A. Kusenko, M. Sasaki, and V. Takhistov, JCAP **10**, 077 (2019), 1907.10613.
- [310] J. Martin, T. Papanikolaou, and V. Vennin, JCAP **01**, 024 (2020), 1907.04236.
- [311] J. Garcia-Bellido, A. D. Linde, and D. Wands, Phys. Rev. D **54**, 6040 (1996), astro-ph/9605094.
- [312] A. M. Green and K. A. Malik, Phys. Rev. D **64**, 021301 (2001), hep-ph/0008113.
- [313] J. Hidalgo, L. Urena-Lopez, and A. R. Liddle, Phys. Rev. D **85**, 044055 (2012), 1107.5669.
- [314] E. Torres-Lomas, J. C. Hidalgo, K. A. Malik, and L. A. Ureña-López, Phys. Rev. D **89**, 083008 (2014), 1401.6960.
- [315] T. Suyama, T. Tanaka, B. Bassett, and H. Kudoh, Phys. Rev. D **71**, 063507 (2005), hep-ph/0410247.
- [316] T. Suyama, T. Tanaka, B. Bassett, and H. Kudoh, JCAP **04**, 001 (2006), hep-ph/0601108.
- [317] E. Cotner, A. Kusenko, and V. Takhistov, Phys. Rev. D **98**, 083513 (2018), 1801.03321.
- [318] S. Khlebnikov and I. Tkachev, Phys. Rev. D **56**, 653 (1997), hep-ph/9701423.
- [319] R. Easther and E. A. Lim, JCAP **04**, 010 (2006), astro-ph/0601617.
- [320] R. Easther, J. Giblin, John T., and E. A. Lim, Phys. Rev. Lett. **99**, 221301 (2007), astro-ph/0612294.
- [321] J. Garcia-Bellido, D. G. Figueroa, and A. Sastre, Phys. Rev. D **77**, 043517 (2008), 0707.0839.
- [322] J. F. Dufaux, A. Bergman, G. N. Felder, L. Kofman, and J.-P. Uzan, Phys. Rev. D **76**, 123517 (2007), 0707.0875.
- [323] J.-F. Dufaux, G. Felder, L. Kofman, and O. Navros, JCAP **03**, 001 (2009), 0812.2917.

## Bibliography

---

- [324] S.-Y. Zhou *et al.*, JHEP **10**, 026 (2013), 1304.6094.
- [325] L. Bethke, D. G. Figueroa, and A. Rajantie, Phys. Rev. Lett. **111**, 011301 (2013), 1304.2657.
- [326] L. Bethke, D. G. Figueroa, and A. Rajantie, JCAP **06**, 047 (2014), 1309.1148.
- [327] S. Antusch, F. Cefala, and S. Orani, Phys. Rev. Lett. **118**, 011303 (2017), 1607.01314, [Erratum: Phys.Rev.Lett. 120, 219901 (2018)].
- [328] S. Antusch *et al.*, JHEP **01**, 083 (2018), 1708.08922.
- [329] S. Antusch, F. Cefala, and S. Orani, JCAP **03**, 032 (2018), 1712.03231.
- [330] J. Liu, Z.-K. Guo, R.-G. Cai, and G. Shiu, Phys. Rev. D **99**, 103506 (2019), 1812.09235.
- [331] D. G. Figueroa and F. Torrenti, JCAP **10**, 057 (2017), 1707.04533.
- [332] C. Fu, P. Wu, and H. Yu, Phys. Rev. D **97**, 081303 (2018), 1711.10888.
- [333] K. D. Lozanov and M. A. Amin, Phys. Rev. D **99**, 123504 (2019), 1902.06736.
- [334] C. Armendariz-Picon, JCAP **08**, 012 (2019), 1905.05724.
- [335] C. Caprini and D. G. Figueroa, Class. Quant. Grav. **35**, 163001 (2018), 1801.04268.
- [336] M. Hindmarsh and T. Kibble, Rept. Prog. Phys. **58**, 477 (1995), hep-ph/9411342.
- [337] E. J. Copeland and T. Kibble, Proc. Roy. Soc. Lond. A **A466**, 623 (2010), 0911.1345.
- [338] G. Vincent, N. D. Antunes, and M. Hindmarsh, Phys. Rev. Lett. **80**, 2277 (1998), hep-ph/9708427.
- [339] N. Bevis, M. Hindmarsh, M. Kunz, and J. Urrestilla, Phys. Rev. D **75**, 065015 (2007), astro-ph/0605018.
- [340] M. Hindmarsh, K. Rummukainen, T. V. I. Tenkanen, and D. J. Weir, Phys. Rev. D **90**, 043539 (2014), 1406.1688, [Erratum: Phys.Rev.D 94, 089902 (2016)].
- [341] D. Daverio, M. Hindmarsh, M. Kunz, J. Lizarraga, and J. Urrestilla, Phys. Rev. D **93**, 085014 (2016), 1510.05006, [Erratum: Phys.Rev.D 95, 049903 (2017)].
- [342] J. Lizarraga, J. Urrestilla, D. Daverio, M. Hindmarsh, and M. Kunz, JCAP **10**, 042 (2016), 1609.03386.
- [343] M. Hindmarsh, J. Lizarraga, J. Urrestilla, D. Daverio, and M. Kunz, Phys. Rev. D **99**, 083522 (2019), 1812.08649.
- [344] M. Hindmarsh, J. Lizarraga, A. Lopez-Eiguren, and J. Urrestilla, Phys. Rev. Lett. **124**, 021301 (2020), 1908.03522.

- 
- [345] D. G. Figueroa, M. Hindmarsh, and J. Urrestilla, Phys. Rev. Lett. **110**, 101302 (2013), 1212.5458.
- [346] M. A. Amin, R. Easther, H. Finkel, R. Flauger, and M. P. Hertzberg, Phys. Rev. Lett. **108**, 241302 (2012), 1106.3335.
- [347] K. D. Lozanov and M. A. Amin, Phys. Rev. D **97**, 023533 (2018), 1710.06851.
- [348] M. A. Amin *et al.*, Phys. Rev. D **98**, 024040 (2018), 1803.08047.
- [349] N. Kitajima, J. Soda, and Y. Urakawa, JCAP **10**, 008 (2018), 1807.07037.
- [350] S. Antusch, F. Cefalà, and F. Torrentí, JCAP **10**, 002 (2019), 1907.00611.
- [351] S. Kasuya, M. Kawasaki, F. Otani, and E. Sonomoto, (2020), 2001.02582.
- [352] K. Enqvist, S. Kasuya, and A. Mazumdar, Phys. Rev. D **66**, 043505 (2002), hep-ph/0206272.
- [353] M. A. Amin and P. Mocz, Phys. Rev. D **100**, 063507 (2019), 1902.07261.
- [354] J. C. Niemeyer and R. Easther, (2019), 1911.01661.
- [355] A. Diaz-Gil, J. Garcia-Bellido, M. Garcia Perez, and A. Gonzalez-Arroyo, PoS **LAT2005**, 242 (2006), hep-lat/0509094.
- [356] A. Diaz-Gil, J. Garcia-Bellido, M. Garcia Perez, and A. Gonzalez-Arroyo, PoS **LATTICE2007**, 052 (2007), 0710.0580.
- [357] T. Fujita and R. Namba, Phys. Rev. D **94**, 043523 (2016), 1602.05673.
- [358] S. Vilchinskii, O. Sobol, E. Gorbar, and I. Rudenok, Phys. Rev. D **95**, 083509 (2017), 1702.02774.
- [359] E. W. Kolb, A. D. Linde, and A. Riotto, Phys. Rev. Lett. **77**, 4290 (1996), hep-ph/9606260.
- [360] E. W. Kolb, A. Riotto, and I. I. Tkachev, Phys. Lett. B **423**, 348 (1998), hep-ph/9801306.
- [361] J. Garcia-Bellido, D. Y. Grigoriev, A. Kusenko, and M. E. Shaposhnikov, Phys. Rev. D **60**, 123504 (1999), hep-ph/9902449.
- [362] R. Allahverdi, B. A. Campbell, and J. R. Ellis, Nucl. Phys. B **579**, 355 (2000), hep-ph/0001122.
- [363] J. Cornwall, D. Grigoriev, and A. Kusenko, Phys. Rev. D **64**, 123518 (2001), hep-ph/0106127.

## Bibliography

---

- [364] A. Tranberg, A. Hernandez, T. Konstandin, and M. G. Schmidt, Phys. Lett. B **690**, 207 (2010), 0909.4199.
- [365] K. Kamada, K. Kohri, and S. Yokoyama, JCAP **01**, 027 (2011), 1008.1450.
- [366] K. D. Lozanov and M. A. Amin, Phys. Rev. D **90**, 083528 (2014), 1408.1811.
- [367] D. I. Podolsky, G. N. Felder, L. Kofman, and M. Peloso, Phys. Rev. D **73**, 023501 (2006), hep-ph/0507096.
- [368] K. D. Lozanov and M. A. Amin, Phys. Rev. Lett. **119**, 061301 (2017), 1608.01213.
- [369] D. G. Figueroa and F. Torrenti, JCAP **02**, 001 (2017), 1609.05197.
- [370] T. Krajewski, K. Turzyński, and M. Wieczorek, Eur. Phys. J. C **79**, 654 (2019), 1801.01786.
- [371] S. Antusch, D. G. Figueroa, K. Marschall, and F. Torrenti, (2020), 2005.07563.
- [372] M. A. Garcia and M. A. Amin, Phys. Rev. D **98**, 103504 (2018), 1806.01865.
- [373] A. Rajantie and E. J. Copeland, Phys. Rev. Lett. **85**, 916 (2000), hep-ph/0003025.
- [374] A. Brandenburg *et al.*, Phys. Rev. D **96**, 123528 (2017), 1711.03804.
- [375] A. Brandenburg *et al.*, Phys. Rev. Fluids. **4**, 024608 (2019), 1710.01628.
- [376] M. Hindmarsh, S. J. Huber, K. Rummukainen, and D. J. Weir, Phys. Rev. Lett. **112**, 041301 (2014), 1304.2433.
- [377] M. Hindmarsh, S. J. Huber, K. Rummukainen, and D. J. Weir, Phys. Rev. D **92**, 123009 (2015), 1504.03291.
- [378] M. Hindmarsh, S. J. Huber, K. Rummukainen, and D. J. Weir, Phys. Rev. D **96**, 103520 (2017), 1704.05871, [Erratum: Phys.Rev.D 101, 089902 (2020)].
- [379] D. Cutting, M. Hindmarsh, and D. J. Weir, Phys. Rev. D **97**, 123513 (2018), 1802.05712.
- [380] D. Cutting, M. Hindmarsh, and D. J. Weir, (2019), 1906.00480.
- [381] A. Roper Pol, S. Mandal, A. Brandenburg, T. Kahniashvili, and A. Kosowsky, (2019), 1903.08585.
- [382] D. Cutting, E. G. Escartin, M. Hindmarsh, and D. J. Weir, (2020), 2005.13537.
- [383] M. Hindmarsh and A. Rajantie, Phys. Rev. Lett. **85**, 4660 (2000), cond-mat/0007361.
- [384] A. Rajantie, Int. J. Mod. Phys. A **17**, 1 (2002), hep-ph/0108159.
- [385] A. Rajantie, Phys. Rev. D **68**, 021301 (2003), hep-ph/0212130.

- 
- [386] M. Donaire, T. Kibble, and A. Rajantie, *New J. Phys.* **9**, 148 (2007), cond-mat/0409172.
- [387] T. Hiramatsu, M. Kawasaki, K. Saikawa, and T. Sekiguchi, *JCAP* **01**, 001 (2013), 1207.3166.
- [388] M. Kawasaki, K. Saikawa, and T. Sekiguchi, *Phys. Rev. D* **91**, 065014 (2015), 1412.0789.
- [389] L. M. Fleury and G. D. Moore, *JCAP* **05**, 005 (2016), 1602.04818.
- [390] B. Eggemeier, J. Redondo, K. Dolag, J. C. Niemeyer, and A. Vaquero, (2019), 1911.09417.
- [391] M. Gorghetto, E. Hardy, and G. Villadoro, *JHEP* **07**, 151 (2018), 1806.04677.
- [392] T. Hiramatsu, M. Kawasaki, and K. Saikawa, *JCAP* **02**, 031 (2014), 1309.5001.
- [393] E. W. Kolb and I. I. Tkachev, *Phys. Rev. D* **49**, 5040 (1994), astro-ph/9311037.
- [394] M. Buschmann, J. W. Foster, and B. R. Safdi, *Phys. Rev. Lett.* **124**, 161103 (2020), 1906.00967.
- [395] H. Fukunaga, N. Kitajima, and Y. Urakawa, *JCAP* **06**, 055 (2019), 1903.02119.
- [396] T. Patel, H. Tashiro, and Y. Urakawa, *JCAP* **01**, 043 (2020), 1909.00288.
- [397] J. T. Giblin, G. Kane, E. Nesbit, S. Watson, and Y. Zhao, *Phys. Rev. D* **96**, 043525 (2017), 1706.08536.
- [398] M. A. Amin, J. Fan, K. D. Lozanov, and M. Reece, *Phys. Rev. D* **99**, 035008 (2019), 1802.00444.
- [399] Y. Akamatsu, A. Rothkopf, and N. Yamamoto, *JHEP* **03**, 210 (2016), 1512.02374.
- [400] K. Boguslavski, A. Kurkela, T. Lappi, and J. Peuron, *Phys. Rev. D* **98**, 014006 (2018), 1804.01966.
- [401] S. Schlichting, D. Smith, and L. von Smekal, *Nucl. Phys. B* **950**, 114868 (2020), 1908.00912.
- [402] M. Laine, G. D. Moore, O. Philipsen, and M. Tassler, *JHEP* **05**, 014 (2009), 0902.2856.
- [403] M. Laine and A. Rothkopf, *JHEP* **07**, 082 (2013), 1304.4443.
- [404] M. Panero, K. Rummukainen, and A. Schäfer, *Phys. Rev. Lett.* **112**, 162001 (2014), 1307.5850.
- [405] K. Boguslavski, A. Kurkela, T. Lappi, and J. Peuron, (2020), 2005.02418.
- [406] J. Sainio, *Comput. Phys. Commun.* **181**, 906 (2010), 0911.5692.
- [407] M. Pippig, *SIAM J. Sci. Comput.* **35**, C213 (2013).



## Bibliography

---

- [408] D. G. Figueroa, A. Florio, and F. Torrenti, In preparation. .
- [409] P. M. Saffin and A. Tranberg, *JHEP* **07**, 066 (2011), 1105.5546.
- [410] P. M. Saffin and A. Tranberg, *JHEP* **02**, 102 (2012), 1111.7136.
- [411] Z.-G. Mou, P. M. Saffin, and A. Tranberg, *JHEP* **11**, 097 (2013), 1307.7924.
- [412] Z.-G. Mou, P. M. Saffin, and A. Tranberg, *JHEP* **06**, 163 (2015), 1505.02692.
- [413] G. Aarts and J. Smit, *Nucl. Phys. B* **555**, 355 (1999), hep-ph/9812413.
- [414] S. Borsanyi and M. Hindmarsh, *Phys. Rev. D* **79**, 065010 (2009), 0809.4711.
- [415] D. G. Figueroa, J. Garcia-Bellido, and A. Rajantie, *JCAP* **11**, 015 (2011), 1110.0337.
- [416] A. Lopez-Eiguren, J. Lizarraga, M. Hindmarsh, and J. Urrestilla, *JCAP* **07**, 026 (2017), 1705.04154.
- [417] *openQCD*, <https://luscher.web.cern.ch/luscher/openQCD/>.
- [418] M. Clark, R. Babich, K. Barros, R. Brower, and C. Rebbi, *Comput. Phys. Commun.* **181**, 1517 (2010), 0911.3191.
- [419] Planck, N. Aghanim *et al.*, (2018), 1807.06209.
- [420] H. Yoshida, *Phys. Lett. A* **150**, 262 (1990).
- [421] W. Kahan and R.-C. Li, *Mathematics of Computation* **66**, 1089 (1997).
- [422] R. Kallosh and A. Linde, *JCAP* **07**, 002 (2013), 1306.5220.
- [423] M. S. Turner, *Phys. Rev. D* **28**, 1243 (1983).
- [424] D. G. Figueroa, J. Garcia-Bellido, and F. Torrenti, In preparation. .
- [425] V. Kasper, F. Hebenstreit, and J. Berges, *Phys. Rev. D* **90**, 025016 (2014), 1403.4849.
- [426] A. Krasnitz, *Nucl. Phys. B* **455**, 320 (1995), hep-lat/9507025.
- [427] K. Peeters, (2007), hep-th/0701238.
- [428] K. Peeters, *Journal of Open Source Software* **3**, 1118 (2018).
- [429] F. Dyson, *Phys. Rev.* **85**, 631 (1952).
- [430] O. Costin, *Asymptotics and Borel Summability* Monographs and Surveys in Pure and Applied Mathematics (Taylor & Francis, 2008).
- [431] M. Mariño, *Fortsch. Phys.* **62**, 455 (2014), 1206.6272.
- [432] I. Aniceto, G. Basar, and R. Schiappa, *Phys. Rept.* **809**, 1 (2019), 1802.10441.

- 
- [433] M. A. Escobar-Ruiz, E. Shuryak, and A. V. Turbiner, Phys. Rev. **D92**, 025046 (2015), 1501.03993, [Erratum: Phys. Rev.D92,no.8,089902(2015)].
- [434] M. Escobar-Ruiz, E. Shuryak, and A. Turbiner, Phys. Rev. D **92**, 025047 (2015), 1505.05115.
- [435] G. V. Dunne and M. Unsal, Phys. Rev. **D89**, 105009 (2014), 1401.5202.
- [436] A. Behtash, G. V. Dunne, T. Schäfer, T. Sulejmanpasic, and M. Ünsal, Ann. Math. Sci. Appl. **02**, 95 (2017), 1510.03435.
- [437] G. V. Dunne and M. Unsal, JHEP **12**, 002 (2016), 1609.05770.
- [438] S. Gukov, M. Mariño, and P. Putrov, (2016), 1605.07615.
- [439] A. Ahmed and G. V. Dunne, JHEP **11**, 054 (2017), 1710.01812.
- [440] M. Mariño and T. Reis, (2019), 1905.09569.
- [441] M. Marino and T. Reis, (2020), 2006.05131.
- [442] O. Costin and G. V. Dunne, J. Phys. **A52**, 445205 (2019), 1904.11593.
- [443] M. Serone, G. Spada, and G. Villadoro, JHEP **08**, 148 (2018), 1805.05882.
- [444] M. Serone, G. Spada, and G. Villadoro, JHEP **05**, 047 (2019), 1901.05023.
- [445] G. V. Dunne, Heisenberg-Euler effective Lagrangians: Basics and extensions, in *From fields to strings: Circumnavigating theoretical physics. Ian Kogan memorial collection (3 volume set)*, edited by M. Shifman, A. Vainshtein, and J. Wheeler, pp. 445–522, 2004, hep-th/0406216.
- [446] O. Costin and G. V. Dunne, J. Phys. **A51**, 04 (2018), 1705.09687.
- [447] S. Chadha and P. Olesen, Phys. Lett. **72B**, 87 (1977).
- [448] J.-M. Drouffe and J.-B. Zuber, Phys. Rept. **102**, 1 (1983).
- [449] C. Brezinski and M. Redivo-Zaglia, Journal of Computational and Applied Mathematics **284**, 69 (2015), OrthoQuad 2014.
- [450] A. Alexandru, G. Basar, P. F. Bedaque, and N. C. Warrington, (2020), 2007.05436.
- [451] AuroraScience, M. Cristoforetti, F. Di Renzo, and L. Scorzato, Phys. Rev. D **86**, 074506 (2012), 1205.3996.
- [452] G. Aarts *et al.*, JHEP **06**, 034 (2017), 1703.09246.



Chemin de la Gravière 6, Donneloye

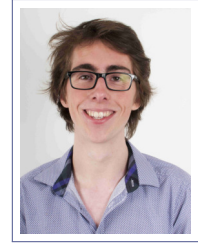
+41787368790

✉ adrien.florio@epfl.ch

Age: 26 (03.04.1994)

Status: single

Nationality: Swiss



# Adrien Florio

*PhD Student in Physics*

## Education

- Exp. 09/2020 **PhD in Physics**, EPFL, Lausanne, Switzerland.  
Supervisor: Pr. M. Shaposhnikov
- 2016 **MSc in Physics**, EPFL, Lausanne, Switzerland.
- 2016 **Minor in Mathematics**, EPFL, Lausanne, Switzerland.
- 2014 **BSc in Physics**, EPFL, Lausanne, Switzerland.
- 2014 **ERASMUS Exchange**, Imperial College London, London, United Kingdom.
- 2011 **Maturité Suisse**, Gymnase d'Yverdon, Cheseaux-Noréaz, Switzerland.

## Talks

- 2019 • Informal talk, Imperial College London    *"Schwinger Pair-Production from Padé-Borel Reconstruction"*
- 2020 • Seminar, Bielefeld University    *"Abelian Finite Temperature Chiral Charge Dynamics"*
- 2019 • Seminar, Basel University
- Seminar, INT, Seattle
- Seminar, UChicago
- Lunch Seminar, Stony Brook
- RIKKEN Lunch Seminar, Brookhaven National Lab
- Informal Seminar, NYU
- Seminar, IFIC, Valencia
- CosmoCoffee, CERN
- 2018 • Lattice2018, MichiganU    *"Real Time Evolution of  $U(1)$  Chiral Charge"*
- 2018 • Seminar, DESY Zeuthen    *"Open vs Periodic Boundary Conditions in the Deconfined Phase"*
- Lattice Seminar, CERN
- 2017 • Lattice2017, Granada    *"Thermal Simulations, Open Boundary Conditions and Switches"*
- HISS, Dubna
- 2016 • Bielefeld University, Bielefeld    *"Open-Boundary Conditions and Sampling of the Topological Charge"*
- 2016 • CERN, Geneva    *"COMBI, Improved Field Solvers"*

---

## Experience

- 2015 CERN internship CERN, Geneva  
2 months internship with Dr. T. Pieloni and Dr. X. Buffat. Development of a new Poisson solver for the COMBI multiparticle tracking software.

---

## Teaching

- 2019-2020 Master project supervision of one student  
2016-2019 Teaching Assistant
  - General Relativity and Cosmology for 1st year Master students
  - Quantum Mechanics III for 1st year Master students
  - Remedial General Physics for 1st year Bachelor students

2017 Teaching Toolkits  
1 day workshop to improve teaching skills, EPFL's Teaching Support Centre.

---

## Languages

- French Mother tongue  
English Fluent CAE in 2014  
German B1-B2  
Italian Good written and oral comprehension

---

## Computing Skills

- C/C++ 2 semester course on C++ and object-oriented programming, with a 1 semester practical project. Course on computational physics. Worked on a particle tracking code at CERN and on Lattice QCD simulations. Currently developing a modern C++ Expression Template field theory library.  
● ● ● ● ●
- MPI/OpenMP Term course on parallel computing. Parallelised field theory simulations.  
● ● ● ● ●
- Python Good knowledge of the language. Mainly used to treat and analyse data.  
● ● ● ● ●
- Bash Relatively good scripting knowledge.  
● ● ● ● ●
- Julia Some experience with the language.  
● ● ● ● ●
- Others Some experience with MATLAB® and ROOT/RooFit.